# Wetting, de-icing and anti-icing behavior of microstructured and plasma-coated polyurethane films

Von der Fakultät Energie-, Verfahrens- und Biotechnik der Universität Stuttgart
zur Erlangung der Würde eines Doktors der
Naturwissenschaften (Dr. rer. nat.) genehmigte Abhandlung

Vorgelegt von

Philipp E. S. Grimmer

aus Stuttgart

| | |
|---|---|
| Hauptberichter: | Prof. Dr. rer. nat. Thomas Hirth |
| Mitberichter: | Prof. Dr.-Ing. Ulrich Nieken |
| Mitberichter: | Hon.-Prof. Dr. rer. nat. Christian Oehr |

Tag der mündlichen Prüfung: 11.12.2018

Institut für Grenzflächenverfahrenstechnik und Plasmatechnologie der
Universität Stuttgart

2019

For
my sister
and
my parents

# Declaration

Hereby I declare that this thesis has been independently completed by me without the help of any other aids than those that are given in the thesis. All references like information or figures from other sources are properly cited.

Stuttgart, May 2018

Philipp Grimmer

# Acknowledgments

I would like to thank those who directed my interest to the topics of materials science, micro- and nanotechnology, surface physics and chemistry, ice adhesion, nucleation and crystallization. They supported my work and guided me through the course of this PhD thesis. My acknowledgments are addressed to the following persons:

Prof. Dr. Thomas Hirth as the first academic supervisor enabled my PhD thesis at the Institute of Interfacial Process Engineering and Plasma Technology.

Prof. Dr. Ulrich Nieken from the Institute of Chemical Process Engineering and the Graduate School for Energy Efficiency took over the part as one further academic supervisor.

Prof. Dr. Christian Oehr encouraged my participation in very informative conferences in Paris (2013), in Garmisch-Partenkirchen (2014) and in Prague (2015). He organized various interesting trips for a project on renewable resources about hydrophilization of cotton rests for medical products and consented to become another academic supervisor.

Dr. Michael Haupt who was leading the group of plasma technology and thin films at the Fraunhofer IGB during my PhD thesis helped me in discussions on important aspects of anti-ice surfaces that always lead to the next steps of experimental work.

Special acknowledgments are owed to my supervisor Dr. Jakob Barz who instructed me in plasma technology, surface physics / chemistry and the lab work and supported me in organizational arrangements, especially regarding the Graduate and Research School of Energy Efficiency at the University of Stuttgart.

Dr. Monika Bach and Prof. Dr. Günter Tovar supported and encouraged me to carry out my PhD thesis in the working group on chemical-physical interfaces at the Institute of Interfacial Process Engineering and Plasma Technology. In the seminar, and on the

seminar trips, I was able to learn a lot about the different aspects of surface chemistry and functionalization methods.

Further special acknowledgments go to my colleagues Bentsian Elkin for technical assistance, to Monika Riedl for all the SEM measurements, to Joachim Mayer for all the ESCA measurements and to Hendrik Schikora and Felix Remppel for realisation of the sand trickling test stand and the icing test chamber.

Acknowledgments also belong to some colleagues of the Fraunhofer IPA, namely to Mathias Maier and Serhat Sahalkajkan for the possibility to use the laser scanning microscope and to Dennis Koch for doing the weathering stability tests of the functionalized PU samples.

Big thanks also belong to the students who have done their thesis on the topic of anti-icing surfaces for their experimental work and discussions, namely Marcus Bachmayr, Swarupini Ganesan, Andre Michele, Johannes Eller, Nadine Dannehl and Maike Hartstern.

The PhD colleagues of the seminar on work techniques and project management are thanked for helping to organize such an interesting seminar on automation of a special biotechnological process.

Further thanks belong to all the other students and colleagues of the work group of plasma technology and thin films (PdS), the department of interfacial engineering and materials science (GTM) of the Fraunhofer IGB and my PhD colleagues for making this PhD an interesting and successful time.

The Graduate and Research School of Energy Efficiency at the University of Stuttgart is acknowledged for financial support of this work and the interesting insight into energy markets and technologies.

Finally, I would like to thank my sister and my parents for enabling my studies of Process, Chemical and Bioengineering and always supporting me during the time of this dissertation.

# Contents

# List of Figures

# List of Tables

# List of symbols and abbreviations

| Symbol Abbreviation | Meaning |
|---|---|
| $a$ | surface-specific constant for calculation of nucleation rate in dependence of reference temperature $T_0$ |
| $a_S$ | surface-specific constant for calculation of nucleation rate in dependence of experimental start temperature $T_S$ |
| $\alpha_{tilt}$ | Critical tilt or roll-off angle in Furmidge equation |
| $\alpha_{cooling}$ | Cooling rate for calculation of nucleation temperature |
| $\alpha$ | Heat transfer coefficient at an interface in heat convection or heat transport |
| $\alpha_{H_2O}$ | Heat transfer coefficient at the water-PU interface |
| $A_{sl}$ | Solid-liquid interface between a water drop and a rough surface |
| $A_f$ | Apparent contact area, flat projected surface of the water drop |
| $A_L$ | Lateral area of a microstructure |
| $A_T$ | Top area of a microstructure |
| $A_B$ | Base area of a microstructure |
| $A_{drop}$ | Apparent water drop base area |
| CA / $\theta$ | Static contact angle |
| ACA / $\theta_{adv}$ | Advancing contact angle |
| RCA / $\theta_{rec}$ | Receding contact angle |
| CAH | Contact angle hysteresis |
| $\theta_W$ | Wenzel contact angle |
| $\theta_{CB}$ | Cassie-Baxter contact angle |
| $\theta_M$ | Mixed state (Wenzel/Cassie-Baxter) contact angle |
| $\theta_{IW}$ | Contact angle between ice/water interface and ice/quasiliquid layer interface of an ice nucleus |
| $\chi$ | Fraction of water drop contact area that has transitioned to the Wenzel state |
| $A$ | Truncated ellipse microstructure base major half-axis |

| Symbol Abbreviation | Meaning |
|---:|---|
| $a$ | Truncated ellipse microstructure top major half-axis |
| $B$ | Truncated ellipse microstructure base minor half-axis |
| $b$ | Truncated ellipse microstructure top minor half-axis |
| $c$, $c_p$ | Specific heat capacity (at constant pressure) |
| $D$ | Truncated cone microstructure bottom diameter |
| $d$ | Truncated cone microstructure top diameter |
| $\eta$ | Density of microstructures on a surface |
| $\epsilon$ | emission coefficient for heat radiation |
| $E^*$ / $E^*_{\mathrm{i,PU}}$ | Combined Young's modulus of the ice and the surface (PU) |
| $E_{\mathrm{ice}}$ | Young's modulus of ice |
| $E_{\mathrm{s}}$ | Young's modulus of the surface |
| $f$ | Factor correlating heterogeneous with homogeneous nucleation, depends on ice-water contact angle $\theta_{\mathrm{IW}}$ and mean surface roughness radius of curvature $R$ |
| $f_{\mathrm{sl}}$ | Solid-liquid fraction of area under a droplet resting on a rough surface |
| $f_{\mathrm{lg}}$ | Liquid-gas fraction of area under a droplet resting on a rough surface |
| $F_{\mathrm{adhesion}}$ | Measured force of ice adhesion |
| $\Delta F_{\mathrm{diff}}$ | Diffusion activation (Helmholtz) energy of a water molecule to cross the water-ice interface |
| g | Acceleration of gravity |
| $\Delta G_{\mathrm{V}}$, $\Delta G_{\mathrm{f,V}}$ | Volumetric Gibbs energy difference between bulk phase (liquid/water) and nucleated phase (solid/ice) |
| $\Delta G$ | Total Gibbs energy difference |
| $\Delta G^*$ | Maximum Gibbs energy difference, energy barrier for nucleation |
| $\Delta G^*_{\mathrm{homo}}$ | Energy barrier for homogeneous nucleation |
| $\Delta G^*_{\mathrm{hetero}}$ | Energy barrier for heterogeneous nucleation |
| $\Delta H_{\mathrm{f,V}}$ | Difference of volumetric enthalpy of fusion / latent heat of fusion |
| $\Delta h_{\mathrm{f}}$ | Difference of mass specific enthalpy of fusion / latent heat of fusion |
| $\Delta H_{\mathrm{f}}$ | Difference of enthalpy of fusion / latent heat of fusion |
| $\Delta H_{\mathrm{f,recalescence}}$ | Difference of enthalpy of fusion / latent heat of fusion released during the recalescence step |
| $\Delta H_{\mathrm{f,C}}$ | Difference of enthalpy of fusion / latent heat of fusion released during the crystallization step |

| Symbol Abbreviation | Meaning |
|---|---|
| $\gamma$ | Surface tension or interfacial / surface free energy of a material |
| $\gamma_{\mathrm{s}}$ | Surface free energy of a solid material surface |
| $\gamma_{\mathrm{sg}}$ | Surface free energy of the solid-gas interface |
| $\gamma_{\mathrm{sl}}$ | Surface free energy of the solid-liquid interface |
| $\gamma_{\mathrm{lg}}$ | Surface tension of the liquid-gas interface |
| $\gamma_{\mathrm{IW}}$ | Surface free energy of the ice-water interface |
| $\gamma_{\mathrm{IA}}$ | Surface free energy of the ice-air interface |
| $\gamma_{\mathrm{II}}$ | Surface free energy of the ice-ice interface |
| $\gamma_{\mathrm{s}}^{\mathrm{d}}$ | Disperse surface free energy of a solid material |
| $\gamma_{\mathrm{s}}^{\mathrm{p}}$ | Polar surface free energy of a solid material |
| $\gamma_{\mathrm{s}}^{\mathrm{tot}}$ | Total surface free energy of a solid material |
| $H$ | Microstructure height |
| h | Planck constant |
| $J\left(T\right)$ | Nucleation rate |
| $K\left(T\right)$ | Kinetic factor describing the diffusion and adsorption of water molecules into a nucleus |
| $\mathrm{k_B}$ | Boltzmann constant |
| $k$ | Total thermal transmittance in heat conduction through a solid layer with two interfaces |
| $\lambda$ | wavelength in heat radiation |
| $\lambda_i$ | heat conduction coefficient in heat conduction |
| $m$ | Mass of a water drop |
| $\mu$ | Mean surface height |
| $\nu_{\mathrm{ice}}$ | Poisson's ratio of ice |
| $\nu_{\mathrm{s}}$ | Poisson's ratio of the surface |
| $P$ | Pitch distance, closest distance between two microstructures |
| $p_{\mathrm{C}}$ | |
| $Q$ | Heat |
| $R$ | Truncated cone microstructure bottom radius |
| $r$ | Truncated cone microstructure top radius |
| $R$ | Surface roughness radius of curvature (nm) for calculation of theoretical median nucleation temperature $T_N$, calculated with AFM roughness parameter surface curvature, $R = 1/S_{\mathrm{sc}}$ |
| $rf$ | Microstructure roughness factor for calculation of the contact angle in Wenzel or Cassie-Baxter state |
| $\rho$ | reflexion coefficient for heat radiation |

| Symbol Abbreviation | Meaning |
|---:|---|
| $\rho_\mathrm{l}$ | density of liquid phase (water) |
| $\rho_\mathrm{s}$ | density of solid phase (ice) |
| $r_\mathrm{c}$ | Critical ice nucleus radius for start of nucleation |
| $S_\mathrm{a}$ | Average or arithmetic sourface roughness (nm) |
| $S_\mathrm{q}$ / RMS | Quadratic surface roughness / Root Mean Square (nm) |
| $S_\mathrm{dr}$ | Surface area ratio (%) |
| $S_\mathrm{sc}$ | Mean surface roughness summit curvature (1/nm), for calculation of surface roughness radius of curvature $R$ |
| $\sigma$ | Stefan-Boltzmann constant for heat radiation |
| $\sigma_\mathrm{ice}$ | Ice adhesion, tensile strength (pulled off) |
| $\tau_\mathrm{ice}$ | Ice adhesion, shear strength (sheared off) |
| $\tau_i$ | transmission coefficient of material or part $i$ for heat radiation |
| $\langle\tau(T)\rangle$ | Theoretical nucleation delay time in dependence of temperature, expected by probability calculation with a Poisson distribution |
| $\tau$ | Measured mean freezing delay time, duration from start of cooling of a water drop until its nucleation, for comparison with expected nucleation delay time |
| $t_\mathrm{C}$ / $\Delta t_\mathrm{C}$ | Measured mean crystallization time, duration of the crystallization phase during freezing process of a water drop |
| $t_\mathrm{F}$ | Measured mean total freezing time, consists of freezing delay time and crystallization time, duration from start of cooling until end of crystallization |
| $T$ | Temperature |
| $T_\mathrm{m}$ | Equilibrium melting temperature (0 °C for water) |
| $T_\mathrm{C}$ | Crystallization temperature (equal to $T_\mathrm{m}$) |
| $T_\mathrm{N}$ | Surface specific nucleation temperature, either measured or expected by probability calculation with a Poisson distribution (median) |
| $U_i$ | Voltage signal caused by heat radiation of the real object, the reflections or the atmosphere; for calculation of object temperature by the IR camera |
| $V_\mathrm{d}$ | Volume of a water drop |
| $V_\mathrm{recalescence}$ | Part of volume of a water drop that freezes during the recalescence step |
| $V_\mathrm{C}$ | Part of volume of a water drop that freezes during the crystallization step |

| Symbol<br>Abbreviation | Meaning |
|---|---|
| $w$ | Width of droplet perpendicular to the direction of sliding in the Furmidge equation |
| $W_i$ | Emitted energy by heat radiation, of the black body, the real object, the reflections or the atmosphere |
| $W_{\mathrm{ad}}$ | Work of adhesion calculated by the Dupré equation |
| $W_{\mathrm{e}}$ | Equilibrium work of adhesion, calculated with $\cos\theta_{\mathrm{e}}$ |
| $W_{\mathrm{p}}$ | Practical work of adhesion, calculated with $\cos\theta_{\mathrm{rec}}$ |
| $W_{\mathrm{ad,VdW}}$ ($\Delta\gamma$) | Work of adhesion characteristic for the Van der Waals interaction |
| $W_{\mathrm{ad,flat}}$ ($\Delta\gamma_{\mathrm{flat}}$) | Work of adhesion between a liquid and a solid surface |
| $W_{\mathrm{ad,crack}}$ ($\Delta\gamma_{\mathrm{crack}}$) | Release of stored energy from crack formation |
| $W_{\mathrm{ad,total}}$ ($\Delta\gamma_{\mathrm{total}}$) | Total work of adhesion between two solids |
| $W_{\mathrm{ad,IS}}$ ($\Delta\gamma_{\mathrm{IS}}$) | Work of adhesion between ice and the surface |

# Kurzfassung

Die Eisbildung auf Oberflächen, beispielsweise auf Flügeln von Flugzeugen oder auf Rotorblättern von Windkraftanlagen, beeinträchtigt die Funktionalität von Verkehrsmitteln oder technischen Anlagen und reduziert deren Sicherheit. Deswegen werden funktionale Anti-Eis-Oberflächen erforscht und entwickelt, welche die Vermeidung oder Reduzierung von Eis auf den gefährdeten Oberflächen bewirken sollen. Die Ausgangshypothese dieser Arbeit ist, dass superhydrophobe Polyurethan-Folien mit Mikrostruktur-Basisdurchmessern von 35 µm oder mehr die Benetzung durch Wasser reduzieren und dabei gleichzeitig eine niedrige Eisadhäsion für eine leichte Ablösung von Eis aufweisen sowie die Eisbildung verringern oder verzögern. Superhydrophobe PU-Folien als mögliche passive Anti-Eis- und Enteisungsmethode wurden durch Heissprägen und plasmagestützte chemische Gasphasenabscheidung (PECVD) hergestellt. Der Einfluss unterschiedlicher Prozessparameter des Heissprägeprozesses sowie verschiedener Plasmaprozesse zur Beschichtung und Ätzung auf die Oberflächeneigenschaften wurde untersucht. Die funktionalisierten PU-Folien wurden in Bezug auf ihre Oberflächentopographie, Oberflächenchemie, Stabilität der Funktionalisierungen, Benetzung durch Wasser, Eisadhäsion sowie Eisbildung charakterisiert. Die Eisadhäsion und Eisbildung wurde zum Vergleich auf relevanten technischen Materialien (Aluminium, Titan, Kupfer, Glas, Epoxidharz von carbonfaserverstärktem Kunststoff und andere fluorhaltige Polymere) und einigen kommerziellen Anti-Eis-Beschichtungen untersucht. Die Kapitel theoretische Grundlagen, Materialien und Methoden sowie Ergebnisse und Diskussion sind jeweils in zwei Teile untergliedert. Dabei behandelt jeweils der erste Teil die Funktionalisierung der PU-Folien, während der zweite Teil die Charakterisierung im Hinblick auf die Anwendung, also die Benetzung, die Eisadhäsion und die Eisbildung, enthält.

Die PU-Folien wurden durch IR-Spektroskopie chemisch analysiert. Im ersten Prozessschritt der Funktionalisierung wurden durch ein Heissprägeverfahren mit verschiedenen, durch ns-gepulste Laserbohrung mikrostrukturierten Stempeln zylindrische, elliptische

und linienförmige Mikrostrukturen in PU-Folien abgeformt. Elliptische und linienförmige Mikrostrukturen wurden für ein eventuell richtungsabhängiges Abrollen von Wassertropfen gewählt. Die so erzeugte Mikrorauheit wurde mit mehreren mikroskopischen Methoden charakterisiert. Die Mikrostrukturen besaßen Höhen von 15 µm bis 140 µm, Durchmesser oder Breiten von 35 µm bis 300 µm und Abstände von 50 µm bis 500 µm. Der Heissprägeprozess wurde in Bezug auf die Prozessparameter Temperatur, Druck, Prozesszeit und Ablösetemperatur der PU-Folie sowie in Bezug auf die Reproduzierbarkeit der Mikrostrukturen analysiert und optimiert.

In einem zweiten Prozessschritt wurden diese Oberflächen durch plasmagestützte chemische Gasphasenabscheidung (PECVD) mit dünnen hydrophoben Plasmapolymeren beschichtet. Dazu wurden verschiedene Fluorkohlenstoff-Präkursoren ($CHF_3$, $C_3F_6$ und $C_4F_8$) und der Präkursor Hexamethyldisiloxan (HMDSO) eingesetzt. Verschiedene Prozessparameter zur Plasmabeschichtung und -ätzung (Ar oder $O_2$ Plasmen) wurden benutzt, um unterschiedliche Nanorauheiten zu erzeugen. Elektronen-Spektroskopie zur chemischen Analyse (ESCA), spektroskopische Ellipsometrie und Rasterkraftmikroskopie (AFM) kamen für die Analyse der chemischen Zusammensetzung, der Dicke und der Nanorauheit der Plasmapolymere zum Einsatz.

Für eine längere Anwendung im Außenbereich ist eine ausreichende Stabilität der funktionalisierten Oberflächen gegenüber Erosion durch Witterungseinflüsse wichtig. Die Stabilität der Funktionalisierungen, insbesondere der Plasmabeschichtungen, wurde getestet und mittels ESCA untersucht. Die optischen Eigenschaften einiger beschichteter, flacher und mikrostrukturierter PU-Folien wurden durch UV/Vis-Spektroskopie bestimmt. Sowohl die Mikrostrukturen als auch die Plasmaschichten sind stabil gegenüber Sanderosion (Sandrieseltest, DIN 52348), während der industrielle Bewitterungstest (1000 h UV-Strahlung und Wasser, X1a CAM 180 Test, SAE J-2527) die Plasmaschichten nahezu komplett abgetragen hat. Ein Langzeittest im Außenbereich über etwa 13,5 Monate führte nur zu einem leichten Abtrag der Plasmaschichten. Durch fünffach wiederholtes Abziehen des Eises wurden die HMDSO-Plasmabeschichtungen nicht beschädigt, während die Fluorkohlenstoff-Plasmabeschichtungen deutlich abgetragen wurden.

Die erste Hypothese in Bezug auf das Benetzungsverhalten ist, dass die derart funktionalisierten PU-Folien mit Mikrostruktur-Basisdurchmessern von mehr als 35 µm einfaches Abrollen von Wassertropfen ermöglichen und superhydrophob sind. Als erster

Schritt der Charakterisierung der PU-Folien wurde deshalb das Benetzungsverhalten von Wasser durch Vorrück- und Rückzugsrandwinkel-Messungen bestimmt. Vorrückrandwinkel von über 150° und sehr niedrige Kontaktwinkelhysteresen von unter 10° konnten auf einigen der zylindrisch und elliptisch strukturierten PU-Oberflächen mit Mikrostruktur-Durchmessern im Bereich von 35 µm bis 50 µm erreicht werden. Im Gegensatz zu den elliptischen Mikrostrukturen zeigten die linienförmigen Strukturen ein makroskopisch richtungsabhängiges Benetzungsverhalten (größere Kontaktwinkel bei paralleler Blickrichtung), erreichten allerdings nicht den superhydrophoben Bereich. Folglich konnte die erste Hypothese für einige zylindrische und elliptische Mikrostrukturen bestätigt werden. Diese superhydrophoben PU-Folien sind deutlich wasserabweisender als die flachen, plasmabeschichteten PU-Oberflächen oder die zum Vergleich gemessenen Materialien. Statische Kontaktwinkel-Messungen mit Diiodmethan (DIM) ermöglichten die Bestimmung der freien Oberflächenenergie der relevanten Oberflächen. Die gemessenen Vorrück-Randwinkel wurden mit den theoretischen Cassie-Baxter- und Wenzel-Benetzungszuständen verglichen, welche mit den Vorrück-Randwinkeln einer PU-Oberfläche und einer hydrophoben Fluorkohlenstoffoberfläche berechnet wurden. Die Messwerte erreichten nicht die theoretische Grenze des Cassie-Baxter-Zustands und gingen von einem gemischten Benetzungszustand nahe Cassie-Baxter im Fall der superhydrophoben PU-Oberflächen mit einem zunehmenden Abstands/Durchmesser-Verhältnis (P/d) in den Wenzel-Zustand über. Zusätzlich wurden Fluoreszenz-Laser-Scanning-Mikroskopiebilder einiger mikrostrukturierter, unbeschichteter oder beschichteter Proben während der Benetzung durch einen Fluoreszenz-Farbstoff enthaltenden Wassertropfen aufgenommen. Diese Bilder zeigen den Wenzel-Zustand bzw. einen gemischten Benetzungszustand anhand der Grenzfläche zwischen Wassertropfen und Oberfläche.

Die zweite Hypothese in Bezug auf die Enteisungseigenschaften ist, dass die superhydrophoben PU-Folien eine niedrigere Eisadhäsion aufweisen als die flachen, plasmabeschichteten, hydrophoben PU-Oberflächen und die zum Vergleich getesteten Materialien. Deshalb wurden eine Eis-Testkammer und ein Versuchsstand für Eisadhäsions- und Eisbildungsmessungen entwickelt. Die Eisadhäsion (Zugmodus) wurde auf flachen und mikrostrukturierten PU-Oberflächen mit verschiedenen Plasmabeschichtungen und den Vergleichsoberflächen gemessen und mit theoretischen Werten und dem Benetzungsverhalten verglichen. Dazu wurde hochreines Wasser ($<$0.056 µS/cm) in einem

Polycarbonat-Zylinder mit einem Innendurchmesser von 4 mm (ähnlich dem Durchmesser großer Regentropfen) auf die Oberfläche gesetzt und sowohl die Oberfläche als auch der Wasserzylinder wurden simultan auf -20 °C abgekühlt. Nach Ausfrieren des Wassers wurde der Eiszylinder vertikal nach oben abgezogen und so ein Adhäsions- oder Kohäsionsbruch erzeugt. Die zum Vergleich gemessenen Metalloberflächen zeigten eine hohe Eisadhäsion, was zu Kohäsionsbrüchen führte, während einige kommerzielle Anti-Eis-Beschichtungen Adhäsionsbrüche mit niedrigen Eisadhäsionswerten aufwiesen. Die flachen, plasmabeschichteten PU-Oberflächen zeigten Adhäsionsbrüche mit einer gegenüber den Vergleichsoberflächen und unbeschichtetem PU reduzierten Eisadhäsion, welche gut mit dem Benetzungsverhalten von Wasser (Adhäsionsarbeit) korreliert. Dagegen wiesen die mikrostrukturierten PU-Oberflächen eine im Vergleich deutlich erhöhte Eisadhäsion auf, welche durch die Plasmaschichten nochmals weiter erhöht wurde. Folglich korreliert die Eisadhäsion nicht mit dem Benetzungsverhalten im Fall der mikrostrukturierten Oberflächen. Der Grund dafür ist der Übergang der Benetzung vom Cassie-Baxter- in den Wenzel-Zustand während des Abkühlens oder Gefrierens, was die Kontaktfläche zwischen Eis und Oberfläche vergrössert und ein mechanisches Ineinandergreifen des Eises und der Mikro- und Nanostrukturen verursacht. Trotz der Superhydrophobie können diese Mikrostrukturen mit Basisdurchmessern von mehr als 35 µm den Cassie-Baxter-Zustand eines gefrierenden Wasserzylinders nicht stabilisieren und weisen daher keine niedrigere, sondern eine stark erhöhte Eisadhäsion bei vertikalem Abzug auf.

Die dritte Hypothese in Bezug auf die Anti-Eis-Eigenschaften lautet, dass die Eisbildung durch die funktionalisierte PU-Oberfläche reduziert oder verzögert wird. Die reduzierte Benetzungsfläche von Wassertropfen auf den superhydrophoben Oberflächen und die Nanostrukturen der hydrophoben Plasmabeschichtung sollen zu einer Verzögerung der Nukleation und Verlängerung der Kristallisationszeit sowie Verringerung der Nukleationstemperatur führen. Für die Charakterisierung des Vereisungsverhaltens wurde das Gefrierverhalten von Wassertropfen auf den genannten Oberflächen im thermodynamischen Gleichgewicht (statisches Experiment) und unter quasi-stationären Bedingungen (dynamisches Experiment) untersucht.

Im statischen Experiment wurden 15 µl Wassertropfen (entspricht mittleren bis großen Regentropfen) mit Raumtemperatur auf eine kalte Oberfläche mit konstanter Temperatur von -20 °C gegeben, anschließend wurde die Gefrierverzögerungszeit, die Kristallisa-

tionszeit sowie die gesamte Gefrierzeit gemessen und mit berechneten Erwartungswerten verglichen. Die Plasmabeschichtung konnte die Gefrierverzögerungszeit verlängern, insbesondere auf den flachen Oberflächen. Auf den mikrostrukturierten Proben konnte die Nukleation weiter verzögert werden, wenn Unterkühlung der Wassertropfen im Cassie-Baxter Zustand auftrat. Allerdings war diese Unterkühlung nicht immer reproduzierbar aufgrund eines instabilen Cassie-Baxter Zustands.

Im dynamischen Experiment wurden die Probenoberfläche, die 25 µl Wassertropfen (entspricht großen Regentropfen) und die umgebende Luft mit geringer, konstanter Rate (1 K/min) unter quasi-stationären Bedingungen bis zum vollständigen Ausfrieren der Tropfen abgekühlt und dabei deren Temperatur mithilfe einer IR-Kamera gemessen. Es konnte eine verringerte Nukleationstemperatur auf den hydrophoben, plasmabeschichteten Oberflächen im Vergleich zu unbeschichtetem PU und den hydrophilen Glas- und Metalloberflächen gemessen werden. Die superhydrophoben Oberflächen zeigten keine weitere Absenkung der Nukleationstemperatur aufgrund eines instabilen Cassie-Baxter Zustands. Die so festgestellten Nukleationstemperaturen wurden mit den theoretischen Erwartungswerten verglichen, welche mittels einer erweiterten Nukleationstheorie und eines Poisson-Prozesses berechnet wurden.

Laut der erweiterten Nukleationstheorie, welche eine quasi-flüssige Grenzschicht des Eis-Nukleationskeims berücksichtigt, wird die Nukleationstemperatur deutlich abgesenkt, sobald der Radius der Wölbungen der Oberflächenrauheit $R$ kleiner als das Zehnfache des kritischen Nukleationskeimradius $r_c \approx 2$ nm ($R$ im Bereich von 20 nm) auf 100 % der Oberfläche wird. Eine entsprechende Absenkung der Nukleationstemperatur aufgrund der Nanorauheit konnte nicht beobachtet werden. Der Grund dafür ist die bisher unpassende Nanorauheit der Plasmabeschichtungen ($R$ im Bereich von etwa 2000 nm bis 40000 nm). Die Nukleationstemperaturen korrelieren nicht mit der Mikrorauheit, dem statischen Kontaktwinkel oder der freien Oberflächenenergie der funktionalisierten PU Oberflächen und der Vergleichsoberflächen. Die Kristallisationsdauer auf den superhydrophoben PU-Oberflächen war im Vergleich zu den übrigen Oberflächen erhöht. Sie steigt mit steigendem Kontaktwinkel, sinkender freier Oberflächenenergie und steigendem Mikrostruktur-Rauheitsfaktor.

Insgesamt wird gezeigt, dass das Heissprägen und die Plasmaprozesse im Hinblick auf einen Rolle-zu-Rolle Prozess gut geeignete Verfahren zur Funktionalisierung und Her-

stellung superhydrophober PU-Folien sind. Die aus den Laborversuchen gewonnene Kenntnis der Einflüsse der Prozessparameter auf die Oberflächeneigenschaften könnte das Hochskalieren auf eine Pilotanlage oder industrielle Anlage ermöglichen. Diese superhydrophoben PU-Folien sind deutlich wasserabweisender als die flachen, plasmabeschichteten PU-Folien und die technischen Vergleichsoberflächen. Allerdings können die Mikrostrukturen mit Basisdurchmessern von 35 µm oder mehr in Verbindung mit der bisherigen Nanorauheit der Plasmabeschichtungen den Cassie-Baxter Zustand eines gefrierenden Wassertropfens nicht ausreichend stabilisieren, um eine geringere Eisadhäsion oder eine stärkere Absenkung der Nukleationstemperatur im Vergleich zu den flachen, plasmabeschichteten PU-Folien zu erzielen. Diese superhydrophoben PU-Folien sind deshalb nicht eisphober als die flachen, plasmabeschichteten PU-Folien. Die flachen, plasmabeschichteten PU Folien zeigen eine reduzierte Eisadhäsion und geringere Nukleationstemperaturen im Vergleich zu den relevanten technischen Materialoberflächen. Im Ausblick wird u. a. die Verkleinerung der geometrischen Abmessungen der Mikrostrukturen (Durchmesser $D$, Abstand $P$) und Nanostrukturen (Wölbungsradius $R$) für niedrigere Eisadhäsionswerte und Nukleationstemperaturen vorgeschlagen.

# Abstract

Ice build-up on surfaces, for example on wings of airplanes or on rotor blades of wind turbines, impairs the functionality of transportation vehicles or technical systems and reduces their safety. Therefore, functional anti-ice surfaces are being researched and developed, which shall prevent the build-up or reduce the amount of ice on the surfaces at risk. The starting hypothesis for this work is that superhydrophobic polyurethane (PU) films with microstructure base diameters of 35 µm or more reduce the wetting by water, show a low ice adhesion for easy removal of ice and reduce or delay icing. Superhydrophobic PU films for passive anti- and de-icing were created by hot embossing and plasma enhanced chemical vapor deposition (PECVD). The hot embossing as well as the plasma coating and etching processes were analyzed for the dependence of the surface characteristics on different process parameters. The functionalized PU films were characterized for their surface topography, surface chemistry, stability of the functionalizations, wettability, ice adhesion and icing behavior. For comparison, the ice adhesion and icing behavior was examined on relevant technical materials (aluminum, titanium, copper, glass, epoxy resin of carbon fiber reinforced polymer and other fluoropolymers) and on some commercial anti-ice coatings. The chapters theoretical basics, materials and methods as well as results and discussion are each divided into two parts. The first part describes the functionalization of the PU films, whereas the second part contains the characterization with regard to the application, namely the wettability, the ice adhesion and the icing behavior.

The PU films were chemically analyzed by IR spectroscopy. As the first process step for functionalization, a hot embossing technique with different ns-pulsed laser-microstructured stamps was used to imprint microstructures of cylindrical, elliptical or linear shape in PU films. Elliptical and linear microstructures were chosen to create a possibly direction-dependent roll-off of water drops. The microstructures, which generate

a micrometer roughness, were characterized by several microscopy methods. The microstructures had heights of 15 µm to 140 µm, diameters or widths of 35 µm to 300 µm and distances (pitch values) of 50 µm to 500 µm. The embossing process was analyzed and optimized in terms of the process parameters temperature, pressure, time, PU film release temperature and in terms of reproducibility.

In a second process step, the samples were coated by PECVD with thin hydrophobic plasma polymers. For this, different fluorocarbon precursors ($CHF_3$, $C_3F_6$ and $C_4F_8$) and the precursor hexamethyldisiloxane (HMDSO) were used. Different plasma coating and etching (Ar or $O_2$ plasmas) process parameters were used in order to create various nanoscale roughness values. Electron spectroscopy for chemical analysis (ESCA), spectroscopic ellipsometry and atomic force microscopy (AFM) were used for analysis of the chemical composition, the thickness and the nano-roughness of the plasma polymers.

For a longer application in the outdoor environment a sufficient stability of the functionalized PU films against erosion by weather influences is of major importance. The stability of the functionalizations, especially of the plasma coatings, was tested and characterized by ESCA. The optical properties of some functionalized PU films were determined by UV/Vis spectroscopy. Both types of plasma coatings and also the microstructures are stable against sand erosion (sand trickling test, DIN 52348), but the industrial weathering test (1000 h UV radiation and water, X1a CAM 180 test, SAE J-2527) nearly completely degraded both plasma coatings. The plasma coatings were only partly damaged by a longterm outdoor test for about 13.5 months. After de-icing repeated for five times, the HMDSO plasma coating is hardly degraded and shows a higher stability than the fluorocarbon plasma coating which was significantly abraded.

The first hypothesis with regard to the wetting behavior reads that the PU films functionalized in this way enable easy roll-off of water drops and are superhydrophobic. As a first step of the characterization of the PU films, the wetting behavior of water was determined by advancing and receding contact angle measurements. Advancing contact angles of over 150° and very low contact angle hysteresis values below 10° were reached on some of the cylindrically and elliptically structured PU samples with microstructure base diameters in the range of 35 µm to 50 µm. In contrast to the elliptical microstructures, the linear structures showed a macroscopic, direction-dependent wetting behavior (larger contact angles at parallel view) but did not reach the superhydrophobic regime.

Therefore, the first hypothesis could be confirmed for some of the cylindrical and elliptical structures. These superhydrophobic PU films are far more water repellent than the flat, plasma coated PU surfaces or the other materials measured for comparison. Additional static contact angle measurements with diiodomethane (DIM) were made for determination of the surface free energies of the relevant surfaces. The measured water advancing contact angles were compared to the theoretical Cassie-Baxter and Wenzel state limits, calculated with the advancing contact angles of a polyurethane surface and a hydrophobic fluorocarbon surface. The measured values did not reach the Cassie-Baxter state and changed from a mixed wetting state near Cassie-Baxter to the Wenzel state with an increasing pitch/diameter (P/d) factor. Additionally, fluorescence laser scanning microscopy images were taken of some microstructured, uncoated or plasma coated samples during the wetting by a water drop containing a fluorescent dye. These images show the Wenzel state or a mixed wetting state by visualization of the interface between the water droplet and the surface.

The second hypothesis in terms of the de-icing properties is an expected lower ice adhesion of the superhydrophobic PU films compared to the flat, plasma coated, hydrophobic PU films and the materials tested for comparison. Therefore, a new icing test chamber and a test setup for ice adhesion and ice nucleation measurements were developed. The tensile ice adhesion was measured on flat or microstructured PU surfaces with different plasma coatings and on the reference surfaces and compared to the theoretical values and the wetting behavior. Therefore, highly purified water ($<0.056$ µS/cm) in a polycarbonate cylinder with an inner diameter of 4 mm (similar to the diameter of large rain drops) was placed on the surface, then the surface and the water cylinder were cooled down simultaneously to -20 °C. After freezing of the water, the ice cylinder was pulled off vertically upwards and so an adhesive or a cohesive fracture was generated. The technical material surfaces measured for comparison showed a high ice adhesion, which led to cohesive fractures especially on the metal surfaces, whereas some of the commercial anti-ice coatings showed lower ice adhesion values. The flat, plasma coated PU surfaces showed adhesive fractures with a reduced ice adhesion compared to the technical material surfaces and uncoated PU and revealed a good correlation of the ice adhesion with the wetting behavior of water (work of adhesion). On the other hand, the microstructured PU surfaces showed a greatly increased ice adhesion in comparison to the flat PU and technical material surfaces which was enhanced even further by the

plasma coatings and did not correlate with the wetting behavior. The reason for this is the wetting transition from the Cassie-Baxter to the Wenzel state during the cooling or freezing process, leading to an increased ice-surface contact area and mechanical interlocking of the ice with the micro- and nanostructures. Although being superhydrophobic, these microstructures with base diameters above 35 µm cannot stabilize the Cassie-Baxter state of a freezing water cylinder and do not show a lower but a highly increased tensile ice adhesion in case of vertical pull-off.

The third hypothesis regarding the anti-icing properties is that the icing is reduced or retarded by the functionalized PU surface. The reduced wetting area of water drops on the superhydrophobic surfaces and the nanostructures of the hydrophobic plasma coating should lead to a delay of nucleation and enhancement of the crystallization time as well as a reduction of the nucleation temperature. For characterization of the icing behavior, water drop freezing experiments were carried out on the mentioned surfaces in thermodynamic equilibrium (static experiment) and under quasi-steady conditions (dynamic experiment).

In the static experiment, 15 µl water drops (corresponding to medium to large rain drops) at room temperature were dispensed onto a cold surface at a constant temperature of -20 °C. The freezing delay times, the crystallization times and the total freezing times were measured and compared to calculated expected values. On the flat samples, the freezing delay times could be extended by the plasma treatments. On the microstructured samples, the nucleation could be delayed even further, if supercooling of the water drops occurred in Cassie-Baxter state. However, this supercooling was not always reproducible because of an unstable Cassie-Baxter state.

In the dynamic experiment, 25 µl water drops (corresponding to large rain drops) were cooled down in quasi-steady conditions with the surface and the surrounding atmosphere by a constant, low cooling rate of 1 K/min until the drops were completely frozen while the water drop temperature was measured by an IR camera. A lower nucleation temperature could be measured on the plasma coated PU surfaces compared to uncoated PU and the hydrophilic glass and metal surfaces. The microstructured surfaces did not show a further reduction of the nucleation temperature because of an unstable Cassie-Baxter state. The resulting measured nucleation temperatures were compared to the expected values calculated with an enhanced nucleation theory and a Poisson process.

The enhanced nucleation theory including a quasi-liquid interfacial layer of the ice nucleus predicts a strong reduction of the nucleation temperature for a nanometer surface roughness radius of curvature $R$ smaller than the 10-fold critical nucleation radius $r_c \approx 2\,\text{nm}$ ($R$ of about 20 nm) on 100 % of the surface. A corresponding reduction of the nucleation temperature because of the nanoroughness could not be measured. This is due to the incorrectly sized nanostructures of the plasma coatings ($R$ values in the range of 2000 nm to 40000 nm). For the nucleation temperature, no clear correlation could be seen with the microroughness factor, the contact angle or the surface free energy. The crystallization time could be extended on the superhydrophobic PU surfaces compared to the other surfaces. It increases with an increasing contact angle, a decreasing surface free energy and an increasing microstructure roughness factor.

Overall, it is shown that hot embossing and PECVD are useful processes for creating superhydrophobic PU surfaces with regard to a roll-to-roll process. The knowledge from the lab experiments of the dependence of the surface properties on the corresponding process parameters could enable the scale-up to a pilot plant or industrial plant. These functionalized PU films are far more water repellent than the flat, plasma coated PU surfaces or the other technical materials. However, the microstructures with base diameters of 35 µm or more and the nanoroughness of the plasma coatings cannot stabilize the Cassie-Baxter state of a freezing water drop enough for a low ice adhesion or a significant decrease of the nucleation temperature. These superhydrophobic PU films are therefore not more icephobic than the flat, plasma coated PU films. The flat, plasma coated PU films show a reduced ice adhesion and lowered nucleation temperature compared to the relevant technical material surfaces. In the outlook the reduction of the geometrical parameters of the microstructures (diameter $D$, distance $P$) and nanostructures (curvature radius $R$) of the surface functionalizations for lower ice adhesion values and nucleation temperatures is proposed.

# 1. Introduction

## 1.1. Icing of surfaces

Icing of surfaces can have a significant impact on safety and functionality of technical devices. This concerns apparatus and facilities, e.g. wind turbines [3, 4, 5, 6, 7] or power lines [8, 9], as well as the transportation sector, e.g. aircrafts, trains or vehicles [10].

If the sensors of a wind turbine become iced, the measured wind speed and direction becomes faulty and the wind turbine gets controlled incorrectly. Rotor blade icing is the main problem and can have several unwanted effects, like unbalanced turning because of uneven rotor blade icing which can lead to the damage of the turbine. The aerodynamic properties are impaired leading to less power production [3]. Ice parts thrown off by the rotating rotors fly at high speed and can cause significant damage or personal injuries. Therefore, laws have been introduced which regulate the placement of wind turbines. They specify the need for anti-icing systems or, if not installed, require a production stop during icing conditions [11, 12]. Icing of power lines can lead to increased weight on the masts and even fracture of them [8]. Ice and snow on roads or car windscreens often lead to crashes during winter. Icing of an airplane during flight is especially dangerous. If the Pitot sensor becomes iced, height and velocity are measured incorrectly. If the leading edges or other surfaces of the wings or the hull become iced, the aerodynamic properties are worsened which can lead to a loss of lift and an unstable and dangerous flying situation [13]. This can even result in a crash of the airplane, like the crash of a Bombardier Q400 Dash 8 (USA continental flight 3407) in 2009 [10].

In order to solve the technical problem of surface icing, different de-icing methods have been developed for the detachment of ice accretions that have built up. Furthermore, anti-icing methods have been developed, which shall prevent icing on certain surfaces. Nowadays, environmental icing as well as energy-efficient de- and anti-icing methods

are an important topic in research and development. Although different mechanical, chemical and thermal de- and anti-icing techniques are available and widely established, these have several disadvantages like high expenditure of energy, limited effectivity and in case of the chemicals also pollution [14, 15]. In order to increase effectivity and reduce energy consumption, functional icephobic surfaces and materials have been developed and examined, which might also be used in combination with the mentioned conventional methods. Therefore, functional surfaces as a passive method for de- and anti-icing have become an important research area, which this work makes a contribution to. The different de- and anti-icing systems or methods are explained in more detail in chapter 2.

## 1.2. Motivation - Anti-ice polyurethane films

The research on passive de- or anti-icing by functional surfaces tries to minimize the disadvantages of the active methods. If a functional surface could somehow shed off accreted ice by itself or prevent or reduce ice accumulation, no other systems would be needed. Different concepts exist for such functional anti-ice surfaces and several production methods are possible for each concept. For an industrial application, such an anti-icing surface needs a sufficiently long lasting stability and has to function reliably in the icing condition corresponding to the specific application. Furthermore, it should be producible on an adequately large scale and at a low cost in order to be a benefit for clients. For some applications, e.g. car or building windows, it should also be transparent.

Technical facility or vehicle nacelles are usually made of common metals, like aluminum or steel, or some polymers, like carbon or glass fiber reinforced polymers. Both the metals, with a metal-oxide layer at their surface, and the epoxy resin coatings used for fiber reinforced polymers have a high surface free energy. Although they are usually covered by a thin layer of aliphatic hydrocarbons in ambient atmosphere, they still show a high ice adhesion. Atmospheric pressure microplasma jet processes are not suited for large area functionalization of these machine parts. The large scale functionalization by low pressure plasma processes is difficult and expensive because very large vacuum chambers would be needed. A better way is to functionalize a polymer film which can

then be applied on the specific surfaces of the technical system. Hydrophobic plasma polymer coatings by low pressure plasma enhanced chemical vapor deposition (PECVD) for tailored surface functionalization, e.g. reduction of wetting, ice adhesion or friction have been developed at the Fraunhofer IGB [16, 17, 18, 19]. Low ice adhesion values on flat polymer films with these hydrophobic plasma coatings have been measured before at the Fraunhofer IGB [20]. For further development, a microstructuring process should be combined with the PECVD process in order to create superhydrophobic anti-ice PU films. Polyurethane is often used for outdoor applications, because it has a high toughness and is resistant against erosion by abrasion, water and UV-radiation. The functionalization processes and surface wetting, de- and anti-icing characteristics need to be analyzed at lab scale. Then a scale up to a larger pilot plant process could be possible.

A schematic drawing of a superhydrophobic PU film created by hot embossing of microstructures and a subsequent PECVD process is shown in Figure 1.1.

Figure 1.1.: Schematic drawing of a superhydrophobic PU film created by hot embossing of microstructures and subsequent plasma enhanced chemical vapor deposition (PECVD).

Reduced water wettability, decreased ice adhesion as well as reduced ice accretion shall be reached by this design. The hot embossing and plasma processes were chosen with the aim of a roll-to-roll functionalization process for large areas of polymer films because they could be easily combined in a film production plant. If the large-area production became possible, the field of application of these films could reach from technical facilities like wind energy plants to transportation vehicles like airplanes and others. The PU films could be easily applied on their outer surfaces with different geometrical forms. If they were damaged in one area, they would still be functioning on the remaining area and could easily be replaced by new films. These anti-ice PU films could increase technical functionality and safety in icing conditions and reduce the amount of energy, costs and pollution for de-icing.

## 1.3. Aim, hypothesis and tasks

Superhydrophobic surfaces have generated a lot of interest among scientific researchers for anti-icing. Many researchers have reported rebounding of impacting droplets or easy rolling-off of lying water drops. The general idea is that nearly no water remains on a superhydrophobic surface, if exposed to water or rain. Ice formation is reduced if the surface stays dry. Due to their low adhesion to water drops, these surfaces are expected to also show a low adhesion to ice. This has been confirmed by some authors, although some have reported different results and do not report superhydrophobic surfaces as being also icephobic. Furthermore, reduced icing is expected because of a freezing delay time or lower freezing temperature (nucleation) and a slower freezing process (crystallization). Icing can involve different physical processes and the anti- and de-icing properties are determined by the surface properties of different length scale. All these processes have to be considered for a successful outdoor application.

The aim for this work was the research on the relationship between the surface chemistry, micro- and nanostructure and the wetting, anti- and de-icing properties (structure-property relationship) in order to optimize the anti-ice PU film surface functionalization. Therefore, superhydrophobic anti-ice PU films should be created by hot embossing and PECVD processes and their wetting, anti- and de-icing behavior should be characterized. This work investigates in detail the functionalization parameters, surface properties, effectivity and limitations of these functionalized PU films.

Since the microstructures of the hot embossing stamps were created by a ns-pulsed laser drilling process, their base diameters are in the range of 35 µm to 100 µm with smaller top diameters because of the cone-shaped laser drilling holes. As drilling of holes with smaller diameters requires a ps-pulsed laser and becomes very expensive, this was the lower base diameter limit for the microstructures of the hot embossing stamps for this work.

The central hypothesis of this thesis is as follows: Superhydrophobic PU films created by these hot embossing and plasma processes with microstructure diameters above 35 µm show simultaneously good water-repellent properties, low ice adhesion and reduced icing by delayed freezing of water drops.

Therefore, the first task is to create a superhydrophobic surface on polyurethane films for use as anti-icing finishings by hot embossing and plasma technology and to characterize their surface properties.

The second task is to analyze the microstructuring and plasma technology processes at lab scale in order to understand the influences of the different process parameters on the resulting topographical and chemical surface properties. The PU films are functionalized by lab processes that could be scaled-up to a large scale roll-to-roll process in the future. The production of the anti-ice films on an industrial scale is a requirement for application in reality, and therefore the understanding of the effects of the functionalization parameters is of great importance.

The third task is to characterize, understand and explain the wetting behavior, ice adhesion and icing behavior on these functionalized PU films. The question is, how the ice adhesion and icing behavior are determined by the wetting behavior and the surface characteristics. This is important for optimization of the surface properties and of the functionalization processes for effective de- and anti-icing.

## 1.4. Structure of the thesis

The thesis is structured according to the aim and the tasks outlined above. The active and passive anti- and de-icing methods and concepts mentioned in the introduction (chapter 1) are described in more detail in the chapter on the state of the art (chapter 2). The chapters on the theoretical background (chapter 3), materials and methods (chapter 4 and chapter 5) as well as results and discussion (chapter 6 and chapter 7) are divided into two parts. The first part is about the functionalization of the surface, regarding the material, the microstructuring by hot embossing, the plasma polymer coatings and the stability of the functionalizations. The second part regards the characterization of the surface functionalizations and describes the wetting, de-icing (ice adhesion) and anti-icing (nucleation and crystallization) behavior. The thesis is concluded by a summary (chapter 8) and an outlook (chapter 9).

The structure of this thesis is shown schematically in Figure 1.2.


Figure 1.2.: Structure of this thesis.

# 2. State of the art

## 2.1. Commonly used surface materials

As icing occurs on the outer surface of cars, trains, airplanes or other machines, it has contact to the typical materials of engineering, which therefore have to be examined for their ice adhesion and icing behavior. Iron or steel alloys are used for heavier machines, whereas aluminum is used widely as bulk and also surface material in the transportation sector, e.g. for the bodies of cars or airplanes. The surfaces exposed to environmental impacts, like the wing leading edges of an airplane, are often made of the light but very stable titanium [13, 21]. Among the polymers, polyurethane is often used for outdoor applications because it is resistant against erosion and UV-light as well as tough and flexible at the same time, e.g. in form of coatings on cars or films on wind energy turbines [22]. As the development of electric mobility demands lighter materials, the importance of composite polymer materials increases. Glass fiber reinforced polymers have been used for smaller airplanes like sailplanes for a longer time already, carbon fiber reinforced polymers (CFRP) will be increasingly used in the automotive and aviation industry because of their low weight and high strength. Because of the significantly reduced heat transfer coefficients, new de- and anti-icing methods are being developed for these fiber reinforced materials. Finally, in the building or architecture sector glass is an important material for windows and copper is often used in heat transfer applications, like heat exchanger tubes or in heat accumulators for heat pumps. These material surfaces were characterized for comparison with the functionalized PU films and will be referred to as “technical material” or “engineering material” surfaces in this thesis.

## 2.2. Active anti- and de-icing methods

The established anti- and de-icing methods can be described as "active" and are divided into mechanical (2.2.1), chemical (2.2.2) and thermal (2.2.3) methods. An "anti-ice" method tries to prevent the build-up of ice on a surface in icing conditions. In contrast, a "de-icing" method is used for removing already accreted ice from a surface in order to restore its proper function.

### 2.2.1. Mechanical methods

The mechanical de-icing methods have been developed for and are mainly used in aviation.

#### Inflatable rubber boots

A de-icing boot is installed on leading edges of aircraft wings or control surfaces (e.g. horizontal and vertical stabilizers) for mechanical in-flight de-icing. If atmospheric icing occurs, a pneumatic system inflates a rubber boot with compressed air. The sudden expansion in size cracks the ice which is then blown away into the airflow. Afterwards, the boot is deflated to return the wing or surface to its optimal shape. De-icing boots are most commonly seen on small and medium-sized airliners and utility aircraft without jet engines [23, 13].

#### Piezoelectric de-icing elements

A similar mechanical de-icing system employs multiple juxtaposed electro-expulsive elements placed within an elastomeric or metal clad boot that is attachable to airfoil surfaces. By application of an electrical impulse, the elements impulsively separate from one another and mechanically throw off thin accretions of ice [24, 25, 26].

#### Other mechanical methods

Another mechanical de-icing system consists of an electrothermal heating element and a syncronized scraper system, that removes the ice after it has been dislodged at the interface by the heating element [27]. There also exists a system with a shape memory alloy sheet mounted on the surface that debonds the ice by expanding and contracting [28].

Disadvantages are that each of these mechanical ice removal systems adds weight, is expensive, requires visual attention to the degree of icing and careful timing of activation for maximum effectiveness. All mechanical systems are de-icing methods, none of these systems can prevent ice from forming (anti-icing).

### 2.2.2. Chemical methods

For roads usually sodium or magnesium chloride salts are used in granulate form, whereas at airports mainly liquids are used. Several liquids are used for both anti- and de-icing of large area surfaces like runways at airports or airplanes. The basis of these anti- or de-icing liquids is propylene or ethylene glycol, isopropyl alcohol, urea, acetate, or formate [23]. The freezing point reduction for anti-icing is due to the increase of dissolved particles in water, e.g. ions from a salt like sodium chloride, which is also called the colligative effect [29]. Many anti- or de-icing liquids have negative environmental impacts, like impairing the health of the vegetation because of osmotic stress, eutrophication, their high biological oxygen demand for degradation or their toxicity for aquatic organisms [30].

Nowadays, more and more acetates or formates (e.g. potassium or sodium formates / acetates) are used. They are regarded as least environmentally harmful, because they have a very low biological oxygen demand for degradation. However, they can react alkaline in aqueous solutions and change the pH value of the ground [30].

Chemical in-flight anti-icing systems prevent the build-up of ice on the leading edges of wings, including propeller and rotor blades, by the weeping of alcohol from a plurality of holes in an attached titanium cuff. Drawbacks of such on-board chemical systems

include their high expense, high weight and the necessity to rely on a finite supply of anti-icing liquid during flight [23, 13].

### 2.2.3. Thermal methods

The thermal de- and anti-icing methods have been developed for aircraft, automobiles and wind energy turbines.

#### Electrothermal heating

A common way to keep surfaces free of ice (anti-icing) or to de-ice them is electrothermal heating. In the aircraft industry this technique is applied often, especially for medium and large aircraft. Heating systems installed underneath the wing's leading edges, on propeller or rotor blades are used, keeping them constantly warm to prevent ice from forming or quickly heating them up for de-icing [13]. Electrothermal systems use resistive heating by an electrical current in resistive parts, wires, layers or conductive coatings. The electric energy comes from a generator driven by one or more of the aircraft engines [31, 32, 33]. The automotive industry also uses electrothermal heating by small wires attached to the inner window surfaces, e.g. of the front or rear window, for de-icing or de-fogging [34].

Several electrically conductive and heatable coatings or layers based on carbon have been developed, like graphite foils [35], heatable graphene thin films incorporating graphene nanoribbons [36], nanostructured layers including carbon nanotubes, nanowires and nanofibers [37] or a sprayable anti-ice paint with carbon nanotubes [38].

Another technology used are transparent, conductive, heatable coatings made up of several layers of dielectric and conductive material containing metals (silver, gold, aluminum, molybdenum, copper, zinc) or metal oxides (indium tin oxide, tin zinc oxide or differently doped tin oxides). Transparent conductive coatings have been developed especially in the automotive industry [39, 40, 41, 42].

One disadvantage of typical thermal systems is the tendency of the protective cover to break down due to cutting, abrasion or erosion. A further big disadvantage is the

high electrical energy consumption. In modern vehicles the electrical energy is limited due to the limited battery capacity, furthermore the energy is also needed for electric propulsion. Therefore de-icing via resistive heating is not attractive in terms of energy efficiency.

### Heating by convection from hot air or fluids

Another method is heating with hot air or hot fluids. Hot air or fluid anti-icing systems have been developed for aircraft [43] and wind energy turbines [44]. For aircraft, these "bleed air" systems use high-temperature air from the engine compressor sections and conduct it towards the wing surface or leading edges for de-icing [45]. However, the use of hot air is not very energy efficient, because the aircraft loses a substantial amount of the forward propulsion power. An emerging problem is the growing amount of light-weight, fiber reinforced polymer compound materials because these materials have a very low heat conductivity and the surface does not heat up sufficiently. Furthermore, modern and fuel-efficient engines do not produce as much heat as older ones.

### Heating by microwave or infrared radiation

Heating of surfaces [46] or directly of the ice [47] is also possible by application of microwaves. The microwaves are generated at a gyrotron or magnetron and led into the wings by waveguides. There, they are radiated towards the surface and heat up the surface and the ice itself. Infrared radiation heating systems for de-icing of aircraft and other structures have also been developed and examined [48].

Overall, the thermal methods can be used for both anti- and de-icing of many types of surfaces or structures. A lot of different systems have been developed. They function reliably and guarantee safety, but they need a significant amount of energy and therefore cause high costs. Furthermore, they cannot be used in combination with new composite materials like fiber reinforced polymers.

## 2.3. Passive anti-icing by functional surfaces

The idea of passive anti-icing comes from the area of functional surfaces, which are developed in modern research areas like interfacial chemistry, micro- or nanotechnology. Functional surfaces were developed for applications like self-cleaning, water-repellency, anti-icing, anti-friction, anti-corrosion, anti-bacteria or others. The concepts are derived from nature, e.g. the superhydrophobic surfaces are derived from the water-repellent, self-cleaning plant leaves, like the Lotus leaf [49, 50] or from the water strider legs [51]. The specified function can be achieved by several different technical concepts. In case of anti-ice surfaces there are the different concepts of protein coatings (2.3.1), various surface concepts with embedded liquids (2.3.2) or other physical-chemical functionalizations like superhydrophobic surfaces (2.3.3). These concepts are briefly described below.

### 2.3.1. Biological functionalization with anti-freeze protein coatings

It is also possible to functionalize surfaces with biological material like proteins for anti-icing. The anti-freeze proteins (AFP) can be found in some animals or plants that live in cold environments and protect their tissue from freezing with these proteins. For example, fish in the arctic sea can survive temperatures of down to -1.9 °C. These proteins can lower the freezing point, although the melting point stays at around 0 °C, leading to a thermal hysteresis. They adsorb to the interfaces of freshly developed ice nucleation seeds, in this way preventing further adsorption of water molecules for normal crystal growth or inhibiting recrystallization. Many different antifreeze proteins have been isolated and their molecular structure and ice crystal adsorption mechanism was analyzed [29].

They can be extracted from natural sources or produced by biotechnology, for example in yeast. Artificial antifreeze molecules have been synthesized to prevent recrystallization in several different applications, e.g. in transplantable tissues [52, 53, 54, 55] or in frozen food, like ice cream [56].

Some groups have coated surfaces with these proteins by covalent binding (bioconjugation) to create anti-ice surfaces with reduced ice accretion and a lowered freezing point [57, 58]. Even an antifreeze protein coating on metal has been reported [59]. Apart from these proteins, an anti-ice coating for outdoor equipment containing covalently linked polysaccharides has been reported, that can incorporate water and has low ice adhesion [60]. For technical application, antifreeze proteins have successfully been integrated into coatings for wind energy turbines [61, 62, 63], into coatings for aircraft or as biocatalytic surfaces [64, 65].

An advantage is the good anti-icing functionality because the anti-freeze protein surface structure corresponds well to the ice crystal surface structure. A disadvantage of this concept is the difficult and costly way to extract or synthesize these anti-freeze proteins and the bad long term durability of these protein coatings.

### 2.3.2. Porous liquid containing or releasing anti-ice surface concepts

Coalescence induced self-removal of condensed water drops has been reported [66, 67], where the drops jump off the surface by the release of energy due to coalescence. Furthermore, porous surfaces can be infused with organic [68, 69] or aqueous [70, 71] liquids as a lubricating layer, leading to a very low ice adhesion. These surfaces have become known as “slippery liquid-infused porous surfaces” (SLIPS).

Another interesting concept is a surface releasing a functional liquid, e.g. an anti-icing liquid [72]. The opposite concept is the absorption of water in a porous coating for anti-fogging or anti-icing, based on inorganic [73] or organic material [74].

### 2.3.3. Physical-chemical anti-ice surface functionalizations

Phase change materials can shed off the ice by controlled contraction or expansion [75].

### Transparent anti-ice surfaces

Transparent anti-ice surfaces are especially interesting for window glasses in architecture, in the automotive industry and in other areas (e.g. as covers for solar panels). An interesting concept is a low thermal emissivity coating, which keeps the heat in the material and prevents cooling down by heat radiation towards the surroundings. Such a "low e" coating was developed for automotive windscreens [76]. This coating is also used for facade elements in the building area [77]. A lot of transparent, hydrophobic coatings are known that do not use any microroughness [78, 63, 79, 80, 81]. As the micro- and nanostructures on a superhydrophobic surface scatter the visible light, they are usually not transparent. However, high optical transmittance might be achieved if the microstructure dimensions are small enough. Superhydrophobic surfaces on PDMS with microstructure diameters of 5 µm to 10 µm and microstructure distances of 10 µm to 30 µm, having up to 80 % optical transmittance, were reported [82]. Furthermore, a superhydrophobic $Al_2O_3$ surface coated with a fluorosilane agent having a roughness of 20 nm to 50 nm and a transmittance for visible light of 92 % was described [83]. Another superhydrophobic, nanorough surface with high transmittance was created on polystyrene by a plasma etching process with a $CF_4/O_2$ mixture combining roughening and fluorination of the surface [84].

### Superhydrophobic anti-ice surfaces

On a superhydrophobic surface, water forms spheroidal droplets with a small solid-liquid contact area, which easily bounce or roll off and the surface remains dry. Therefore, only little or no ice accumulates on such surfaces and they are not only regarded as superhydrophobic, but also as icephobic. Superhydrophobic coatings are being researched since the mid 1990s. Advantages of superhydrophobic surfaces are the possible functionalization of different substrates and their suitability for different industrial applications. Commercially available are so far only superhydrophobic paints, textiles and glasses. Surfaces for the marine, automotive, aviation, electronic industries and the medical technology, microfluidics and architecture areas are still under development. Many material combinations and production processes exist today. An important research topic

is the improvement of the robustness and stability against environmental and mechanical influences. Another problem is the use under humid conditions where condensation, rime or frost formation let the surfaces loose their superhydrophobic properties. Additionally, the commercial market demands also colored and transparent surfaces, better performance, e.g. also under frost or condensation conditions, and sustainable resources and processes [85].

Coating processes include CVD, plasma technology, sol-gel processes, electrodeposition, galvanization processes, polyelectrolytic multilayers by layer-by-layer processes, lithography, molding, embossing, self-assembly, thermal and electron beam evaporation [85, 86, 87, 88, 89].

Superhydrophobic behavior can be achieved by generating a surface topography with a superposition of a micro- and nanometer scale roughness, also referred to as hierarchically micro- and nanostructured topography. This topography then has to be combined with a hydrophobic coating [90, 91, 92]. These hydrophobic coatings can be of polymeric origin like fluorocarbon as well as silane or siloxane polymers [93, 94, 16, 18]. Another superhydrophobic concept uses nanostructured coatings of rare-earth oxides on microstructures [95].

Hydrophobic or water repellent coatings have been patented for electric cables [96, 97], for aircraft (polysiloxane(amide-ureide) coating) and other surfaces [98]. Hydrophobic plasma coatings have been patented by the Fraunhofer IGB for different applications [99, 100, 101, 102]. Some research groups, e.g. B. Bhushan *et al.* [103] and D. Gao *et al.* [104], have patented their superhydrophobic surfaces. Several other patents for superhydrophobic anti-ice surfaces exist from industry or research institutes [105, 106, 107, 81, 108, 109, 110].

The main research topics concerning superhydrophobic surfaces with respect to anti-icing are the condensation and frost formation behavior, the roll-off of water drops, the rebound of impacting water drops, the delay and duration of freezing (nucleation and crystallization processes), the ice adhesion and the durability of the structures and coatings against environmental influences [111].

The biological functionalization is currently too expensive for large areas of polymer films because of the need for extraction or artificial synthesis of a large amount of the

anti-freeze proteins. Various other concepts have been researched lately, but they often rely on embedded liquids and are therefore only functional for a limited time or are not created by plasma technology. Superhydrophobic surfaces have been thoroughly researched and can be created by microstructuring and plasma technology. As these two processes can be combined for an economic, large scale functionalization process, this concept was chosen for this thesis.

# 3. Experimental and theoretical basics

The first section describes the chemical and thermal properties of polyurethane (3.1.1) and the experimental basics for the surface functionalization, the processes of hot embossing (3.1.2) and plasma technology (3.1.3).

In the following section, the theoretical basics of the relevant physical and thermodynamical aspects are given. The physics of surface wetting (3.2.1), superhydrophobic surfaces (3.2.2), ice adhesion (3.2.3) and icing (3.2.4), especially the nucleation theory are described. The physical principles of heat transfer are given as well (3.2.5) because infrared radiation was used for the water drop temperature measurements in the icing experiments.

## 3.1. Experimental basics of surface functionalization

The experimental basics of the surface functionalization processes, especially of plasma technology are given in this section.

### 3.1.1. Chemical and thermal properties of polyurethanes

#### Chemistry of polyurethanes

Polyurethanes are the 6th most produced polymers in the world and belong to the polymer group of duroplasts [22]. Duroplasts are synthesized by crosslinking to a network and therefore are very stable against breakdown, e.g. by hydrolysis in the outdoor environment. The urethane group is created by the reaction of an isocyanate (R-N=C=O)

with alcohols (R-OH), which also creates an alcohol molecule as a byproduct. The characteristic urethane group has one oxygen atom more than the amide group, as shown in Figure 3.1. Polyurethane is made from diisocyanates and diols or polyols. Several side reactions are possible, forming urea, allophanates, biurets, uretidions, carbodiimides, uretonimines or amides [22].

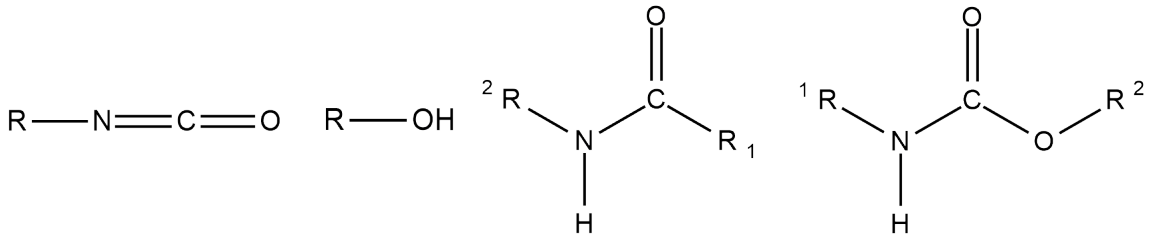


Figure 3.1.: Chemical structures of an isocyanate group, an alcohol group, an amide group, and a urethane group.

Polyurethanes are usually divided by the type of di-isocyanates used, for which there are three different groups: toluene di-isocyanate (TDI) and diphenylmethane-di-isocyanate (MDI) - which are both aromatic - and aliphatic di-isocyanate. The synthesis of the aromatic isocyanates is usually done with phosgene, which is toxic and environmentally harmful. Quite often, polymer chain extenders are used like hexamethylene-di-isocyanate (HDI), iso-phorene-di-isocyanate (IPDI) or di-isocyanate-di-cyclohexyl-methane ($H_{1,2}$MDI) [22].

Around 90 % of polyurethanes are made from TDI or MDI which are used mainly for foams. Only about 10 % are made from aliphatic diisocyanates, of which about 90 % are used for coatings and about 10 % are used for thermoplastic PU films [22].

The polyols can be polyethers, polyesters, acrylics, carbonates or poly(tetra-methylene-ether-glycol)s. For certain syntheses, also "filled" polyols, seed-oil derived polyols or prepolymers (polyol terminated by an isocyanate at each end) are used [22]. Polyether-based polyurethane is suited better against breakdown by hydrolysis in an outdoor environment than polyurethanes based on the other polyols.

#### Glass transition and melting temperature of polyurethanes

Duroplasts do not show melting, but decomposition above a certain temperature. Because of their thermoplastic characteristic these PU films can be reshaped to a certain degree by heating up above the glass transition or melting temperature of the thermoplast. The glass transition characterizes the temperature above which the solidified amorphous parts (comparable to glass) turn into movable polymer chains (comparable to liquid glass). The melting point is the temperature above which the crystalline parts melt and are converted from a solid into a liquid phase. Polyurethanes can have both crystalline and amorphous phases that form hard and soft segments. In case of the former diisocyanates or diols, the same parts in the polymer chains can be arranged side by side because of hydrogen bonding forming the crystalline-like phase. Depending on the degree of phase separation, the hard and soft segments can be more or less separated [22].

### 3.1.2. Microstructuring by hot embossing

Microstructures in polymers can be made by injection moulding, replication, lithography (e.g. with a plasma etching process step), material printing, hot embossing or incorporation of micro- and nanoparticles. Hot embossing has become an important method for easily controllable, low-cost and large area microstructuring of polymers [112, 113, 114]. For hot embossing of a polymer film, the film has to be heated above the glass transition temperature (for the amorphous parts) and the melting temperature (for the crystalline parts) and be pressed onto a stamp with negative mircostructures. Then the polymer fills the negative mold and adapts its positive shape. Air trapping, which randomly occurs at atmospheric pressure, can be avoided by embossing under vacuum.

### 3.1.3. Plasma technology

#### Definition and properties of a plasma

A partly or fully ionized gas is called a plasma when it contains equal amounts of positive and negative charge carriers. It is composed of free electrons, ions, radicals,

neutral atoms, metastable species and also photons in a range from IR to UV radiation. Since the number of positive and negative particles is equal, it is also described as being "quasineutral". The temperature is determined by the average energy and degrees of freedom of the particles. Since these particles have a different mass they absorb the energy differently. The energy distribution is different for each species like electrons, ions, radicals and neutrals. These energy distributions determine the temperature of the plasma which is dependent on the process parameters, like pressure and power. Plasmas can be created thermally, electrically or by other methods and at different pressures, like atmospheric, medium, or low pressure ($< 1$ mbar). Power sources with either direct current, e.g. for glow discharges, or alternating current, e.g. for radio frequency (RF) discharges, can be used [115].

Electrical, microwave and laser discharges are usually used for technical plasmas. In low pressure plasmas, the electrons have a median energy of about 2 eV to 8 eV which would, in case of a Boltzmann-distribution, correspond to a temperature of about 20 000 K and above [116]. As their mass is a lot smaller than that of ions or neutral atoms, hardly any kinetic energy is transferred by elastic collisions. Accordingly, the ion and neutral particle temperature is very low with less than 0.1 eV and the plasma is at about room temperature [116]. This makes low pressure plasma processes ideal for the treatment of polymeric material, which would otherwise be damaged in higher pressure plasmas.

### Applications of plasma technology

Plasma technology is used widely for different applications, like plasma cleaning, sterilization, chemical conversion, etching or coating of surfaces [115]. Plasma processes generally have a low use of resources, are environmentally friendly, can be used for treatment of parts and volumes of all sorts of geometries and at different scales. This makes them also suitable for large scale roll to roll coating processes. In chemical vapor deposition processes the volatile monomer molecules, called precursors, dissociate and react to a product, e.g. a polymer coating on a surface. If the dissociation of the precursors is caused by a plasma, this process is called "plasma enhanced chemical vapor deposition" (PECVD). Plasma etching of surfaces is caused by a chemical (e.g. reduction-oxidation reactions), physical (e.g. sputtering) or combined process [115].

### Plasma polymerization

The polymer synthesis within a plasma is called plasma polymerization [115]. Another process is the plasma-induced polymerization where the reactions of a substance on a surface are started by plasma particles and UV-light [115].

The dissociated precursor gas radicals and ions are both involved in polymer synthesis, which is also influenced by the UV radiation of the plasma. Yasuda described this polymerization process and introduced the Yasuda factor, combining radical and ionic polymerization [117]. The deposition processes can be counteracted by simultaneous etching processes that degrade the material, depending on the process parameters like added gases or RF power. These opposing processes are shown in Figure 3.2.

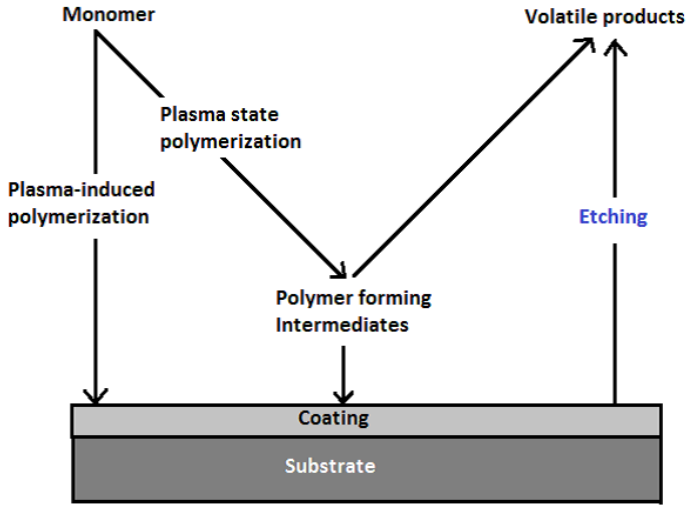


Figure 3.2.: Scheme of different plasma polymerization routes for deposition (plasma-induced polymerization or deposition of polymer forming intermediates) and opposing etching process. Reprinted from Ref [1].

The polymerization can start in the plasma gas phase (plasma state polymerization), where oligomers are created that accumulate on the surface, or takes place directly on the surface (plasma-induced polymerization). Plasma polymers are highly crosslinked and can have a dense structure. They usually have a better adhesion to most substrates than wet chemical coatings. The properties of the plasma polymer depend on the precursor gas (mixture), the gas flow, the process pressure and the RF power. The plasma coating process is quite slow, because the thin film grows from the bottom upwards

by incorporation of radicals or ions from the gas phase. The thickness of the thin film increases linearly with process time [115].

### Fluorocarbon plasma polymer coating

Different fluorocarbon monomer precursors were used, namely Trifluoromethane ($CHF_3$, CAS number 75-46-7), Hexafluoropropylene ($C_3F_6$, CAS number 116-15-4) and Octafluorocyclobutane ($C_4F_8$, CAS number 115-25-3). Both $C_4F_8$, which is a cyclic molecule, and $C_3F_6$ are good precursors for plasma polymerization as they enable high polymerization rates. With all fluorocarbon precursors, the typical surface groups CF, $CF_2$, $CF_3$ and C-$CF_X$ are created. Figure 3.3 shows the chemical structures of the monomers. Figure 3.4 shows a schematic example of a resulting cross-linked fluorocarbon (FC) plasma polymer. On account of the CF groups, this plasma polymer is similar in structure and properties to PTFE, which is shown for comparison in Figure 3.4.

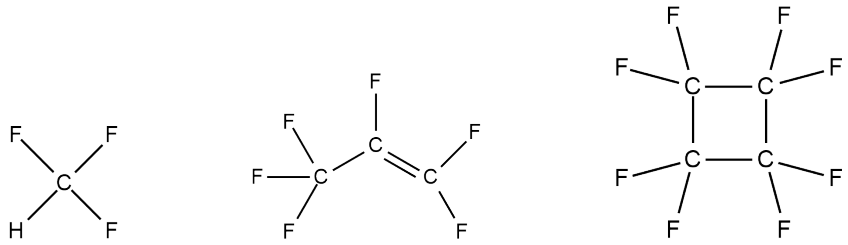

Figure 3.3.: Chemical structure of the fluorocarbon monomer precursors $CHF_3$, $C_3F_6$ and $C_4F_8$.

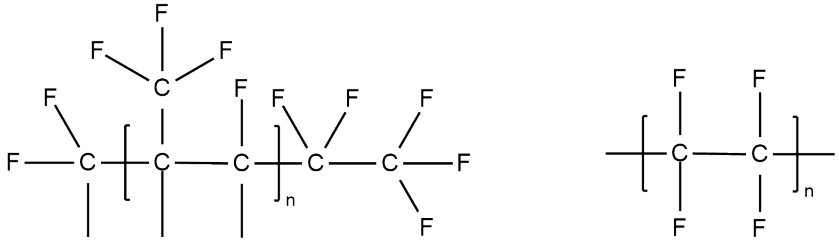

Figure 3.4.: Schematic example of the chemical structure of a crosslinked fluorocarbon plasma polymer (left) and of the chemical structure of polytetrafluoroethylene (PTFE, right).

Especially with fluorine containing precursors, the opposing processes of deposition and etching can occur simultaneously. The fluorocarbon radicals lead to surface polymeriza-

tion whereas atomic fluorine leads to degradation of the surface by etching. A higher C/F ratio usually enhances the plasma polymerization rate whereas a lower C/F ratio enhances the etching rate. The addition of oxygen to the gas mixture enhances the fluorine concentration and therefore the etching rate. Fluorine can react with hydrogen from the polymer surface or added hydrogen to hydrofluoric acid (HF) which is transported into the freezing trap and has to be neutralized there by a base solution. The addition of hydrogen to the plasma gas mixture binds free fluorine radicals and therefore enhances the polymerization rate [118, 119].

The hydrophobic fluorocarbon plasma polymer coatings have a low surface energy, low friction coefficient, high thermal stability and high stability against many chemicals and solvents. The coating consists of a dense, highly cross-linked carbon backbone that is covered by the fluorine atoms on the surface. The CF bond is characterized by a high strength, a strong polarity because of the electronegativity difference between carbon and fluorine and can hardly be broken up by other substances. Because of their high electronegativity, the fluorine atoms create an electron cloud at the surface, which shields the surface against chemical reactions or adhesion of adjacent substances [120]. This is responsible for the hydrophobic and oleophobic character of fluorocarbon surfaces.

### Silicone-like plasma polymer coating

Siliconorganic plasma coatings with the precursor hexymethyldisiloxane (HMDSO, CAS number 107-46-0) were also deposited. The HMDSO molecule is shown in Figure 3.5 and a scheme of the resulting silicone-like plasma polymer in Figure 3.6.

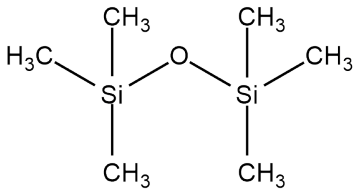


Figure 3.5.: Chemical structure of the HMDSO precursor.

Two different types of polymer coatings can be made by adding either oxygen or other gases to the precursor gas and adjusting especially the process power. By addition of oxygen a hydrophilic, glass-like siliconoxide coating is created [18]. The glass-like,

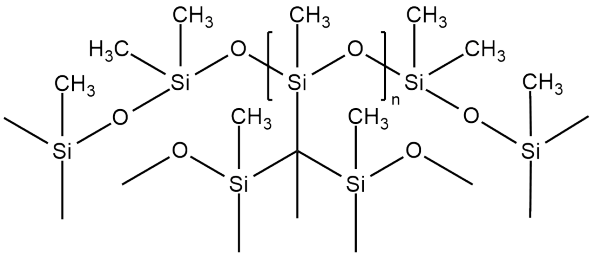


Figure 3.6.: Schematic example of the chemical structure of a silicone-like plasma polymer.

amorphous films show high transparency and high hardness. Typical applications for the glass-like films are coatings for corrosion protection of metals, optical filters, e.g. for protection against UV-light, scratch resistance of polymers or as a diffusion barrier against water vapor and gas for packaging material or solar cells [18]. Without admixture of oxygen, a hydrophobic siliconorganic polymer coating with a silicon oxygen backbone can be made. The hydrophobic character is due to the unpolar methyl groups at the surface which do not create strong, polar interactions by hydrogen bonds with the polar water molecules. The number of methyl groups at the surface depends on the degree of cross-linking of the backbone.

## 3.2. Theoretical basics of wetting, ice adhesion, icing and heat transfer

### 3.2.1. Wetting behavior and interfacial energy

#### Surface tension and surface free energy

The energetical state of a system is described by the free enthalpy or Gibbs energy $G$. A change of the energetical state of a system can be described by the total differential of the Gibbs energy:

$$\mathrm{d}G = \left(\frac{\partial G}{\partial T}\right)_{p,n,A} \mathrm{d}T + \left(\frac{\partial G}{\partial p}\right)_{T,n,A} \mathrm{d}p + \sum \left(\frac{\partial G}{\partial n_i}\right)_{T,p,A} \mathrm{d}n_i + \left(\frac{\partial G}{\partial A}\right)_{T,p,n} \mathrm{d}A. \quad (3.1)$$

Here, $T$, $p$, $n_i$ and $A$ denote the temperature, the pressure, the molar amount of substance $i$ and the interfacial area of a thermodynamic system.

The term surface refers to an interface between a condensed phase and the surrounding gas phase or vacuum. The total differential of the Gibbs energy without mass exchange at isothermal and isobaric conditions is

$$\mathrm{d}G = \left(\frac{\partial G}{\partial A}\right)_{T,p,n} \mathrm{d}A = \gamma \, \mathrm{d}A. \tag{3.2}$$

The differential quotient $(\partial G/\partial A)_{T,p}$ is called the surface free energy, or surface tension in case of liquids, denoted by $\gamma$ or by $\sigma$. In this thesis, $\gamma$ will be used for the surface free energy. It is equivalent to the energy or reversible work that has to be used in order to enlarge an interface for one standard unit under isothermal and isobaric conditions. The surface tension of water is 72.75 mN/m at 293 K [121].

### Wetting of surfaces and contact angles

If a drop is in contact with a solid surface, three different interfacial free energies have to be accounted for: the surface free energy between solid and liquid $\gamma_{\mathrm{sl}}$, the surface free energy between solid and gas $\gamma_{\mathrm{sg}}$ and the surface tension between liquid and gas $\gamma_{\mathrm{lg}}$. This is shown schematically in Figure 3.7.

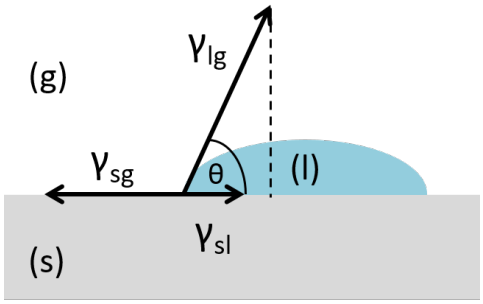


Figure 3.7.: Scheme of the interfacial energies at the three phase contact line of a liquid drop.

The contact angle $\theta$ of the liquid at the three phase line can be correlated with the interfacial energies by the Young equation:

$$\cos\,\theta = \frac{\gamma_{\mathrm{sg}} - \gamma_{\mathrm{sl}}}{\gamma_{\mathrm{lg}}}. \tag{3.3}$$

The wetting behavior and surface free energy of a solid material can be characterized by contact angle measurements. With a static water contact angle of less than 90°(on the entire surface), the surface is called hydrophilic and a water drop takes on the shape of a fraction of less than a hemisphere. For more than 90°(on the entire surface), it is called hydrophobic and the water drop gets pulled into a shape resembling a fraction of a sphere or an ellipsoid. If the advancing contact angle exceeds 150° and the contact angle hysteresis is very small (below 10°), the surface is called superhydrophobic [122, 123, 124, 111].

The reasons for more or less spreading of the drop on the surface are the intermolecular, electrostatic forces between the surface and the liquid phase molecules. These forces can be separated into disperse and polar interactions. The disperse interactions are the London-van der Waals interactions between two induced dipoles in neutral atoms or molecules. The polar interactions are the Coulomb interactions between charged atoms or molecules, the Keesom-van der Waals interactions between two permanent dipoles, the Debye-van der Waals interactions between a permanent dipole and an induced dipole or hydrogen bonds. The specific work of adhesion $W_{\mathrm{ad}}$ is equal to the interfacial energies of the two separate systems which get reduced by the solid-liquid interfacial energy. This is expressed by the Dupré equation [90]:

$$W_{\mathrm{ad}} = \gamma_{\mathrm{sg}} + \gamma_{\mathrm{lg}} - \gamma_{\mathrm{sl}}. \tag{3.4}$$

Combined with the Young equation, the Dupré equation can be rewritten to the Young-Dupré equation for the equilibrium work of adhesion $W_{\mathrm{e}}$:

$$W_{\mathrm{e}} = \gamma_{\mathrm{lg}}\,(1 + \cos\theta_{\mathrm{e}})\,, \tag{3.5}$$

where $\theta_{\mathrm{e}}$ denotes the equilibrium contact angle.

During advancing or receding contact angle measurements, the water drop triple phase line is moved across the surface, and thereby the advancing and receding contact angles can be determined. The advancing contact angle is higher than or equal to the static

one, whereas the receding contact angle is lower than or equal to the static one. This is caused by the molecular interactions and surface adsorption or desorption processes of the water molecules at the triple phase line. The advancing of the three phase contact line corresponds to a wetting process where energy is released. In contrast, a receding three phase contact line corresponds to a dewetting process which consumes energy in order to create two new interfaces. The difference between the advancing and the receding contact angle is called the hysteresis. In addition to that, a stick-slip behavior can be caused by chemical and topographical inhomogeneities of the surface at the triple phase line.

The sliding of a drop across a surface, corresponding to a shearing process, is described by the Furmidge equation:

$$(mg/w)\sin\alpha_{\mathrm{tilt}} = \gamma_{\mathrm{lg}}\left(\cos\theta_{\mathrm{rec}} - \cos\theta_{\mathrm{adv}}\right). \tag{3.6}$$

Here, $m$ is the drop mass, g is the gravitational constant, $w$ is the width of the drop perpendicular to the sliding direction, $\alpha$ is the sliding angle, $\gamma_{\mathrm{lg}}$ is the liquid-gas surface tension of the liquid and $\theta_{\mathrm{rec}}$ and $\theta_{\mathrm{adv}}$ are the receding and advancing contact angles of the liquid, respectively.

### Wetting states of Wenzel and Cassie-Baxter

Most real surfaces possess a certain degree of roughness. While hydrophobic coatings reduce the surface energy, this roughness or a topographical structuring of surfaces can additionally alter the contact area between water droplets and the surface, depending on the wetting state [122, 123, 124, 111]. The wetting state of a water drop on a rough surface is always between the two theoretical limits of wetting which were described by Wenzel [125] and Cassie and Baxter [126]. In one case, the water droplet completely fills the gaps between the surface structures which was described by Wenzel as wetting on "rough" surfaces [125]. In the other case, it only wets the top surface of the structure peaks which leads to air pockets between the structures under the droplet, therefore described as wetting on "porous" surfaces by Cassie and Baxter [126]. Both wetting cases are shown schematically in Figure 3.8.

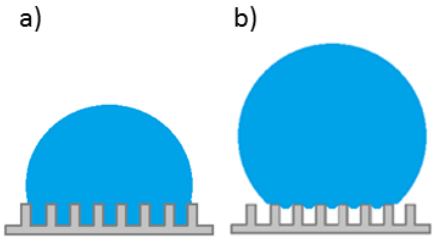


Figure 3.8.: Schematic drawings of the Wenzel wetting state (a) and the Cassie-Baxter wetting state (b) of a water drop. Reprinted from [1].

The Wenzel state model assumes the static contact angle $\theta_{\mathrm{W}}$ to be determined by the real surface roughness. A non-dimensional surface roughness factor $rf$ is introduced for calculation of the real solid-liquid interface area $A_{\mathrm{sl}}$ from the flat projection of the solid-liquid interface area $A_{\mathrm{f}}$. With this factor, Young's contact angle is altered to the Wenzel state contact angle [125, 90]:

$$rf = \frac{A_{\mathrm{sl}}}{A_{\mathrm{F}}}, \tag{3.7}$$

$$\cos\,\theta_{\mathrm{W}} = rf \cdot \cos\,\theta. \tag{3.8}$$

The factor $rf$ is equal to one for a perfectly flat surface, but larger than one for real surfaces. Therefore, the amount of the factor $\cos\,\theta$ is enlarged. The roughness enhances wetting on a hydrophilic surface (the contact angle becomes smaller), whereas the contact angle becomes larger on a hydrophobic surface. The effect of the surface free energy of the specific material is enhanced.

In the Cassie-Baxter state, air is trapped between the surface structures leading to a low water wettability and easy roll-off of water drops, e.g. by wind or gravitational forces. This is known as the Lotus effect. The interface beneath the drop is regarded as combined of a solid-liquid (fraction $f_{\mathrm{sl}}$) and a liquid-gas (fraction $f_{\mathrm{lg}}$) interface, the corresponding contact angle terms are added, the roughness is introduced by the factor $rf$ for the solid-liquid interface and it is rearranged to the Cassie-Baxter contact angle [126, 90]:

$$\cos\ \theta_{\mathrm{CB}} = f_{\mathrm{sl}}\ \cos\ \theta_{\mathrm{sl}} + f_{\mathrm{lg}}\ \cos\ \theta_{\mathrm{lg}}, \tag{3.9}$$

$$f_{\mathrm{lg}} = 1 - f_{\mathrm{sl}}, \tag{3.10}$$

$$\cos\ \theta_{\mathrm{lg}} = -1, \tag{3.11}$$

$$\cos\ \theta_{\mathrm{sl}} = \cos\ \theta, \tag{3.12}$$

$$\cos\ \theta_{\mathrm{CB}} = rf\ f_{\mathrm{sl}}\ \cos\ \theta - 1 + f_{\mathrm{sl}}. \tag{3.13}$$

A liquid drop continues spreading on a surface until simultaneously the Young equation is satisfied locally at the triple phase line and the minimal surface condition ($1/R_1 + 1/R_2 = \text{const.}$) is satisfied over the entire liquid-air interface. Then, the liquid drop has reached the state of minimal surface energy [90]. Whether a homogeneous or a composite interface forms depends on the history of the system, e.g. whether the drop results from condensation or was placed upon the surface from above. The Wenzel state is energetically stable, while the Cassie-Baxter state is only metastable and can be destroyed by interfacial wave perturbations like vibrations [90]. In this case, a transition from the Cassie-Baxter to the Wenzel state can be observed. During transition from the Cassie-Baxter to the Wenzel state the liquid interface can be stabilized on the microstructure sides by nanoasperities [90]. This was described to be the reason for the nanostructures being superimposed on the microstructures of the Lotus leaf. For a superhydrophobic surface, the static contact angle in Cassie-Baxter state is above 150°, while it is between about 120° and 150° in the Wenzel state.

Zheng *et al.* proposed a model to describe wetting states, where the water drop is neither in Wenzel nor in Cassie-Baxter state, but in a mixed wetting state [127]. In this state, only parts of the water-air interface have been able to sink down to the bottom of the valleys between the surface asperities:

$$\cos\theta_{\mathrm{M}} = \chi\cos\theta_{\mathrm{W}} + (1-\chi)\cos\theta_{\mathrm{CB}}. \tag{3.14}$$

Here, $\chi$ is the fraction of the total surface area where the water has transitioned to the Wenzel state.

If a part of a water drop moves into the Wenzel wetting state, this part gets stuck on

the surface. This is called "pinning", where the advancing or receding triple phase line gets stuck at the surface. It is caused by chemical or topographical inhomogeneities on the surface. This can happen in particular on a microstructured surface, if sharp edges are present on the microstructures. Therefore, it is important that the structures have rounded side and top surfaces in order to prevent pinning and enable good roll-off [90]. The easiest microstructure arrangement for laser drilling is quadratic, but for maximum structure density on a surface a hexagonal arrangement is needed, as calculated below. The microstructures have a certain base and top area and the shortest distance between them is $P$ (pitch), as shown in Figure 3.9 for quadratically and hexagonally arranged patterns.

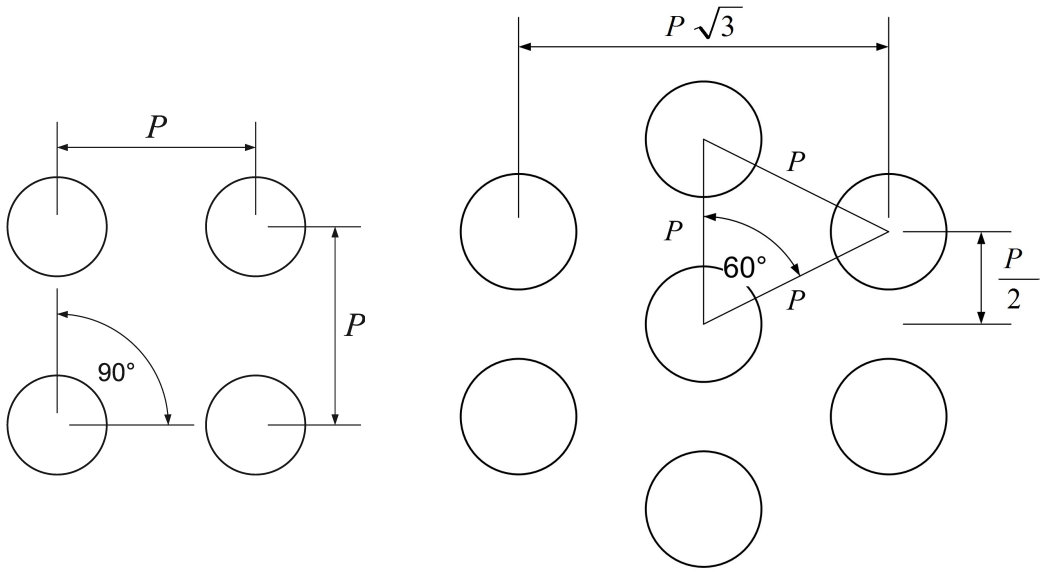


Figure 3.9.: Quadratic (left) and hexagonal (right) arrangement of microstructures on a surface and important geometrical parameters.

In order to calculate the Cassie-Baxter contact angle, the microstructure density $\eta$, the roughness factor $rf$ and the solid-liquid fraction $f_{\mathrm{sl}}$ are needed.

For a quadratic arrangement (see Figure 3.9, left), the structure density $\eta$ is:

$$\eta = \frac{1}{P} \cdot \frac{1}{P} = \frac{1}{P^2}. \tag{3.15}$$

For a hexagonal arrangement (see Figure 3.9, right), the structure density $\eta$ is:

$$\eta = \frac{1}{\sqrt{3}P} \cdot \frac{1}{P/2} = \frac{2}{\sqrt{3}\,P^2} \approx \frac{1.155}{P^2}, \tag{3.16}$$

where $P$ denotes the shortest distance between two microstructures.

The cylindrical microstructures have a lateral area $A_{\mathrm{L}}$, bottom radius $R$, base area $A_{\mathrm{B}}$, top radius $r$, top area $A_{\mathrm{T}}$ and height $h$, as shown in Figure 3.10.

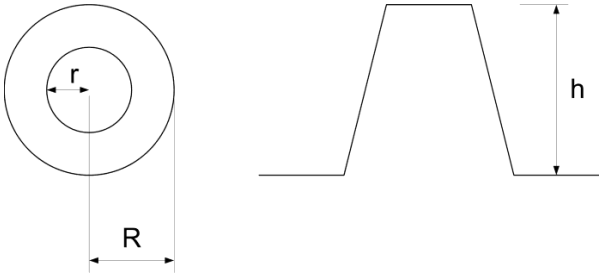


Figure 3.10.: Schematic drawing of a cylindrical microstructure with geometric parameters.

The roughness factor $rf$ and the solid-liquid interface fraction $f_{\mathrm{sl}}$ of cylindrical microstructures are calculated as follows [90]:

$$A_{\mathrm{L}} = \pi \cdot (R + r) \cdot \sqrt{h^2 + (R - r)^2}, \tag{3.17}$$

$$A_{\mathrm{T}} = \pi\, r^2, \tag{3.18}$$

$$A_{\mathrm{B}} = \pi\, R^2, \tag{3.19}$$

$$rf = 1 + \eta \cdot (A_{\mathrm{L}} + A_{\mathrm{T}} - A_{\mathrm{B}}), \tag{3.20}$$

$$f_{\mathrm{sl}} = \eta \cdot A_{\mathrm{T}} = \eta \cdot \pi\, r^2. \tag{3.21}$$

The elliptical microstructures have a lateral area $A_{\mathrm{L}}$, bottom major radius $A$ and minor radius $B$, base area $A_{\mathrm{B}}$, top major radius $a$ and minor radius $b$, top area $A_{\mathrm{T}}$ and height $h$, as shown in Figure 3.11.

The roughness factor $rf$ and the solid-liquid interface fraction $f_{\mathrm{sl}}$ of elliptical microstruc-

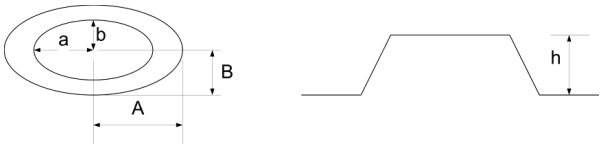


Figure 3.11.: Schematic drawing of an elliptical microstructure with geometric parameters.

tures are calculated as follows [90]:

$$A_{\mathrm{L}} = \pi \cdot \left[\left(\frac{A+B}{2}\right) + \left(\frac{a+b}{2}\right)\right] \cdot \sqrt{h^2 + \left[\left(\frac{A+B}{2}\right) - \left(\frac{a+b}{2}\right)\right]^2}, \tag{3.22}$$

$$A_{\mathrm{T}} = \pi \left(\frac{a+b}{2}\right)^2, \tag{3.23}$$

$$A_{\mathrm{B}} = \pi \left(\frac{A+B}{2}\right)^2, \tag{3.24}$$

$$rf = 1 + \eta \cdot (A_{\mathrm{L}} + A_{\mathrm{T}} - A_{\mathrm{B}}), \tag{3.25}$$

$$f_{\mathrm{sl}} = \eta \cdot \ A_{\mathrm{T}} = \eta \cdot \pi \left(\frac{a+b}{2}\right)^2. \tag{3.26}$$

### Models for calculation of surface free energy of solids

As the surface free energy of surfaces cannot be measured directly, it has to be derived by contact angle measurements with minimum two liquids with different polarity and surface tensions. The liquids are chosen according to material compatibility, e.g. water as a polar liquid, diiodomethane (DIM) as an unpolar liquid and ethyleneglycol as a liquid with an intermediate polarity. The polar and disperse parts of the surface tensions of the liquids are known. The surface free energy can be calculated by different methods, e.g. of Wu [128, 129], of Fowkes [130], of Girifalco and Good [131] or of Owens, Wendt, Rabel, Kaelble (OWRK) [121]. The critical surface free energy, where complete wetting is achieved by a fluid with the same surface tension, can be derived with the Zisman method [132]. The surface free energies in this thesis were calculated with the OWRK model which assumes that both disperse and polar interactions between solid and liquid phase are present. It uses the geometrical mean for determination of these interactions:

$$\gamma_{sl} = \gamma_{sg} + \gamma_{lg} - 2(\sqrt{\gamma_s^d \gamma_l^d} + \sqrt{\gamma_s^p \gamma_l^p}). \tag{3.27}$$

Here, the indices s and l represent the solid and liquid phase, d and p represent the disperse and the polar interactions. This is combined with the Young equation (3.3) and rearranged to an equation for a linear regression:

$$\frac{1+\cos\theta}{2}\frac{\gamma_{lg}}{\sqrt{\gamma_{lg}^d}} = \sqrt{\gamma_{sg}^p} \cdot \sqrt{\frac{\gamma_{lg}^p}{\gamma_{lg}^d}} + \sqrt{\gamma_{sg}^d}, \tag{3.28}$$

$$\gamma_s^{tot} = \gamma_s^d + \gamma_s^p. \tag{3.29}$$

With the values of the slope and the y-axis intersection, the polar and disperse parts of the surface free energy of the solid can be determined. They are combined to the total surface free energy.

### 3.2.2. Ice adhesion and icing on superhydrophobic surfaces

A superhydrophobic surface can be generated by a superposition of a micro- and nanometer scale roughness, also referred to as hierarchically micro- and nanostructured topography. Furthermore, a hydrophobic surface chemistry is needed which can be created by a hydrophobic coating. A superhydrophobic surface is essentially a self-cleaning surface, where water drops take dirt particles with them while they easily roll off from the surface [133].

Icing involves different physical processes leading to different types of ice. The de- and anti-icing properties of a superhydrophobic surface are determined by its different topographical length scales, which are described here briefly.

If a water drop is gently placed on a superhydrophobic surface, it will stay in the Cassie-Baxter state and roll off. But the Cassie-Baxter state is an energetically metastable

state. The water drop can transition into the Wenzel wetting state because of destabilization of the water-air interface under the drop by environmental influences and is then pinned to the surface [90]. This behavior is determined on the micrometer scale.

In an outdoor environment, falling rain drops impact with a certain velocity or dynamic pressure on the surface. If the dynamic pressure is higher than the capillary pressure created by the microstructures, the drops get stuck on the surface in the Wenzel wetting state [134, 135, 136, 137]. Being superhydrophobic under normal rain conditions, these surfaces might lose their functionality at high impact speeds, which can occur during flight or on turning rotors of a wind turbine.

Freezing rain conditions are especially dangerous because then supercooled large droplets (SLD) can occur. While in the air, supercooled water droplets are liquid, but they instantly freeze when hitting a surface leading to ice accumulation. Therefore, experiments with impacting supercooled droplets at different speeds have been done. It was shown that droplets can rebound from superhydrophobic surfaces without freezing because of their interfacial tension in case the micro- and nanostructure geometry creates a sufficiently high capillary pressure ($p_C = -4f_{sl}/(d(1-f_{sl}))\gamma\cos\theta$). It is the resistive pressure that has to be overcome by the droplet weight and impact pressure for penetration of the liquid into the surface structures [138, 139, 140, 141].

Further problematic processes are condensation, rime formation and frost formation (by desublimation) which occur if the surface is colder than the ambient air with a certain humidity. These processes are determined by the surface nanometer length-scale, which has been examined lately [142, 143, 144]. By condensation, rime or frost formation, the superhydrophobic wetting behavior of a surface can be lost [145, 146, 147]. In this case, the Wenzel wetting state leads to an increased wetting area of droplets and therefore higher ice adhesion after freezing [148, 149]. Condensation or frost formation is difficult to prevent, although nanostructures have been reported on which drops formed by condensation accumulate on top of the nanostructures and run off [150].

If water remains on a superhydrophobic surface and freezes, the ice adhesion is expected to be significantly lower than on normal or hydrophilic surfaces. Ice adhesion depends on the surface chemistry and the total contact area, determined by the surface topography. After freezing of a water drop, a large contact area between the ice and the surface, especially in the Wenzel state, results in strong adhesion. In contrast, freezing

in the Cassie-Baxter state should lead to reduced adhesion due to the air-filled structure gaps and the smaller contact area. On this topic, different results and opinions exist in the literature. Some articles report a reduced ice adhesion on superhydrophobic surfaces compared to flat, hydrophobic surfaces, especially if the microstructure geometrical dimensions are only a few micrometers large [151, 86, 152, 153, 154, 87, 155, 156]. In contrast, others have measured a higher ice adhesion and conclude that superhydrophobic surfaces do not automatically show a low ice adhesion, which depends on the microstructure shape and dimensions, atmospheric influences like condensation and the size of initial microcracks in the ice [157, 158, 159, 160, 161, 162, 154, 163].

Icing has been studied on various surfaces with wetting behavior ranging from hydrophilic to superhydrophobic under atmospheres of various humidity. Water drops can be supercooled down to different temperatures below 0 °C depending on the surface wettability. Water drops were given onto surfaces held constantly at a certain temperature or they were cooled down together with the surface at a certain cooling rate. Their freezing behavior has been analyzed by IR measurements [164].

One effect of superhydrophobic surfaces is the reduction of the heat transfer across the water-surface interface. The air trapped between the microstructures creates an insulating layer between the surface and the water drop in Cassie-Baxter state. Therefore, it reduces the heat transfer across the interface for cooling down the drop and for release of latent heat during crystallization [164, 165].

Another effect is the influence on the heterogeneous nucleation rate for the start of freezing. The nucleation rate can be calculated with the classical nucleation theory. For intermediate supercooling down to about -20 °C, heterogeneous nucleation at the water-substrate interface is the dominant factor for icing. Then, a small water-substrate contact area leads to a reduced water-substrate interface nucleation rate and a reduced total nucleation rate. This results in a significant freezing delay. However, at lower supercooling temperatures the bulk and water-air interface nucleation rates become dominant, which limits the effectiveness of superhydrophobic surfaces against icing at very low temperatures (about -25 °C to -40 °C) [164]. Furthermore, it has been reported that the water contact angle, the water surface tension and the water-substrate interface area are depending on the temperature, which also influences the nucleation rate [166]. For different nanostructures or nanoroughness (RMS) values, extremely low nucleation

temperatures of about -24 °C and long freezing delays have been measured on superhydrophobic surfaces. It has been reported that the classical nucleation theory should be enhanced by a quasiliquid interfacial layer between the ice nucleus and the surface. With this enhanced model, nucleation temperatures and freezing delays could be calculated that matched the experimental values. The theoretical dependencies of nucleation temperature reduction and freezing delay on the nanostructure dimensions were shown [167, 168].

In order to prevent or delay these different processes connected to icing (run-off or rebound of water, condensation, rime or frost formation, nucleation, crystallization), the micro- and nanostructure geometrical dimensions have to be chosen accordingly. However, the lower limits of their geometrical dimensions are determined by the functionalization processes.

### 3.2.3. Adhesion of ice

Adhesion in general depends on the interface area and the adhesive and cohesive forces. These forces are caused by the eletrostatic, polar or disperse interactions between the atoms or molecules. Cohesive forces are the attractive forces between the atoms or molecules within one bulk phase, e.g. within an ice crystal. Adhesive forces are the forces between the two different phases, e.g. between the ice and the surface. If divided by the interface area, the adhesion force is specific for the surface chemistry and roughness. The ice adhesion is determined by the intermolecular forces between the surface and the ice which depends on the surface chemistry and the surface-ice interface area. Furthermore, it is also influenced by the surface roughness $rf$ which alters the contact area between water/ice and surface ($A_{\mathrm{sl}} = rf \cdot A_{\mathrm{f}}$). Ice adhesion is usually measured either by pulling off or by shearing off an ice test specimen from a surface. The measured ice adhesion can be significantly different depending on whether it is measured as tensile strength ($\sigma_{\mathrm{ice}}$) or as shear strength ($\tau_{\mathrm{ice}}$). It has been stated that a combination of both strength types is also possible depending on the ice adhesion measurement setup [163]. For this thesis, the ice adhesion was measured as tensile strength by pulling off an ice cylinder vertically from the surface.

As the ice results from water on the surface it is important to know the relationship between ice adhesion and wettability. Although the rolling off of water drops is determined by the contact angle hysteresis, the hysteresis term is not related to ice adhesion. The ice adhesion is rather related to the adhesion of water to the surface. Meuler *et al.* measured the (shear-off) ice adhesion on bare steel and 21 different test coatings (200 nm to 300 nm thick) of commercially available polymers or fluorinated polyhedral oligomeric silsesquioxane (fluorodecyl POSS) on nominally smooth steel discs. Meuler *et al.* correlated their shear strength values of ice adhesion to the factors $\cos\theta_{\mathrm{rec}} - \cos\theta_{\mathrm{adv}}$ from the Furmidge equation, $1 + \cos\theta_{\mathrm{e}}$ from the Young-Dupré equation (equilibrium work of adhesion), and $1 + \cos\theta_{\mathrm{rec}}$ from the practical work of adhesion, calculated with $\theta_{\mathrm{rec}}$ [169]. These correlations are shown in Figure 3.12.

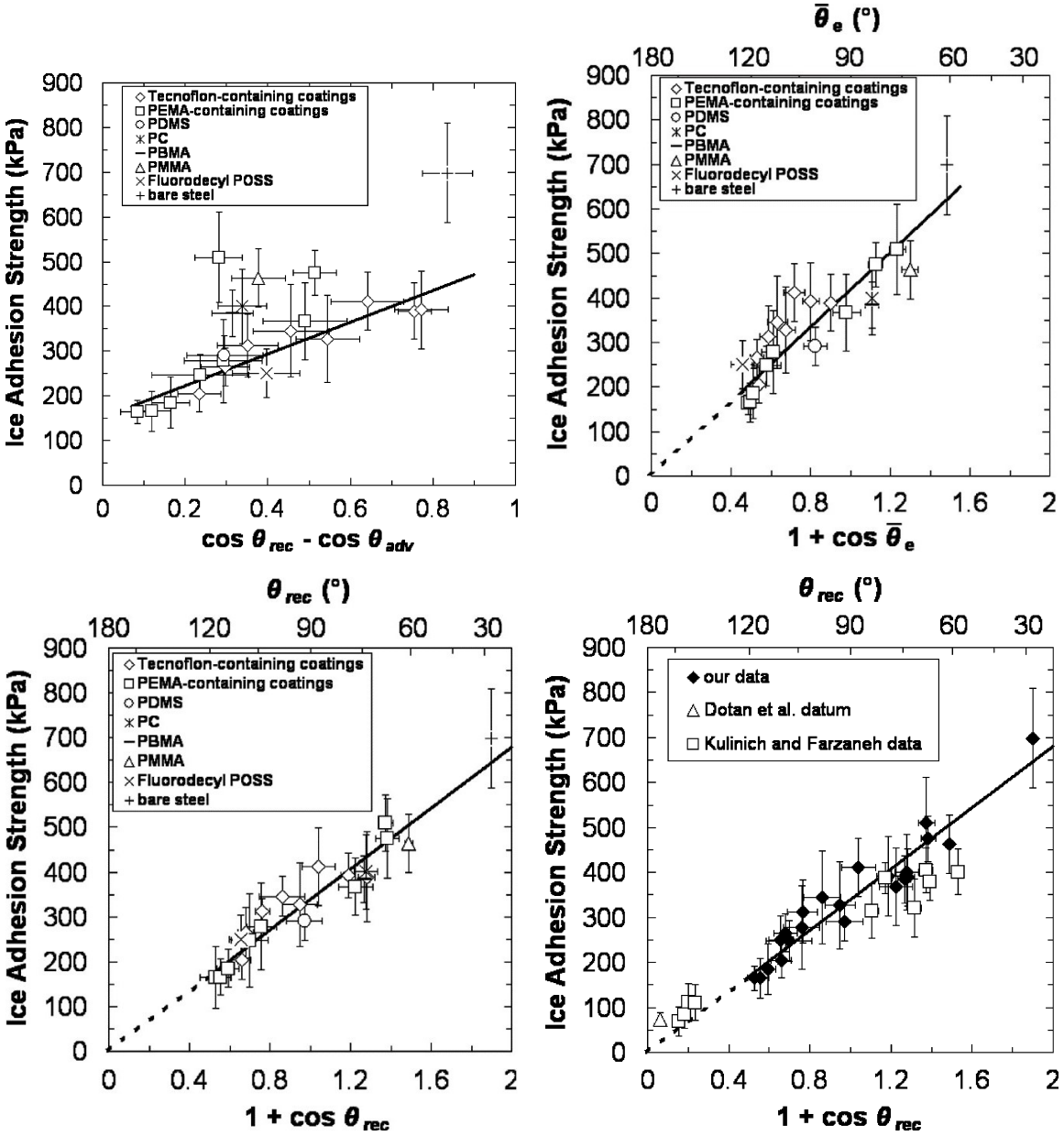


Figure 3.12.: Correlation of average ice adhesion shear strength values measured at -10 °C on bare steel, commercially available polymer coatings and fluorodecyl POSS coatings, drawn over different wetting terms that scale with liquid drop roll-off ($\cos\theta_{\mathrm{rec}} - \cos\theta_{\mathrm{adv}}$), equilibrium work of adhesion ($1+\cos\theta_{\mathrm{e}}$) or practical work of adhesion ($1+\cos\theta_{\mathrm{rec}}$) of liquid water, by Meuler *et al.* The straight lines are the linear best fits of the data. The solid portions encompass the measured data, whereas the dashed portions represent the extrapolations through the origin. Adapted with permission from Ref [169]. Copyright 2010 American Chemical Society.

Accordingly, the ice adhesion correlates with $\cos\theta_{\mathrm{rec}} - \cos\theta_{\mathrm{adv}}$, because the ice slides on a quasi-liquid interface layer during shear-off on flat surfaces. It also correlates with one of the work of adhesion factors as the shear-off of ice creates two new interfaces to air [169]. The best correlation for the ice adhesion measured by shearing off was found for the factor $1 + \cos\theta_{\mathrm{rec}}$ with a $R^2 = 0.92$, leading to the following linear fit [169]:

$$\tau_{\mathrm{ice}} = (340 \pm 40)(1 + \cos\theta_{\mathrm{rec}}). \tag{3.30}$$

The authors state that no known flat, hydrophobic materials show significantly higher receding contact angles, so the term $1+\cos\theta_{\mathrm{rec}}$ has reached a minimum for flat surfaces. Therefore, textured surfaces are proposed for further reduction of the ice adhesion [169]. This will be tested with the microstructured surfaces prepared for this thesis.

Generally, the ice adhesion (measured as shear strength) on flat surfaces can be derived from the relation for practical work of adhesion for shear-off of a liquid from a surface $W_{\mathrm{ad,flat}}$ [163]:

$$W_{\mathrm{ad,flat}} = \gamma_{\mathrm{lg}} \cdot (1 + \cos\theta_{\mathrm{rec}}). \tag{3.31}$$

Nosonovsky *et al.* stated that dewetting depends on contact angle hysteresis while ice adhesion depends on the receding contact angle and initial size of micrometer-scale cracks [162]. Therefore, the work of adhesion between two solid surfaces does not only depend on the practical work of adhesion between a solid and a liquid, but additionally on the release of stored energy from crack formation $W_{\mathrm{ad,crack}}$:

$$W_{\mathrm{ad,total}} = W_{\mathrm{ad,flat}} + W_{\mathrm{ad,crack}}. \tag{3.32}$$

This is especially important for microstructured surfaces and described by Griffith's law for crack initiation. The adhesion between ice and surface is approximated as $W_{\mathrm{ad,IS}} \approx R_{\mathrm{crit}}\sigma_{\mathrm{crack}}^2/E^*$, where $R_{\mathrm{crit}}$, $\sigma_{\mathrm{crack}}$ and $E^*$ denote the radius of the interfacial contact area of each ice/substrate contact point, the tensile stress for adhesive failure and the combined Young's modulus [163, 170]. The combined Young's modulus can be derived as

$$\frac{1}{E^*} = \frac{(1-\nu_{\mathrm{ice}}^2)}{E_{\mathrm{ice}}} + \frac{(1-\nu_{\mathrm{s}}^2)}{E_{\mathrm{s}}}, \tag{3.33}$$

where $\nu$ and $E$ are the Poisson's ratio and Young's modulus of ice and the surface (s), respectively [163, 170]. For contacts below a certain critical size (represented by $R_{\mathrm{crit}}$) the adhesion strength becomes independent of surface roughness (shape independent). Then, the surfaces can be regarded as ideally matching and the adhesion strength reaches a maximum, the theoretical van der Waals bond strength, $\sigma_{\mathrm{th}} \approx W_{\mathrm{ad,VdW}}/b \approx 20\,\mathrm{MPa}$. Here, $W_{\mathrm{ad,VdW}}$ is the work of adhesion ($\approx$10 mJ m$^{-2}$) and $b$ is the characteristic length of surface interaction ($\approx 0.5\,\mathrm{nm}$), both for the van der Waals interaction [170]. Above the critical scale $R_{\mathrm{crit}} \approx E^* \cdot b/\sigma_{\mathrm{th}}$, the shape-independent adhesion strength $\sigma_{\mathrm{th}}$ changes to the shape-dependent adhesive strength $\sigma_{\mathrm{crack}}$ with a stress distribution associated to crack initiation.

In case of tensile strength (mode 1 fracture), the shape-dependent adhesive strength $\sigma_{\mathrm{crack}}$ can be approximated by Griffith's model for brittle linear elastic fracture within a bulk phase (e.g. ice, cohesive fracture) [171]:

$$\sigma_{\mathrm{ice}} = \sqrt{\frac{\gamma_{\mathrm{II}} E_{\mathrm{ice}}}{\pi L}}, \tag{3.34}$$

where L denotes a characteristic length for crack propagation and $\gamma_{\mathrm{II}}$ denotes the surface free energy of the ice-ice interface.

For an adhesive mode 1 fracture at the ice-surface (e.g. PU) interface, it makes sense to use the combined Young's modulus of the ice and the surface as described by Maitra *et al.* [163, 170]:

$$\sigma_{\mathrm{ice,s}} = \sqrt{\frac{\gamma_{\mathrm{II}} E^*}{\pi L}}. \tag{3.35}$$

In case of shear strength (mode 2 fracture), it can better be calculated with the term $(1 + \cos\theta_{rec})$ from the practical work of adhesion, the surface free energy of ice to air, $\gamma_{\mathrm{IA}}$, and the receding contact angle of water or ice, $\theta_{\mathrm{rec}}$ [162]. As before, the Young's modulus of ice $E_{\mathrm{ice}}$ is used for calculating a cohesive fracture:

$$\tau_{\mathrm{ice}} = \sqrt{\frac{E_{\mathrm{ice}} \cdot \gamma_{\mathrm{IA}}(1 + \cos\theta_{\mathrm{rec}})}{\pi L}}. \tag{3.36}$$

An adhesive fracture is calculated with the combined Young's modulus at the ice-surface

interface $E^*$:

$$\tau_{\mathrm{ice,s}} = \sqrt{\frac{E^* \cdot \gamma_{\mathrm{IA}}(1+\cos\theta_{\mathrm{rec}})}{\pi L}}. \tag{3.37}$$

## 3.2.4. Physics of icing

### Properties of water

The water molecule $H_2O$ is $sp^3$ hybridized and would normally be a tetrahedral with a bond angle of 109°47'. However, it is not perfectly tetrahedral, as it has two free electron pairs which lead to a slight distortion of the molecule and a reduced bond angle of 104°45'. The higher electronegativity of the oxygen atom compared to the hydrogen atoms pulls the electron pairs closer to the oxygen atom which causes the permanent dipole moment of the water molecule. Water molecules can build hydrogen bonds to their near neighbor molecules. If multiple molecules act together, there is a "cooperative phenomenon", where one bond stabilizes further bonds of the molecule. By this, the hybridization is enhanced and the bond angle approaches 109°. There are two types of molecules in liquid water: The unbound ones and the ones connected to clusters by hydrogen bonds. These clusters have a very short lifetime of about $10^{-11}$ s and they change their molecule number and shape steadily [172]. Water has several unusual thermodynamic anomalies, e.g. of the density at 3.98 °C (increasing density with decreasing temperature down to 3.98 °C, maximum density at 3.98 °C, decreasing density with further decreasing temperature.) [173].

### Types of icing

The type of ice formed and the icing process depend on the humidity, air and surface temperatures and pressure. Some types of ice can only be made in the laboratory. Ice always exists in a crystal structure with an anisotropic growth mechanism. By this growth mechanism, the overall system energy becomes minimal. Only the hexagonal crystal structure $I_h$ occurs naturally.

When looking at the micrometer and above scale, two different cases have to be distinguished. In the first case, a water drop with a temperature above the melting point of

0 °C hits and stays on a surface cooled to below 0 °C. Then the drop will be cooled down by the surface and eventually freeze because of heterogeneous nucleation. An example would be rain on cold ground forming glaze ice. This process takes time for cooling down the drop until nucleation occurs and crystallization is finished. The heat transfer rate, the time until nucleation or the nucleation temperature are dependent on the surface topography and chemistry. In the other case, freezing rain drops (below 0 °C, down to about -40 °C possible, e.g. supercooled large droplets) hit a surface (below 0 °C) and almost instantly turn to ice after heterogeneous nucleation. This process is very fast and forms clear ice. This is a type of atmospheric icing, which is known from aviation to happen in clouds and can be very dangerous for flying airplanes [13].

At the nanometer scale, there are the processes of condensation and desublimation. It depends on the air temperature, humidity, wind speed and surface characteristics, whether soft rime, hard rime or a type of frost forms. If the air humidity exceeds the dew point, condensation leads to nanometer and then larger water drops in the air or on a surface. The drops in the air form clouds, fog or mist and can also be supercooled. These supercooled water drops of clouds, fog or mist will eventually freeze if contacting a surface, forming soft rime (from small droplets) or hard rime (from large droplets) at medium or high humidity. Otherwise, if the surface is below the frost point of the air at low humidity, which is not enough for condensation of liquid water, frost formation occurs. Frost formation is the desublimation of water from humid air to crystalline ice spicules on the surface.

### Thermodynamics of ice nucleation

For formation of ice, the water molecules need to be cooled down enough in order to get arranged into a crystal structure, which corresponds to the state of minimal inner energy. The freezing process starts with nucleation (lat. "nucleus" = seed), forming a stable cluster consisting of water molecules. Clusters form and dissolve constantly with a lifetime of the order of $10^{-11}$ s, but only if water is cooled down enough and a cluster gets stable, nucleation starts there. This depends on the difference of the Gibbs energy of the surface and of the volume of a cluster which is shown in Figure 3.13 in dependence of the number of water molecules $i$ in the cluster.

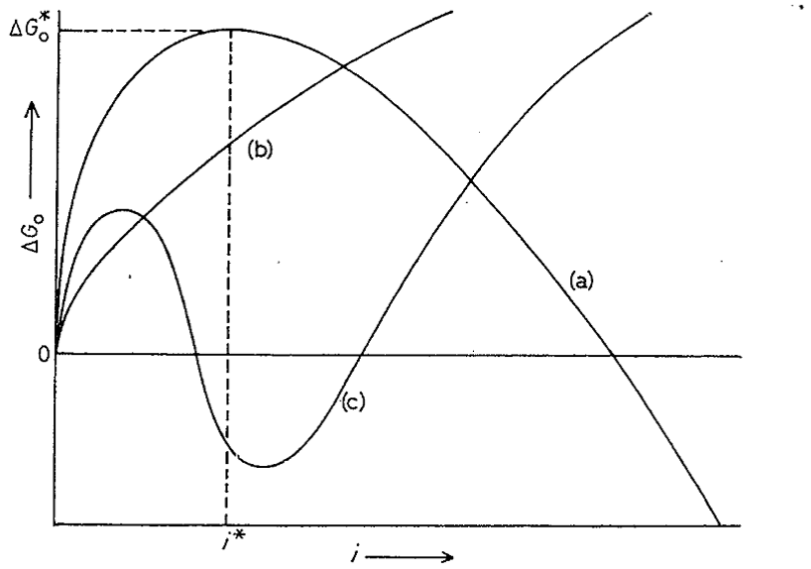


Figure 3.13.: Gibbs energy change $\Delta G_0$ at standard conditions of a cluster containing i water molecules: a) in an ice-like (crystal) structure, b) in a non ice-like (random) structure and c) in a structure giving optimum bonding when small in size. In all cases the temperature is assumed to be below 0 °C and the curves only have meaning for integral i. Reproduced from Ref [172] with permission of Science Reviews 2000 Ltd.

If the number of water molecules in the cluster is smaller than the critical number ($i < i^*$), further molecule addition increases the difference of the Gibbs energy, the cluster becomes instable and dissolves. Only if more molecules than the critical number at the corresponding temperature have accumulated in the cluster ($i > i^*$), the thermodynamic nucleation barrier has been overcome. As further incorporation of water molecules lowers the difference of the Gibbs energy, the cluster becomes stable and turns into a nucleation seed [172]. The development of ice-like clusters into stable nuclei is not an equilibrium problem but rather one of kinetic growth and melting equations [172].

The thermodynamics of nucleation were described by Fletcher [172] with the model of a cluster consisting of $i$ water molecules. These molecules have a lower Gibbs energy $G$ than an average molecule in the bulk liquid. The molecules at the surface of the cluster contribute positively to the difference of the Gibbs energy proportional to the factor $i^2$ in order to create the surface, whereas the molecules in the bulk volume of the cluster lower the difference of the Gibbs energy proportional to the factor $i^3$. A cluster has a

total Gibbs energy, relative to the same number of $i$ molecules in the bulk liquid, of [172]:

$$\Delta G = A \cdot i^2 - B \cdot i^3. \tag{3.38}$$

The constants $A$ and $B$ depend on the temperature and form of the cluster [172].

If the cluster is approximated as spherical, the Gibbs energy difference can be rewritten as [172]:

$$\Delta G = 4\pi r^2 \gamma_{\mathrm{IW}} - \frac{4}{3}\pi r^3 \Delta G_{\mathrm{V}}. \tag{3.39}$$

Here, $r$ is the radius of the spherical cluster, $\gamma_{\mathrm{IW}}$ is the ice-water interfacial energy and $\Delta G_{\mathrm{V}}$ is the difference of the volumetric Gibbs energy. Maximization of $\Delta G$ using the average volumetric entropy of fusion $\overline{\Delta S_{\mathrm{f,V}}}$ over the supercooling range $\Delta T$ for the difference of the volumetric Gibbs energy of fusion $\Delta G_{\mathrm{f,V}}$ then gives the thermodynamic barrier for nucleation [172]:

$$\Delta G^* = \frac{16\pi\gamma_{\mathrm{IW}}^3}{3(\overline{\Delta S_{\mathrm{f,V}}}\Delta T)^2}. \tag{3.40}$$

If the difference of the volumetric Gibbs energy of fusion $\Delta G_{\mathrm{f,V}}$ is expressed with the difference of the volumetric enthalpy of fusion $\Delta H_{\mathrm{f,V}}$, the critical nucleation barrier becomes [168]:

$$\Delta G^* = \frac{16\pi\gamma_{\mathrm{IW}}^3}{3\left(\Delta H_{\mathrm{f,V}}\left(\frac{T_{\mathrm{m}}-T}{T_{\mathrm{m}}}\right)\right)^2}, \tag{3.41}$$

where $T_{\mathrm{m}}$ denotes the melting temperature.

### Nucleation rate of the classic model with constant $\theta_{\mathrm{IW}}$

The nucleation rate $J(T)$ of ice within a water droplet can be expressed as [168]

$$J(T) = K(T) \cdot A_{\mathrm{sl}} \cdot \exp\left(\frac{-\Delta G^*(T)}{\mathrm{k_B}T}\right), \tag{3.42}$$

where $K(T)$ is a kinetic factor representing the adsorption and integration of free water molecules into an ice embryo, $A_{\mathrm{sl}}$ is the solid-liquid contact area, $\Delta G^*(T)$ is the thermodynamically derived Gibbs energy barrier or combined volumetric and surface

work (for homogeneous or heterogeneous nucleation) for the formation of a stable ice embryo, $k_B$ is the Boltzmann constant and $T$ is the temperature [174]. The factor $K(T)$ is determined by the diffusivity of the water, which depends on temperature, liquid composition, impurities and thermodynamic boundaries [174]:

$$K(T) = \frac{n k_B T}{h} \cdot \exp\left(\frac{-\Delta F_{diff}(T)}{k_B T}\right), \tag{3.43}$$

where $n$, h and $\Delta F_{diff}$ are the number density of the water molecules at the ice nucleus/water interface ($n \approx 10^{19}$ m$^{-2}$), the Planck constant and the difference of the Helmholtz energy for diffusion of a water molecule across the water-ice embryo interface, respectively.

Two types of nucleation are possible. Homogeneous nucleation, where nucleation starts in the bulk phase, can be delayed until down to about -40 °C, if the system remains undisturbed. Heterogeneous nucleation is caused by either dissolved molecules or suspended particles, like dirt or a solid surface. An ice cluster with a particle on one side has a lower free energy than an independent ice cluster. Supercooling is also possible for heterogeneous nucleation, but usually not far below 0 °C. Then, the contact area, surface topography and chemistry of the particle or surface determine the nucleation temperature. The energy barrier of the heterogeneous nucleation $\Delta G^*_{hetero}$ is reduced by $f$ ($0 \leq f \leq 1$) compared to the homogeneous nucleation barrier $\Delta G^*_{homo}$:

$$\Delta G^*_{hetero}(T) = \Delta G^*_{homo}(T) \cdot f. \tag{3.44}$$

The factor $f$ depends on the surface energy (surface chemistry and surface topography) of the nucleation particle (or surface). With an increasing particle size and a reducing contact angle the factor $f$ decreases and the nucleation barrier is reduced towards zero. Then, no supercooling will be seen and nucleation will already occur at 0 °C [2].

For a given temperature, an ice nucleus must reach a critical stable radius $r_c$ for freezing to initiate and propagate [175]:

$$r_c = \frac{2\,\gamma_{IW}}{\Delta G_{f,V}}, \tag{3.45}$$

where $\gamma_{IW}$ is the ice-water interfacial energy and $\Delta G_{f,V}$ is the difference of the solid (ice) and liquid (water) volumetric Gibbs energy of fusion. At -25 °C, a critical nucleation radius of about 1.7 nm is reached [167].

### Nucleation rate of the model with a quasi-liquid interfacial layer and variable $\theta_{IW}$

The nucleation and freezing behavior of water drops has been extensively analyzed on nanostructured surfaces with various RMS roughness values [167]. The factor $f$ is dependent on the surface roughness radius of curvature $R$, which is not the RMS roughness of the surface, but the radius of curvature of every pit (concave structure) or bump (convex structure), and also on the ice-water contact angle $\theta_{IW}$ [174]. Therefore, the critical energy barrier for heterogeneous nucleation is not only a function of temperature, but also of the ice-water contact angle and the surface roughness [174]. According to the classical nucleation theory, the nucleation rate is strongly dependent on the surface nanostructures, if the surface roughness radius of curvature $R$ is in the range of $10r_c$ and below [174]. The factor $f$ in dependence of $x = R/r_c$ is shown in Figure 3.14 for concave ($f_c$) and for convex ($f_v$) nanostructures.

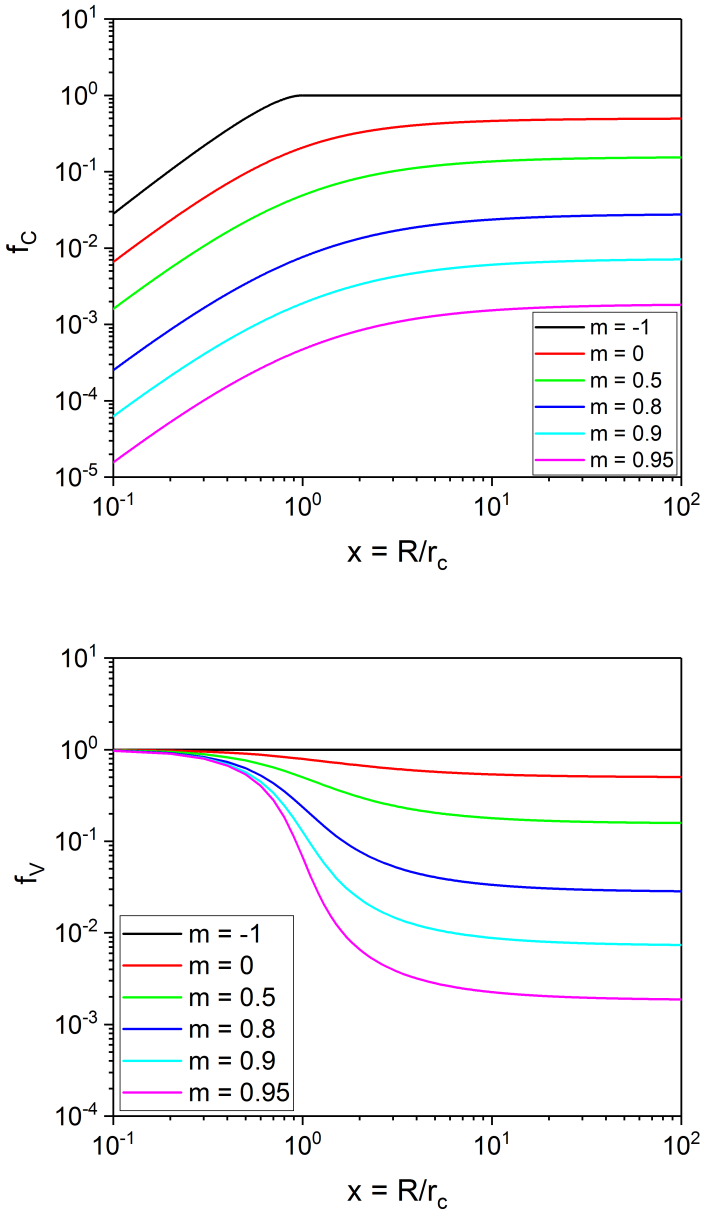


Figure 3.14.: Nucleation factor $f$ in dependence of the surface roughness radius of curvature and critical nucleation radius ($x = R/r_c$) for concave (pits, $f_c$) and for convex (bumps, $f_v$) spherical nanostructures, according to equations S22 and S23 in Ref [168]. The different curves are obtained for $\cos\theta_{IW}$ = -1 (black), 0 (red), 0.5 (green), 0.8 (blue), 0.9 (cyan), 0.95 (magenta), starting from the top and corresponding to $\theta_{IW}$ values of 180° to 18.2°. Adapted from Ref [167] with permission of the Royal Society of Chemistry.

In experiments with a low cooling rate of 0.31 K/min for the cooling of the water drops, surface and surroundings in a quasi thermodynamic equilibrium, very similar nucleation temperatures $T_N$ were measured by Eberle *et al.* on all of the nanostructured samples, although the RMS values and accordingly the surface roughness curvature radius values $R$ ($R = 1/H$, e.g. being large on a very smooth surface) varied over three orders of magnitude. From a practical point of view this is of advantage, because perfectly precise tuning of nanostructures is not needed for a robust icephobic surface. For the physical explanation, a model of the nucleation in a nanopit is created and a quasi-liquid layer, which is a disordered amorphous layer of a crystallized water cluster, is introduced between the ice embryo and the surface [167].

The nucleation rates and temperatures are determined by a quasi-liquid layer (LL) at the interface of the solid surface (S) and the ice nucleus (I), which forms in supercooled water. The surface roughness radius of curvature $R$ determines the thickness of this quasi-liquid layer and therefore the ice-water contact angle $\theta_{IW}$. A schematic model is shown in Figure 3.15.

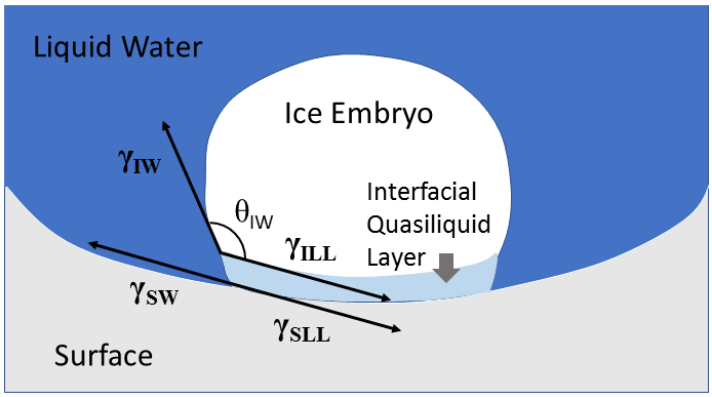


Figure 3.15.: Scheme of an ice nucleus with an interfacial quasiliquid layer in a concave nanoscale pit with roughness radius of curvature R surrounded by supercooled water and corresponding surface energies, denoted by $\gamma$ with indexes S = surface, LL = quasiliquid layer, I = ice, W = water. Adapted from Ref [167] with permission of the Royal Society of Chemistry.

This leads to an enhanced nucleation theory where the influence of the surface roughness curvature radius $R$, the quasi-liquid layer thickness and the variable ice-water contact angle $\theta_{IW}$ are included. The nucleation temperatures $T_N$ in dependence of the surface

roughness curvature radius $R$, predicted by the different nucleation models, are shown in Figure 3.16.

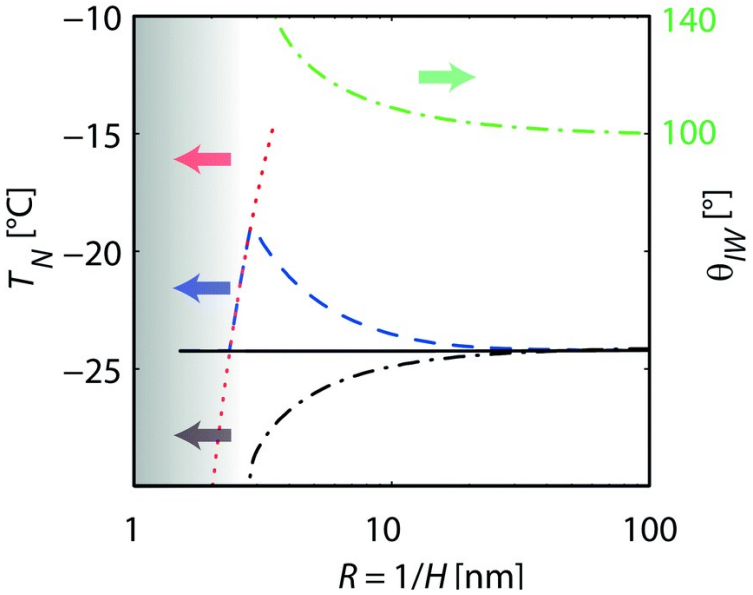


Figure 3.16.: $T_N$ calculations from nucleation theory as a function of roughness curvature radius for a substrate with 15 % of its area covered with concave nanoscale pits. The blue dashed line shows the results for constant $\theta_{IW} = 100°$ and the black solid line for $\theta_{IW}$ progressively increasing with decreasing roughness radius of curvature for the nanopits. The $\theta_{IW}$ variation (green dash-dotted line) occurs due to the presence of a quasiliquid layer (see [168], Section 6). The red dotted line shows the depressed melting point in the nanoscale pits according to the Gibbs-Thomson relation (see [168], Section 6) and the grey shaded area represents the range of roughness curvature radius where the melting point is depressed through confinement effects below the $T_N$ of a flat substrate. The black dash-dotted line shows the $T_N$ relationship for a hypothetical surface with 100 % of its area occupied by concave nanoscale pits and the coexisting bumps being perfectly sharp (R = 0). Reproduced from Ref [167] with permission of the Royal Society of Chemistry.

The dependence of the variable $\theta_{IW}$ on the nanometer roughness radius of curvature $R$, the quasi-liquid layer thickness and the temperature was derived in [168] and can be calculated. The temperature dependence of $\theta_{IW}$ is caused by the temperature dependent flexibility of the surface layer, e.g. the FDTS monolayer of Eberle *et al.* [168]. Real surfaces usually have a random distribution of surface roughness curvature radii. The variation of the ice-water contact angle $\theta_{IW}$ counteracts the curvature dependent ice

nucleation promotion in the nanoscale pits. Therefore, the nucleation rate is determined by the "flat" regions, with larger roughness radii above $10r_c$, leading to similar nucleation temperatures on differently nanostructured surfaces with about 15 % surface coverage of nanostructures.

For a small temperature change $\Delta T$ around a reference temperature $T_0$, the substrate specific nucleation rate was linearized and rearranged to [168]:

$$J(T_0 + \Delta T) \approx a \cdot \exp(-\lambda \cdot \Delta T), \tag{3.46}$$

where $a$ and $\lambda$ are substrate specific constants and $T_0$ is a temperature close to the expected nucleation temperature $T_N = T_0 + \Delta T$. The derivations for the substrate specific constants $a$ and $\lambda$ are shown in the appendix (see A.7).

The dynamic freezing experiments for this thesis with a constant cooling rate $\alpha$ for the cooling of the water drop and the surroundings in thermodynamic quasi steady state started at the temperature $T_S$ (0 °C). For the temperature change $\Delta T_S$ around $T_S$, the nucleation rate can also be expressed as [168]:

$$J(T_S + \Delta T_S) = a \cdot \exp(-\lambda(T_S - T_0 + \Delta T_S)) = a_S \cdot \exp(-\lambda \Delta T_S), \tag{3.47}$$

where $\Delta T = T_S - T_0 + \Delta T_S$ and $a_S = a \cdot \exp(-\lambda(T_S - T_0))$ were used. The temperature change is a linear relation of the cooling rate $\alpha_{cooling}$ and time from start of the experiment $t$, $\Delta T_S = \alpha_{cooling} \cdot t$.

### Prediction of nucleation temperature and nucleation delay time

For the dynamic freezing experiment, the stochastic freezing with a changing nucleation rate $J(T)$ caused by the changing temperature can be described by a nonhomogeneous Poisson process. By setting the probability distribution function of the frozen drop to 0.5 (median), the expected median nucleation temperature $T_N$ can be calculated [168]:

$$T_N = \frac{-1}{\lambda} \ln\left(1 - \ln(2)\frac{\lambda\alpha}{a_S}\right) + T_S = \frac{-1}{\lambda} \ln\left(-\alpha\lambda \ln(2)\right) + T_1, \tag{3.48}$$

where $T_1$ is the temperature at which the nucleation rate equals one, $J(T_1) = 1\,s^{-1}$.

This leads to the following relation for the nucleation rate at the expected median nucleation temperature [168]:

$$J(T_{\mathrm{N}}) = -\alpha \cdot \lambda \cdot \ln(2). \tag{3.49}$$

In the static freezing experiment, the surface is held at a constant temperature. For a constant temperature in the vicinity of the expected median nucleation temperature $T_{\mathrm{N}}$, it is convenient to rearrange the nucleation rate as [167]:

$$J(T_{\mathrm{N}} + \Delta T) = a \cdot \exp(-\lambda\, \Delta T), \tag{3.50}$$

where $\Delta T$ is the difference between $T_{\mathrm{N}}$ and the actual constant temperature.

By modeling the freezing with a homogeneous Poisson process, the expected nucleation delay time at a constant temperature for a surface with known expected median nucleation temperature $T_{\mathrm{N}}$ can be calculated as [168]:

$$\langle \tau(T) \rangle = \frac{1}{J(T)} = \frac{1}{J(T_{\mathrm{N}} + \Delta T)}. \tag{3.51}$$

This predicted value can be compared to the measured mean nucleation delay time $\tau = \frac{1}{n} \sum_{x=1}^{n} \tau_x$.

It was shown that the nucleation rate is negligible already a few degrees above the surface specific expected nucleation temperature [168]. Eberle *et al.* calculated that for a hierarchically structured, superhydrophobic surface with an expected median nucleation temperature of about -24 °C, a temperature rise of 1 K results in a nucleation rate decrease by a factor of 10. When they tested this surface at -21 °C ($\Delta T = 3$ K under ideal lab conditions), an extreme nucleation delay time of about 25 h was published in the literature. This corresponds well with the nucleation delay time $\langle \tau \rangle$ predicted for this surface by the theory [167].

For characterization of the icing behavior of the surfaces examined in this thesis, the nucleation (freezing) delay times at a constant temperature were determined in the static experiment (at $T_{\mathrm{N}} + \Delta T_{\mathrm{N}}$) and the nucleation temperatures $T_{\mathrm{N}}$ were determined

in the dynamic experiment (expected values calculated with $T_0 + \Delta T$ or $T_S + \Delta T_S$). The temperatures used for the theoretical calculations are shown in Figure 3.17.

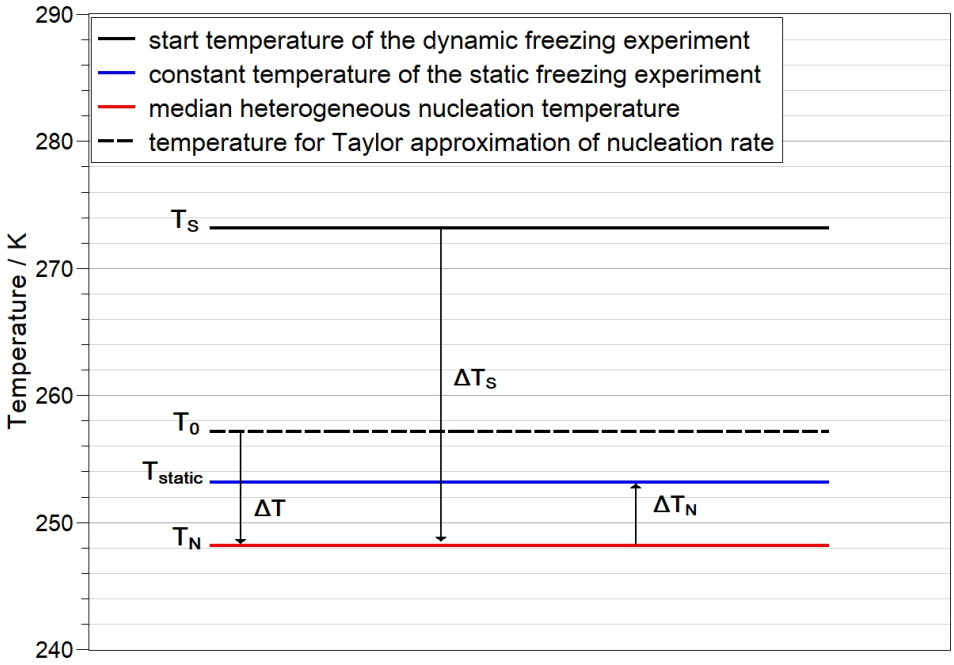


Figure 3.17.: Temperatures of the static and the dynamic icing experiment and theoretical relations of the Taylor approximation for calculation of the expected nucleation delay time $\langle \tau(T) \rangle$ and the expected nucleation temperature $T_N$. The arrows show the temperature step $\Delta T_i$ from the point of linearization to the temperature of interest.

Hierarchically structured surfaces have a lower nucleation temperature than only nanostructured surfaces, as the effective water drop surface contact area is reduced due to the Cassie-Baxter state. The difference of nucleation temperature can be expressed as [167]:

$$T_{N,Hierarchical} - T_{N,Nano} \approx \frac{-1}{\lambda} \cdot ln\left(\frac{A_{Nano}}{A_{Hierarchical}\, f_{sl}}\right), \tag{3.52}$$

where $A$ denotes the solid-liquid contact area, $f_{sl} = \eta \cdot A_T$ (equals $2/(\sqrt{3}P^2) \cdot \pi r^2$ in case of the hexagonally arranged cylindrical microstructures) is the solid-liquid fraction of the apparent droplet contact area touching the top area of the microstructures, and $\lambda$ is a substrate-specific constant. Eberle *et al.* found a reduction of $T_N$ of about 2.5 °C when going from nanostructured to hierarchically structured surfaces [167].

### The freezing process

If both the freezing and the melting point are reduced to lower temperatures than 0 °C, this is called a freezing point depression and caused by the colligative effect, e.g. of ions from salts or gases in solution. For deionized water on functionalized surfaces, only the freezing temperature can be lowered through supercooling, whereas the equilibrium melting temperature stays at 0 °C. This is called the thermal hysteresis [29].

During crystallization, the latent heat is released and transferred into the surroundings by the heat transfer processes, most of it over the surface as the heat conduction of the surface is higher than the heat conduction of the air, the heat radiation of the water and the natural heat convection with no externally applied gas flow. When recording the temperature of a freezing drop, a sharp temperature rise at the beginning of the crystallization is observed. This is called recalescence [176], during which the crystal growth is driven by the supercooling. It happens directly after nucleation and is caused by the sudden crystallization of a part of the supercooled water drop and the corresponding release of latent heat or heat of fusion $\Delta h_\mathrm{f} = 333\,\mathrm{kJ/kg}$. During the sudden recalescence step, ice forms almost instantly in form of many thin spicules.

During the following crystallization phase the remaining liquid material is turned into a crystal structure at the equilibrium melting temperature $T_\mathrm{m}$ (0 °C). The crystallization front moves from the cold ground upwards. The crystallization time depends on the heat transfer of the latent heat out of the water or ice through the surface. Once the crystallization is finished, the ice crystal is cooled down further to ambient temperature. Images of these steps are shown in Figure 3.18 and a schematic temperature curve is shown in Figure 3.19.

With the mass of a water drop and the specific enthalpy of fusion for water ($\Delta h_\mathrm{f} = 333\,\mathrm{kJ/kg}$), the released energy of one water drop during the freezing experiment can be calculated as $\Delta H_\mathrm{f} = \Delta h_\mathrm{f} \cdot m$. This energy is conducted mainly through the surface ($\lambda_\mathrm{PU} = 0.22\,\mathrm{W/(m{\cdot}K)}$) because the heat conduction through air is lower by one order of magnitude ($\lambda_\mathrm{air} = 0.0262\,\mathrm{W/(m{\cdot}K)}$). Heat transfer rates by convection and radiation are lower as well and therefore neglected for this estimation.

The heat transfer during crystallization of a water drop is determined by the heat transfer coefficient $\alpha$, the actual solid-liquid contact area $A_\mathrm{sl} = rf \cdot A_\mathrm{f}$, the temperature

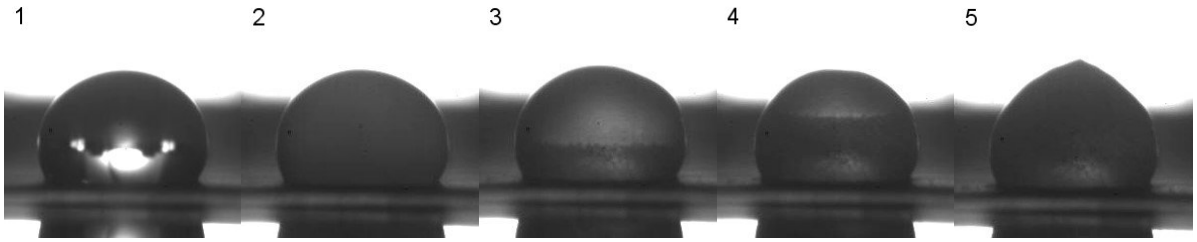


Figure 3.18.: Images of the important steps during freezing of a water drop, 1) cooling of the liquid drop, 2) recalescence step, 3)/4) crystallization phase with crystallization front moving up from the bottom, 5) cooling of the frozen drop.

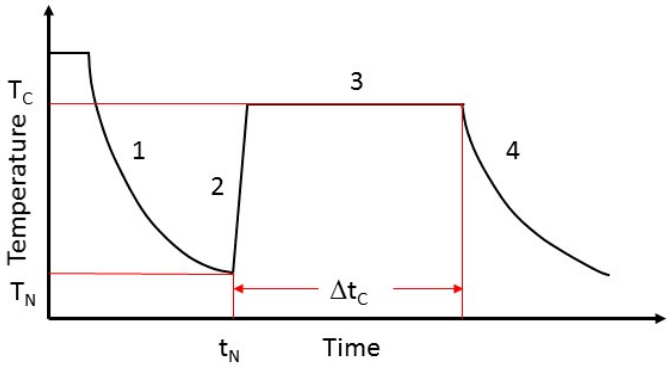


Figure 3.19.: Schematic temperature curve of a freezing water drop, 1) cooling of the liquid (water), 2) recalescence step, 3) crystallization phase, 4) cooling of the solid (ice). The data points of nucleation temperature $T_\mathrm{N}$, equilibrium melting or crystallization temperature $T_\mathrm{C}$, nucleation time $t_\mathrm{N}$ and crystallization time (duration) $\Delta t_\mathrm{C}$ are indicated.

difference $\Delta T$ between water equilibrium melting temperature $T_\mathrm{m} = 273.15\,\mathrm{K}$ and surface nucleation temperature $T_\mathrm{N}$ and the crystallization time $\Delta t_\mathrm{C}$:

$$\Delta Q = \Delta H_\mathrm{f,C} = \alpha \cdot A_\mathrm{sl} \cdot \Delta T \cdot \Delta t_\mathrm{C}. \tag{3.53}$$

The recalescence is driven by the supercooling of the water drop and causes the sudden freezing of a part of the water drop volume $V_\mathrm{d}$ corresponding to a part of the latent heat $\Delta H_\mathrm{f}$. This volume part $V_\mathrm{recalescence}$ and part of latent heat $\Delta H_\mathrm{f,recalescence}$ can be

calculated for water in dependence of the nucleation temperature $T_N$ [176]:

$$V_{\text{recalescence}} = V_d \cdot \frac{c_l \rho_l}{\rho_s} \cdot \frac{T_m - T_N}{\Delta h_f},$$
$$\Delta H_{f,\text{recalescence}} = V_{\text{recalescence}} \cdot \rho_s \cdot \Delta h_f. \tag{3.54}$$

The remaining liquid volume $V_C = V_d - V_{\text{recalescence}}$ is frozen by crystallization because of heat transfer across the ice-surface interface. Therefore, the crystallization front is moving upwards from the surface. The latent heat to be transferred after the recalescence step is $\Delta H_{f,C} = \Delta H_f - \Delta H_{f,\text{recalescence}}$. Therefore, the crystallization time $\Delta t_C$ can be calculated as:

$$\Delta t_C = \frac{\Delta H_{f,C}}{\alpha \cdot A_{sl} \cdot \Delta T},$$
$$\Delta t_C = \frac{\Delta H_{f,C}}{\alpha \cdot A_{sl} \cdot (T_m - T_N)}. \tag{3.55}$$

The total freezing time consists of the nucleation time (time until nucleation occurs) and the crystallization time. The nucleation time is combined of the time for cooling to surface temperature and the freezing delay time.

### 3.2.5. Heat transfer mechanisms for water drop freezing tests

Heat ($Q$) is the thermal form of energy, together with the inner work of volume change ($W_i$) it describes the inner energy ($U$) of a system:

$$U = Q + W_i = m \cdot c \cdot T + p \cdot V. \tag{3.56}$$

Here, $m$ is the mass, $c$ is the specific heat capacity, $T$ the temperature, $p$ the pressure and $V$ the volume of the system, e.g. of a water drop. The heat can be transferred by heat conduction, by convective heat transfer or by heat radiation. Heat conduction (no mass transport involved) and convective heat transfer (mass transport connected) determine the freezing process of a water drop, because its latent heat is transferred away through

the surface material and the surrounding air. Heat radiation is used for measuring the water drop temperature during cooling and freezing by an infrared camera.

### Convective heat transfer

Convective heat transfer is the transport of heat connected to mass transport, e.g. by molecules of a moving fluid in contact with a surface. There is "forced convection", if the fluid is moved by external forces, e.g. a pump, and "natural convection" which is caused by gravity and the presence of density or temperature gradients inside of the fluid or gas. The heat transfer at the interface of a surface and a fluid is proportional to the heat transfer coefficient $\alpha_i$. It depends on the fluid velocity and type of flow (laminar or turbulent), materials, geometry and surface properties and can be approximated by correlations including dimensionless numbers like the Nusselt number (Nu). The heat transfer is then calculated as:

$$\dot{Q} = \alpha_i \cdot A \cdot (T_\mathrm{f} - T_\mathrm{s}) = \alpha_i \cdot A \cdot \Delta T, \tag{3.57}$$

where $A$, $T_\mathrm{f}$ and $T_\mathrm{s}$ are the area, the temperature of the fluid and of the surface, respectively.

### Heat conduction

Heat is transported through any material by heat conduction which is similar to the diffusion mechanism. It always flows along the path with a temperature gradient. The heat flux is determined by the heat conduction coefficient $\lambda_i$ inside of a material, the heat transfer coefficients $\alpha_i$ at the interfaces and the thickness $d_i$ of a material. In the general three dimensional case, it is described by the surface specific heat flux density $q$:

$$\vec{q} = -\lambda_i \cdot grad\, T. \tag{3.58}$$

In the one dimensional simplified case of a solid body with two parallel interfaces it is described by Fourier's law:

$$\dot{Q} = \frac{\lambda_i}{d_i} \cdot A \cdot \Delta T. \tag{3.59}$$

For two or more heat transfer processes in series, the heat transfer coefficients have to be added inversely. Therefore, the heat conduction through a layer with thickness $d_i$ and two interfaces, denoted by indexes 1 and 2, is:

$$\dot{Q} = \left( \frac{1}{\frac{1}{\alpha_1} + \frac{d_i}{\lambda_i} + \frac{1}{\alpha_2}} \right) \cdot A \cdot \Delta T = k \cdot A \cdot \Delta T. \tag{3.60}$$

Here, $k$ is the total thermal transmittance.

### Heat radiation

Heat radiation is electromagnetic radiation in the infrared wavelength region, where near (NIR, 0.75 µm to 3 µm), medium (MIR, 3 µm to 6 µm), far (FIR, 6 µm to 15 µm) and extreme (15 µm to 100 µm) infrared radiation can be separated. A black body has the maximum emissivity of one. For real objects, the emissivity is between 0 and 1. Distilled water and ice both have an emissivity of 0.96, whereas white-colored snow reflects more of the heat radiation and absorbs or emits a smaller part of it, therefore it has an emissivity of 0.8 to 0.85 [177]. A polished surface, like the icing test chamber aluminum surfaces, has an emissivity of below 0.1, therefore not disturbing the water drop heat radiation for IR temperature measurement by emission. The amount of absorption is equal to the amount of emission which is stated by Kirchhoff's law of thermal radiation. The total heat radiation properties of an object consist of absorption ($\alpha$) = emission ($\epsilon$), reflection ($\rho$) and transmission ($\tau$), which add up to 1:

$$1 = \alpha_\lambda + \rho_\lambda + \tau_\lambda, \tag{3.61}$$

where $\lambda$ denotes the radiation wavelength.

The emission of an object is defined as its emitted radiation $W_\lambda$ compared to the radiation of a blackbody of same temperature $W_{\lambda,black}$:

$$\epsilon_\lambda = \frac{W_\lambda}{W_{\lambda,\mathrm{black}}}. \tag{3.62}$$

The spectral distribution of the radiation of a blackbody is described by the law of

Planck:

$$W_{\lambda,\text{black}} = \frac{2\,\pi\,\text{h}\,\text{c}^2}{\lambda^5\ (e^{\text{h}\,\text{c}/\lambda\,\text{k}_\text{B}\,T} - 1)} \times 10^{-6}\ , \tag{3.63}$$

where h, c, $k_B$ and $T$ denote the Planck constant, the speed of light, the Boltzmann constant and the temperature, respectively.

Therefore, only radiation in the infrared region, near the maximum radiative emission at low temperature, should be used for measurement of low temperature objects. The law of Wien describes the wavelength of maximum radiative emission (in µm) for a certain temperature $T$ (in K), corresponding to the visible color of an object:

$$\lambda_\text{max} = \frac{2898}{T}\ . \tag{3.64}$$

By integration of the law of Planck over all the wavelengths, one obtains the total radiation of a black body, the law of Stefan-Boltzmann:

$$W_\text{black} = \sigma \cdot A \cdot T^4\ , \tag{3.65}$$

where $\sigma$ is the Stefan-Boltzmann constant and $A$ is the surface of the object.

For a real, gray object, the emitted energy is determined by its emissivity $\epsilon$:

$$W = \epsilon \cdot \sigma \cdot A \cdot T^4\ . \tag{3.66}$$

For a correct temperature measurement by an infrared (IR) camera, some options have to be set correctly. These are the object emissivity ($\epsilon$), the temperature of the surrounding atmosphere that is reflected from the object ($T_\text{refl}$), the measurement distance, the relative humidity, the temperature of the surrounding atmosphere ($T_\text{atm}$) and the transmission coefficient ($\tau$) of any external optical components and the atmosphere in the measurement pathway between object and camera [177].

The total radiation received by the IR camera is made up of the actual object radiation $W_\text{obj}$, the reflected radiation of the surroundings $W_\text{refl}$ and the atmospheric radiation $W_\text{atm}$ [177]:

$$W_\text{tot} = \epsilon\,\tau\,W_\text{obj} + (1-\epsilon)\,\tau\,W_\text{refl} + (1-\tau)\,W_\text{atm}. \tag{3.67}$$

The received total radiation $W(T)$ creates a voltage signal $U$ in the IR camera with a linear relationship [177]:

$$U = C \cdot W(T) \ , \tag{3.68}$$

where $C$ is constant defined by the calibration of the camera.

Equation 3.67 can be multiplied by the constant $C$. After replacement with the voltages $U$ and rearrangement, it becomes the general object temperature measurement equation [177]:

$$U_{\mathrm{obj}} = \frac{1}{\epsilon\,\tau} U_{\mathrm{tot}} - \frac{1-\epsilon}{\epsilon} U_{\mathrm{refl}} - \frac{1-\tau}{\epsilon\,\tau} U_{\mathrm{atm}} \ . \tag{3.69}$$

# 4. Experimental methods for the surface functionalization and analysis of the PU films

In this chapter, the materials and experimental methods for the surface functionalizations are given. The PU films, relevant engineering material surfaces and commercial anti-ice surface coatings, which were characterized for their wetting, anti- and de-icing behavior in this thesis, are listed in the first section (4.1). Afterwards, the hot embossing (4.2) and the plasma processes (4.3) are described. Finally, the methods of surface analytics (4.4) and the methods for measurement of the stability of the surface functionalizations (4.5) are given.

## 4.1. Materials: polyurethane films, competing technical materials and commercial anti-ice coatings

The PU elastomer film 8674 from 3M was chosen because it is used in aviation for protection of wing surfaces. The thermoplastic PU films LPT 4800 and LPT 4802 by epurex films, Covestro (formerly Bayer MaterialScience) are newly developed (laboratory products) aliphatic Polyether-PU films with better UV stability compared to aromatic PU films. They are transparent and well suited for large scale, visible areas. The thermoplastic PU films 63615 and 63630 (superseded by 63330) from CMC Klebetechnik are of the aliphatic Polyether-PU type. The PU films are produced by Gerlinger Industries, Netzschkau, Germany, and the adhesive layer on the back is applied by CMC Klebetechnik. They are more economical and therefore the best choice for surface functionalization on a larger scale in the future. Table 4.1 shows the different PU films that were available for this work.

Table 4.1.: Polyurethane films and their technical properties.

| Company<br>- | Product name<br>- | Temperature range<br>(°C) | Density<br>(kg/m$^3$) | Hardness<br>(Shore) | Film thickness<br>(µm) | Adhesive thickness<br>(µm) | PU film / adhesive type<br>- |
|---|---|---|---|---|---|---|---|
| 3M | 8674 | -40 to 135 | 1115 | - | 150 | 50 | PU elastomer / acrylate |
| Epurex Films, Covestro | LPT 4800 TT | -40 to 130 | 1140 | A 85 | 200 | - | aliphatic, thermoplastic Polyester-PU / - |
| Epurex Films, Covestro | LPT 4802 T | -40 to 110 | 1120 | D 55 | 200 | - | aliphatic, thermoplastic Polyether-PU / - |
| CMC Klebetechnik | 63615 | -40 to 120 | 1101 | A 90 | 150 | 55 | aliphatic, thermoplastic Polyether-PU / acrylate |
| CMC Klebetechnik | 63630 | -40 to 120 | 1512 | A 98 | 300 | 55 | aliphatic, thermoplastic Polyether-PU / acrylate |
| CMC Klebetechnik | 63330 | -40 to 120 | 1101 | A 92 | 300 | 55 | aliphatic, thermoplastic Polyether-PU / acrylate |

The microstructuring and plasma-coating functionalizations were done on the PU films from CMC Klebetechnik, Germany. The topography of the PU films was modified by thermal imprinting of micrometer-sized structures, subsequently thin hydrophobic polymer layers were deposited by a PECVD process. For the other PU films, the wetting, de- and anti-icing characterization results will be given only of the untreated PU films for comparison in this thesis.

The relevant technical materials are shown in Table 4.2 and the commercially available anti-ice coatings are shown in Table 4.3. They were analyzed for their wetting, de- and anti-icing behavior for comparison with the functionalized PU surfaces. The copper,

aluminum and titanium plates were cut out and finished in the workshop. A flat glass microscope slide (Menzel glass) was used as glass surface. The epoxy resin surface was prepared in order to resemble a carbon-fiber reinforced polymer (CFRP) surface. The resin and the hardener components were mixed at a ratio of 1:1 and cast onto a flat glass microscope slide, where they cross-linked over night at room temperature. The commercial anti-ice surface samples consist of aluminum slides with various coatings of a thickness of several micrometers. They were provided for a former project about ice adhesion on surfaces by the project partners.

Table 4.2.: Technical material surfaces.

| Company | Material | Type |
|---|---|---|
| Nowofol | Fluorinated ethylene propylene (Nowoflon FEP) | film |
| Nowofol | Perfluoroalkoxy alkane (Nowoflon PFA) | film |
| Thermo Fisher Scientific | Glass, silicon oxide at surface (SiOx) | float glass |
| - | Copper (Cu), copper oxide at surface (CuOx) | metal sheet |
| - | Aluminum (Al), aluminum oxide at surface (AlOx) | metal sheet |
| - | Titanium (Ti), titanium oxide at surface (TiOx) | metal sheet |
| Henkel | UHU 2 component epoxy resin (CFRP surface model) | coating |

Table 4.3.: Commercial anti-ice coatings.

| Company<br>- | Product<br>- | Material<br>- | Type<br>- | Thickness<br>(µm) |
|---|---|---|---|---|
| provided by Airbus Group (EADS) | PUR Topcoat | hydrophobic PU | coating | 25 |
| provided by Airbus Group (EADS) | System 5 GH60-5 | Basecoat / Clearcoat system, active nanostructured PU | coating | 50 |
| NuSil Technology | Nusil R2180 | Silicone | coating | 20 |
| MicroPhase Coatings | IcePhob ESL | Epoxy based coating with embedded freezing point depressing salt particles | coating | 200 |

## 4.2. Microstructuring by hot embossing

A hot embossing technique was used in order to imprint microstructures onto the surface of the polyurethane films.

### 4.2.1. Microstructures

Overall four chromated copper plates with small, separated fields differently micropatterned by laser ablation were acquired from Schepers GmbH, Vreden, Germany and were used as hot embossing stamps. The micromachined pattern is the negative of the final microstructures. Simple designs of standalone microstructures were chosen because of economic production by laser micromachining. Microstructures of cylindrical, elliptical and linear shape were chosen in order to find the best shape in terms of stability, hydrophobicity and icephobicity. The geometric values, namely the diameter ($D$), height ($h$) and distance (pitch $P$) between each structure, were varied in order to analyze which structure creates the most stable, hydrophobic and icephobic surface. The optimal combination of high superhydrophobicity, requiring small diameters and pitch values, and of high stability, which could be improved by larger diameters, needed to be found. The

cylindrical and elliptical microstructures on stamp 1, 2 and 3 are arranged hexagonally for maximum density on the surface. For a larger surface functionalization for various stability and outdoor application tests, additional stamps of DIN A5 and DIN A4 size were acquired. On these stamps, the structures were arranged quadratically because of faster and more economic production. Table 4.4 gives an overview of the acquired hot embossing stamps used as molds.

Table 4.4.: Microstructured stamps for hot embossing.

| Stamp | Company | Fields | Size | Type of microstructures | Arrangement of structures |
|---|---|---|---|---|---|
| Stamp 1 | Schepers | 60 | 1 x 1 cm | cylinders, ellipses, lines | hexagonal |
| Stamp 2 | Schepers | 6 | 2 x 2 cm | cylinders, ellipses | hexagonal |
| Stamp 3 | Schepers | 18 | 2 x 2 cm | cylinders, ellipses, lines | hexagonal |
| Stamp 4 #1 | Schepers | 1 | DIN A5 | cylinders | quadratic |
| Stamp 4 #2 | Schepers | 1 | DIN A4 | cylinders | quadratic |

The microstructured fields on the stamps were unambiguously named by using capital letters C for cylinders, E for ellipses and L for lines, and then adding an increasing number, e.g. C1, C2, etc. The assignment of the microstructure names to the different stamps and their geometrical parameters are given in the appendix (A.2).

### 4.2.2. Glass transition and melting temperature

Differential scanning calorimetry (DSC) was used in order to determine the glass transition and melting temperatures of the different PU films. The DSC 200 F3 Maia from NETZSCH, Selb, Germany, was used. Two complete runs of heating and cooling were made for each PU film sample. Each run consisted of one heating cycle up to a temperature of 160 °C and one cooling cycle down to -30 °C at a rate of 10 K/min [178]. The glass transition and melting temperatures were determined from the heating cycle of the first run.

### 4.2.3. Hot embossing process

Several stamping experiments with different temperatures (80 °C to 130 °C), different pressures (30 bar to 150 bar) and varied imprinting duration times (5 s to 10 min) were done in order to find the optimal process parameters. The first experimental set in order to determine the hot embossing parameters was made on a hydraulic press (Bike Machinery, Bagnatica, Italy) at various temperatures and pressures with a process time of 10 minutes. Further experiments for parameter optimization were carried out on a pneumatic press (LabEcon 150, Fontijne Grotnes, Vlaardingen, Netherlands). This pneumatic press had a plate area of 320 mm x 320 mm, a maximum closing force of 150 kN and a maximum temperature of 300 °C, separately adjustable for the upper and lower plate. Over the course of time, the older stamps were replaced by newer stamps with smaller microstructure dimensions or larger microstructured area (DIN A4). However, the most superhydrophobic microstructures on each stamp still had similar dimensions with diameters of 70 µm or below. The final samples were made at 150 bar and 85 °C with a process time of 5 minutes. After embossing, the stamp and PU film were removed from the press, were let cool down to about 40 °C and then the imprinted PU film was removed from the stamp. The experimental sets for optimization of the hot embossing parameters are shown in Table 4.5.

The hot embossing process is schematically drawn in Figure 4.1.

Table 4.5.: Process parameters for hot embossing.

| Stamp<br>- | Process<br>- | Press<br>- | Temperature<br>(°C) | Pressure<br>(bar) | Time<br>(s) |
|---|---|---|---|---|---|
| Stamp 1 | parameter determination | BikeMachinery, Bike Machinery (hydraulic) | 100, 110, 115 | 30, 50, 80 | 600 |
| Stamp 2 | temperature optimization | LabEcon 150, Fontijne Grotnes (pneumatic) | 85 to 90 | 150 | 600 |
| Stamp 3 | process time optimization | LabEcon 150, Fontijne Grotnes (pneumatic) | 85 | 150 | 5 to 600 |
| Stamp 4 | optimization for uniform pressure distribution on DIN A4 scale | LabEcon 150, Fontijne Grotnes (pneumatic) | 85 | 150 | 300 |

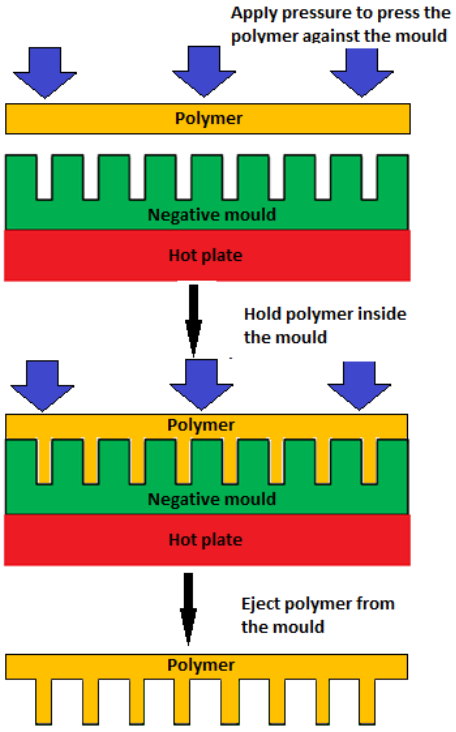


Figure 4.1.: Scheme of the hot embossing process for microstructuring of polyurethane films, reprinted from [1].

## 4.3. Plasma processes

Once the polymer films were imprinted, they were plasma-coated by a PECVD process. Plasma coated silicon wafers were used as supporting samples for the thickness and chemical composition analysis of the coatings.

### 4.3.1. PECVD process parameters

Both fluorocarbon ($C_XF_Y$) and silicone-like plasma polymers were deposited on the PU film samples and additionally on silicon wafers for further analysis. The aim was a film thickness of about 200 nm. Trifluoromethane ($CHF_3$), Hexafluoropropylene ($C_3F_6$, purity ≥99.0 %) and Octafluorocyclobutane ($C_4F_8$, purity ≥99.998 %) were used as precursor gases to generate fluorocarbon plasma polymer coatings. Hexamethyldisiloxane (HMDSO, purity ≥98.5 %) was evaporated and used together with nitrogen (Air Liquide Deutschland GmbH, Düsseldorf, Germany) for a silicone-like plasma coating. The process parameters were adapted from [179] and are listed with the corresponding precursors in Table 4.6.

Table 4.6.: PECVD coating parameters.

| Gas<br>- | Company<br>- | CAS Nr.<br>- | Gas flow<br>(sccm) | Pressure<br>(mbar) | RF power<br>(W) |
|---|---|---|---|---|---|
| $CHF_3$ | Air Liquide Deutschland GmbH, Düsseldorf, Germany | 75-46-7 | 10, 30 | 0.2 | 50, 100 |
| $C_3F_6$ | Chempur Feinchemikalien GmbH, Karlsruhe, Germany | 116-15-4 | 20, 30 | 0.1 to 0.15 | 50 |
| $C_4F_8$ | Linde AG, Pullach, Germany | 115-25-3 | 10, 20 | 0.1 to 0.2 | 50 |
| HMDSO/$N_2$ | Chempur Feinchemikalien GmbH, Karlsruhe, Germany | 107-46-0 | 7 / 100 | 0.09 to 0.18 | 60, 200 |

The leakage rate of the HMDSO mass flow controller was about 2.5 sccm which results in a total HMDSO gas flow of about 10 sccm.

### 4.3.2. Plasma etching process parameters

The processes of plasma coating and plasma etching were combined in order to create a hierarchically micro-nanostructured surface. As no information on the adhesion of the plasma polymers to PU was available, both the etching of the plasma polymer after coating as well as the direct etching of the polyurethane substrate before coating was tested. The combined process of plasma coating and etching of the plasma polymer is schematically shown in Figure 4.2.

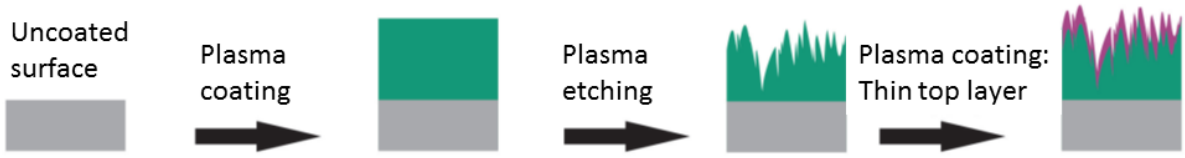


Figure 4.2.: Subsequent coating and etching processes for creation of a nanostructured, hydrophobic surface, scheme adapted from [2].

At first, the PU surface was coated with a plasma polymer. Next, this polymer coating was exposed to an argon (Air Liquide Deutschland GmbH, Düsseldorf, Germany) plasma (ionic etching) or oxygen (Air Liquide Deutschland GmbH, Düsseldorf, Germany) plasma (chemical etching) with the aim of creating nanostructures at the surface. Finally, the etched surface was coated again with a thin plasma polymer layer in order to restore the hydrophobic surface chemistry, because the etching process leaves a slightly hydrophilic surface. Etching of the PU surfaces was done by applying an oxygen plasma because of the higher etching rate. The process parameters are listed in Table 4.7 (pp = plasma polymer).

Table 4.7.: PECVD etching parameters.

| Surface<br>- | Gas<br>- | Gas flow<br>(sccm) | Pressure<br>(mbar) | RF power<br>(W) | Time<br>(min) |
|---|---|---|---|---|---|
| pp($C_3F_6$) / pp(HMDSO) | Ar | 50 / 100 | 0.28 / 0.2 | 100 | 10 |
| pp($C_3F_6$) / pp(HMDSO) | Ar | 50 / 100 | 0.38 / 0.26 | 200 | 10 |
| pp($C_3F_6$) / pp(HMDSO) | Ar | 50 / 100 | 0.38 / 0.26 | 300 | 10 |
| pp($C_3F_6$) | $O_2$ | 30 | 0.2 | 100 | 1 |
| PU | $O_2$ | 30 | 0.27 | 200 | 3 |

### 4.3.3. PECVD laboratory setup

Both the fluorocarbon reactor and the HMDSO reactor were of the low pressure, capacitively coupled plasma (CCP) setup type. The reactors were of the rectangular DIN A3 size. The top and bottom electrodes were parallely arranged, flat plates separated by 40 mm (FC reactor) and 70 mm (HMDSO reactor). The process gases are led into the reactor chamber through a gas shower at the top for uniform gas distribution and flow. The exhaust gases from the reactors were frozen in a cooling trap which was cooled down by liquid nitrogen (-196 °C). The plasma chamber was evacuated to a base pressure of $10^{-2}$ mbar to $10^{-3}$ mbar before the PECVD process was started. By turning on the gas flow and the RF power (13.56 MHz) a working pressure of 0.1 mbar to 0.2 mbar (depending on the reactor and process parameters) was set.

The CCP reactor is shown schematically in Figure 4.3.

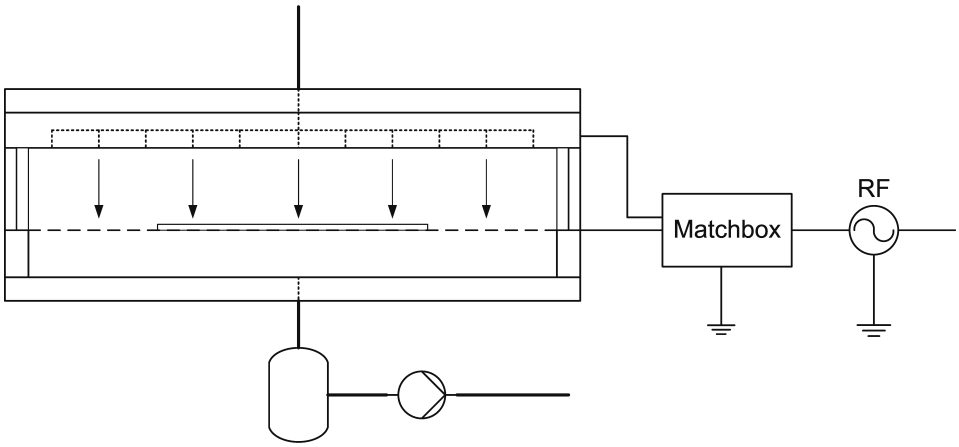


Figure 4.3.: Scheme of a capacitively coupled plasma reactor.

A scheme of a general PECVD laboratory system is shown in Figure 4.4.

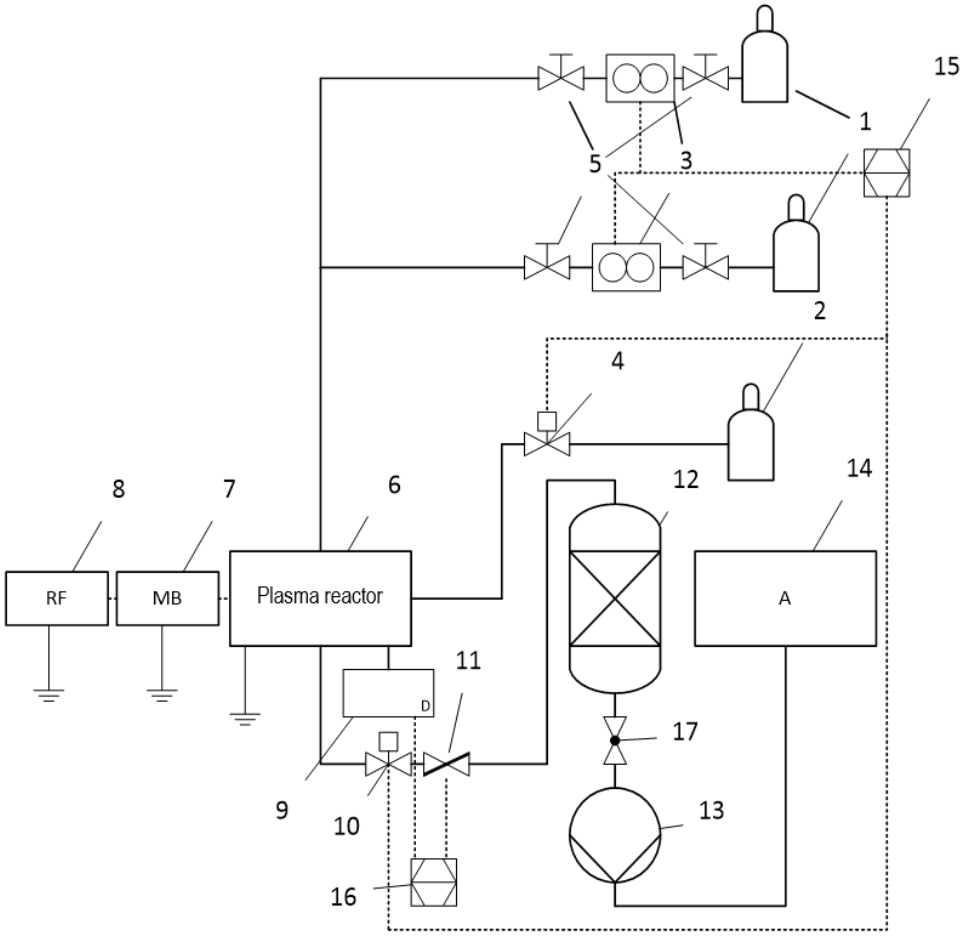


Figure 4.4.: Scheme of the PECVD laboratory setup. 1: process gas (precursor), 2: inert gas (Ar), 3: gas / mass flow controller (MFC), 4: magnetic valve, 5: screw valve, 6: DIN A3 plasma reactor, 7: impedance matching network, 8: RF generator, 9: pressure sensor, 10: magnetic valve, 11: throttle valve, 12: cooling trap, 13: rotary pump, 14: exhaust gas line, 15: gas control unit, 16: pressure / throttle control unit, 17: manual valve. Adapted from [180].

### Components of the fluorocarbon plasma reactor

At the fluorocarbon reactor, the vacuum was generated by a rotary pump (Alcatel Hochvakuum Technik GmbH, Wertheim, Germany). The process gas flows were regulated by mass flow controllers (MFC) with a range of 200 sccm (MKS Instruments, Andover, USA), which were connected to a multi gas controller type 647C (MKS Instruments, Andover, USA). Two pressure sensors were used, a Convectron Gauge D with display unit 375 Convectron (Granville-Phillips) and a Baratron sensor (MKS In-

struments, Andover, USA) connected to the pressure control unit. The pressure was regulated by a throttle valve (VAT, Sennwald, Switzerland) connected to a MKS pressure control unit of the 600 series type (MKS Instruments, Andover, USA). The top and bottom electrodes were connected to the RF generator Cesar (dressler Hochfrequenztechnik GmbH, Stolberg, Germany) which supplied the power for creating the plasma. Impedance matching was carried out manually with a matchbox (MB IV A, WM. M. NYE Company Inc., Pries River, USA), which minimizes the power that is reflected from the reactor setup back to the RF generator (in the ideal case 0 W). At the fluorocarbon reactor, the bottom of the cooling trap was filled with a calcium hydroxide solution ($Ca(OH)_2$) for neutralization of the HF gas, which reacts to calcium fluoride ($CaF_2$) and water.

### Components of the HMDSO plasma reactor

At the HMDSO reactor, a heater was used for evaporating the liquid HMDSO (FAP Forschungs- und Applikationslabor Plasmatechnik, Dresden, Germany) which is not shown in the PECVD laboratory system scheme. The vapor pressure of HMDSO is 43 mbar at 292 K, therefore the substance is present as a colorless, inflammable liquid under normal lab conditions. By heating, the liquid is evaporated and can be led into the reactor as a gas. The container with the liquid HMDSO was kept at 37 °C and both the mass flow controller and the gas lines were kept at 47 °C in order to prevent condensation of the HMDSO. Two pump stages including a roots pump were used for the HMDSO reactor because of the pipe and reactor system with higher volume. The pumps were a Ruvac WS251 (Leybold, Cologne, Germany) for pressures until 80 mbar and a Trivac D40B (Leybold, Cologne, Germany) for pressures until 0.1 mbar. The gas flows were controlled by a multi gas controller type 647B (MKS Instruments, Andover, USA) connected to several mass flow controllers with a range of 100 sccm or 200 sccm (MKS Instruments, Andover, USA). A special UNIT 7300 high performance mass flow controller (Celerity, Yorba Linda, California, USA) with a range of 150 sccm was used for the evaporated HMDSO. Two pressure sensors were used, a Convectron Gauge D with display unit 375 Convectron (Granville-Phillips) and a Baratron sensor (MKS Instruments, Andover, USA). The Baratron sensor was connected to a VAT pressure controller (VAT, Sennwald, Schweiz) which regulated the pressure by a slide controlled throttle

valve VAT F4664601. The power was supplied by the RF generator type Cesar (dressler Hochfrequenztechnik GmbH, Stolberg, Germany) connected to an automatic matchbox dressler VM 1500 AW (dressler Hochfrequenztechnik GmbH, Stolberg, Germany).

## 4.4. Physical and chemical analysis methods

### 4.4.1. Microscopic methods

The negative structures on the stamps and the positive structures on the imprinted polyurethane films were analyzed for their geometric dimensions by digital light microscopy and laser scanning microscopy. Furthermore, fluorescence laser scanning microscopy, scanning electron microscopy and atomic force microscopy were used. The PU samples of stamp 1 were analyzed by white light interferometry (Optical 3D-Profilometer ZeGage, ZygoLOT, Darmstadt, Germany).

#### Light microscopy

A digital light microscope, VHX 600 from Keyence, Neu-Isenburg, Germany, was used to generate two-dimensional images with high depth of field. The zoom objective VH-Z100 with a magnification factor from 100 to 1000 was used for the images with normal view from above. These were used for measuring the microstructure diameters or widths and structure distances, both of the stamps and of the embossed samples. The objective VH-Z20 with a magnification factor from 20 to 200 was used for tilted angle views of the microstructures in order to characterize their shape.

#### Laser scanning microscopy

The microstructures on the stamps and the imprinted PU samples were also characterized by a VK 9700 laser scanning microscope from Keyence, Neu-Isenburg, Germany at the Fraunhofer IPA. The surface is scanned linewise by a laser and the reflection makes an exact measurement of their shape and height possible.

### Fluorescence laser scanning microscopy

The inverse fluorescence laser scanning microscope LSM 710 from Carl Zeiss, Oberkochen, Germany, was used in order to see the wetting behavior on superhydrophobic surfaces. The exact position of the water interface should be visualized on the most relevant surfaces in order to determine whether the drop was in the Wenzel, the Cassie-Baxter or a mixed state. Green fluorescent water drops were placed on microstructured PU samples or microstructured, red fluorescent silicone samples. The surface was then tilted (with the water drop rolling off) and placed upside down on the sample table. In this way, the objective was looking at the top of the surface that was wetted before. The water was colored by addition of green fluorescent fluorescein sodium salt (CAS Nr. 518-47-8, Merck, absorption maximum at 485 nm). The silicone (Wacker Silicones, type Elastosil RT 602) was prepared by mixing the silicone base (component A) with the crosslinker (component B) in the ratio of 9:1 (45 g: 5 g) and adding the dye "fluorescent red" (94720) from Kremer Pigmente.

### Scanning electron microscopy

Scanning electron microscopy (SEM) was used in order to visualize the microstructure shapes and plasma coatings. With SEM, very high magnification factors of up to 50000x can be achieved. As the sample material has to be electrically conductive, the PU samples were sputtered with about 5 nm of platinum. The instrument LEO 1530VP from Carl Zeiss, Oberkochen, Germany, was used with an in lens detector.

### Atomic force microscopy

The plasma coating topography or nanometer scale roughness was measured by atomic force microscopy (AFM), on a Solver PRO from NT-MDT, Moscow, Russia. In contact-mode, the cantilever is constantly on the surface, whereas it only swings above it in non-contact mode. The cantilever types NSG-20 and NSG-11 from NT-MDT were used in semi-contact mode (tapping mode) for the measurements discussed in this thesis. With the software SPIP (Image Metrology) the topography images were evaluated and the roughness values $S_a$ (average roughness), $S_q$ (quadratic roughness or Root Mean

Square RMS), $S_{\mathrm{dr}}$ (surface area ratio) and $S_{\mathrm{sc}}$ (mean summit curvature, average of the principal curvature of the local maximums on the surface) were calculated. The mean summit curvature was used for calculation of surface mean radius of curvature $R = 1/S_{\mathrm{sc}}$, which was needed for calculation of the nucleation temperatures. The surface ratio $S_{\mathrm{dr}}$ is the amount of surface enlargement compared to the planar surface. A completely flat surface would have a $S_{\mathrm{dr}} = 0\,\%$. The nanoscale roughness values were determined on own samples with a preferably homogeneous area of 10 µm x 10 µm. Values from other theses determined on an area of 15 µm x 15 µm [2] and 20 µm x 20 µm [179] were added for comparison. Before each roughness calculation, a slope correction by a $2^{nd}$ order polynomial was applied linewise to the measurement data.

## 4.4.2. Spectroscopic methods

### Spectroscopic ellipsometry

The thickness and the refractive index of the plasma polymer coatings was measured on coated silicon wafers by spectroscopic ellipsometry. The instrument Sentech SE 801 from Sentech Instruments, Berlin, Germany, with a spectral range from 250 nm to 850 nm was used.

A Cauchy model was used, which describes the refractive index n in dependence of the wavelength $\lambda$ with a polynomial function:

$$n_\lambda = n_0 + C_0\frac{n_1}{\lambda^2} + C_1\frac{n_2}{\lambda^4} \tag{4.1}$$

$C_0$ and $C_1$ are constants. The parameters $n_0$, $n_1$ and $n_2$ are changed by fitting the theoretical values to the measurement values. In this way, the refractive index n and the thickness of the plasma coating are derived. The given measurement error is only in the picometer range. However, a rough surface or inhomogeneous coatings can lead to diffuse scattering of the incidence light beam which changes the polarization of the light beam (measurement signal). Therefore, the thickness measurement values cannot be treated as absolute but have a standard deviation of up to 5 nm.

### UV/Vis spectroscopy

The transparency or optical parameters like direct and diffuse transmission of the plain and functionalized PU samples were determined by ultraviolet/visible (UV/Vis) radiation spectroscopy. The transmission was measured in the range of 190 nm to 800 nm. Therefore, an integrating sphere with sample holders for solid surfaces was inserted into the UV-2450 from Shimadzu, Kyoto, Japan.

### IR spectroscopy

The chemistry of the plain and functionalized PU foils was determined by Fourier-transformed infrared (FTIR) spectroscopy (Equinox 55, Bruker, Billerica, USA) using the diamond-ATR mode (attenuated total reflection). A wave number spectrum is generated by Fourier transformation. The transmission or absorption bands can be related to the chemical structures. All FTIR spectra were normalized for the maximum of intensity of the spectra and their baseline was corrected.

### X-ray photoelectron spectroscopy

The surface chemistry of the plasma coatings was examined by x-ray photoelectron spectroscopy (XPS), also known as electron spectroscopy for chemical analysis (ESCA). With ESCA, information about the elementary composition as well as about the chemical groups and bonds can be gathered. The instrument Axis Ultra from Kratos Analytical, Manchester, UK, was used, giving an information depth of about 5 nm - 10 nm from the surface. Measurements were carried out with X-ray radiation from a monochromatic Al-$K_\alpha$ source (1486.6 eV), using a hemispherical detector and the slot mode. The samples were neutralized by slow electrons from a filament. The original binding energy can be calculated by measuring the kinetic energy:

$$E_{\text{binding}} = \text{h} \cdot \nu - E_{\text{kin}} - \phi_{\text{sp}}. \tag{4.2}$$

Here, h, $\nu$, $E_{\mathrm{kin}}$ and $\phi_{\mathrm{sp}}$ are the Planck constant, the X-ray frequency, the kinetic energy of the photoelectrons and the device specific work function, respectively. The obtained high resolution spectra in VAMAS file format were fitted using the software CasaXPS. The correction of the samples charging was done with the C-C/C-H bonds of the C 1s region which were assigned a binding energy of 284.6 eV.

## 4.5. Methods for measurement of stability and optical properties

Only a sufficient stability of the surface functionalizations, namely the microstructures and nanostructured plasma coatings, enables a real application of the anti-ice PU films. If the microstructures or plasma coatings are eroded too quickly in an outdoor environment, the anti-ice PU films are not economically useful. As the long-term durability is of major importance, the functionalized PU samples were tested for durability by several methods.

### Stability against sand erosion

In order to analyze the functionalized surface stability against erosion by sand or dirt particles, a sand trickling test according to DIN 52348 was built. This test characterizes the surface abrasion by sand impacting from about 1.5 m at an inclined angle [181]. It was designed for analysis of wear of glass and polymer surfaces for viewing windows. The sieves are made of stainless steel wires (mean mesh width of 1.6 mm) and the tube parts of polycarbonate (PC). The test stand is shown in Figure 4.5.

Two samples of every surface are mounted on the turn table inclined at 45°which rotates at 250 rpm. About 3 kg of fine quartz sand (corn size 0.4 to 0.8 mm) fall from the reservoir at the top through two sieves onto the samples at room temperature. After the test, the samples were cleaned in an ultrasonic bath, rinsed with deionized water and dried by nitrogen gas ($N_2$ 5.0). The transmission (direct and diffuse) and turbidity are measured at the UV/Vis spectrometer with the integrating sphere adapter before and after sand trickling for each sample. The increase of the diffuse transmission is

Figure 4.5.: Images of the sand trickling test stand corresponding to the standard DIN 52348.

calculated by the difference before and after sand trickling. In addition, the corrected turbidity is calculated. Further details can be found in the standard [181] or in the construction report [182]. Furthermore, contact angle, SEM and ESCA measurements were done of the samples before and after the sand trickling test.

## Stability against UV/water weathering

The stability against weathering (water and UV radiation) was tested according to the standard test method X1a CAM 180 described in SAE J-2527, former SAE J-1960, at

the Fraunhofer IPA. Two samples of each surface were placed in the testing machine Weather-o-meter (Atlas Material Testing Technology, Linsengericht-Altenhaßlau, Germany). There, they were exposed to water spray and radiation that is comparable to the sunlight spectrum (wavelength of 290 nm and above), being composed of UV-B, UV-A, visible range and NIR radiation (UV-B increased as compared to sunlight). One cycle lasts for 3 h and is composed of 4 phases: 40 min dry irradiation, 20 min irradiation with wetness by rain, 60 min dry irradiation and 60 min darkness with wetness by rain, with a maximum temperature of 70 °C. Further details can be found in the test method description SAE J-2527. The test was run for about 1000 h which is a typical test duration in the coating industry for a following surface analysis. Afterwards, one sample of each surface was measured by ESCA for determination of the surface chemistry.

## Long term outdoor stability

Various sample surfaces (plain PU, HMDSO (60 W) plasma coated PU and $C_4F_8$ (50 W) plasma coated PU films) were exposed to the outdoor environment for about 13.5 months. Therefore, they were glued to a test stand on the roof of the Fraunhofer IGB. The surface with the samples was inclined at 45°from the horizontal plane and facing the south. They were put out in January 2015 and brought in again in March 2016. Afterwards, the samples were removed, immersed in deionized water for 2 hours and rinsed with highly purified (65 µS/ml) water. Then, their surface chemistry was analyzed by ESCA. The climate data from the measuring station Stuttgart-Mitte (operated by the city of Stuttgart and the Department of Environmental Protection) during this period are shown in Figure 4.6 and Figure 4.7.

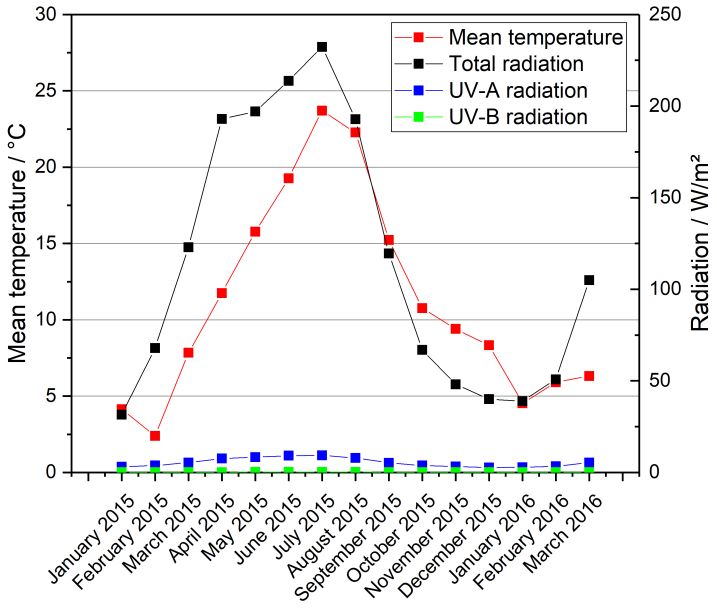


Figure 4.6.: Mean monthly temperature and radiation values during the long term outdoor stability test, climate data from the measuring station Stuttgart-Mitte [183].

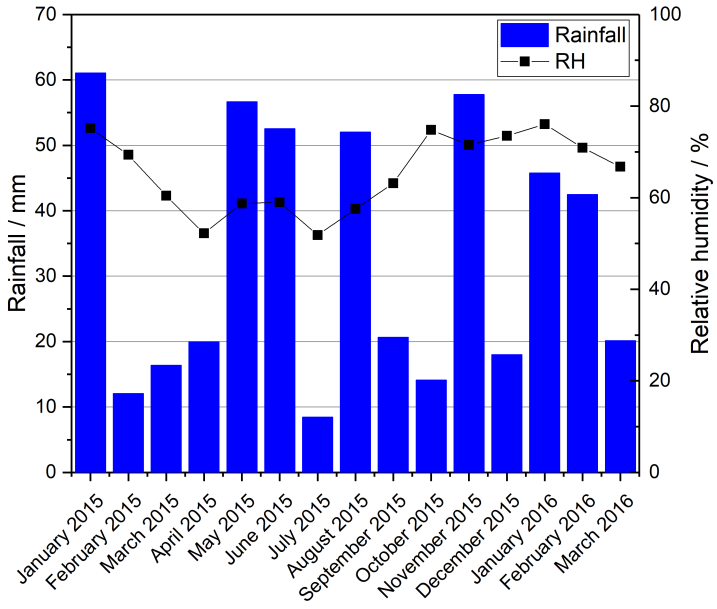


Figure 4.7.: Mean monthly rainfall and relative humidity values during the long term outdoor stability test, climate data from the measuring station Stuttgart-Mitte [183].

## Stability tests for repeated icing/de-icing

The stability of the functionalizations against repeated icing and de-icing was tested as well. Before each ice pull-off test, the surface was rinsed with highly purified water and dried with nitrogen 5.0 gas. Then, an ice cylinder with a diameter of 4 mm was frozen on the surface at the same spot and pulled off. This was repeated for five times. The spot was marked by a black circle. The surface chemistry was characterized by ESCA on the flat samples. The microstructured samples were analyzed by LSM for their shape after 5x ice pull-off.

## Optical properties

The optical properties of the functionalized PU films were characterized by UV/Vis spectroscopy and by testing on a small solar panel on the roof of the institute. The solar panel was inclined at 45°from the horizontal plane and facing the south. A USB voltage logger was connected to the solar panel via a 5 $\Omega$ resistor. The voltage of the solar panel was logged with different cover setups, at first uncovered, then covered with the flat, $C_3F_6$ plasma-coated PU films and finally with the C16 microstructured and $C_3F_6$ plasma-coated PU films. The different cover setups were tested at sunny weather conditions during one day for comparison. Additionally, each cover setup was tested for a longer period of up to 11 days.

# 5. Experimental methods for the characterization of the wetting, de-icing and anti-icing behavior

In this chapter, the experimental methods used for the characterization of the functionalized anti-ice surfaces are given. The contact angle measurements for the determination of the wetting behavior are described in the first section (5.1). Then, the icing test chambers (5.2), the characterization of the ice adhesion (de-icing, 5.3) and the icing behavior (anti-icing, 5.4) are described.

## 5.1. Water contact angle measurements for the characterization of the wetting behavior

PC-controlled contact angle measurements were performed to analyze the wetting behavior of the functionalized PU films and the other surfaces (OCA 40 device and the Software SCA 20 from DataPhysics Instruments, Filderstadt, Germany). A 3 µl droplet was generated at the tip of the needle and placed on the surface. Static contact angles of highly purified water (Type I, $\leq$0.056 µS/cm) and diiodomethane (DIM) were measured on the flat and microstructured PU film samples and on the reference materials for surface free energy determination. The surface free energy was calculated by the software using the OWRK method. Advancing and receding contact angles were determined on all samples with highly purified water (Type I, $\leq$0.056 µS/cm). For these advancing / receding contact angle measurements, the volume of the droplet was first increased and afterwards decreased by 10 µl at a rate of 0.5 µl/s, while the needle remained in the droplet (needle-in method). A video was captured by a CCD high-speed camera with

the measurement software (SCA 20), which automatically determines the drop contour by the contrast in the image. For every frame, the contact angles are determined by the intersection of the baseline and an ellipse which is fitted to the drop contour. The values reported in the results chapter, in the section on wetting behavior, are the average of three measurements, each on a different part of the sample, carried out at 21 °C and a relative humidity of 56 %. Images of advancing and receding three-phase contact lines during measurement with the needle-in method are shown in Figure 5.1.

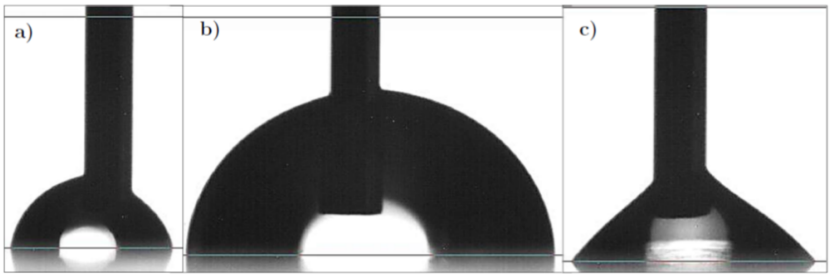


Figure 5.1.: Images of the water drop during dynamic contact angle measurement with the needle-in method: a) start (static contact angle), b) increase of drop volume (advancing contact angle), c) decrease of drop volume (receding contact angle), reprinted from [184].

The determination of the advancing and receding contact angle from measurement data is shown schematically in Figure 5.2.

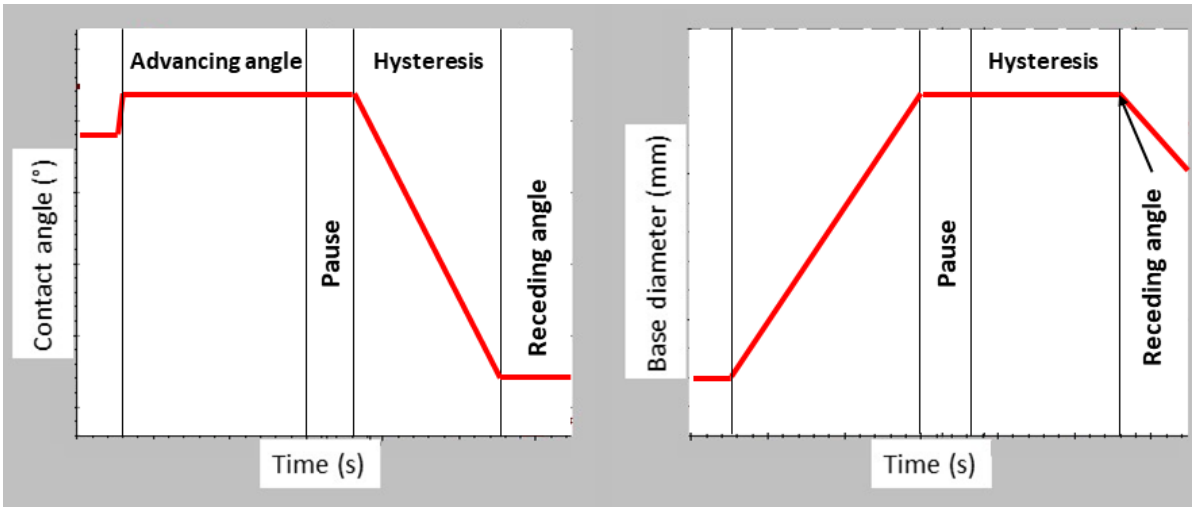


Figure 5.2.: Schematic example for determination of the advancing and receding contact angle from a dynamic contact angle measurement.

## 5.2. Icing test setups

### 5.2.1. Cooling chamber of previous icing test setup

The icing tests with constant surface temperature were done with the cooling chamber of the contact angle measurement device OCA 40.

A cooling chamber (TPC 150), connected to a temperature control unit (TC 150), a water-glycol cooling thermostat (RC 6, Lauda Dr. R. Wobser, Lauda-Königshofen, Germany) together with a diaphragm pump (Liquiport, KNF Neuberger, Freiburg, Germany) for cooling of the TPC 150 Peltier element, and a precision scale (Precisa ES 2220M, Precisa Gravimetrics, Dietikon, Switzerland) were used in the test setup. The chamber ground (with the sample) is cooled down by a Peltier element which dissipates heat from the inner to the outer side by the thermoelectric effect if an electric current flows. Therefore, the outer side becomes hot and is cooled by a cold water-glycol mixture, provided by the thermostat. The chamber atmosphere is measured by a temperature and a relative humidity sensor. Nitrogen gas was used to create a dry atmosphere.

### 5.2.2. Newly developed icing test setup

#### Motivation for development of a new icing test chamber

The ice adhesion measurements using the cooling chamber of the contact angle measurement device often showed a cohesive break, especially on the microstructured samples. This setup resulted in measurements of greatly varying ice adhesion forces on the same surface. No reproducible results could be generated. Furthermore, the temperature distribution in the chamber was very uneven, as the temperature sensor in the ground and in the air showed. Not enough sensors were available for measurement of the exact temperatures of the ground, the sample surface, the walls and the air. Finally, the cooling power was not sufficient resulting in very long freezing times of up to 30 minutes per sample.

The design of a new icing test chamber should allow for the examination of ice adhesion, icing behavior and impacting droplets on different surfaces. This icing test chamber

should have a large cooling power for freezing of water drops in an acceptably short time, a homogeneous and precisely controllable temperature and humidity distribution within the chamber and enough sensors at all relevant spots to log the climatic conditions.

### Components of the icing test chamber

The main part of the icing test chamber consists of an aluminum block with a horizontal, rectangular opening for the samples and a hole in the chamber lids for applying the hollow test cylinder filled with water (or ice) on the samples. The chamber is cooled down electrically by Peltier elements on the bottom, left and right side of the inner aluminum block with a water cooling installed on the outer side and temperature sensors on both sides of each Peltier element. The Peltier elements are surrounded by a polystyrene insulation and attached by thermal compound to the inner aluminum block and the water cooling blocks.

Copper microscope slides with the functionalized samples glued onto them were slid in until the aluminum end strip mounted with two screws. Then, the copper slides were screwed down onto the heat conductive tape (Keratherm KL 90, Kerafol, Eschenbach, Germany) on the ground of the aluminum block. The PT100 thin film temperature sensor (Telemeter Electronic, Donauwörth, Germany) for the PID controller (UR484802, Wachendorff Prozesstechnik, Geisenheim, Germany) was placed in a pit under the heat conductive tape. This temperature signal is used for regulating the lab power supply (Voltcraft HPS13030, Conrad Electronic SE, Wernberg-Köblitz, Germany) for the Peltier elements. The temperature right underneath the heat conductive tape, in the lateral middle of the sample on the copper slide, is crucial for sensing and controlling the temperature of the water drops on the sample.

The temperatures, relative humidity and ice adhesion forces are measured by USB-linked sensors and logged by a PC. The relative humidity sensor (Sensirion EK-H5 SHT2x) is fixed in the channel at the chamber wall side. The thermocouples (Type J with USB TC-08 data logger, Omega Engineering, USA) are installed on the inside and outside of each Peltier element. Additional thermocouples were placed in the pit underneath the heat conductive tape, in the chamber air and on the copper slide surface. Inside of the chamber lid, a meandering gas channel was milled for cooling of dry $N_2$ 5.0 gas (purity

≥99.999 %), before the gas is conducted into the chamber for creating a dry atmosphere with nearly 0 % relative humidity. For the 0 % relative humidity experiments, nitrogen 5.0 gas was turned on at 0.5 bar. With the nitrogen gas turned off, the lab atmosphere created about 50 % relative humidity in the chamber. Double glass windows at the front and the back were used in order to prevent fogging when the chamber is cooled down. Normal glass was used for the back, whereas infrared-transparent ZnS glass (CLEAR type, VITRON Spezialwerkstoffe, Germany) was used for the front in order to enable water drop temperature measurements by an IR camera.

The ice adhesion measurements and dynamic freezing tests were done with the newly developed icing test chamber. Technical drawings of the new icing test chamber with geometrical parameters are shown in the appendix. A scheme of the ice test setup is shown in Figure 5.3.

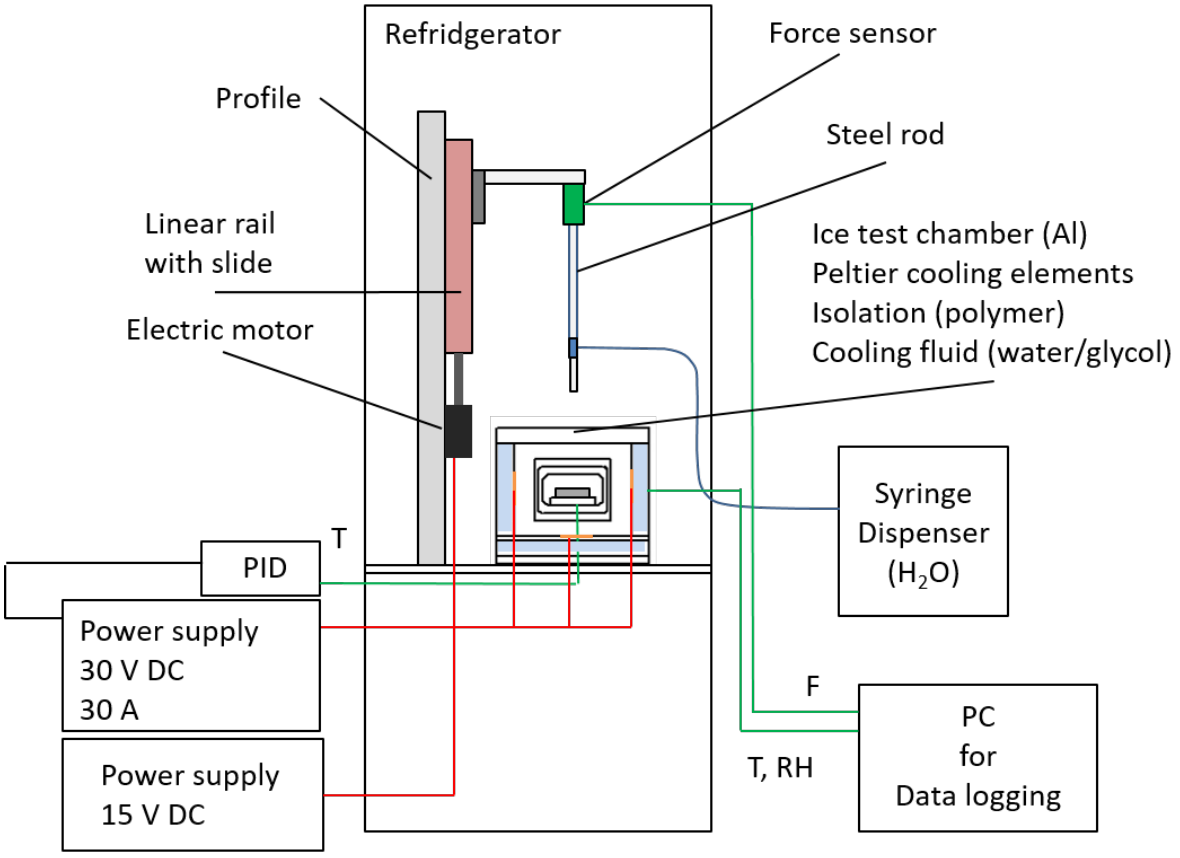


Figure 5.3.: Scheme of newly developed icing test stand.

## 5.3. Ice adhesion measurements for characterization of the de-icing behavior

Adhesive fractures, where the fracture is located at the surface-ice interface, or cohesive fractures, where the fracture is located within the ice, can occur. Only adhesive fractures give information about the dependence of ice adhesion on the surface properties. In this case, the ice test cylinder base diameter is measured and a circular area is calculated. The maximum of the measured tensile force is normalized to the apparent (flat projected) circular contact area and the ice adhesion in kPa is derived:

$$\sigma_{\text{ice}} = \frac{F_{\text{adhesion}}}{A_{\text{f}}}. \tag{5.1}$$

At least three measurements were done for each surface.

A non-transparent aluminum or transparent polycarbonate cylinder (selfmade, outer diameter of 6 mm, inner diameter of 4 mm) was connected rigidly to the force sensor by a steel rod in order to guarantee stability, ensure a vertical alignment of the cylinder and exclude measurement errors because of torque in the ice test specimen. It can be moved up and down by a slide on linear rails driven by an electrical engine. Before each ice adhesion or freezing measurement, the sample surface was rinsed with ethanol and deionized water and dried with nitrogen 5.0. For the ice adhesion measurements, the cylinder was filled with highly purified water (Type I, $\leq$0.056 µS/cm) until a meniscus at the lower end was visible. Then it was moved down until the water wetted the sample surface. Subsequently the ice test chamber was cooled down to -20 °C until the water cylinder was frozen. The force sensor was set to zero in order to exclude errors caused by the water volume change during freezing. Finally, the ice cylinder was pulled off vertically from the surface at a very low velocity and the corresponding force was measured. The force sensor KD40s from ME Messsysteme with a rated force scale of $\pm$20 N (pressure or tension, maximum safe value of $\pm$80 N) was used to measure and log the adhesion force of the ice cylinder by vertical pull-off. Typical measurement curves for each surface type are shown in Figure 5.4.

The force sensor curves show the maximum tensile force which was used for calculation of the ice adhesion. Images of the ice cylinder were taken before and after ice fracture by a

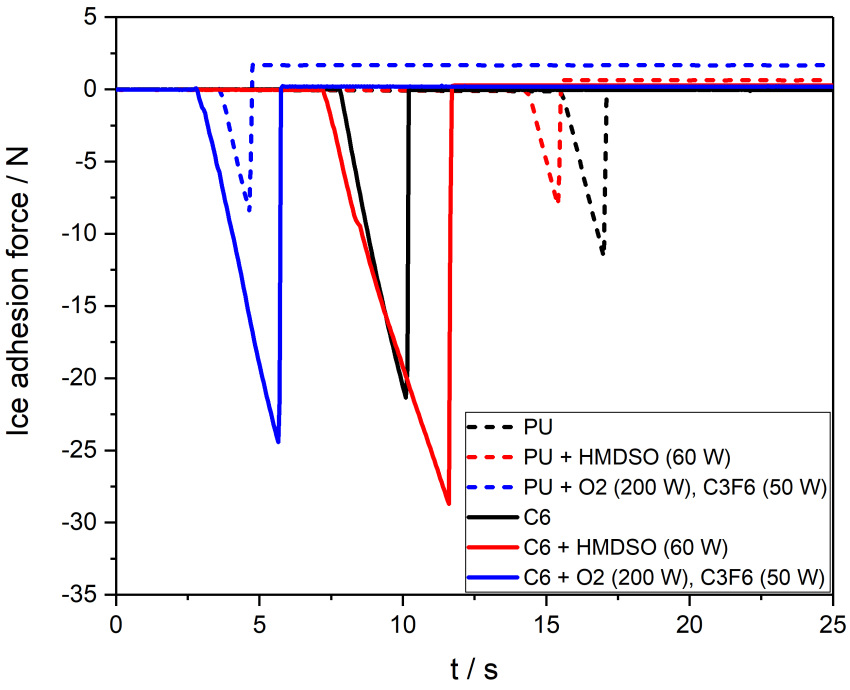


Figure 5.4.: Exemplary ice adhesion force sensor graphs of the samples plain PU, PU coated in an HMDSO plasma, PU etched with $O_2$ and coated in a $C_3F_6$ plasma, uncoated microstructure C6, microstructure C6 coated in an HMDSO plasma and microstructure C6 etched with $O_2$ and coated in a $C_3F_6$ plasma.

CMOS camera (1312DR1, photonfocus AG, Lachen, Switzerland) with a zoom objective (Zoom 7000, focal length = 18 mm to 108 mm, Navitar, Rochester, New York). The ice test cylinder base diameter was determined by these images with ImageJ. In the images, the outer diameter of the cylinder was used for calibration of the linear measurement tool, then the actual ice specimen diameter for calculation of the apparent contact area $A_f$ and the ice adhesion was measured.

## 5.4. Water drop icing measurements for characterization of the anti-icing behavior

The wavelength of maximum radiative emission of an object at -20 °C, which was the minimal temperature in the icing measurements, is 11.45 µm. The IR camera (P620, FLIR Systems, USA) uses the equation 3.69 with a focal plane array (FPA) detector in the range of 7.5 µm to 13 µm for determination of the water drop temperature.

### 5.4.1. Static freezing experiment with constant surface temperature

The freezing experiment at constant surface temperature was done in order to measure the nucleation time, which is defined as the duration from setting a water drop onto a cold surface (constant temperature) until its nucleation. Furthermore, the total freezing time, consisting of the freezing delay time and the crystallization time, was determined. The static experiment was carried out in the cooling chamber of the contact angle measurement device with uncoated and coated samples of flat PU and microstructure C6. Once the temperature sensor in the chamber ground indicated -20 °C, the chamber lid was opened and the IR camera was installed above the surface. Then, multiple 15 µl drops were placed on flat or C6 microstructured, uncoated or plasma-coated PU samples on the sample table that was constantly set to -20 °C at the temperature control unit. The temperature of the surface and the drops was recorded by the IR camera looking perpendicularly from above with a set scale from -10 °C to +10 °C [2]. The setup is shown in Figure 5.5.

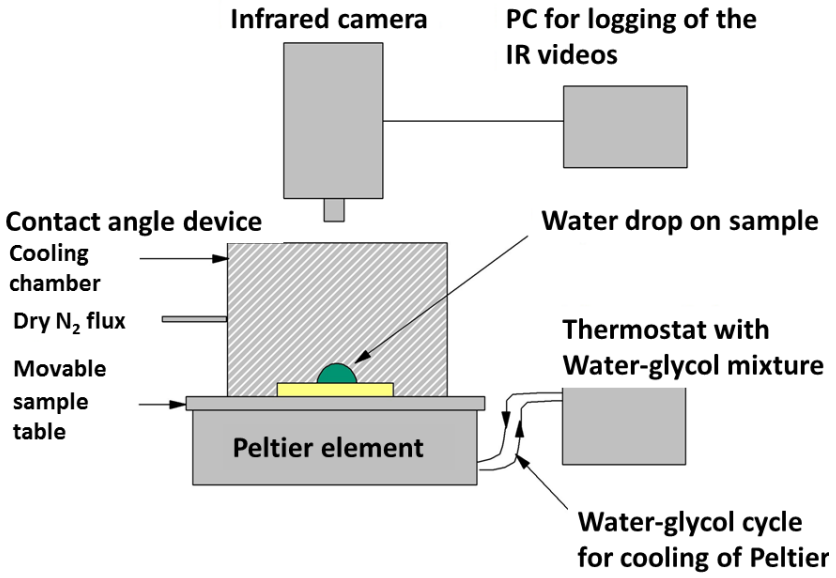


Figure 5.5.: IR camera measurement setup for static freezing experiments with constant surface temperature of -20 °C, adapted from [2].

### 5.4.2. Dynamic freezing experiment with constant cooling rate

The freezing experiments with dynamic surface temperature (constant cooling rate) were carried out in the icing test chamber. A cooling rate of 1 K/min (0.0167 K/s) was set at the PID controller. This low rate was chosen for simultaneous cooling of the layered sample system, the water drops and the surrounding air. From this experiment, the surface specific nucleation temperature and time were determined for the surface in thermodynamic equilibrium with the surroundings. Here, nucleation of the highly purified water drops is only dependent on the solid-liquid contact area, surface roughness, surface chemistry and the current temperature. A calculation of the heat fluxes in order to prove the thermodynamic quasi-steady state of the measurement setup is shown in the appendix (A.7). A schematic illustration of the measurement setup for the dynamic freezing experiment is shown in Figure 5.6.

For the freezing measurements, at least three drops were placed on the sample surface which was then inserted into the icing test chamber. The chamber was closed with the CVD zinc sulfide (ZnS) glass (VITRON Spezialwerkstoffe GmbH, Jena, Germany) window. For measurement of the temperature of the water drops, a video was recorded

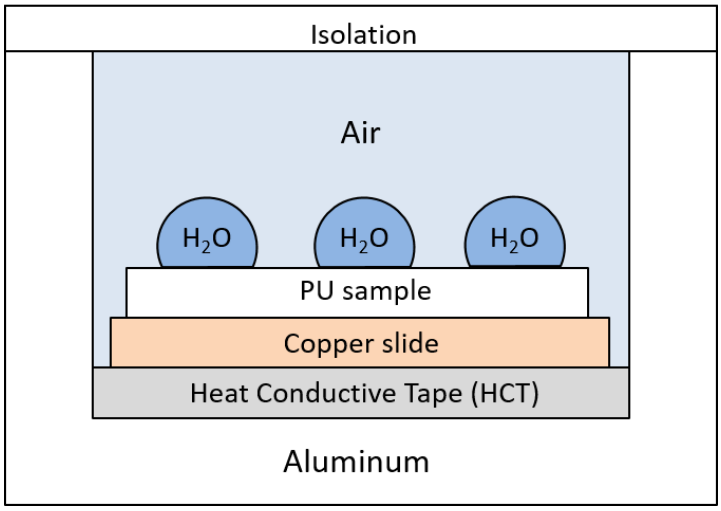


Figure 5.6.: Schematic illustration of the experimental setup for dynamic water drop freezing experiments with constant cooling rate (1 K/min).

by the IR camera looking through the ZnS window. The transmission of the ZnS window is shown in Figure 5.7.

The IR camera with the macrolens was placed directly in front of the ZnS window. The temperatures, the relative humidity and the IR camera video were logged by a laptop. The video pattern was set to gray-scale and the temperature scale was set constant from -20 °C to +10 °C. The following parameters important for heat radiation were set in the IR camera software:

- emissivity $\epsilon = 0.96$ (distilled water/ice)
- transmission coefficient $\tau_{\text{total}} = \tau_{\text{ZnS}} \cdot \tau_{\text{ZnS}} \cdot \tau_{\text{macrolens}} = 0.7 \cdot 0.7 \cdot 0.97 = 0.48$
- reflected temperature = -5 °C (radiation from inner chamber walls, mean value of +10 °C and -20 °C)
- temperature of external optics = 22 °C
- atmospheric temperature = 22 °C
- relative humidity = 50 %
- distance = 0.1 m (distance between water drop and CCD chip)

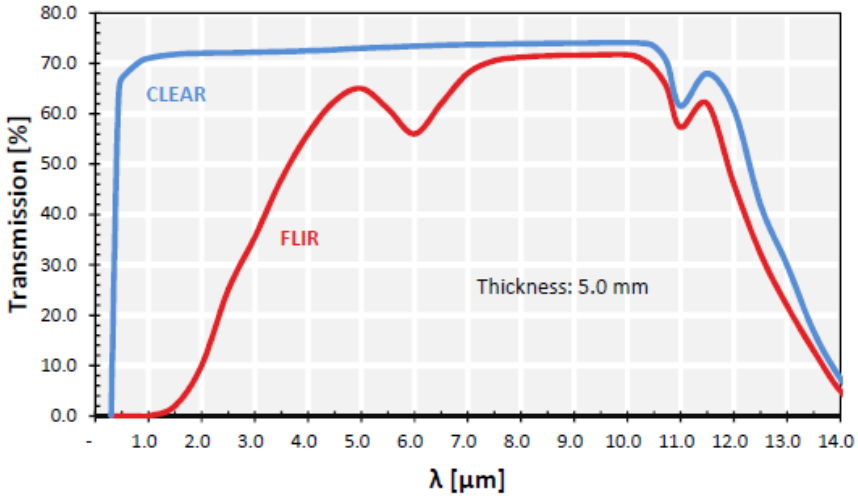


Figure 5.7.: Transmission of the infrared transparent zinc sulfide (ZnS) glass in dependence of the wavelength; FLIR = regular grade, transparent in the IR region from 7 µm to 12 µm, CLEAR = multispectral grade, transparent in the visible and IR region from 0.45 µm to 12 µm (used for measurements), reprinted from [185].

The parameters were set according to known data or estimated for the reflected and atmospheric temperatures. These parameters were varied, checked and verified experimentally by measuring a water drop on a surface held constantly at 5 °C.

The water drop temperature curves were determined from the grayscale IR videos by ImageJ using the point measurement tool and setting measurement points into the uppermost part of each water drop. Then, the grayscale values ($x$, in the range of 0 to 255) were converted to the temperature ($T$) by the following formula:

$$T = [(x/255 - 0.66666) \cdot 30] \ . \tag{5.2}$$

This gives the temperature curves of the water drops in °C.

The time scales (total measurement durations) of the IR camera, of the thermocouples and of the humidity sensors deviated because of different internal capture and saving times. As the IR camera time scale differed from the time scales of the other sensors, its time scale was normalized to the one from the thermocouples for each measurement individually (usually about $t_{\mathrm{TC}} = 0.9 \cdot t_{\mathrm{IR}}$). Furthermore, the temperature curve of the IR camera was usually about 5 K to 10 K above the temperature curve of the thermocouple

on the copper sheet. The copper surface thermocouple values were regarded as absolute and the water drop temperature as being the same as the sample surface, because the thermal conductivities of the solids ($\lambda_{Al} = 230\,W\,m^{-1}K^{-1}$, $\lambda_{HCT} = 1.4\,W\,m^{-1}K^{-1}$, $\lambda_{Cu} = 330\,W\,m^{-1}K^{-1}$, $\lambda_{PU} = 0.245\,W\,m^{-1}K^{-1}$) are much higher than of the air ($\lambda_{air} = 0.0262\,W\,m^{-1}K^{-1}$). Therefore, the IR camera temperature curve was shifted down in a way that for each drop, the nucleation temperature was equal to the corresponding temperature of the copper surface thermocouple at the given time point.

Examples of the uncorrected and resulting corrected temperature curves for uncoated PU CMC 63630 are shown in Figure 5.8.

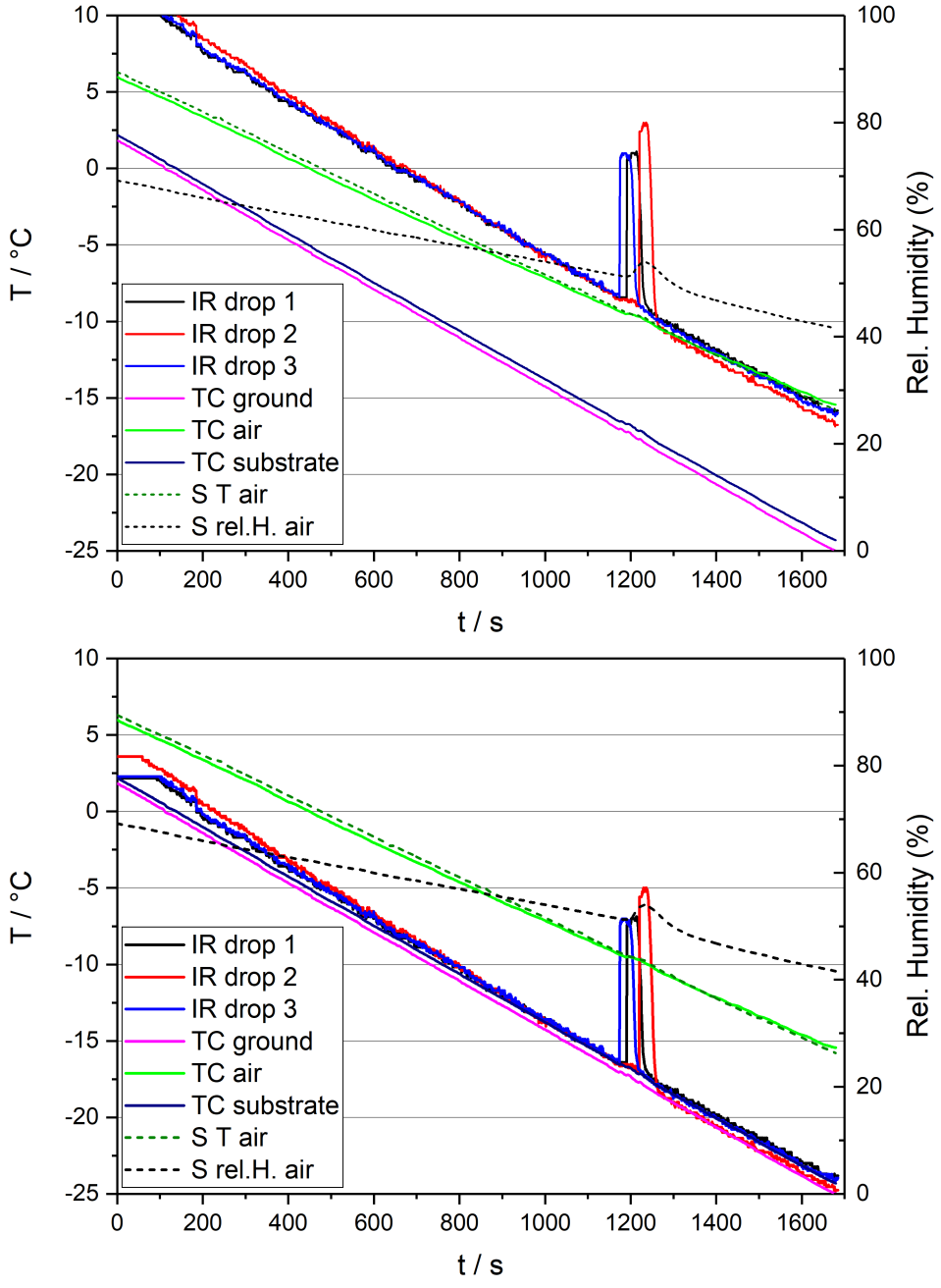


Figure 5.8.: Exemplary temperature curves of the water drops on uncoated PU CMC 63630 measured by the IR camera ("IR"), of the thermocouples ("TC") and of the relative humidity sensor by Sensirion ("S"), top: before correction, bottom: after correction by shifting the IR curves to the sample temperature curve measured by the thermocouple ("TC substrate").

From these temperature graphs, the nucleation temperatures $T_N$ as well as the nucleation times, crystallization times ($t_C$) and total freezing times were extracted. Box plot diagrams were created for the nucleation temperatures with the data of at least three drops for each surface (up to nine drops in case of the microstructured samples).

# 6. Results and discussion of the PU film surface functionalization

In the following sections the results regarding the functionalizations are presented, especially of the hot embossing (6.2) and the plasma coating and etching processes (6.3). The functionalized PU surfaces were characterized by several different spectroscopic and microscopic methods. The results of their bulk chemistry (6.1), their surface microstructure topography (6.2), surface chemistry and nanometer roughness (6.3) are presented. The influence of the process parameters of the hot embossing and PECVD processes on the surface properties is discussed. The last section describes the results of several stability tests of the differently functionalized PU films, including their optical properties (6.4).

## 6.1. Chemistry of the PU films

The different PU films were analyzed by IR spectroscopy for their chemical composition in the bulk phase. The spectra were recorded in order to see differences between the PU films and as a reference for later IR spectrometry measurements of plasma coated films.

The IR spectra of the PU films 8674 from 3M, LPT4800TT and LPT4802T from Covestro are shown in Figure 6.1.

The IR spectrum of the 3M PU film shows a broad band for the hydroxyl (-OH, 3500 $cm^{-1}$ to 3300 $cm^{-1}$) and amino (-NH, 3350 $cm^{-1}$ to 3300 $cm^{-1}$) group vibrations, and two distinct bands for the hydrocarbon group stretching vibrations (-$CH_2$ asymmetric/symmetric at 2920/2850 $cm^{-1}$ and -$CH_3$ asymmetric/symmetric at 2960/2870 $cm^{-1}$). The next band, with overall highest intensity, at around 1700 $cm^{-1}$ is caused by the

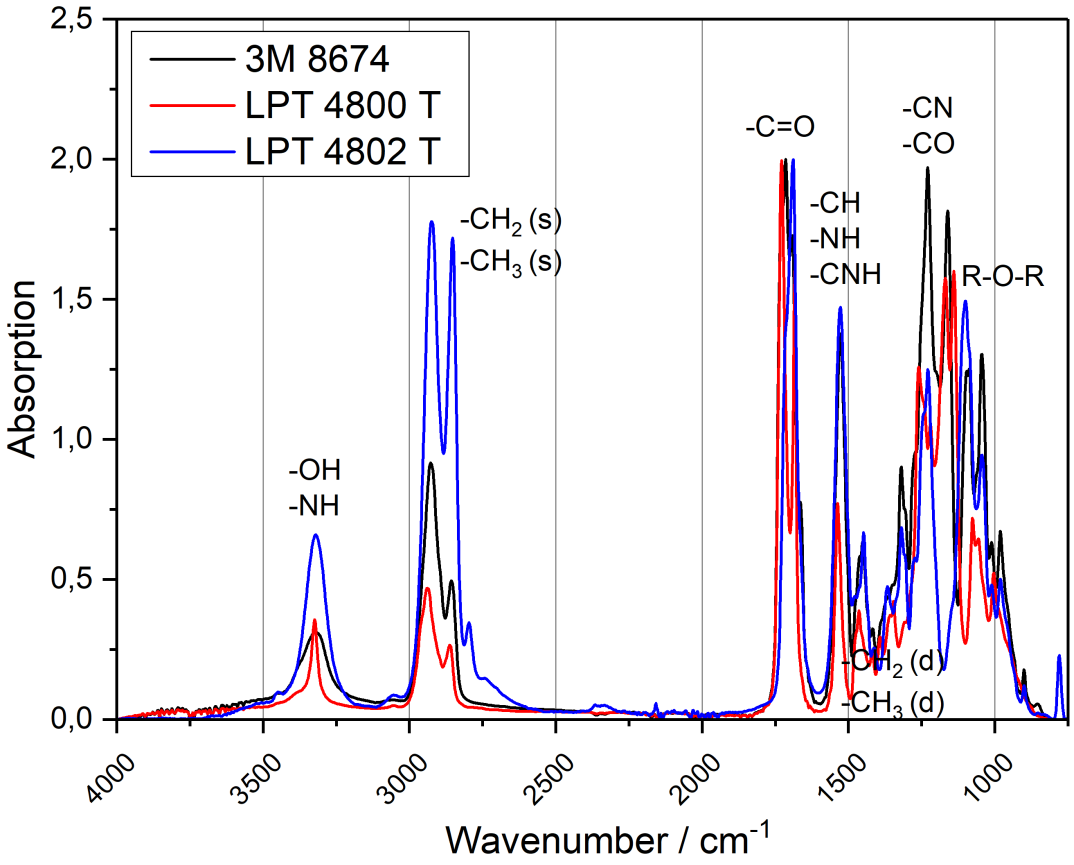


Figure 6.1.: IR-spectra of the PU films type 8674 from 3M, LPT4800TT and LPT4802T from Covestro.

carbonyl group (-C=O, 1690 $cm^{-1}$), which is part of the urethane group within the polyurethane. Another strong band found around 1550 $cm^{-1}$ corresponds to the -CH, -NH or -CNH stretching vibrations. This band at 1550 $cm^{-1}$ and the carbonyl group band at 1690 $cm^{-1}$ indicate the polyurethane structure. Below 1500 $cm^{-1}$ the fingerprint region is found that clearly identifies a polymer, but the bands overlap here and are difficult to distinguish. The following two smaller bands at around 1450 $cm^{-1}$ and 1350 $cm^{-1}$ originate from the asymmetric and symmetric deformational vibrations of the $-CH_2$ and $-CH_3$ groups. The next two bands with high intensity just above and below 1200 $cm^{-1}$ are due to the -CN and -CO group vibrations (1230 $cm^{-1}$), which are also part of the urethane group.

The IR spectra of both LPT PU films are similar to the one of the 3M PU film and similar to each other. Both have the bands for the -OH/-NH groups, for the -$CH_2$/-$CH_3$ groups, for the carbonyl and for the -NH/-CH/-CNH groups. The large bands between 1100 $cm^{-1}$ and 1200 $cm^{-1}$ belong to -CO, -CN or ether (R-O-R) groups. There are differences in wavenumber between the two LPT PU film spectra for the carbonyl group and the -CO/-CN group bands in the fingerprint region. The type LPT 4802T is of main interest for anti-ice functionalization, because it is a polyether-based polyurethane. Therefore, it is thought to be more stable against breakdown by water in an outdoor environment. The ether band (R-O-R) occurs typically at about 1100 $cm^{-1}$, where the LPT4802T has a large, distinctive band compared to the LPT4800T type.

The IR spectra of the PU films 63615 and 63630 from CMC Klebetechnik (one with and one without the adhesive polyacrylate layer) are shown in Figure 6.2.

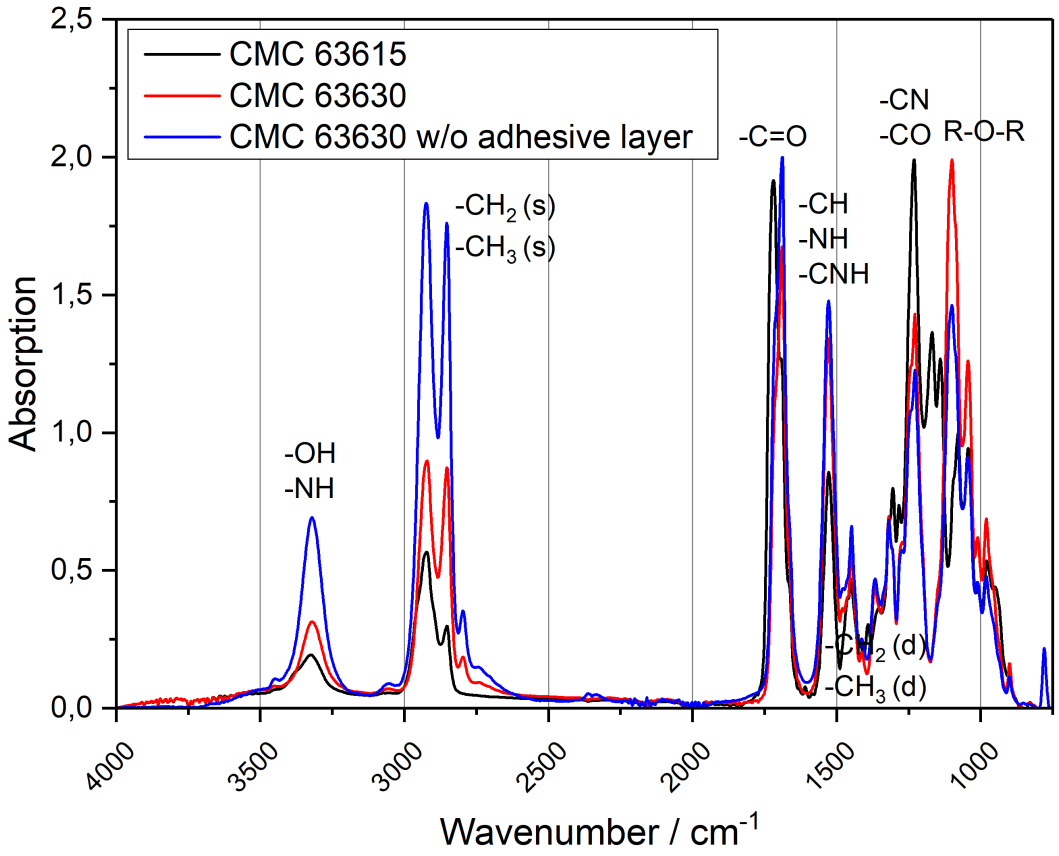


Figure 6.2.: IR-spectra of the PU films 63615 and 63630 (with and without polyacrylate adhesive layer on the back) from CMC Klebetechnik.

The IR spectra look similar to the spectra of the preceding PU films from Covestro and 3M. The distinctive bands appear for the -OH/-NH group, the -$CH_2$/-$CH_3$ group, the -C=O group, the -CH/-NH group, and the -CN/-CO group vibrations. The difference between the two types of PU films from CMC Klebetechnik is the thickness (150 µm and 300 µm). The IR spectra of the two different types are similar, but not identical. The CMC 63630 type shows an additional small band at 2800 $cm^{-1}$ corresponding to the -CH group vibration and the carbonyl group band at around 1690 $cm^{-1}$ is slightly shifted towards lower wavenumbers. In the fingerprint region the CMC 63630 type shows a large band at around 1100 $cm^{-1}$, which indicates an ether group (R-O-R). The CMC 63615 does not have this band at 1100 $cm^{-1}$, but instead a larger band at around 1230 $cm^{-1}$ due to the -CN/-CO group of the PU. Therefore, the PU film 63630 is expected to be

more stable against breakdown by water and is used for further sample preparation.

The IR spectra of the PU film CMC 63630 with and without adhesive layer show the same bands, apart from some variations in intensity. The acrylate adhesive would show the bands of an alkene ($3095\,\mathrm{cm}^{-1}$ to $3075\,\mathrm{cm}^{-1}$, $1650\,\mathrm{cm}^{-1}$ and $890\,\mathrm{cm}^{-1}$) and the strong characteristic bands of the salt ($1650\,\mathrm{cm}^{-1}$ to $1550\,\mathrm{cm}^{-1}$) or the ester ($1750\,\mathrm{cm}^{-1}$ to $1735\,\mathrm{cm}^{-1}$) of the acrylic acid. The depth of analysis of the ATR method was estimated to be about 1 µm [186]. Therefore, the adhesive layer on the back of the PU film cannot be detected. However, it is shown that the chemical structure of the PU type 63630 front side is not altered by the adhesive layer on the back. Therefore, the adhesive layer on the back will not influence the functionalization on the front side.

## 6.2. Microstructures created by hot embossing

The hot embossing process was analyzed in order to identify the process parameters for best shape and reproducibility of the microstructures. At first, the melting and glass transition temperatures of the PU films determined by differential scanning calorimetry measurements are given. Then, the best embossing parameters determined by several sets of embossing experiments at different temperatures and pressures are listed. Furthermore, the chemical structure of the PU film after hot embossing and the reproducibility of the microstructures was analyzed. Finally, the dependence of the microstructure height on the removal temperatures of the PU film from an embossing stamp and on the embossing process times was analyzed. A summary of the optimized embossing parameters is given at the end.

### 6.2.1. Characterization of the microstructures

The microstructured fields and PU films were analyzed by digital light microscopy, confocal laser scanning microscopy and scanning electron microscopy for their geometrical dimensions. Light microscopy was used to determine the top and bottom diameters $d$ and $D$, and distances $P$ of the microstructures. It has to be noted that the bottom diameter $D$ on the PU film is the top diameter $d$ on the stamp which also applies for the corresponding other diameter. For exact measurement of the height $H$ and top diameter $d$ on the PU films, laser scanning microscopy was used. SEM measurements showed the surface of the microstructures in detail. With these geometric parameters it was possible to calculate the surface roughness factor $rf$ and therefore the theoretical contact angles described by the Wenzel [125] and Cassie-Baxter [126] theories.

Exemplary microscopy images of the best superhydrophobic, cylindrical microstructures C6 and C9 (holes) in the stamp are shown in Figure 6.3.

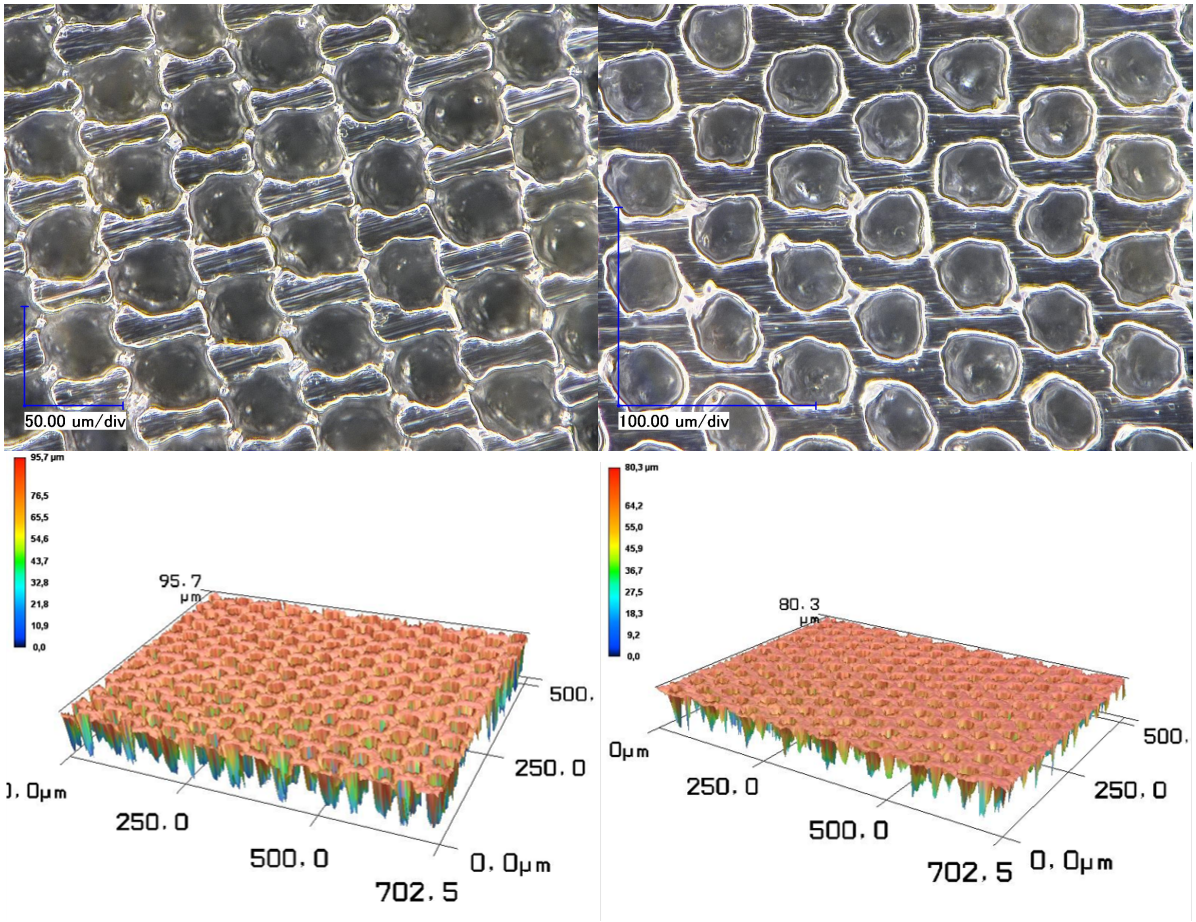


Figure 6.3.: LM (top) and LSM (bottom) images of the laser-drilled holes of the microstructures C6 (left) and C9 (right) in the embossing stamp.

Exemplary microscopy images of the best superhydrophobic, cylindrical microstructures C6 and C9 on PU are shown in Figure 6.4.

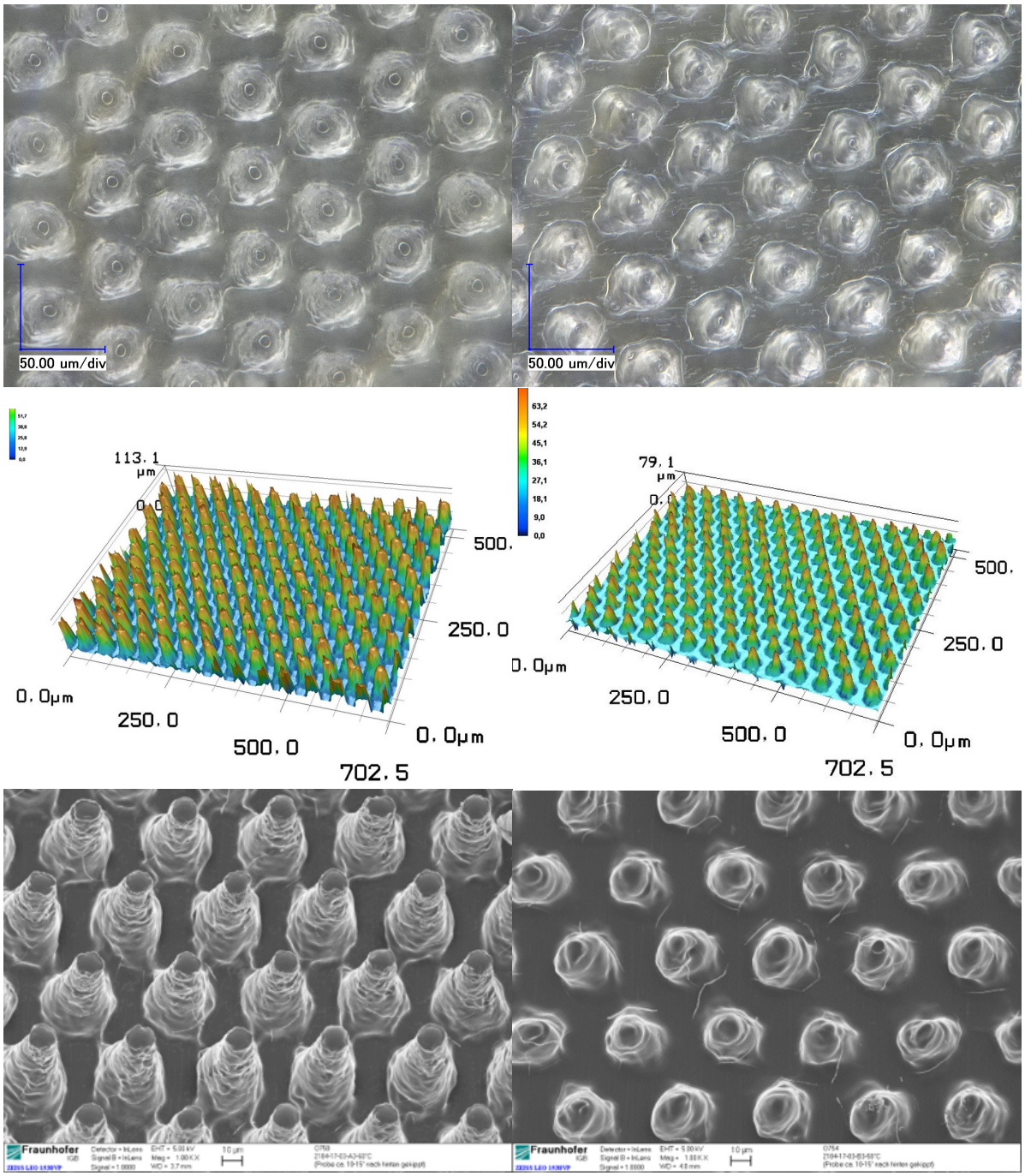


Figure 6.4.: LM (top), LSM (middle) and SEM (bottom) images of the microstructures C6 (left) and C9 (right) imprinted on the PU film.

Exemplary microscopy images available of the most hydrophobic, elliptical and linear microstructures E4 and L2 are shown in Figure 6.5.

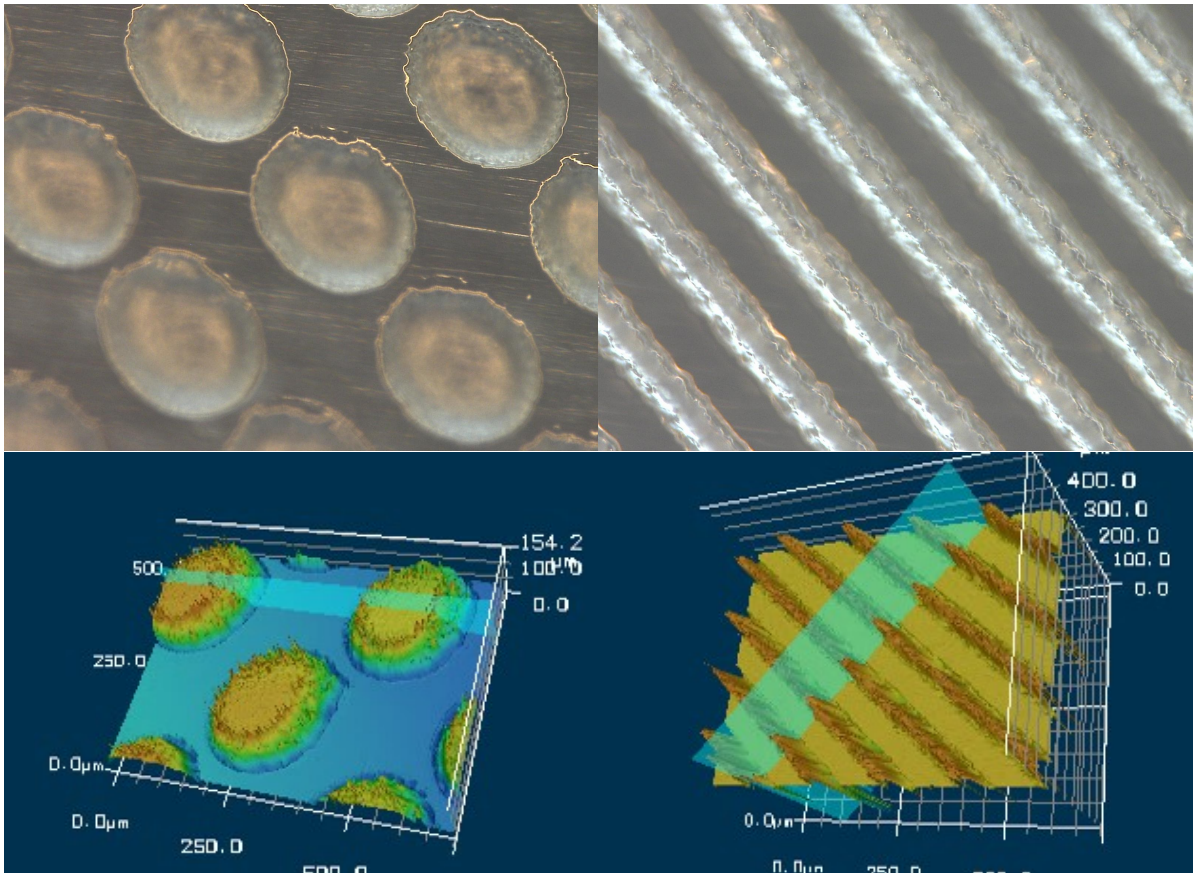


Figure 6.5.: LM (top) and LSM (bottom) images of microstructures E4 (left) and L2 (right) imprinted on the PU film.

A detailed list of the geometric dimension parameters of all microstructures on PU films are shown in the appendix (section A.2). The geometrical parameters of the most hydrophobic microstructures that will be chosen from wetting behavior measurements described later on and used for further characterization (see section 7.1) are shown in Table 6.1.

Table 6.1.: Geometrical dimensions of the most hydrophobic microstructures for further characterization.

| Structure name | Type of microstructure | Arrangement of structures | Field name | Height H | Base diameter D | Top diameter d | Distance (pitch) P | Spacing factor P/D | Spacing factor P/d | Aspect ratio H/d | Roughness factor rf |
|---|---|---|---|---|---|---|---|---|---|---|---|
| - | - | - | - | (µm) | (µm) | (µm) | (µm) | - | - | - | - |
| E1 | Ellipse | hexagonal | 2-A1 | 56 | 44 | 22 | 68 | 1.5 | 3.08 | 2.54 | 2.20 |
| C1 | Cylinder | hexagonal | 2-B1 | 114 | 51 | 14 | 70 | 1.4 | 5.02 | 8.14 | 3.32 |
| C6 | Cylinder | hexagonal | 3-A3 | 71 | 37 | 20 | 50 | 1.36 | 2.45 | 3.5 | 3.65 |
| C9 | Cylinder | hexagonal | 3-B3 | 43 | 34 | 14 | 49 | 1.41 | 3.60 | 3.2 | 2.24 |
| C16 | Cylinder | quadratic | DIN A4 | 50 | 70 | 35 | 90 | 1.29 | 2.57 | 1.43 | 1.72 |
| C17 | Cylinder | quadratic | DIN A5 | 50 | 60 | 30 | 90 | 1.5 | 3.00 | 1.67 | 1.65 |

The microstructure base dimensions $D$ and distances $P$ on the stamps and the imprinted PU films were analyzed by digital light microscopy. The dimension $D$ corresponds to the base diameter in case of cylinders, the mean value of base major and minor half-axis (mean diameter) in case of ellipsoids and the base width in case of linear ridges. An overview showing the microstructure dimension $D$ over the spacing factor $P/D$ or the roughness factor $rf$ is given in Figure 6.6 and Figure 6.7.

The diagram shows the variation of the diameters $D$, with the lower limit of 35 µm given by the laser micromachining process, and of the distance $P$, resulting in various spacing factors $P/D$ or roughness factors $rf$.

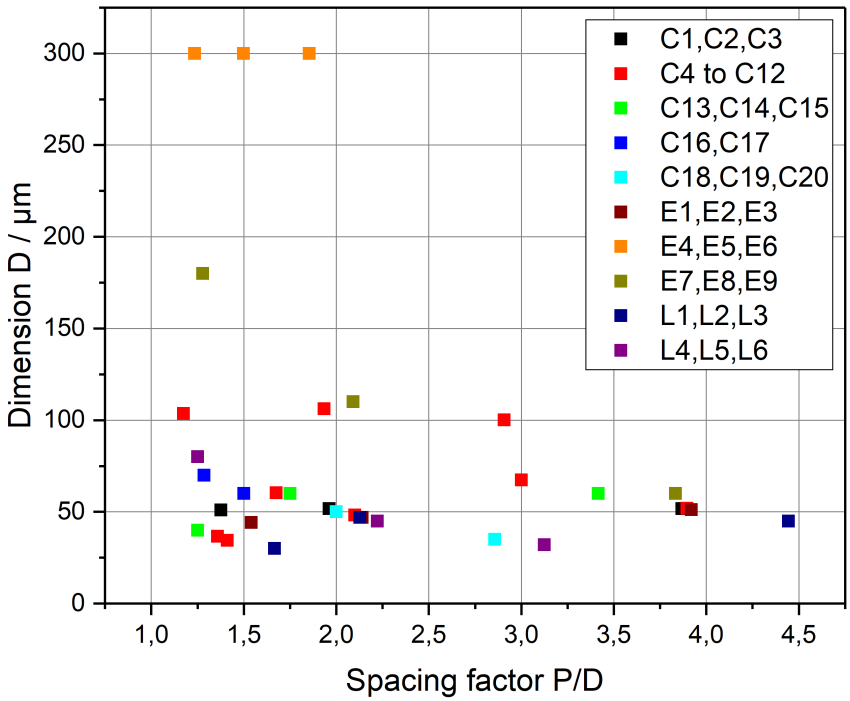


Figure 6.6.: Overview of the dimensions $D$ (diameter in case of cylinders, mean diameter in case of ellipsoids, width in case of linear ridges) over spacing factors $P/D$ of the different microstructures.

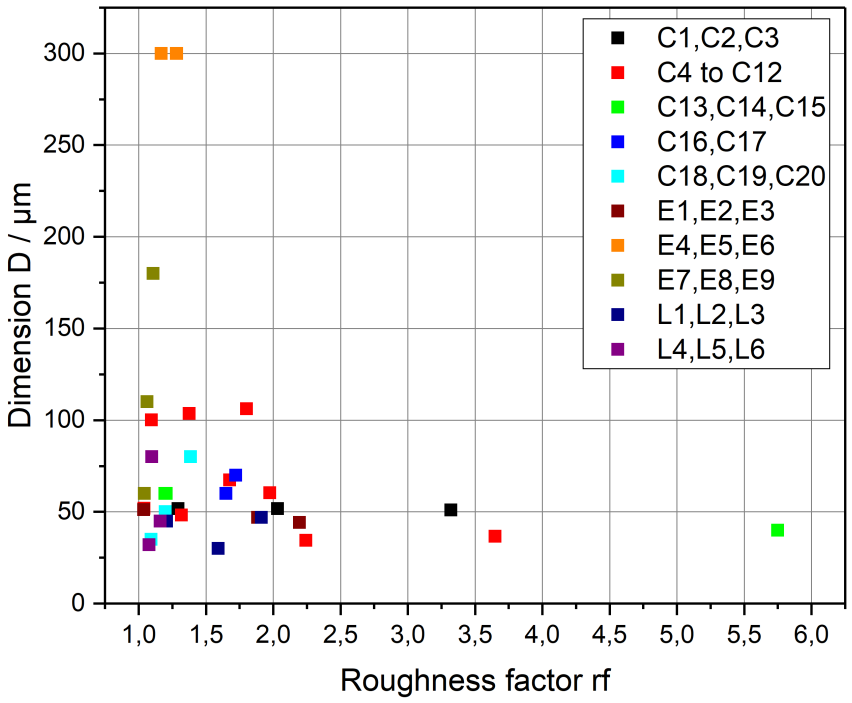


Figure 6.7.: Overview of the dimensions $D$ (diameter in case of cylinders, mean diameter in case of ellipsoids, width in case of linear ridges) over roughness factors $rf$ of the different microstructures.

### 6.2.2. Characterization of the hot embossing process

The different process parameters of the hot embossing process like embossing temperature, pressure, release temperature and process duration were varied in order to find the optimum for microstructure geometry and reproducibility. During the hot embossing process the partly crystalline PU is heated above the glass transition point and the melting point by the hot plates, then it gets pressed into the microstructure cavities of the metal stamps by the applied pressure. After the process time, the PU film is let cool down and is released from the stamp.

#### Thermal properties of the PU films

Differential scanning calorimetry (DSC) measurements (2 heating and cooling runs) were carried out in order to clearly specify the glass transition temperature and the melting temperature of the different PU films. These temperatures determine the hot embossing temperature of the corresponding PU films. Although the values of the second run are normally given for characterization of the thermal properties of a polymer, the values of the first run correspond better to the hot embossing process, where only one heating run and no cooldown is made during one embossing process step.

The DSC data curve of the PU film CMC 63630 with an adhesive layer is given in Figure 6.8. The other DSC data curves are given in Figure A.1 to Figure A.6 in the appendix.

The glass transition and melting temperatures were determined during the first heating cycle from -20 °C to 160 °C and are given in Table 6.2.

The results are similar for the different PU films, except for type LPT4800TT. The glass transition temperature is around 23 °C for the 3M 8674 and the Covestro LPT4802T films, and around 30 °C to 36 °C for the CMC films. Only for the Covestro LPT4800TT neither in run 1 nor in run 2 a glass transition could be seen. A glass transition shows that the PU material changes its flexibility and mechanical properties when used in cold environment below 20 °C against icing. The melting range is between about 66 °C and 92 °C for all PU films. For the Covestro LPT4800TT, two peaks were recorded, one between -3 °C and 21 °C, and one between 52 °C and 67 °C. The second peak was shifted

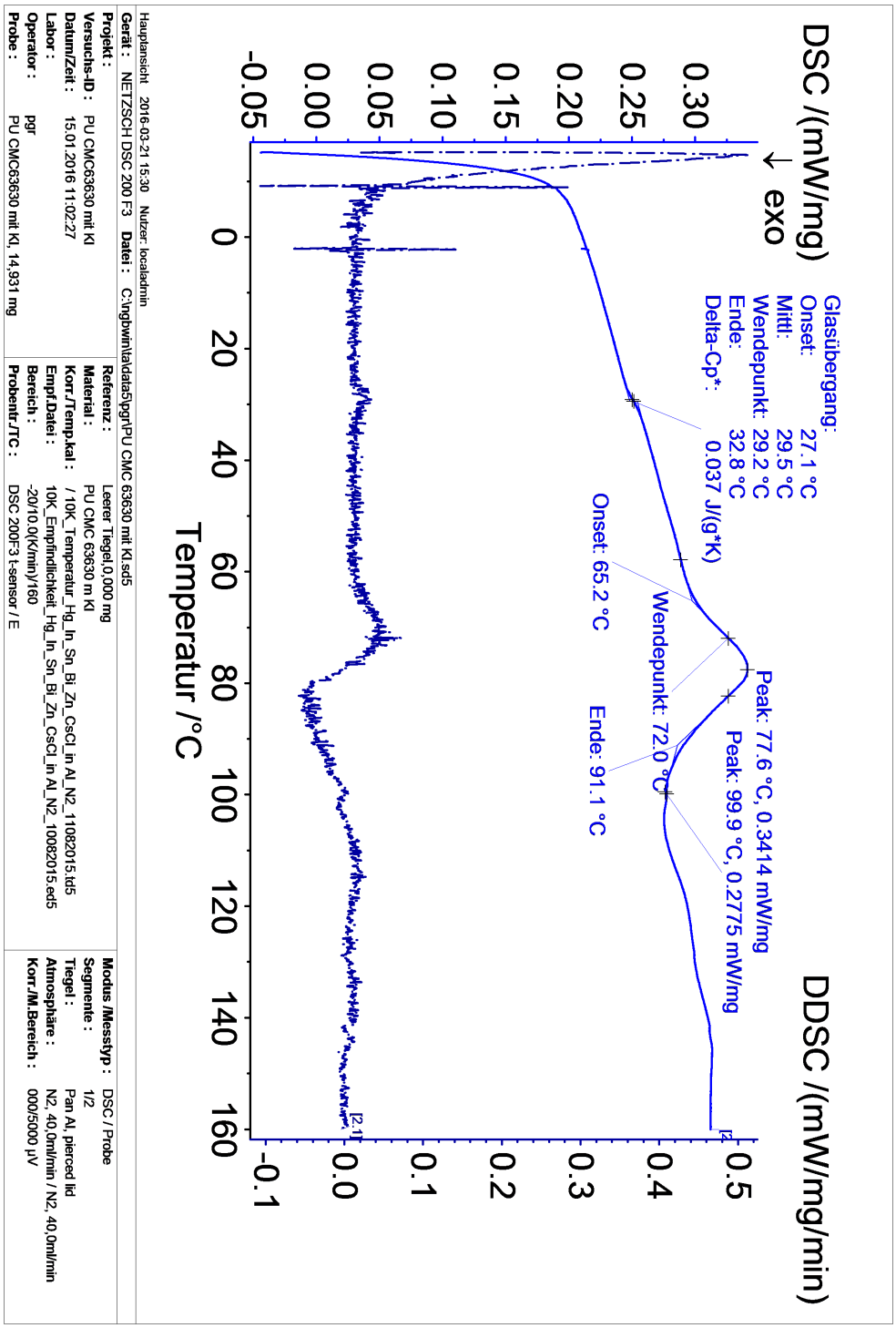


Figure 6.8.: DSC melting curve of the PU film 63630 with adhesive layer from CMC Klebetechnik.

Table 6.2.: Glass transition and melting temperatures of the different PU films determined by DSC.

| PU film | Run | Glass transition | Melting range | | |
|---|---|---|---|---|---|
| - | - | $T_G$ (°C) | $T_M$ Onset (°C) | $T_M$ Peak (°C) | $T_M$ End (°C) |
| 3M 8674 | 1 | 23.2 ± 1.6 | 67.2 | 82.5 | 93.9 |
| Covestro LPT 4800TT | 1 | - | -3.5 / 51.8 | 10.7 / 58.9 | 21.4 / 66.7 |
| Covestro LPT 4800TT | 2 | - | -1.2 / 105.2 | 18 / 132.4 | 33.1 / 148.9 |
| Covestro LPT 4802T | 1 | 22.4 ± 1.0 | 67.8 | 81.3 | 91.2 |
| CMC 63630 w/o. adhesive layer | 1 | 31.7 ± 2.5 | 67.8 | 80.3 | 93.3 |
| CMC 63630 w. adhesive layer | 1 | 29.5 ± 2.8 | 65.2 | 77.6 | 91.1 |
| CMC 63330 w. adhesive layer | 1 | 36.2 ± 1.0 | 64.5 | 77.8 | 90.3 |

towards higher temperatures in the second run. All the PU films had a melting range with a peak at about 80 °C and end at about 90 °C. Therefore the optimal embossing temperature lies in this range of 80 °C to 90 °C.

### Simulation of different embossing methods

Different hot embossing methods were examined in terms of the resulting microstructure shape and contour sharpness. A roll-to-roll embossing process was simulated by an aluminum cylinder.

At first, static embossing with two heatable aluminum plates pressed together by lead weights (pressure of about 1 bar to 5 bar) at 90 °C, 100 °C, 120 °C and 140 °C was examined. The PU film started to become damaged above 120 °C. No microstructures could be imprinted into the PU film with this setup [187].

The imprinting was carried out with an aluminum cylinder of about 10 cm diameter in order to simulate the linear pressure of an imprinting calender in the final roll-to-roll

process. The aluminum cylinder was rolled by hand over the heated PU film on the stamp at 120 °C, 130 °C and 135 °C. With this setup, only 2D shapes of the microstructures with nearly no height could be created on the PU film at 120 °C and 130 °C [187].

In order to imitate a roll-to-roll embossing process, the PU film was fixed to the aluminum cylinder by heat-stable capton tape. In the first case, the cylinder with the PU film was pressed down on the stamp without rolling which is referred to as "static roll imprinting". In the second case, it was pressed down on the stamp and rolled from side to side which should simulate a roll-to-roll process and is referred to as "dynamic roll imprinting" .

By only heating up the PU film above the melting temperature but not applying pressure, it was not possible to imprint microstructures with the heated plate or the cylinder setup. If pressure was applied on the cylinder, static roll imprinting created microstructures with an uneven height distribution, whereas dynamic roll imprinting created microstructures with an even height distribution. However, the pressure was too low in order to create microstructures with the full height given by the microstructure cavities in the embossing stamps [187]. As shown by the dynamic roll imprinting test, an increased line pressure of a real roll-to-roll process is expected to imprint microstructures with larger height.

### Temperature and pressure

The hot embossing parameter search was run on a hydraulic press using two aluminum plates connected to a heating unit for heating up the stamp and the PU film. The first set of hot embossing experiments was carried out at 100 °C, 110 °C and 115 °C, at pressures of 30 bar, 50 bar and 80 bar, in order to find the optimal temperature and pressure for creating well-shaped microstructures [187]. Undamaged microstructures with sharp contours could be created with the highest pressure of 80 bar and 100 °C or 110 °C. A temperature of 115 °C was too high and led to damaged microstructures [187].

The further parameter optimization of the hot embossing process and the final sample preparation was carried out on a pneumatic press equipped with two heatable, flat plates. Therefore, a set of embossing experiments with temperatures of 80 °C, 85 °C, 90 °C and 100 °C and pressures of 50 bar, 100 bar and 150 bar was done. On the basis

of these experiments and the DSC measurements, the embossing temperature was set to 85 °C. The maximum pressure of 150 bar and a process time of 5 minutes were used for sample preparation [1, 180, 2, 184].

### Influence of hot embossing on the chemical structure of the PU films

IR spectra of the PU films before and after the hot embossing process were recorded in order to check whether the chemical structure of the PU is changed or damaged during the hot embossing process. The IR spectra of the PU film 63630 from CMC Klebetechnik show the bands typical for PU, as discussed before in the section on materials (6.1). The spectra are the same before and after hot embossing, so the chemical structure of the PU is not damaged or altered during the hot embossing process, as shown in Figure 6.9.

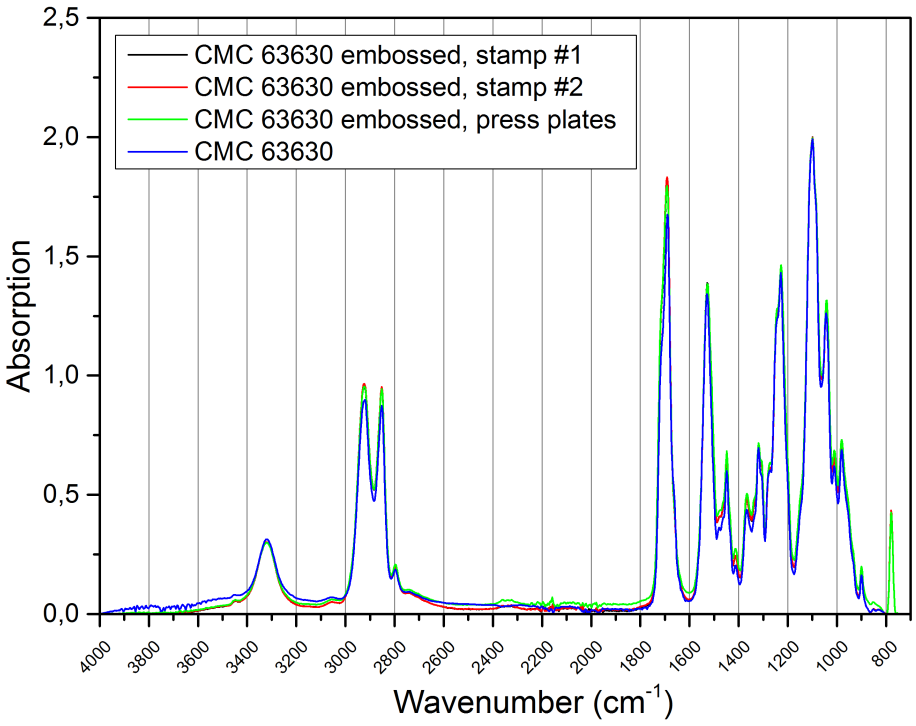


Figure 6.9.: IR spectra of the PU film CMC 63630 before and after hot embossing. Two parts positioned on the stamp ("stamp #1 and #2") and one part positioned directly on the plates of the press ("press plates") were analyzed.

### Reproducibility of the microstructure shape

For an industrially applied production process, the quality and reproducibility of the created surface are of major importance. In the case of microstructuring the PU surface, the microstructures need a reproducible geometrical shape and quality. The sample surfaces were analyzed by LM, LSM and SEM. The first samples showed that the microstructures did not always have the same shape when imprinted with the same parameters [188].

The misshaped, bent microstructures of C6 only occur if the microstructure height reaches the full height of the laser-drilled holes as shown by casted silicone reprints (see subsection on fluorescence laser scanning microscopy in section on wetting behavior 7.1.3). These bent microstructures occured only randomly in PU as usually air trapping during hot embossing prevents the microstructures from reaching the full height.

For analysis of the reproducibility, a set of four embossing experiments with the same process parameters (85 °C, 150 bar, 10 min) was done. A preheating step was introduced before the embossing step, so that the PU film was raised to the right temperature first and the crystalline parts in the surface were melted (85 °C, 10 bar, 1 min). The temperature for removal of the PU film from the stamp was 24 °C [184].

The light microscopy and laser scanning microscopy images of the microstructures C6 and C9 proved that these structures could be imprinted with reproducible geometrical dimensions of the diameter $D$, distance $P$ and height $H$ [184]. Some microstructures had flat tops and some had craters at the top because of entrapped air in the stamp holes during hot embossing. Exemplary laser scanning microscopy profiles of microstructures C6 and C9, with and without craters at their top, are shown in Figure 6.10.

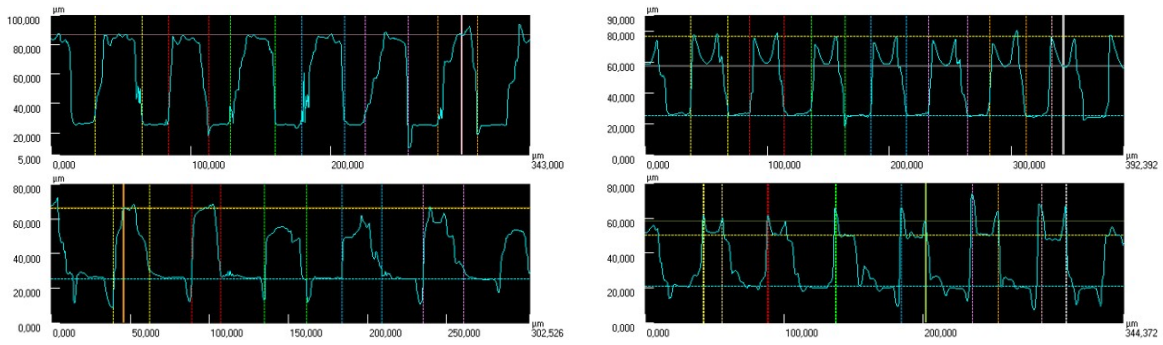

Figure 6.10.: Exemplary laser scanning microscopy profiles of microstructures C6 (top) and C9 (bottom), left: with normal top, right: with crater at the top because of entrapped air in the stamp holes during hot embossing.

### Removal temperature of the PU film

In order to analyze the influence of delamination of the PU film from the stamp after hot embossing, the PU films were delaminated at various temperatures. The tests were done with the established process parameters for preheating (85 °C, 10 bar, 1 min) and hot embossing (85 °C, 150 bar, 10 min) [184]. Afterwards, the microstructures were analyzed with light microscopy and laser scanning microscopy. The height depending on the removal temperature is shown in Figure 6.11 for microstructure C6, Figure 6.12 for microstructure C9 and Figure 6.13 for microstructure C16.

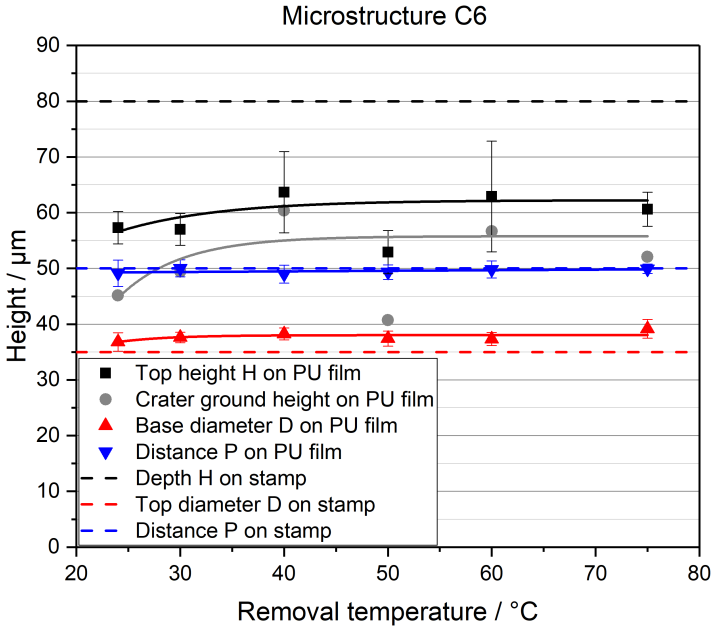


Figure 6.11.: Influence of PU film removal temperature: height of the microstructure C6 in dependence of the removal temperature of the preheated and hot embossed PU film.

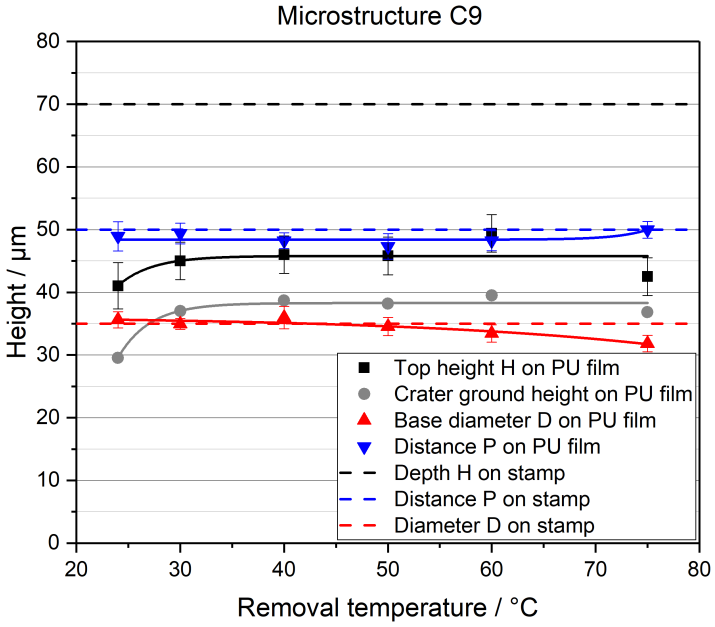


Figure 6.12.: Influence of PU film removal temperature: height of the microstructure C9 in dependence of the removal temperature of the preheated and hot embossed PU film.

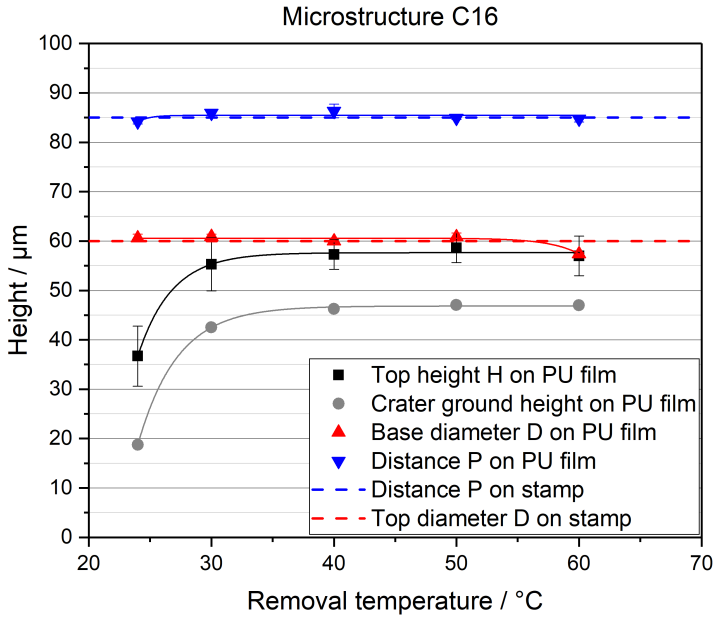


Figure 6.13.: Influence of PU film removal temperature: height of the microstructure C16 in dependence of the removal temperature of the preheated and hot embossed PU film.

For all the examined microstructures, the base diameters D and distances P of the microstructures on PU correspond well to the given parameters on the stamps and do not depend on the removal temperature. The removal temperature graphs show that the removal temperature has an impact on the final microstructure top height and crater ground height (craters are caused by air trapping during hot embossing). The height increases with increasing removal temperature up to 40 °C. If the removal temperature is below 40 °C, the height is reduced. At 75 °C the microstructure height is reduced because this temperature is close to the melting range peak of 80 °C of the PU and the microstructures get damaged during removal. The optimal temperature for PU film removal is therefore between 40 °C and 60 °C. However, the full height - given by the depth of the holes on the stamps - is not reached by any microstructure. Only about 60 µm of 80 µm for C6, 45 µm of 70 µm for C9 and 58 µm of 85 µm for C16 could be reached. A removal temperature of 60 °C corresponds best to the removal in a roll-to-roll process.

### Hot embossing process time

Process time is a critical parameter for a roll-to-roll production and should be kept as low as possible. In order to find the optimum process time, where the microstructures still have the required height, a set of embossing experiments was done with varied process times. The experiments were done with the established process parameters for preheating (85 °C, 10 bar, 1 min) and hot embossing (85 °C, 150 bar). The temperature for removal of the PU film from the stamp was 60 °C [184]. The height in dependence of the process time is shown in Figure 6.14 for microstructure C6 and Figure 6.15 for microstructure C9.

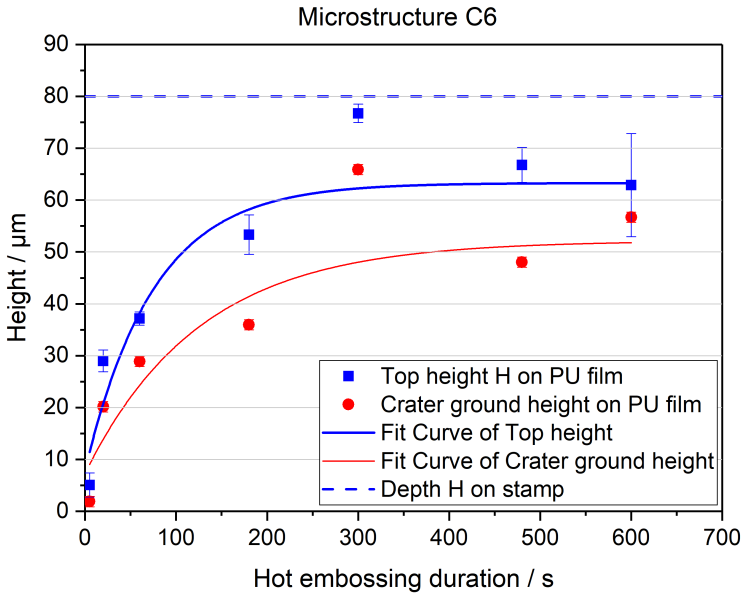


Figure 6.14.: Influence of hot embossing process duration: height of the microstructure C6 in dependence of the hot embossing duration of the preheated and hot embossed PU film.

The embossing time graphs show that the embossing duration time significantly influences the microstructure height. The microstructure height increases with increasing hot embossing duration, until it reaches a limit after about 300 s (see the exponential fit curves). The largest height, which was also closest to the maximum, was reached by microstructure C6 at 300 s. A similar result could not be reached on microstructure C9. For both microstructures, even with longer embossing process times the maximum

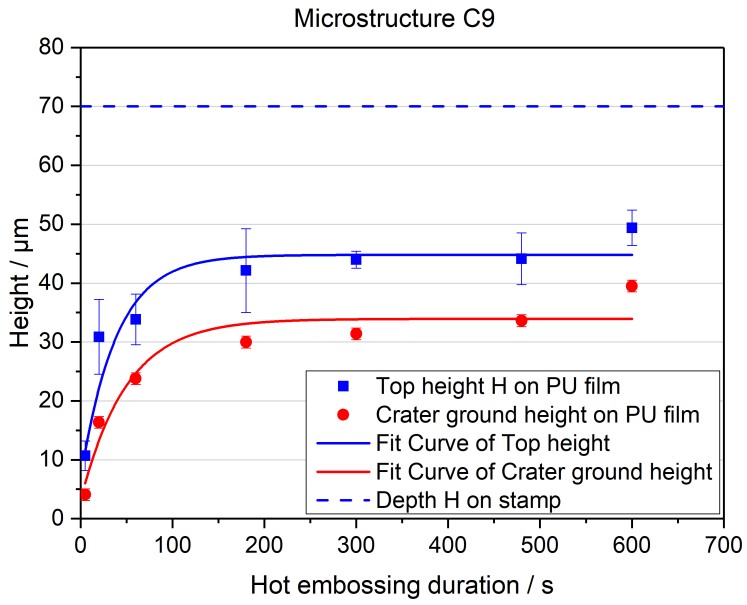


Figure 6.15.: Influence of hot embossing process duration: height of the microstructure C9 in dependence of the hot embossing duration of the preheated and hot embossed PU film.

height given by the holes of the stamp could not be reached. Therefore, the embossing process duration was set down from 10 min to 5 min for the sample preparations for further characterization of wetting, icing and de-icing.

### Comparison of microstructure dimensions from hot embossing without and with preheating

In order to see the influence of the preheating step before the hot embossing step, the geometrical dimensions of microstructures C6 and C9 embossed without and with the preheating step are compared in Table 6.3.

As can be seen, the preheating step does not alter the geometrical dimensions of the microstructures C6 and C9 significantly.

Table 6.3.: Comparison of geometrical dimensions of microstructures hot embossed without and with preheating.

| Preheating | Microstructure | Diameter | Pitch | Spacing factor | Top height | Crater base height |
|---|---|---|---|---|---|---|
| - | - | D (µm) | P (µm) | P/D | H (µm) | (µm) |
| no | C6 | $41 \pm 1$ | $48 \pm 2$ | $1.2 \pm 0.1$ | 69 | 55 |
| no | C9 | $35 \pm 3$ | $50 \pm 2$ | $1.4 \pm 0.2$ | 45 | 40 |
| yes | C6 | $37 \pm 2$ | $49 \pm 2$ | $1.3 \pm 0.1$ | $57 \pm 3$ | $45 \pm 12$ |
| yes | C9 | $36 \pm 1$ | $49 \pm 2$ | $1.4 \pm 0.1$ | $41 \pm 4$ | $30 \pm 11$ |

### Summary of the hot embossing process parameters

The PU elastomer film 8674 from 3M was chosen because it is used in aviation for protection of wing surfaces. The thermoplastic PU films LPT 4800 (Polyester-based) and LPT 4802 (Polyether-based) by Epurex Films, Covestro (formerly Bayer MaterialScience) are newly developed aliphatic PU films (laboratory products) with better UV stability compared to common aromatic PU films. They are transparent and well suited for large scale, visible areas. The thermoplastic PU films 63615 and 63630 (superseded by 63330) from CMC Klebetechnik are based on aliphatic Polyethers but are more economical and therefore the best choice for surface functionalization on a larger scale in the future. The DSC measurements showed that the PU films all had a melting range from 65 °C to 90 °C with a peak at 80 °C. The lab-scale roll imprinting was done for simulating a line pressure distribution. With the dynamic roll imprinting well-shaped microstructures could be generated, but not with their full height because the pressure was not high enough. This was only achieved with the flat pressure distribution of the pneumatic plate press using high pressure. Further embossing experiments led to the parameters of 85 °C and the maximum possible pressure of 150 bar for sample preparation. IR spectroscopy measurements showed that the chemistry of the PU film CMC 63630 is not altered during the hot embossing process (see Figure 6.9). A preheating step was introduced before the hot embossing step in order to melt the PU film surface before embossing. The reproducibility of the microstructures produced on the plate press was

good. Craters occurred often on the microstructure tops because of trapped air during hot embossing. Bent cylinders were microscopically seen randomly for microstructure C6, if its full height of about 80 µm was reached. The removal temperature of the PU film from the stamp after hot embossing does not have an influence on the microstructure height, if it is above 40 °C. The microstructure height increases with increasing embossing time and reaches a maximum after 5 minutes. The overall best PU film type cannot be given here because some parameters were only analyzed on the PU film CMC 63630 which was chosen for further large scale functionalization in the future. Therefore, the materials used during the optimization tests are given for each parameter. Table 6.4 summarizes the tested and optimal hot embossing process parameters.

Table 6.4.: Summary of the varied and optimal hot embossing process parameters.

| Process parameter | Tested PU film | parameter variation | optimal parameter |
|---|---|---|---|
| Temperature | 3M 8674, LPT 4800, LPT 4802, CMC 63630, CMC 63615, CMC 63330 | 80 °C to 115 °C | 85 °C |
| Pressure | LPT 4800, CMC 63630 | 30 bar to 150 bar | 150 bar |
| Removal temperature of PU film | CMC 63630 | 25 °C to 75 °C | >40 °C |
| Embossing duration | CMC 63630 | 5 s to 600 s | 300 s |

## 6.3. Plasma polymer coatings

Hydrophobic surface chemistry on the microstructures is needed for a superhydrophobic surface. It was created by PECVD. The hydrophobic plasma polymer coatings were analyzed by several methods. In the following subsections, the process parameters are listed along with the thickness, coating rates, surface roughness and surface chemistry of the coatings.

### 6.3.1. PECVD process parameters for standard plasma polymers

The aim was to deposit plasma polymer thin films of about 200 nm thickness. The coating thickness of the normal hydrophobic plasma polymers was measured by spectroscopic ellipsometry. The process parameters are shown in Table 6.5 (dc = duty cycle on time fraction).

The resulting coating thickness increases with increasing process time. The deposition rate also depends on the gas flow, process pressure and power. For the fluorocarbon plasma coatings, $C_3F_6$ and $C_4F_8$ were used for further plasma etching experiments and the final sample preparation because of the higher deposition rates compared to $CHF_3$. In case of HMDSO the gas flow was adjusted from 10 sccm to 7 sccm because of the leakage rate of the mass flow controller of up to 2.5 sccm. Coating thicknesses of about 150 nm to 200 nm were achieved for all the fluorocarbon and the HMDSO precursors.

Table 6.5.: Plasma process parameters, film thickness and coatings rates of the standard plasma coatings determined by spectroscopic ellipsometry.

| | | Plasma process | | | | Plasma coating | |
|---|---|---|---|---|---|---|---|
| Coating name | Precursor | Gas flow (sccm) | $p$ (mbar) | RF (W) | $t$ (min) | $d$ (nm) | Rate ($\frac{nm}{min}$) |
| $CHF_3$ [179] | $CHF_3$/Ar | 10/60 | 0.8 | 50 | 3 (dc 0.35) | 34 | 11 |
| $CHF_3$ [179] | $CHF_3$/Ar | 10/60 | 0.8 | 100 | 3 (dc 0.35) | 73 | 24 |
| $CHF_3$ [187] | $CHF_3$/Ar | 10/60 | 0.8 | 50 | 3 | 24 | 8 |
| $CHF_3$ [1] | $CHF_3$ | 30 | 0.2 | 100 | 10 | 148 | 15 |
| $C_4F_8$ [179] | $C_4F_8$ | 10 | 0.1 | 50 | 2 | 53 | 26 |
| $C_4F_8$ [179] | $C_4F_8$ | 10 | 0.1 | 100 | 2 | 75 | 37 |
| $C_4F_8$ [187, 180] | $C_4F_8$ | 10 | 0.1 | 50 | 2 | 68 | 34 |
| $C_4F_8$ [1, 2] | $C_4F_8$ | 20 | 0.2 | 50 | 7 | 216 | 31 |
| $C_3F_6$ [187] | $C_3F_6$ | 20 | 0.15 | 60 | 3 | 176 | 59 |
| $C_3F_6$ [184] | $C_3F_6$ | 30 | 0.11 | 50 | 7 | 236 | 34 |
| $C_3F_6$ | $C_3F_6$ | 30 | 0.13 | 50 | 5 | 199 | 40 |
| HMDSO [179] | HMDSO/$N_2$ | 10/100 | 0.15 | 60 | 5 | 236 | 47 |
| HMDSO [179] | HMDSO/$N_2$ | 10/100 | 0.15 | 350 | 2 | 599 | 300 |
| HMDSO [187, 180, 189] | HMDSO/$N_2$ | 10/100 | 0.15 | 60 | 5 | 157 | 31 |
| HMDSO [2] | HMDSO/$N_2$ | 10/100 | 0.18 | 60 | 6 | 296 | 49 |
| HMDSO | HMDSO/$N_2$ | 7/100 | 0.09 | 60 | 5 | 245 | 49 |
| HMDSO | HMDSO/$N_2$ | 7/100 | 0.09 | 200 | 3 | 420 | 140 |

### 6.3.2. Plasma etching process parameters for plasma polymers with increased nanoroughness

In order to generate a nanoscale roughness overlaying the microstructures, the plasma polymer coatings were etched in an oxygen or argon plasma in the DIN A3 reactors. Afterwards, they were shortly coated again to create a closed, thin, hydrophobic top layer after etching. An oxygen or argon gas flow was set similar to that of the corresponding coating process and the throttle valve was completely opened leading to the final process

pressure. The dependence of different surface nano-roughness values on different etching power parameters was analyzed. Therefore, the etching process with argon was carried out at 100 W, 200 W and 300 W on both the fluorocarbon and the silicone-like plasma coatings. The etching and coating parameters are given in Table 6.6. The achieved nano-roughness is discussed in the following subsection about the AFM measurements.

Table 6.6.: Process parameters and etching rates of the used oxygen and argon plasma etching processes.

| Surface preparation | | | Plasma process parameters | | | | | | Coating |
|---|---|---|---|---|---|---|---|---|---|
| Step 1 Coating | Step 2 Etching | Step 3 Coating | Gas - | Flow (sccm) | $p$ (mbar) | RF (W) | $t$ (min) | $d$ (nm) | Rate ($\frac{nm}{min}$) |
| $C_3F_6$ [184] | $O_2$ | - | $O_2$ | 30 | 0.2 | 100 | 1 | -64 | -64 |
| $C_3F_6$ [184] | $O_2$ | $C_3F_6$ | $C_3F_6$ | 30 | 0.11 | 50 | 1 | 37 | 37 |
| $C_4F_8$ [2] | Ar | - | Ar | 50 | 0.2 | 100 | 10 | - | -5 |
| $C_4F_8$ [2] | Ar | $C_4F_8$ | $C_4F_8$ | 20 | 0.11 | 50 | 0.5 | 19 | 38 |
| $C_3F_6$ [184] | Ar | - | Ar | 50 | 0.28 | 100 | 10 | -30 | -3 |
| $C_3F_6$ [184] | Ar | $C_3F_6$ | $C_3F_6$ | 30 | 0.11 | 50 | 1 | 35 | 35 |
| $C_3F_6$ | Ar | - | Ar | 50 | 0.38 | 200 | 10 | - | -4 |
| $C_3F_6$ | Ar | - | Ar | 30 | 0.38 | 300 | 10 | - | -6 |
| HMDSO [2] | Ar | - | Ar | 100 | 0.2 | 100 | 10 | - | -2 |
| HMDSO [2] | Ar | HMDSO | HMDSO/$N_2$ | 10/100 | 0.18 | 60 | 0.166 | 8 | 48 |
| HMDSO | Ar | - | Ar | 100 | 0.26 | 200 | 10 | - | -1 |
| HMDSO | Ar | - | Ar | 100 | 0.26 | 300 | 10 | - | -3 |

As the thickness measurements show, etching in an $O_2$ plasma leads to a higher etching rate than in an argon plasma because of the oxidative effect of the oxygen. Increasing the power in the argon plasma from 100 W to 300 W increased the etching rate. The etching rates of the silicone-like plasma polymers were lower than those of the fluorocarbon plasma polymers but are in the same range. Overall, the erosion of the plasma coatings is only minimal by these low etching rates of the argon plasma.

In another experimental set, a nanorough surface was generated by first etching the PU film and then coating it with a hydrophobic plasma polymer. The etching and coating parameters are shown in Table 6.7.

Table 6.7.: Process parameters used for oxygen plasma etching of the PU film

| Surface preparation | | | Plasma process parameters | | | | | Coating | |
|---|---|---|---|---|---|---|---|---|---|
| Coating name | Step 1 Etching | Step 2 Coating | Gas - | Flow (sccm) | $p$ (mbar) | RF (W) | $t$ (min) | $d$ (nm) | Rate ($\frac{nm}{min}$) |
| - | $O_2$ | - | $O_2$ | 30 | 0.28 | 200 | 3 | - | - |
| $O_2$, $C_3F_6$ | $O_2$ | $C_3F_6$ | $C_3F_6$ | 30 | 0.13 | 50 | 5 | 199 | 40 |

No rate of etching the PU film can be given, since the PU film thickness could not be measured for nanometer changes by ellipsometry.

### Discussion of the plasma etching process for creating a nanoscale roughness

In the literature, similar plasma etching experiments have been done for combined roughening and fluorination of a polystyrene (PS) surface in a $CF_4/O_2$ plasma [84]. Here, etching and coating takes place simultaneously. A RF capacitively coupled parallel plate plasma reactor was used with a constant $CF_4/O_2$ gas flow rate of 60 sccm at a constant pressure of 0.08 mbar. The effects of the $O_2$ fraction (0 %, 17 %, 33 %, 50 % and 100 %) in the gas mixture, of the input power (from 50 W to 300 W) and of the treatment duration were investigated by SEM, AFM, ESCA and advancing / receding water contact angle measurements. The highest F/C ratio was achieved for an $O_2/CF_4$ mixture containing 17 % $O_2$ (10 sccm $O_2$/50 sccm $CF_4$). For this ratio, the power and the process time were varied. For a process time of 5 min and variable power values up to 150 W, the contact angle hysteresis was quite similar at around 20°, but with an increasing power up to 300 W, it could be reduced by increased receding contact angle values. The highest advancing contact angle (162°) and lowest hysteresis (2°) could be obtained with the treatment at 300 W for 5 min. A surface with nanostructure heights of about 400 nm to 500 nm, a density of nanostructures on the surface of about 18 $\mu m^{-2}$ (calculated by ImageJ imaging software elaboration of SEM top view images) and an overall RMS value of 35 nm resulted from this. A treatment at 150 W for 20 min resulted

in a sticky surface, although it had a nanostructure height of about 600 nm, a density of nanostructures on the surface of about 9 $\mu m^{-2}$ and an RMS value of 75 nm. This shows that superhydrophobic surfaces can be either sticky or slippery, depending on the height, top surface area and spacing (lateral density) of the nanostructures [84].

### 6.3.3. Plasma polymer surface chemistry

The plasma polymers have to create a hydrophobic coating on the microstructures needed for a superhydrophobic surface. The surface chemistry of the first 10 nm of the plasma polymer coatings was analyzed by ESCA in order to see whether a hydrophobic composition was achieved. The ESCA measurement results of the fluorocarbon plasma coatings on PU are shown in Figure 6.16.

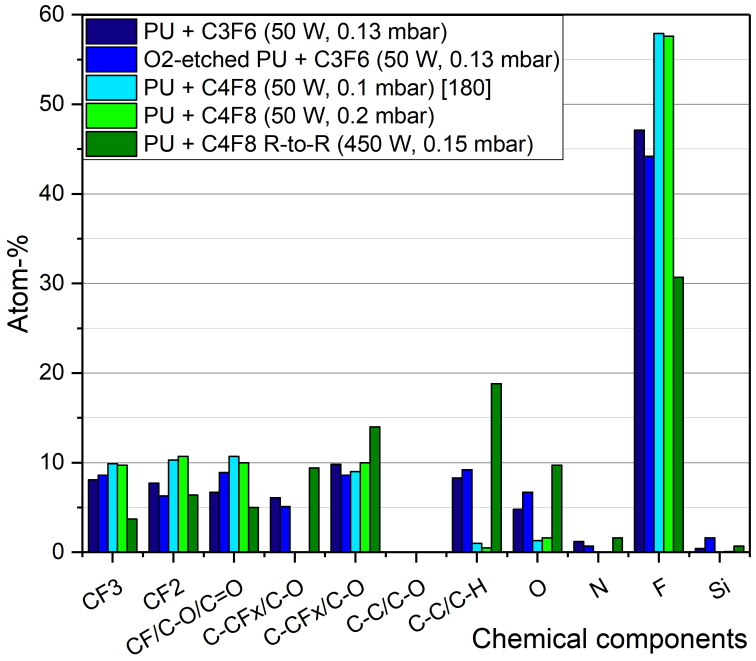


Figure 6.16.: Surface chemistry of several fluorocarbon plasma coatings on PU film CMC 63630, determined by ESCA.

The plasma coating thicknesses measured on silicon wafers are as follows: 236 nm for sample PU + $C_3F_6$ (50 W, 0.13 mbar), 200 nm for sample $O_2$-etched PU + $C_3F_6$ (50 W,

0.13 mbar), 214 nm for sample PU + $C_4F_8$ (50 W, 0.1 mbar) [180] and 175 nm for sample PU + $C_4F_8$ (50 W, 0.2 mbar). No thickness has been determined for sample PU + $C_4F_8$ R-to-R (450 W, 0.15 mbar). The significant peaks of a fluorocarbon plasma polymer can be seen for all coatings, namely $CF_3$, $CF_2$, CF, C-$CF_X$, C-C/C-H and F. The oxygen, nitrogen and silicon peaks do not belong to the fluorocarbon polymer, as these materials are not used for the plasma. The $C_4F_8$-plasma coatings have a very high fluorine content of nearly 60 %. The $C_3F_6$-plasma coatings have a lower fluorine content of only about 45 % and the roll-to-roll $C_4F_8$-plasma coating consists to only 30 % of fluorine. These coatings have larger peaks for the C-C/C-H group (nearly 10 % or 20 %), oxygen (5 % or 10 %) and nitrogen. The oxygen and nitrogen peaks are caused by either the incorporation of oxygen and nitrogen from air in the plasma reactor or from gases of the PU or acrylate adhesive or by oxidation on ambient air after the plasma process.

Figure 6.17 shows the ESCA measurement results of the fluorocarbon plasma coatings on silicon wafers.

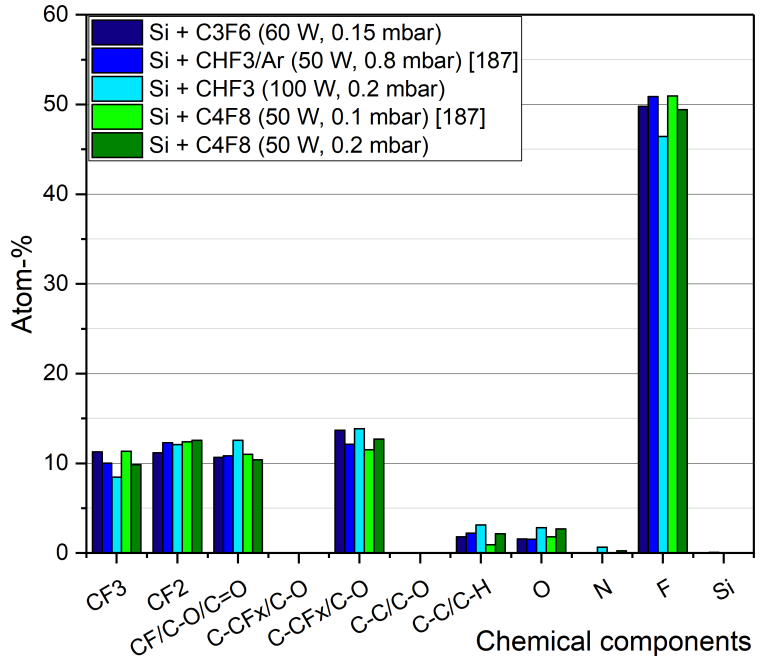


Figure 6.17.: Surface chemistry of several fluorocarbon plasma coatings on Si-wafers, determined by ESCA.

The thickness values of the plasma coatings on silicon wafers are as follows: 176 nm for sample Si + $C_3F_6$ (60 W, 0.15 mbar), 24 nm for sample Si + $CHF_3$/Ar (50 W, 0.8 mbar) [187], 148 nm for sample Si + $CHF_3$ (100 W, 0.2 mbar), 68 nm for sample Si + $C_4F_8$ (50 W, 0.1 mbar) [187] and 326 nm for sample Si + $C_4F_8$ (50 W, 0.2 mbar). The fluorocarbon plasma coatings on silicon wafers all show a very similar peak distribution with a fluorine content of about 50 %. The oxygen and nitrogen peaks are caused either by the incorporation of oxygen and nitrogen from air in the plasma reactor or from gases of the PU or acrylate adhesive or by oxidation on ambient air after the plasma process.

Figure 6.18 shows the ESCA measurement results of silicone-like plasma polymers.

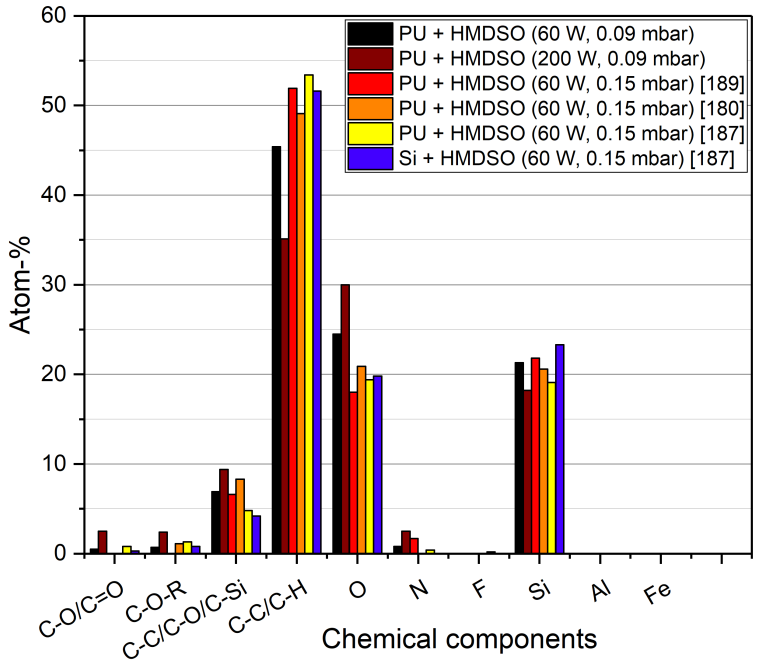


Figure 6.18.: Surface chemistry of several HMDSO plasma coatings on PU film CMC 63630, determined by ESCA.

Here, the plasma coating thickness values measured on silicon wafers are 245 nm for sample PU + HMDSO (60 W, 0.09 mbar), 445 nm for sample PU + HMDSO (200 W, 0.09 mbar), 243 nm for sample PU + HMDSO (60 W, 0.15 mbar) [189], 212 nm for sample PU + HMDSO (60 W, 0.15 mbar) [180], 157 nm for sample PU + HMDSO (60 W, 0.15 mbar) [187] and 157 nm for sample Si + HMDSO (60 W, 0.15 mbar) [187]. The significant peaks of the HMDSO-plasma polymer are C=O, C-O, C-Si, C-C/C-H, O and Si. About 45 % to 50 % of the polymer are C-C or C-H groups. Also incorporated are silicon at an amount of about 20 % (30 % if the C-Si peak is included) and oxygen at an amount of about 20 %. The nitrogen peaks are caused by the incorporation either from ambient air in the plasma reactor or from gases of the PU or the acrylate adhesive. The 200 W HMDSO-plasma coating has a higher content of oxygen (30 %) and a lower content of C-C/C-H groups (35 %) compared to the 60 W HMDSO-plasma coatings. Therefore, it is expected to be less hydrophobic than the 60 W HMDSO-plasma coating.

ESCA-spectra of some of these plasma coatings are given in the appendix.

### 6.3.4. Bulk chemistry of the plasma coated PU films determined by IR spectroscopy

Additional IR measurements of the plasma coated PU films show the bulk chemistry up to a depth of approximately a few micrometers, including the plasma coating of about 200 nm thickness.

#### $C_XF_Y$ plasma coatings on a PU film

The typical IR spectra of the PU film CMC 63630 coated with $C_XF_Y$ plasma polymers, determined by IR spectroscopy with the ATR method, are shown in Figure 6.19.

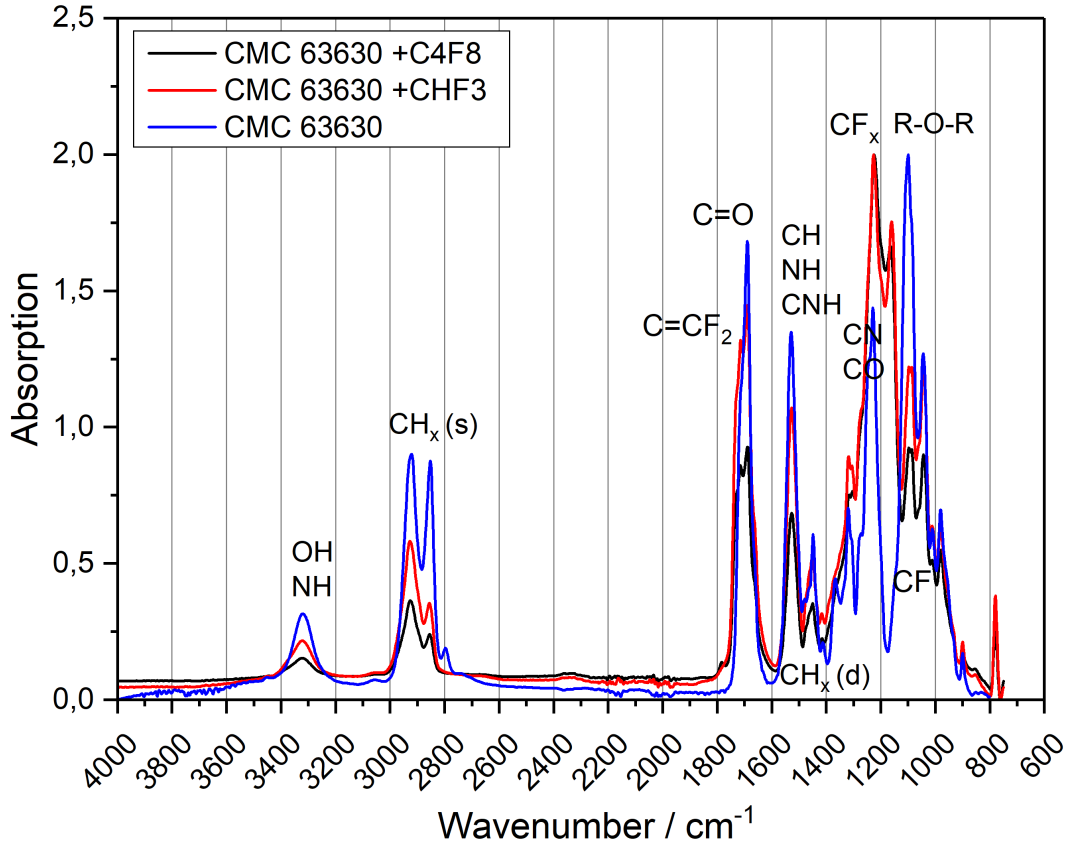


Figure 6.19.: IR spectra of the $C_XF_Y$ plasma coatings on PU film CMC 63630.

The bands typical for PU can be seen, namely of OH (3300 $cm^{-1}$), $CH_2$ and $CH_3$ (2850 $cm^{-1}$/ 2950 $cm^{-1}$ and 1340/1475 $cm^{-1}$), carbonyl (C=O, 1690 $cm^{-1}$), CH or NH (1550 $cm^{-1}$), CN or CO (1230 $cm^{-1}$) and the ether group (1100 $cm^{-1}$). On the coated samples, a broad band between 1000 $cm^{-1}$ and 1400 $cm^{-1}$ because of the $CF_X$ groups and bands for CF (1070 $cm^{-1}$) and $C{=}CF_2$ (1730 $cm^{-1}$) appear which are characteristic of the fluorocarbon plasma polymer [190, 186]. The bands of the PU have decreased in intensity and the newly appeared bands can be attributed to the fluorocarbon plasma polymer. The IR spectrum shows that the bulk chemical structure of the PU is not altered by the plasma coating process because no other new bands have appeared.

### HMDSO plasma coatings on a PU film

The typical IR spectra of the PU film CMC 63630 coated with HMDSO plasma polymers, determined by IR spectroscopy with the ATR method, are shown in Figure 6.20.

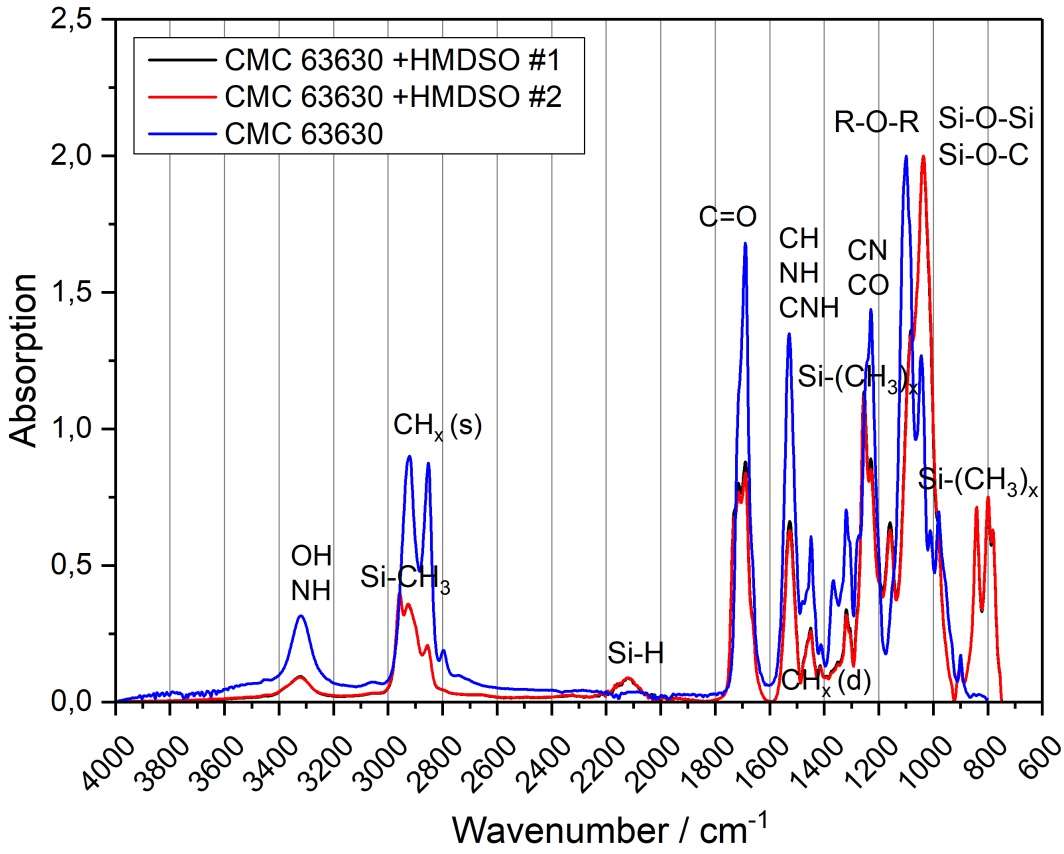


Figure 6.20.: IR spectra of the HMDSO plasma coatings on PU film CMC 63630.

The same bands typical for PU as described above can be seen. The silicone-like coating generates the additional bands of Si-$CH_3$ (2960 $cm^{-1}$), Si-H (2100 $cm^{-1}$), Si-$(CH_3)_X$ (1260 $cm^{-1}$), Si-$(CH_3)_3$ (840 $cm^{-1}$), Si-$(CH_3)_2$ (800 $cm^{-1}$) and Si-O-Si (1070/1150 $cm^{-1}$) or Si-O-C (1035/1100 $cm^{-1}$) [191, 192]. The bands of the PU have decreased in intensity and the newly appeared bands can be attributed to the silicone-like plasma polymer. The IR spectrum shows that the bulk chemical structure of the PU is not altered by the plasma coating process.

### 6.3.5. Nanoscale topography of the standard and etched plasma polymers

The nanoroughness values acquired by the plasma processes described above are given in this subsection. By the combination of coating and etching processes, three types of surfaces were created: the polyurethane film with a coating layer (type I), with a coating layer that was subsequently etched (type II) or with a coating layer that was subsequently etched and thinly coated again (type III). The AFM image area for determination of the roughness factors was 10 µm x 10 µm measured by an NSG-11 AFM tip. In additional measurements for comparison, the AFM image area was 15 µm x 15 µm measured by an NSG-11 AFM tip [2, 184] or 20 µm x 20 µm measured by an NSG-11 AFM tip [179]. All AFM measurements were done on plasma coatings on PU film substrates, except for the values from [184] which were measured on plasma coatings on silicon wafers. High $S_a$ roughness values correspond to tall peaks / deep valleys, therefore the aim was to generate a surface with a high $S_a$ value. At the same time the diameter of the nanobumps should be as small as possible. As this would increase the actual surface area, a high $S_{dr}$ value must be achieved simultaneously in order for the surface nanoroughness to resemble that of a lotus leaf.

#### Nanometer roughness values of the $C_4F_8$ plasma polymer

Table 6.8.: Nanometer roughness values of $C_4F_8$ plasma polymers determined by AFM.

| Type | step 1: coating | step 2: etching | step 3: coating | Scan length | Roughness average $S_a$ | Root mean square $S_q$ | Surface area ratio $S_{dr}$ | Mean summit curvature $S_{sc}$ | Radius of curvature $R$ |
|---|---|---|---|---|---|---|---|---|---|
| - | - | - | - | (µm) | (nm) | (nm) | (%) | (1/nm) | (nm) |
| I [179] | $C_4F_8$ (50 W) | - | - | 20 | 17 | 25 | - | - | - |
| I [179] | $C_4F_8$ (100 W) | - | - | 20 | 7 | 10 | - | - | - |
| I [2] | $C_4F_8$ (50 W) | - | - | 15 | 5.21 | 7.27 | 0.124 | $5.31 \cdot 10^{-5}$ | 18800 |
| II [2] | $C_4F_8$ (50 W) | Ar (100 W) | - | 15 | 14.2 | 18 | 0.389 | $5.66 \cdot 10^{-5}$ | 17700 |
| III [2] | $C_4F_8$ (50 W) | Ar (100 W) | $C_4F_8$ | 15 | 6.32 | 9.61 | 0.079 | $2.34 \cdot 10^{-5}$ | 42700 |

The roughness values depend on the process power and gas flow as can be seen for the plain $C_4F_8$ plasma coatings. The values could be slightly increased by 100 W Ar-plasma etching, but were decreased again by the following thin hydrophobic $C_4F_8$ plasma coating. Additionally, the $S_{dr}$ value is very small for the etched and coated surfaces. The corresponding AFM images are shown in the appendix.

### Nanometer roughness values of the $C_3F_6$ plasma polymer

The nanoscale roughness values of the etched $C_3F_6$ plasma coatings are shown in Table 6.9.

Table 6.9.: Nanometer roughness values of $C_3F_6$ plasma polymers determined by AFM.

| Type | step 1: coating | step 2: etching | step 3: coating | Scan length | Roughness average $S_a$ | Root mean square $S_q$ | Surface area ratio $S_{dr}$ | Mean summit curvature $S_{sc}$ | Radius of curvature $R$ |
|---|---|---|---|---|---|---|---|---|---|
| - | - | - | - | (µm) | (nm) | (nm) | (%) | (1/nm) | (nm) |
| I | $C_3F_6$ | - | - | 10 | 21.6 | 27.6 | 3.44 | $13.8 \cdot 10^{-5}$ | 7246 |
| I [184] | $C_3F_6$ | - | - | 15 | 0.14 | 0.19 | 0.001 | $0.403 \cdot 10^{-5}$ | 248000 |
| II [184] | $C_3F_6$ | O2 (100 W) | - | 15 | 0.88 | 1.15 | 0.074 | $1.28 \cdot 10^{-5}$ | 78100 |
| III [184] | $C_3F_6$ | O2 (100 W) | $C_3F_6$ | 15 | 0.21 | 0.27 | 0.002 | $0.675 \cdot 10^{-5}$ | 148000 |
| II [184] | $C_3F_6$ | Ar (100 W) | - | 1 | - | 1 | - | - | - |
| III [184] | $C_3F_6$ | Ar (100 W) | $C_3F_6$ | 1 | - | 0.25 | - | - | - |
| II | $C_3F_6$ | Ar (200 W) | - | 10 | 6.5 | 10.2 | 0.097 | $4.2 \cdot 10^{-5}$ | 23810 |
| II | $C_3F_6$ | Ar (300 W) | - | 10 | 3.64 | 4.79 | 0.007 | $1.62 \cdot 10^{-5}$ | 61728 |
| I [179] | $CHF_3$ (50 W) | - | - | 20 | 8 | 15 | - | - | - |
| I [179] | $CHF_3$ (100 W) | - | - | 20 | 16 | 24 | - | - | - |

The plain $C_3F_6$ plasma coating had higher roughness values than the $C_4F_8$ plasma coating. The etching in an oxygen or argon plasma led to decreased instead of increased $S_a$ and $S_q$ values. Also the $S_{dr}$ value could not be increased compared to the plain

plasma coating. Here, the etching did not lead to a higher nanoroughness. The $CHF_3$-plasma coating showed higher roughness values with a power of 100 W than with 50 W, corresponding to the higher coating rate. The corresponding AFM images are shown in the appendix.

### Nanometer roughness values of the plain and etched PU film

As the roughness values for the $C_3F_6$- and $C_4F_8$-plasma coatings could not be increased by a following etching process, the PU film was directly etched before applying a thin plasma coating in order to restore the hydrophobic surface chemistry.

The AFM images of the plain PU foil CMC 63630 are shown in Figure 6.21.

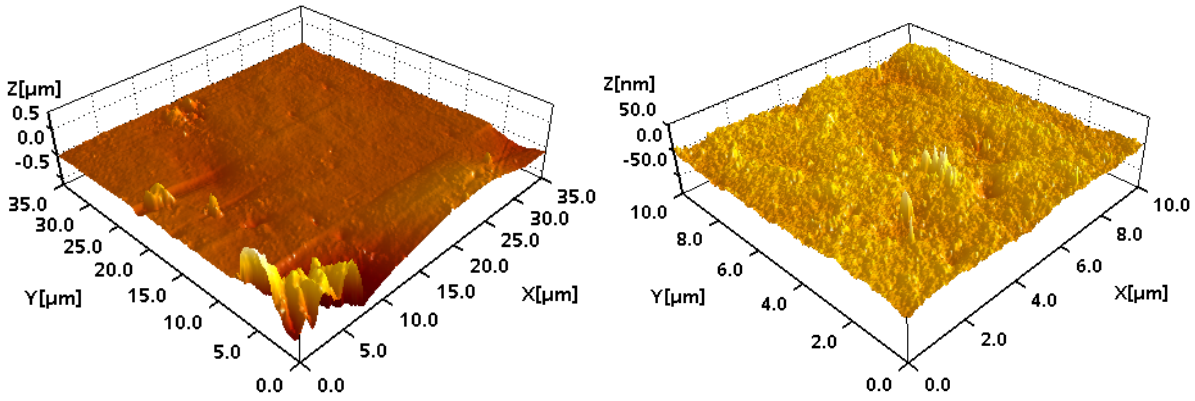


Figure 6.21.: AFM images of sample PU CMC 63630, 35 µm and 10 µm scan length.

The AFM images of the $O_2$-plasma etched PU foil CMC 63630 are shown in Figure 6.22 and of the nanostructured $C_3F_6$-plasma coating in Figure 6.23.

The AFM images show a smooth surface for the untreated PU film CMC 63630. The nanoroughness is increased by the $O_2$ plasma etching, which creates many little spikes, and then decreased again by the subsequent plasma coating, as can be seen by the reduced number of spikes.

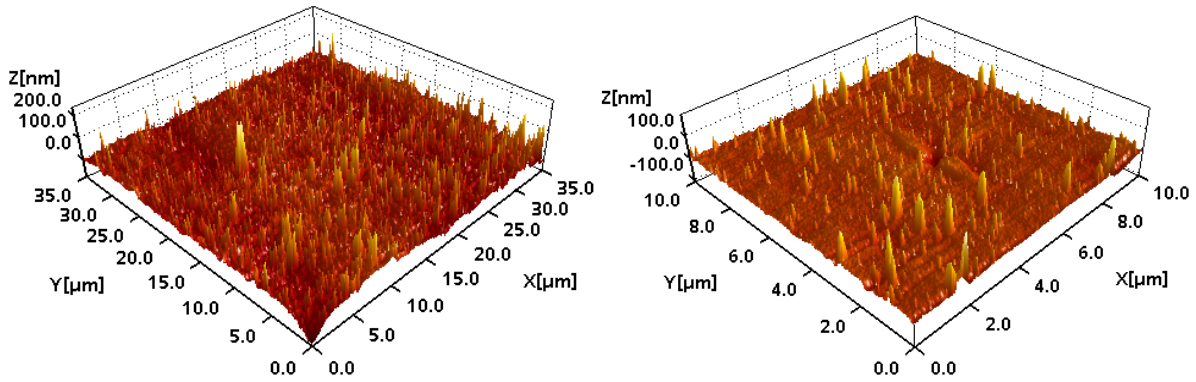


Figure 6.22.: AFM images of sample PU CMC 63630, etched in an $O_2$ plasma, 35 µm and 10 µm scan length.

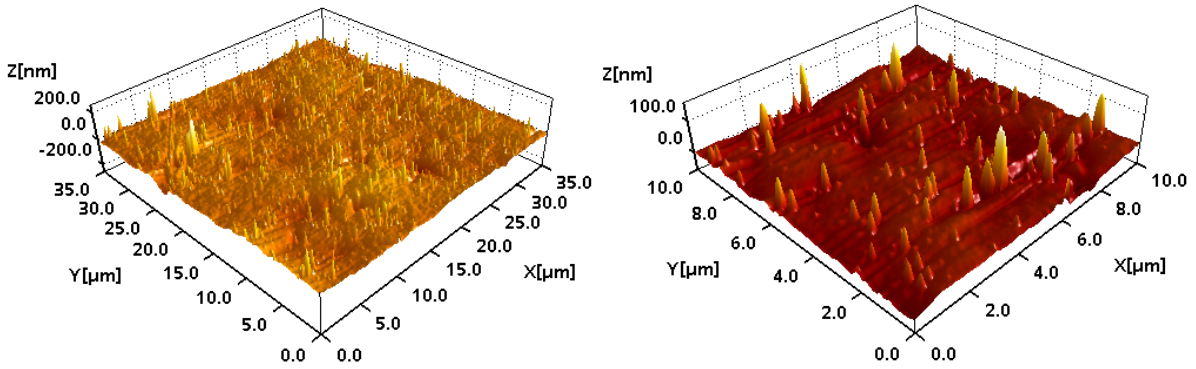


Figure 6.23.: AFM images of sample PU CMC 63630, etched in an $O_2$ plasma and thinly coated again in a $C_3F_6$ plasma, 35 µm and 10 µm scan length.

The corresponding roughness values are shown in Table 6.10.

With plasma etching the PU film before coating, it was possible to increase the nanoroughness values, as can be seen for the $O_2$-etched PU sample. The $S_{dr}$ value is decreased again after another thin plasma coating, whereas the $S_a$ and $S_q$ values stay the same. Therefore, the created nanoroughness is retained after the plasma coating in order to restore the hydrophobic surface chemistry. This is important for the creation of a superhydrophobic and icephobic surface, as nucleation is influenced by the nanometer roughness.

Table 6.10.: Nanometer roughness values of etched and $C_3F_6$ plasma coated PU determined by AFM.

| Type | Substrate | step 1: etching | step 2: coating | Scan length | Roughness average $S_a$ | Root mean square $S_q$ | Surface area ratio $S_{dr}$ | Mean summit curvature $S_{sc}$ | Radius of curvature $R$ |
|---|---|---|---|---|---|---|---|---|---|
| - | - | - | - | (µm) | (nm) | (nm) | (%) | (1/nm) | (nm) |
| I [2] | PU | - | - | 15 | 3.57 | 6.12 | 0.193 | $7.41 \cdot 10^{-5}$ | 13500 |
| I | PU | - | - | 10 | 3.56 | 4.58 | 0.011 | $2.44 \cdot 10^{-5}$ | 40984 |
| II | PU | $O_2$ | - | 10 | 7.5 | 14 | 3.5 | $12.9 \cdot 10^{-5}$ | 7752 |
| III | PU | $O_2$ | $C_3F_6$ | 10 | 8.1 | 13.9 | 0.931 | $30.3 \cdot 10^{-5}$ | 3300 |

### Nanometer roughness values of the HMDSO plasma polymer

The nanoscale roughness values of the etched HMDSO plasma coatings are shown in Table 6.11.

The plain HMDSO plasma coatings all had similar, small roughness values, which are also similar to the plain fluorocarbon coatings. Very large $S_a$ values were only achieved with high powers of 200 W or 350 W, also corresponding to a higher coating rate than at 60 W. The Ar-plasma etching of the silicone-like coatings with a power of 100 W increased the roughness values persistently, even after coating again. However, decreased roughness values were obtained with increased etching powers of 200 W or 300 W. The Ar-plasma etching at 100 W gave the best result for surface nanoscale roughness, although it was not as high as for direct coating at high powers. The corresponding AFM images are shown in the appendix.

Table 6.11.: Nanometer roughness values of HMDSO plasma polymers determined by AFM.

| Type | Step 1: coating | Step 2: etching | Step 3: coating | Scan length | Roughness average $S_a$ | Root mean square $S_q$ | Surface area ratio $S_{dr}$ | Mean summit curvature $S_{sc}$ | Radius of curvature $R$ |
|---|---|---|---|---|---|---|---|---|---|
| - | - | - | - | (µm) | (nm) | (nm) | (%) | (1/nm) | (nm) |
| I | HMDSO (60 W) | - | - | 10 | 7.84 | 10.1 | 3.92 | $7.8 \cdot 10^{-5}$ | 12821 |
| I [179] | HMDSO (60 W) | - | - | 20 | 8 | 13 | - | - | - |
| I [2] | HMDSO (60 W) | - | - | 15 | 5.35 | 7.83 | 0.055 | $2.22 \cdot 10^{-5}$ | 45000 |
| II [2] | HMDSO | Ar (100 W) | - | 15 | 17.7 | 23.9 | 1.15 | $17.8 \cdot 10^{-5}$ | 5620 |
| III [2] | HMDSO | Ar (100 W) | HMDSO | 15 | 19.4 | 23.9 | 0.478 | $19.1 \cdot 10^{-5}$ | 5240 |
| II | HMDSO | Ar (200 W) | - | 10 | 7.73 | 10.5 | 2.35 | $6.45 \cdot 10^{-5}$ | 15504 |
| II | HMDSO | Ar (300 W) | - | 10 | 5.41 | 7.25 | 1.5 | $5.91 \cdot 10^{-5}$ | 16920 |
| I | HMDSO (200 W) #1 | - | - | 10 | 86 | 106 | 2.1 | $43.3 \cdot 10^{-5}$ | 2310 |
| I | HMDSO (200 W) #2 | - | - | 10 | 115 | 139 | 4.53 | $49.2 \cdot 10^{-5}$ | 2033 |
| I [179] | HMDSO (350 W) | - | - | 20 | 83 | 100 | - | - | - |

### 6.3.6. Selection of plasma polymers for further characterization

Based on the nanoroughness values of the AFM measurements, a selection of plasma coatings was made for the preparation of the samples for further characterization. The aim was to create hydrophobic plasma coatings with a maximally rough nanoscale topography in addition to the normal plasma coatings with a smooth topography. The set of samples for further characterization was therefore created in a normal version (type 1) and a version with increased nanoroughness (type 2) for both the fluorocarbon and the silicone-like plasma polymer. The AFM measurements showed that the silicone-

like coating with the highest nanoroughness could be achieved by applying a HMDSO plasma coating using 200 W. The fluorocarbon coating with the highest nanoroughness could be created by first etching the PU film in an oxygen plasma and then by coating in a $C_3F_6$ plasma. Furthermore, the standard $C_4F_8$ plasma coating was made both in a lab reactor and in a roll-to-roll (R-to-R) reactor in order to compare the coatings by the different reactor setups. The $CHF_3$ plasma coating was not used for further sample preparation because the coating process is significantly slower than for the other fluorocarbon precursors. The plasma polymers used for characterization of the wetting, de- and anti-icing behavior in the icing test chamber are listed in Table 6.12.

Table 6.12.: Process parameters for the plasma coatings for further characterization.

| | | Plasma process | | | | | | Coating | |
|---|---|---|---|---|---|---|---|---|---|
| | Surface | | | Flow | $p$ | RF | $t$ | $d$ | Rate |
| Name | Type | step 1 | step 2 | (sccm) | (mbar) | (W) | (min) | (nm) | ($\frac{nm}{min}$) |
| $C_4F_8$ (50 W) | - | $C_4F_8$ | - | 20 | 0.15 | 50 | 7 | 216 | 31 |
| $C_4F_8$ R-to-R | - | $C_4F_8$ | - | 30 | 0.15 | 450 | 10 $\frac{cm}{min}$ | - | - |
| $C_3F_6$ (50 W) | 1 | $C_3F_6$ | - | 30 | 0.11 | 50 | 10 | 329 | 33 |
| - | 2 | $O_2$ | - | 30 | 0.28 | 200 | 3 | - | - |
| $O_2$ (200 W), $C_3F_6$ (50 W) | 2 | $O_2$ | $C_3F_6$ | 30 | 0.13 | 50 | 5 | 169 | 34 |
| HMDSO (60 W) | 1 | HMDSO/$N_2$ | - | 7/100 | 0.09 | 60 | 5 | 245 | 49 |
| HMDSO (200 W) | 2 | HMDSO/$N_2$ | - | 7/100 | 0.09 | 200 | 3 | 420 | 140 |

The samples are named by the substrate (flat PU or microstructure name) plus the plasma coating with the corresponding process power in order to distinguish between the normal and the rougher coatings. Since these plasma coatings can be distinguished by the process power, the process pressure is not added to the names. This naming scheme will be used throughout the rest of this thesis.

## 6.4. Stability and optical properties

For outdoor application, a sufficient stability against environmental influences is important. The results of the different stability tests are given in the following subsections.

### 6.4.1. Stability against sand erosion

#### Plasma coating stability against sand erosion - ESCA measurement results

In some situations, like on airplanes or wind energy turbines, these functionalized PU films would be exposed to air flows at high speed and therefore abrasion by dirt particles. The sand erosion test should show the stability of the different PU surfaces against abrasive erosion according to the test method DIN 52348.

The ESCA measurement result of the plain PU film CMC 63630 is shown in Figure 6.24.

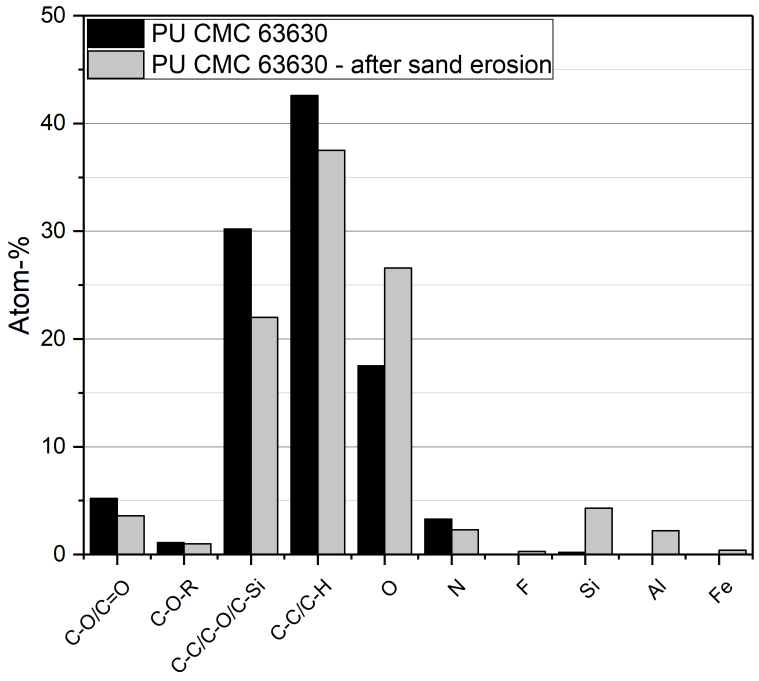


Figure 6.24.: Stability against erosion of the PU film: ESCA-measurements before and after a sand trickling test.

The plain PU film is characterized by the large peaks of the C-C/C-O, C-C/C-H and O groups and the smaller peaks of the C-O, C=O and N groups. After sand trickling the peaks of the C-C/C-O and C-C/C-H groups are reduced, whereas the peaks of the O, Si, Al and Fe groups are higher. The Si, Al and Fe peaks show that not all the sand could be washed away and some is still stuck on the surface, leading also to the increased O peak because of the stoichiometry of sand ($SiO_2$) and the metal-oxides.

The ESCA results of the HMDSO plasma coating before and after the sand erosion test are shown in Figure 6.25.

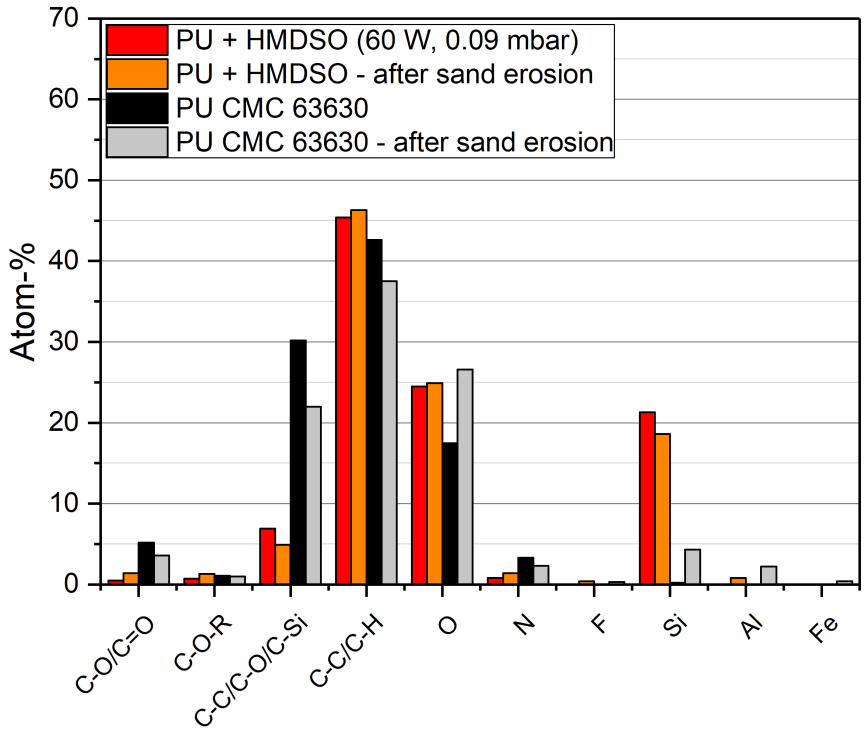


Figure 6.25.: Stability against erosion of the HMDSO plasma coating: ESCA measurements before and after a sand trickling test.

The silicone-like coating is characterized by the peaks of the C=O, C-O, C-C/C-Si, C-C/C-H, O and Si groups. The nitrogen peak is caused either by the PU or by nitrogen from air incorporated in the plasma coating. After the sand erosion test the peaks have almost the same height, although the coating has become thinner as seen by the lower C-Si and Si peaks as well as the larger C-C/C-H peak. It can be concluded that the silicone-like coating is very stable against this kind of sand erosion.

The ESCA results of the fluorocarbon plasma coatings before and after the sand erosion test are shown in Figure 6.26.

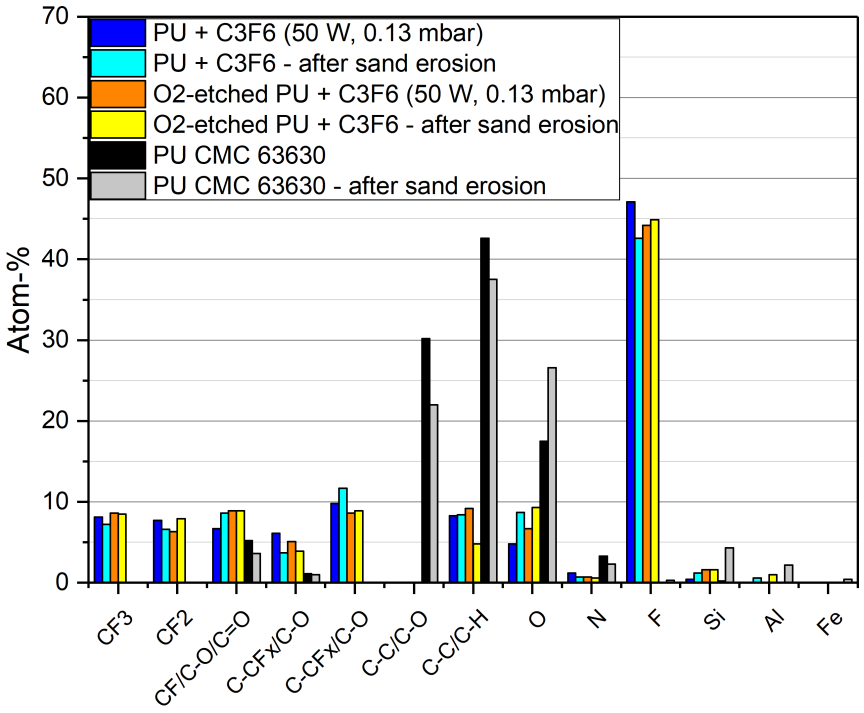


Figure 6.26.: Stability against erosion of the CF plasma coating: ESCA measurements before and after a sand trickling test

The fluorocarbon coatings can be seen by the peaks of the $CF_3$, $CF_2$, CF, C-$CF_X$, C-C/C-H and F groups. The O and N peaks are caused either by the PU, by oxidation of the plasma coatings or by incorporation into the plasma polymers from air in the reactor. Both fluorocarbon coatings have nearly the same surface chemistry, where the $O_2$-etched PU and $C_3F_6$ plasma coated sample has more oxygen and less fluorine in the coating. After the sand erosion test the peaks have not changed significantly. Some sand was still sticking on the surface after the sand erosion test shown by the increased O, Si and Al peaks. Overall, also the fluorocarbon coatings are very stable against this kind of erosion test.

### Microstructure stability against sand erosion - SEM images

Besides the plasma coating stability, the stability of the microstructures is also important for the functionality of the surface. Therefore, the samples were rinsed with deionized water after the sand erosion test and the microstructures were analyzed by SEM images.

A set of SEM images was taken of microstructures C6 and C9. After the sand erosion test, the samples were cleaned in an ultrasonic bath with deionized water in order to make sure all of the sand is removed. The SEM images of the uncoated and the $C_3F_6$ plasma coated microstructure C6, both after the sand erosion test, are shown in Figure 6.27.

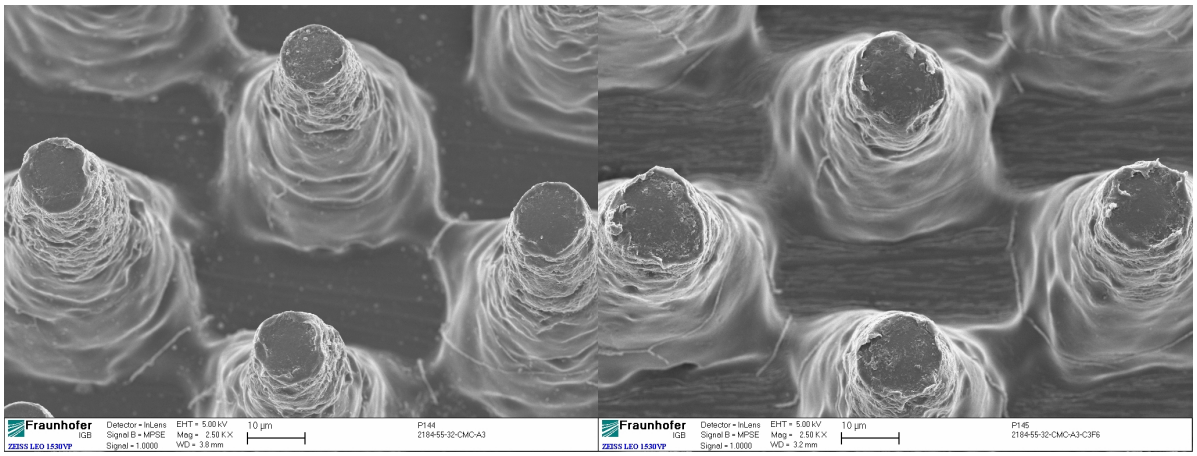


Figure 6.27.: Microstructure stability against sand erosion: SEM images of the uncoated (left) and $C_3F_6$ plasma coated (right) microstructure C6, after the sand erosion test.

The SEM images of the uncoated and the $C_3F_6$ plasma coated microstructure B3, both after the sand erosion test, are shown in Figure 6.28.

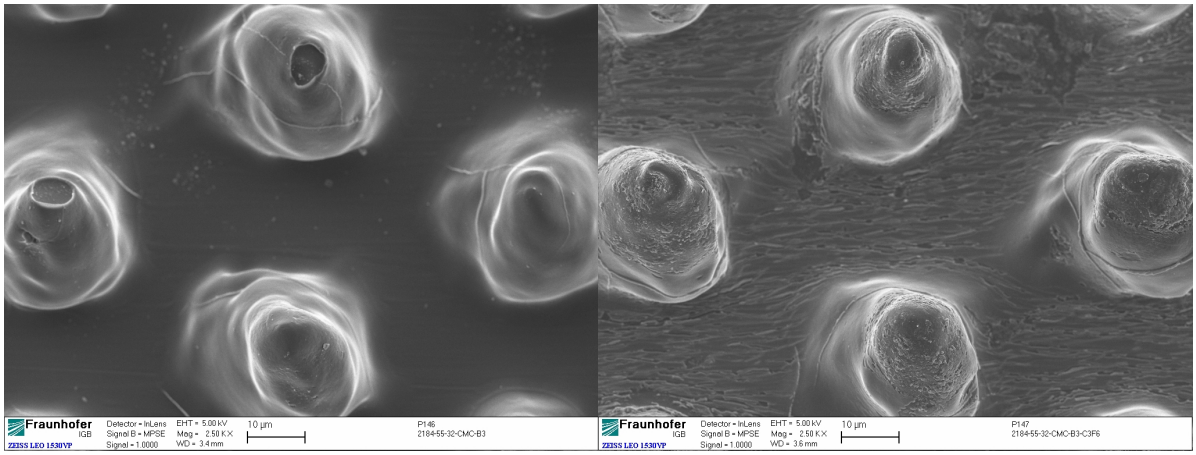


Figure 6.28.: Microstructure stability against sand erosion: SEM images of the uncoated (left) and $C_3F_6$ plasma coated (right) microstructure C9, after the sand erosion test.

For both structures, the plasma coating can be seen in the SEM images. The microstructures themselves do not get damaged by the sand and are therefore stable against this kind of erosion.

### Surface wettability and optical properties before and after sand erosion

Further, the wetting behavior and optical transmission were measured after the sand erosion test.

Figure 6.29 shows the static water contact angle values before and after the sand erosion test.

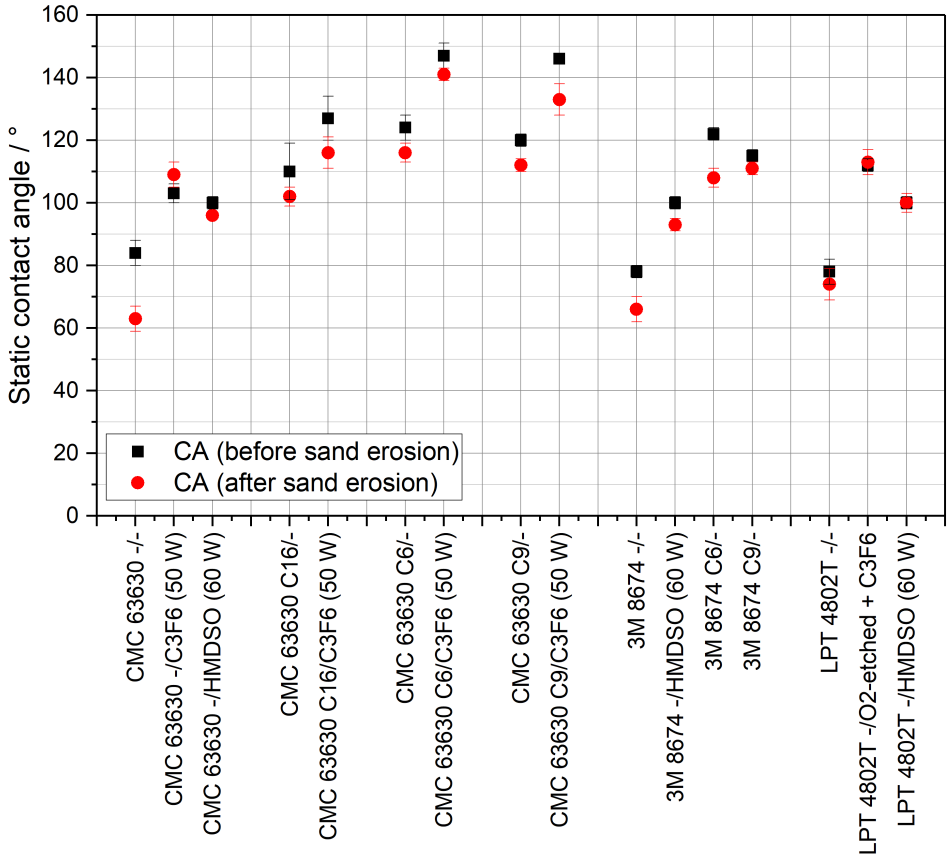


Figure 6.29.: Static water contact angle values before and after the sand erosion test.

The static contact angles are about 5° to 10° lower after the sand erosion test, so the surfaces became more hydrophilic than before. The wetting behavior was not changed significantly by this test. However, the superhydrophobic PU surfaces C6/$C_3F_6$ and C9/$C_3F_6$ lost their superhydrophobic functionality, because their static water contact angle decreased to a value below 150° after the sand erosion test. Therefore, it is possible that a superhydrophobic PU surface looses its functionality in an outdoor environment with longer exposure to sand or dirt erosion.

Figure 6.30 shows the optical transmission values before and after the sand erosion test.

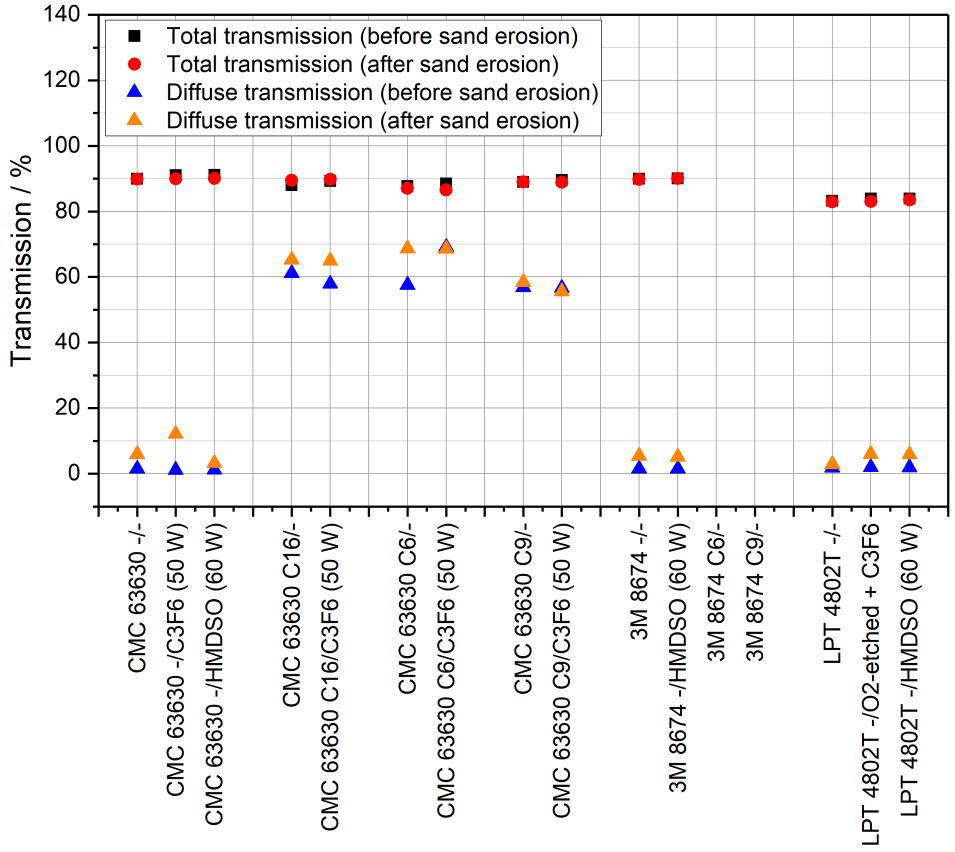


Figure 6.30.: Total and diffuse transmission values before and after the sand erosion test.

The total transmission after the sand erosion test is the same as before, whereas the diffuse transmission has increased by about 5 % to 10 %.

Overall, it can be concluded that both the plasma coatings and the microstructures showed good stability in this erosion test. However, the wetting behavior and optical transmission have been impaired. The sand impact speed can be higher than in this test in some applications which could lead to a higher erosion. Therefore, long term tests in real applications are needed in order to show the performance of these functionalizations.

### 6.4.2. Stability against UV/water weathering

Another very important factor for outdoor application is the stability against erosion by UV light and water.

Two samples of each surface (PU CMC 63630, PU CMC 63330, PU + HMDSO (60 W), PU + $C_3F_6$) were weathered for about 1000 h in the testing machine "Weather-o-meter" according to the industrial X1a CAM 180 test method. The aim for the thickness of the plasma coatings was 300 nm. The HMDSO (60 W) plasma coating was 430 nm thick. The $C_3F_6$ plasma coating thickness was not measured and is assumed to be about 300 nm thick corresponding to the plasma process parameters.

The ESCA measurement results of the plain PU films are given in Figure 6.31.

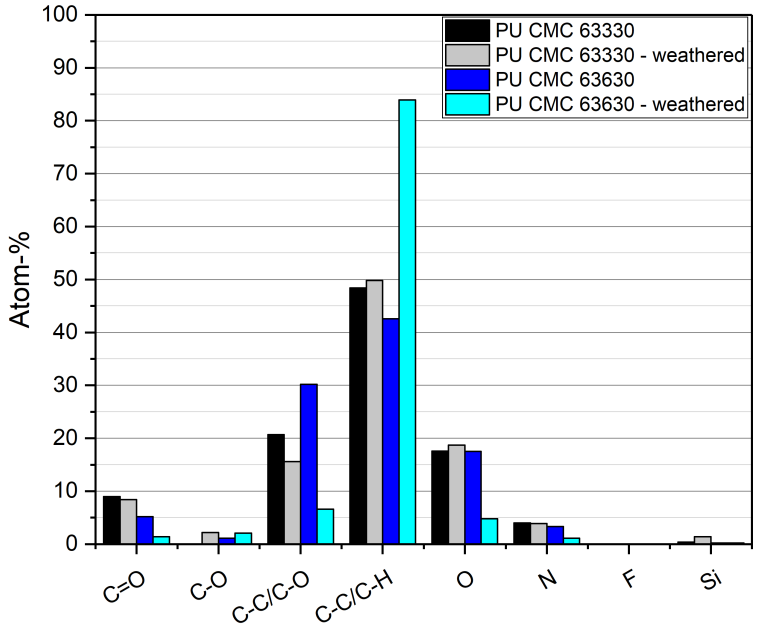


Figure 6.31.: Stability against UV/$H_2O$ weathering of the PU films: ESCA measurements before and after 1000 h of the industrial weathering test.

For the CMC 63630 film, the C=O, C-C/C-O, O and N peaks are significantly reduced after weathering, whereas the C-C/C-H peak is increased. The reduction of oxygen-containing components indicates that the chemical structure of the CMC 63630 type PU has changed and especially the oxygen- and nitrogen-containing bonds have been broken up by the weathering. In contrast to that, the peaks of the other PU film CMC 63330 after the weathering test are nearly the same as before. Here, the chemical structure has not changed which shows that the PU CMC 63330 film is more suitable against outdoor weathering than the 63630 type.

Figure 6.32 shows the ESCA results for the weathered HMDSO-plasma coating.

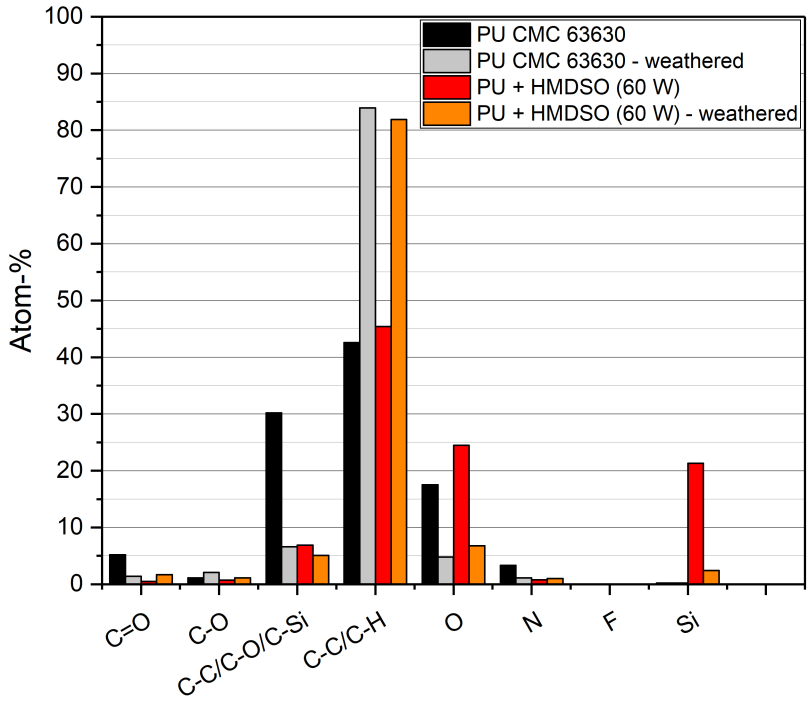


Figure 6.32.: Stability against UV/$H_2O$ weathering of the HMDSO plasma coating: ESCA measruements before and after 1000 h of the weathering test.

The amounts of the O and Si groups are distinctively decreased after weathering, whereas the amount of C-Si is similar to before and that of C-C/C-H is increased. The increase of the C-C/C-H peak is similar for the plain PU film and caused by the change of the PU chemical structure by the weathering test. The reduction in O and Si indicates that the silicone-like coating has been largely damaged and taken away. This silicone-like plasma coating is not stable against UV and water weathering. A gradient layer with a higher oxygen content, which decreases from the hydrophilic base (PU) to the hydrophobic surface, could increase the adhesion and stability of the silicone-like plasma coating.

Figure 6.33 shows the ESCA results for the weathered $C_3F_6$-plasma coating.

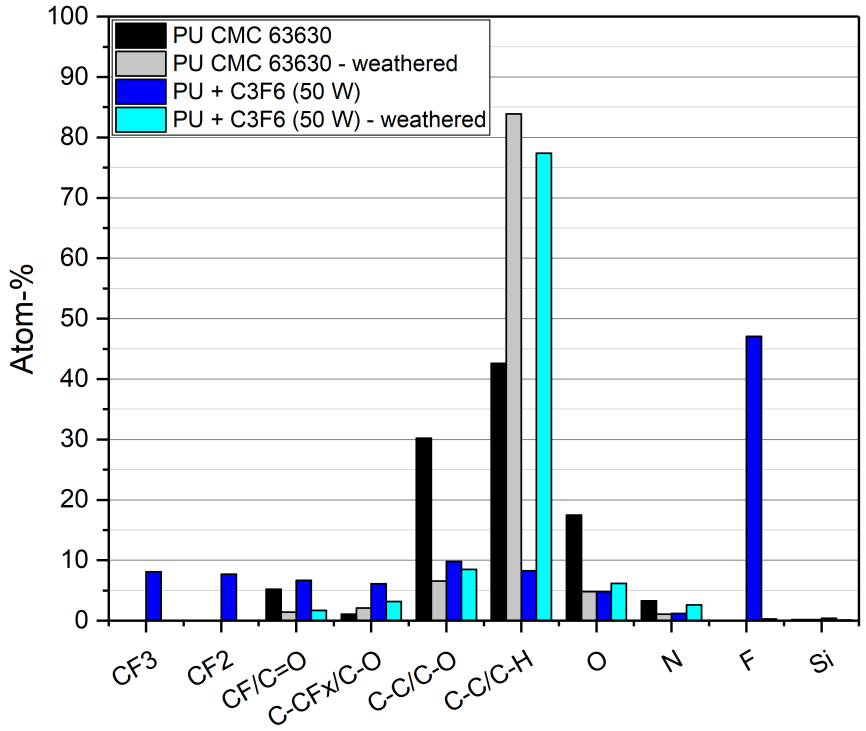


Figure 6.33.: Stability against UV/$H_2O$ weathering of the CF plasma coating: ESCA measurements before and after 1000 h of the weathering test.

Also in case of the fluorocarbon coating, the characteristic peaks of the $CF_3$, $CF_2$, CF, C-$CF_X$ and F components are reduced to almost zero, whereas the C-C/C-H amount is significantly enhanced after the weathering test. The degraded PU film is detected, indicated by the C-C/C-H, O and N groups. The fluorocarbon coating is completely gone and not stable at all against this kind of UV and water weathering.

This weathering test showed that the PU film CMC 63330 is stable against UV and water weathering, whereas the chemical structure of the PU film CMC 63630 gets changed. The HMDSO (60 W, 430 nm thick) and $C_3F_6$ (50 W, about 300 nm thick) plasma coatings get eroded within 1000 h of weathering.

### 6.4.3. Long term outdoor stability

In addition to the industrial weathering test described above, the stability was tested over a period of about 13.5 months, from january 2015 to march 2016, in normal outdoor conditions. Afterwards, the PU film samples were ultrasonicated in and rinsed with highly purified water in order to wash away the accumulated dirt. Then the surface chemistry was analyzed by ESCA.

The ESCA measurement results of the HMDSO-plasma coated films are shown in Figure 6.34.

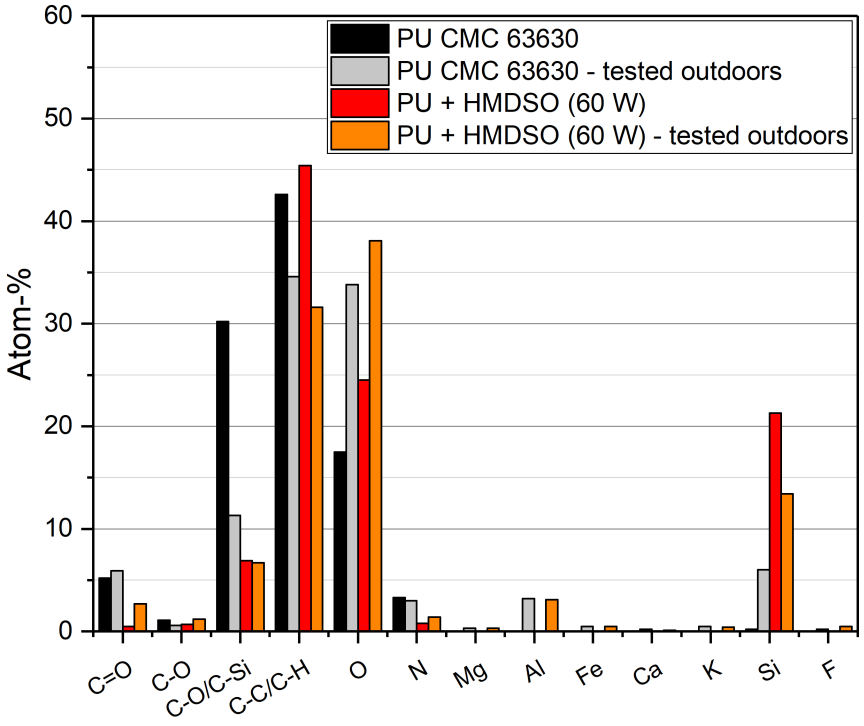


Figure 6.34.: Chemical composition of the silicone-like plasma coating after long term outdoor exposure.

The PU surface chemistry has changed after outdoor exposure. The C-C/C-O and C-C/C-H peaks are reduced whereas the O peak has increased and Al and Si peaks

have appeared. The increased oxygen amount is caused either by oxidation because of outdoor weathering or by $SiO_2$ and $Al_2O_3$ because of accumulated dirt. The reduced C-C/C-O and C-C/C-H peaks are lower because of the accumulated dirt, as the total amount of all peaks is always 100 %. Therefore, no significant change of the chemical structure of the PU CMC 63630 can be seen by the outdoor exposure.

The silicone-like plasma coating surface chemistry has changed, the C-C/C-H and Si amounts are reduced, whereas the O, Al, Fe and K amounts are increased. This indicates the accumulation of dirt, which consists in parts of $Al_2O_3$, $Fe_2O_3$ and $SiO_2$ and contributes to the Al, Fe, Si and O peaks. The enhanced nitrogen and reduced silicon amount indicate that the plasma coating is damaged by the outdoor weathering but not completely taken off.

Figure 6.35 shows the ESCA measurement results of the $C_4F_8$-plasma coated films.

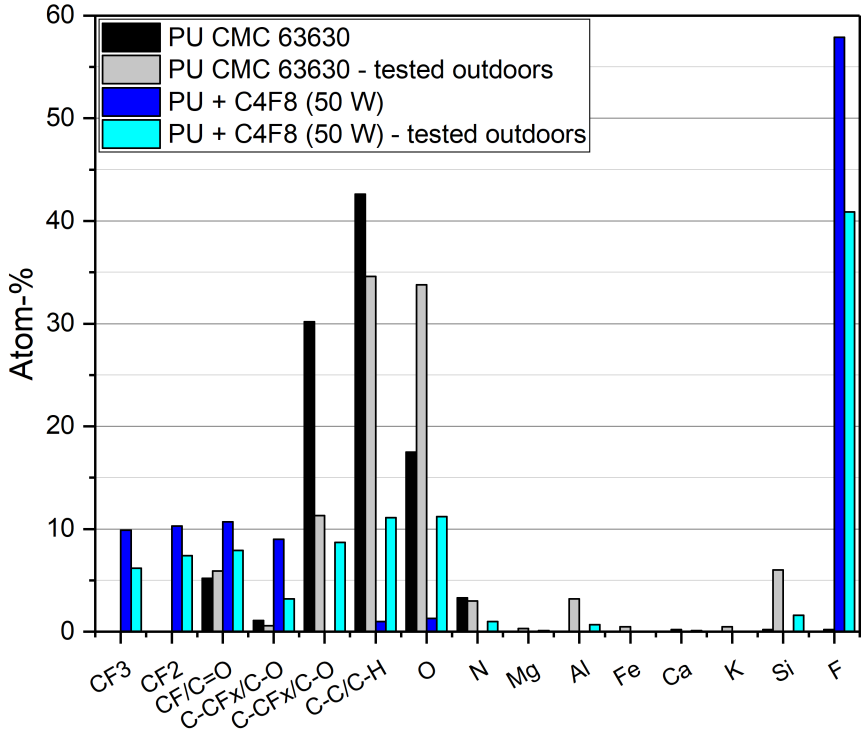


Figure 6.35.: Chemical composition of the fluorocarbon plasma coating after long term outdoor exposure.

The peaks characteristic for the fluorocarbon coating are decreased after the long term outdoor exposure by about 25 % to 60 %. The Al and Si peaks have appeared because of the rests of dirt which also raised the O amount because of the $SiO_2$ and $Al_2O_3$. Furthermore, the C-O, C-C/C-H, O and N peaks have increased and the F peak has decreased. This shows that the plasma coating is damaged but not completely eroded, and the PU film chemistry is detected after long term outdoor exposure.

### 6.4.4. Stability against repeated icing and de-icing cycles

It was published that the anti-icing performance deteriorates with multiple icing/de-icing cycles because the microstructures get damaged. Their height gets reduced by ripping off the parts that are enclosed in the ice during ice shear-off [152, 161]. For real application, the surface microstructures and coatings have to be stable against repeated de-icing at the same spot.

Figure 6.36 shows the ESCA results of the HMDSO-plasma coated surfaces before and after repeated de-icing.

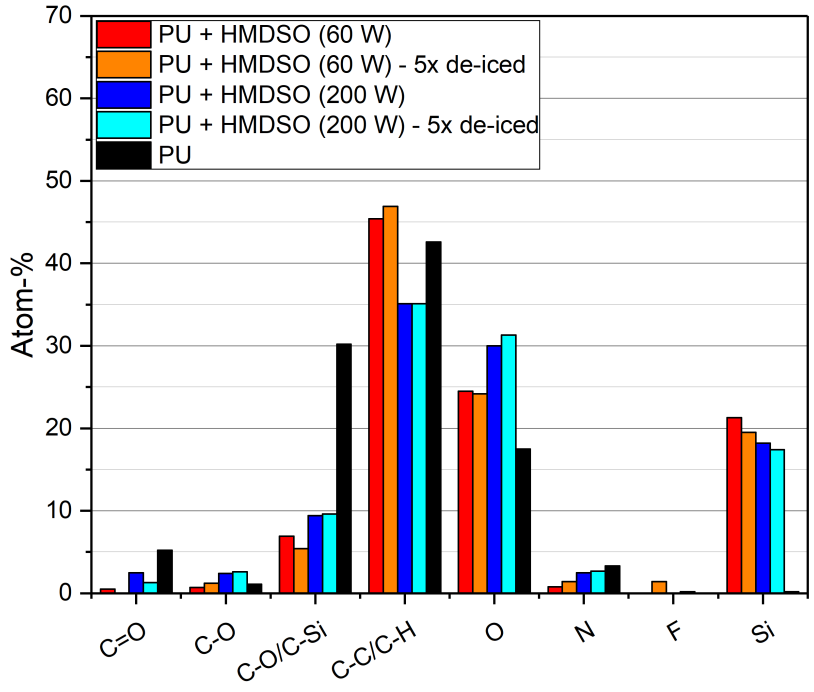


Figure 6.36.: Chemical composition of the silicone-like plasma coatings before and after 5 de-icing tests, determined by ESCA.

The peaks of the HMDSO (60 W) plasma coating after the 5 deicing tests are similar to before, with smaller peaks for the C-Si and Si groups and larger peaks for the C-C/C-H and N groups, which belong to the PU. In case of the HMDSO (200 W) plasma coating the peaks after the deicing tests are nearly unchanged. Overall, the silicone-like plasma coatings are very stable against multiple ice detachments.

Figure 6.37 shows the ESCA results of the CF-plasma coated surfaces before and after repeated de-icing.

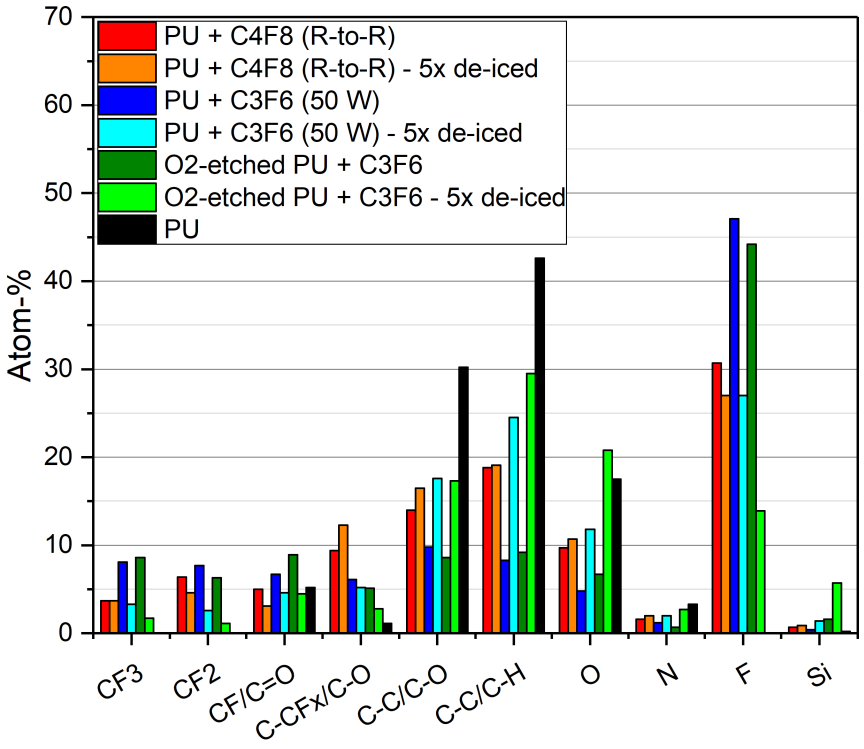


Figure 6.37.: Chemical composition of the fluorocarbon plasma coatings before and after 5 de-icing tests, determined by ESCA.

The N peak might be caused by remaining air in the plasma reactor during the coating process and the Si peak by remaining dirt on the surface. The $C_4F_8$ roll-to-roll plasma coating shows similar peaks before and after the 5 de-icing tests. The $CF_2$, CF and F peaks are reduced, whereas the C-$CF_X$, C-C/C-O, C-C/C-H and O peaks are increased. This coating is very stable against repeated deicing, although the initial F content is only about 30 % and quite low compared to the other fluorocarbon coatings. For both the $C_3F_6$ plasma coatings on normal and on $O_2$-etched PU, the peaks of the $CF_X$ and F groups were significantly decreased by the de-icing tests, whereas the C-C/C-O, C-C/C-H, O and N peaks were increased. This shows that the fluorocarbon plasma coatings were significantly damaged by the de-icing tests. The fluorocarbon plasma coating on

oxygen-etched PU is less stable than the same coating on untreated PU. In contrast to the silicone-like plasma coatings, the fluorocarbon plasma coatings do not seem very stable against repeated de-icing.

LSM images taken of microstructure C6 before and after five times of de-icing (same spot of ice cylinder pull-off) showed that the microstructures are not damaged by 5 times of repeated de-icing, see Figure 6.38.

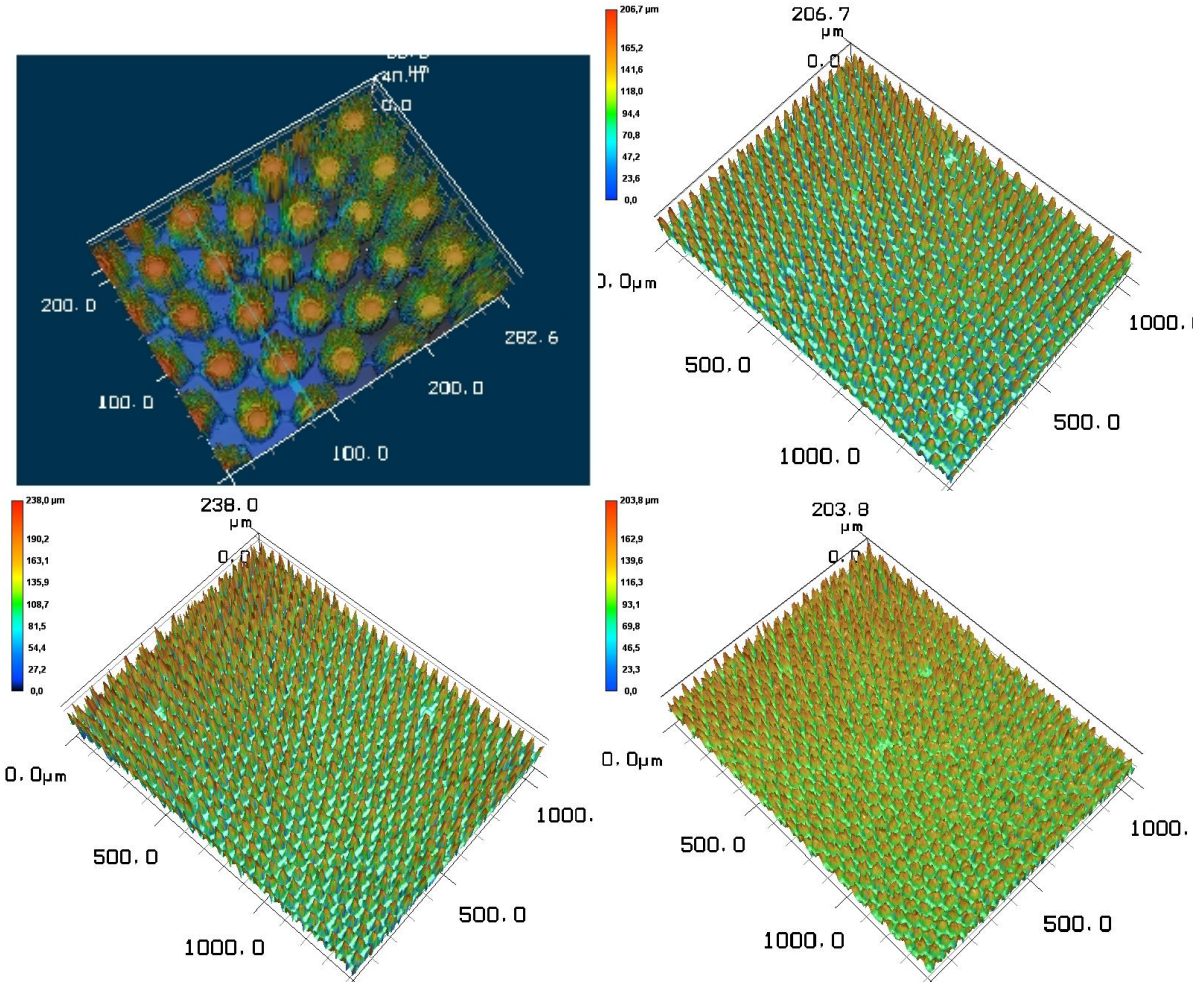


Figure 6.38.: Comparison of the microstructure A3 of stamp 3 before (uncoated, upper left) and after 5 de-icing tests (upper right: $O_2$-etched A3+$C_3F_6$, lower left: A3+HMDSO 60W, lower right: A3+HMDSO 200W), determined by Laser scanning microscopy.

### 6.4.5. Optical properties and test as a solar panel cover

For application on viewing windows or as solar panel covers, the optical properties and the transparency are important. Therefore, the PU films were tested as solar panel covers and their total, direct and diffuse transmission was measured by UV/Vis spectroscopy.

The rated data of the solar panel are 16.9 V for voltage, 3.56 A for current and 60 W for peak power. All three cover setups (uncovered, $C_3F_6$ plasma-coated, flat PU film and $C_3F_6$ plasma-coated, C16 microstructured PU film) were tested over a multiple day period and during a single, nearly cloudless day. For the single day test, the voltage logging was stopped during change of the cover and afterwards the measurement was started again. The voltage of the uncovered setup from the multiple day measurements during the corresponding time is shown for comparison with the single day measurements (the voltage increase is caused by the changing height of the sun around midday). The logged voltages are shown in Figure 6.39.

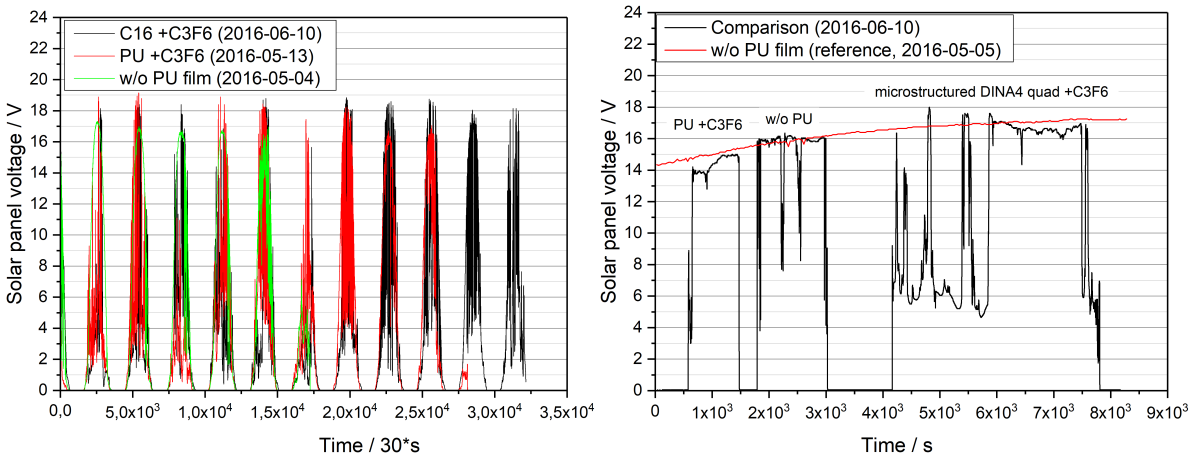


Figure 6.39.: Comparison of solar panel voltages for different cover setups: uncovered, $C_3F_6$ plasma-coated, flat PU film and $C_3F_6$ plasma-coated, C16 microstructured PU film. Left: multiple day solar panel test, right: single day solar panel test.

The day-cycle can be seen for the multiple day measurements, the maximum voltage reaches nearly 19 V. The fluctuations of the voltage are caused by clouds moving across the sky and decreasing the incoming sunlight temporarily.

From the voltage measurements, the mean maximum voltage of the 11 day test and the

maximum voltage of the 1 day test was determined. The optical transmission values, which were already measured by UV/Vis spectroscopy for evaluation of the preceding sand erosion test, are shown together with the measured maximum voltages in Figure 6.40 for the different cover setups.

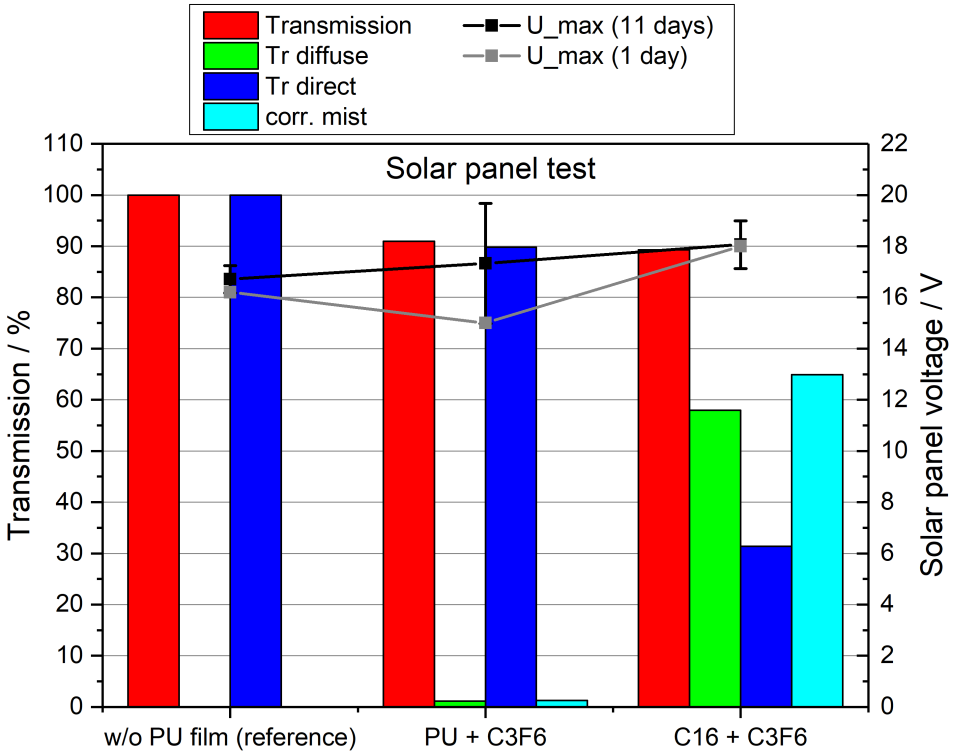


Figure 6.40.: Comparison of the total, direct and diffuse transmission values determined by UV/Vis spectroscopy of the different cover setups (without cover, with fluorocarbon plasma-coated, flat PU film and with fluorocarbon plasma-coated, C16 microstructured PU film) and measured peak voltage of the solar panel (maximum from 1 day test and mean from 11 days test).

The $C_3F_6$ plasma-coated PU film has a slightly decreased total transmission value of about 91 %, where about 90 % are direct transmission and only about 1 % is diffuse transmission, and a corrected mist value of about 1.3 %. In contrast, the microstructured (C16) and plasma-coated PU film has 89 % total transmission, where nearly 58 % are diffuse transmission and only about 31 % are direct transmission. Here, the corrected mist value is almost 65 %. The C16 microstructured film is not transparent anymore and creates a lot of light scattering and diffuse transmission.

Overall, the functionalized PU films do not decrease the voltage and therefore the power

of the solar test panel significantly compared to the uncovered reference setup which is important for real application. Both the flat, plasma-coated and the microstructured, superhydrophobic PU films can be used as solar panel covers without reducing the power generation. For an application where transparency is needed, like viewing window or windshield covers, the superhydrophobic PU films are not useful yet because of their high diffuse transmission.

# 7. Results and discussion of the wetting, de-icing and anti-icing behavior

The contact angle measurement results are reported and compared to the theories of Wenzel and Cassie-Baxter, in order to characterize the wetting behavior of the functionalized PU films and select the most interesting microstructures for further characterization (7.1). Afterwards, the results of the ice adhesion measurements (7.2) and then those of the icing tests (7.3) are described. The de- and anti-icing behavior is correlated with the wetting behavior and the surface properties in order to identify the parameters most important for the design of a functional anti-ice PU film.

## 7.1. Water wetting behavior

The icing behavior and ice adhesion on a surface are determined by the wetting behavior of water on that surface. Superhydrophobic surfaces are water repellent and therefore promising for anti-icing. The first hypothesis is that superhydrophobic PU films can be created by hot embossing and plasma processes of etching and coating. For the wetting behavior analysis, static and advancing / receding contact angle measurements with water were carried out on the flat and microstructured PU films. The contact angle measurement results are used for determination of the superhydrophobic, most water repellent surfaces for further analysis of their de- and anti-icing behavior. In the following sections the water contact angle measurement results are shown and compared to the theoretical limits given by the Wenzel and Cassie-Baxter states for the microstructures C4 to C12, L1 to L3 and E4 to E6. The contact angle values of the other microstructured samples and the technical materials are listed in the appendix. Finally, a visualization of the water-air interface beneath the water droplet by fluorescence laser

scanning microscopy is given for better determination of the exact wetting state on the most superhydrophobic surfaces.

### 7.1.1. Dynamic water contact angles on microstructured, uncoated or plasma-coated PU surfaces

#### Cylindrical microstructures with diameters of 35 µm and above

In Figure 7.1 the contact angle measurement results of the uncoated and plasma coated cylindrical microstructures are presented. The detailed process parameters and description of the plasma coated and plasma etched samples are given in the corresponding subsections of the results section on the plasma processes 6.3.

The contact angles were increased by the microstructures compared to the flat PU, depending on the diameters $D$ or $d$ and distance $P$. They were increasing with decreasing $P/D$ or $P/d$ factors (see Table A.2 and Table A.3 in the appendix, section A.2). The contact angles were raised further by the plasma coatings for both the flat and microstructured PU samples. Superhydrophobic states with advancing contact angles above 150° and contact angle hysteresis values below 10° could be measured for the coated, microstructured samples C5, C6 and C9. For C6 and C9, both the fluorocarbon and the silicone-like plasma coating render the surface superhydrophobic. The contact angles were further increased by argon plasma etching of the $C_4F_8$ or HMDSO plasma coatings and subsequent thin plasma coating of the etched samples leading to an improved superhydrophobicity, with advancing contact angles up to 157° and a contact angle hysteresis below 10°. The oxygen plasma etching of the $C_3F_6$ plasma coating and subsequent thin coating lead to an increased advancing contact angle (160°), but also an increased contact angle hysteresis (above 10°) and therefore to an overall worse superhydrophobicity compared to the unetched, $C_3F_6$ plasma coated sample. The oxygen-etched and subsequently $C_3F_6$ plasma coated samples created superhydrophobicity in case of microstructure C6, but not in case of C9. The HMDSO (200 W) plasma coating did not lead to superhydrophobicity because of the lower hydrophobicity by a lower C-C/C-H content of this plasma coating (see ESCA measurements in 6.3).

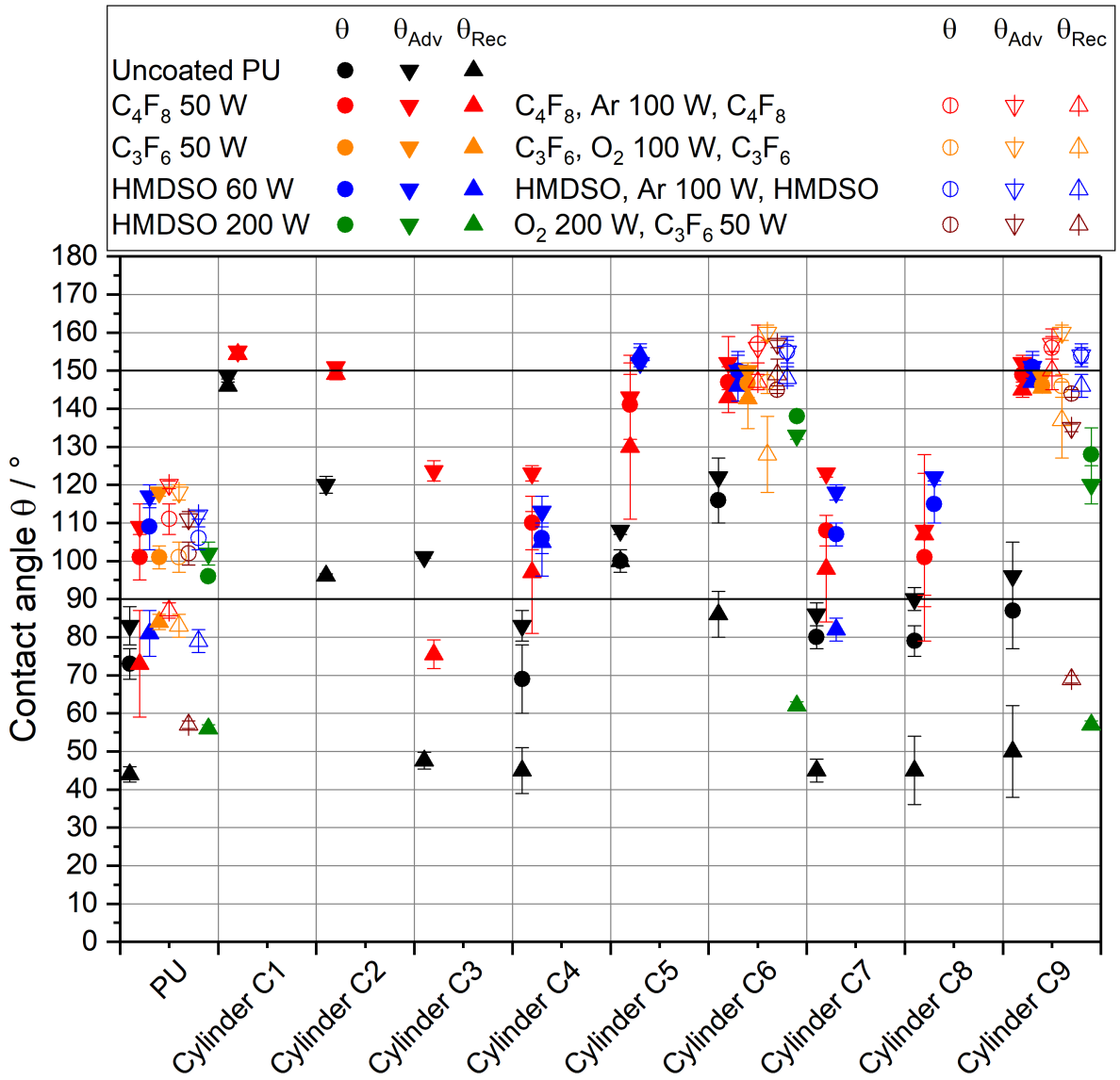


Figure 7.1.: Dynamic and static water contact angle values of uncoated or plasma coated cylindrical microstructures. The superhydrophobic state with contact angles above 150° is reached by plasma coated microstructures C5, C6 and C9. The contact angles are raised further on the plasma etched samples.

### Elliptical and linear microstructures with widths of 35 µm and above

In Figure 7.2 the contact angle measurement results of the uncoated or plasma coated elliptical and linear microstructures are shown.

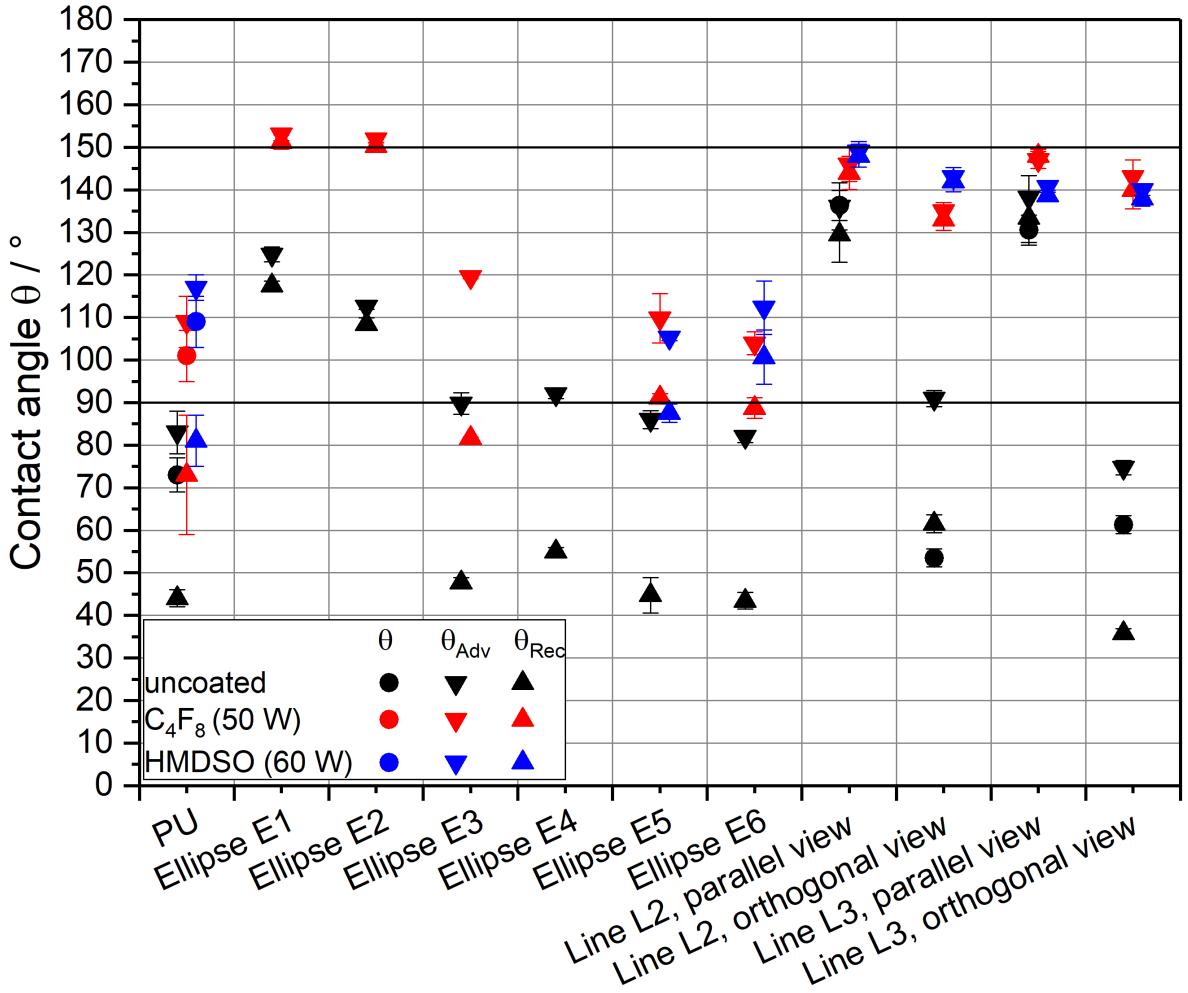


Figure 7.2.: Dynamic and static water contact angle values of uncoated or plasma coated elliptical and linear microstructures. The superhydrophobic state with contact angles above 150° is only reached by the elliptical microstructure E1 and, in case of the linear ridges, only in the direction looking in parallel to the ridges.

Among the elliptical microstructures, the superhydrophobic state could be achieved with the $C_4F_8$ plasma coating on E1 and in parts on E2. For the HMDSO (60 W) plasma-

coated linear microstructure L2, superhydrophobic contact angles could be measured when looking along the ridges (parallel view), whereas the contact angles are lower when looking orthogonally to the ridges (orthogonal view). An advantage of superhydrophobic linear ridges is a direction-dependent roll-off behavior of water drops (roll-off perpendicular to the ridges because of high contact angle with parallel view). In this way, accumulating water drops could be guided along a certain direction, e.g. for fluidic applications.

As the elliptical microstructures showed no sufficient superhydrophobicity except for E1, and the linear microstructures showed superhydrophobicity only in one direction, only the elliptical microstructure E1 is further characterized. The most superhydrophobic behavior was seen on the cylindrical microstructures C1, C6 and C9. Therefore, these hexagonally arranged, elliptical and cylindrical microstructures and the quadratically arranged, cylindrical microstructure C16 are chosen for further de- and anti-icing characterization.

#### Surface free energy of the functionalized PU surfaces and further surfaces

In addition to the contact angles measured with water, static contact angles of diiodomethane (DIM) were also measured in order to determine the surface free energy of the examined surfaces. From the DIM and $H_2O$ static contact angle values, the surface free energies of the functionalized PU surfaces and the engineering material surfaces were determined by the software SCA 20 with the OWRK model. These values were used for correlation with the icing behavior or ice adhesion. The surface free energy values are given in the appendix, in Table A.8.

### 7.1.2. Comparison of measured water contact angles with Wenzel and Cassie-Baxter wetting state limits

#### Cylindrical microstructures with diameters of 35 µm and above

The measured advancing contact angles were compared with the calculated values of the Wenzel and Cassie-Baxter wetting state equations for comparison of the superhydropho-

bicity of the functionalized PU films with these calculated limits. The theoretical values were calculated for all $P/d$ values according to the Wenzel (3.8) and Cassie-Baxter (3.13) equations given in the chapter of theoretical and experimental basics (3.2.1). In contrast to distance $P$ / base diameter $D$, which was used in the graphs before, the factor distance $P$ / top diameter $d$ was chosen here because the water drop only contacts the top of the microstructures if in Cassie-Baxter state. This comparison is given for cylindrical microstructures in Figure 7.3 as well as for elliptical and linear microstructures in Figure 7.4.

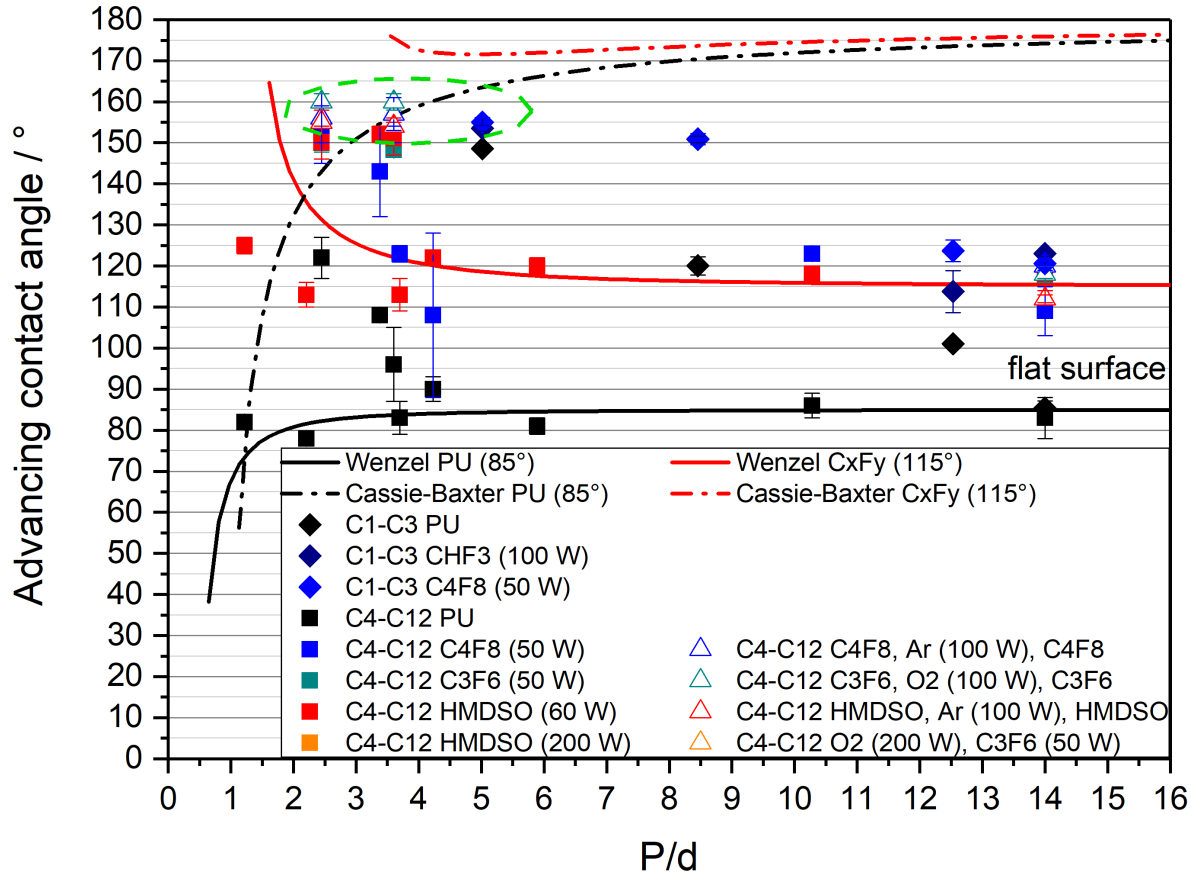


Figure 7.3.: Comparison of measured advancing contact angles with theories of Wenzel (solid lines) and Cassie-Baxter (dash-dotted lines), for cylindrical microstructures with different nanoroughness (uncoated, normal and etched plasma coatings). The theoretical curves were calculated for a PU surface ($\theta_{adv} = 85°$) and a fluorocarbon or silicone-like plasma coating ($\theta_{adv} = 115°$). Values for flat PU shown at $P/d = 14$ for comparison. The superhydrophobic samples are marked by the green, dashed ellipse.

For the cylindrical microstructures (equations 3.21), the Wenzel curves for uncoated and coated samples were calculated with the geometrical parameters of microstructure C10 (highest $P/d$ and lowest measured $\theta_{\mathrm{Adv}}$) and an advancing contact angle of 85° for the uncoated (PU) or of 115° for a plasma-coated coated ($C_XF_Y$) surface. The fluorocarbon and the silicone-like plasma coating are modeled with the assumption of being similarly hydrophobic. In contrast, the Cassie-Baxter curves were calculated with the geometrical parameters of microstructure C6 (lowest $P$ and $P/d$, highest measured $\theta_{\mathrm{Adv}}$) and an advancing contact angle of 85° (PU) or 115° ($C_XF_Y$). For both wetting state models, these curves represent the theoretical minima (C10) and maxima (C6) for both the uncoated and coated type of all cylindrical microstructures. Both the measurement values and the theoretical curves are drawn with their corresponding $P/d$ values (for comparison, the values for flat PU were drawn over $P/d = 14$).

For large $P/d$ factors (above 4 for C4-C12 of stamp 3) the measurement values correspond to the Wenzel wetting state. For $P/d$ factors increasing from small to large values (5 to 12.5 for C1-C3 of stamp 2, 2.5 to 10 for C4-C12 of stamp 3) the measurement values close to the Cassie-Baxter state curve approach the Wenzel state curve, although some measured values at low $P/d$ values are also close to the Wenzel state. This can be seen for both the uncoated and plasma coated surfaces.

The approach from the Cassie-Baxter to the Wenzel state with an increasing $P/d$ factor (or decreasing microstructure density) was described by a stochastic model in literature [193] and can be seen among the measured values. It can be concluded that among these microstructures, the smallest $P/d$ factor created the most superhydrophobic surface (microstructure C6 with $P/d = 2.45$). The maximum advancing contact angle of nearly 180° has not been reached yet so the dimensions of the cylindrical microstructures need to be further optimized. However, at the time of ordering the microstructured stamps, the diameters of the holes could not be reduced further because of the used ns-pulsed laser-drilling process (base diameter ≈ 35 µm, top diameter ≈ 20 µm).

#### Elliptical and linear microstructures with widths of 35 µm and above

For the elliptical and linear microstructures (equations 3.26), the Wenzel curves were calculated with the geometrical parameters of microstructure E6 (largest $P/d$ of ellip-

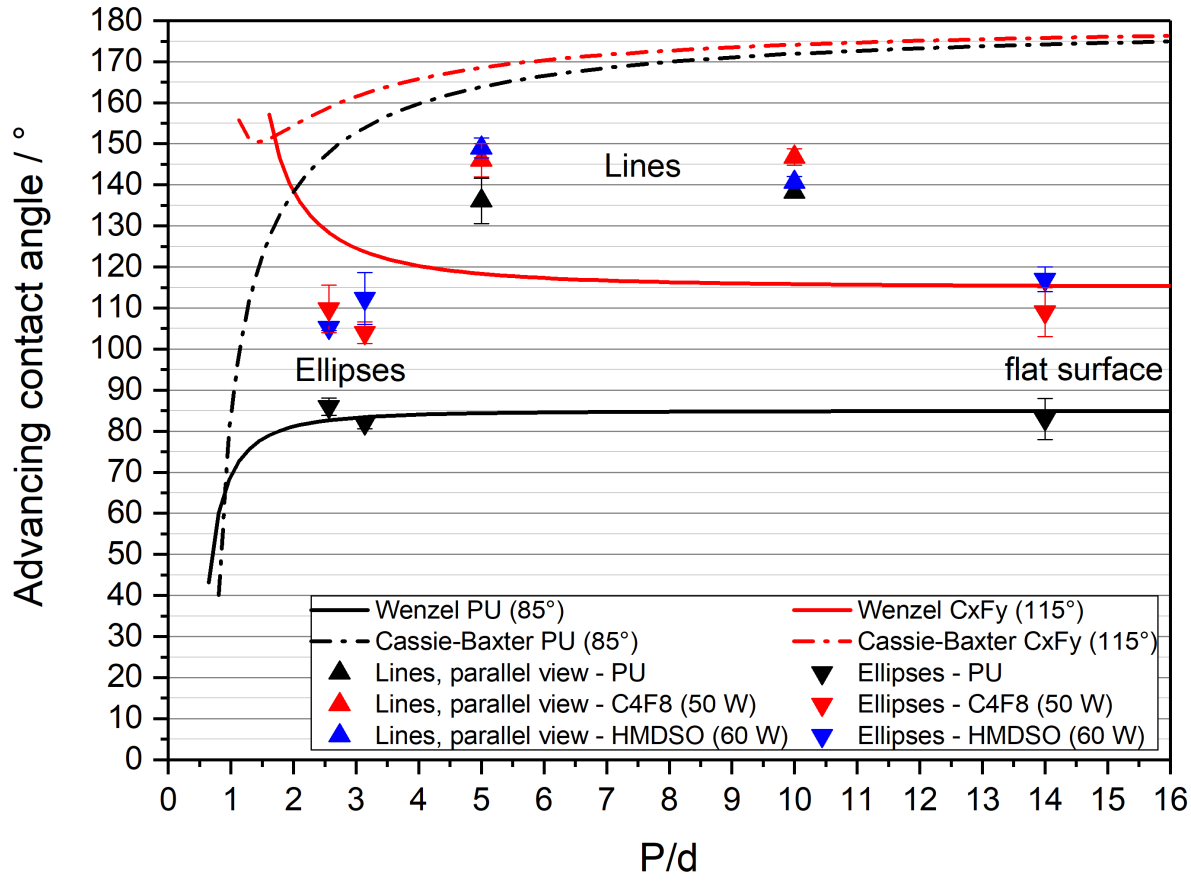


Figure 7.4.: Comparison of measured advancing contact angles with theories of Wenzel (solid lines) and Cassie-Baxter (dash-dotted lines), for elliptical and linear microstructures (uncoated and with normal plasma coatings). The theoretical curves were calculated for a PU surface ($\theta_{adv} = 85°$) and a fluorocarbon or silicone-like plasma coating ($\theta_{adv} = 115°$). Values for flat PU shown at $P/d = 14$ for comparison. The elliptical microstructures do not show direction dependent macroscopic wetting behavior. Values on linear microstructures obtained with view parallel to linear ridges.

tical structures) whereas the Cassie-Baxter curves were calculated with the geometrical parameters of microstructure E4 (smallest $P/d$ of elliptical structures). For calculation, an advancing contact angle of 85° for the uncoated PU surface and of 115° for the plasma coated surface was used. The fluorocarbon and the silicone-like plasma coating are modeled with the assumption of being similarly hydrophobic. Both the measurement values and the theoretical curves are drawn with their corresponding $P/d$ values ($d$ representing the mean top diameter for ellipses, mean top width for lines).

The measurement values of the linear microstructures lie between the calculated Wenzel and Cassie-Baxter curves. The measured values of the elliptical microstructures lie on or below the Wenzel wetting state curve.

For the elliptical microstructures, no direction-dependent macroscopic wetting behavior could be seen. It has to be kept in mind that the theoretical curves for the ellipses were modeled with only one diameter in the Wenzel and Cassie-Baxter equations which was composed of the major and minor half-axis ($D = A + B$). In case of the linear structures, the highest advancing contact angles were measured looking in parallel to the linear ridges (shown here) and the lowest advancing contact angles were measured looking orthogonally to the linear ridges. For the linear structures no separate theoretical curves of the Wenzel and Cassie-Baxter states were calculated, as the density of the structures is different (no hexagonal arrangement).

These measurement values only represent the macroscopic wetting behavior, but both the elliptical and linear microstructures might have a direction-dependent microscopic wetting behavior.

Neither the elliptical nor the linear microstructures could create sufficient superhydrophobicity, because the elliptical microstructures only showed advancing contact angles below 120° (except for E1 and E2), and the linear microstructures showed advancing contact angles near 150° only in the direction looking in parallel to the linear ridges. The geometric dimensions have to be optimized for a stable Cassie-Baxter state with an advancing contact angle of nearly 180°. Therefore, these elliptical and linear microstructures will not be examined further for de- or anti-icing behavior (except for E1). The cylindrical microstructures do not show direction dependent wetting behavior, and the most superhydrophobic samples C6 and C9 will be analyzed further for their wetting state.

### 7.1.3. Determination of the wetting state by FLSM images of the solid-liquid interface

A transition of the measured advancing contact angles from being close to the Cassie-Baxter state curve at small $P/d$ values towards being close to the Wenzel state curve

with increasing values of $P/d$ can be seen on the plasma coated microstructures. This transition is also described in the literature [193, 194]. For thermodynamical reasons, the water drop can only change its state from heterogeneous wetting (Cassie state, local energy minimum) to homogeneous wetting (Wenzel state, global energy minimum). The water-air interface beneath the drop can get stabilized at different positions along the way down to the bottom of the microstructure gaps because of local energy minima created by the superimposed nanostructures [195, 196].

The measured advancing contact angles on the most superhydrophobic samples (microstructures C6 and C9) still did not completely reach the Cassie-Baxter state curve. They seem to correspond more to a mixed wetting state with the water-air interface stabilized at a position between the Cassie-Baxter and the Wenzel state. Although showing high contact angles, these mixed wetting states can significantly influence the ice adhesion and icing behavior because the water already partially fills the gaps and the surface-water interface is increased.

In order to better determine the exact wetting state on the quadratically arranged microstructure C16 and the hexagonally arranged microstructures C6 and C9, fluorescence laser scanning microscopy images were taken of these microstructures in uncoated or plasma coated PU and silicone (shown below). A green fluorescent water drop was put either on the microstructured, non-fluorescent PU or red-fluorescent silicone samples. The silicone was used to create samples with optimal reproduction of the microstructures in the stamp, because the silicone is liquid before cross-linking. Therefore, no air trapping occurs in contrast to using PU as the substrate. The green fluorescence of the water or red fluorescence of the silicone surface should enable better detection by the FLSM and visualization of the corresponding water-air and surface-air or surface-water interfaces.

For each sample, the top view (x-y plane) with the corresponding orthogonal views (x-z and y-z cuts) on the sides are shown in this section. The position of the cuts is marked by the colored lines and the cuts are surrounded by frames of the same color (x-z = green, y-z = red). The cuts are drawn from the lowest position z = 0 (on the upper side for x-z cuts, on the right side for y-z cuts) to the highest position z = max (on the lower side for x-z cuts, on the left side for y-z cuts). A green fluorescent water drop was placed on the sample. The sample with the water drop was turned upside down

and put onto the inversely looking fluorescence laser scan microscope. In this way, the scattering was reduced, as the microscope now looked directly through the water drop at the sample surface. Therefore, the microstructures are pointing towards z = 0 in the FLSM images.

### Fluorescent water on microstructure C16 on red fluorescent silicone

The images taken of the quadratically arranged microstructures C16 are shown in Figure 7.5.

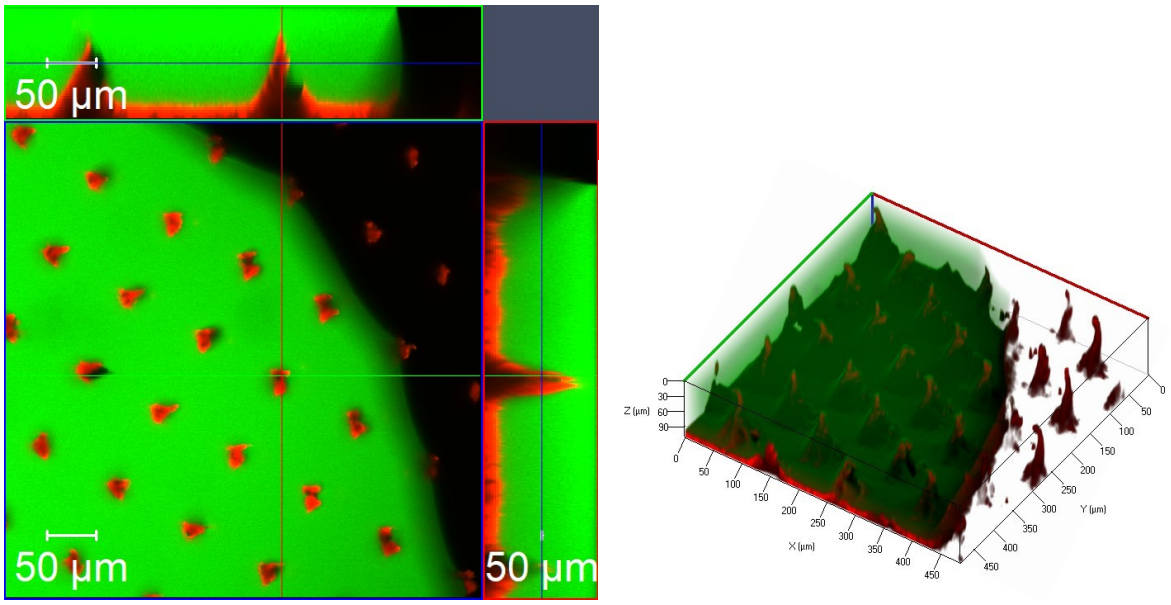


Figure 7.5.: Fluorescence laser scan microscopy images of microstructure of the DIN A4 stamp in red fluorescent silicone, wetted by a green fluorescent water drop, (485.82 x 485.82 x 114.86) µm, 0.7x zoom.

The fluorescent water is in the Wenzel wetting state on the coated silicone surface with microstructure C16. On the plasma coated microstructure C16 in the PU film the water contact angles were at about 130°, therefore also in the Wenzel wetting state. The quadratical arrangement of microstructures on the surface leads to a lower structure density as compared to the hexagonal arrangement. Therefore these surfaces, although coated, are more easily wetted by the water down to the surface bottom. These quadratically arranged microstructures are not suited for stabilization of water drops in the Cassie-Baxter or a mixed wetting state close to it.

### Fluorescent water on microstructure C6 on PU

The images of a fluorescent water drop on microstructure C6 on a PU surface are shown in Figure 7.6.

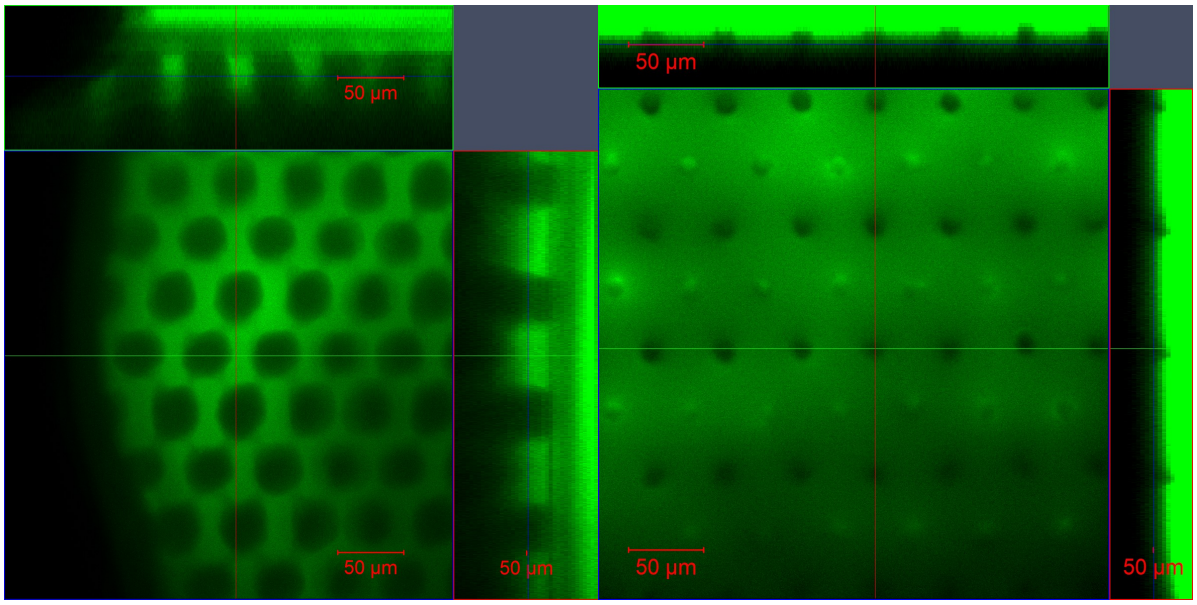


Figure 7.6.: Fluorescence laser scan microscopy images of a green fluorescent water drop on microstructure C6 in non-fluorescent PU, left: uncoated, (340.08 x 340.08 x 109.11) µm, 1x zoom, right: fluorocarbon plasma coated, (340.08 x 340.08 x 54.56) µm, 1x zoom.

It can be seen that the green water moves deeper into the gaps on the uncoated than on the coated surface. On the uncoated surface, the water interface is near the base of the structures, which is shown by the larger dark spots being the non-fluorescent polyurethane microstructures. On the coated surface, only the smaller tops of the microstructures can be seen.

It can be concluded that the wetting state on plasma coated microstructure C6 is close to the Cassie-Baxter state.

### Microstructure C6 on red fluorescent silicone

The microstructure C6 made of red fluorescent silicone is shown in Figure 7.7.

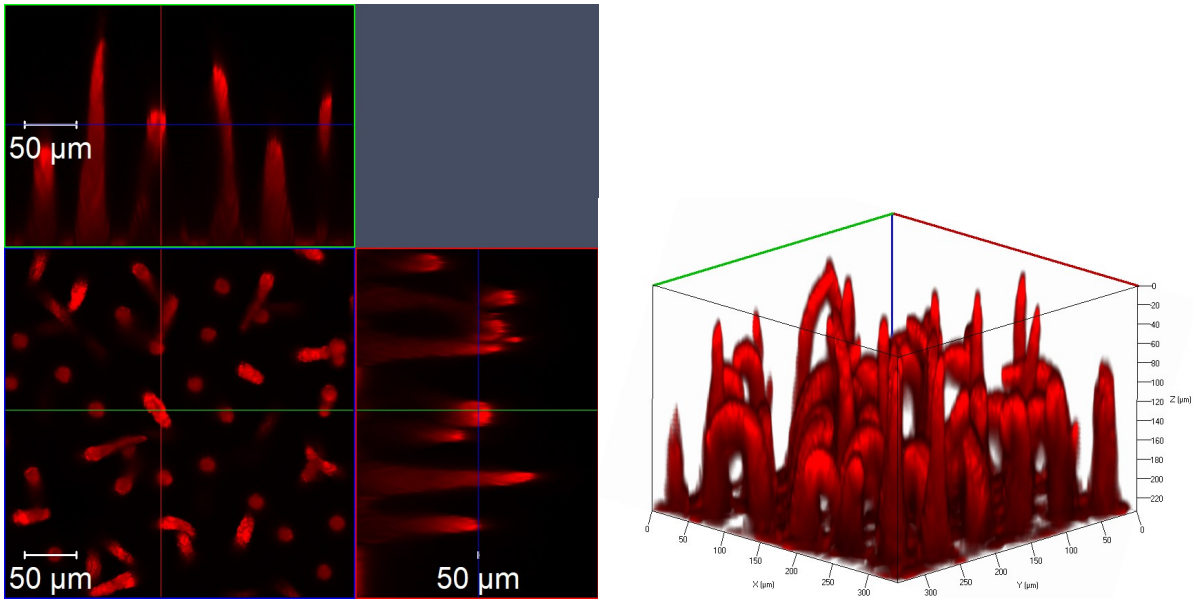


Figure 7.7.: Fluorescence laser scan microscopy images of microstructure C6 in red fluorescent silicone, (340.08 x 340.08 x 235.10) µm, 1x zoom.

As the liquid silicone-mixture flows down to the bottom of the holes of the microstructuring stamp and allows air to evade before hardening, the microstructures become very long and then sometimes get bent, as shown by the FLSM images above. This can also happen for microstructures in PU if all the air evades during hot embossing and the height of the microstructures becomes too large (full height = 80 µm).

### Fluorescent water on microstructure C9 on PU

The images taken of microstructure C9 are shown in Figure 7.8 for a PU surface.

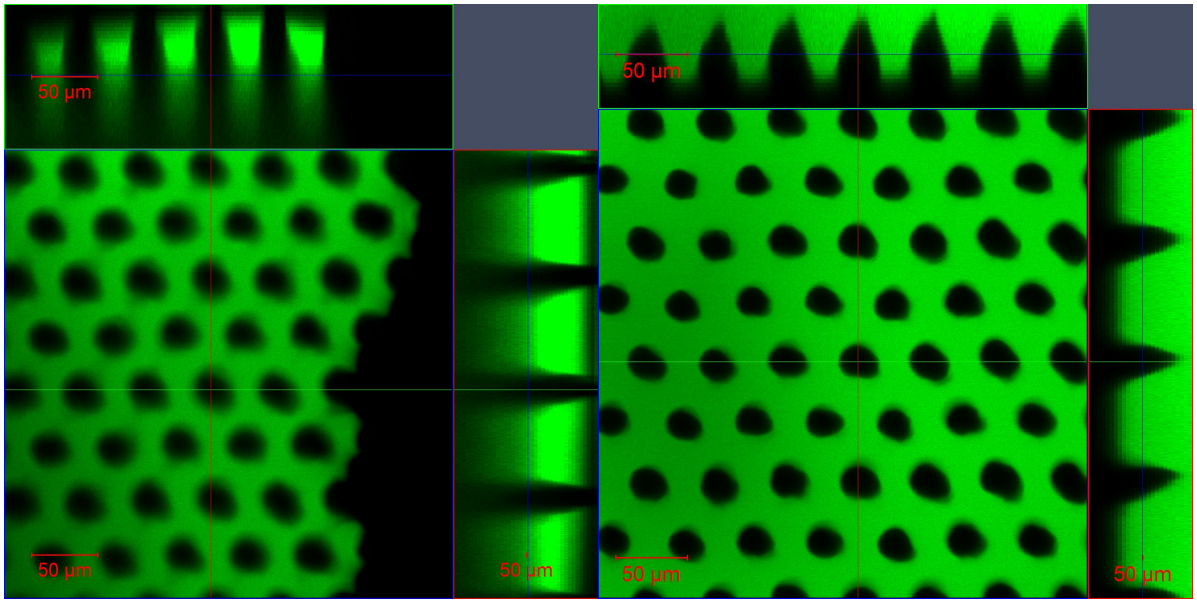


Figure 7.8.: Fluorescence laser scan microscopy images of a green fluorescent water drop on microstructure C9 in non-fluorescent PU, left: uncoated, (340.08 x 340.08 x 109.11) µm, 1x zoom, right: fluorocarbon plasma coated, (340.08 x 340.08 x 71.78) µm, 1x zoom.

These images show that both the uncoated and the plasma-coated sample of microstructure C9 get wetted between the microstructures. The depth of wetting is larger on the uncoated than on the coated microstructures. The reason is the lower height and higher $P/d$ factor of microstructure C9 compared to C6. The lower height leads to less positions for stabilization of the water-air interface on the microstructure sides and the probability for it to reach the bottom (Wenzel state) is increased.

### Microstructure C9 on red fluorescent silicone

The microstructure C9 made of red fluorescent silicone is shown in Figure 7.9.

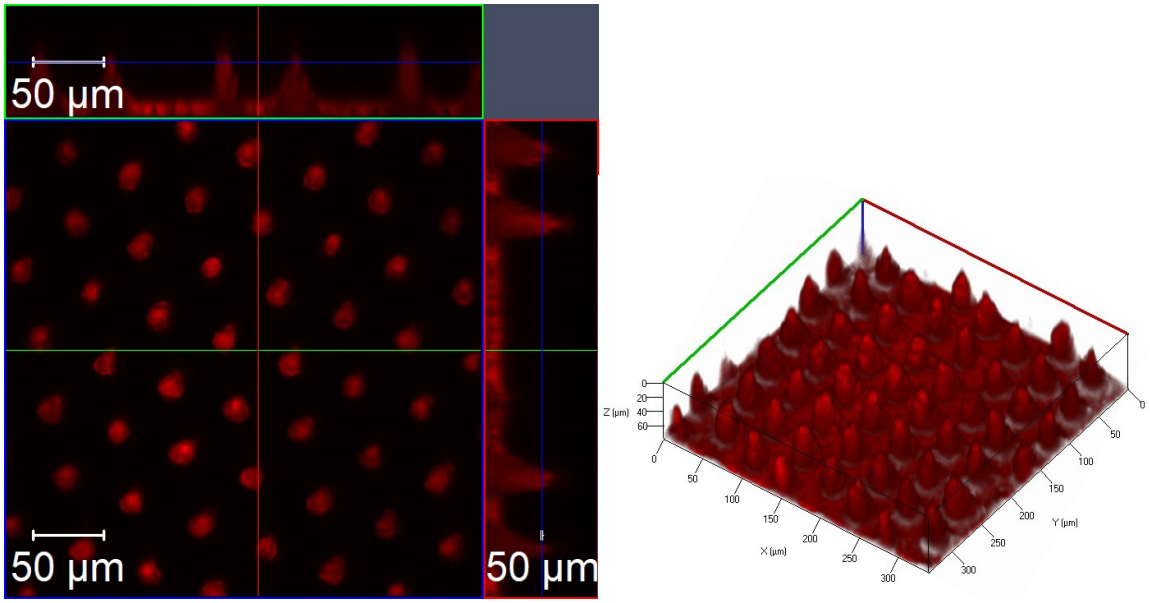


Figure 7.9.: Fluorescence laser scan microscopy images of microstructure C9 in red fluorescent silicone, (340.08 x 340.08 x 79.74) µm, 1x zoom.

As microstructure C9 is lower than C6, no bent microstructures can be seen for this surface.

Microstructure C9 has the same diameter and distance values as C6, only the height is lower (about 40 µm compared to about 70 µm). Therefore, this microstructure C9 cannot stabilize the water in a mixed wetting state state as well as microstructure C6.

These fluorescence laser scan microscopy images are able to show the surface and water interfaces on the most interesting microstructures C16, C6 and C9. Because of the inverse microscopy method, the light was scattered by the sample in case of upright sample positioning, where the real wetting behavior could be visualized. For less light scattering, the wetted samples were turned upside down and the water drops rolled off. These images show the wetting behavior by visualization of the formerly wetter areas.

The different wetting states (Wenzel state on uncoated samples, mixed state on coated samples) can be seen for the hexagonally structured samples C6 and C9. The stabi-

lization of a mixed wetting state close to Cassie-Baxter was seen on microstructure C6 with increased height compared to C9, where the mixed state was closer to the Wenzel state. Furthermore, the better stabilization on hexagonally arranged microstructures compared to quadratically arranged microstructure C16 becomes clear.

The hypothesis was that a superhydrophobic surface can be generated on PU by hot embossing of microstructures with diameters of 35 µm and above and subsequent plasma processes. The superhydrophobic state with contact angles above 150° was not fully reached by using elliptical or linear microstructures. The linear microstructures showed a direction dependent macroscopic wetting behavior. It could also not be achieved with quadratically arranged, cylindrical microstructures with a diameter of 70 µm. However, superhydrophobicity was reached with hexagonally arranged, cylindrical microstructures with diameters of 50 µm and 35 µm. As the comparison of the measured with the theoretical values and the FLSM images of green fluorescent water drops on these hexagonally arranged, cylindrical microstructures in PU have shown, the Cassie-Baxter state has not been fully reached and the water drops were in a mixed wetting state. Therefore, the microstructure dimensions need to be optimized further in order to increase the water contact angles and reach a complete Cassie-Baxter state.

The characterization of the ice adhesion and icing behavior is given in the following sections. The results of the wetting behavior of the different functionalized PU surfaces and other technical material surfaces will be correlated with the ice adhesion and icing measurements.

## 7.2. Ice adhesion - de-icing behavior

In case not all water runs off the surface and the remaining water cannot be prevented from freezing, the ice has to be removed from the functionalized anti-ice surface. The force needed for removal depends on the adhesion between the ice and the surface. For an effective de-icing, the ice should be easily removable, preferably without mechanical or electrical energy, just by wind or gravitational forces. The hypothesis is that the ice adhesion is determined by the surface free energy or wetting behavior of a surface, therefore it is expected to be the lowest on superhydrophobic surfaces. In this section, the measured ice adhesion values are given, compared to theoretical fracture values and to values from literature, and the observed ice adhesion measurement values are explained. Finally, the ice adhesion is correlated with the wetting behavior and the surface topography of the examined surfaces in order to derive ideas for optimization of the design for an effective de-icing behavior.

### 7.2.1. Calculation of theoretical ice adhesion values

In order to classify the experimental ice adhesion values, they are compared to theoretical values. The theoretical ice adhesion values were calculated with Griffith's law for a plane crack initiation according to linear elastic fracture mechanics [163, 162] (see equations 3.34 to 3.37 in chapter on theoretical basics 3.2.3). Values of 1 µm, 10 µm and 100 µm were used as characteristic length $L$ of a microcrack in the ice or at the ice-surface interface. The value of 65 mN m$^{-1}$ was used for the surface free energy of the ice-to-ice interface $\gamma_{II}$ [197, 198] for calculation of a pull-off (mode 1) cohesive and adhesive fracture (see equations 3.34 and 3.35, respectively). 109 mN m$^{-1}$ was used as ice-to-air surface free energy $\gamma_{IA}$ and 145° was used as the receding contact angle $\theta_{\mathrm{rec}}$ of water or ice on a superhydrophobic surface for calculation of a shear-off (mode 2) cohesive and adhesive fracture (see equations 3.36 and 3.37, respectively). Table 7.1 and Figure 7.10 show the calculated theoretical tensile (mode 1) and shear (mode 2) strength values for the different fracture types.

Table 7.1.: Theoretical strength values for cohesive or adhesive mode 1 and mode 2 ice fractures in dependence of microcrack length.

| | pulled, mode I cohesive, microcrack in ice<br>$\gamma_{II} = 65\ mN\ m^{-1}$<br>$E_{ice} = 10\ GPa$ | pulled, mode I adhesive, microcrack at interface<br>$\gamma_{II} = 65\ mN\ m^{-1}$<br>$E^*_{i,PU} = 0.5091\ GPa$ | sheared, mode II cohesive, microcrack in ice<br>$\gamma_{IA} = 109\ mN\ m^{-1}$<br>$E_{ice} = 10\ GPa$ | sheared, mode II adhesive, microcrack at interface<br>$\gamma_{IA} = 109\ mN\ m^{-1}$<br>$E^*_{i,PU} = 0.5091\ GPa$ |
|---|---|---|---|---|
| $L$ (µm) | $\sigma_{ice}$ (kPa) | $\sigma_{ice,PU}$ (kPa) | $\tau_{ice}$ (kPa) | $\tau_{ice,PU}$ (kPa) |
| 1 | 14384 | 3246 | 7921 | 1787 |
| 10 | 4549 | 1026 | 2505 | 565 |
| 100 | 1438 | 325 | 792 | 179 |

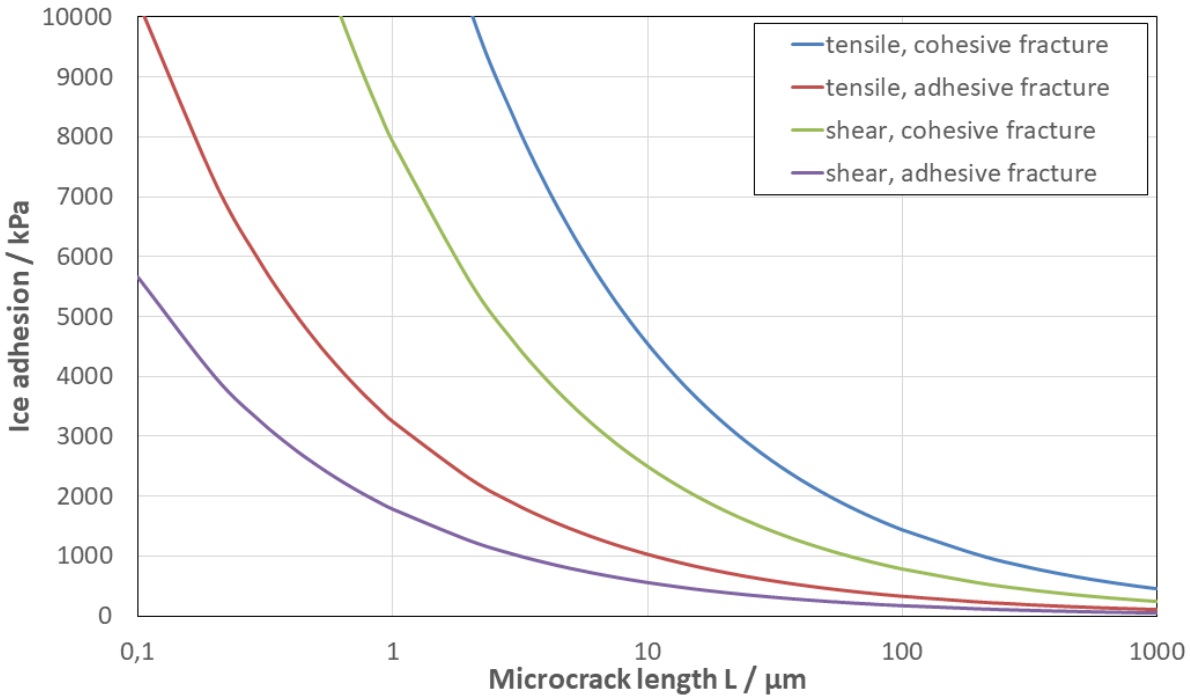


Figure 7.10.: Theoretical strength values for cohesive or adhesive mode 1 and mode 2 ice fractures in dependence of microcrack length.

### 7.2.2. Ice adhesion measurement results

All ice adhesion measurements were done at ambient atmosphere in the ice test chamber at about 50 % relative humidity, except for the measurements in dry atmosphere at about 0 % to 5 % relative humidity.

#### Ice adhesion on flat plasma-coated PU samples

As the surface free energy of the PU was lowered by the plasma coatings to values below those of the metal oxide and polymer surfaces, the ice adhesion on the plasma coated PU surfaces was expected to be even lower. Figure 7.11 shows the ice adhesion values of plain and plasma-coated PU surfaces.

Adhesive fractures on the whole circular ice-surface contact area occurred on all of the uncoated and plasma coated PU surfaces. No images of the fractures are shown here because no ice rests remained on any of these flat PU surfaces.

The uncoated PU surface showed the highest ice adhesion of $(447 \pm 77)$ kPa. An ice adhesion value of $(820 \pm 40)$ kPa measured by shearing off is reported by Bharatidasan *et al.* [199].

The plasma coatings all reduced the ice adhesion. On the $C_3F_6$-plasma coated PU surface the ice adhesion was lowest with a value of $(287 \pm 8)$ kPa. The ice adhesion on the $O_2$-etched and then $C_3F_6$ plasma coated PU is higher at $(371 \pm 66)$ kPa because of the different nanoroughness and lesser hydrophobia.

For the HMDSO plasma coated surfaces, the sample coated in the 200 W plasma has a lower ice adhesion of $(365 \pm 46)$ kPa than the one coated in the 60 W plasma with a value of $(413 \pm 208)$ kPa, despite of the higher oxygen content and lesser hydrophobia. This could be caused by the different nanoroughness.

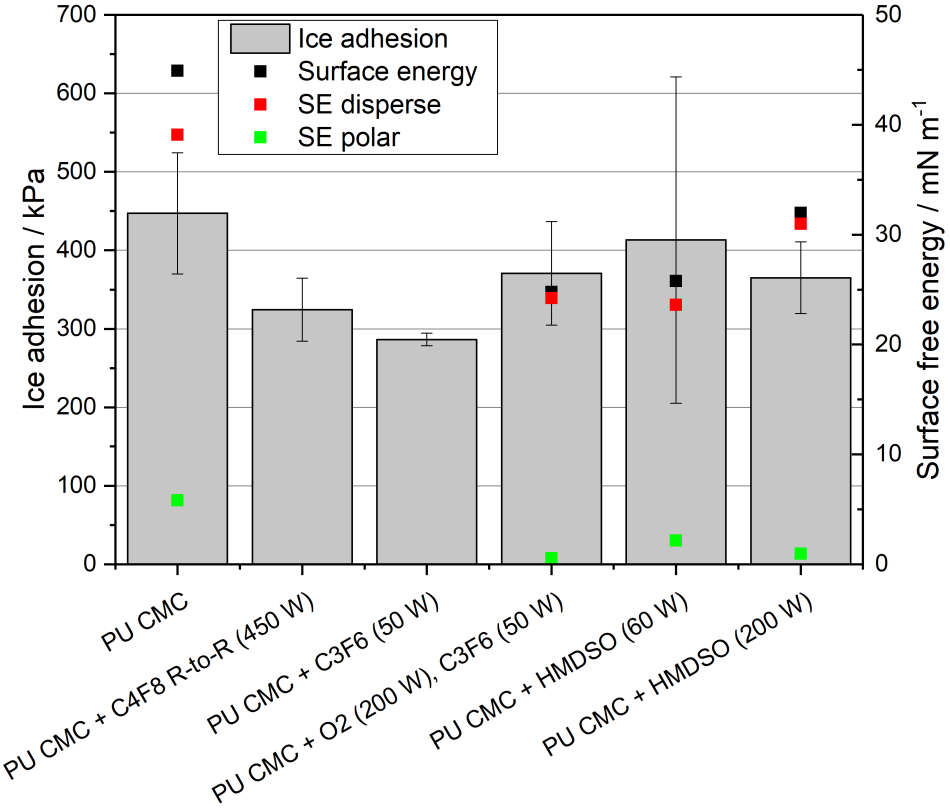


Figure 7.11.: Ice adhesion values of uncoated and plasma coated, flat PU surfaces. Surface free energy values were determined for some surfaces by static water and DIM contact angle measurements (not shown, if no DIM values available). The uncoated PU film shows the highest ice adhesion.

### Discussion of ice adhesion on flat plasma-coated PU samples

For comparison with the fluorocarbon plasma coatings, fluorinated sol-gel coatings have a reported shear strength ice adhesion of about 100 kPa to 500 kPa, Teflon of about 300 kPa [157]. Jafari *et al.* report a sheared ice adhesion on a RF-sputtered PTFE coating on polished or anodized aluminum of $(110 \pm 22)$ kPa or $(72 \pm 12)$ kPa, respectively [87]. Furthermore, an ice adhesion shear strength (mode II) of $(238 \pm 38)$ kPa on perfluoropolyether (PFPE) and $(394 \pm 70)$ kPa or $(284 \pm 90)$ kPa on fluorinated polyurethane polyols (FPU) is reported [200].

Regarding the silicone-like plasma coatings, shear strength (mode II) ice adhesion values of $(264 \pm 19)$ kPa and $(33 \pm 2)$ kPa are reported for PDMS with high and low crosslink-

ing degree, respectively [200]. Very low ice adhesion values have been reported on elastomeric coatings with low cross-linking degree, but these plasma coatings are naturally highly cross-linked [200]. On room temperature vulcanized silicone an ice adhesion of $(24.8 \pm 8)$ kPa was measured [199].

Adhesion is caused by different mechanisms like mechanical interlocking, electrostatic interactions or adsorption. The surface forces are caused by the van der Waals short range weak interactions between the hydroxyl group of the adsorbed water molecules and the surface atoms. The nature of the surface forces (attractive or repulsive) is determined by the thermal expansion of ice and the solid and the lattice mismatch between the ice and the solid. At -20 °C the lattice mismatch is expected to have a greater effect than the thermal expansion. A solid which displays good lattice matching with ice shows good adhesive strength [201]. Polymers have a lower coefficient of thermal expansion compared to ice. In case of an ice-polymer interface at -20 °C the ice experiences a compressive force and the hydroxyl bond length is shortened [201]. In the case of polymers, the interatomic C-C distance of the backbone determines the surface forces on the hydroxyl groups and the adhesion of the ice. For PTFE, the average C-C distance is 4 Å which is larger than the lattice constant (O-O distance of 2.78 Å in polycrystalline ice) of ice and causes low adhesion because of the high lattice mismatch [201].

Overall, the fully adhesive mode I fractures allowed the determination of the ice adhesion on these plasma coated PU surfaces. The plasma coatings lowered the surface free energy and therefore also the ice adhesion to values between $(287 \pm 8)$ kPa and $(413 \pm 208)$ kPa.

### Ice adhesion on quadratically arranged cylindrical microstructures with $D = 70$ µm

According to the hypothesis, the ice adhesion was expected to be the lowest on the microstructured, plasma-coated PU surfaces which showed high water contact angles or even superhydrophobic wetting behavior. Because the cylindrical microstructures C16 (diameter of 70 µm) were arranged quadratically, the corresponding plasma-coated surfaces did not show superhydrophobic wetting behavior, but a Wenzel state wetting behavior (see water contact angles in the appendix A.4). Figure 7.12 shows the ice

adhesion values of the quadratically arranged, cylindrical microstructures C16 and of the flat PU surfaces.

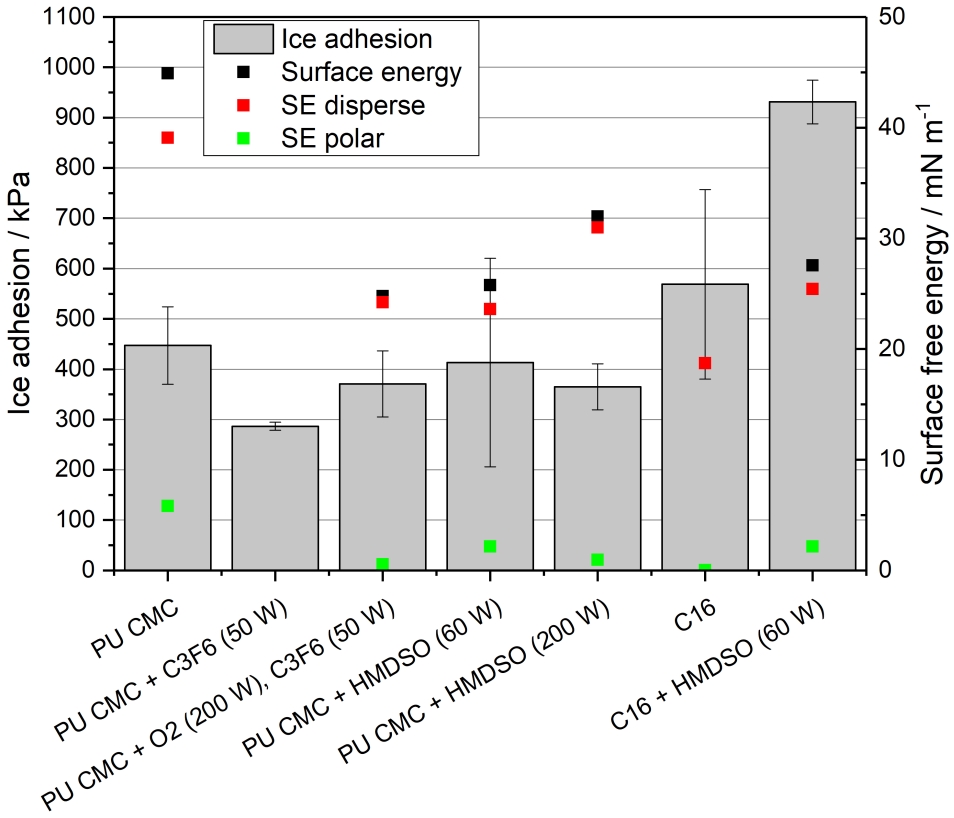


Figure 7.12.: Ice adhesion values of uncoated or plasma coated, flat PU surfaces and quadratically arranged, cylindrical microstructure C16. Surface free energy values were determined for some surfaces by static water and DIM contact angle measurements (not shown, if no DIM values available). The ice adhesion is higher on the microstructured surfaces than on the flat surfaces.

In contrast to the hypothesis, the ice adhesion is higher on the microstructured PU samples than on the flat PU samples. A value of (569 ± 188) kPa was measured on uncoated microstructure C16. The ice adhesion value for the microstructured and plasma-coated sample was even higher ((931 ± 43) kPa on the HMDSO 60 W plasma coated microstructure C16).

The fracture was adhesive on HMDSO 60 W plasma coated microstructure C16 as no ice residues can be seen in the corresponding image, see Figure 7.13. The images of the ice fractures after the ice adhesion tests of further microstructured surfaces are shown

in the appendix (A.6).

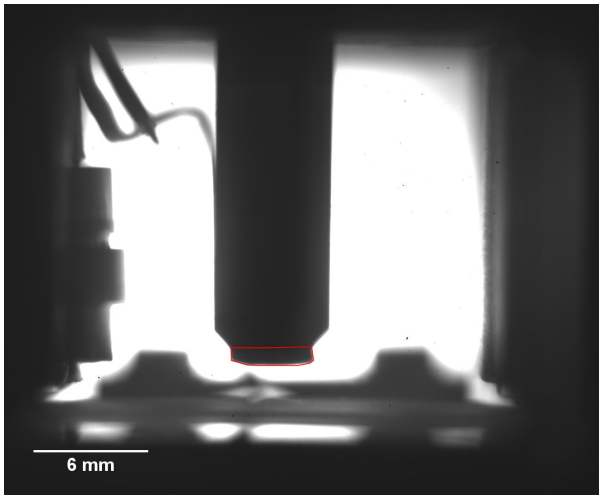


Figure 7.13.: Image of ice adhesion measurement fracture on sample C16 + HMDSO (60 W).

### Discussion of the ice adhesion on quadratically arranged cylindrical microstructures with $D = 70$ µm

These measured fracture strength values between $(569 \pm 188)$ kPa and $(931 \pm 43)$ kPa on the microstructured surface are in the range of theoretical adhesive mode I fractures with a microcrack length of 100 µm (325 kPa) to 10 µm (1026 kPa, see Table 7.1).

It becomes clear that surfaces with quadratically arranged microstructures of 70 µm base diameter create a Wenzel wetting state and a high ice adhesion because of the increased contact area, although the fracture was adhesive and not cohesive.

### Ice adhesion on hexagonally arranged cylindrical microstructures with $D = 50$ µm

The plasma-coated, hexagonally arranged, cylindrical microstructures C1 (diameter of 50 µm) showed superhydrophobicity. Figure 7.14 shows the ice adhesion values of the hexagonally arranged, cylindrical microstructures C1 and of the flat PU surfaces.

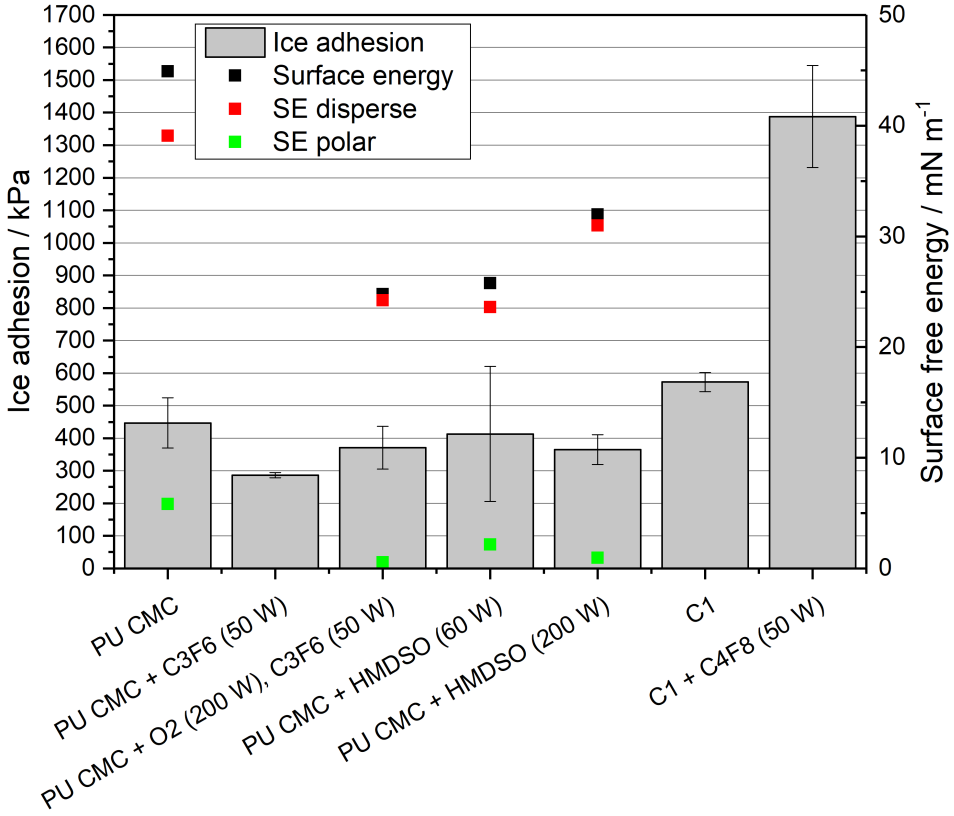


Figure 7.14.: Ice adhesion values of uncoated or plasma coated, flat PU surfaces and hexagonally arranged, cylindrical microstructure C1. Surface free energy values were determined for some surfaces by static water and DIM contact angle measurements (not shown, if no DIM values available). The ice adhesion is higher on the microstructured surfaces than on the flat surfaces.

Values of $(573 \pm 29)$ kPa for the microstructure C1 and $(1388 \pm 157)$ kPa for the $C_4F_8$ plasma-coated microstructure C1 were measured although this surface showed superhydrophobicity.

In the images of the uncoated C1 sample shown in Figure 7.15 it can be seen that ice rests remain on the surfaces, between the microstructures in shape of the circular ice-surface contact area. Here, the fractures were in parts cohesive (along the edge or the circular area) and in parts adhesive (in the middle of the circular area). On the plasma coated C1 samples cohesive fractures occured (see Figure 7.15 and images in the appendix, A.6).

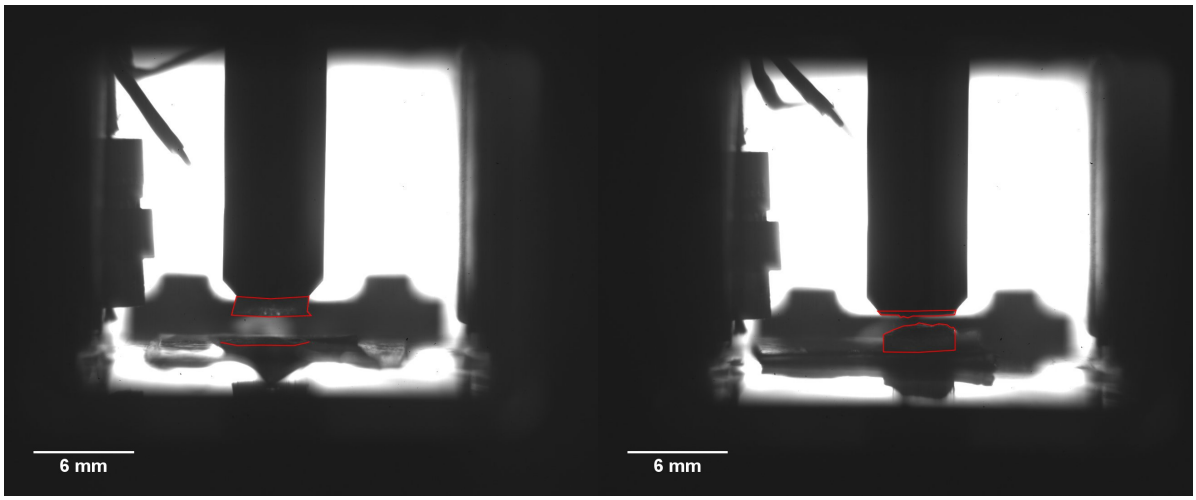


Figure 7.15.: Images of ice adhesion measurement fractures on uncoated C1 (left) and C1 + $C_4F_8$ (right).

**Discussion of the ice adhesion on hexagonally arranged cylindrical microstructures with $D = 50$ µm**

These values are in the range of theoretical adhesive mode I fractures with microcrack lengths of 100 µm (325 kPa) to 10 µm (1026 kPa) and cohesive mode I fractures with microcrack lengths of 100 µm (1438 kPa) or more (see Table 7.1).

In the earlier literature, superhydrophobic surfaces were postulated to be also icephobic and to show a low ice adhesion [87, 154, 156, 133, 151, 155, 202]. Furthermore, the ice adhesion strength has been correlated to the work of adhesion of water and textured surfaces have been proposed for further reduction of ice adhesion [169]. A low ice adhesion has also been attributed to a low wetting hysteresis [203].

However, a larger ice adhesion on rough surfaces compared to flat surfaces with the same chemistry has also been reported in literature [204, 157]. Zou *et al.* have reported that ice adhesion on sand-blasted aluminum surfaces was 1.5 to 1.9 times that of the adhesion on flat, untreated aluminum surfaces with same surface chemistry [204]. Cao *et al.* stated that the determining roughness for superhydrophobicity is of a different length scale than for icephobicity [86].

The reason for the high strength values is the wetting in Wenzel state where the water fills the gaps between the microstructures. The superhydrophobic wetting state is metastable

and water can fill the microstructure gaps during cooldown and freezing [193, 205, 194]. This has happened during the cooling process as shown by the images showing ice rests between the microstructures after the fracture. The increased surface-ice contact area and the mechanical interlocking of the ice with the micro- and nanostructures enhance the ice adhesion on these superhydrophobic PU surfaces.

These measurements show that superhydrophobic surfaces are not always icephobic which has been reported by some authors before [204, 162, 158]. It becomes clear that superhydrophobic surfaces with hexagonally arranged microstructures of 50 µm base diameter cannot stabilize the Cassie-Baxter state sufficiently during simultaneous cooldown of the water and the surface which results in the Wenzel wetting state and high ice adhesion. The reason for the higher ice adhesion on the more hydrophobic, plasma-coated microstructures compared to the uncoated microstructures could be the different nanoroughness and its effect on microcrack length.

#### Ice adhesion on hexagonally arranged cylindrical microstructures with $D = 35$ µm

As the diameters of the hexagonally arranged microstructures C6 and C9 were even smaller than of C1, these plasma coated surfaces showed the best superhydrophobicity and were expected to show the overall lowest ice adhesion values. Figure 7.16 shows the measured ice adhesion values of uncoated or plasma coated microstructures C6 and C9.

The ice adhesion strength on the uncoated, microstructured surfaces is higher than on the flat surfaces, with $(1125 \pm 364)$ kPa for uncoated C6 and $(866 \pm 15)$ kPa for uncoated C9. The ice adhesion strength values are increased further on the plasma-coated samples, e.g. to $(2780 \pm 270)$ kPa for C6 + $O_2$, $C_3F_6$ and to $(1186 \pm 259)$ kPa for C9 + $O_2$, $C_3F_6$. For each structure, the $O_2$ (200 W) etching and subsequent $C_3F_6$ (50 W) coating and the HMDSO (60 W) coating led to similar high ice adhesion values.

The HMDSO 200 W coatings reduced the ice adhesion below the values of the uncoated microstructures ($(930 \pm 135)$ kPa for C6 and $(839 \pm 88)$ kPa for C9). This can only be caused by the different nanoroughness with lesser, but rounder bumps on the HMDSO 200 W plasma coating compared to the nanoroughness with more and sharper needles

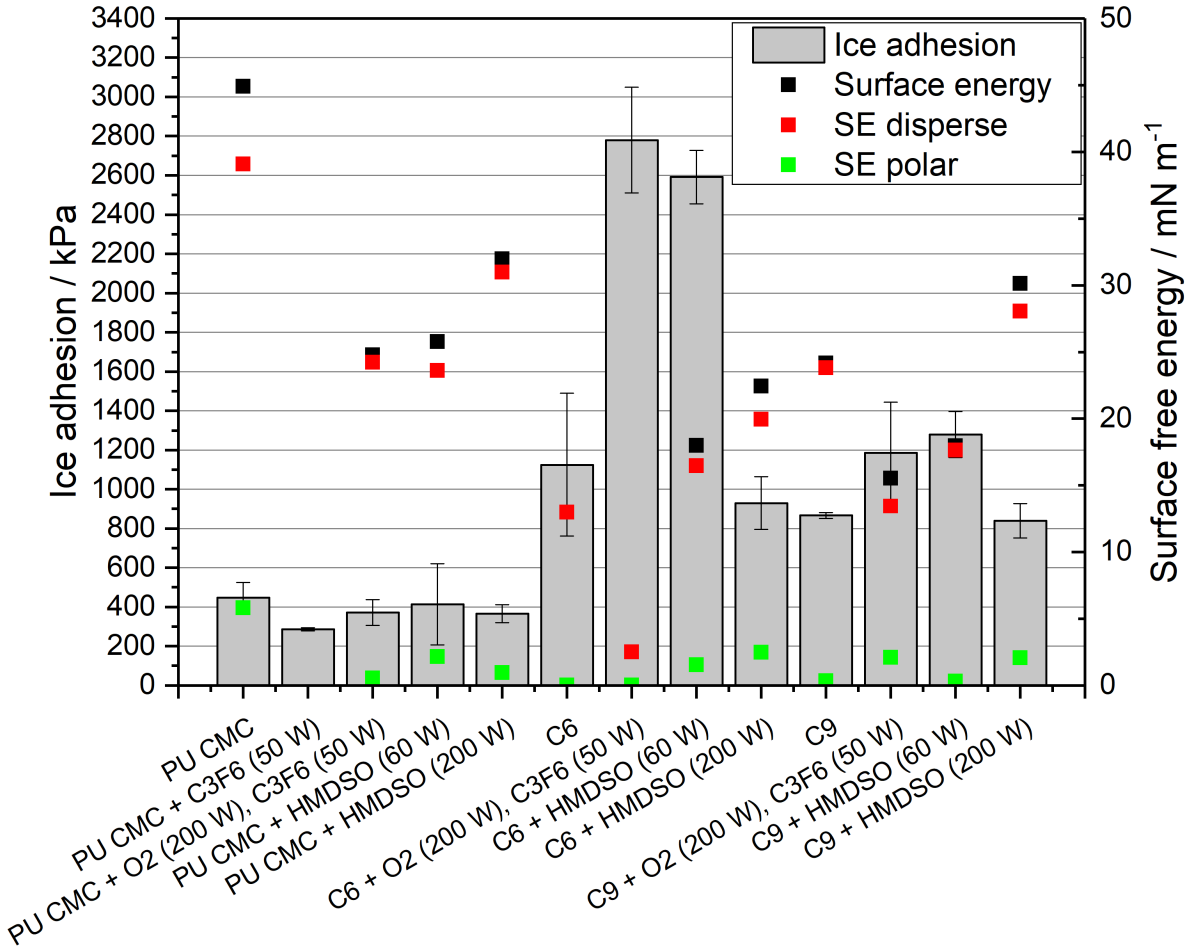


Figure 7.16.: Ice adhesion values of uncoated or plasma-coated, flat PU surfaces and hexagonally arranged microstructures C6 and C9, which showed the best superhydrophobicity. Surface free energy values were determined for some surfaces by static water and DIM contact angle measurements (not shown, if no DIM values available). The ice adhesion is higher on the microstructured surfaces than on the flat surfaces and it is further increased on the $C_3F_6$ and HMDSO (60 W) plasma-coated microstructures.

on the other plasma coatings (see AFM images of the various plasma coatings in the appendix A.3).

The images taken after the ice adhesion measurements show that ice rests remain on the HMDSO 60 W and $C_3F_6$ plasma-coated surfaces in the shape of the circular contact area because ice remains stuck between the microstructures (see ice fracture images in Figure 7.17, Figure 7.18 and the appendix A.6). Mixed fractures occurred for these plasma-coated samples.

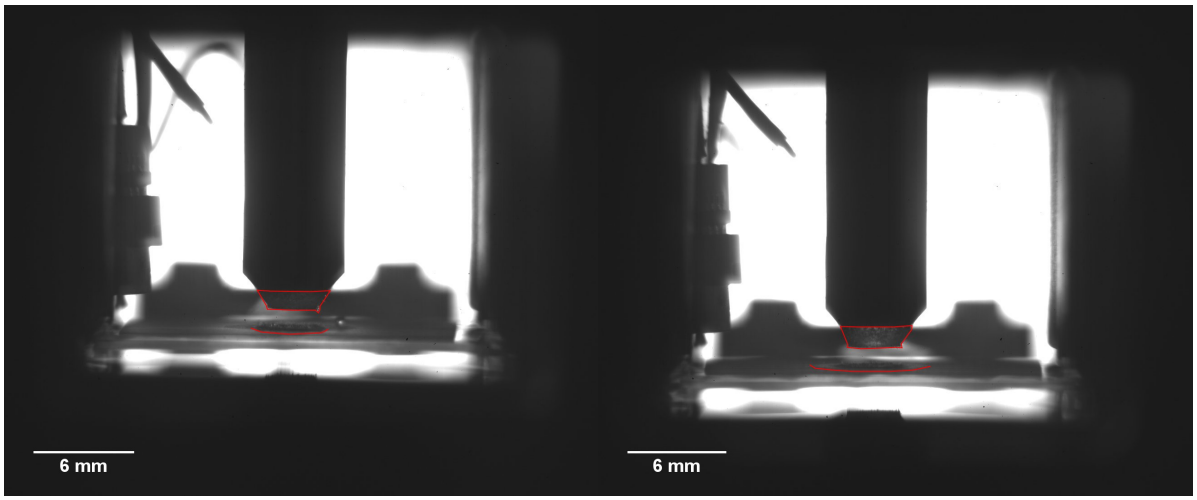


Figure 7.17.: Images of ice adhesion measurement fractures on samples $O_2$-etched C6 + $C_3F_6$ (left) and $O_2$-etched C9 + $C_3F_6$ (right).

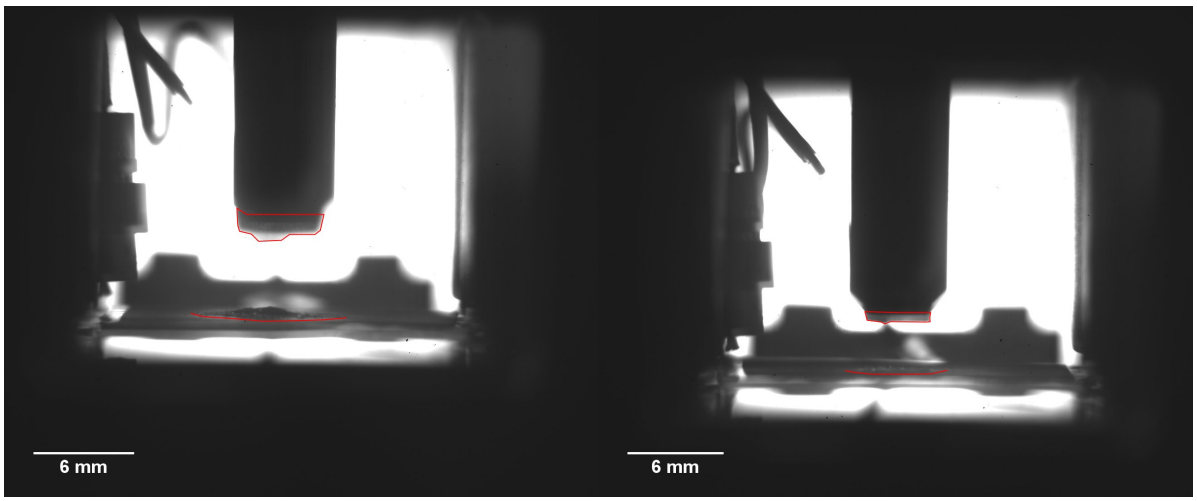


Figure 7.18.: Images of ice adhesion measurement fractures on samples C6 + HMDSO 60 W (left) and C9 + HMDSO 60 W (right).

The images of the HMDSO 200 W coatings show that ice rests remain mostly on the outside of the circular ice contact area which happens because of condensation from

the water cylinder during cooldown on every surface (see Figure 7.19). Therefore, the fractures on the HMDSO 200 W coatings were largely adhesive.

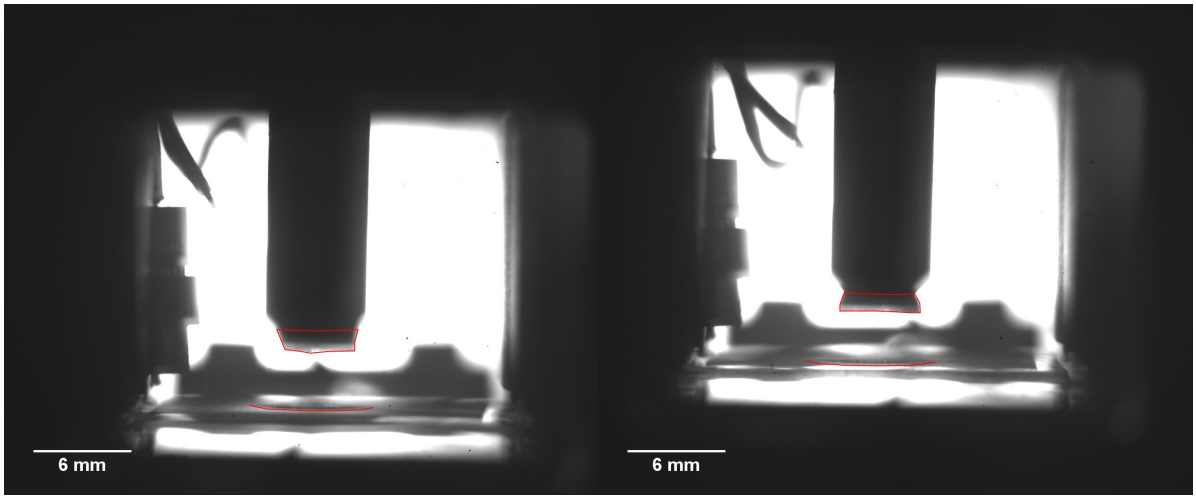


Figure 7.19.: Images of ice adhesion measurement fractures on samples C6 + HMDSO 200 W (left) and C9 + HMDSO 200 W (right).

### Discussion of the ice adhesion on hexagonally arranged cylindrical microstructures with $D = 35$ µm

When compared to the theoretical values, these measured high ice adhesion values between 800 kPa and 2800 kPa are in the range of cohesive mode I fractures for initial microcracks within the ice of 10 µm (4549 kPa) to 100 µm (1438 kPa) length. The fractures on the HMDSO 200 W coating can be compared with adhesive mode I fractures with microcracks of 10 µm (1026 kPa, see Table 7.1).

The reason for these high ice adhesion values is the Cassie-to-Wenzel transition during the cooling process and the freezing of the water in the Wenzel wetting state. The Wenzel state leads to a larger ice-surface contact area because the water moves into the air filled pores of the structured surface during freezing which creates a larger adhesive strength. The ice-surface contact area is enhanced further on the plasma coatings because of their higher nanoroughness leading to even higher fracture strength values. Additionally, a mechanical interlocking effect created by the micro- and nanostructures between the surface and the ice was postulated which further enhances the adhesion [204, 158].

According to Chen *et al.*, on microstructured surfaces the adhesive and cohesive strengths have to be combined according to the fractions of microstructures and ice-filled pores. For removal of the ice, the adhesive strength to the microstructure top surfaces as well as the cohesive strength of the ice parts in the pores has to be overcome. The cohesive strength of ice was estimated by an extrapolation method to be about 1916 kPa to 1970 kPa by Chen *et al.* [158] which is similarly high as some of the measured values. The fracture strength has been reported to increase with increasing density of microstructures or pores [158]. Therefore, the measured strength values are higher on microstructured surfaces as compared to flat surfaces.

The ice adhesion for the plasma coated microstructures C6 is the highest because these microstructures have the largest height of about 70 µm. If the water fills the microstructure gaps during freezing, the surface-to-ice interface becomes largest on these surfaces. As the microstructure C9 is only about 40 µm high, the surface-to-ice interface and therefore also the ice adhesion is lower here.

The Cassie-to-Wenzel transition has occurred during the cooling process which is shown by the ice fracture images showing ice rests between the microstructures in the circular contact area. The significantly increased ice-to-surface contact area leads to partly cohesive fractures and very high fracture values. It has to be concluded that these superhydrophobic surfaces with hexagonally arranged cylindrical microstructures with the smallest base diameters of about 35 µm still cannot prevent the Cassie-to-Wenzel transition during the cooling or freezing process and therefore do not enable a low ice adhesion.

Another reason for the Cassie-to-Wenzel transition could be the destabilization of the Cassie-Baxter state because of condensing microdroplets from ambient air between the microstructures on the cooled surface. These condensed microdroplets could lead to coalescence with the water-air interface under the water drop. In order to exclude this possibility, ice adhesion measurements in dry atmosphere were carried out.

### Ice adhesion on hexagonally arranged cylindrical nanorough microstructures with $D$ = 35 µm in dry atmosphere

The influence of condensation on ice adhesion has been reported before, where higher relative humidity has led to higher measured ice adhesion strengths [152, 161]. The ice adhesion measurements described before were carried out at about 50 % relative humidity (icing test chamber $N_2$ gas turned off). In order to see whether the Cassie-to-Wenzel transition is caused by condensation from ambient air during the cooling process, some ice adhesion measurements (on $O_2$ etched and $C_3F_6$ plasma coated microstructures C6 and C9) were done in dry atmosphere (about 0 % to 5 % relative humidity, $N_2$ gas turned on at 0.5 bar). It was expected that the water freezes in Cassie state and these superhydrophobic surfaces show low ice adhesion in dry atmosphere. Figure 7.20 shows the ice adhesion values of plasma coated, microstructured surfaces C6 and C9 in dry atmosphere.

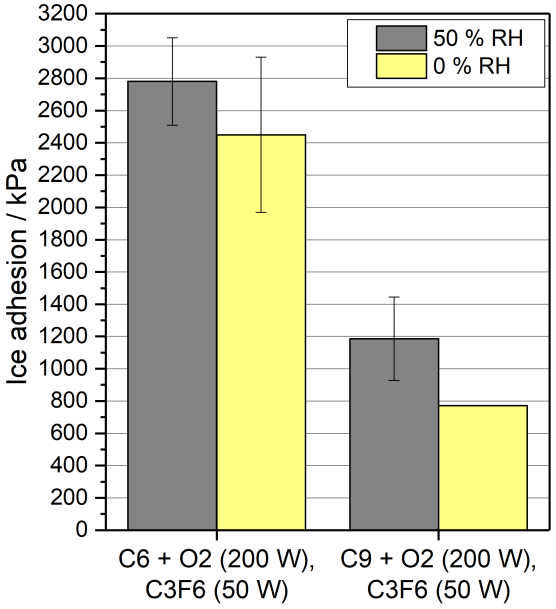


Figure 7.20.: Ice adhesion values of plasma-coated, nanorough, hexagonally arranged microstructures C6 and C9 at 0 % relative humidity.

The ice adhesion values for $O_2$ etched and $C_3F_6$ plasma-coated microstructures C6 and C9 are reduced in dry atmosphere compared to at about 50 % relative humidity but

are still too high for a properly functioning de-icing surface which should have an ice adhesion of 200 kPa or below.

The images of the ice adhesion fractures on microstructures C6 and C9 in dry atmosphere are shown in Figure 7.21. Cohesive fractures occurred during the measurements on C6 ((2450 ± 481) kPa) whereas an adhesive fracture occurred on C9 (771 kPa).

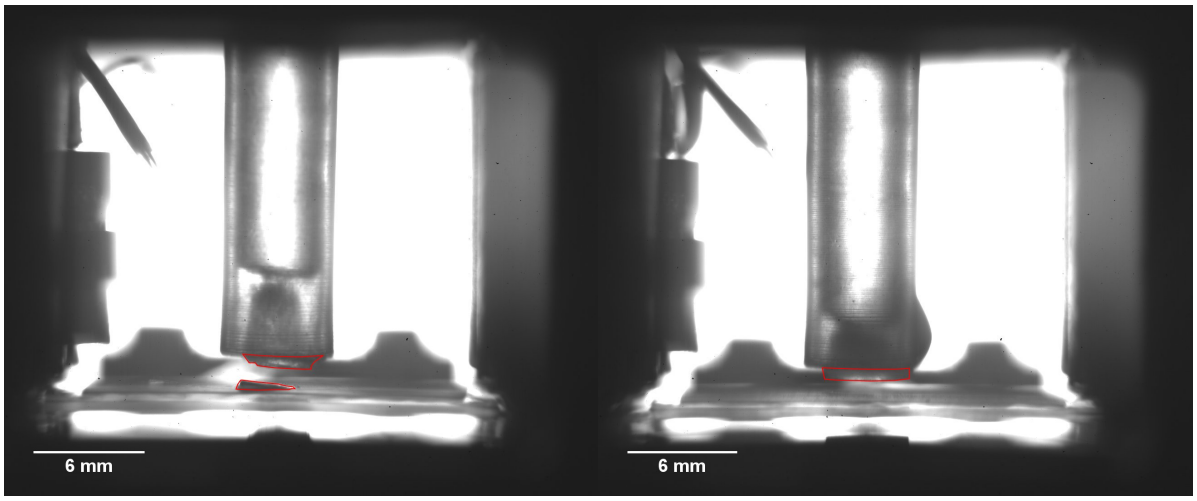


Figure 7.21.: Images of ice adhesion measurement fractures at 0 % rel. humidity on $O_2$-etched C6 + $C_3F_6$ (left) and $O_2$-etched C9 + $C_3F_6$ (right).

### Discussion of the ice adhesion on hexagonally arranged cylindrical nanorough microstructures with $D$ = 35 µm in dry atmosphere

The measured value on C6 is in the range of a cohesive mode I fracture with a microcrack length between 100 µm (1438 kPa) and 10 µm (4549 kPa). The measured value on C9 is in the range of an adhesive mode I fracture with a microcrack length of 10 µm (1026 kPa, see Table 7.1).

No condensation from ambient air occurs in dry atmosphere so that water drops stay longer in Cassie-Baxter state than at normal atmosphere with about 50 % rel. humidity. However, it has been reported that the water contact angle decreases and wetting increases with decreasing temperature and increasing water drop evaporation over time which is the reason for the observed Cassie-to-Wenzel state transition in dry atmosphere [206].

The water droplets have transitioned to a Wenzel wetting state during cooling and the measured fracture values are far above 200 kPa even in dry atmosphere. Reasons for this are the increased wetting area because of the cooldown process or the condensation from evaporation of the water drop itself. Therefore, it has to be concluded that these superhydrophobic surfaces ($O_2$ etched and $C_3F_6$ plasma coated microstructures C6 and C9) cannot prevent the Wenzel wetting state even in dry atmosphere and are not suited as an effective de-icing surface because of their high ice adhesion values.

### Ice adhesion on technical material surfaces and commercial anti-ice coatings

On the metallic (aluminum, titanium and copper) technical material surfaces a high ice adhesion above 500 kPa was expected because of their hydrophilic metal oxide surface (silicon oxide in case of glass).

Figure 7.22 shows the ice adhesion values of several technical material surfaces and commercial anti-ice coatings.

However, quite low strength values of $(140 \pm 58)$ kPa on the aluminum sample, $(62 \pm 9)$ kPa on the titanium sample and $(160 \pm 29)$ kPa on the glass sample were measured. Only on copper the measured value of $(394 \pm 234)$ kPa was in the expected region.

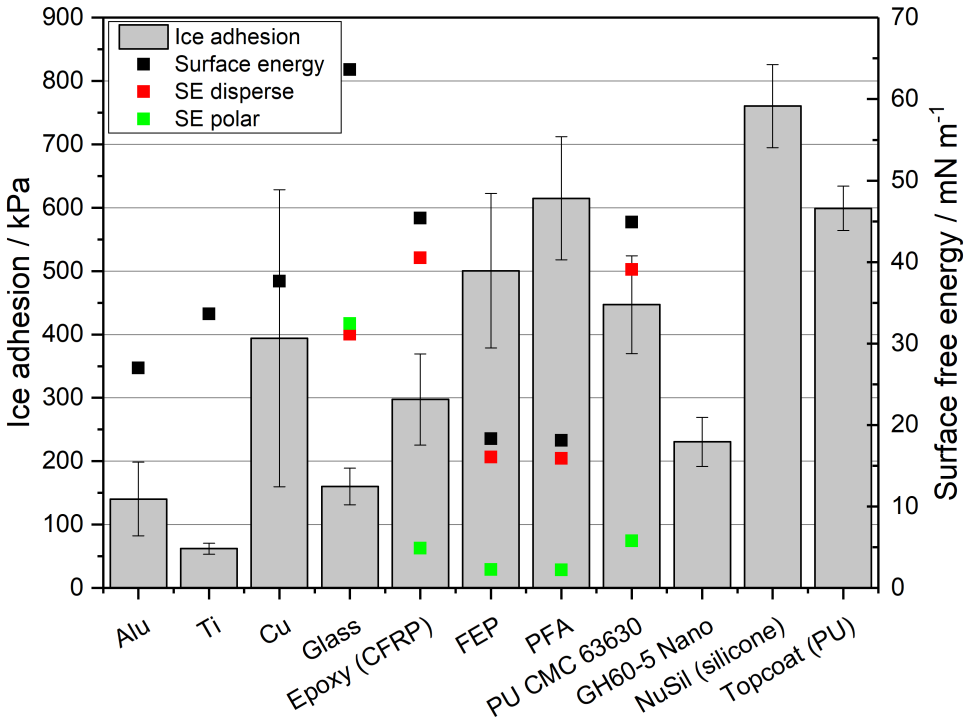


Figure 7.22.: Ice adhesion values of technical material surfaces and commercial anti-ice coatings (GH60-5 Nano, NuSil (silicone) and Topcoat (PU)) for comparison. Surface free energy values were determined for some surfaces by static water and DIM contact angle measurements (not shown, if no DIM values available).

### Discussion of the ice adhesion on the metal oxide surfaces

In case of the pure substance under vacuum, these materials have a very high surface free energy (aluminum: 1160 mN/m to 1381 mN/m [207], 1199 mN/m in the (111) plane [208]; titanium: 1935 mN/m to 2100 mN/m [207], 2632 mN/m in the (0001) plane [208]; copper: 1683 mN/m to 1830 mN/m [207], 1952 mN/m in the (111) plane; glass: 254 mN/m at 30 °C in vacuum [209]). In application, alloys of these materials are used which are covered by a metal oxide layer on the surface. This surface layer consists of the metal cations which are shielded by oxygen anions in order to minimize the surface free energy of the system [210]. This shielding by oxygen is created either by retraction of the metal cations or by adsorption of gases from the atmosphere [210].

Measured surface free energy values are 31 mN/m to 50.5 mN/m for aluminum oxide ($Al_2O_3$), 43.1 mN/m to 112.9 mN/m for glass ($SiO_2$) or 27.7 mN/m to 42.9 mN/m for titanium dioxide ($TiO_2$), depending on the type of alloy or composition [211].

The ice adhesion depends on temperature and surface roughness and increases with decreasing temperature and increasing roughness [212]. The measured values in the literature vary significantly. For example, a pull-off (mode I fracture) ice adhesion on aluminum of 330 kPa on a flat surface or 610 kPa on a sandblasted surface was measured [204]. Other pull-off ice adhesion values were $(369 \pm 89)$ kPa on as-received Al and $(444 \pm 32)$ kPa on etched Al [151], 558 kPa [212] or 931 kPa [213].

It has to be noted that the strength values are different when measured as shearing-off of ice (mode II fracture). For example, sheared ice adhesion values on bare aluminum of $(2000 \pm 140)$ kPa [202], of 1600 kPa [157] and of $(1072 \pm 120)$ kPa [199] were measured.

If an ice cylinder is pulled off vertically, the tensile force is effective on the complete circular contact area, as opposed to horizontal shear-off of an ice cylinder where half of the circular contact area experiences tensile force and the other half experiences pressure. Therefore, the measured force is different for mode I and mode II fractures which can also be seen among the theoretical values in Table 7.1.

For titanium, copper or glass, the ice adhesion values from literature are higher but also inconsistent. For titanium, 1103 kPa [213], $(254 \pm 36)$ kPa [214] or 436 kPa [201] were measured. Ice adhesion values of 422 kPa [201], 625 kPa [215] and 107 kPa [216] are reported for copper. An ice adhesion of about 560 kPa at -18 °C and 370 kPa at -10 °C was reported for glass [217].

The variation in ice adhesion values can be explained by different surface roughnesses, different measurement setups or fracture modes and different initial crack sizes at the surface-ice interface or within the ice because of local stresses.

On the examined metal and glass surfaces, parts of the ice cylinders after cohesive fracture remained on all the surfaces, see Figure 7.23 and Figure 7.24.

The measured low forces can be caused by several possible reasons outlined below. It has been reported that the solidification of ice on these metal surfaces causes high tensile stresses at the interface which can lead to brittle, cohesive failures [218].

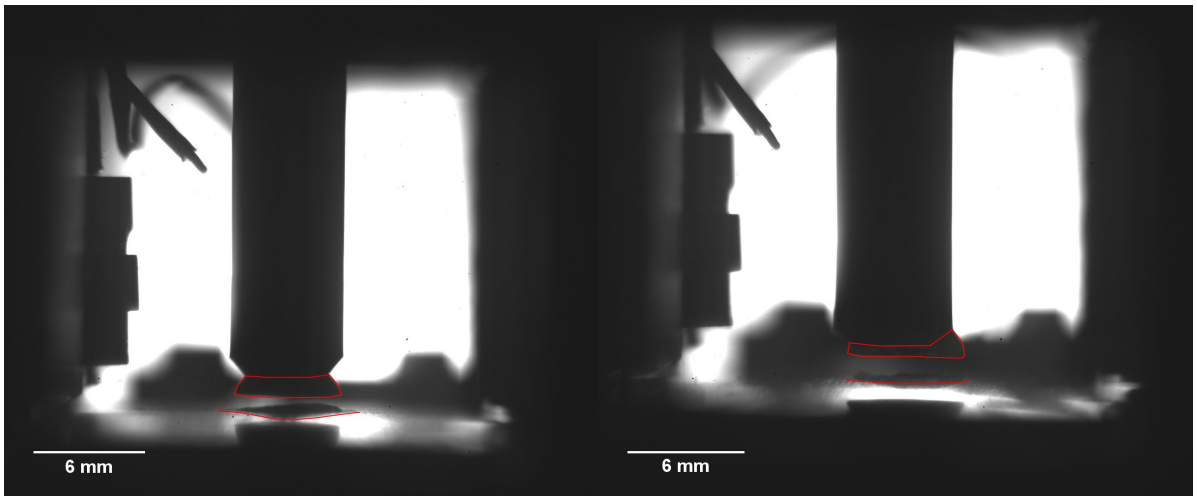


Figure 7.23.: Images of an ice fracture on the aluminum (left) and the titanium (right) surface.

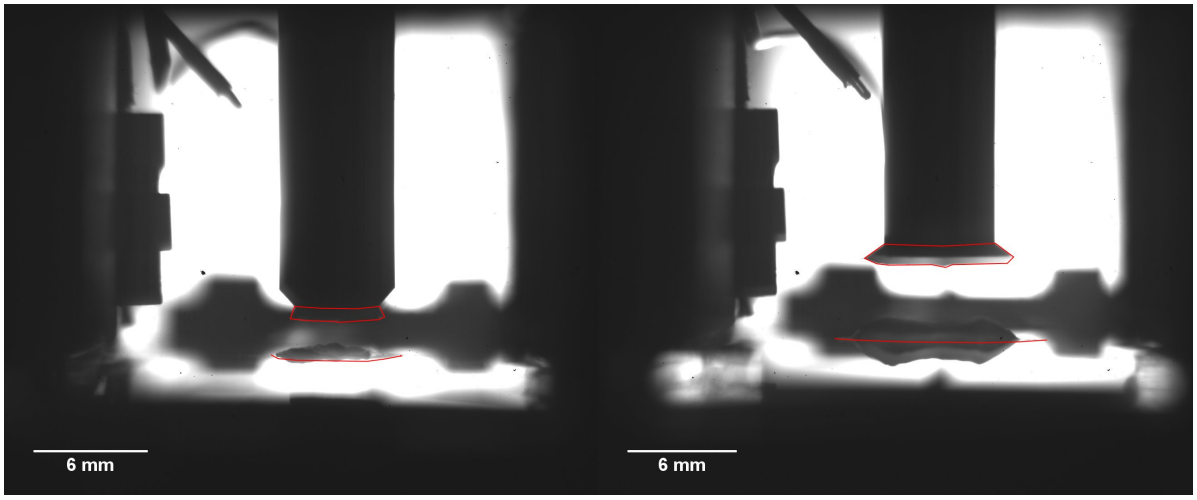


Figure 7.24.: Images of an ice fracture of the copper (left) and the glass (right) surface.

The degree of atomic lattice mismatch at the interface influences the ice adhesion. The ice adhesion is caused by the surface forces between the adsorbed hydroxyl groups of the ice and the surface atoms. These surface forces are determined by the lattice matching of the ice and the solid material. The distance between two oxygen atoms in ice is 2.78 Å in polycrystalline ice. The lattice constants are 2.95 Å for titanium and 2.87 Å for iron, leading to a good match with the oxygen atoms of the ice, high adhesion and low tensile stresses at the interface. For copper and aluminum the lattice constants are 3.61 Å and 4.05 Å, respectively. This creates higher tensile stresses at the interface, lower adhesion

and promotes larger microcracks and therefore brittle failures [201].

Another important property is the thermal expansion of ice and the solid material. Metals have a higher coefficient of thermal expansion than ice. If water is frozen on a metal surface, the metal will shrink more and create a tensile force at the ice interface leading to high adhesion [201].

Whether a brittle or ductile failure occurs is determined by the ice-to-surface adhesion and the tensile stresses at the ice-to-surface interface. If the failure occurs at the interface, it is ductile and dependent on temperature, with adhesion strength increasing with decreasing temperature [218]. In case of high local stresses, the failure is brittle and occurs within the ice as a cohesive fracture. The force for fracture then depends on the size of initial microcracks within the ice or at the interface, caused by the local stresses. Large initial cracks (e.g. 100 µm) lead to a low force for failure, whereas small initial cracks (e.g. 1 µm) cause a higher force for failure [162].

Therefore, a possible reason for these measured low values are large micrometer-sized cracks in the ice cylinder or at the interface. These large microcracks could have led to the brittle, partly cohesive fractures and the low measured forces on the materials aluminum, titanium and glass.

The images of the further measurements on these surfaces look similar, the fractures were always cohesive in parts, not fully adhesive (see appendix A). Therefore, the measured values derived by partly cohesive fractures are not representative of the true ice adhesion on these metal oxide surfaces. However, it can be concluded that these metal oxide surfaces have a high ice adhesion because of their high surface free energy.

### Discussion of the ice adhesion on the polymeric surfaces and commercial anti-ice coatings

Owing to their lower surface free energy, the ice adhesion on the polymeric and commercial anti-ice surfaces were expected to be lower than on the metal oxide surfaces.

However, the forces on the polymer surfaces were higher than those on the metal oxide surfaces, all of them measured in the ice test chamber. The ice adhesion value of $(447 \pm 77)$ kPa on uncoated PU (CMC 63630) is in the region of the theoretical values

$\sigma_{ice,PU}$ for an adhesive fracture and a microcrack length between 100 µm (325 kPa) and 10 µm (1026 kPa). The here measured forces on the other polymeric surfaces were even higher, except for the epoxy-resin surface (model for a CFRP coating) with a value of $(298 \pm 72)$ kPa and the nanostructured GH60-5 surface, for which a value of only $(230 \pm 39)$ kPa was measured.

Polymers have a lower coefficient of thermal expansion compared to ice. In this case, a compressive force and low adhesion is the result [201]. No high tensile stresses are created at the interface between ice and these soft materials, leading to smaller initial cracks and a ductile failure type. In case of a fully adhesive fracture, the force of failure is representative of the ice adhesion force at the interface [218].

For an epoxy-polyamide primer coating, an ice adhesion of $(340 \pm 94)$ kPa at -10 °C, $(570 \pm 107)$ kPa at -15 °C and $(590 \pm 128)$ kPa at -20 °C is reported [219]. This is nearly twice as much as the measured value at -20 °C during this thesis. Ice adhesion values of $(290 \pm 140)$ kPa at -10 °C, $(370 \pm 60)$ kPa at -15 °C and $(470 \pm 90)$ kPa at -20 °C were measured on a PU top coating [219], which is comparable to the here measured value.

For clarification the observed fractures have to be regarded which are shown in Figure 7.25.

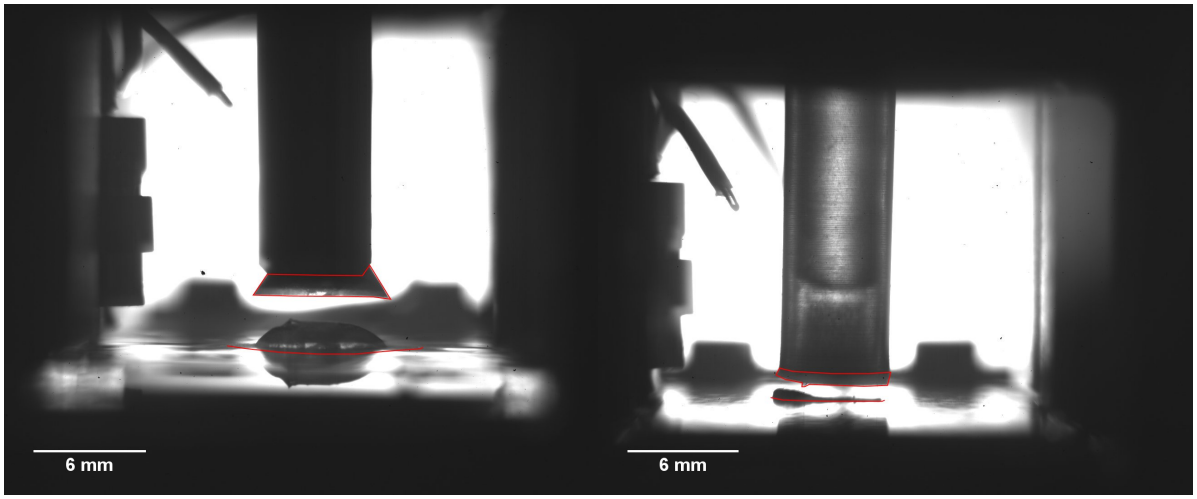


Figure 7.25.: Images of an ice fracture on the epoxy coating (CFRP surface model, left) and the PUR Topcoat coating (right).

The measurements on the epoxy coating and the PUR Topcoat surface led to partly

cohesive fractures which could have been caused by differently sized initial microcracks. Therefore, the measured values do not resemble the true ice adhesion on these surfaces.

A very low ice adhesion value of $(42.5 \pm 15)$ kPa for a NuSil R2180 coating is reported [199]. The corresponding ice fractures are shown in Figure 7.26.

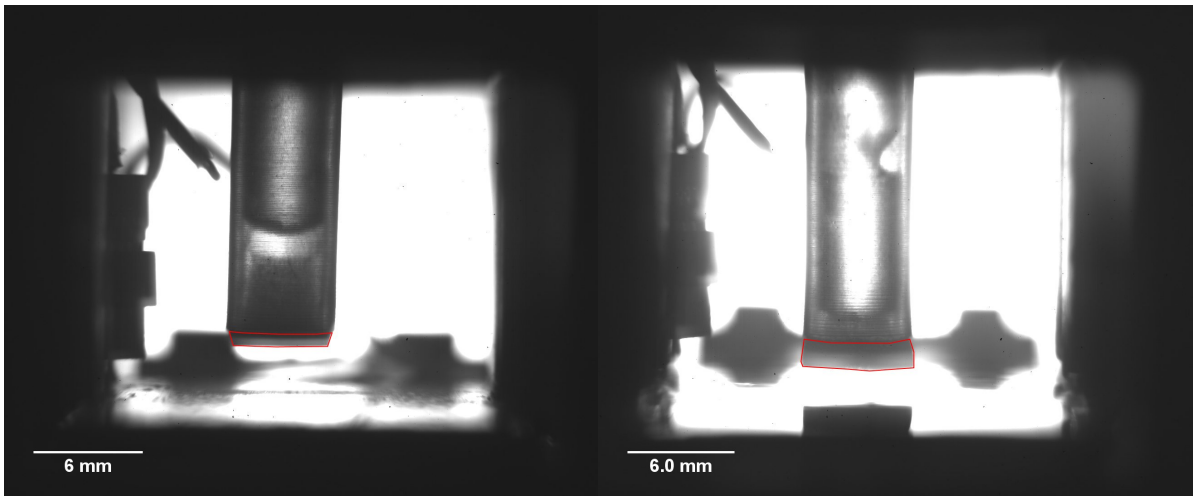


Figure 7.26.: Images of an ice fracture on the NuSil R2180 silicone coating (left) and the nanostructured GH60-5 PU coating (right).

Fully adhesive fractures were measured on the NuSil silicone coating ($(760 \pm 66)$ kPa) and the nanostructured GH60-5 coating ($(230 \pm 39)$ kPa). These values represent the true ice adhesion on these surfaces.

The hypothesis of lowest ice adhesion on these superhydrophobic PU surfaces with microstructure diameters of 35 µm and lowest wettability is falsified. Overall, it has to be concluded that all the superhydrophobic PU surfaces showed a very high vertical pull-off force. As the water cylinder sitting on the surface was cooled down, the water changed from the Cassie-Baxter to the Wenzel state and led to these high ice adhesion values. No ice adhesion values in numbers can be given for the hydrophilic metal-oxide surfaces because only cohesive fractures occured. The ice adhesion is high on these metal-oxide surfaces because of their high surface free energy leading to cohesive fractures. The ice adhesion on the hydrophobic polymer surfaces and flat, plasma coated PU surfaces was low. Here, the $C_3F_6$ plasma coated PU surface had the lowest ice adhesion with $(287 \pm 8)$ kPa. The overall lowest ice adhesion was measured on the nanostructured GH60-5 coating ($(230 \pm 39)$ kPa).

## 7.2.3. Correlation of ice adhesion with surface wetting behavior

### Dependence of ice adhesion on wetting behavior for microstructured surfaces

The hypothesis was that the ice adhesion is lowest on the superhydrophobic surfaces with microstructure diameters of 35 µm and above and correlates with the water wetting behavior. In Figure 7.27 the correlation between the measured ice adhesion values and the wetting term $1 + \cos\theta_{\mathrm{Rec}}$ is shown for all the different types of the characterized surfaces. These include the hexagonally arranged, cylindrical microstructures showing lowest wettability (C1, C6 and C9), the quadratically arranged microstructure C16 and the flat PU and technical material surfaces. The cohesive failure measurements were not included (masked = ignored by the fitting method) for the linear fits and are marked with orange color. The correlations with the other wetting terms are shown in the appendix (A.6).

For the surface wetting terms $1 + \cos\theta$, $1 + \cos\theta_{Rec}$, and $\cos\theta_{Rec} - \cos\theta_{Adv}$, the ice adhesion values should increase with the increasing terms according to the examples from literature presented in the chapter on theoretical basics 3.2.3. This is only the case for the flat, plasma coated PU surfaces and in parts for the flat technical material surfaces. For the surface free energy, the ice adhesion is expected to decrease with decreasing surface free energy. Again, this applies only for the flat, plasma coated PU surfaces and partly for the flat engineering material surfaces. The ice adhesion on all of the microstructured samples does not correlate with the wetting terms or the surface free energy because the ice adhesion increases with the decreasing wetting terms or the decreasing surface free energy.

Therefore, it has to be concluded that the ice adhesion is not directly correlated to the water wetting behavior or the surface free energy on these micro- and nanostructured surfaces. This shows that ice adhesion is not dependent only on the wetting behavior and these correlations cannot be applied for micro- and nanostructured coatings which was also stated by Susoff *et al.* [157].

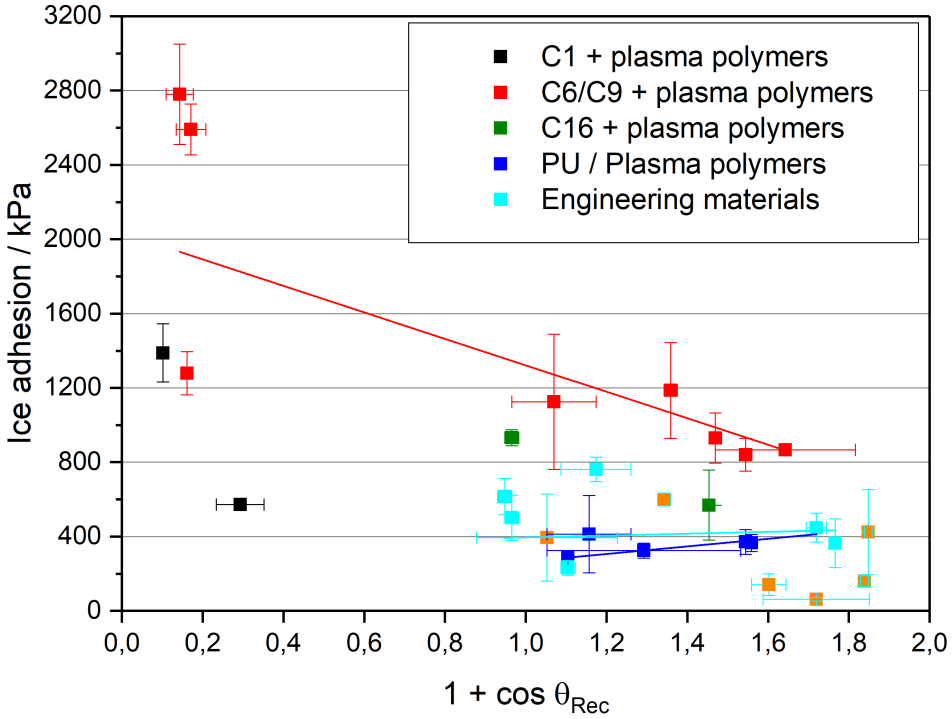


Figure 7.27.: Ice adhesion values of all flat and microstructured surfaces correlated with the practical work of adhesion term. The cohesive failure measurements were masked (ignored by the fitting method) and are marked with orange color. The expected correlation of increasing ice adhesion with increasing practical work of adhesion cannot be seen for the microstructured surfaces.

### Dependence of ice adhesion on wetting behavior for flat surfaces

Because of the correlations of ice adhesion with surface wetting terms described before, it was assumed that the ice adhesion can only be correlated to the wetting behavior or surface free energy on flat surfaces. In Figure 7.28 to Figure 7.31 the correlation between the measured ice adhesion values and different surface wetting terms or surface free energy is shown for the examined engineering material surfaces and the PU surfaces, in comparison with measurement data from Meuler *et al.* [169]. Except for the term $\cos\theta_{\mathrm{Rec}} - \cos\theta_{\mathrm{Adv}}$, the linear fit was forced to intersect at $y = 0$ according to literature [169]. The cohesive failures were masked for the linear fits and are marked with orange color.

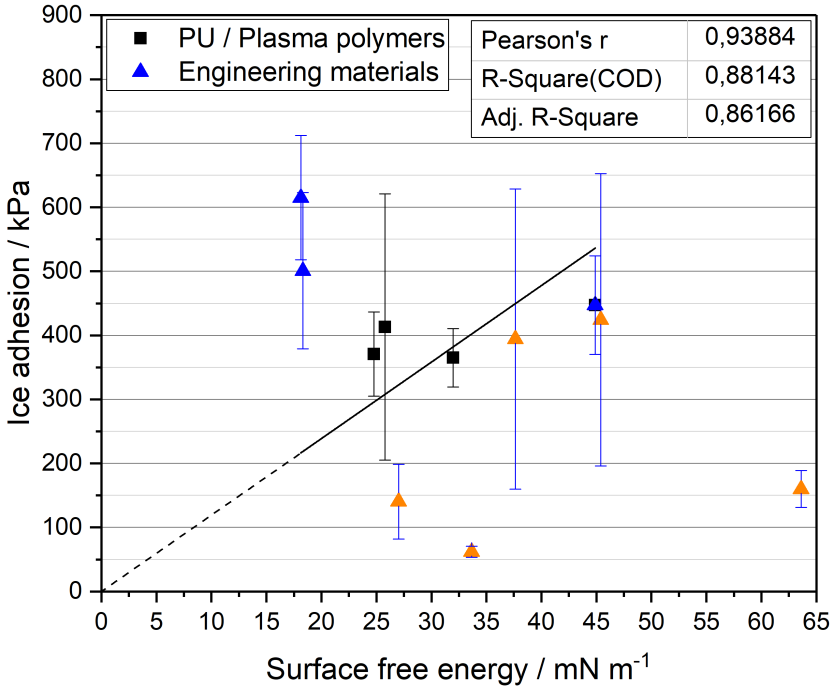


Figure 7.28.: Ice adhesion values of the flat, plasma-coated PU surfaces, of the technical material surfaces and of Meuler *et al.* drawn over the surface free energy. The solid line is the linear best fit. The cohesive failure measurements were masked (ignored by the fitting method) and are marked with orange color.

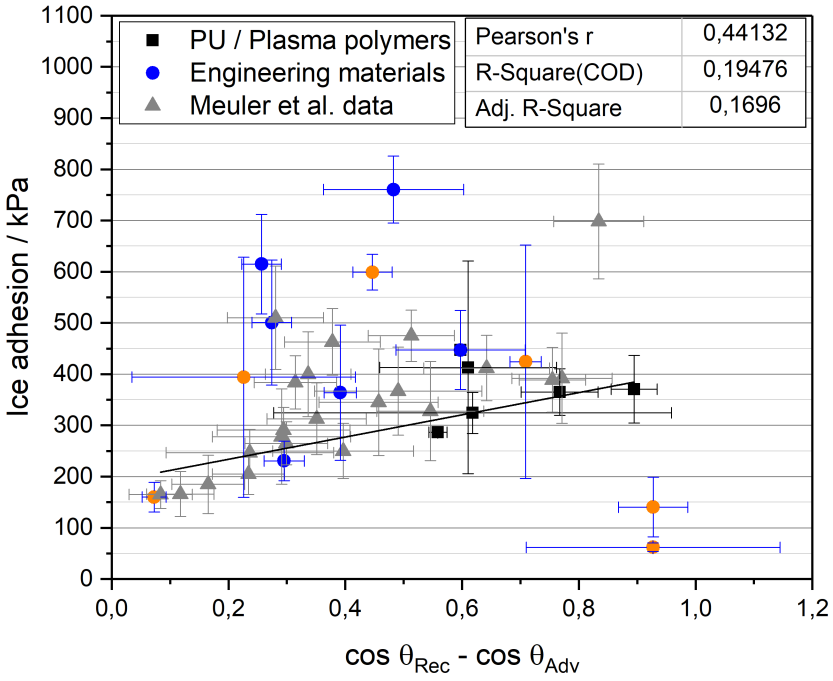


Figure 7.29.: Ice adhesion values of the flat, plasma-coated PU surfaces, of the technical material surfaces and of Meuler *et al.* drawn over the drop roll-off term. The solid line is the linear best fit. The cohesive failure measurements were masked (ignored by the fitting method) and are marked with orange color.

The coefficients of determination (COD) for the surface free energy ($R^2 = 0.8814$) and the term $\cos\theta_{Rec} - \cos\theta_{Adv}$ ($R^2 = 0.1948$) are lower, so the correlation is not as good but the linear fit still shows the correct trend.

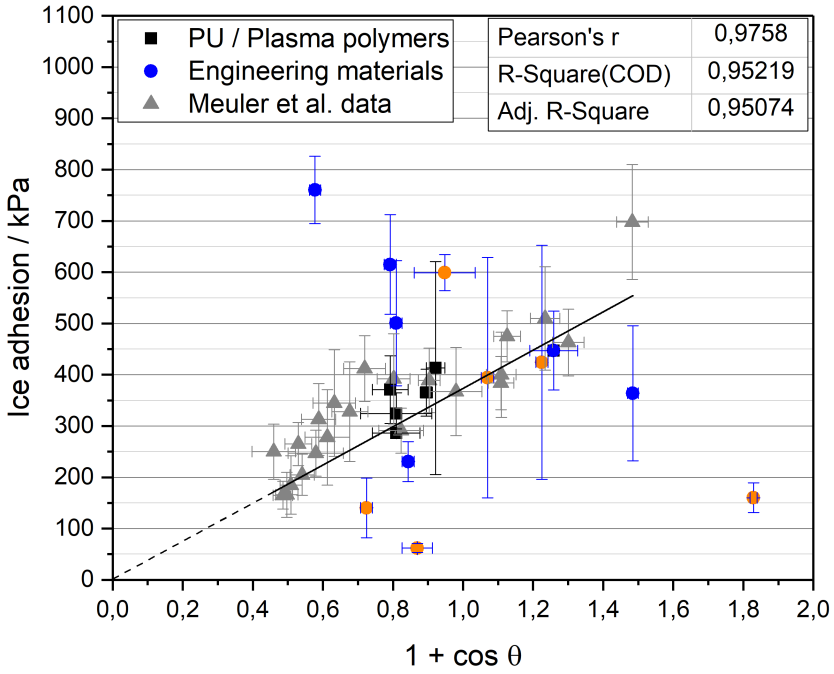


Figure 7.30.: Ice adhesion values of the flat, plasma-coated PU surfaces, of the technical material surfaces and of Meuler *et al.* drawn over the equilibrium work of adhesion term. The solid line is the linear best fit and the dashed line represents the extrapolation through the origin. The cohesive failure measurements were masked (ignored by the fitting method) and are marked with orange color.

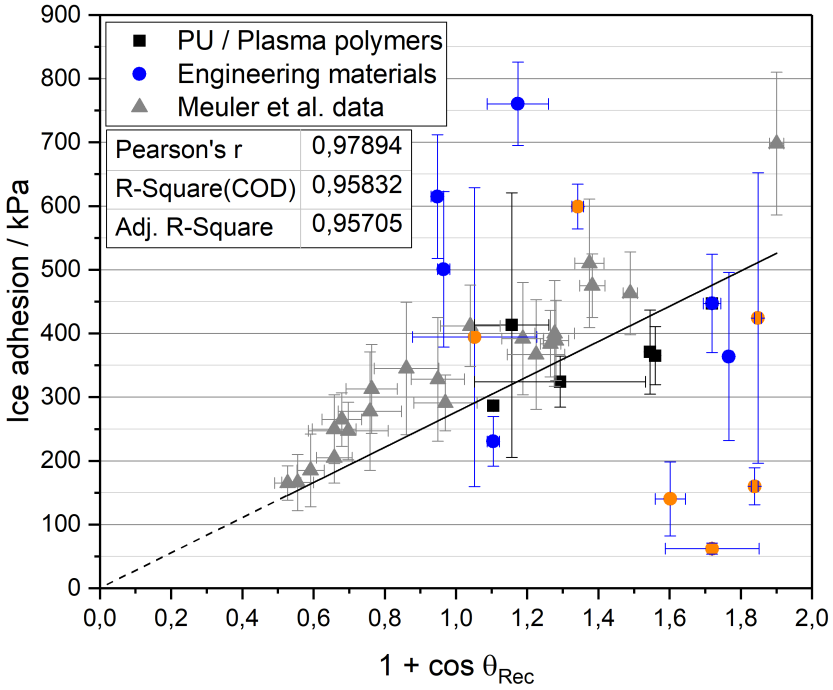


Figure 7.31.: Ice adhesion values of the flat, plasma-coated PU surfaces, of the technical material surfaces and of Meuler *et al.* drawn over the practical work of adhesion term. The solid line is the linear best fit and the dashed line represents the extrapolation through the origin. The cohesive failure measurements were masked (ignored by the fitting method) and are marked with orange color.

For the flat surfaces, the correlation is very good for the factors $1+\cos\theta$ ($R^2 = 0.9522$) and $1+\cos\theta_{Rec}$ ($R^2 = 0.9583$).

The ice adhesion values by Meuler *et al.* were derived by shearing-off of ice (mode II fractures) from different polymeric surfaces at -10 °C. In contrast, the ice was pulled off vertically (mode I fractures) at -20 °C from the plasma coated PU surfaces and the engineering material surfaces which consist of both metal-oxide and polymeric surfaces.

The correlation of ice adhesion and surface wetting behavior or surface free energy cannot be seen for all the technical material surfaces which included some cohesive fractures, especially on the metal-oxide surfaces. However, the ice adhesion correlates with the surface wetting behavior or the surface free energy of the polymeric surfaces from Meuler *et al.* and of the plasma coated PU surfaces. The ice adhesion does not correlate with

the wetting behavior of micro- and nanostructured surfaces. On these surfaces, the dependence on the surface topography has to be regarded as well.

### 7.2.4. Correlation of ice adhesion with surface topography

#### Dependence of ice adhesion on micrometer surface roughness

Chen *et al.* have published that the ice fracture strength increases with increasing density of microstructures or pores [158]. This shall be checked for the ice adhesion measurements on the different types of microstructured and plasma coated PU surfaces listed above.

Figure 7.32 shows the ice adhesion on the microstructured surfaces depicted over the surface roughness parameter $rf = A_{\mathrm{sl}}/A_{\mathrm{f}}$. The dashed line was drawn as a guide to the eye in order to show the increasing ice adhesion with increasing roughness factor for the $C_3F_6$ (50 W) and HMDSO (60 W) plasma coatings and as upper limit of the measured ice adhesion values.

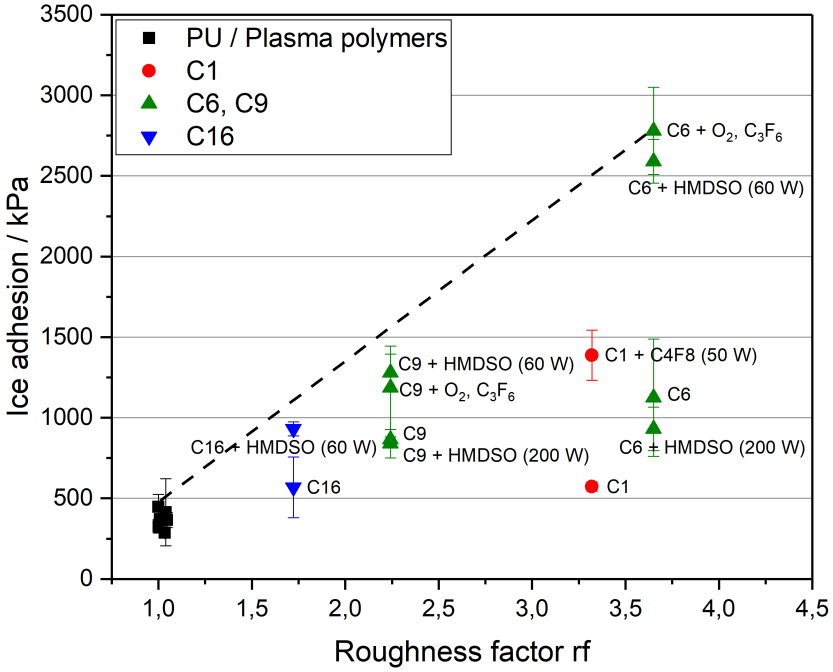


Figure 7.32.: Ice adhesion on microstructured and plasma coated samples in dependence of the surface roughness factor $rf = A_{\mathrm{sl}}/A_{\mathrm{f}}$. The drawn dashed line represents an upper limit of ice adhesion.

The ice adhesion increases with an increasing roughness factor, because the water freezes in Wenzel state leading to higher fracture values on surfaces with higher density of microstructures. This is caused by the larger contact area and the mechanical interlocking of the ice between the micro- and nanostructures. The increase in ice adhesion is clearly visible for the $C_3F_6$ and HMDSO 60 W plasma coated surfaces. The influence of microstructure roughness is not as strong for the uncoated and HMDSO 200 W plasma coated surfaces, but still visible. A possible reason for this is the different nanoroughness of the HMDSO 200 W coating ($S_a = 115$ nm) compared to the other plasma coatings ($S_a \approx 3$ nm to 22 nm).

This overview shows that the ice adhesion values on the flat PU surfaces cannot be lowered further by the superhydrophobic surfaces with the smallest diameters of 35 µm and these plasma coatings. On the microstructured surfaces, the ice adhesion is determined by the surface nanoroughness and surface chemistry.

### Dependence of ice adhesion on nanometer surface roughness

Although the $C_3F_6$ and HMDSO 60 W plasma coatings created superhydrophobic surfaces, the ice adhesion on these surfaces was significantly higher than on uncoated and HMDSO 200 W plasma coated surfaces. It is postulated that the different nanoroughness of the plasma coatings with otherwise similarly hydrophobic surface chemistry mainly determines the ice adhesion on microstructured surfaces. Therefore, the ice adhesion is drawn over the surface nanoroughness for flat surfaces. Figure 7.33 shows the ice adhesion on the flat, plasma coated PU surfaces in dependence of the nanoscale surface roughness average $S_a$ determined by AFM measurements. The ice adhesion in dependence of the AFM roughness parameters $S_q$ and $S_{dr}$ are shown in the appendix (see section A.6).

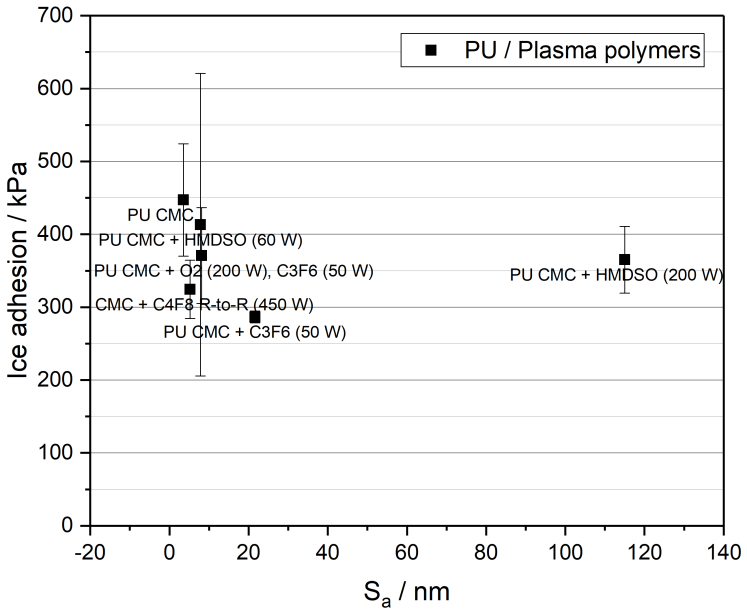


Figure 7.33.: Ice adhesion on flat plasma-coated PU surfaces in dependence of nanoscale roughness average $S_a$ determined by AFM measurements. The ice adhesion does not correlate with the nanoroughness on the flat, plasma-coated PU surfaces.

The nanometer surface roughness average is very similar for all the flat, coated PU surfaces, except for the HMDSO 200 W coating, which shows a significantly higher $S_a$

value compared to the other surfaces. The AFM images showed lesser, but bigger and rounder convex nanostructures on this plasma coating as opposed to many little spikes of the other plasma coatings (see AFM images of the plasma coatings in the appendix A.3).

No correlation between the ice adhesion and the AFM surface roughness parameters $S_a$, $S_q$ and $S_{dr}$ can be seen. On all the flat PU surfaces in Figure 7.33, the ice adhesion is around 300 kPa to 400 kPa, independent of the nanoroughness.

A reason may be that the nanostructures are arranged pointing vertically upwards on the flat surfaces and therefore do not cause mechanical interlocking. As they only marginally increase the water-surface contact area, the ice adhesion on the flat surfaces is mainly determined by the surface chemistry. On the microstructured surfaces, the nanostructures on the side walls of the microstructures may lead to mechanical interlocking of the ice and higher failure strengths. This could explain the lower ice adhesion values on the microstructured, HMDSO 200 W plasma-coated surfaces with larger, rounder nanostructures compared to the microstructured samples with spiky nanostructures of the other plasma coatings.

The hypothesis was that the ice adhesion correlates with the wetting behavior and is lowest on the superhydrophobic PU surfaces with microstructure diameters of 35 µm and above. The ice adhesion does in fact correlate with the wetting behavior for the flat, plasma-coated PU surfaces, but it does not correlate for these microstructured, plasma-coated PU surfaces. In case that not all water rebounds or runs off the superhydrophobic PU surfaces and the remaining water freezes, it has to be concluded that the ice adheres strongly to these superhydrophobic surfaces with base diameters of 35 µm or more. The release by external forces without the use of energy is not possible yet. Therefore, the microstructure dimensions have to be further reduced in order to guarantee a stabilization of the drops in Cassie-Baxter state and a low ice adhesion.

## 7.3. Water drop nucleation and crystallization - anti-icing behavior

If not all the water rebounds or runs off the superhydrophobic PU surfaces instantly, the remaining water will eventually freeze. Therefore, the freezing of the water drops should be delayed or prevented. If this were achieved by the surface because of thermodynamic reasons, the remaining water would be given more time to eventually run off the surface which would remain free of ice.

The ice adhesion is mainly determined by the surface micrometer roughness. The freezing of water drops consists of the processes of nucleation and of crystallization. These processes are determined by the surface chemistry and especially the surface nanometer roughness. If the surface nanoroughness is created correctly, the energetical possibility of water molecules building clusters and finally an ice nucleus on the surface leading to crystallization of the water drop can be reduced. The related hypothesis is that the icing can be reduced or delayed by these superhydrophobic PU surfaces with micrometer diameters of 35 µm and above. Therefore, the nucleation temperatures must be reduced (or the nucleation must be delayed) by the correct nanostructures, and the crystallization times must be extended by the Cassie-Baxter wetting state.

The icing behavior of the surfaces was characterized by measuring the nucleation delay times, the crystallization times and the total freezing times as well as the nucleation temperatures of the different surfaces (see the chapter on experimental methods 5.4).

The water drop freezing experiment was carried out statically and dynamically. For the static freezing experiment in the cooling chamber of the contact angle device, the water drops were placed on the surface constantly held at a subzero temperature (-20 °C set at the temperature control unit) until they were fully frozen. In this way the nucleation delay or freezing delay times, the crystallization times and the total freezing times were measured. For the dynamic freezing experiment in the new icing test chamber, the water drops were first applied at 0 °C and then cooled down in a quasi-steady manner (quasi thermodynamic equilibrium) with their surroundings at a constant rate of 1 K/min (0.0167 K/s) until nucleation in order to determine the surface specific nucleation temperature.

### 7.3.1. Static icing experiment measurement results

#### Theoretical nucleation delay times $\langle\tau(T)\rangle$

The theoretical nucleation delay time at a constant temperature $\langle\tau(T)\rangle = 1/J(T)$ of a water drop on the sample surfaces of the static icing experiment was calculated according to equation 3.51 in the chapter on theoretical basics of icing (3.2.4). It is an expectation value derived from probability calculation and will be compared with the measured mean freezing delay times. The samples used consisted of uncoated or HMDSO (60 W) plasma coated, flat PU and uncoated or HMDSO (60 W) plasma coated (normal and etched version) microstructure C6 because this showed the best superhydrophobicity of all microstructures. The Wenzel wetting state was assumed on uncoated microstructure C6 ($rf = 3.65$, $f_{\mathrm{SL}} = 1$) and the Cassie-Baxter state was assumed on the HMDSO (60 W) plasma coated microstructure C6 ($rf = 3.65$, $f_{\mathrm{SL}} = 0.1$).

$T_0$ for linearization of the nucleation rate $J(T_0+\Delta T)$ (equation 3.46) was set to 257.15 K which was approximately the measured median nucleation temperature of plain PU. The same ice-water contact angle $\theta_{\mathrm{IW}}$ was assumed on PU and on the HMDSO (60 W) coating, based on the chemically similar perfluorodecyltrichlorosilane (FDTS) monolayer with temperature dependent flexibility of Eberle *et al.*. It was calculated in dependence of temperature with a constant slope $\theta_{\mathrm{IW}}(T) = (100 - 2.5 \cdot (T - 249.15))$ (in degrees) based on the fit of Eberle *et al.* [168]. The temperature dependent thermodynamic values at $T_0 = 257.15\,\mathrm{K}$ were $\theta_{\mathrm{IW}} = 80°$, $r_{\mathrm{c}} = 2.94\,\mathrm{nm}$, $\Delta H_{\mathrm{f,V}} = 299.72 \times 10^6\,\mathrm{J/m^3}$ and $\gamma_{\mathrm{IW}} = 25.8\,\mathrm{mN/m}$.

$J(T)$ was calculated at the different temperatures with the relation $J(T_{\mathrm{S}} + \Delta T_{\mathrm{S}})$ (equation 3.47, $T_{\mathrm{S}} = 273.15\,\mathrm{K}$). For temperatures of -10 °C, -15 °C and -20 °C, 15 µl water drops and the relevant wetting and surface parameters, the values of the expected nucleation delay time $\langle\tau(T_{\mathrm{S}} + \Delta T_{\mathrm{S}})\rangle$ are listed in Table 7.2.

For plain PU, the calculated nucleation delay is shorter on microstructure C6 than on the flat surface because of an increased wetting area in the assumed Wenzel wetting state. For the HMDSO (60 W) coating, the calculated nucleation delay is longer on microstructure C6 than on the flat surface because of a decreased wetting area in the assumed Cassie-Baxter wetting state. No longer nucleation delay time is calculated

Table 7.2.: Theoretical (expected) nucleation delay times $\langle\tau(T_S + \Delta T_S)\rangle$ of a 15 µl water drop on uncoated or HMDSO (60 W) plasma-coated, flat PU and microstructure C6 at -10 °C, -15 °C and -20 °C.

| - | - | - | - | T = -10 °C | T = -15 °C | T = -20 °C |
|---|---|---|---|---|---|---|
| Sample | $rf$ | $f_{sl}$ | $R$ | $\theta_{IW}$ / $\langle\tau(T)\rangle$ | $\theta_{IW}$ / $\langle\tau(T)\rangle$ | $\theta_{IW}$ / $\langle\tau(T)\rangle$ |
| - | - | - | (nm) | (°) / (s) | (°) / (s) | (°) / (s) |
| PU | 1 | 1 | 40984 | 65 / $1.67\times10^{51}$ | 77.5 / $6.63\times10^{25}$ | 90 / 2.63 |
| PU + HMDSO (60 W) | 1 | 1 | 12821 | 65 / $1.61\times10^{51}$ | 77.5 / $6.47\times10^{25}$ | 90 / 2.60 |
| C6 | 3.65 | 1 | 40984 | 65 / $0.46\times10^{51}$ | 77.5 / $1.82\times10^{25}$ | 90 / 0.72 |
| C6 + HMDSO (60 W) | 3.65 | 0.1 | 12821 | 65 / $4.41\times10^{51}$ | 77.5 / $17.73\times10^{25}$ | 90 / 7.13 |

for the HMDSO plasma coating than for the plain PU, because the same temperature dependent $\theta_{IW}$ was used for both surfaces. It is not dependent on $R$, because the $R$ values are far above $10r_c = 29.4$ nm.

The calculated nucleation rates $J(T)$ and $J(T_S + \Delta T_S)$ and corresponding expected nucleation delay times $\langle\tau\rangle = 1/J(T)$ and $\langle\tau_{TS}\rangle = 1/J(T_S + \Delta T_S)$ of a 15 µl water drop are shown in Figure 7.34.

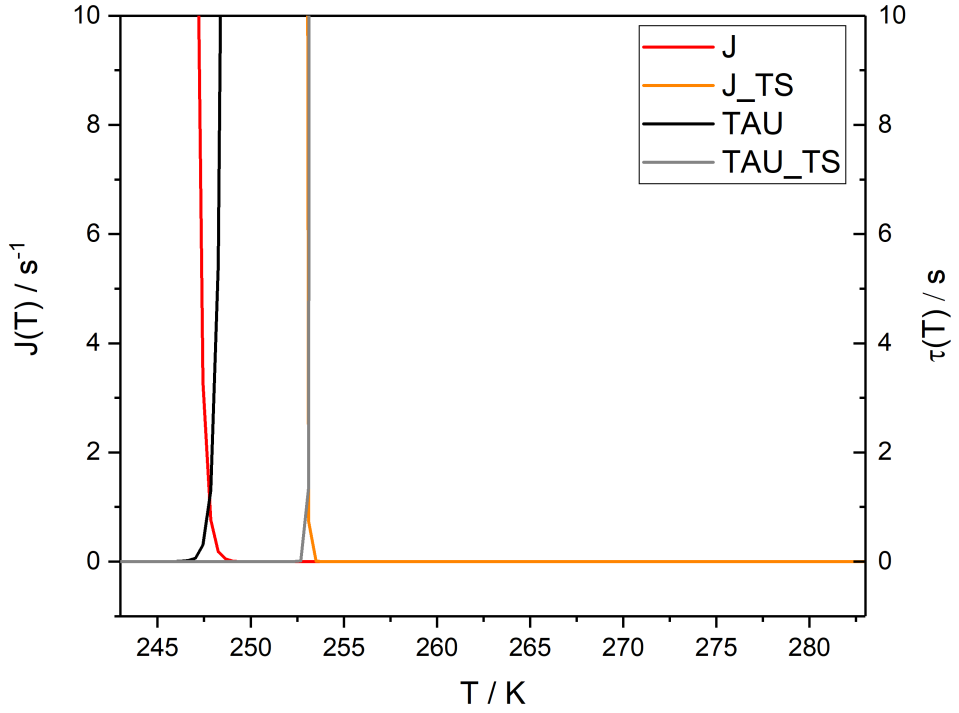


Figure 7.34.: Theoretical nucleation delay times $\langle\tau\rangle = 1/J(T)$ and $\langle\tau_{\mathrm{TS}}\rangle = 1/J(T_{\mathrm{S}} + \Delta T_{\mathrm{S}})$ of a 15 µl water drop on uncoated PU, derived from the normal nucleation rate $J(T)$ and approximated nucleation rate $J(T_{\mathrm{S}} + \Delta T_{\mathrm{S}})$, in dependence of the temperature. $T_0 = 257.15\,\mathrm{K}$ and $T_{\mathrm{S}} = 273.15\,\mathrm{K}$ were used for the Taylor approximation of the nucleation rate. The reason for the different nucleation rates and times is the calculation of the approximated nucleation rate with the thermodynamic values at $T_0$, whereas the normal nucleation rate was calculated with temperature dependent thermodynamic values.

### Theoretical crystallization times $t_{\mathrm{C}}(T)$

The crystallization times were calculated for different nucleation temperatures $T_{\mathrm{N}}$, the roughness factors $rf$ of the examined, flat PU and C6 microstructured samples and the contact area of a 15 µl half-sphere of $1.1673 \times 10^{-5}\,\mathrm{m}^2$ (radius $= 1.928 \times 10^{-3}\,\mathrm{m}$), according to equation 3.55 in the chapter on theoretical basics of icing (3.2.4). Heat radiation, heat convection by the air and heat conduction through the air were neglected. Only the heat transfer at the solid-liquid interface was considered. The heat transfer coefficient at the solid-water/ice interface depends on the surface topography and wetting state. For this estimation, the heat transfer coefficient at the water-PU interface of

$\alpha_{H_2O} = 500\,W/(m^2{\cdot}K)$ was used [220]. The crystallization times were calculated for a flat PU surface and for the C6 microstructured surfaces with the water drop in Wenzel ($f_{sl} = 1$), mixed ($f_{sl} = 0.5$) and Cassie-Baxter ($f_{sl} = 0.1$) wetting states. The calculated crystallization times of a 15 µl water drop at -10 °C, -15 °C and -20 °C are listed in Table 7.3.

Table 7.3.: Theoretical crystallization times of a 15 µl water drop at -10 °C, -15 °C and -20 °C for flat PU and uncoated or plasma-coated microstructure C6.

| Sample | Wetting state | Roughness factor | solid-liquid fraction | solid-liquid interface | T = -10 °C | T = -15 °C | T = -20 °C |
|---|---|---|---|---|---|---|---|
| - | - | $rf$ | $f_{sl}$ | $A_{sl}$ | $t_C$ | $t_C$ | $t_C$ |
| - | - | - | - | ($m^2$) | (s) | (s) | (s) |
| PU | flat | 1 | 1 | $1.17 \times 10^{-5}$ | 75 | 46 | 32 |
| C6 | Wenzel | 3.65 | 1 | $4.26 \times 10^{-5}$ | 20 | 13 | 9 |
| C6 + HMDSO (60 W) | Mixed | 3.65 | 0.5 | $2.13 \times 10^{-5}$ | 41 | 25 | 18 |
| C6 + HMDSO (60 W) | Cassie-Baxter | 3.65 | 0.1 | $0.43 \times 10^{-5}$ | 205 | 127 | 88 |

The calculated crystallization times of a 15 µl water drop in different wetting states are shown in Figure 7.35.

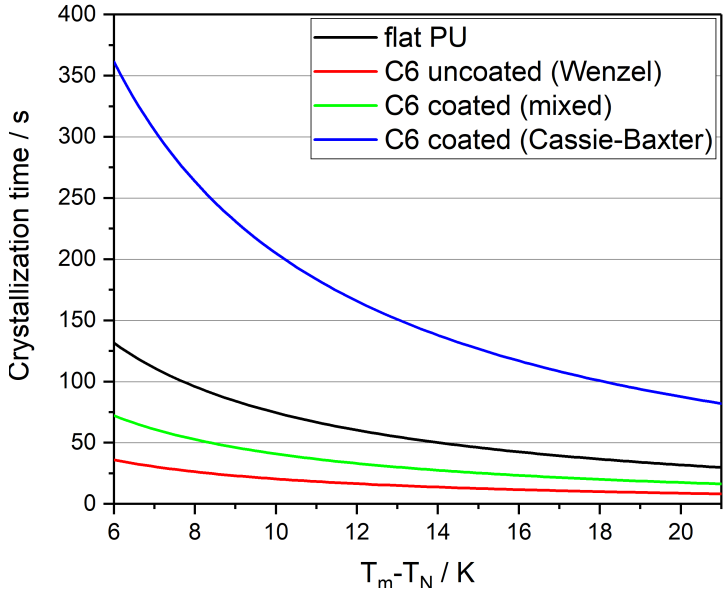


Figure 7.35.: Theoretical crystallization times of a 15 µl water drop on flat PU and uncoated or plasma-coated microstructure C6 in dependence of the supercooling $T_m - T_N$. The Wenzel state ($f_{sl} = 1$) was assumed on uncoated C6 and a mixed ($f_{sl} = 0.5$) or Cassie-Baxter state ($f_{sl} = 0.1$) was assumed on HMDSO (60 W) plasma coated C6.

### Temperature curves of the static freezing experiment

It was expected that the surface nanoroughness and chemistry of the plasma coatings leads to a significant supercooling and a larger nucleation delay compared to uncoated PU surfaces. The nucleation delay depends on the difference between the temperature of the surface and the specific nucleation temperature ($\Delta T = T - T_N$). This nucleation delay and the crystallization time should be enhanced further by the reduced water-surface contact area in the Cassie-Baxter state on the superhydrophobic surfaces.

The typical temperature curves of a freezing water drop on a surface with constant temperature $T_{start}$ (= start temperature, sample surface temperature measured by the IR camera at the start of the experiment) are shown in Figure 7.36.

Two types of temperature curves of a freezing water drop can be seen, one for instant freezing without supercooling (gray), and the other one for supercooling and subsequent freezing at the elevated crystallization or equilibrium melting temperature $T_m$ (green). The equilibrium melting temperature of water is 0 °C. The measured crystallization

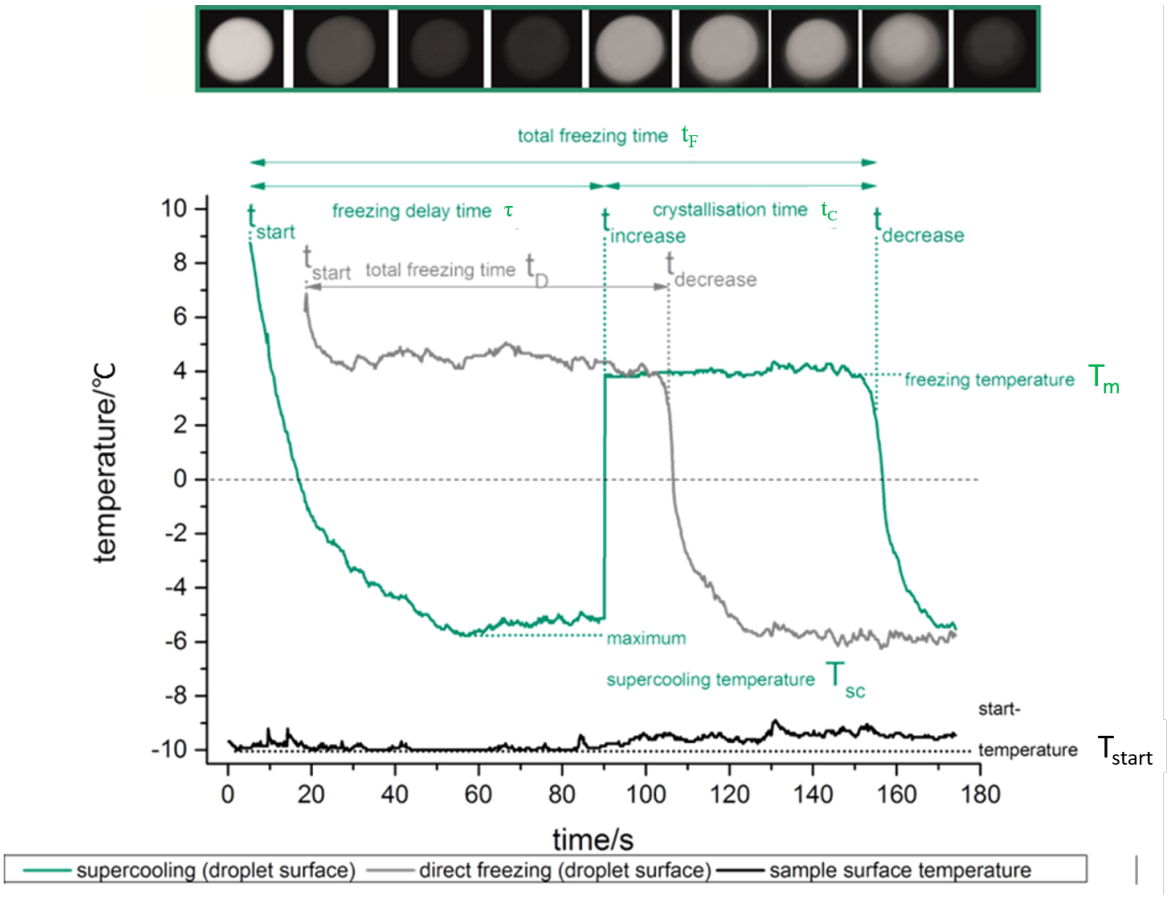


Figure 7.36.: Exemplary temperature curves drawn over time of static water drop freezing experiments on a surface constantly set to -20 °C. The IR camera measurement range was set from -10 °C to +10 °C. Temperature curves of a freezing water drop without supercooling (gray) and with supercooling (green, with corresponding IR-images at the top). The start temperature $T_{start}$ (black) is the sample surface temperature at the start of the experiment, increasing over time because of the warmer surrounding atmosphere. The temperature curves have an offset of about +4 °C because of the manually set IR camera parameters. Adapted from [2].

temperature deviated by about 4 °C because the IR camera measured the top surface of the water drop. The water surface reflects IR radiation of the surroundings. This measurement error is caused by the manually set measurement parameters of the IR camera, especially the "reflected temperature" and the "atmospheric temperature".

From these curves, the freezing delay times, crystallization times and total freezing times

were derived [2]. The time from the start of the experiment to the nucleation of the drop is the freezing delay time $\tau$ (for comparison with the expected nucleation delay time $\langle\tau\rangle$). The crystallization time $t_C$ is the duration of the phase change of liquid water to ice. The total freezing time $t_F$ consists of the crystallization time $t_C$ if no supercooling occurs, or it consists of the freezing delay time $\tau$ and the crystallization time $t_C$ if supercooling occurs.

The freezing delay times and total freezing times were measured on the flat, uncoated or HMDSO 60 W plasma coated PU, uncoated or HMDSO 60 W plasma coated microstructure C6 and additionally C6 that was HMDSO 60 W plasma coated, then etched in an argon plasma and finally thinly coated again. The microstructure C6 was chosen because it showed the best superhydrophobicity of all microstructures with a plasma coating [2].

### Measured freezing delay times $\tau$

The mean values of the measured freezing delay times are shown in Figure 7.37.

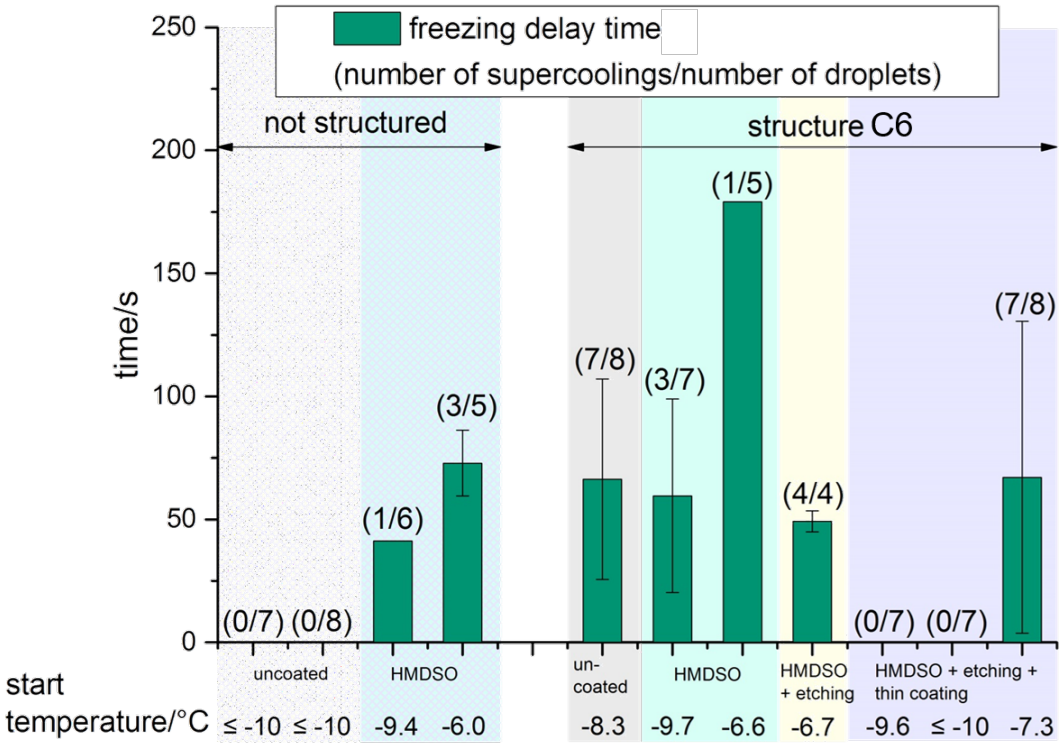


Figure 7.37.: Freezing delay times (mean values) on uncoated or HMDSO 60 W plasma-coated flat PU (left) and on uncoated, HMDSO 60 W plasma-coated, HMDSO 60 W plasma-coated and Ar (100 W) etched or HMDSO 60 W plasma-coated, Ar (100 W) etched and finally HMDSO 60 W plasma-coated microstructure C6 (right). Up to three experiments were made for each surface corresponding to the number of bars per surface. The numbers in brackets denote the number of supercooled drops per total number of drops for each experiment. The start temperature denotes the sample surface temperature measured by the IR camera at the start of each experiment. Adapted from [2].

A problem of these experiments was the inconsistent sample surface temperature at the start of the experiment and the inconsistent occurrence of water drop supercooling, for

both the flat and the microstructured, plasma-coated surfaces. On the flat samples, a freezing delay could only be seen with the HMDSO 60 W plasma coating (see sample "not structured, HMDSO")). Regarding the microstructured samples, the freezing delay was enhanced on the HMDSO 60 W plasma coated sample compared to the uncoated one, if supercooling occured (see samples "structure C6, uncoated and HMDSO"). The amount of supercooled drops was enhanced on the plasma coated/etched/coated samples (sample "structure C6, HMDSO + etching + thin coating"), but the freezing delay was not increased compared to the normally coated, microstructured sample.

According to theory, at the surface specific expected median nucleation temperature $T_N$ (expected value derived by probability calculation, see next subsection) the nucleation starts within seconds after the water drop has reached the surface temperature and no nucleation delay occurs. The nucleation delay should be seen if the surface temperature is raised above the expected median nucleation temperature. The theoretical (expected) nucleation delay time $\langle\tau(T)\rangle$ increases with increasing difference between surface temperature and expected median nucleation temperature $\Delta T = T - T_N$. It has to be noted that the surface temperature was set to -20 °C at the temperature control unit, although the IR camera measurements show surface temperatures around -10 °C. The measured freezing delay times are of the order of a few tens of seconds and are in the range of the calculated nucleation delay values $\langle\tau(T_S + \Delta T_S)\rangle$ for temperatures between -20 °C and -15 °C. They do not correspond to the calculated values for the temperatures of -15 °C or -10 °C. According to the theoretical freezing delay times, the surface must have been cooled to around -20 °C.

### Measured crystallization times $t_C$

The measured crystallization times $t_C$ were derived from the difference of the measured total freezing times $t_F$ and the measured freezing delay times $\tau$ and are shown in Figure 7.38.

The mean values of the measured crystallization times are in the range of the calculated crystallization time values of the corresponding flat PU or C6 microstructured surfaces (see Table 7.3 or Figure 7.35). The measured crystallization times on uncoated or HMDSO plasma coated C6 samples are higher than the calculated values of the Wenzel

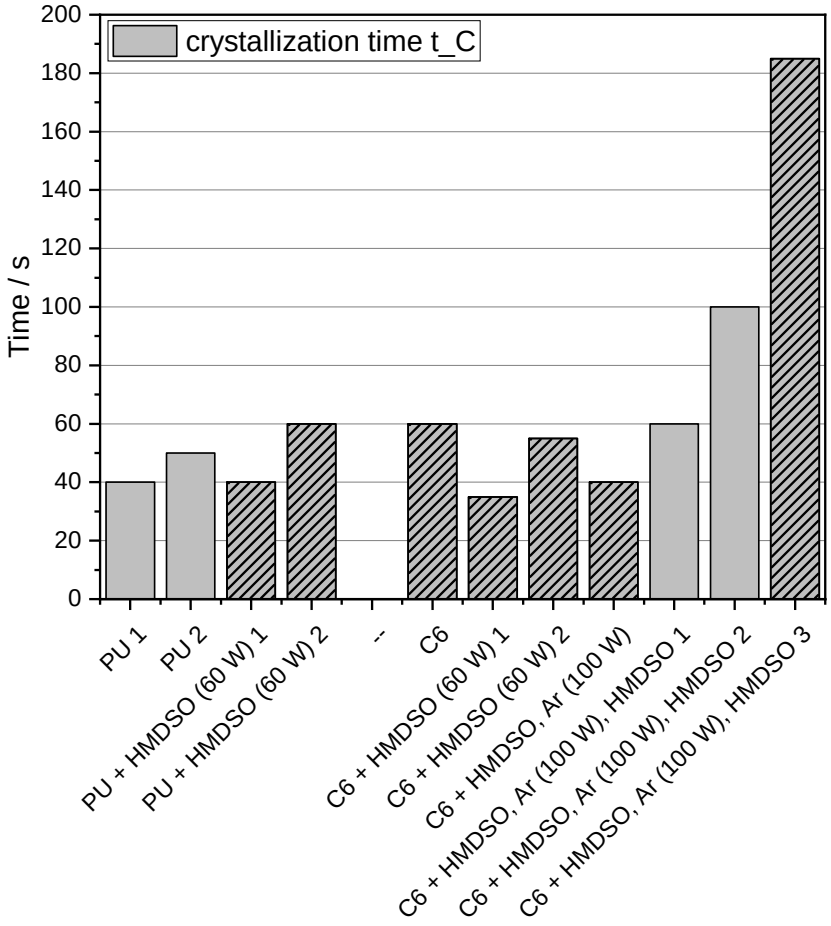


Figure 7.38.: Crystallization times (mean values) on uncoated or HMDSO 60 W plasma-coated flat PU (left) and on uncoated, HMDSO 60 W plasma-coated, HMDSO 60 W plasma-coated and Ar (100 W) etched or HMDSO 60 W plasma-coated, Ar (100 W) etched and finally HMDSO 60 W plasma-coated microstructure C6 (right). Up to three experiments were made for each surface corresponding to the number of bars. The hatched areas show that supercooling of water drops has occurred. Derived from data of [2].

or mixed state at -20 °C and correspond better to those at -10 °C. The longer crystallization times on the coated/etched/coated C6 samples are similar to the calculated values of the Cassie-Baxter state in the range of -12 °C to -20 °C.

### Measured total freezing times $t_F$

The measured total freezing times $t_F$ consist of the measured freezing delay times and crystallization times and are shown in Figure 7.39.

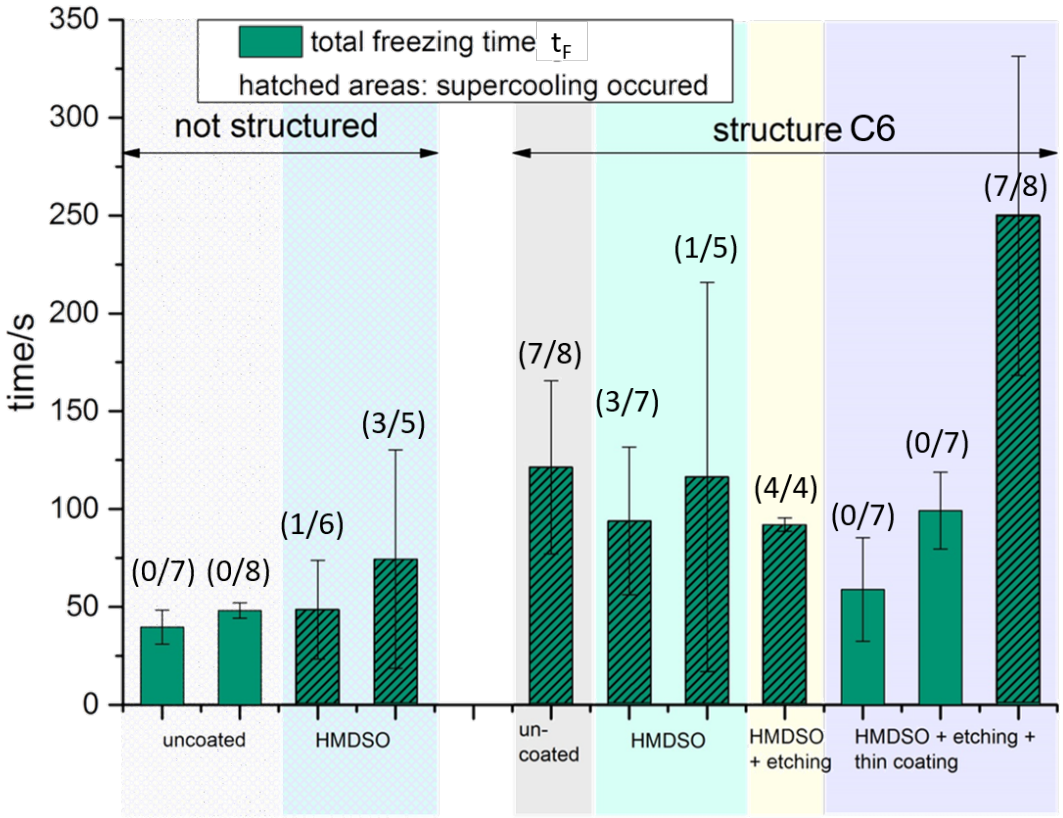


Figure 7.39.: Total freezing times (mean values) on uncoated or HMDSO 60 W plasma-coated flat PU (left) and on uncoated, HMDSO 60 W plasma-coated, HMDSO 60 W plasma-coated and Ar (100 W) etched or HMDSO 60 W plasma-coated, Ar (100 W) etched and finally HMDSO 60 W plasma-coated microstructure C6 (right). Up to three experiments were made for each surface corresponding to the number of bars. The hatched areas show that supercooling of water drops has occurred. The numbers in brackets denote the number of supercooled drops per total number of drops for each experiment. Adapted from [2].

For the flat PU samples ("not structured"), the total freezing time is clearly longer on the hydrophobic HMDSO 60 W plasma coating (about 50 s to 75 s, with supercooling)

than on uncoated PU (about 50 s, without supercooling). The longer total freezing time is caused by the supercooling on the HMDSO 60 W plasma coating.

For the microstructured samples ("structure C6") the mean total freezing time on the plasma coated samples is not longer than on the uncoated samples (about 125 s). Reasons are the similar freezing delay times on the uncoated and plasma coated samples and similar crystallization times. The similar crystallization times could be caused by similar surface-ice interface areas or the Wenzel wetting state in both cases.

On the coated, etched and thinly coated, microstructured sample the total freezing time was longest and could be prolonged significantly to about 250 s on the sample with supercooling. This is caused by an enhanced freezing delay time because of the HMDSO 60 W plasma coating and enhanced crystallization time because of better stabilization of a mixed wetting state or the Cassie-Baxter state compared to the plain HMDSO 60 W plasma coated microstructure C6.

It has to be noted that the surface starting temperature was inconsistent (increasing over time because of the open lid towards the ambient air during the static experiments) and varied by up to 4 °C. The temperature of the surface and the water drop is the thermodynamic force that drives the nucleation and crystallization process and therefore also determines the freezing delay time, crystallization time and total freezing time.

A reason that not every water drop could be supercooled is the open cooling chamber, because the lid had to be opened for the IR camera videos. Consequently, the samples on the cooled surface were exposed to warmer lab air which led to condensation or frost formation on the samples. The frost formation enhances the freezing probability, because the frost crystals act like ice nuclei when contacting a water drop which then instantly starts to crystallize.

As expected, the flat, plasma-coated samples showed better anti-icing behavior than the flat, uncoated PU because of the supercooling and increased nucleation delay time caused by the HMDSO 60 W plasma coating. This was further improved by the superhydrophobic surfaces with prolonged total freezing times because of a longer crystallization time caused by a better stabilization of the Cassie-Baxter state, if supercooling could be achieved.

Because of possible experimental problems like inconsistent surface temperature and frost formation on the samples, dynamic freezing measurements in the better insulated new icing test chamber were made to determine the surface specific nucleation temperatures and reliably characterize the icing behavior. These measurement results will be discussed in the next subsection.

## 7.3.2. Dynamic icing experiment measurement results

The dynamic water drop icing experiments were done in the new icing test chamber with a constant cooling rate of 1 K/min. 25 µl water drops were applied on the samples and the samples were inserted into the chamber at about 0 °C. Then, the Peltier cooling with constant rate, the logging of the temperatures and the humidity and the IR camera video were started. From the grayscale IR video the droplet temperature curves were extracted and the nucleation temperatures and crystallization times were read out manually (see chapter methods for details).

The freezing process of three water drops recorded with the photonfocus DR1-D1312 camera is shown in Figure 7.40.

### Theoretical prediction of the nucleation temperature $T_N$

The theoretical nucleation temperatures were calculated for the flat, uncoated and plasma-coated samples with the equations given in the section on theoretical basics of icing (3.2.4). These are expected values derived with probability calculation by setting the probability function of the frozen drop to 0.5 (median). Therefore, they are called expected median nucleation temperatures [168]. The calculated values given here were derived with the equation including $T_S$ (0 °C, see equation 3.48). Calculation with $T_1$ (equation 3.48) leads to the same calculated nucleation temperatures.

For calculation of the approximated nucleation rate, $T_0$ was set to 257.15 K (-16 °C), because it is the mean of the measured nucleation temperatures of the flat samples (about -12 °C to -22 °C), most being between -14 °C and -18 °C. With this $T_0$ value, the constants in the nucleation rate equation were calculated, giving $\lambda = 7.94$, $a = 7.52 \times 10^{-8}$ and $a_S = 4.92 \times 10^{-63}$. The thermodynamic parameters used for calculation were the

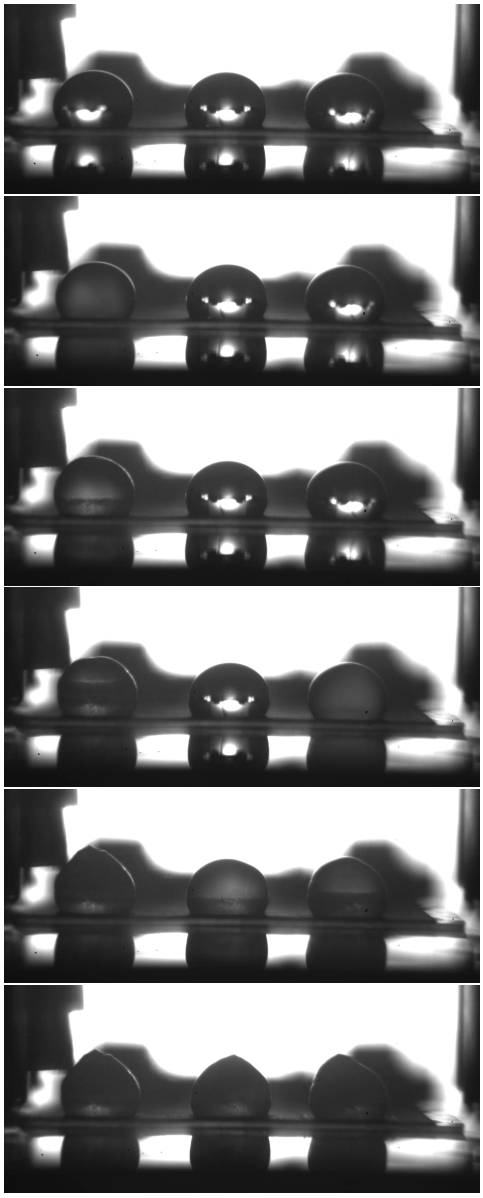

Figure 7.40.: Freezing process of three 25 µl water drops on a PU surface with microstructure C6, etched in an $O_2$ plasma and coated in a $C_3F_6$ plasma. Images taken by the DR1-D1312 digital camera during a dynamic icing experiment for determination of the nucleation temperature (between -16 °C and -19.5 °C). After the nucleation, indicated by the recalescence which turns the whole drop into a homogeneous light gray, the crystallization front moves up from the bottom to the top of the water drop while turning the remaining water to ice (dark gray).

ice-water interfacial tension $\gamma_{IW} = 21.7\,mN/m$ and the volumetric enthalpy of fusion $\Delta H_{f,v} = 281 \times 10^6\,J/m^3$, determined for -25 °C by empirical relations, similar to [168].

The starting temperature $T_S$ for the dynamic freezing experiments was 273.15 K and the rate of temperature change $\alpha$ was -0.0167 K/s (-1 K/min). The temperature $T_1$ with a nucleation rate of $1\,s^{-1}$ was calculated as 255.08 K. The other constants were $T_m = 273.15\,K$, $T_R = 118\,K$ and $E = 892\,K$ [168]. $T_R$ and $E$ were determined experimentally in the temperature range from 150 K to 273 K, according to [168].

A water drop of 25 µl in the shape of a half-sphere was assumed, giving a radius of 2.29 mm and a flat contact area $A_f = 16.4 \times 10^{-6}\,m^2$. The actual solid-liquid contact area was calculated as $A_{sl} = rf \cdot f_{sl} \cdot A_f$ for each sample. On the flat surfaces, the values of $rf$ and $f_{sl}$ were set to 1. On the uncoated, microstructured surfaces, the Wenzel wetting state was assumed and $f_{sl}$ was set to 1. On the plasma-coated, microstructured surfaces, various mixed wetting states were assumed and $f_{sl}$ was set to values between 0.2 and 1 according to the water contact angle measurements. The Wenzel state was assumed on all quadratically arranged microstructures C16 and C17 ($f_{sl} = 1$). A solid-liquid fraction $f_{sl}$ of 0.2 was assumed for the superhydrophobic microstructure C6 and 0.6 for the hydrophobic sample C6 + HMDSO (200 W). A solid-liquid fraction $f_{sl}$ of 0.4 was assumed for the superhydrophobic microstructure C9 and 0.8 for the hydrophobic sample C9 + HMDSO (200 W). $f_{sl}$ was set to 0.4 for superhydrophobic microstructure C1 and to 0.6 for superhydrophobic microstructure E1. During the experiments at 0 % relative humidity, the Cassie-Baxter state was assumed (better stabilization of the water drop because of no condensation from ambient air) and therefore $f_{sl}$ was set to 0.1 for the plasma-coated and microstructured surfaces. Further details are given in the appendix (see A.7).

The surface parameter $f$ for heterogeneous nucleation was calculated for convex nano-bumps with the parameters $R$, $r_c = 2.94\,nm$, $x$, $m$, $g_v$ and $\theta_{IW} = 80°$ at $T_0 = 257.15\,K$. For $\theta_{IW}$ a linear decrease of -2.5°/K from 100° at -24 °C was assumed, caused by the plasma coating surface groups with temperature dependent flexibility, similar to the FDTS monolayer of Eberle *et al.* [168]. The mean roughness radius of curvature $R = 1/H$ was calculated for each sample from the mean summit curvature $H$ (AFM parameter $S_{sc}$) determined by AFM measurements.

With these parameters, the expected median nucleation temperature $T_N$ (equation 3.48), the expected nucleation rate $J(T_N)$ (equation 3.49) and the expected nucleation delay time $\langle\tau(T_N)\rangle$ (equation 3.51) were calculated. These icing behavior values and corresponding plasma polymer surface parameters are listed in Table 7.4. The calculated median nucleation temperatures are shown as black spots in the graphs below in comparison to the measured values in form of box plots (with the mean value as a hollow square and the median value as the middle horizontal line).

Table 7.4.: AFM surface parameters of the plasma polymers and corresponding icing behavior values (expected nucleation rate $J(T_N)$, expected median nucleation temperature $T_N$ and expected nucleation delay time $\langle\tau(T_N)\rangle$) calculated with the enhanced nucleation theory including a variable ice-water contact angle $\theta_{IW}$.

| Sample<br>- | $S_a$<br>(nm) | $S_q$<br>(nm) | $S_{sc}$, $H$<br>(1/nm) | $R$, $1/H$<br>(nm) | $J(T_N)$<br>(1/s) | $T_N$<br>(K) | $T_N$<br>(°C) | $\langle\tau(T_N)\rangle$<br>(s) |
|---|---|---|---|---|---|---|---|---|
| PU | 3.56 | 4.58 | $0.24 \times 10^{-4}$ | 40984 | 0.0917 | 255.392 | -17.76 | 10.91 |
| PU + $C_4F_8$ | 5.21 | 7.27 | $0.53 \times 10^{-4}$ | 18800 | 0.0916 | 255.394 | -17.76 | 10.91 |
| PU + $C_3F_6$ | 21.6 | 27.6 | $1.38 \times 10^{-4}$ | 7246 | 0.0917 | 255.392 | -17.76 | 10.91 |
| PU + $O_2$, $C_3F_6$ | 8.1 | 13.9 | $3.03 \times 10^{-4}$ | 3300 | 0.0917 | 255.389 | -17.76 | 10.91 |
| HMDSO (60 W) | 7.84 | 10.1 | $0.78 \times 10^{-4}$ | 12821 | 0.0916 | 255.393 | -17.76 | 10.91 |
| HMDSO (200 W) | 115 | 139 | $4.92 \times 10^{-4}$ | 2033 | 0.0917 | 255.385 | -17.77 | 10.90 |

### Measured nucleation temperatures $T_N$

The measured nucleation temperatures for every surface were obtained by the dynamic freezing experiments with 25 µl water drops and a cooling rate of 1 K/min.

### Water drop freezing on flat plasma-coated PU films

Figure 7.41 shows the nucleation temperatures on the plasma coated PU surfaces.

The measured nucleation temperature of uncoated PU is in the range of -17 °C. This corresponds well to the calculated median nucleation temperature $T_N$ in Table 7.4. The HMDSO 60 W and $C_3F_6$ coated samples have a lower measured $T_N$ because of the

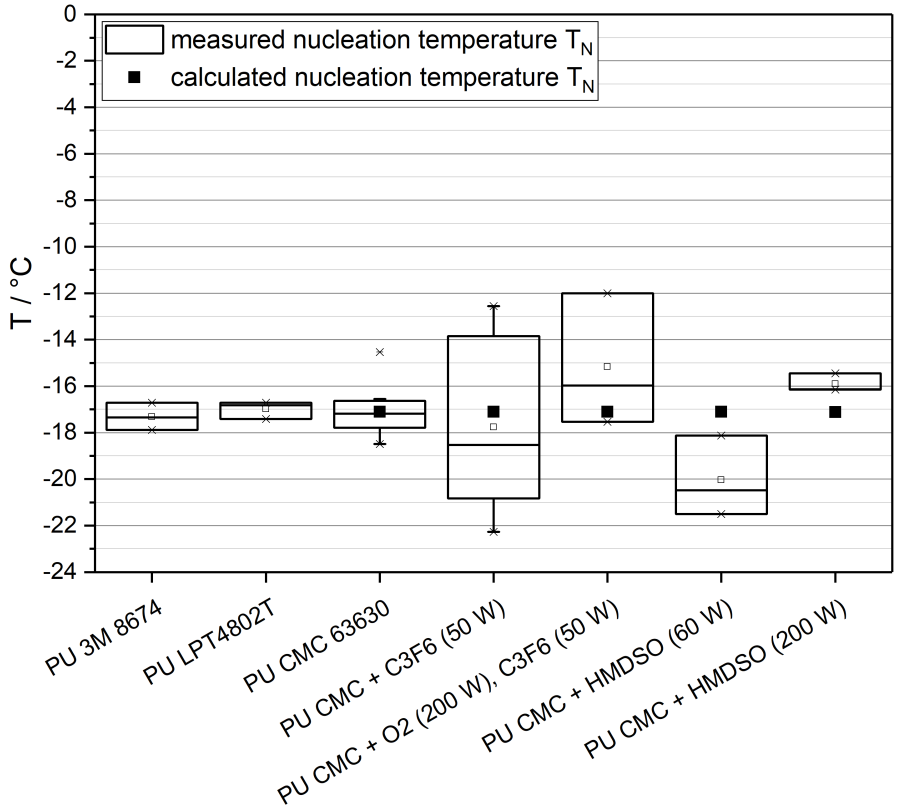


Figure 7.41.: Nucleation temperatures of the uncoated and plasma-coated, flat PU surfaces.

reduced water-surface contact area. The HMDSO 200 W as well as the $O_2$-etched and then $C_3F_6$ coated samples have a higher measured $T_N$ because of the lesser hydrophobia (increased oxygen content) of the plasma coatings and therefore increased water-surface contact area. In consideration of the unpreventable measurement error, the predicted median nucleation temperatures correspond well to the measurement values.

### Discussion of water drop freezing on flat plasma-coated PU films

The RMS ($S_q$) values are at about 5 nm for the uncoated PU and between about 7 nm to 139 nm for the different plasma coatings. Eberle *et al.* have measured RMS values ranging from about 0.17 nm (on polished silicon with a $SiO_2$ layer) to about 173 nm on their samples which were created by varying the ICP etching time of the $SiO_2$ layer and coating with a self-assembled FDTS monolayer. The cooling rate of Eberle *et*

*al.* was 0.31 K/min starting from -14 °C as opposed to 1 K/min starting from 0 °C of this dynamic freezing experiment [167]. The RMS values and hydrophobicity of the plasma coatings are comparable to those of the etched silicon samples with a FDTS monolayer. Although the surface nanoscale roughness and chemistry are similar, the measured nucleation temperatures are different. Eberle *et al.* measured median nucleation temperatures of about -24 °C as opposed to about -16 °C to -20.5 °C on the plasma coatings.

### Water drop freezing on quadratically arranged cylindrical microstructures with $D = 70$ µm

The question is, whether lower nucleation temperatures can be measured on the plasma coated, quadratically arranged cylindrical microstructures than on the flat, plasma coated surfaces because of the higher contact angle and a reduced water-surface contact area. Figure 7.42 shows the nucleation temperatures of microstructure C16 and C17 surfaces.

For the C16 and C17 microstructures the median values of the measured nucleation temperatures are in the range of about -19 °C to -13 °C. This is higher than on the flat samples, on which the median values are in the range of -20.5 °C to -16 °C. As the water contact angles on the plasma coated C16 and C17 samples did not reach 150°, the drops were not in the Cassie-Baxter state. The increased water-surface contact area in a mixed state or the Wenzel state leads to a higher nucleation rate and higher nucleation temperatures. The uncoated C16 sample shows the lowest nucleation temperature, whereas the coated C16 samples show a higher one. As the water drops sit in the Wenzel state on all the C16 samples, the increased nanoroughness on the plasma coatings enhances the nucleation rate and results in higher median values of the measured nucleation temperature.

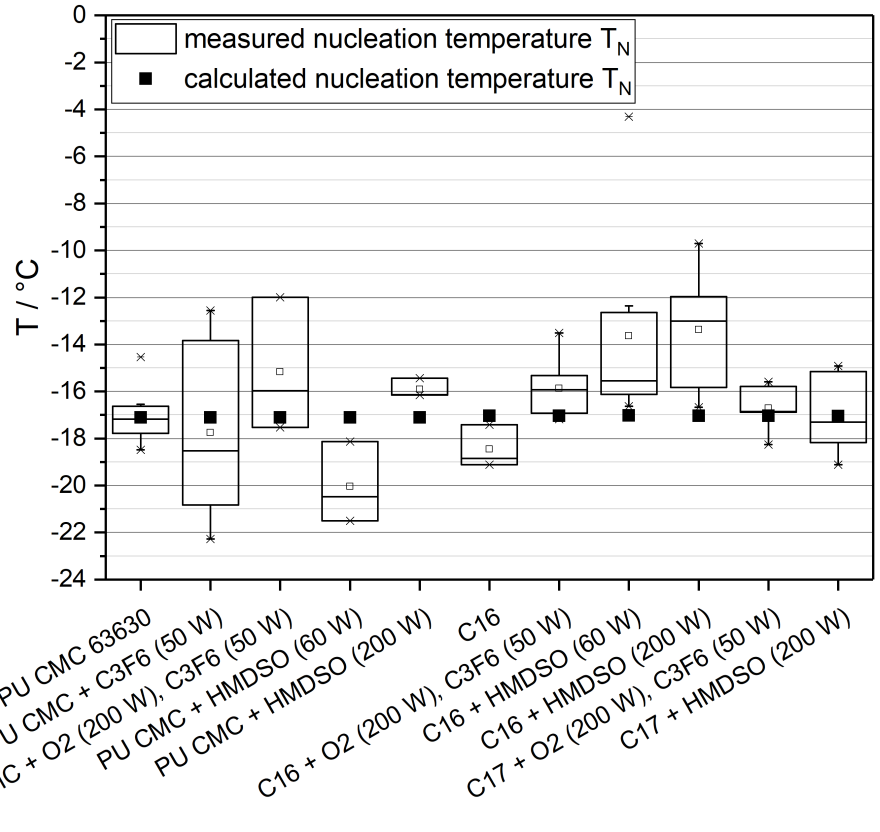


Figure 7.42.: Nucleation temperatures of the uncoated and plasma-coated, quadratically arranged microstructure C16 and C17 samples.

### Discussion of water drop freezing on quadratically arranged cylindrical microstructures with $D = 70$ µm

Eberle *et al.* created quadratically arranged, cylindrical microstructures in silicon by photolithography and cryogenic ICP etching. Their microstructures had diameters of 2.5 µm to 13 µm, heights of 6 µm to 10 µm and pitch values of 4.5 µm to 33 µm. These values are smaller than those of the cylindrical microstructures C16 and C17 in PU, with diameters of about 60 µm to 70 µm, a height of about 50 µm and a pitch of about 90 µm (C16 and C17 are larger by a factor of about 5 to 10). Eberle *et al.* used 4 µl drops of highly purified (type 1) water as opposed to 25 µl drops (larger by a factor of about 6) in the dynamic icing experiments for this thesis [167]. Both the microstructure dimensions and the water drop volume used for this thesis are larger. However, the wetting behavior is determined by the capillary pressure of the microstructure gaps and

the gravitational force of the water drops. These forces are different to those of Eberle *et al.*.

It can be concluded that the median value of the measured nucleation temperature could not be lowered further than on the flat, plasma coated PU surfaces by the plasma-coated microstructures C16 and C17, unlike on the microstructured samples of Eberle *et al.*. The reason is that these quadratically arranged microstructures with a base diameter of 70 µm do not show a stable Cassie-Baxter state and cause an increased water-surface contact area in the Wenzel wetting state leading to an increased nucleation rate.

### Water drop freezing on hexagonally arranged microstructures with $D = 50$ µm

The hexagonally arranged microstructures C1 and E1 with a mean base diameter of 50 µm and distance $P$ of 70 µm showed superhydrophobic wetting behavior and were expected to show a lowered nucleation temperature compared to the flat PU surfaces and the quadratically arranged microstructures. Figure 7.43 shows the nucleation temperatures of the cylindrical C1 and elliptical E1 microstructures.

Regarding these samples, the nucleation temperatures are higher than on flat PU which can be explained by a higher nucleation rate because of a higher contact area in Wenzel state or a mixed state. For the plasma coated, cylindrical microstructure C1 with a roughness factor of 3.32 and a height of 114 µm and the plasma coated, elliptical microstructure E1 with a roughness factor of 2.2 and a height of 50 µm the median measured nucleation temperatures are between -12.5 °C and -14 °C.

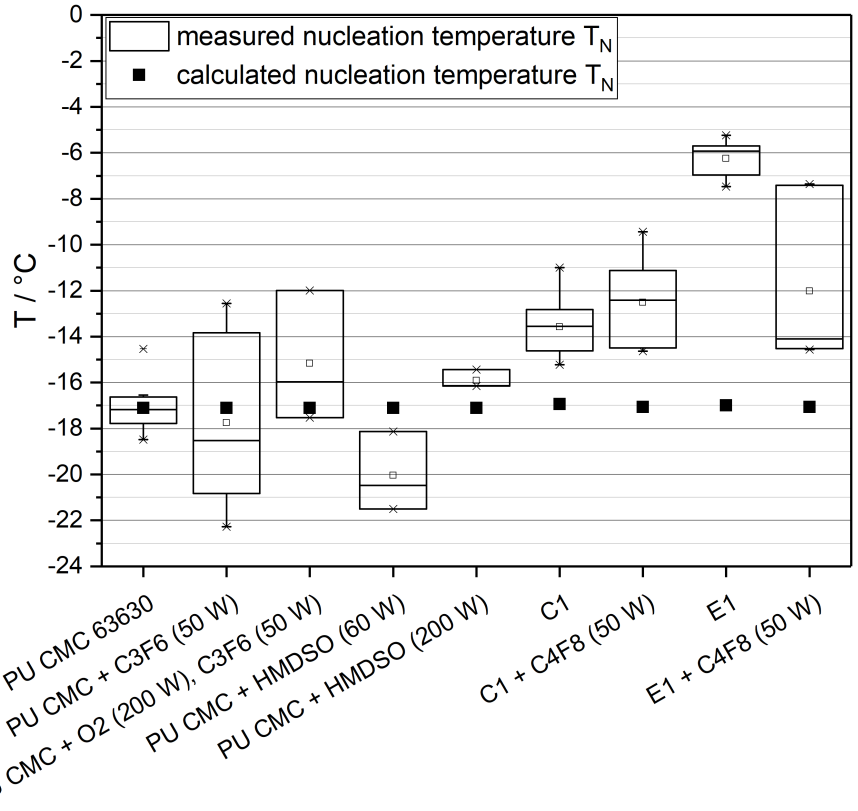


Figure 7.43.: Nucleation temperatures of the uncoated and plasma-coated, hexagonally arranged microstructure C1 and E1 samples.

**Discussion of water drop freezing on hexagonally arranged microstructures with $D$ = 50 µm**

Overall, the plasma coated, hexagonally arranged microstructures with a base diameter of 50 µm showed higher contact angles than the flat PU samples and the quadratically arranged microstructures (C16 and C17). The measured nucleation temperatures were not lower but higher on these samples. This shows that the water drops could not be stabilized sufficiently in the Cassie-Baxter state during the cooling process. Furthermore it can be concluded that higher nucleation temperatures can occur even in Cassie-Baxter state on the coated samples due to the surface nanoroughness and chemistry which mainly determines the nucleation temperature regardless of the microstructure.

### Water drop freezing on hexagonally arranged cylindrical microstructures with $D$ = 35 µm

The hexagonally arranged microstructures C6 ($rf$ = 3.65, $h$ = 71 µm) and C9 ($rf$ = 2.24, $h$ = 43 µm) had a smaller base diameter of 35 µm and smaller distance $P$ of 50 µm compared to the microstructures C1, E1 and C16, C17. The plasma coated samples also showed superhydrophobicity and were expected to better stabilize the Cassie-Baxter state during the cooling process. This should lead to lower nucleation temperatures compared to the microstructures C1, E1, C16, C17 and the flat samples with the corresponding plasma polymer coating type.

Figure 7.44 shows the nucleation temperatures of microstructures C6 and C9.

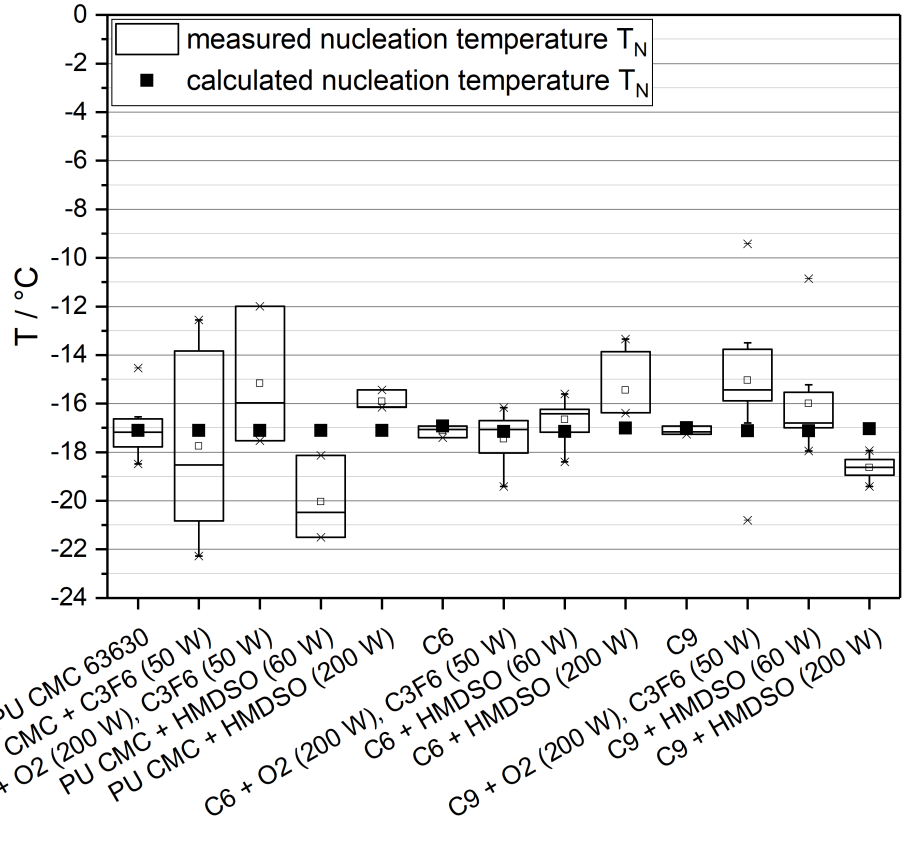


Figure 7.44.: Nucleation temperatures of the uncoated and plasma-coated, hexagonally arranged microstructure C6 and C9 samples.

The microstructured samples have similar or even higher nucleation temperatures compared to the flat surfaces.

### Discussion of water drop freezing on hexagonally arranged cylindrical microstructures with $D = 35$ µm

The median measured nucleation temperatures of the uncoated C6 and C9 samples are on a similar level as of uncoated, flat PU, at about -17 °C because of the same surface chemistry. The water drop is in a mixed wetting state here that does not decrease the water-surface interface area compared to the flat, uncoated PU. When the HMDSO 60 W plasma coatings are compared, both the median and the mean value of the measured nucleation temperatures on the C6 and C9 microstructure samples are higher than on the flat samples because no Cassie-Baxter state occured and the mixed wetting state increased the water-surface contact area and the nucleation rate. This can also be seen for the $C_3F_6$ plasma coatings on oxygen etched PU. An exception is the sample C6 + $O_2$ (200 W), $C_3F_6$ (50 W), where the median measured nucleation temperature is lower because of a reduced water-surface contact area in a mixed wetting state close to the Cassie-Baxter state.

The rate of ice nucleation is determined by the surface nanoroughness and chemistry and is proportional to the water-surface contact area. According to theory, the hierarchical micro-nanostructures reduce the nucleation temperature compared to flat surfaces by reducing the water-surface contact area in Cassie-Baxter state.

Overall, the nucleation temperature decreasing effect of the microstructures compared to the flat surfaces cannot be seen for the C6 and C9 samples. Obviously, the micro- and nanostructures cannot stabilize the water drops of this large size sufficiently long in the Cassie-Baxter state during the cooling process.

The water drops could have slowly transferred to a Wenzel wetting state during the long cooling period because of destabilization of the Cassie-Baxter state by condensation from the ambient air with about 50 % to 60 % relative humidity. Therefore, dynamic freezing experiments with uncoated and plasma coated microstructure C6 were repeated in dry atmosphere.

### Water drop freezing on hexagonally arranged cylindrical microstructures with $D$ = 35 µm in dry atmosphere

No condensation from ambient air can occur in dry atmosphere (about 0 % to 5 % relative humidity) and so the possibility for destabilization of the Cassie-Baxter state of the water drops by condensated microdrops between the microstructures is reduced. A reduced water-surface interface area leading to a reduced nucleation rate and nucleation temperature was expected on plasma coated microstructure C6 in dry atmosphere. Figure 7.45 shows the nucleation temperatures of microstructure C6 surfaces at 0 % relative humidity.

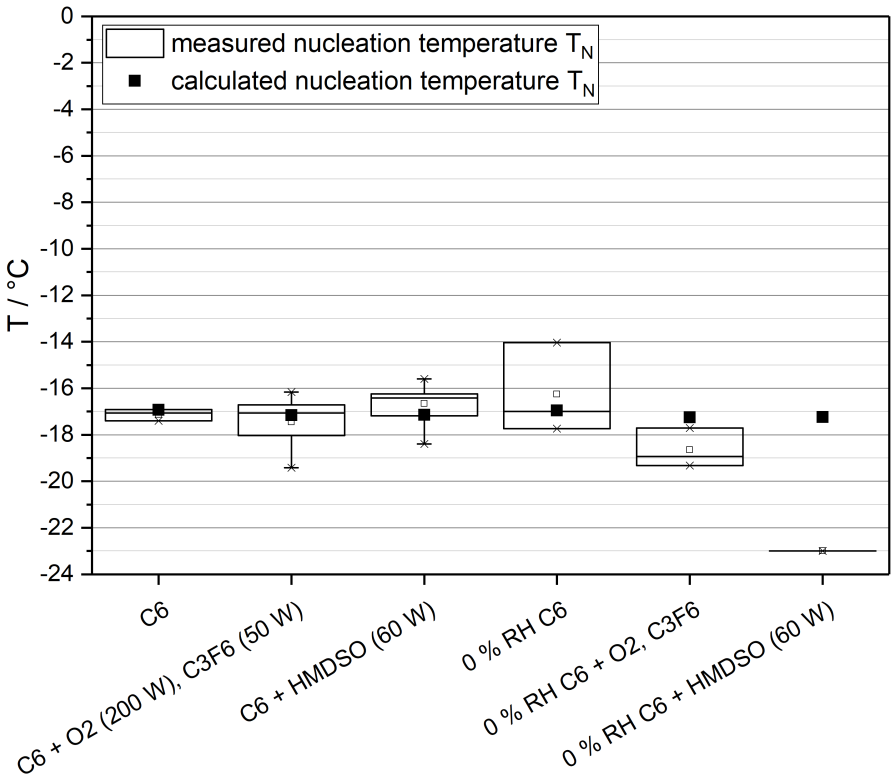


Figure 7.45.: Nucleation temperatures of the plasma-coated, nanorough, hexagonally arranged microstructure C6 samples at 0 % rel. humidity.

A difference can be seen regarding the nucleation temperatures of microstructure C6 samples in dry atmosphere (about 0 % to 5 % relative humidity) compared to normal atmosphere (about 50 % relative humidity, although the absolute humidity is very low at negative temperatures). The median value of the measured nucleation temperature $T_N$ is

similar for the uncoated sample where the water drop can only be in the Wenzel state or a mixed state close to the Wenzel state. However, the nucleation temperatures are lower for the plasma coated samples at 0 % relative humidity; on the HMDSO 60 W plasma coated sample the water drops did not freeze at all until the end of the experiment (30 minutes, -30 °C, measurement value drawn manually only for completion of Figure 7.45).

### Discussion of water drop freezing on hexagonally arranged cylindrical microstructures with $D = 35$ µm in dry atmosphere

Eberle *et al.* conducted their freezing experiments with an ice bath surrounding the sample table. In this way the humidity was always saturated with respect to ice and the relative humidity was at about 75 % to 80 % with respect to liquid water. This high humidity atmosphere was used in order to suppress homogeneous nucleation at the water-air interface because of evaporative cooling of the droplets [168]. The high relative humidity did not destabilize the Cassie-Baxter state or increase the nucleation temperatures because the air and the surface had the same temperature and so condensation was prevented.

In the dynamic freezing experiment with dry atmosphere, no condensation from ambient air could occur. The drops could be stabilized longer in the Cassie-Baxter state on the plasma coated microstructure C6 and therefore could be supercooled further than in the normal lab atmosphere with about 50 % relative humidity. In the Cassie-Baxter state, the nucleation temperature is decreased by the plasma coated microstructure C6 because of a smaller water-surface interface area and a smaller nucleation rate.

### Water drop freezing on technical material surfaces and commercial anti-ice coatings

For comparison, the nucleation temperatures were also measured on the technical material surfaces and commercial anti-ice coatings. Because of the more hydrophilic surface chemistry leading to higher water-surface interface areas and higher nucleation rates, higher nucleation temperatures are expected on the technical material surfaces compared

to the functionalized PU surfaces. The nucleation temperatures on the commercial anti-ice coatings are expected to be similar to the functionalized PU films. Figure 7.46 shows the nucleation temperatures of the technical material surfaces and commercial anti-ice coatings.

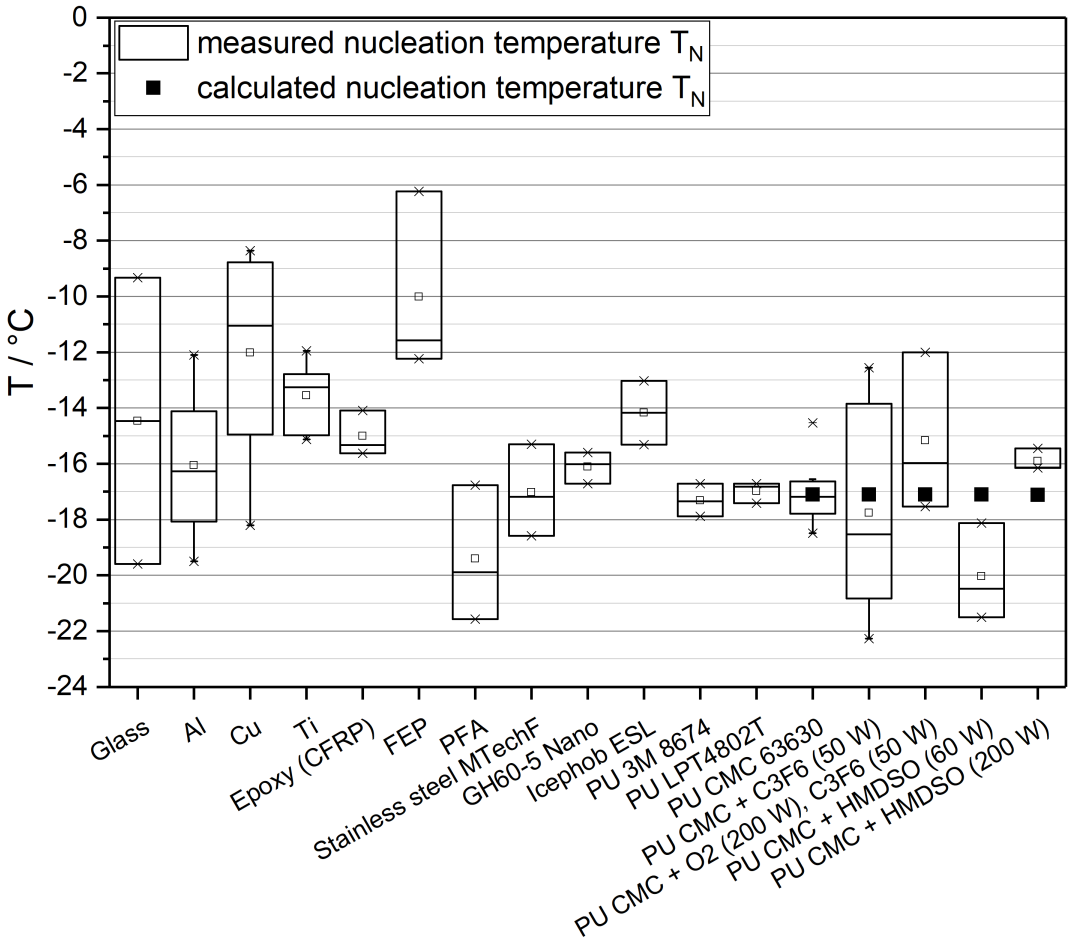


Figure 7.46.: Nucleation temperatures of the technical material surfaces and commercial anti-ice coatings.

The mean nucleation temperatures lie between about -10 °C and -17 °C, except for the PFA film surface. The different PU surfaces have about the same mean nucleation temperature at -17 °C. The hydrophilic metal-oxide and epoxy surfaces have different mean nucleation temperatures from -12 °C to -16 °C, determined by their nanoroughness. The mean nucleation temperatures of the commercial anti-ice surfaces are not lower than those of uncoated PU, although the Icephob ESL surface has salt particles embedded in

the coating.

It can be concluded that from the surfaces examined for comparison, both the technical material surfaces and the commercial anti-ice surfaces show higher nucleation temperatures compared to uncoated or plasma coated, flat PU surfaces.

### Discussion of influence of nanoroughness on measured and calculated nucleation temperatures

The calculated nucleation temperatures are all very similar, being between -17 °C and -18 °C. The microstructuring does not alter the theoretical values because the Wenzel ($rf = 1$) or a mixed state is assumed for the calculations. Even the assumed Cassie-Baxter state ($rf = 0.1$) for the 0 % relative humidity experiments does not significantly change the nucleation temperatures (see Table 7.4 and the appendix A.7). As a nucleation seed is around 2 nm to 3 nm, the nanometer roughness is the critical influence on the nucleation temperature. It is characterized by the mean surface curvature ($H$ or $S_{sc}$) or the mean surface roughness radius of curvature ($R = 1/H$), which is used for calculation of the heterogeneous nucleation factor $f$, the nucleation rate $J(T)$ and the nucleation temperature $T_N$. A depression of the nucleation temperature can be expected for $R \leq 10\, r_c$ [167]. Therefore, $R$ would have to be maximally around 20 nm to 30 nm on 100 % of the surface. Eberle *et al.* measured and calculated values of the median nucleation temperature of about -24 °C to -25 °C (using a value for $T_0$ close to 248.15 K), which is about 7 K to 8 K lower than the calculated values of this thesis (using $T_0 = 257.15$ K). $T_0 = 257.15$ K was chosen because it is close to the measured nucleation temperature on uncoated PU, but it remains unclear which $T_0$ has to be chosen for the Taylor approximation of the nucleation rate on the various plasma-coated PU surfaces. A constant $\theta_{IW}$ of 100° (calculated at $T_N$ = -24.4 °C) for hydrophilic $SiO_2$ and a variable $\theta_{IW}$ (99° at $T_N$ = -24.2 °C with an assumed linear decrease of -2.5°/K because of the temperature dependent flexibility of the fluorinated alkylsilane chains) for the hydrophobic FDTS monolayer were assumed by Eberle *et al.*. The question remains, what the exact values for the interfacial quasiliquid layer thickness of the ice nucleus and the dependent ice-water contact angle $\theta_{IW}$ on the uncoated or plasma-coated PU surfaces are. The exact values would enable a more precise calculation of the median

nucleation temperature. The $R$ values of the plasma coatings determined on flat samples by AFM measurements are in the range of 41000 nm (uncoated PU) to 2000 nm (HMDSO 200 W), corresponding to an average roughness $S_a$ of 3.56 nm (PU) to 115 nm (HMDSO 200 W). This is too high by a factor of 100 to 1000 and explains the almost identical calculated median nucleation temperatures on the different coatings and microstructures. The nanometer roughness has to be further optimized (increasing the $S_a$ value for decreasing the $R$ value towards 20 nm) in order to achieve a reduction of the median nucleation temperatures by the "nanoscale interface confinement effect".

### Correlation of nucleation temperatures $T_N$ with the surface wetting behavior

It shall further be checked whether the nucleation temperature is determined by the wetting behavior. It was assumed that a high static water contact angle or a low surface free energy leads to a small water-surface interface area, a low nucleation rate and therefore a low nucleation temperature. Therefore, the mean measured nucleation temperatures of all types of the examined surfaces are correlated with the mean values of the static water contact angles and surface free energies in Figure 7.47 and Figure 7.48. The surfaces include the quadratically arranged microstructures C16 and C17, the most hydrophobic hexagonally arranged microstructures C6 and C9 and the flat PU and technical material surfaces.

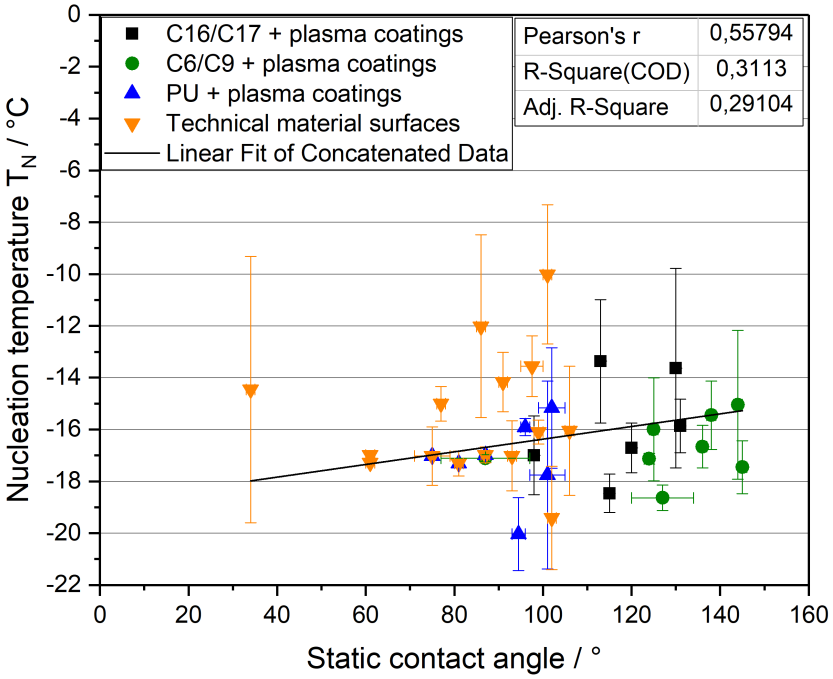


Figure 7.47.: Nucleation temperature $T_N$ (mean value) of the flat and microstructured surfaces in dependence of the static water contact angle. The solid line is the linear best fit.

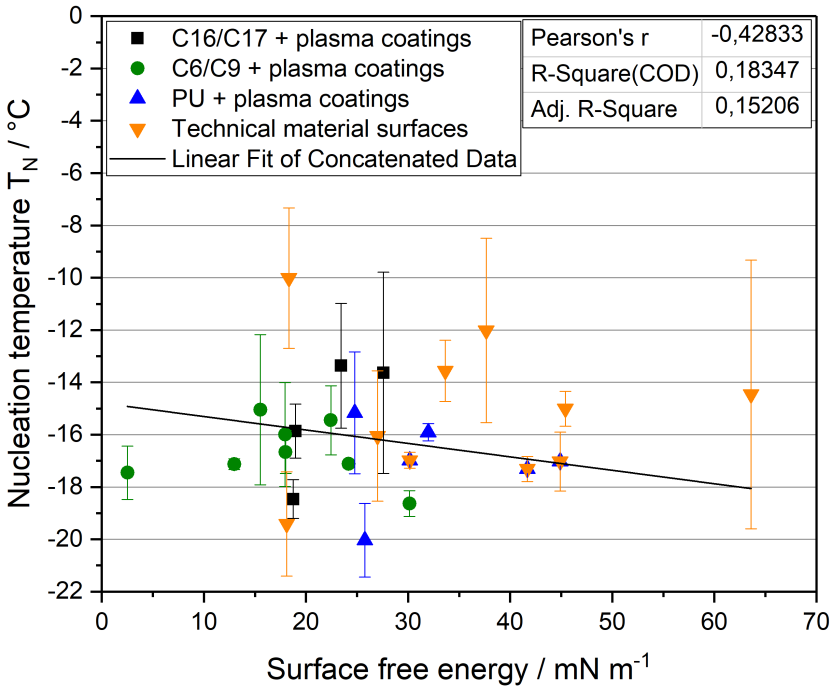


Figure 7.48.: Nucleation temperature $T_N$ (mean value) of the flat and microstructured surfaces in dependence of the surface free energy. The solid line is the linear best fit.

No linear correlation between the nucleation temperature and the static water contact angle or the surface free energy can be seen. This is also shown by the low adjusted $R^2$ values (adj. $R^2 = 0.29$ for static contact angle and adj. $R^2 = 0.15$ for surface free energy).

A higher contact angle or a lower surface free energy leads to a smaller water-surface contact area and therefore lower nucleation rate which is proportional to the contact area. However, the nucleation rate (and temperature) is determined as well by the nanoroughness and, depending on the absolute value of the factors in the nucleation rate equation, the influence of the nanoroughness might be bigger than that of the contact area.

### Correlation of nucleation temperatures $T_N$ with the surface micrometer roughness

Furthermore, it was assumed that a decreasing water-surface contact area (the wetting state getting closer to the Cassie-Baxter state) on the superhydrophobic samples leads to a decreasing nucleation temperature compared to the flat samples. Therefore, the mean measured nucleation temperatures of all types of the examined surfaces are correlated with the micrometer roughness values $rf = A_{sl}/A_f = 1+\eta\cdot(A_L+A_T-A_B)$ in Figure 7.49.

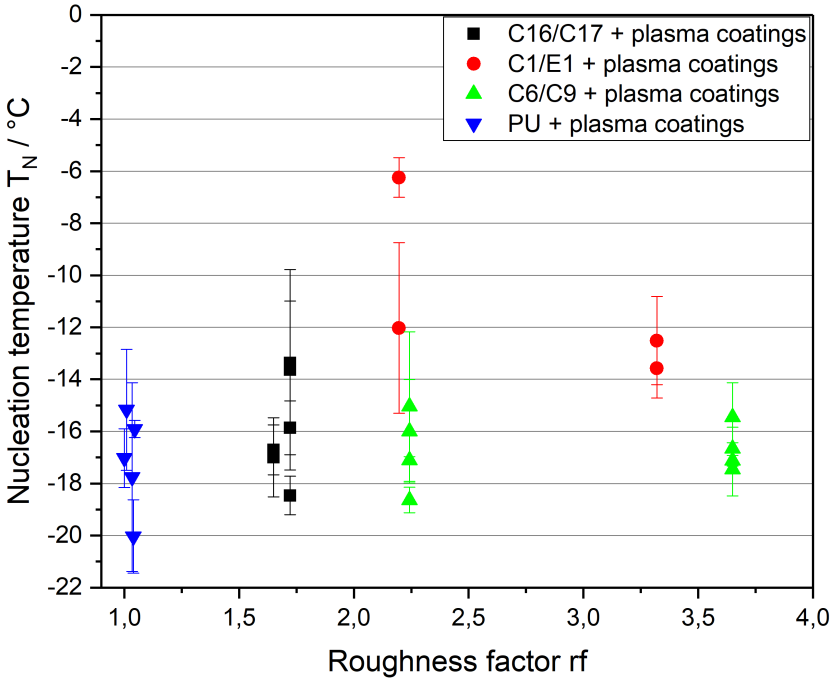


Figure 7.49.: Nucleation temperature $T_N$ (mean value) of the flat and microstructured surfaces in dependence of the micrometer roughness $rf$.

For each roughness factor value, the mean measured nucleation temperatures vary which can be attributed to different water-surface contact areas and nanoroughness values. A slight increase in nucleation temperature with increasing roughness value can be seen compared to the flat PU surfaces.

As the Cassie-Baxter state could not be stabilized during the cooling process, a higher micrometer roughness value has led to a larger water-surface interface area in Wenzel state or a mixed wetting state and therefore also to a larger ice nucleation probability and higher nucleation temperature. However, the main influence is the nanoroughness of the plasma coatings which is similar on the different microstructures leading to similar nucleation temperatures.

### Correlation of measured crystallization times $t_C$ with the surface wetting behavior

If nucleation has occured, the freezing of the water drop is determined by the crystallization process. If the water drop is not fully crystallized yet, some of the water can still be

removed by external forces. The crystallization times depend on the amount of latent heat released and the heat transfer rate through the ice-surface interface. If the water drop freezes in Cassie-Baxter state or a mixed state close to it, the crystallization time is enhanced by the lower ice-surface interface and the insulating air pockets between the microstructures under the drop. The calculated crystallization times (see equation 3.55 in the chapter on theoretical basics of icing, 3.2.4) of a 25 µl water drop in different wetting states are shown in Figure 7.50 for comparison with the measured values.

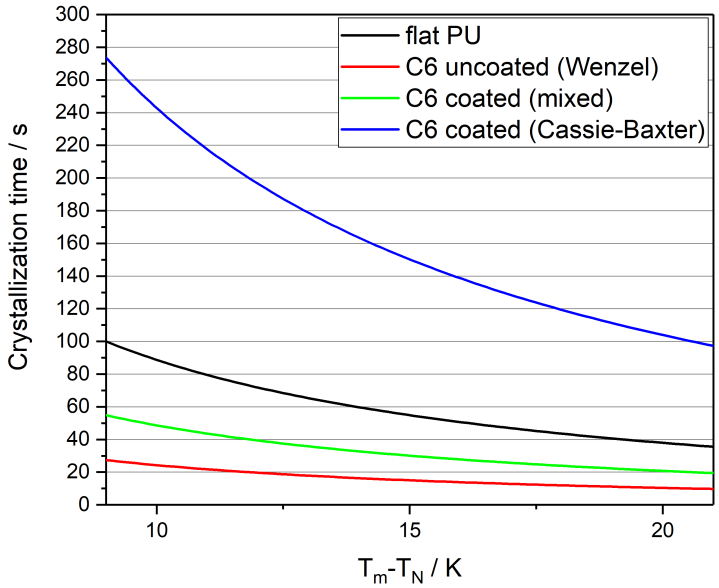


Figure 7.50.: Theoretical crystallization times of a 25 µl water drop on flat PU and uncoated or plasma-coated microstructure C6 in dependence of the supercooling $T_\mathrm{m} - T_\mathrm{N}$. The Wenzel state ($f_\mathrm{sl} = 1$) was assumed on uncoated C6 and a mixed ($f_\mathrm{sl} = 0.5$) or Cassie-Baxter state ($f_\mathrm{sl} = 0.1$) was assumed on HMDSO (60 W) plasma coated C6.

It is assumed that the crystallization times were enhanced by the superhydrophobic surfaces. Figure 7.51 and Figure 7.52 show the mean measured crystallization times of all types of the examined surfaces correlated with the corresponding mean values of the static water contact angle and surface free energy. The surfaces include the quadratically arranged microstructures C16 and C17, the most hydrophobic hexagonally arranged microstructures C6 and C9 and the flat PU and technical material surfaces.

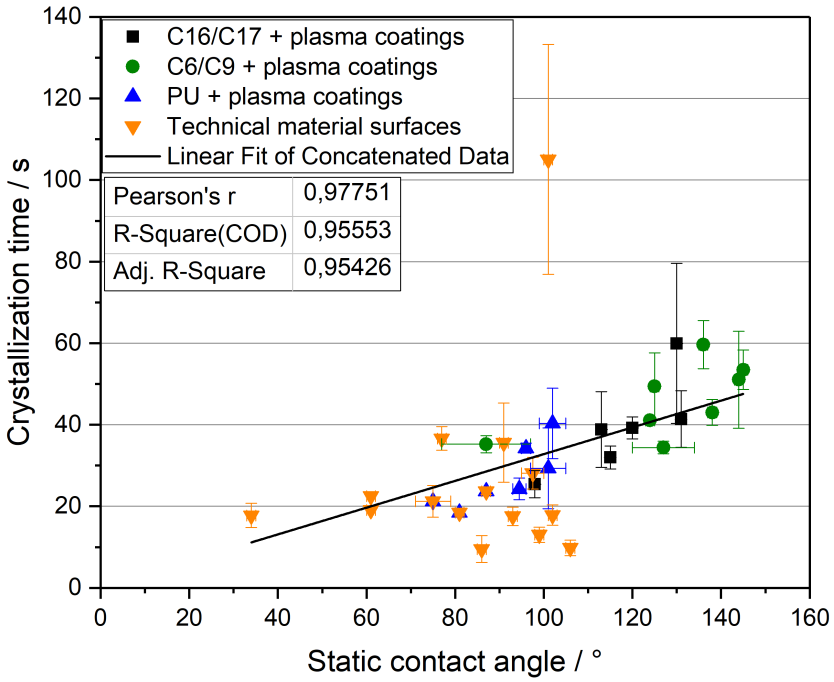


Figure 7.51.: Crystallization times $t_C$ (mean value) of the flat and microstructured surfaces in dependence of the static water contact angle. The solid line is the linear best fit.

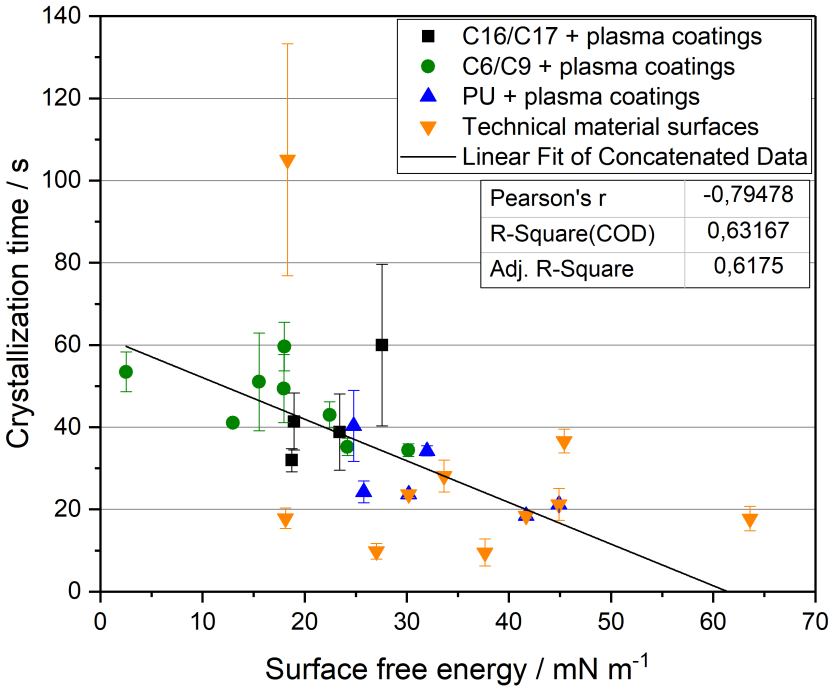


Figure 7.52.: Crystallization times $t_C$ (mean value) of the flat and microstructured surfaces in dependence of the surface free energy. The solid line is the linear best fit.

The measurements show a clear increase of crystallization time with an increasing static water contact angle or a decreasing surface free energy. The crystallization time is increased by a decreased heat transfer rate of the latent heat during crystallization.

On the flat samples, the heat transfer rate is determined by the water-surface interface area which decreases with an increasing contact angle or a decreasing surface free energy of the material. The correlation can also be seen for the microstructured samples, although the water-interface area cannot be directly derived from the contact angle or the notional surface free energy, because the different wetting states have to be regarded additionally. The closer the water drop wetting state is to the Cassie-Baxter state, the better the isolation because of the air-filled gaps is, which leads to a decreased heat transfer rate and increased crystallization time. As long as the water drop is not fully frozen, the liquid part can be taken off the surface easily, which is a contribution to the anti-ice functionality of the surface.

### Correlation of measured crystallization times $t_C$ with the surface micrometer roughness

As the contact angle measurements have shown, the water drops were not in Cassie-Baxter state, but in a mixed wetting state on the microstructured samples, resulting in an increased water-surface interface area. However, even in the mixed wetting state some air remains between the microstructures under the drop which would reduce the heat transfer rate and increase the crystallization time. The insulating amount of air between the microstructures under a water drop should be maximized and the ice-surface interface area minimized in order to minimize the heat transfer for cooldown or crystallization of a water drop.

The mean measured crystallization times of all types of the examined surfaces are correlated with the micrometer roughness values $rf = A_{sl}/A_f = 1 + \eta \cdot (A_L + A_T - A_B)$ in Figure 7.53.

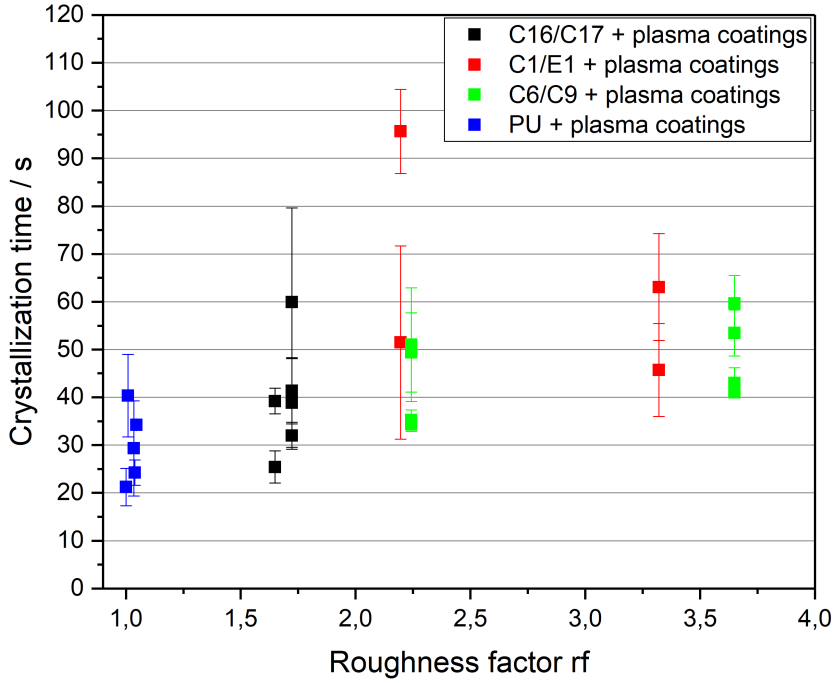


Figure 7.53.: Crystallization times $t_C$ (mean value) of all the examined surfaces in dependence of the micrometer roughness $rf$.

Varying crystallization times were measured for each roughness factor (microstructure), which is caused by the different wetting states, dependent on the varying nanoroughness and surface chemical groups. Overall, the crystallization times are clearly increasing with an increasing micrometer roughness value $rf$. With an increasing roughness factor rf the water wetting state goes from a Wenzel state or mixed state close to Wenzel towards a mixed state close to Cassie-Baxter state. This increases the amount of air within the heterogeneous solid-air interface under the water drop and lowers the heat transfer during crystallization.

The mixed wetting state was pushed towards a Cassie-Baxter state and the crystallization time was increased by an increasing roughness factor.

### Summary of the anti-icing behavior measurements

The hypothesis was that the nucleation temperatures could be lowered and the crystallization durations could be enhanced by the superhydrophobic PU surfaces with mi-

crostructure diameters of 35 µm and above and the described plasma coatings.

In the static freezing experiment, the nucleation of water drops could be delayed and the total freezing time prolonged on the functionalized PU surfaces at a constant surface temperature of -20 °C. The HMDSO 60 W plasma coating caused the nucleation delay time. The crystallization time was increased by the lower heat transfer in a mixed wetting state close to Cassie-Baxter state on the microstructure C6, especially with the etched HMDSO 60 W plasma coating with an increased nanoroughness.

The dynamic freezing experiment showed that the mean nucleation temperature could be reduced from -12 °C on a hydrophilic copper surface or -17 °C on an uncoated PU surface down to -20 °C on the flat, HMDSO 60 W plasma-coated PU surfaces. No further reduction of the mean nucleation temperature could be measured on the microstructured, superhydrophobic PU surfaces compared to the flat, plasma-coated PU surfaces because the water-surface interface area could not be reduced by a stable Cassie-Baxter state and the nanostructures did not have the right geometrical dimensions. The mean crystallization time could be enhanced from about 20 s on the flat, uncoated PU surface to about 60 s on the superhydrophobic surfaces.

With further optimization of the micro- and nanostructures a better stabilization of the Cassie-Baxter state, a further increased crystallization time, a further reduction of the nucleation temperature and therefore also a further increase of the nucleation delay time and overall freezing time could be achieved.

# 8. Summary

The central hypothesis of this thesis is that superhydrophobic polyurethane films created by hot embossing and low pressure plasma processes with microstructure base diameters above 35 µm show simultaneously good water-repellent properties, low ice adhesion and reduced icing (delayed freezing characteristics of water drops) for application as a passive de- and anti-icing method, in particular when compared to reference surfaces, like common technical material surfaces and commercial anti-ice coatings. Therefore, a superhydrophobic surface should be created on a PU film by functionalization with a hot embossing process and different plasma processes (PECVD, plasma etching). The dependence of the resulting surface characteristics on the process parameters should be analyzed. The wetting, de- and anti-icing behavior should be characterized by adequate test methods.

Several aliphatic, thermoplastic PU films were characterized for their thermal and chemical properties by DSC and IR spectroscopy. They showed similar IR spectra and in most cases also similar DSC curves with a melting range from about 65 °C to 95 °C with a peak at about 80 °C. Relevant technical material surfaces and available commercial anti-ice surface coatings were characterized as well for their wetting, de- and anti-icing behavior and compared with the functionalized PU films.

The hot embossing process parameters were determined and optimized. The first and second embossing stamps (no. 1 and 2) with ns-pulsed laser-drilled negative microstructures of different shape, size and distance were acquired and multiple test series in a heatable plate press were done to find the optimal embossing temperature and pressure at around 85 °C and 150 bar. Further chromated copper embossing stamps (no. 3.1 and 3.2) with microstructures of smaller size (H = 15 µm to 140 µm, D = 35 µm to 275 µm) and distance (P = 50 µm to 500 µm) were used for the sample preparations. The microstructures were hexagonally arranged and of cylindrical, elliptical and linear

(side by side arrangement) shape with base diameters or widths above 35 µm. Elliptical and linear microstructures were included in order to create a possible macroscopic, direction-dependent wetting behavior for directed roll-off of the water drops. They were characterized by light microscopy, laser scanning microscopy and scanning electron microscopy. The reproducibility of the microstructure shape, various embossing times and various removal temperatures of the PU film were analyzed as well. The hot embossing method produces reproducible microstructures at an optimal embossing time of five minutes. If the removal temperature of the PU film from the stamp is above 40 °C, it does not have an influence on the structure height.

Hydrophobic plasma polymers using different fluorocarbon precursors and HMDSO were deposited on flat and microstructured samples. The aim was to create superhydrophobic surfaces with a hierarchical micro- and nanostructure inspired by the surface of a Lotus leaf. Therefore, not only the established plasma polymers ($C_XF_Y$ (50 W), HMDSO (60 W)) were deposited, but also coatings with an increased nanoroughness. This was done by etching the plasma polymers with argon (100 W, 200 W and 300 W) or oxygen (100 W) plasmas, etching the PU film by an oxygen plasma (200 W, for the $C_3F_6$ plasma coating), or increasing the process power (HMDSO (200 W)). The nanoscale roughness was analyzed by AFM, the film thickness by spectroscopic ellipsometry, the surface chemistry by ESCA and the overall chemistry by IR spectroscopy. In all cases, about 200 nm thick plasma coatings were deposited. The Ar- and $O_2$-plasma etching of the plasma polymers led to a smoother surface. However, increased surface nanoroughness values could be produced by either $O_2$-etching (200 W) the PU film before coating (with $C_3F_6$ at 50 W) or by varying the HMDSO plasma power (increase to 200 W).

The stability of the microstructures and plasma coatings against erosion was characterized by several tests. The microstructures and plasma coatings are both stable against erosion by sand particles (sand trickling test, DIN 52348). However, an industrial (UV/water) weathering test (X1a CAM 180 test, SAE J-2527) nearly completely degraded the plasma coatings, and damaged also the PU film type 63630, whereas the type 63330 was stable (both from CMC Klebetechnik). The plasma coatings are degraded but still present after long-term outdoor exposure for about 13.5 months, from January 2015 to March 2016. Most important, they are stable against de-icing repeated for five times on the same spot. The silicone-like plasma coating is more suitable because it is more stable against repeated de-icing than the fluorocarbon plasma coating accord-

ing to ESCA measurements. The optical properties of some functionalized PU films were characterized as well. The plasma coated PU film reduces the total transmission, equal to direct transmission, to about 90 % as compared to without any PU film. The microstructures do not reduce the total transmission, but lower the direct transmission to about 30 % and create diffuse transmission of nearly 60 %, therefore the transparency of the flat PU film is lost on the superhydrophobic PU films.

As the topic of icing is connected to water wetting, the wetting behavior of water on the functionalized PU surfaces was analyzed by advancing / receding contact angle measurements (water drops with 3 µl volume, increased / decreased by 10 µl). High advancing contact angles of more than 150° and contact angle hystereses below 10°, which are characteristic for a superhydrophobic surface, could be measured on the best samples (e.g. hexagonally arranged, cylindrical microstructures C6 and C9 with base diameters of 35 µm). Some elliptical microstructures (E1 and E2) reached the superhydrophobic state without showing a macroscopic, direction-dependent wetting behavior, whereas the linear microstructures showed a macroscopic, direction-dependent wetting behavior (highest contact angles at parallel view) but did not reach the superhydrophobic wetting regime. The advancing contact angle values were compared to the theoretical limits given by the Wenzel and Cassie-Baxter wetting states, calculated with advancing contact angles for a PU and a fluorocarbon plasma polymer surface. The transition from a mixed state close to Cassie-Baxter to the Wenzel state with increasing pitch/diameter ($P/d$) factors could be seen for the measurement values. Additional static contact angle measurements with diiodomethane (DIM) were made for determination of the surface free energies of the relevant surfaces. Furthermore, fluorescence laser scanning microscopy images (inverse mode) for determination of the wetting state by visualization of the water interface underneath the droplets on the uncoated and plasma-coated microstructures C6, C9 and C16 were taken. The different wetting states on uncoated and plasma-coated samples could be visualized. The first aim of creation of a superhydrophobic surface on PU films by hot embossing and plasma coating was reached by the microstructures with correct geometrical parameters (base diameters of 35 µm and pitch values of 50 µm).

Following the analysis of their wetting behavior, the tensile ice adhesion on the functionalized PU surfaces was measured in a newly developed ice test chamber at -20 °C by pulling off large ice cylinders (about 4 mm diameter, corresponding to large rain drops) connected to a force sensor. With this ice test chamber, fast cooling down to a target

temperature with controlled humidity is possible. The chamber wall, ground and sample temperatures and the air temperature and relative humidity were monitored by USB-linked sensors. Highly purified water (<0.056 µS/cm) inside of a cylinder (aluminum or polycarbonate) was placed on the surface, then the surface and the water cylinder were cooled down simultaneously to about -20 °C. The ice test cylinder diameters at the interface correlating with the ice-surface interface areas were determined by images of an industrial high-speed camera with a zoom objective and an image analysis software. The ice adhesion correlates well with the wetting behavior (equilibrium or practical work of adhesion of water) or surface free energy only on the flat plasma polymer samples. The metal surfaces showed lower ice failure strengths because of cohesive breaks caused by larger microcracks created by higher local stresses at the interface. In contrast, the failure strengths on the polymeric surfaces were higher because of smaller initial microcracks. The ice adhesion is reported to be temperature dependent, but for these samples it was not measured at other temperatures yet. The ice adhesion values on these flat samples from simultaneous cool-down (water cylinder of 4 mm diameter) differ in parts from the ice adhesion values of previous research work obtained by applying warm water (smaller drop diameters) on a cold surface, and therefore absolute values should not be compared directly. As the water of the test cylinder transitions from Cassie-Baxter to Wenzel state on the superhydrophobic PU surfaces during the cooling or freezing process, the ice adhesion is significantly increased because of the increased ice-surface interface area. This was also reported in literature. It is increased even further on the plasma-coated microstructures, most likely because of a mechanical interlocking effect between the ice and the nanostructures of the plasma polymers. Therefore, the hypothesis that superhydrophobic surfaces with microstructure base diameters of 35 µm and above show low ice adhesion in vertical pull-off mode after simultaneous cool-down of the surface and the water to -20 °C could not be confirmed.

The icing behavior of the functionalized PU surfaces and the additional surfaces for comparison was characterized by freezing of water droplets. Therefore, water drop freezing experiments were carried out in a thermodynamically equilibrated (constant surface temperature, static experiment) and in a quasi-steady (slowly decreasing surface temperature, dynamic experiment) way.

In the static experiment, carried out in the cooling chamber of the contact angle measurement device, room temperature water drops of 15 µl (corresponding to medium to

large rain drops) were given onto a cold surface with a constant temperature of -20 °C and different characteristic freezing times (freezing delay time, duration of crystallization and total freezing time) were recorded. On the flat samples, the freezing delay times and total freezing times could be extended by the plasma coatings. On the microstructured and plasma-coated samples the nucleation could be delayed even further (increased freezing delay times), but the supercooling of the droplets was not always reproducible and the surface temperature was not consistent. The longest total freezing time was achieved on the plasma-coated, etched and finally thinly coated (HMDSO 60 W), microstructured (most superhydrophobic) sample.

The dynamic experiment was done in the new icing test chamber. The sample surface, the 25 µl water droplets (corresponding to large rain drops) and the surrounding air were cooled down in a quasi-steady state by a constant cooling rate of 1 K/min. In this way, the characteristic nucleation and freezing behavior dependent only on surface chemistry and topography was determined for each surface. The water drop temperature curves were recorded by an IR camera. From these temperature curves, the measured nucleation temperatures and crystallization times were derived and visualized by box plots. The mean measured values were compared to the expected values determined by thermodynamic calculations. The nucleation temperatures correlate with the surface chemistry on the flat, plasma coated PU samples. They are lowered by the $C_3F_6$ (50 W) and HMDSO (60 W) plasma polymers to about -18 °C and -20 °C, respectively. Although expected because of a smaller surface-water interface area in Cassie-Baxter state, among the microstructured samples no lowered nucleation temperature in comparison to the flat samples can be seen. In fact, the nucleation temperature is sometimes even higher on the microstructured, plasma-coated PU films. If the wetting transitions to a Wenzel state on these microstructures, the nucleation temperature is raised because of the increased nucleation rate by the increased surface-water interface area. This shows that the microstructures with base diameters above 35 µm do not always show a stable Cassie-Baxter state, but sometimes a Cassie-to-Wenzel transition during simultaneous cooling of the water drops and the surface. The nucleation temperatures and crystallization times were correlated with the surface properties. On the microstructured samples, the nucleation temperature does not change significantly with varying contact angles or surface free energies. It stays nearly the same on the microstructured surfaces with increasing roughness factors, except for some samples where wetting in the Wen-

zel state occured. The crystallization times correlate well with the wetting behavior. They increase with an increasing water contact angle, decreasing surface free energy or increasing roughness factor because of the latent heat transfer rate being dependent on the wetting state and interface area.

To summarize, the crystallization time can be enhanced by the microstructures, if a stable Cassie-Baxter state or mixed state close to it is achieved. The nucleation temperature depends mainly on the surface nanostructures which are determined by the plasma polymer coatings. The nanostructures of the plasma coatings are not optimally sized yet, with a mean surface roughness radius of curvature $R$ in the range of 2000 nm to 40000 nm as shown by AFM measurements. For a significant nucleation temperature decrease, a mean surface roughness radius of curvature $R < 10r_c$ (about 20 nm to 30 nm) is needed on 100 % of the surface. The nucleation temperatures could not be reduced further by the plasma-coated microstructures compared to the flat plasma polymer coatings and was sometimes even increased because of wetting in the Wenzel state. The icing experiments have shown that these superhydrophobic PU surfaces with microstructure base diameters above 35 µm are not automatically also icephobic and the third main hypothesis could not be confirmed.

Many different anti-ice properties have to be fulfilled by the surface simultaneously, like high water repellency, repellency against impacting supercooled droplets (including supercooled large droplets, SLD, in freezing drizzle or freezing rain with diameters above 0.1 mm), low ice adhesion, low nucleation temperature and even prevention of condensation and frost formation, which is not achieved by these functionalized PU films yet. Therefore, these functionalized PU films can only be used in combination with conventional thermal anti- and de-icing systems so far. The relevant geometrical dimensions of both the microstructures (diameter $D$, pitch $P$) and the nanostructures (radius of curvature $R$) need to be reduced for improved anti- and de-icing properties.

# 9. Outlook

As the de- and anti-icing behavior of the functionalized PU films is not convincing yet, the micro- and nanoroughness needs to be improved. The correct model and physical laws regarding the size for a sufficiently stable Cassie-Baxter state have to be followed. The size and pitch values of the microstructures have to become smaller, but the lower limit with a conventional "ns pulsed" laser is reached by our hot embossing stamps. For smaller microstructures, a "ps pulsed" laser micromachining process or a (reactive) ion beam etching process, e.g. the Bosch process, is needed. However, it might be difficult to apply ion beam etching processes on metals like steel or copper. A plasma etching process (soft lithography) could also create an adequate microroughness directly on a polyurethane film. Then, there would be no need for an optimized hot embossing stamp.

If the nanoroughness could be adjusted precisely and made stable against external influences, the surface might prevent or reduce condensation and frost formation. Some condensation and frost formation tests with the functionalized PU samples were made in the freezing chamber with the lid taken off, so that ambient air provided the humidity. More data from condensation, rime ice and frost formation tests has to be collected, evaluated and compared to the relevant physical models.

Also some experiments with impacting droplets from a height of about half a meter were done with the industrial high speed camera photonfocus DR1-1312, but the drops only partly bounced off from the superhydrophobic surfaces. More tests have to be made, including impacting supercooled large droplets, and the measurements have to be related to the physical models on the topic of rebounding water drops.

If the micro- and nanostructures can be optimized as proposed, further ice adhesion and icing tests should lead to good and reproducible de- and anti-icing values. Then, the processes could be scaled-up, first to a pilot plant scale and in a second step to an industrial plant scale. If larger areas of anti-ice PU films could be functionalized, they

should be applied in outdoor field tests, e.g. on wind energy turbines or airplanes, in order to assess their performance.

Apart from the micro-/nanostructured anti-ice surfaces, the antifreeze protein (AFP) coatings should be further developed. These proteins are too expensive for industrial application if isolated from natural sources, but they can be synthesized chemically or by molecular biotechnology. The other concepts for anti-ice surfaces are also interesting for further research. These include more stable closed-cell microstructures, e.g. by inkjet printing of PU dispersions, slippery liquid infused porous plasma coatings, or coatings with embedded polymer particles that automatically release freezing point depressant liquids in icing conditions.

# Bibliography


[1] Ganesan, Swarupini: *Design of plasma deposited anti-ice coatings on microstructured polyurethane films.* Stuttgart, University of Stuttgart, Master thesis, 2013 (document), 3.2, 3.8, 4.1, 6.2.2, 6.5

[2] Dannehl, Nadine: *Untersuchung der Eisbildung auf strukturierten, plasmabeschichteten Oberflächen.* Gießen and Stuttgart, University of Gießen, Master thesis, 2015 (document), 3.2.4, 4.2, 4.4.1, 5.4.1, 5.5, 6.2.2, 6.5, 6.6, 6.3.5, 6.8, 6.10, 6.11, 7.36, 7.3.1, 7.37, 7.38, 7.39

[3] Botta, G. ; Cavaliere, M. ; Holttinen, H.: *Ice accretion at acqua spruzza and its effects on wind turbine operation and loss of energy production: BOREAS IV.* Hetta, Finland, 1998 1.1

[4] Frohboese, Peter ; Anders, Andreas: Effects of Icing on Wind Turbine Fatigue Loads. In: *Journal of Physics: Conference Series* 75 (2007), S. 12061. http://dx.doi.org/10.1088/1742-6596/75/1/012061. – DOI 10.1088/1742–6596/75/1/012061. – ISSN 1742–6596 1.1

[5] Parent, Olivier ; Ilinca, Adrian: Anti-icing and de-icing techniques for wind turbines: Critical review. In: *Cold Regions Science and Technology* 65 (2011), Nr. 1, S. 88–96. http://dx.doi.org/10.1016/j.coldregions.2010.01.005. – DOI 10.1016/j.coldregions.2010.01.005. – ISSN 0165232X 1.1

[6] Laakso, T. ; Talhaug, L. ; Ronsten, G. ; Horbaty, R. ; Baring-Gould, I. ; Lacroix, A. ; Peltola, E. ; Wallenius, T. ; Durstewitz, M. ; IEA Program for Research, Development and Deployment of Wind Energy Conversion Systems (Hrsg.): *Wind energy in cold climates: Final report: IEA Task 19.* 2009 1.1

[7] Durstewitz, M. ; Laakso, T. ; Talhaug, L. ; Ronsten, G. ; Cattin, R. ; Baring-Gould, I. ; Lacroix, A. ; Peltola, E. ; Wallenius, T. ; Hulkkonen, M. ; Krenn, A.: *Wind Energy in Cold Climates: Cold Climate Challenges: IEA Wind Task 19.* Brussels, Belgium, 16.03.2011 (EWEA 2011 side event) 1.1

[8] Farzaneh, M.: *Atmospheric icing of power networks*. Dordrecht and London : Springer, 2008 http://www.worldcat.org/oclc/272307944. – ISBN 978–1–4020–8530–7 1.1

[9] Laforte, J.L ; Allaire, M.A ; Laflamme, J.: State-of-the-art on power line deicing. In: *Atmospheric Research* 46 (1998), Nr. 1-2, S. 143–158. http://dx.doi.org/10.1016/S0169-8095(97)00057-4. – DOI 10.1016/S0169–8095(97)00057–4. – ISSN 01698095 1.1

[10] Mosher, Frederick ; Schaum, Debbie ; Herbster, Chris ; Guinn, Tom: *Analysis of Causes of Icing Conditions which Contributed to the Crash of Continental Flight 3407*. http://commons.erau.edu/db-applied-aviation/21. Version: 2010 1.1

[11] Ministerium für Bauen und Verkehr (MBV), Ministerium für Umwelt und Naturschutz, Landwirtschaft und Verbraucherschutz (MUNLV), Ministerium für Wirtschaft, Mittelstand und Energie: *Grundsätze für Planung und Genehmigung von Windkraftanlagen - WKA-Erl. MBI. NRW. 2005 S. 2310*. 21.10.2005 1.1

[12] Bundesministerium für Verkehr, Bau und Stadtentwicklung: *Anlage 2.7/12 zur Richtlinie "Windenergieanlagen; Einwirkungen und Standsicherheitsnachweise für Turm und Gründung"*. 2012 1.1

[13] Scholz, Dieter ; MSME, Aircraft Design and Systems Group (AERO), Department Fahrzeugtechnik und Flugzeugbau (Hrsg.): *Flugzeugsysteme: Kapitel 9 - Eis- und Regenschutz (ATA 30)*. http://handbuch.profscholz.de. Version: 2013 1.1, 2.1, 2.2.1, 2.2.2, 2.2.3, 3.2.4

[14] Fay, L., Shi, X.: Environmental Impacts of Chemicals for Snow and Ice Control: State of the Knowledge. In: *Water Air Soil Pollution* 223 (2012), Nr. 5, S. 2751–2770. http://dx.doi.org/10.1007/s11270-011-1064-6. – DOI 10.1007/s11270–011–1064–6 1.1

[15] Ramakrishna, D.M., Viraraghavan, T.: Environmental impact of chemical deicers: A review. In: *Water Air Soil Pollution* 166 (2005), Nr. 1, S. 49–63. http://dx.doi.org/10.1007/s11270-005-8265-9. – DOI 10.1007/s11270–005–8265–9 1.1

[16] Barz, J. ; Haupt, M. ; Vohrer, U. ; Hilgers, H. ; Oehr, C.: Ultrathin carbon–fluorine film processing. In: *Surface and Coatings Technology* 200 (2005), Nr. 1-4, S. 453–457. http://dx.doi.org/10.1016/j.surfcoat.2005.02.064. – DOI 10.1016/j.surfcoat.2005.02.064. – ISSN 02578972 1.2, 2.3.3

[17] Haupt, Michael ; Barz, Jakob ; Vohrer, Uwe ; Hilgers, Heinz ; Oehr, Christian: Fluor-Kohlenstoff-Nanoschichten zur gezielten OberflächenfunktionalisierungFluorine-Carbon Nano Coatings for Specific Surface Functionalization. In: *Vakuum in Forschung und Praxis* 17 (2005), Nr. 6, S. 329–335. http://dx.doi.org/10.1002/vipr.200500272. – DOI 10.1002/vipr.200500272. – ISSN 0947–076X 1.2

[18] Jacoby, B. ; Bock, W. ; Haupt, M. ; Hilgers, H. ; Kopnarski, M. ; Molter, J. ; Oehr, C. ; Rühle, T. ; Wahl, M.: Abscheidung, Charakterisierung und Anwendung von Plasma-Polymerschichten auf HMDSO-Basis. In: *Vakuum in Forschung und Praxis* 18 (2006), Nr. 4, S. 12–18. http://dx.doi.org/10.1002/vipr.200600289. – DOI 10.1002/vipr.200600289. – ISSN 0947–076X 1.2, 2.3.3, 3.1.3

[19] Haupt, Michael ; Bergrath, Beate ; Barz, Jakob ; Oehr, Christian ; Wemhöner, Jens: Lager wie geschmiert. In: *Vakuum in Forschung und Praxis* 25 (2013), Nr. 3, S. 38–43. http://dx.doi.org/10.1002/vipr.201300521. – DOI 10.1002/vipr.201300521. – ISSN 0947076X 1.2

[20] Haupt, Michael ; Barz, Jakob: Anti-Eis-Oberflächenbeschichtungen. In: *Vakuum in Forschung und Praxis* 27 (2015), Nr. 1, S. 28–32. http://dx.doi.org/10.1002/vipr.201500573. – DOI 10.1002/vipr.201500573. – ISSN 0947076X 1.2

[21] Federal Aviation Administration (FAA), Flight Standards Service: *Aviation Maintenance Technician-Airframe Handbook (FAA-H-8083-31): Volume 2: Chapter 15: Ice and Rain Protection*. Bd. 2. Oklahoma City : Airmen Testing Standards Branch, 2012 2.1

[22] Sonnenschein, Mark F.: *Polyurethanes: Science, technology, markets, and trends*. Hoboken, New Jersey : Wiley, 2015 (Wiley series on polymer engineering and technology). – ISBN 9781118737835 2.1, 3.1.1, 3.1.1, 3.1.1

[23] Federal Aviation Administration ; Federal Aviation Administration (Hrsg.): *International De/Anti-icing chapter: Part of the Standardized International Aircraft Ground Deice Program (SIAGDP): FAA 121*. https://www.faa.gov/other_visit/aviation_industry/airline_operators/airline_safety/deicing/. Version: 2010 2.2.1, 2.2.2

[24] Schutzrecht US 20110011056 A1 . (2011). Le Docte, T. (Erfinder); Aircelle (Anmelder)., *Piezoelectric De-Icing of an Air Inlet* 2.2.1

[25] Schutzrecht US 20100288882 A1 . (2010). Olson, R. A. ; Bridgeford, M. R. (Erfinder); Ice Management Systems, Inc. (Anmelder)., *Electro-expulsive de-icing system for aircraft and other applications* 2.2.1

[26] Schutzrecht US 5584450 . (1996). Pisarski, N. (Erfinder); B. F. Goodrich Company (Anmelder)., *Metal clad electro-expulsive deicer with segmented elements* 2.2.1

[27] Schutzrecht US 20110259880 A1 . (2011). Petrenko, V. F. ; Sullivan, C. (Erfinder); Icecode LLC (Anmelder)., *Mechanical scraper system with synchronized pulse electrothermal deicing* 2.2.1

[28] Schutzrecht US 5686003 A . (1997). Ingram, R. B. ; Gerardi, J. J. (Erfinder); Innovative Dynamics Inc. (Anmelder)., *Shape memory alloy de-icing technology* 2.2.1

[29] Feeney, Robert E. ; Yeh, Y.: Antifreeze proteins: structures and mechanisms of function. In: *Chemical Reviews* 96 (1996), Nr. 2, S. 601–618 2.2.2, 2.3.1, 3.2.4

[30] Sarkezi-Selsky, Patrick: *Entwicklung, Herstellung und Umwelteigenschaften von taumittelfreisetzenden Polymerpartikeln.* Stuttgart, University of Stuttgart, Bachelor thesis, 2014 2.2.2

[31] Schutzrecht JP 2004025925 A1 . (2004). Tetsuo, K. ; Rikio, T. (Erfinder); Sumitomo Electric Ind Ltd (Anmelder)., *Electric heating type anti-icing de-icing device for aircraft fixed wings* 2.2.3

[32] Schutzrecht JP 2004017878 A1 . (2004). Tetsuo, K. ; Rikio, T. (Erfinder); Sumitomo Electric Ind Ltd (Anmelder)., *Electric heating type ice prevention removal device for aircraft fixed wing* 2.2.3

[33] Schutzrecht US 20080166563 A1 . (2008). Brittingham, D. L. ; Prybyla, S. G. ; Christy, D. P. (Erfinder); Goodrich Corporation (Anmelder)., *Electrothermal heater made from thermally conducting electrically insulating polymer material* 2.2.3

[34] Schutzrecht WO 2013035778 A1 . (2013). Asaoka, H. ; Sakamoto, T. (Erfinder); Nippon Sheet Glass Company Ltd. (Anmelder)., *Laminated glass with embedded heating element* 2.2.3

[35] Schutzrecht US 6194685 B1 . (2001). Rutherford, R. B. (Erfinder); Northcoast Technologies (Anmelder)., *De-ice and anti-ice system and method for aircraft surfaces* 2.2.3

[36] Schutzrecht WO 2012100178 A1 . (2012). Tour, J. M. ; Volman, V. ; Zhu, Y. (Erfinder); William Marsh Rice University, Lockheed Martin Corporation (Anmelder)., *Graphene-based thin films in heat circuits and methods of making the same* 2.2.3

[37] Schutzrecht US20130043342 . (2013). Nordin, P. ; Strindberg, G. (Erfinder); SAAB AB (Anmelder)., *Multifunctional de-icing/anti-icing system* 2.2.3

[38] Delaney, K. ; Massey, T. R. ; Battelle (Hrsg.): *Battelle's Heat-Coat Anti-Icing Technology for Drones Passes Key Milestone in Wind Tunnel Testing.* `http://www.battelle.org/newsroom/press-releases/battelle-heatcoat-anti-icing-technology-for-drones-passes-milestone`. Version: 2015 2.2.3

[39] Schutzrecht WO 0072635 A1 . (2000). Degand, E. ; Maza, C. (Erfinder); Glaverbel (Anmelder)., *Automotive glazing panel having an electrically heatable solar control coating layer* 2.2.3

[40] Schutzrecht US 4668270 A1 . (1987). Ramus, K. J. (Erfinder); Ford Motor Company (Anmelder)., *Method of making an electrically heated, glass vision unit* 2.2.3

[41] Schutzrecht WO 2012031908 A1 . (2012). Lisinski, S. ; Phan, D. C. ; Schall, G. (Erfinder); Saint-Gobain Glass France (Anmelder)., *Transparent panel having a heatable coating* 2.2.3

[42] Schutzrecht WO 2012110381 A1 . (2012). Reul, B. ; Lisinski, S. ; Schall, G. ; Velden, S. (Erfinder); Saint-Gobain Glass France (Anmelder)., *Transparent pane with an electrical heating layer and production process therefor* 2.2.3

[43] Schutzrecht EP 0376371 A2 . (1989). McLaren, D. ; Orr, W. W. (Erfinder); The Boeing Company (Anmelder)., *Thermal anti-icing system for aircraft* 2.2.3

[44] ENERCON GmbH: Technologie-Spitzenreiter beim Rotorblattenteisungssystem: Validierung der ENERCON Rotorblattenteisung abgeschlossen. In: *Windblatt, Enercon Magazin für Windenergie* (2010), Nr. 4, S. 8–9 2.2.3

[45] Schutzrecht US 5484122 A . (1996). DeSalve, D. W. (Erfinder); Parker-Hannifin Corporation (Anmelder)., *Turbine Exhaust Gas Anti-Ice System* 2.2.3

[46] Schutzrecht US 5615849 A1 . (1997). Salisbury, J. T. (Erfinder); Salisbury, J. T. (Anmelder)., *Microwave deicing and anti-icing system for aircraft* 2.2.3

[47] Schutzrecht DE 19750198 A1 . (1999). Feher, L. ; Schnack, M. (Erfinder); Forschungszentrum Karlsruhe GmbH, DaimlerChrysler Aerospace Airbus GmbH (Anmelder)., *Enteisung von Flugzeugen mit Mikrowellen* 2.2.3

[48] Schultz, L. A. ; Minnick, P. V. ; NKF Engineering Inc., Arctic Technology Group (Hrsg.): *Feasibility of using lasers and infrared heaters as unrep icing countermeasures: Final report.* Annapolis, Maryland, 1989 2.2.3

[49] Butt, Hans-Jürgen ; Auernhammer, Günter ; Vollmer, Doris: Oberflächen mit Phobie. In: *Physik Journal* 14 (2015), Nr. 2, S. 25–30 2.3

[50] Wang, Jiadao ; Chen, Haosheng ; Sui, Tao ; Li, Ang ; Chen, Darong: Investigation on hydrophobicity of lotus leaf: Experiment and theory. In: *Plant Science* 176 (2009), Nr. 5, S. 687–695. http://dx.doi.org/10.1016/j.plantsci.2009.02.013. – DOI 10.1016/j.plantsci.2009.02.013. – ISSN 01689452 2.3

[51] Gao, Xuefeng ; Jiang, Lei: Water-repellent legs of water striders: Biophysics. In: *Nature* 432 (2004), 36. http://dx.doi.org/10.1038/432036a. – DOI 10.1038/432036a. – ISSN 0028–0836 2.3

[52] Schutzrecht US 4484409 A1 . (1984). Caple, G. ; Layton, R. G. (Erfinder); University Patents Inc. (Anmelder)., *Prevention of freezing at moderate supercooling using synthetic polymeric ice nucleation inhibitors* 2.3.1

[53] Schutzrecht WO 9630459 A1 . (1996). Fahy, G. (Erfinder); Organ Inc. and Life Resuscitation Technologies Inc. (Anmelder)., *Novel ice-controlling molecules and their applications* 2.3.1

[54] Schutzrecht WO 9918169 A1 . (1999). Fahy, G. (Erfinder); Life Science Holdings Inc. (Anmelder)., *Methods of using ice-controlling molecules* 2.3.1

[55] Schutzrecht US 5118792 A1 . (1992). Warren, G. J. ; Mueller, G. M. ; McKown, R. L. (Erfinder); DNA Plant Technology Corporation (Anmelder)., *Ice crystal growth suppression polypeptides and method of making* 2.3.1

[56] Meldolesi, Anna: GM fish ice cream. In: *Nature Biotechnology* 27 (2009), Nr. 8, S. 682. http://dx.doi.org/10.1038/nbt0809-682b. – DOI 10.1038/nbt0809–682b. – ISSN 1087–0156 2.3.1

[57] Charpentier, Thibaut V. J. ; Neville, Anne ; Millner, Paul ; Hewson, Rob ; Morina, Ardian: An Investigation of Freezing of Supercooled Water on Anti-Freeze Protein Modified Surfaces. In: *Journal of Bionic Engineering* 10 (2013), Nr. 2, S. 139–147. http://dx.doi.org/10.1016/S1672-6529(13)60208-5. – DOI 10.1016/S1672–6529(13)60208–5. – ISSN 16726529 2.3.1

[58] Esser-Kahn, Aaron P. ; Trang, Vivian ; Francis, Matthew B.: Incorporation of antifreeze proteins into polymer coatings using site-selective bioconjugation. In: *Journal of the American Chemical Society* 132 (2010), Nr. 38, S. 13264–13269.

http://dx.doi.org/10.1021/ja103038p. – DOI 10.1021/ja103038p. – ISSN 0002–7863 2.3.1

[59] Schutzrecht EP 2921539 A1 . (2015). Kim, Hong S. ; Kwon, Myong J. ; Oh, Seung J. ; Gwak, Yunho ; Kim, Young-Pil ; Park, Ji-In ; Jin, Eon S. (Erfinder); Samsung Electronics Co. Ltd. and Industry-University Cooperation Foundation (Anmelder)., *Antifreeze member* 2.3.1

[60] Schutzrecht EP 2960309 A1 . (2014). Scolan, Emmanuel (Erfinder); CSEM Centre Suisse d'Electronique et de Microtechnique SA (Anmelder)., *Method of treatment of outdoor equipment with a polysaccharide coating* 2.3.1

[61] Siegmann, K. ; Kaufmann, A. ; Hirayama, M. ; Bundesamt für Energie BFE, Forschungsprogramm Windenergie, CH (Hrsg.): *Anti-freeze Beschichtungen für Rotorblätter von Windenergieanlagen*. Bern, 18.12.2006 2.3.1

[62] Horbaty, R. ; Bundesamt für Energie BFE, CH (Hrsg.): *Forschungsprogramm Windenergie: Synthesebericht 2008 des BFE-Programmleiters*. Bern, 2009 2.3.1

[63] Schutzrecht US 20130101859 A1 . (2013). Hirayama, M. ; Siegmann, K. ; Meola, G. ; Schaefer, C. ; Daenhardt, K. (Erfinder); Clariant Finance (BVI) Ltd. (Anmelder)., *Surface coatings having anti-ice properties* 2.3.1, 2.3.3

[64] Schutzrecht WO 2009136186 A1 . (2009). Bauer, Karin ; Bolzmacher, Christian ; Friedberger, Alois ; Reidt, Ulrich (Erfinder); Airbus UK Ltd. (Anmelder)., *Surfaces with immobilized enzymes or anti-icing proteins* 2.3.1

[65] Schutzrecht EP 2248607 A1 . (2010). Heller, Christoph ; Reidt, Ulrich ; Friedberger, Alois ; Bauer, Karin (Erfinder); Airbus Operations Limited (Anmelder)., *Self-regenerating biocatalytic and/or anti-icing surface* 2.3.1

[66] Boreyko, Jonathan ; Chen, Chuan-Hua: Self-Propelled Dropwise Condensate on Superhydrophobic Surfaces. In: *Physical Review Letters* 103 (2009), Nr. 18. http://dx.doi.org/10.1103/PhysRevLett.103.184501. – DOI 10.1103/PhysRevLett.103.184501. – ISSN 0031–9007 2.3.2

[67] Zhang, Qiaolan ; He, Min ; Chen, Jing ; Wang, Jianjun ; Song, Yanlin ; Jiang, Lei: Anti-icing surfaces based on enhanced self-propelled jumping of condensed water microdroplets. In: *Chemical Communications* 49 (2013), Nr. 40, S. 4516. http://dx.doi.org/10.1039/c3cc40592c. – DOI 10.1039/c3cc40592c. – ISSN 1359–7345 2.3.2

[68] Wilson, Peter W. ; Lu, Weizhe ; Xu, Haojun ; Kim, Philseok ; Kreder, Michael J. ; Alvarenga, Jack ; Aizenberg, Joanna: Inhibition of ice nucleation by slippery liquid-infused porous surfaces (SLIPS). In: *Physical Chemistry Chemical Physics* 15 (2012), Nr. 2, S. 581. http://dx.doi.org/10.1039/c2cp43586a. – DOI 10.1039/c2cp43586a. – ISSN 1463–9076 2.3.2

[69] Nosonovsky, Michael: Slippery when wetted: Materials Science. In: *Nature* 2011 (2011), Nr. 477, S. 412–413. http://dx.doi.org/10.1038/477412a. – DOI 10.1038/477412a. – ISSN 0028–0836 2.3.2

[70] Chen, Jing ; Dou, Renmei ; Cui, Dapeng ; Zhang, Qiaolan ; Zhang, Yifan ; Xu, Fujian ; Zhou, Xin ; Wang, Jianjun ; Song, Yanlin ; Jiang, Lei: Robust Prototypical Anti-icing Coatings with a Self-lubricating Liquid Water Layer between Ice and Substrate. In: *ACS Applied Materials & Interfaces* (2013), S. 130510105547001. http://dx.doi.org/10.1021/am401004t. – DOI 10.1021/am401004t. – ISSN 1944–8244 2.3.2

[71] Stone, Howard A.: Ice-Phobic Surfaces That Are Wet. In: *ACS Nano* 6 (2012), Nr. 8, S. 6536–6540. http://dx.doi.org/10.1021/nn303372q. – DOI 10.1021/nn303372q. – ISSN 1936–0851 2.3.2

[72] Schutzrecht US 20080175987 A1 . (2008). Carter, J. T. (Erfinder); Carter (Anmelder)., *Active ice-phobic freeze-point reducing anti-ice coating and method for providing anti-ice protection to surfaces* 2.3.2

[73] Schutzrecht WO 2012141150 A1 . (2012). Mori, Y. ; Kishikawa, N. (Erfinder); Asahi glass company Ltd. (Anmelder)., *Functional article, article for transport equipment, article for construction, and composition for coating* 2.3.2

[74] Schutzrecht DE 102006004913 A1 . (2007). Esemann, H. ; Schultheis, B. (Erfinder); Schott AG (Anmelder)., *Erzeugnis mit einer die Vereisung verhindernden Beschichtung und Verfahren zu dessen Herstellung* 2.3.2

[75] Lv, Jianyong ; Song, Yanlin ; Jiang, Lei ; Wang, Jianjun: Bio-Inspired Strategies for Anti-Icing. In: *ACS Nano* 8 (2014), Nr. 4, S. 3152–3169. http://dx.doi.org/10.1021/nn406522n. – DOI 10.1021/nn406522n. – ISSN 1936–0851 2.3.3

[76] Volkswagen AG ; Volkswagen AG (Hrsg.): *Stressfrei durch den Autowinter*. http://autogramm.volkswagen.de/11_10/autoundtechnik/autoundtechnik_05.html. Version: 2010 (autogramm) 2.3.3

[77] Schutzrecht DE 4302375 A1 . (1994). Gartner, F. (Erfinder); Josef Gartner & Co. (Anmelder)., *Verwendung oder Anordnung einer die langwellige Strahlung gering emittierenden Beschichtung auf Oberflächen, insbesondere von Gebäuden* 2.3.3

[78] Schutzrecht US 5071709 A1 . (1991). Berquier, J. M. ; Ausserre, D. ; Leger, L. (Erfinder); Saint-Gobain Vitrage (Anmelder)., *Glazing provided with an anti-frost layer* 2.3.3

[79] Schutzrecht US 20050064101 A1 . (2005). Messere, R. ; Hebert, A.-S. ; Florentin, J.-M. (Erfinder); Saint-Gobain Vitrage (Anmelder)., *Transparent glazing and use thereof in a chilling chamber door comprising in particular a glazing under vacuum* 2.3.3

[80] Schutzrecht DE 20023626 U1 . (2005). Saint-Gobain Vitrage (Erfinder); Saint-Gobain Vitrage (Anmelder)., *Durchsichtige Verglasung und ihre Verwendung in einer Tür eines gekühlten Raumes die insbesondere eine evakuierte Verglasung enthält* 2.3.3

[81] Schutzrecht US 20050202178 A1 . (2005). Roche, J. M. ; Madireddi, S. C. ; Bernheim, E. A. ; Raglin, B. W. (Erfinder); Hussmann Corporation (Anmelder)., *Merchandisers having anti-fog coatings and methods for making the same* 2.3.3, 2.3.3

[82] Pruna, A. ; Ramiro, J. ; Belforte, L.: Preliminary study on different technological tools and polymeric materials towards superhydrophobic surfaces for automotive applications. In: *Journal of Physics and Chemistry of Solids* 74 (2013), Nr. 11, S. 1640–1645. http://dx.doi.org/10.1016/j.jpcs.2013.06.009. – DOI 10.1016/j.jpcs.2013.06.009. – ISSN 00223697 2.3.3

[83] Tadanaga, K. ; Katata, N. ; Minami, T.: Super-Water-Repellent Al2O3 Coating Films with High Transparency. In: *J. Am. Ceram. Soc.* 80 (1997), Nr. 4, 1040–1042. http://dx.doi.org/10.1111/j.1151-2916.1997.tb02943.x. – DOI 10.1111/j.1151–2916.1997.tb02943.x 2.3.3

[84] Di Mundo, Rosa ; Palumbo, Fabio ; d'Agostino, Riccardo: Nanotexturing of polystyrene surface in fluorocarbon plasmas: from sticky to slippery superhydrophobicity. In: *Langmuir : the ACS journal of surfaces and colloids* 24 (2008), Nr. 9, S. 5044–5051. http://dx.doi.org/10.1021/la800059a. – DOI 10.1021/la800059a. – ISSN 1520–5827 2.3.3, 6.3.2

[85] Frost and Sullivan: *Advances in Superhydrophobic Coatings - R&D Management (Technical Insights): Emerging trends in superhydrophobic coatings sector.* 2012 (D2F4-TI) 2.3.3

[86] Cao, Liangliang ; Jones, Andrew K. ; Sikka, Vinod K. ; Wu, Jianzhong ; Gao, Di: Anti-Icing Superhydrophobic Coatings. In: *Langmuir* 25 (2009), Nr. 21, S. 12444–12448. http://dx.doi.org/10.1021/la902882b. – DOI 10.1021/la902882b. – ISSN 0743–7463 2.3.3, 3.2.2, 7.2.2

[87] Jafari, R. ; Menini, R. ; Farzaneh, M.: Superhydrophobic and icephobic surfaces prepared by RF-sputtered polytetrafluoroethylene coatings. In: *Applied Surface Science* 257 (2010), Nr. 5, S. 1540–1543. http://dx.doi.org/10.1016/j.apsusc.2010.08.092. – DOI 10.1016/j.apsusc.2010.08.092. – ISSN 01694332 2.3.3, 3.2.2, 7.2.2, 7.2.2

[88] Meuler, Adam J. ; McKinley, Gareth H. ; Cohen, Robert E.: Exploiting Topographical Texture To Impart Icephobicity. In: *ACS Nano* 4 (2010), Nr. 12, S. 7048–7052. http://dx.doi.org/10.1021/nn103214q. – DOI 10.1021/nn103214q. – ISSN 1936–0851 2.3.3

[89] Stenzel, V. ; Kreider, A. ; Rehfeld, N. ; Stake, A.: Melting the ice. New anti-frost technologies. Das Eis schmelzen. Neue Technologien gegen Eisbildung. In: *European coatings journal* (2011), Nr. 1, S. 36–40 2.3.3

[90] Nosonovsky, Michael ; Bhushan, Bharat: Roughness-induced superhydrophobicity: a way to design non-adhesive surfaces. In: *Journal of Physics: Condensed Matter* 20 (2008), Nr. 22, S. 225009. http://dx.doi.org/10.1088/0953-8984/20/22/225009. – DOI 10.1088/0953–8984/20/22/225009. – ISSN 0953–8984 2.3.3, 3.2.1, 3.2.1, 3.2.1, 3.2.1, 3.2.1, 3.2.1, 3.2.1, 3.2.2

[91] Bhushan, Bharat ; Jung, Yong C. ; Koch, Kerstin: Micro-, nano- and hierarchical structures for superhydrophobicity, self-cleaning and low adhesion. In: *Philosophical transactions. Series A, Mathematical, physical, and engineering sciences* 367 (2009), Nr. 1894, S. 1631–1672. http://dx.doi.org/10.1098/rsta.2009.0014. – DOI 10.1098/rsta.2009.0014. – ISSN 1364–503X 2.3.3

[92] Öner, Didem ; McCarthy, Thomas J.: Ultrahydrophobic Surfaces. Effects of Topography Length Scales on Wettability. In: *Langmuir* 16 (2000), Nr. 20, S. 7777–7782. http://dx.doi.org/10.1021/la000598o. – DOI 10.1021/la000598o. – ISSN 0743–7463 2.3.3

[93] Deng, Xu ; Mammen, L. ; Butt, H.-J. ; Vollmer, D.: Candle Soot as a Template for a Transparent Robust Superamphiphobic Coating: Reports. In: *Science (New York, N.Y.)* 335 (2012), Nr. 6064, S. 67–69. http://dx.doi.org/10.1126/science.1207115. – DOI 10.1126/science.1207115. – ISSN 0036–8075 2.3.3

[94] Kulinich, S. A. ; Farzaneh, M.: Hydrophobic properties of surfaces coated with fluoroalkylsiloxane and alkylsiloxane monolayers. In: *Surface Science* 573 (2004), Nr. 3, S. 379–390. http://dx.doi.org/10.1016/j.susc.2004.10.008. – DOI 10.1016/j.susc.2004.10.008. – ISSN 00396028 2.3.3

[95] Azimi, Gisele ; Dhiman, Rajeev ; Kwon, Hyuk-Min ; Paxson, Adam T. ; Varanasi, Kripa K.: Hydrophobicity of rare-earth oxide ceramics. In: *Nature materials* 12 (2013), Nr. 4, S. 315–320. http://dx.doi.org/10.1038/nmat3545. – DOI 10.1038/nmat3545. – ISSN 1476–1122 2.3.3

[96] Schutzrecht US 20020111402 A1 . (2002). Mizuno et al. (Erfinder); NTT Advanced Technology Corporation (Anmelder)., *Water-repellent coating and coating film* 2.3.3

[97] Schutzrecht DE 19935875 A1 . (2000). Mizuno et al. (Erfinder); NTT Advanced Technology Corp., Nippon Telegraph and Telephone Corp. (Anmelder)., *Wasserabweisendes Beschichtungsmaterial und wasserabweisender Beschichtungsfilm* 2.3.3

[98] Schutzrecht US 20030232201 A1 . (2003). Byrd, N. R. ; Keener, S. G. ; Lally, E. D. ; Peralta, C. (Erfinder); The Boeing Company (Anmelder)., *Polysiloxane coatings for surfaces* 2.3.3

[99] Schutzrecht DE102005034764A1 . (2007). Michael Haupt ; Christian Oehr ; Jakob Barz (Erfinder); Fraunhofer-Gesellschaft zur Förderung der angewandten Forschung e.V. (Anmelder)., *Verfahren zur Herstellung von funktionalen Fluor-Kohlenstoff-Polymerschichten mittels Plasmapolymerisation von Perfluorocycloalkanen* 2.3.3

[100] Schutzrecht DE 10 2012 208 941 A1 . (2013). Michael Haupt ; Christian Oehr (Erfinder); Fraunhofer Gesellschaft zur Förderung der angewandten Forschung e.V. (Anmelder)., *Eisspeicher mit verbessertem Wärmetauscher* 2.3.3

[101] Schutzrecht WO 2014 095 112 A1 . (2014). Michael Haupt ; Christian Oehr (Erfinder); Fraunhofer Gesellschaft zur Förderung der angewandten Forschung e.V. (Anmelder)., *Freezing-point-lowering coating composed of plastics foils for applying to rotor blades of wind turbines* 2.3.3

[102] Schutzrecht DE 10 2012 007 787 A1 . (2013). Michael Haupt ; Jakob Barz ; Christian Oehr (Erfinder); Fraunhofer Gesellschaft zur Förderung der angewandten Forschung e.V. (Anmelder)., *Anti-Eis-Beschichtung von Skiern, Skibindungen und Skibrillen* 2.3.3

[103] Schutzrecht US20110177288A1 . (2011). Bhushan, Bharat ; Jung, Yong C. ; Nosonovsky, Michael (Erfinder); Bhushan (Anmelder)., *Hierarchical structures for superhydrophobic surfaces and methods of making* 2.3.3

[104] Schutzrecht US 20100314575 A1 . (2010). Gao, D. ; Jones, Andrew K. ; Sikka, Vinod K. (Erfinder); Gao et al. (Anmelder)., *Anti-icing superhydrophobic coatings* 2.3.3

[105] Schutzrecht WO 2009097790 A1 . (2009). He, M. ; Song, Y. ; Liu, B. (Erfinder); Institute of Chemistry, Chinese Academy of Sciences (Anmelder)., *An anti-frost coating and the application method thereof* 2.3.3

[106] Schutzrecht US 20130101859 A1 . (2013). Hirayama, M. ; Siegmann, K. ; Meola, G. ; Schaefer, C. ; Daenhardt, K. (Erfinder); Clariant Finance (BVI) Ltd. (Anmelder)., *Surface coatings having anti-ice properties* 2.3.3

[107] Schutzrecht CA 1331240 C . (1994). Murase, H. (Erfinder); Kansai Paint Company Ltd. (Anmelder)., *Anti-Icing Coating Compositions* 2.3.3

[108] Schutzrecht US 6183872 B1 . (2001). Tanaka, Y. ; Hachisuka, H. ; Arase, T. ; Negishi, Y. ; Tatemoto, M. ; Shimizu, T. ; Yamaguchi, S. ; Desaki, K. (Erfinder); Daikin Industries Ltd. (Anmelder)., *Silicon-containing organic fluoropolymers and use of the same* 2.3.3

[109] Schutzrecht US 20130052031 A1 . (2013). Towkan, M. F. (Erfinder); Towkan (Anmelder)., *Propeller blades having icephobic coating* 2.3.3

[110] Schutzrecht US 20020028289 A1 . (2002). Vijayen, S. V. (Erfinder); Guardian Industries Corporation (Anmelder)., *Hydrophobic coating including DLC on substrate* 2.3.3

[111] Boinovich, Ludmila B. ; Emelyanenko, Alexandre M.: Anti-icing Potential of Superhydrophobic Coatings. In: *Mendeleev Communications* 23 (2013), Nr. 1, S. 3–10. http://dx.doi.org/10.1016/j.mencom.2013.01.002. – DOI 10.1016/j.mencom.2013.01.002. – ISSN 09599436 2.3.3, 3.2.1, 3.2.1

[112] Becker, Holger ; Heim, Ulf: Hot embossing as a method for the fabrication of polymer high aspect ratio structures. In: *Sensors and Actuators A: Physical* 83 (2000), Nr. 1-3, S. 130–135. http://dx.doi.org/10.1016/S0924-4247(00)00296-X. – DOI 10.1016/S0924–4247(00)00296–X. – ISSN 09244247 3.1.2

[113] Wagenknecht, T. ; Rattba, K. ; Wagner, S.: Heißprägen von Mikrostrukturen: Fertigung mikrostrukturierter Kunststoffformteile für fluidische Anwendungen. In: *wt Werkstatttechnik online* 96 (2006), Nr. 11/12, 849–853. http://www.werkstattstechnik.de/wt/article.php?data%5Barticle_id%5D=32502 3.1.2

[114] Xia, Younan ; Whitesides, G. M.: Softlithographie. In: *Angewandte Chemie* 110 (1998), Nr. 5, 568–594. http://dx.doi.org/10.1002/(SICI)1521-3757(19980302)110:5{\T1\textless}568::AID-ANGE568{\T1\textgreater}3.0.CO;2-X. – DOI 10.1002/(SICI)1521–3757(19980302)110:5<568::AID–ANGE568>3.0.CO;2–X. – ISSN 0044–8249 3.1.2

[115] Fridman, Alexander A.: *Plasma chemistry*. Cambridge and New York : Cambridge University Press, 2008. – ISBN 9780521847353 3.1.3, 3.1.3, 3.1.3, 3.1.3

[116] Franz, G.: *Oberflächentechnologie mit Niederdruckplasmen: Beschichten und Strukturieren in der Mikrotechnik*. Zweite, völlig neubearbeitete Auflage. Berlin, Heidelberg : Springer Berlin Heidelberg, 1994. – ISBN 3662089793 3.1.3

[117] Yasuda, H.: *Plasma polymerization*. Orlando : Academic Press, 1985. http://dx.doi.org/10.1016/B978-0-12-768760-5.50001-3. http://dx.doi.org/10.1016/B978-0-12-768760-5.50001-3. – ISBN 9780127687605 3.1.3

[118] Jakob Philipp Barz: *Particle dynamics simulation and diagnostics of the PECVD processes in fluorocarbon rf discharges*. Stuttgart, University of Stuttgart, Dissertation, 2010 3.1.3

[119] Barz, Jakob P. ; Oehr, Christian ; Lunk, Achim: Analysis and Modeling of Gas-Phase Processes in a CHF3/Ar Discharge. In: *Plasma Processes and Polymers* 8 (2011), Nr. 5, S. 409–423. http://dx.doi.org/10.1002/ppap.201000095. – DOI 10.1002/ppap.201000095. – ISSN 16128850 3.1.3

[120] Lee, Sangwha ; Park, Joon-Seo ; Lee, T. R.: The wettability of fluoropolymer surfaces: influence of surface dipoles. In: *Langmuir : the ACS journal of surfaces and colloids* 24 (2008), Nr. 9, S. 4817–4826. http://dx.doi.org/10.1021/la700902h. – DOI 10.1021/la700902h. – ISSN 1520–5827 3.1.3

[121] Owens, D. K. ; Wendt, R. C.: Estimation of the surface free energy of polymers. In: *Journal of Applied Polymer Sience* 13 (1969), Nr. 8, 1741–1747. http://dx.doi.org/10.1002/app.1969.070130815. – DOI 10.1002/app.1969.070130815 3.2.1, 3.2.1

[122] Ganesh, V. A. ; Raut, Hemant K. ; Nair, A. S. ; Ramakrishna, Seeram: A review on self-cleaning coatings. In: *Journal of Materials Chemistry* 21 (2011), Nr. 41, S. 16304. http://dx.doi.org/10.1039/c1jm12523k. – DOI 10.1039/c1jm12523k. – ISSN 0959–9428 3.2.1, 3.2.1

[123] Guo, Zhiguang ; Liu, Weimin ; Su, Bao-Lian: Superhydrophobic surfaces: from natural to biomimetic to functional. In: *Journal of colloid and interface science* 353 (2011), Nr. 2, S. 335–355. http://dx.doi.org/10.1016/j.jcis.2010.08.047. – DOI 10.1016/j.jcis.2010.08.047. – ISSN 0021–9797 3.2.1, 3.2.1

[124] Darmanin, Thierry ; Guittard, Frederic: Recent advances in the potential applications of bioinspired superhydrophobic materials. In: *J. Mater. Chem. A* 2 (2014), Nr. 39, S. 16319–16359. http://dx.doi.org/10.1039/C4TA02071E. – DOI 10.1039/C4TA02071E. – ISSN 2050–7488 3.2.1, 3.2.1

[125] Wenzel, Robert N.: Resistance of solid surfaces to wetting by water. In: *Industrial and Engineering Chemistry* 28 (1936), Nr. 8, 988–994. http://dx.doi.org/10.1021/ie50320a024. – DOI 10.1021/ie50320a024 3.2.1, 3.2.1, 6.2.1

[126] Cassie, A. B. D. ; Baxter, S.: Wettability of porous surfaces. In: *Transactions of the Faraday Society* (1944), Nr. 40, S. 546–551 3.2.1, 3.2.1, 6.2.1

[127] Zheng, Q-S ; Yu, Y. ; Zhao, Z-H: Effects of hydraulic pressure on the stability and transition of wetting modes of superhydrophobic surfaces. In: *Langmuir : the ACS journal of surfaces and colloids* 21 (2005), Nr. 26, S. 12207–12212. http://dx.doi.org/10.1021/la052054y. – DOI 10.1021/la052054y. – ISSN 1520–5827 3.2.1

[128] Wu, Souheng: *Polymer Interface and Adhesion*. New York : CRC Press, 1982 https://books.google.de/books?id=tXNgrCbsCfIC. – ISBN 9780824715335 3.2.1

[129] Wu, Souheng: Polymers at interfaces: Polymer symposia. In: *Journal of Polymer Science: Part C* (1971), Nr. 34, 19–30. https://books.google.de/books?id=5zYwAQAAIAAJ 3.2.1

[130] Fowkes, Frederick M. (Hrsg.): *Contact Angle, Wettability, and Adhesion*. WASHINGTON, D.C. : AMERICAN CHEMICAL SOCIETY, 1964 (Advances in Chemistry). http://dx.doi.org/10.1021/advances. http://dx.doi.org/10.1021/advances. – ISBN 0–8412–0044–0 3.2.1

[131] Girifalco, L. A. ; Good, R. J.: A Theory for the Estimation of Surface and Interfacial Energies. I. Derivation and Application to Interfacial Tension. In: *J. Phys. Chem.* 61 (1957), Nr. 7, 904–909. http://dx.doi.org/10.1021/j150553a013. – DOI 10.1021/j150553a013 3.2.1

[132] ZISMAN, W. A.: Relation of the Equilibrium Contact Angle to Liquid and Solid Constitution. Version: 1964. http://dx.doi.org/10.1021/ba-1964-0043.

ch001. In: Fowkes, Frederick M. (Hrsg.): *Contact Angle, Wettability, and Adhesion* Bd. 43. WASHINGTON, D.C. : AMERICAN CHEMICAL SOCIETY, 1964. – DOI 10.1021/ba–1964–0043.ch001. – ISBN 0–8412–0044–0, S. 1–51 3.2.1

[133] Dodiuk, H. ; Rios, P. F. ; Dotan, A. ; Kenig, S.: Hydrophobic and self-cleaning coatings. In: *Polymers for Advanced Technologies* 18 (2007), Nr. 9, S. 746–750. http://dx.doi.org/10.1002/pat.957. – DOI 10.1002/pat.957. – ISSN 10427147 3.2.2, 7.2.2

[134] Reyssat, M. ; Pépin, A. ; Marty, F. ; Chen, Y. ; Quéré, D.: Bouncing transitions on microtextured materials. In: *Europhysics Letters (EPL)* 74 (2006), Nr. 2, S. 306–312. http://dx.doi.org/10.1209/epl/i2005-10523-2. – DOI 10.1209/epl/i2005–10523–2. – ISSN 0295–5075 3.2.2

[135] Bartolo, D. ; Bouamrirene, F. ; Verneuil, É. ; Buguin, A. ; Silberzan, P. ; Moulinet, S.: Bouncing or sticky droplets: Impalement transitions on superhydrophobic micropatterned surfaces. In: *Europhysics Letters (EPL)* 74 (2006), Nr. 2, S. 299–305. http://dx.doi.org/10.1209/epl/i2005-10522-3. – DOI 10.1209/epl/i2005–10522–3. – ISSN 0295–5075 3.2.2

[136] Lafuma, Aurelie ; Quere, David: Superhydrophobic states. In: *Nature materials* 2 (2003), Nr. 7, S. 457–460. http://dx.doi.org/10.1038/nmat924. – DOI 10.1038/nmat924. – ISSN 1476–1122 3.2.2

[137] Deng, Tao ; Varanasi, Kripa K. ; Hsu, Ming ; Bhate, Nitin ; Keimel, Chris ; Stein, Judith ; Blohm, Margaret: Nonwetting of impinging droplets on textured surfaces. In: *Applied Physics Letters* 94 (2009), Nr. 13, S. 133109. http://dx.doi.org/10.1063/1.3110054. – DOI 10.1063/1.3110054. – ISSN 00036951 3.2.2

[138] Jung, Yong C. ; Bhushan, Bharat: Dynamic Effects of Bouncing Water Droplets on Superhydrophobic Surfaces. In: *Langmuir* 24 (2008), Nr. 12, S. 6262–6269. http://dx.doi.org/10.1021/la8003504. – DOI 10.1021/la8003504. – ISSN 0743–7463 3.2.2

[139] Maitra, Tanmoy ; Tiwari, Manish K. ; Antonini, Carlo ; Schoch, Philippe ; Jung, Stefan ; Eberle, Patric ; Poulikakos, Dimos: On the Nanoengineering of Superhydrophobic and Impalement Resistant Surface Textures below the Freezing Temperature. In: *Nano Letters* 14 (2014), Nr. 1, S. 172–182. http://dx.doi.org/10.1021/nl4037092. – DOI 10.1021/nl4037092. – ISSN 1530–6984 3.2.2

[140] Mishchenko, Lidiya ; Hatton, Benjamin ; Bahadur, Vaibhav ; Taylor, J. A. ; Krupenkin, Tom ; Aizenberg, Joanna: Design of Ice-free Nanostructured Surfaces Based on Repulsion of Impacting Water Droplets. In: *ACS Nano* 4

(2010), Nr. 12, S. 7699–7707. http://dx.doi.org/10.1021/nn102557p. – DOI 10.1021/nn102557p. – ISSN 1936–0851 3.2.2

[141] Bird, James C. ; Dhiman, Rajeev ; Kwon, Hyuk-Min ; Varanasi, Kripa K.: Reducing the contact time of a bouncing drop. In: *Nature* 503 (2013), Nr. 7476, S. 385–388. http://dx.doi.org/10.1038/nature12740. – DOI 10.1038/nature12740. – ISSN 0028–0836 3.2.2

[142] Enright, Ryan ; Miljkovic, Nenad ; Al-Obeidi, Ahmed ; Thompson, Carl V. ; Wang, Evelyn N.: Condensation on superhydrophobic surfaces: the role of local energy barriers and structure length scale. In: *Langmuir : the ACS journal of surfaces and colloids* 28 (2012), Nr. 40, S. 14424–14432. http://dx.doi.org/10.1021/la302599n. – DOI 10.1021/la302599n. – ISSN 1520–5827 3.2.2

[143] Enright, Ryan ; Miljkovic, Nenad ; Alvarado, Jorge L. ; Kim, Kwang ; Rose, John W.: Dropwise Condensation on Micro- and Nanostructured Surfaces. In: *Nanoscale and Microscale Thermophysical Engineering* 18 (2014), Nr. 3, S. 223–250. http://dx.doi.org/10.1080/15567265.2013.862889. – DOI 10.1080/15567265.2013.862889. – ISSN 1556–7265 3.2.2

[144] Miljkovic, Nenad ; Enright, Ryan ; Wang, Evelyn N.: Effect of droplet morphology on growth dynamics and heat transfer during condensation on superhydrophobic nanostructured surfaces. In: *ACS Nano* 6 (2012), Nr. 2, S. 1776–1785. http://dx.doi.org/10.1021/nn205052a. – DOI 10.1021/nn205052a. – ISSN 1936–0851 3.2.2

[145] He, Min ; Li, Huiling ; Wang, Jianjun ; Song, Yanlin: Superhydrophobic surface at low surface temperature. In: *Applied Physics Letters* 98 (2011), Nr. 9, S. 93118. http://dx.doi.org/10.1063/1.3558911. – DOI 10.1063/1.3558911. – ISSN 00036951 3.2.2

[146] Mockenhaupt, Bernd ; Ensikat, Hans-Jurgen ; Spaeth, Manuel ; Barthlott, Wilhelm: Superhydrophobicity of biological and technical surfaces under moisture condensation: stability in relation to surface structure. In: *Langmuir : the ACS journal of surfaces and colloids* 24 (2008), Nr. 23, S. 13591–13597. http://dx.doi.org/10.1021/la802351h. – DOI 10.1021/la802351h. – ISSN 1520–5827 3.2.2

[147] Wier, Kevin A. ; McCarthy, Thomas J.: Condensation on ultrahydrophobic surfaces and its effect on droplet mobility: ultrahydrophobic surfaces are not always water repellant. In: *Langmuir : the ACS journal of surfaces and colloids* 22 (2006), Nr. 6, S. 2433–2436. http://dx.doi.org/10.1021/la0525877. – DOI 10.1021/la0525877. – ISSN 1520–5827 3.2.2

[148] Oberli, Linda ; Caruso, Dean ; Hall, Colin ; Fabretto, Manrico ; Murphy, Peter J. ; Evans, Drew: Condensation and freezing of droplets on superhydrophobic surfaces. In: *Advances in colloid and interface science* 210 (2014), S. 47–57. http://dx.doi.org/10.1016/j.cis.2013.10.018. – DOI 10.1016/j.cis.2013.10.018. – ISSN 1873–3727 3.2.2

[149] Varanasi, Kripa K. ; Deng, Tao ; Smith, J. D. ; Hsu, Ming ; Bhate, Nitin: Frost formation and ice adhesion on superhydrophobic surfaces. In: *Applied Physics Letters* 97 (2010), Nr. 23, S. 234102. http://dx.doi.org/10.1063/1.3524513. – DOI 10.1063/1.3524513. – ISSN 00036951 3.2.2

[150] Rykaczewski, Konrad ; Osborn, William A. ; Chinn, Jeff ; Walker, Marlon L. ; Scott, John Henry J. ; Jones, Wanda ; Hao, Chonglei ; Yao, Shuhuai ; Wang, Zuankai: How nanorough is rough enough to make a surface superhydrophobic during water condensation? In: *Soft Matter* 8 (2012), Nr. 33, S. 8786. http://dx.doi.org/10.1039/c2sm25502b. – DOI 10.1039/c2sm25502b. – ISSN 1744–683X 3.2.2

[151] Sarkar, D. K. ; Farzaneh, M.: Superhydrophobic Coatings with Reduced Ice Adhesion. In: *Journal of Adhesion Science and Technology* 23 (2009), Nr. 9, S. 1215–1237. http://dx.doi.org/10.1163/156856109X433964. – DOI 10.1163/156856109X433964. – ISSN 0169–4243 3.2.2, 7.2.2, 7.2.2

[152] Farhadi, S. ; Farzaneh, M. ; Kulinich, S. A.: Anti-icing performance of superhydrophobic surfaces. In: *Applied Surface Science* 257 (2011), Nr. 14, S. 6264–6269. http://dx.doi.org/10.1016/j.apsusc.2011.02.057. – DOI 10.1016/j.apsusc.2011.02.057. – ISSN 01694332 3.2.2, 6.4.4, 7.2.2

[153] Kulinich, S.A ; Farzaneh, M.: Ice adhesion on super-hydrophobic surfaces. In: *Applied Surface Science* 255 (2009), Nr. 18, S. 8153–8157. http://dx.doi.org/10.1016/j.apsusc.2009.05.033. – DOI 10.1016/j.apsusc.2009.05.033. – ISSN 01694332 3.2.2

[154] Kulinich, S. A. ; Farzaneh, M.: On ice-releasing properties of rough hydrophobic coatings. In: *Cold Regions Science and Technology* 65 (2011), Nr. 1, S. 60–64. http://dx.doi.org/10.1016/j.coldregions.2010.01.001. – DOI 10.1016/j.coldregions.2010.01.001. – ISSN 0165232X 3.2.2, 7.2.2

[155] Wang, Fochi ; Lv, Fangcheng ; Liu, Yunpeng ; Li, Chengrong ; Lv, Yuzhen: Ice adhesion on different microstructure superhydrophobic aluminum surfaces. In: *Journal of Adhesion Science and Technology* 27 (2013), Nr. 1, S. 58–67. http://dx.doi.org/10.1080/01694243.2012.701506. – DOI 10.1080/01694243.2012.701506. – ISSN 0169–4243 3.2.2, 7.2.2

[156] Wang, Yuanyi ; Xue, Jian ; Wang, Qingjun ; Chen, Qingmin ; Ding, Jianfu: Verification of Icephobic/Anti-icing Properties of a Superhydrophobic Surface. In: *ACS Applied Materials & Interfaces* 5 (2013), Nr. 8, S. 3370–3381. http://dx.doi.org/10.1021/am400429q. – DOI 10.1021/am400429q. – ISSN 1944–8244 3.2.2, 7.2.2

[157] Susoff, Markus ; Siegmann, Konstantin ; Pfaffenroth, Cornelia ; Hirayama, Martina: Evaluation of icephobic coatings—Screening of different coatings and influence of roughness. In: *Applied Surface Science* 282 (2013), S. 870–879. http://dx.doi.org/10.1016/j.apsusc.2013.06.073. – DOI 10.1016/j.apsusc.2013.06.073. – ISSN 01694332 3.2.2, 7.2.2, 7.2.2, 7.2.2, 7.2.3

[158] Chen, Jing ; Liu, Jie ; He, Min ; Li, Kaiyong ; Cui, Dapeng ; Zhang, Qiaolan ; Zeng, Xiping ; Zhang, Yifan ; Wang, Jianjun ; Song, Yanlin: Superhydrophobic surfaces cannot reduce ice adhesion. In: *Applied Physics Letters* 101 (2012), Nr. 11, S. 111603. http://dx.doi.org/10.1063/1.4752436. – DOI 10.1063/1.4752436. – ISSN 00036951 3.2.2, 7.2.2, 7.2.2, 7.2.4

[159] Jung, Stefan ; Dorrestijn, Marko ; Raps, Dominik ; Das, Arindam ; Megaridis, Constantine M. ; Poulikakos, Dimos: Are superhydrophobic surfaces best for icephobicity? In: *Langmuir : the ACS journal of surfaces and colloids* 27 (2011), Nr. 6, S. 3059–3066. http://dx.doi.org/10.1021/la104762g. – DOI 10.1021/la104762g. – ISSN 1520–5827 3.2.2

[160] Jung, Stefan ; Dorrestijn, Marko ; Raps, Dominik ; Das, Arindam ; Megaridis, Constantine M. ; Poulikakos, Dimos: Are superhydrophobic surfaces best for icephobicity? In: *Langmuir : the ACS journal of surfaces and colloids* 27 (2011), Nr. 6, S. 3059–3066. http://dx.doi.org/10.1021/la104762g. – DOI 10.1021/la104762g. – ISSN 1520–5827 3.2.2

[161] Kulinich, S. A. ; Farhadi, S. ; Nose, K. ; Du, X. W.: Superhydrophobic Surfaces: Are They Really Ice-Repellent? In: *Langmuir* 27 (2011), Nr. 1, S. 25–29. http://dx.doi.org/10.1021/la104277q. – DOI 10.1021/la104277q. – ISSN 0743–7463 3.2.2, 6.4.4, 7.2.2

[162] Nosonovsky, Michael ; Hejazi, Vahid: Why Superhydrophobic Surfaces Are Not Always Icephobic. In: *ACS Nano* 6 (2012), Nr. 10, S. 8488–8491. http://dx.doi.org/10.1021/nn302138r. – DOI 10.1021/nn302138r. – ISSN 1936–0851 3.2.2, 3.2.3, 3.2.3, 7.2.1, 7.2.2, 7.2.2

[163] Maitra, Tanmoy ; Jung, Stefan ; Giger, Markus E. ; Kandrical, Vimal ; Ruesch, Timon ; Poulikakos, Dimos: Superhydrophobicity vs. Ice Adhesion: The Quandary of Robust Icephobic Surface Design. In: *Advanced Materials Interfaces* 2 (2015), Nr. 16, S. 1500330. http://dx.doi.org/10.1002/admi.

201500330. – DOI 10.1002/admi.201500330. – ISSN 21967350 3.2.2, 3.2.3, 3.2.3, 3.2.3, 3.2.3, 3.2.3, 7.2.1

[164] Alizadeh, Azar ; Yamada, Masako ; Li, Ri ; Shang, Wen ; Otta, Shourya ; Zhong, Sheng ; Ge, Liehui ; Dhinojwala, Ali ; Conway, Ken R. ; Bahadur, Vaibhav ; Vinciquerra, A. J. ; Stephens, Brian ; Blohm, Margaret L.: Dynamics of Ice Nucleation on Water Repellent Surfaces. In: *Langmuir* 28 (2012), Nr. 6, S. 3180–3186. http://dx.doi.org/10.1021/la2045256. – DOI 10.1021/la2045256. – ISSN 0743–7463 3.2.2

[165] Tourkine, Piotr ; Le Merrer, Marie ; Quere, David: Delayed Freezing on Water Repellent Materials. In: *Langmuir* 25 (2009), Nr. 13, S. 7214–7216. http://dx.doi.org/10.1021/la900929u. – DOI 10.1021/la900929u. – ISSN 0743–7463 3.2.2

[166] Boinovich, Ludmila ; Emelyanenko, Alexandre M. ; Korolev, Vadim V. ; Pashinin, Andrei S.: Effect of wettability on sessile drop freezing: when superhydrophobicity stimulates an extreme freezing delay. In: *Langmuir : the ACS journal of surfaces and colloids* 30 (2014), Nr. 6, S. 1659–1668. http://dx.doi.org/10.1021/la403796g. – DOI 10.1021/la403796g. – ISSN 1520–5827 3.2.2

[167] Eberle, Patric ; Tiwari, Manish K. ; Maitra, Tanmoy ; Poulikakos, Dimos: Rational nanostructuring of surfaces for extraordinary icephobicity. In: *Nanoscale* 6 (2014), Nr. 9, S. 4874–4881. http://dx.doi.org/10.1039/c3nr06644d. – DOI 10.1039/c3nr06644d. – ISSN 2040–3364 3.2.2, 3.2.4, 3.2.4, 3.14, 3.2.4, 3.15, 3.16, 3.2.4, 3.2.4, 3.2.4, 3.2.4, 7.3.2, 7.3.2, 7.3.2

[168] Eberle, Patric ; Tiwari, Manish K. ; Maitra, Tanmoy ; Poulikakos, Dimos: The rational nanostructuring of surfaces for extraordinary icephobicity: Supplementary Information. In: *Nanoscale* 6 (2014), Nr. 9, S. 1–30. – ISSN 2040–3364 3.2.2, 3.2.4, 3.2.4, 3.14, 3.16, 3.2.4, 3.2.4, 3.2.4, 3.2.4, 3.2.4, 3.2.4, 7.3.1, 7.3.2, 7.3.2

[169] Meuler, Adam J. ; Smith, J. D. ; Varanasi, Kripa K. ; Mabry, Joseph M. ; McKinley, Gareth H. ; Cohen, Robert E.: Relationships between Water Wettability and Ice Adhesion. In: *ACS Applied Materials & Interfaces* 2 (2010), Nr. 11, S. 3100–3110. http://dx.doi.org/10.1021/am1006035. – DOI 10.1021/am1006035. – ISSN 1944–8244 3.2.3, 3.12, 3.2.3, 3.2.3, 7.2.2, 7.2.3

[170] Gao, Huajian ; Yao, Haimin: Shape insensitive optimal adhesion of nanoscale fibrillar structures. In: *Proceedings of the National Academy of Sciences of the United States of America* 101 (2004), Nr. 21, S. 7851–7856. http://dx.doi.org/10.1073/pnas.0400757101. – DOI 10.1073/pnas.0400757101. – ISSN 0027–8424 3.2.3, 3.2.3, 3.2.3

[171] Wikipedia contributors ; Wikipedia - The Free Encyclopedia (Hrsg.): *Material failure theory*. https://en.wikipedia.org/w/index.php?title=Material_failure_theory&oldid=758906451. Version: 2017 3.2.3

[172] Fletcher, N. H.: The freezing of water. In: *Science Progress* 54 (1966), Nr. 214, 227–241. http://www.jstor.org/stable/43419536 3.2.4, 3.13, 3.2.4, 3.2.4, 3.2.4

[173] Mishima, O. ; Stanley, H. E.: The relationship between liquid, supercooled and glassy water. In: *Nature* 396 (1998), 329–335. http://dx.doi.org/10.1038/24540. – DOI 10.1038/24540. – ISSN 0028–0836 3.2.4

[174] Schutzius, Thomas M. ; Jung, Stefan ; Maitra, Tanmoy ; Eberle, Patric ; Antonini, Carlo ; Stamatopoulos, Christos ; Poulikakos, Dimos: Physics of icing and rational design of surfaces with extraordinary icephobicity. In: *Langmuir : the ACS journal of surfaces and colloids* 31 (2015), Nr. 17, S. 4807–4821. http://dx.doi.org/10.1021/la502586a. – DOI 10.1021/la502586a. – ISSN 1520–5827 3.2.4, 3.2.4

[175] Fletcher, N. H.: Size Effect in Heterogeneous Nucleation. In: *The Journal of chemical physics* 29 (1958), Nr. 3, S. 572–576. http://dx.doi.org/10.1063/1.1744540. – DOI 10.1063/1.1744540. – ISSN 0021–9606 3.2.4

[176] Hindmarsh, J.P ; Russell, A.B ; Chen, X.D: Experimental and numerical analysis of the temperature transition of a suspended freezing water droplet. In: *International Journal of Heat and Mass Transfer* 46 (2003), Nr. 7, S. 1199–1213. http://dx.doi.org/10.1016/S0017-9310(02)00399-X. – DOI 10.1016/S0017–9310(02)00399–X. – ISSN 00179310 3.2.4, 3.2.4

[177] FLIR Systems ; FLIR Systems (Hrsg.): *Manual FLIR P6xx series: Publ. No. 1558548 Rev. a506*. 2010 3.2.5, 3.2.5, 3.2.5, 3.2.5

[178] Otto, Matthias: *Analytische Chemie*. 4., überarb. u. erg. Aufl. Weinheim, Bergstr : Wiley-VCH, 2011 (Bachelor). – ISBN 3527328815 4.2.2

[179] Zhang, Chenying: *Oberflächenfunktionalisierung von Kunststofffolien zur Verminderung der Eisbildung und Eishaftung ("Anti-Icing")*. Reutlingen and Stuttgart, Reutlingen University, Master thesis, 2011 4.3.1, 4.4.1, 6.5, 6.3.5, 6.8, 6.9, 6.11

[180] Michele ; Andre: *Herstellung und Charakterisierung von funktionalen Polymeroberflächen zur Verminderung der Eishaftung und Eisbildung*. Reutlingen and Stuttgart, Reutlingen University, Bachelor thesis, 2014 4.4, 6.2.2, 6.5, 6.3.3, 6.3.3

[181] Norm DIN 52348 Februar 1985. *Verschleißprüfung, Sandriesel-Verfahren* 4.5, 4.5

[182] Eller, Johannes: *Untersuchung der Stabilität gegen Erosion von Anti-Eis-Polymerfolien: Aufbau eines Teststandes nach DIN 52348.* Stuttgart, University of Stuttgart, Semester thesis, 2014 4.5

[183] Rainer Kapp ; Landeshauptstadt Stuttgart, Amt für Umweltschutz, Abteilung Stadtklimatologie (Hrsg.): *Stadtklima Stuttgart: Download von Messdaten der Station S-Mitte (Schwabenzentrum).* `https://www.stadtklima-stuttgart.de/index.php?klima_messdaten_download`. Version: 2018 4.6, 4.7

[184] Hartstern, Maike: *Herstellung von mikrostrukturierten und plasmabeschichteten, superhydrophoben Polyurethanoberflächen und Analyse ihrer Anti-Eis-Eigenschaften.* Rüsselsheim and Stuttgart, RheinMain University, Bachelor thesis, 2016 5.1, 6.2.2, 6.2.2, 6.2.2, 6.2.2, 6.5, 6.6, 6.3.5, 6.9

[185] VITRON Spezialwerkstoffe GmbH: *VITRON CVD Zinc Sulfide: Technical Datasheet.* `http://www.vitron.de/english/IR-Glas/Daten-ZnS-Glas.php`. Version: 2015 5.7

[186] Holvoet, Servaas ; Chevallier, Pascale ; Turgeon, Stéphane ; Mantovani, Diego: Toward High-Performance Coatings for Biomedical Devices: Study on Plasma-Deposited Fluorocarbon Films and Ageing in PBS. In: *Materials* 3 (2010), Nr. 3, S. 1515–1532. `http://dx.doi.org/10.3390/ma3031515`. – DOI 10.3390/ma3031515. – ISSN 1996–1944 6.1, 6.3.4

[187] Bachmayr, Marcus: *Mikrostrukturierung und Funktionalisierung von Kunststofffolien zur Verminderung der Eisbildung und Eishaftung.* Aalen and Stuttgart, Aalen University, Master thesis, 2013 6.2.2, 6.2.2, 6.5, 6.3.3, 6.3.3

[188] Dannehl, Nadine: *Physikalisch-chemische Grundlagen und Stand der Forschung zum Thema Anti-Icing: 2. Vertiefungsmodul: Projektpraktikum Physikalische Chemie.* Gießen and Stuttgart, University of Gießen, Report, 2015 6.2.2

[189] Bracke, Johannes: *Modellversuche zur Eisbildung an wasserabweisenden mikro- und nanostrukturierten Rohroberflächen für den Wärmeübertrager eines Eisspeichers.* Stuttgart, University of Stuttgart, Semester thesis, 2015 6.5, 6.3.3

[190] Haïdopoulos, Marie ; Turgeon, Stéphane ; Laroche, Gaétan ; Mantovani, Diego: Chemical and Morphological Characterization of Ultra-Thin Fluorocarbon Plasma-Polymer Deposition on 316 Stainless Steel Substrates: A First Step Toward the Improvement of the Long-Term Safety of Coated-Stents. In: *Plasma Processes and Polymers* 2 (2005), Nr. 5, S. 424–440. `http://dx.doi.org/10.1002/ppap.200400066`. – DOI 10.1002/ppap.200400066. – ISSN 16128850 6.3.4

[191] Blanchard, Noemi E. ; Naik, Vikrant V. ; Geue, Thomas ; Kahle, Olaf ; Hegemann, Dirk ; Heuberger, Manfred: Response of Plasma-Polymerized Hexamethyldisiloxane Films to Aqueous Environments. In: *Langmuir : the ACS journal of surfaces and colloids* 31 (2015), Nr. 47, S. 12944–12953. http://dx.doi.org/10.1021/acs.langmuir.5b03010. – DOI 10.1021/acs.langmuir.5b03010. – ISSN 1520–5827 6.3.4

[192] Rüdiger Reuter: *Silicon-Oxide-Like thin film deposition from HMDSO by means of non-equilibrium atmospheric pressure plasmas: the role of oxygen and surface reactions*. Bochum, Ruhr-Universität, Dissertation, 2012 6.3.4

[193] Nosonovsky, Michael ; Bhushan, Bharat: Stochastic model for metastable wetting of roughness-induced superhydrophobic surfaces. In: *Microsystem Technologies* 12 (2006), Nr. 3, S. 231–237. http://dx.doi.org/10.1007/s00542-005-0048-0. – DOI 10.1007/s00542–005–0048–0. – ISSN 0946–7076 7.1.2, 7.1.3, 7.2.2

[194] Papadopoulos, Periklis ; Mammen, Lena ; Deng, Xu ; Vollmer, Doris ; Butt, Hans-Jürgen: How superhydrophobicity breaks down. In: *Proceedings of the National Academy of Sciences* 110 (2013), Nr. 9, S. 3254–3258. http://dx.doi.org/10.1073/pnas.1218673110. – DOI 10.1073/pnas.1218673110. – ISSN 0027–8424 7.1.3, 7.2.2

[195] Nosonovsky, Michael ; Bhushan, Bharat: Energy transitions in superhydrophobicity: Low adhesion, easy flow and bouncing. In: *Journal of Physics: Condensed Matter* 20 (2008), Nr. 39, S. 395005. http://dx.doi.org/10.1088/0953-8984/20/39/395005. – DOI 10.1088/0953–8984/20/39/395005. – ISSN 0953–8984 7.1.3

[196] Nosonovsky, Michael ; Bhushan, Bharat: Hierarchical roughness makes superhydrophobic states stable. In: *Microelectronic Engineering* 84 (2007), Nr. 3, S. 382–386. http://dx.doi.org/10.1016/j.mee.2006.10.054. – DOI 10.1016/j.mee.2006.10.054. – ISSN 01679317 7.1.3

[197] Petrenko, Victor F. ; US Army Corps of Engineers, Cold Regions Research & Engineering Laboratory (Hrsg.) ; Thayer School of Engineering, Dartmouth College (Hrsg.): *The Surface of Ice: Special Report 94-22*. 1994 7.2.1

[198] Ketcham, W. M. ; Hobbs, P. V.: An experimental determination of the surface energies of ice. In: *Philosophical Magazine* 19 (1969), Nr. 162, S. 1161–1173. http://dx.doi.org/10.1080/14786436908228641. – DOI 10.1080/14786436908228641. – ISSN 0031–8086 7.2.1

[199] Bharathidasan, T. ; Kumar, S. V. ; Bobji, M. S. ; Chakradhar, R.P.S. ; Basu, Bharathibai J.: Effect of wettability and surface roughness on ice-adhesion strength of hydrophilic, hydrophobic and superhydrophobic surfaces. In: *Applied Surface Science* 314 (2014), S. 241–250. http://dx.doi.org/10.1016/j.apsusc.2014.06.101. – DOI 10.1016/j.apsusc.2014.06.101. – ISSN 01694332 7.2.2, 7.2.2, 7.2.2, 7.2.2

[200] Golovin, Kevin ; Kobaku, Sai P. R. ; Lee, Duck H. ; DiLoreto, Edward T. ; Mabry, Joseph M. ; Tuteja, Anish: Designing durable icephobic surfaces. In: *Science advances* 2 (2016), Nr. 3, S. e1501496. http://dx.doi.org/10.1126/sciadv.1501496. – DOI 10.1126/sciadv.1501496. – ISSN 2375–2548 7.2.2

[201] Sonwalkar, Nishikant ; Sunder, S. S. ; Sharma, S. K.: Ice/Solid Adhesion Analysis Using Low-Temperature Raman Microprobe Shear Apparatus. In: *Applied Spectroscopy* 47 (1993), Nr. 10, S. 1585–1593. http://dx.doi.org/10.1366/0003702934334606. – DOI 10.1366/0003702934334606. – ISSN 0003–7028 7.2.2, 7.2.2, 7.2.2, 7.2.2

[202] He, Yang ; Jiang, Chengyu ; Cao, Xiaobao ; Chen, Jun ; Tian, Wei ; Yuan, Weizheng: Reducing ice adhesion by hierarchical micro-nano-pillars. In: *Applied Surface Science* 305 (2014), S. 589–595. http://dx.doi.org/10.1016/j.apsusc.2014.03.139. – DOI 10.1016/j.apsusc.2014.03.139. – ISSN 01694332 7.2.2, 7.2.2

[203] Kulinich, S. A. ; Farzaneh, M.: How wetting hysteresis influences ice adhesion strength on superhydrophobic surfaces. In: *Langmuir : the ACS journal of surfaces and colloids* 25 (2009), Nr. 16, S. 8854–8856. http://dx.doi.org/10.1021/la901439c. – DOI 10.1021/la901439c. – ISSN 1520–5827 7.2.2

[204] Zou, M. ; Beckford, S. ; Wei, R. ; Ellis, C. ; Hatton, G. ; Miller, M. A.: Effects of surface roughness and energy on ice adhesion strength. In: *Applied Surface Science* 257 (2011), Nr. 8, S. 3786–3792. http://dx.doi.org/10.1016/j.apsusc.2010.11.149. – DOI 10.1016/j.apsusc.2010.11.149. – ISSN 01694332 7.2.2, 7.2.2, 7.2.2

[205] Moulinet, S. ; Bartolo, D.: Life and death of a fakir droplet: impalement transitions on superhydrophobic surfaces. In: *The European physical journal. E, Soft matter* 24 (2007), Nr. 3, S. 251–260. http://dx.doi.org/10.1140/epje/i2007-10235-y. – DOI 10.1140/epje/i2007–10235–y. – ISSN 1292–8941 7.2.2

[206] Papadopoulos, Periklis ; Mammen, Lena ; Deng, Xu ; Vollmer, Doris ; Butt, Hans-Jurgen: How superhydrophobicity breaks down. In: *Proceedings of the National Academy of Sciences of the United States of America* 110 (2013), Nr. 9, S. 3254–3258. http://dx.doi.org/10.1073/pnas.1218673110. – DOI 10.1073/pnas.1218673110. – ISSN 0027–8424 7.2.2

[207] Aqra, Fathi ; Ayyad, Ahmed: Surface energies of metals in both liquid and solid states. In: *Applied Surface Science* 257 (2011), Nr. 15, S. 6372–6379. http://dx.doi.org/10.1016/j.apsusc.2011.01.123. – DOI 10.1016/j.apsusc.2011.01.123. – ISSN 01694332 7.2.2

[208] Vitos, L. ; Ruban, A. V. ; Skriver, H. L. ; Kollár, J.: The surface energy of metals. In: *Surface Science* 411 (1998), Nr. 1-2, S. 186–202. http://dx.doi.org/10.1016/S0039-6028(98)00363-X. – DOI 10.1016/S0039–6028(98)00363–X. – ISSN 00396028 7.2.2

[209] Rhee, S. K.: Surface energies of silicate glasses calculated from their wettability data. In: *Journal of Materials Science* 12 (1977), Nr. 4, S. 823–824. http://dx.doi.org/10.1007/BF00548176. – DOI 10.1007/BF00548176. – ISSN 0022–2461 7.2.2

[210] Livey, D. T. ; Murray, P.: Surface Energies of Solid Oxides and Carbides. In: *Journal of the American Ceramic Society* 39 (1956), Nr. 11, S. 363–372 7.2.2

[211] KRÜSS GmbH: *Values for the surface free energy of solids*. https://www.kruss.de/services/education-theory/substance-data/solids/. Version: 2017 7.2.2

[212] Tarquini, Stefania ; Antonini, Carlo ; Amirfazli, Alidad ; Marengo, Marco ; Palacios, Jose: Investigation of ice shedding properties of superhydrophobic coatings on helicopter blades. In: *Cold Regions Science and Technology* 100 (2014), S. 50–58. http://dx.doi.org/10.1016/j.coldregions.2013.12.009. – DOI 10.1016/j.coldregions.2013.12.009. – ISSN 0165232X 7.2.2

[213] Reich, A. ; B. F. Goodrich Aerospace, De-icing systems (Hrsg.): *Interface influences upon ice adhesion to airfoil materials: 32nd Aerospace Sciences Meeting & Exhibit* (AIAA) 7.2.2

[214] Soltis, Jared ; Palacios, Jose ; Eden, Timothy ; Wolfe, Douglas: Evaluation of Ice-Adhesion Strength on Erosion-Resistant Materials. In: *AIAA Journal* 53 (2015), Nr. 7, S. 1825–1835. http://dx.doi.org/10.2514/1.J053516. – DOI 10.2514/1.J053516. – ISSN 0001–1452 7.2.2

[215] Ling, Edwin Jee Y. ; Uong, Victor ; Renault-Crispo, Jean-Sebastien ; Kietzig, Anne-Marie ; Servio, Phillip: Reducing Ice Adhesion on Nonsmooth Metallic Surfaces: Wettability and Topography Effects. In: *ACS applied materials & interfaces* 8 (2016), Nr. 13, S. 8789–8800. http://dx.doi.org/10.1021/acsami.6b00187. – DOI 10.1021/acsami.6b00187. – ISSN 1944–8244 7.2.2

[216] Hejazi, Vahid ; Sobolev, Konstantin ; Nosonovsky, Michael: From superhydrophobicity to icephobicity: Forces and interaction analysis. In: *Scientific reports* 3 (2013), S. 2194. http://dx.doi.org/10.1038/srep02194. – DOI 10.1038/srep02194. – ISSN 2045–2322 7.2.2

[217] Chernyy, Sergey ; Jarn, Mikael ; Shimizu, Kyoko ; Swerin, Agne ; Pedersen, Steen U. ; Daasbjerg, Kim ; Makkonen, Lasse ; Claesson, Per ; Iruthayaraj, Joseph: Superhydrophilic polyelectrolyte brush layers with imparted anticing properties: Effect of counter ions. In: *ACS applied materials & interfaces* 6 (2014), Nr. 9, S. 6487–6496. http://dx.doi.org/10.1021/am500046d. – DOI 10.1021/am500046d. – ISSN 1944–8244 7.2.2

[218] Raraty, L. E. ; Tabor, D.: The adhesion and strength properties of ice. In: *Proceedings of the Royal Society of London. Series A, Mathematical and Physical Sciences* 245 (1958), Nr. 1241, 184–201. http://dx.doi.org/10.1098/rspa.1958.0076. – DOI 10.1098/rspa.1958.0076 7.2.2, 7.2.2

[219] Rajkiran Gouni: *A new technique to study temperature effects on ice adhesion strength for wind turbine materials*. Cleveland, OH, USA, Case Western Reserve University, Master Thesis, January 2011 7.2.2

[220] Herr, Horst: *Europa*. Bd. 50619: *Technische Physik: Band 3: Wärmelehre*. 4. Aufl. Haan-Gruiten : Verl. Europa-Lehrmittel Nourney Vollmer, 2006. – ISBN 9783808550649 7.3.1

[221] Image Metrology: *SPIP (AFM software) Manual: Classic Roughness Parameters for Images*. http://spip.imagemet.com/WebHelp6/Default.htm#RoughnessParameters/Roughness_Parameters.htm A.3.1, A.3.1

[222] Wikibooks-Bearbeiter ; Wikibooks, die freie B. (Hrsg.): *Tabellensammlung Chemie*. https://de.wikibooks.org/w/index.php?title=Tabellensammlung_Chemie&oldid=813993. Version: 2016 A.8

# A. Appendix

## A.1. Materials

### A.1.1. DSC measurement graphs

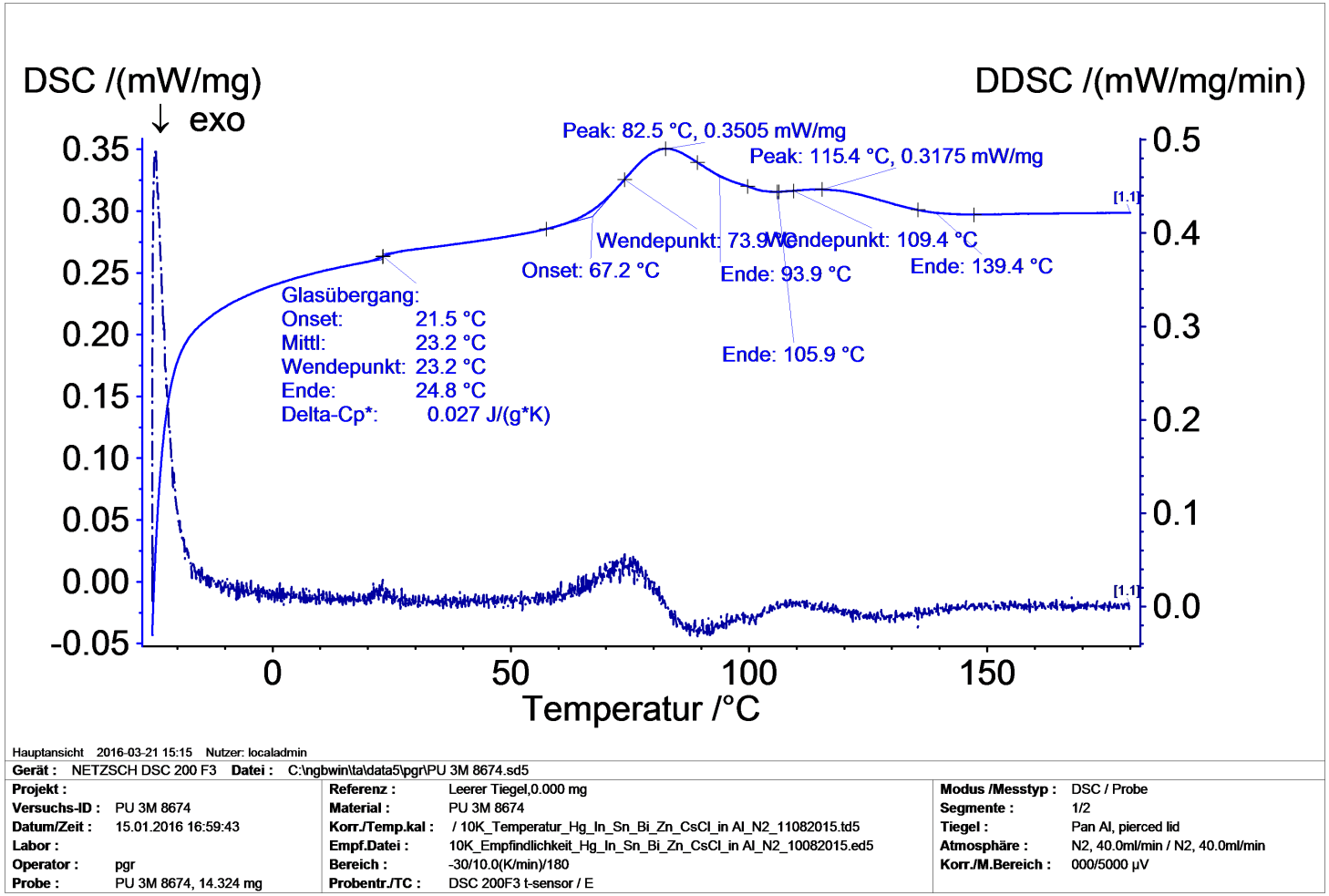


Figure A.1.: DSC melting curve of the PU film 8674 from 3M.

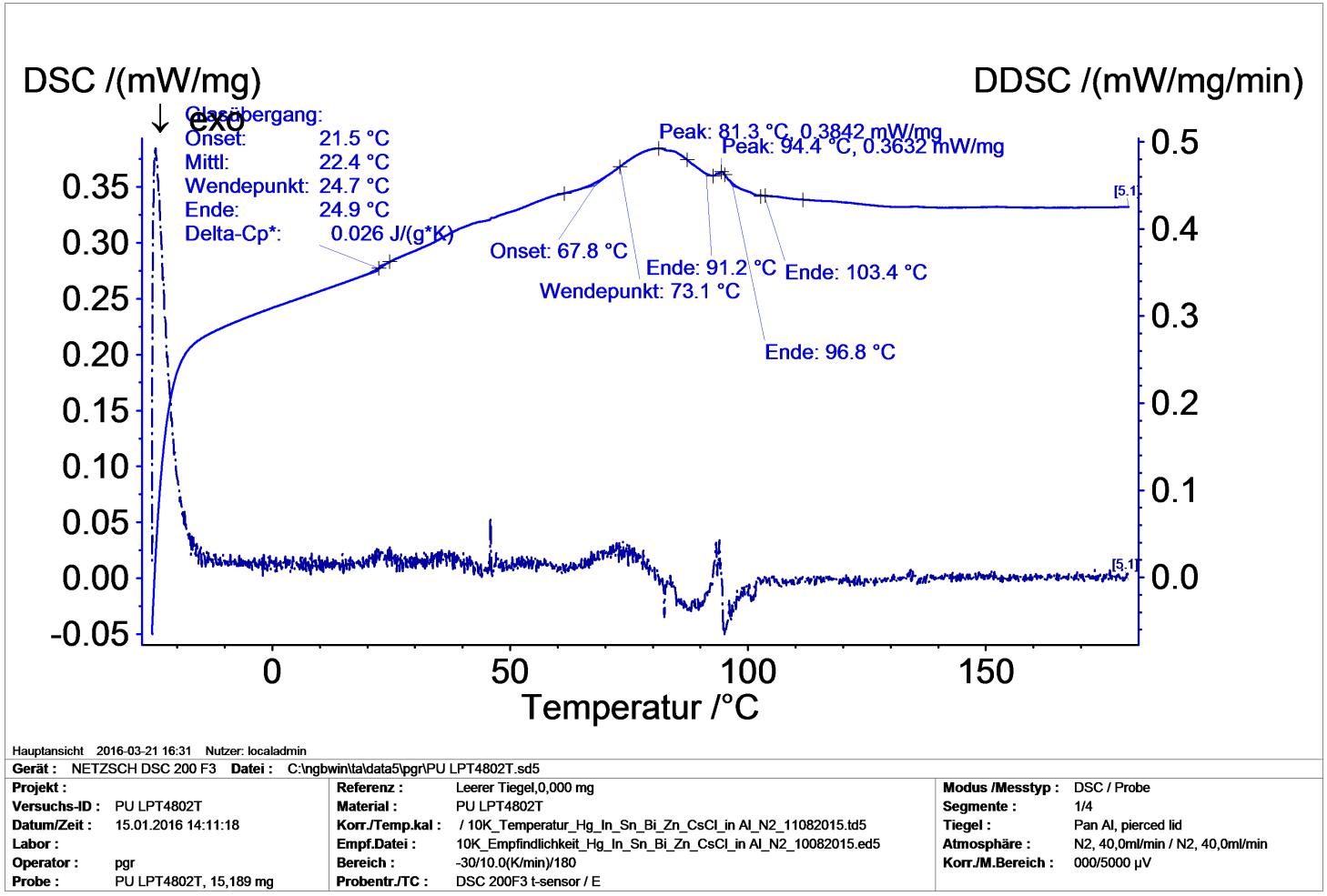


Figure A.2.: DSC melting curve of the PU film LPT 4802 T from Epurex Films, Covestro.

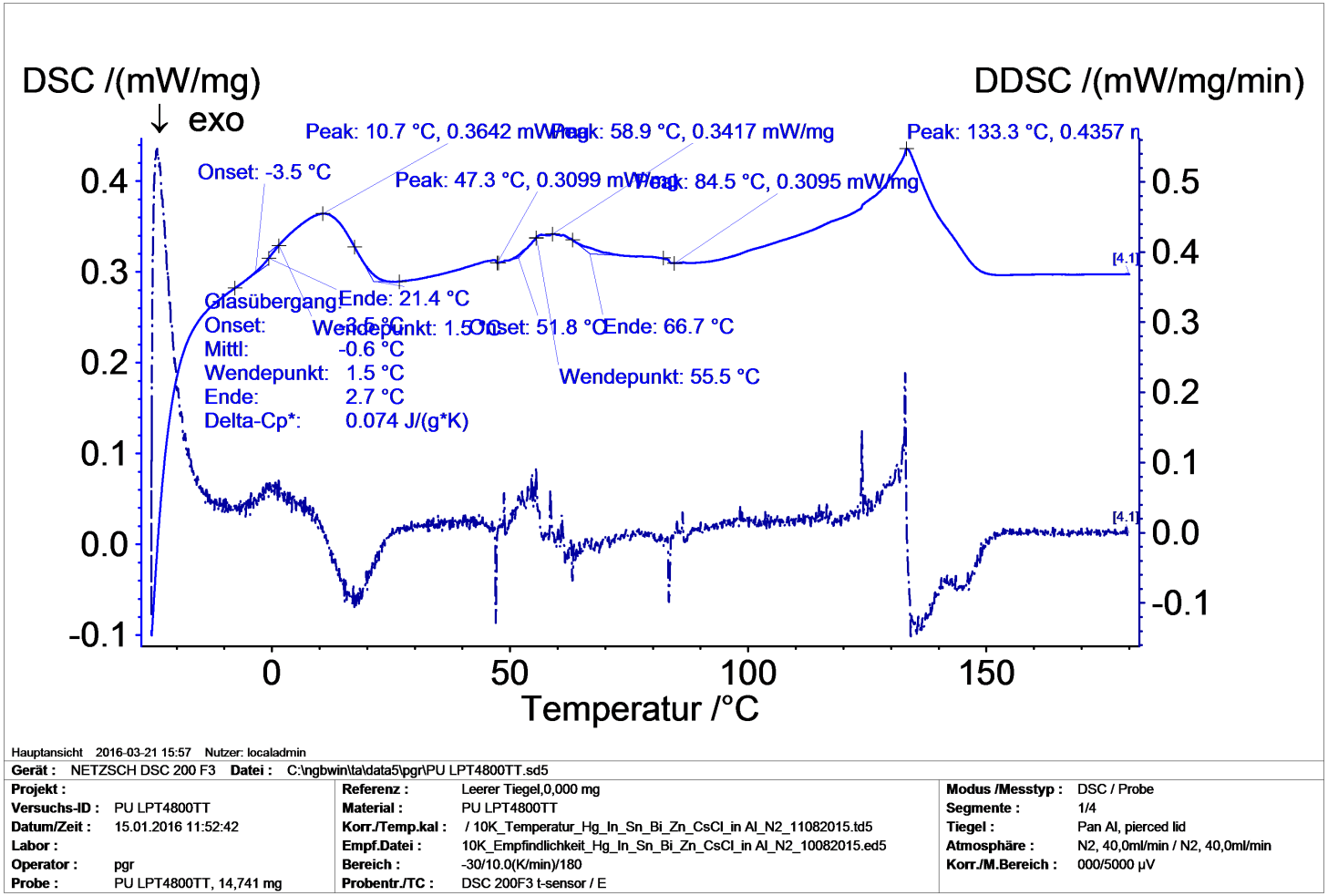


Figure A.3.: DSC melting curve of the PU film LPT 4800 TT from Epurex Films, Covestro, measurement run 1.

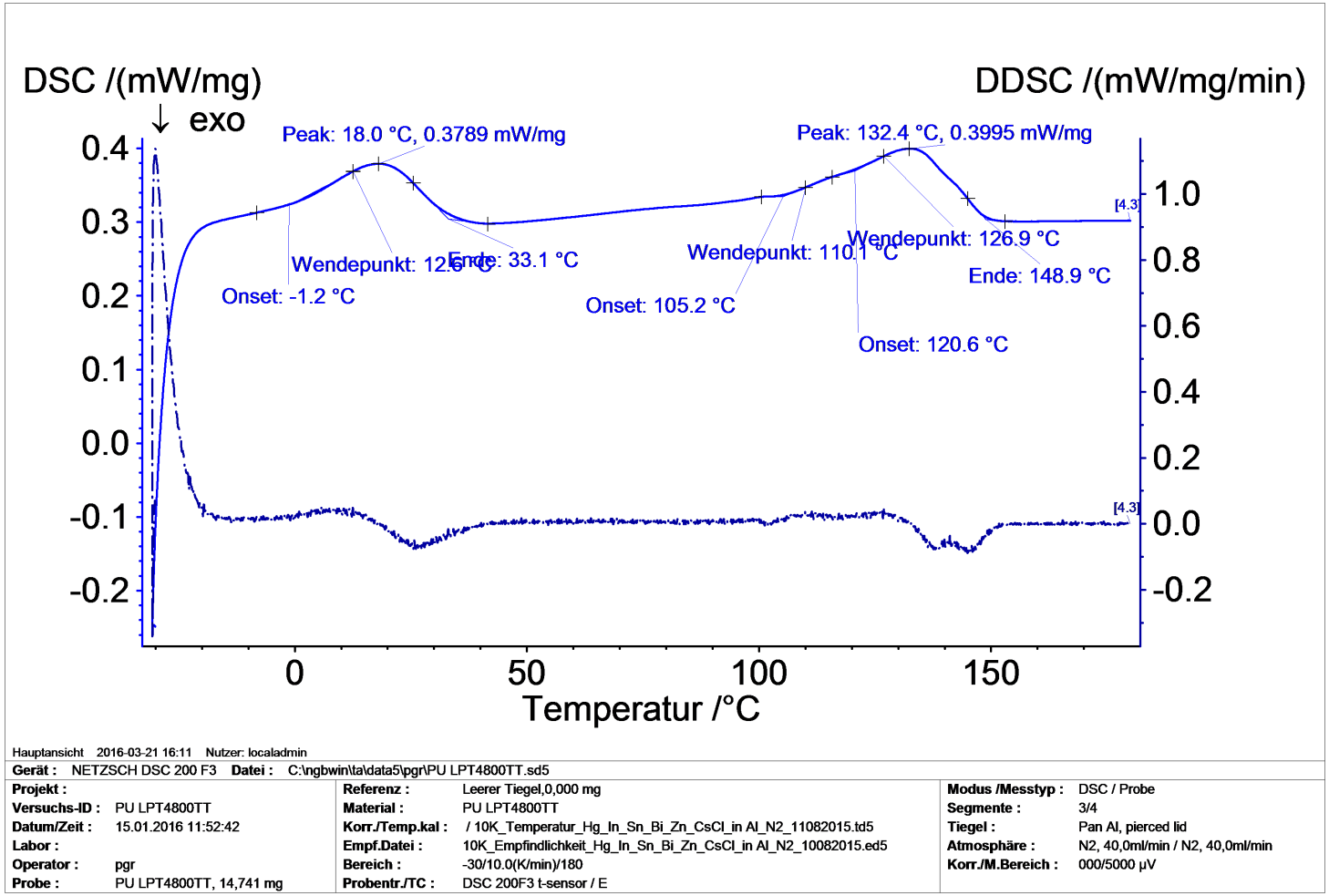


Figure A.4.: DSC melting curve of the PU film LPT 4800 TT from Epurex Films, Covestro, measurement run 2.

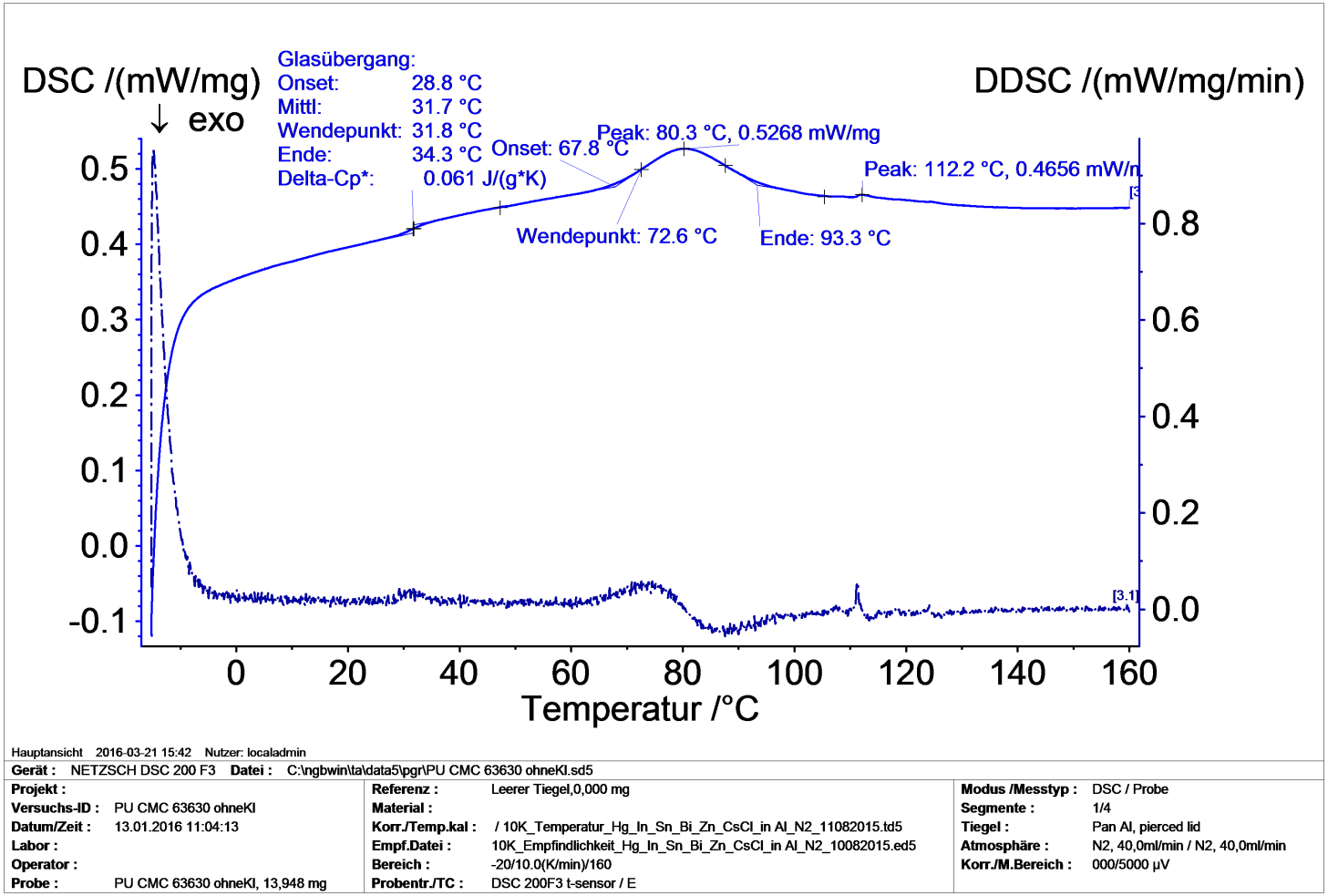


Figure A.5.: DSC melting curve of the PU film 63630 without adhesive layer from CMC Klebetechnik.

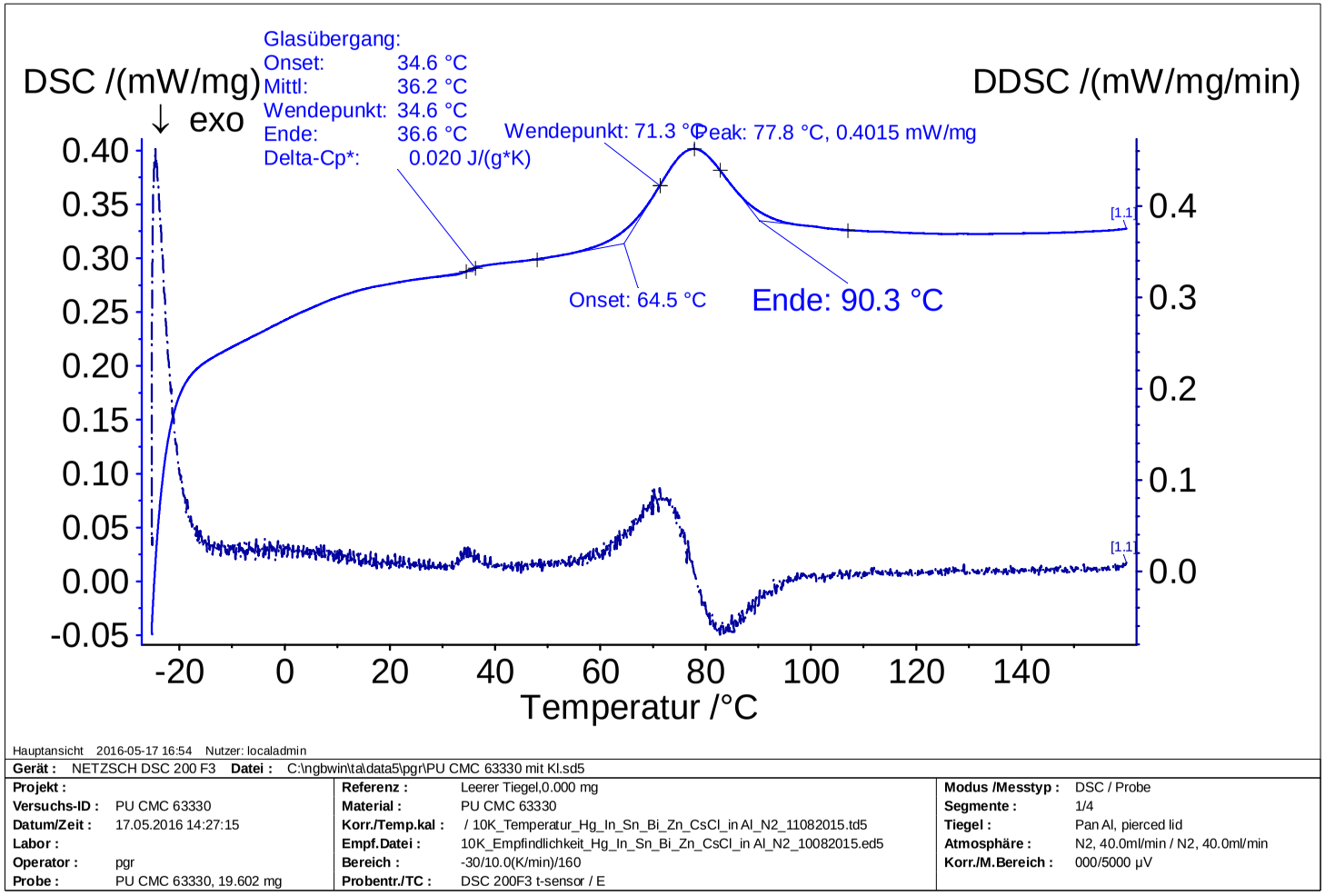




Figure A.6.: DSC melting curve of the PU film 63330 with adhesive layer from CMC Klebetechnik.

# A.2. Microstructuring with a hot embossing process

## A.2.1. Microstructures of stamp 1

Table A.1.: Geometrical dimensions of hexagonally arranged microstructures of stamp 1 (Schepers GmbH).

| Name | Type of structure | Field | H (µm) | D (µm) | d (µm) | P (µm) | P/D (-) | P/d (-) | H/d (-) | rf (-) |
|---|---|---|---|---|---|---|---|---|---|---|
| C18 | Cylinder | A1 | 15 | 35 | 20 | 100 | 2.86 | 5.00 | 0.75 | 1.09 |
| C19 | Cylinder | A5 | 24 | 50 | 25 | 100 | 2.00 | 4.00 | 0.96 | 1.20 |
| C20 | Cylinder | A12 | 32 | 80 | 40 | 100 | 1.25 | 2.50 | 0.80 | 1.39 |
| E7 | Ellipse | B1 | 25 | 60 | 30 | 230 | 3.83 | 7.67 | 0.83 | 1.04 |
| E8 | Ellipse | B5 | 21 | 110 | 75 | 230 | 2.09 | 3.07 | 0.28 | 1.06 |
| E9 | Ellipse | B12 | 32 | 180 | 100 | 230 | 1.28 | 2.30 | 0.32 | 1.11 |
| L4 | Linear ridge | E3 | 17 | 32 | 15 | 100 | 3.13 | 6.67 | 1.13 | 1.08 |
| L5 | Linear ridge | E7 | 17 | 45 | 35 | 100 | 2.22 | 2.86 | 0.49 | 1.16 |
| L6 | Linear ridge | E12 | 19 | 80 | 25 | 100 | 1.25 | 4.00 | 0.76 | 1.10 |

## A.2.2. Microstructures of stamp 2

Table A.2.: Geometrical dimensions of hexagonally arranged microstructures of stamp 2 (Schepers GmbH).

| Name | Type of structure | Field | H (µm) | D (µm) | d (µm) | P (µm) | P/D (-) | P/d (-) | H/d (-) | rf (-) |
|---|---|---|---|---|---|---|---|---|---|---|
| C1 | Cylinder | A1 | 114 | 51 | 14 | 70 | 1.4 | 5.02 | 8.14 | 3.32 |
| C2 | Cylinder | A2 | 110 | 52 | 12 | 102 | 2.0 | 8.46 | 9.17 | 2.03 |
| C3 | Cylinder | A3 | 112 | 52 | 16 | 201 | 3.9 | 12.53 | 7.0 | 1.29 |
| E1 | Ellipse | B1 | 56 | 44 | 22 | 68 | 1.5 | 3.08 | 2.54 | 2.20 |
| E2 | Ellipse | B2 | 81 | 47 | 24 | 101 | 2.1 | 4.28 | 3.45 | 1.89 |
| E3 | Ellipse | B3 | 20 | 51 | 26 | 201 | 3.9 | 7.84 | 0.78 | 1.04 |

## A.2.3. Microstructures of stamp 3

Table A.3.: Geometrical dimensions of hexagonally arranged microstructures of stamp 3.1 (Schepers GmbH).

| Name | Type of structure | Field | H (µm) | D (µm) | d (µm) | P (µm) | P/D (-) | P/d (-) | H/d (-) | rf (-) |
|---|---|---|---|---|---|---|---|---|---|---|
| C4 | Cylinder | A1 | 131 | 67 | 55 | 202 | 3.00 | 3.69 | 2.4 | 1.68 |
| C5 | Cylinder | A2 | 75 | 60 | 30 | 101 | 1.68 | 3.38 | 2.5 | 1.97 |
| C6 | Cylinder | A3 | 71 | 37 | 20 | 50 | 1.36 | 2.45 | 3.5 | 3.65 |
| C7 | Cylinder | B1 | 24 | 52 | 20 | 203 | 3.90 | 10.28 | 1.2 | 1.04 |
| C8 | Cylinder | B2 | 35 | 48 | 24 | 101 | 2.10 | 4.23 | 1.5 | 1.32 |
| C9 | Cylinder | B3 | 43 | 34 | 14 | 49 | 1.41 | 3.60 | 3.2 | 2.24 |
| C10 | Cylinder | C1 | 49 | 100 | 49 | 291 | 2.91 | 5.89 | 1.0 | 1.10 |
| C11 | Cylinder | C2 | 100 | 106 | 93 | 206 | 1.93 | 2.20 | 1.1 | 1.80 |
| C12 | Cylinder | C3 | 17 | 104 | 100 | 122 | 1.17 | 1.22 | 0.2 | 1.38 |

Table A.4.: Geometrical dimensions of hexagonally arranged microstructures of stamp 3.2 (Schepers GmbH).

| Name | Type of structure | Field | H (µm) | D (µm) | d (µm) | P (µm) | P/D (-) | P/d (-) | H/d (-) | rf (-) |
|---|---|---|---|---|---|---|---|---|---|---|
| C13 | Cylinder | A4 | 119 | 40 | 20 | 50 | 1.25 | 2.50 | 5.9 | 5.75 |
| C14 | Cylinder | A5 | 29 | 60 | 20 | 105 | 1.75 | 5.25 | 1.4 | 1.20 |
| C15 | Cylinder | A6 | 66 | 60 | 30 | 205 | 3.42 | 6.83 | 2.2 | 1.20 |
| L1 | Line | B4 | 32 | 30 | 10 | 50 | 1.67 | 5.00 | 3.2 | 1.59 |
| L2 | Line | B5 | 99 | 47 | 20 | 100 | 2.13 | 5.00 | 5.0 | 1.91 |
| L3 | Line | B6 | 106 | 45 | 13 | 200 | 4.44 | 15.38 | 8.2 | 1.21 |
| E4 | Ellipse | C4 | 59 | 275 | 160 | 335 | 1.23 | 2.15 | 0.4 | 1.17 |
| E5 | Ellipse | C5 | 102 | 275 | 160 | 410 | 1.50 | 2.56 | 0.6 | 1.28 |
| E6 | Ellipse | C6 | 138 | 275 | 160 | 510 | 1.85 | 3.14 | 0.8 | 1.28 |

## Light microscopy images of stamp 3.1 - cylinders

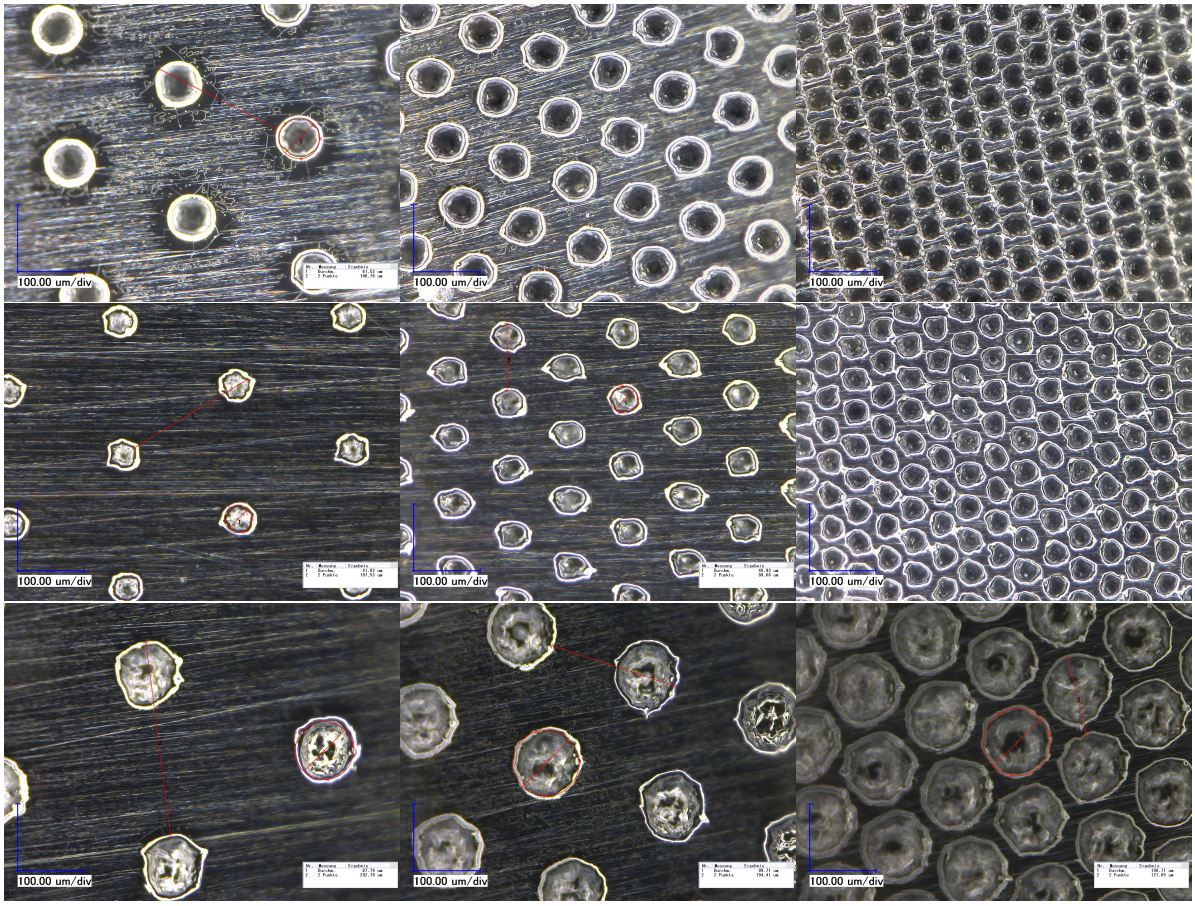


Figure A.7.: Light microscopy images of stamp 3.1, magnification 500x, first row: C4/C5/C6, second row: C7/C8/C9, third row: C10/C11/C12.

**Laser scanning microscopy images of PU films imprinted by stamp 3.1 - cylinders**

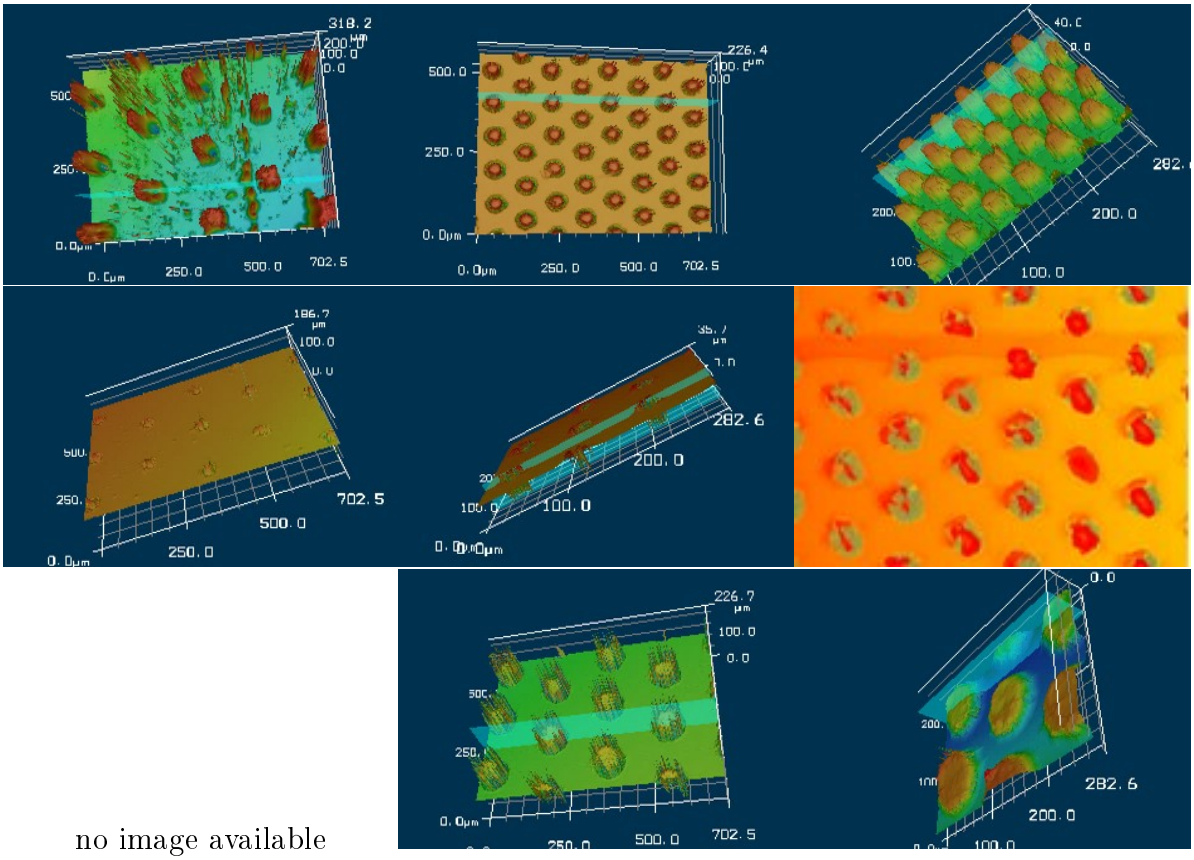


no image available

Figure A.8.: Laser scanning microscopy images of PU films imprinted by stamp 3.1, magnification 20x, first row: C4/C5/C6, second row: C7/C8/C9, third row: C10/C11/C12.

### Laser scanning microscopy images of PU films imprinted by stamp 3.2 - cylinders, lines, ellipses

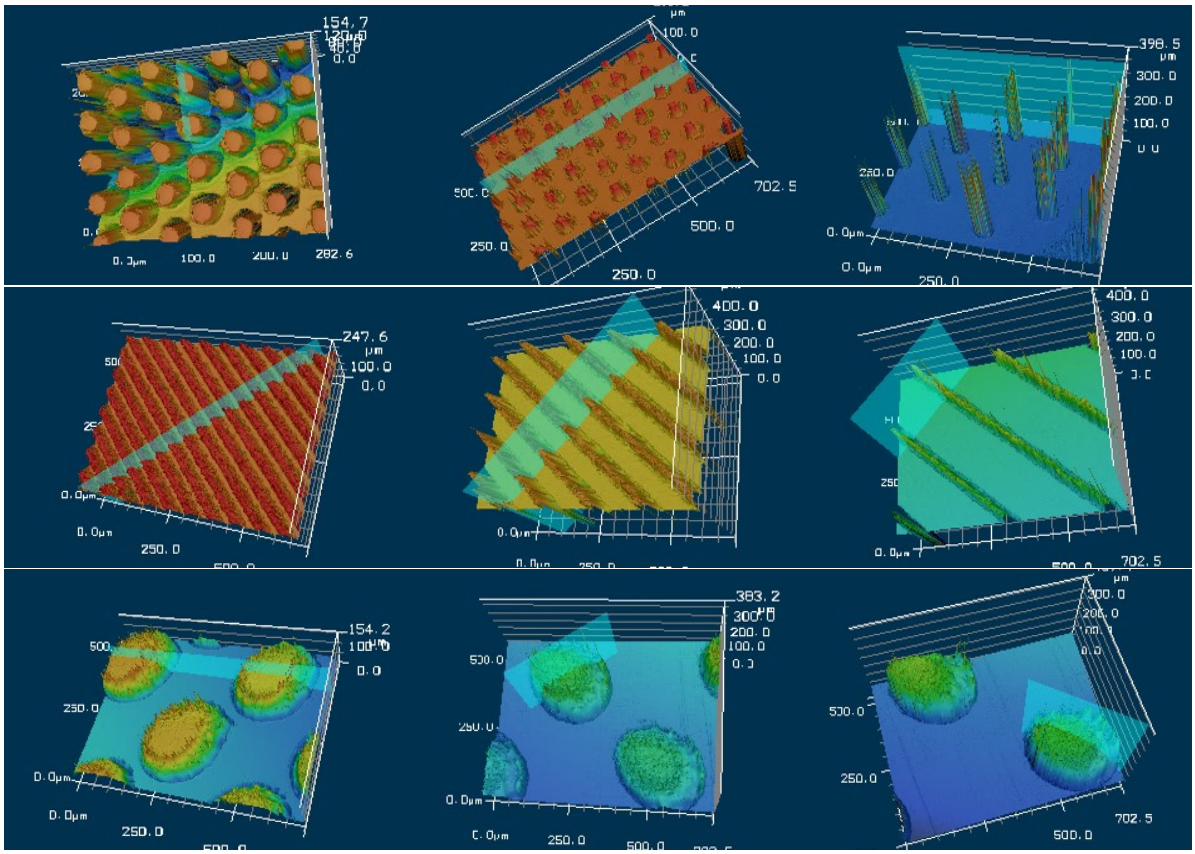

Figure A.9.: Laser scanning microscopy images of PU films imprinted by stamp 3.2, magnification 20x, first row: C13/C14/C15, second row: L1/L2/L3, third row: E4/E5/E6.

## A.2.4. Microstructures of stamp 4

Table A.5.: Geometrical dimensions of the quadratically arranged microstructures of stamp 4 (Schepers GmbH).

| Name | Field | Type of structure | H | D | d | P | P/D | P/d | H/d | rf |
|---|---|---|---|---|---|---|---|---|---|---|
| - | - | - | (µm) | (µm) | (µm) | (µm) | (-) | (-) | (-) | (-) |
| C16 | DIN A4 | Cylinder | 50 | 70 | 35 | 90 | 1.29 | 2.57 | 1.43 | 1.72 |
| C17 | DIN A5 | Cylinder | 50 | 60 | 30 | 90 | 1.5 | 3.00 | 1.67 | 1.65 |

### Light microscopy images of stamp 4

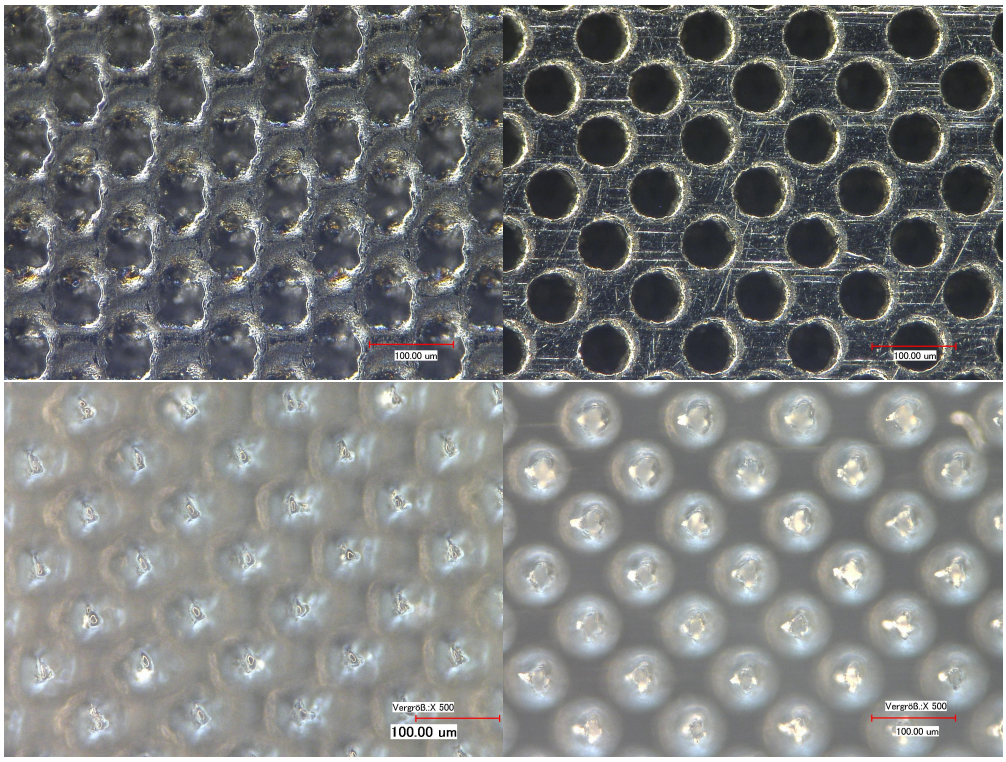


Figure A.10.: Light microscopy images at 500x magnification of the stamps from Schepers GmbH (top) and the imprinted PU films (bottom): DIN A4 (left) and DIN A5 (right).

# A.3. Plasma polymers

## A.3.1. AFM measurements

### $C_4F_8$ 50 W plasma coatings

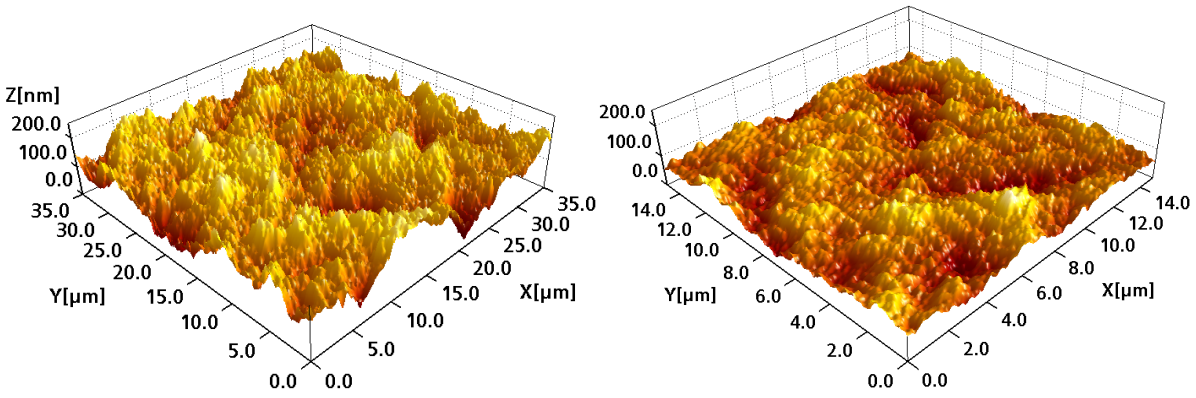


Figure A.11.: AFM images of sample PU + $C_4F_8$ (50 W), etched with Ar (100 W), 35 µm and 15 µm scan length.

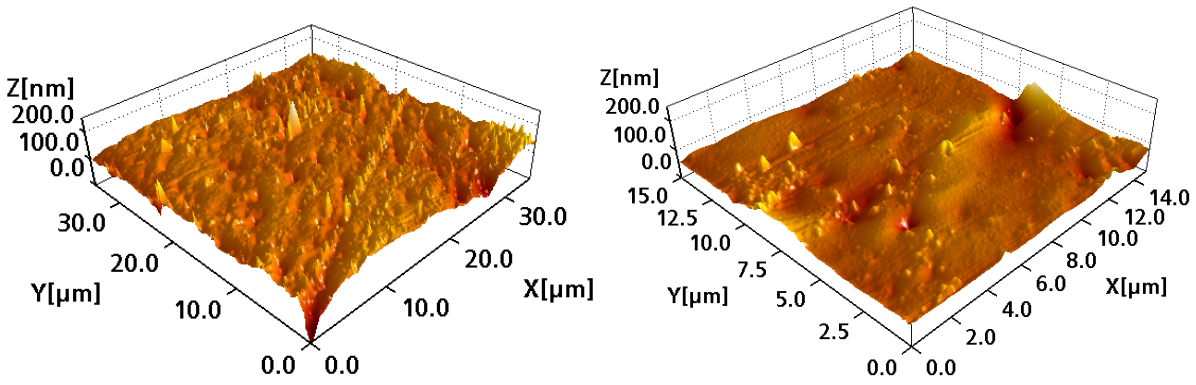


Figure A.12.: AFM images of sample PU + $C_4F_8$ (50 W), then etched with Ar (100 W) and coated again in a $C_4F_8$ (50 W) plasma, 35 µm and 15 µm scan length.

### $C_3F_6$ 50 W plasma coatings

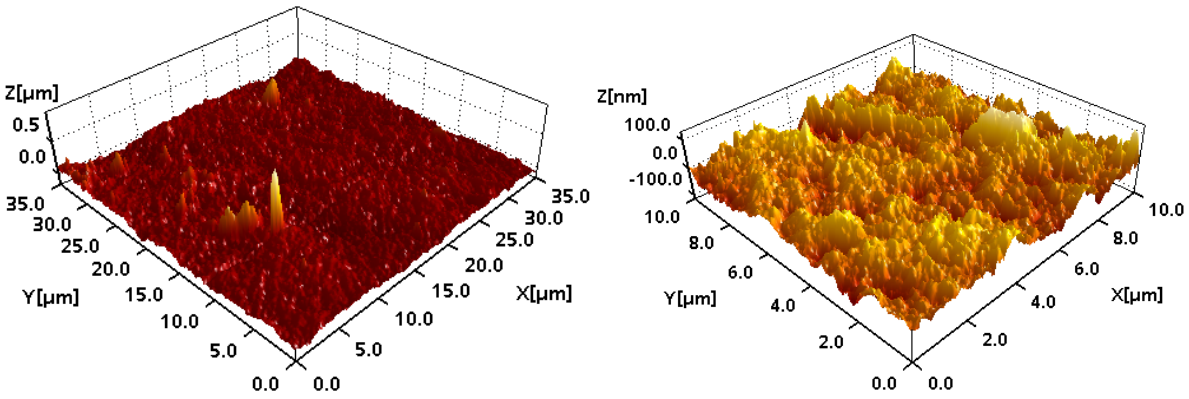


Figure A.13.: AFM images of sample PU + $C_3F_6$ (50 W), 35 µm and 10 µm scan length.

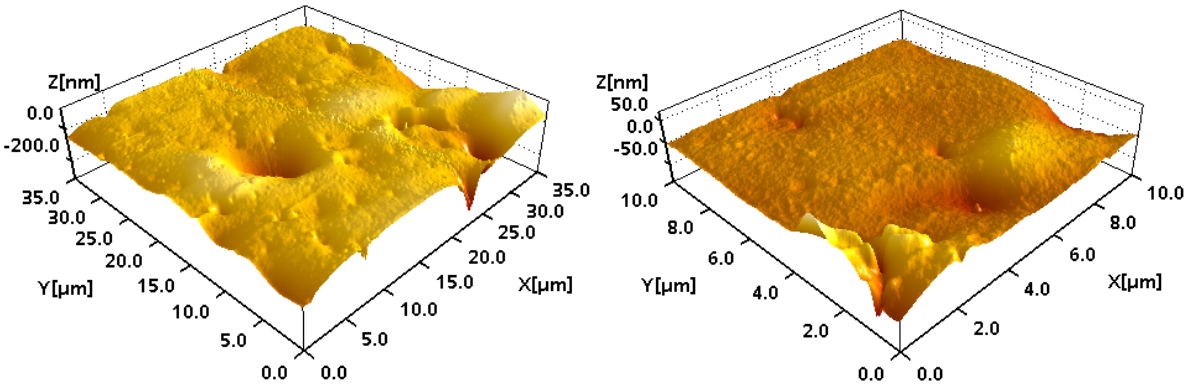


Figure A.14.: AFM images of sample PU + $C_3F_6$ (50 W), etched with Ar (200 W), 35 µm and 10 µm scan length.

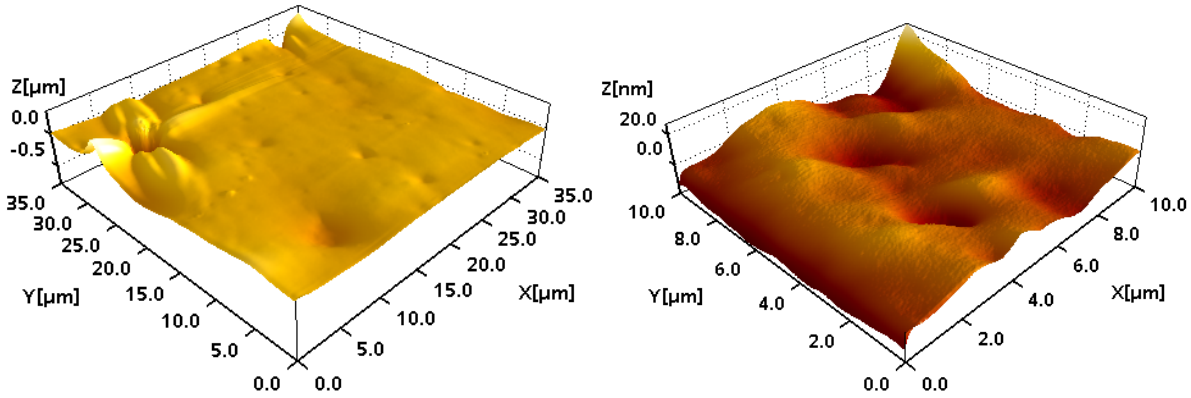


Figure A.15.: AFM images of sample PU + $C_3F_6$ (50 W), etched with Ar (300 W), 35 µm and 10 µm scan length.

### HMDSO 60 W plasma coatings

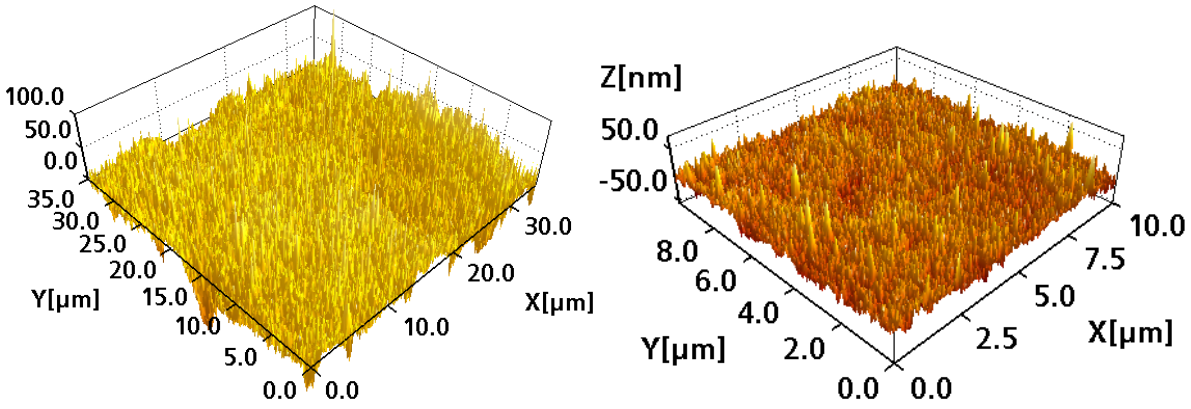


Figure A.16.: AFM images of sample PU + HMDSO (60 W), 35 µm and 10 µm scan length.

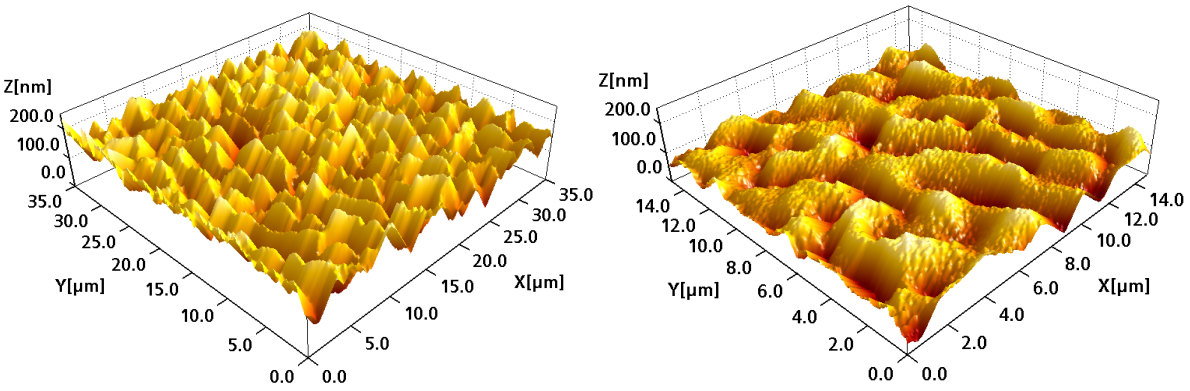


Figure A.17.: AFM images of sample PU + HMDSO (60 W), etched with Ar (100 W), then coated again with HMDSO (60 W), 35 µm and 15 µm scan length.

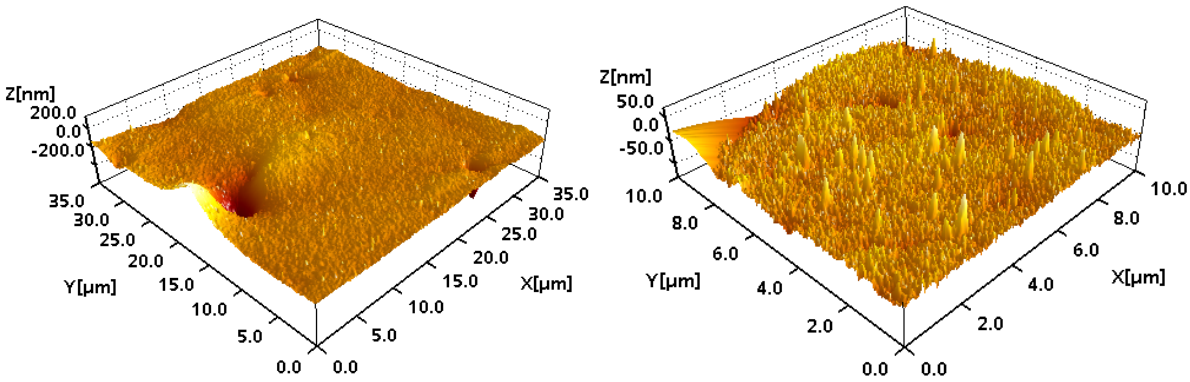


Figure A.18.: AFM images of sample PU + HMDSO (60 W), etched with Ar (200 W), 35 µm and 10 µm scan length.

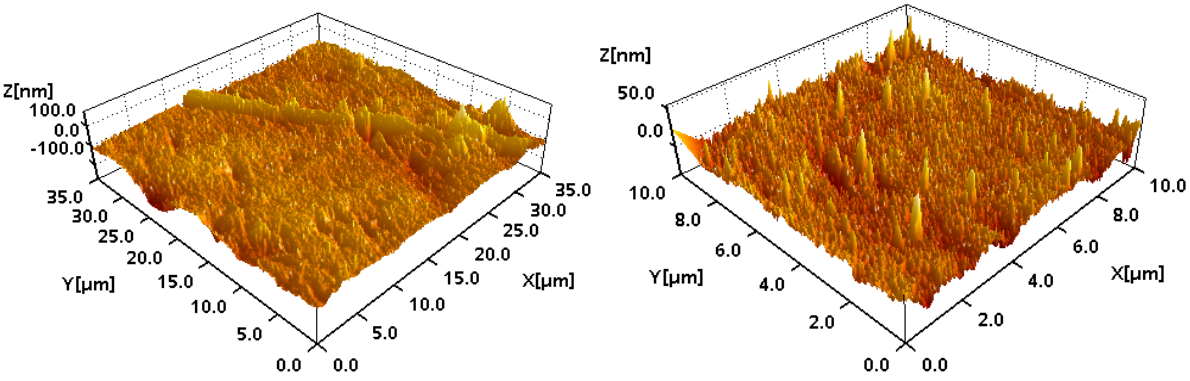


Figure A.19.: AFM images of sample PU + HMDSO (60 W), etched with Ar (300 W), 35 µm and 10 µm scan length.

## HMDSO 200 W plasma coatings

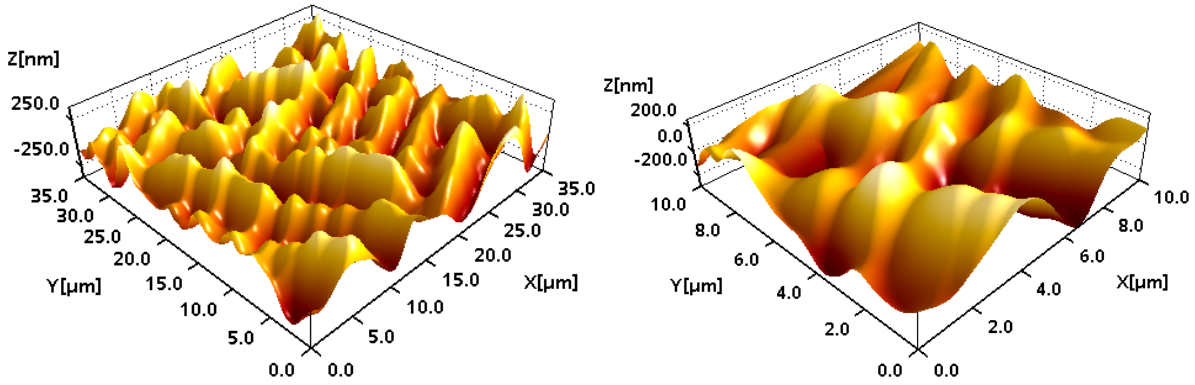


Figure A.20.: AFM images of sample PU + HMDSO (200 W) No.1, 35 µm and 10 µm scan length.

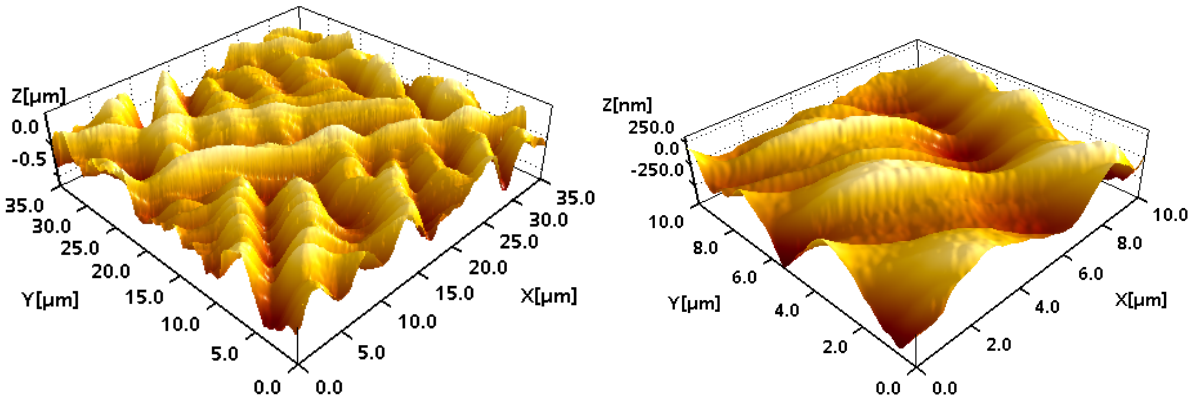


Figure A.21.: AFM images of sample PU + HMDSO (200 W) No.2, 35 µm and 10 µm scan length.

### Calculation of AFM roughness values

For a scan area of M x N, the mean height is calculated as follows [221]:

$$\mu = \frac{1}{MN} \sum_{k=0}^{M-1} \sum_{l=0}^{N-1} z(x_k, y_l) \ . \tag{A.1}$$

The roughness parameters are calculated as follows [221]:

$$S_\mathrm{a} = \frac{1}{MN} \sum_{k=0}^{M-1} \sum_{l=0}^{N-1} |z(x_k, y_l) - \mu| \ , \tag{A.2}$$

$$S_\mathrm{q} = \sqrt{\frac{1}{MN} \sum_{k=0}^{M-1} \sum_{l=0}^{N-1} [z(x_k, y_l) - \mu]^2} \ , \tag{A.3}$$

$$S_\mathrm{dr} = \frac{\left(\sum_{k=0}^{M-2} \sum_{l=0}^{N-2} A_{kl}\right) - (M-1)(N-1)\delta x \delta y}{(M-1)(N-1)\delta x \delta y} \times 100\% \ , \tag{A.4}$$

$$A_\mathrm{kl} = \frac{1}{4} \times \left(\sqrt{\delta y^2 + (z(x_k, y_l) - z(x_k, y_{l+1}))^2} + \sqrt{\delta y^2 + (z(x_{k+1}, y_l) - z(x_{k+1}, y_{l+1}))^2}\right) \times \\ \times \left(\sqrt{\delta x^2 + (z(x_k, y_l) - z(x_{k+1}, y_l))^2} + \sqrt{\delta x^2 + (z(x_k, y_{l+1}) - z(x_{k+1}, y_{l+1}))^2}\right) \ . \tag{A.5}$$

$$S_\mathrm{sc} = \frac{-1}{2n} \sum_{i=1}^{n} \left(\frac{\partial^2 z(x,y)}{\partial x^2}\right) + \left(\frac{\partial^2 z(x,y)}{\partial y^2}\right) \ . \tag{A.6}$$

## A.3.2. ESCA spectra

### $C_3F_6$ plasma coating on a Si-wafer (samples of stamp 1)

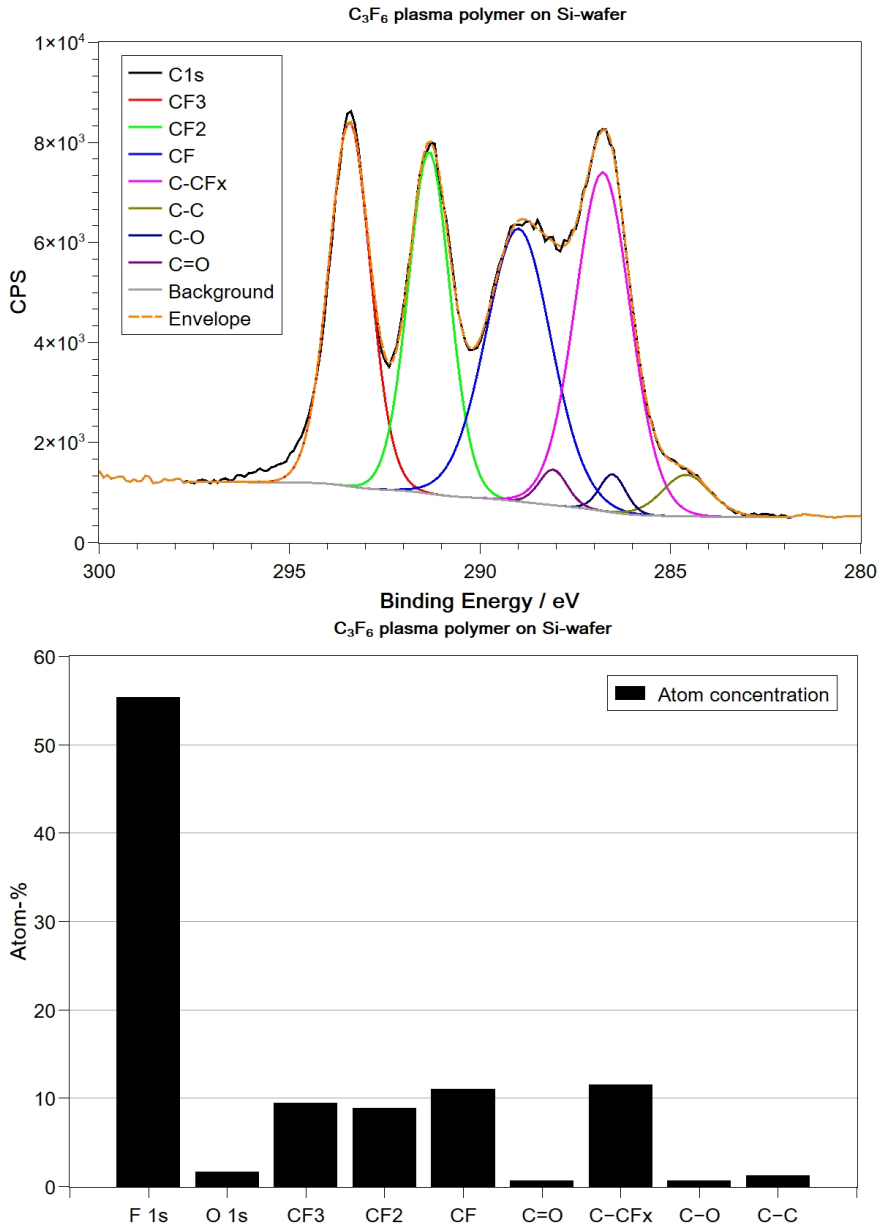


Figure A.22.: ESCA C 1s spectrum and atomic concentrations of the $C_3F_6$-plasma coating on a Si-wafer (samples of stamp 1).

## $C_4F_8$ plasma coating on a Si-wafer (samples of stamp 1)

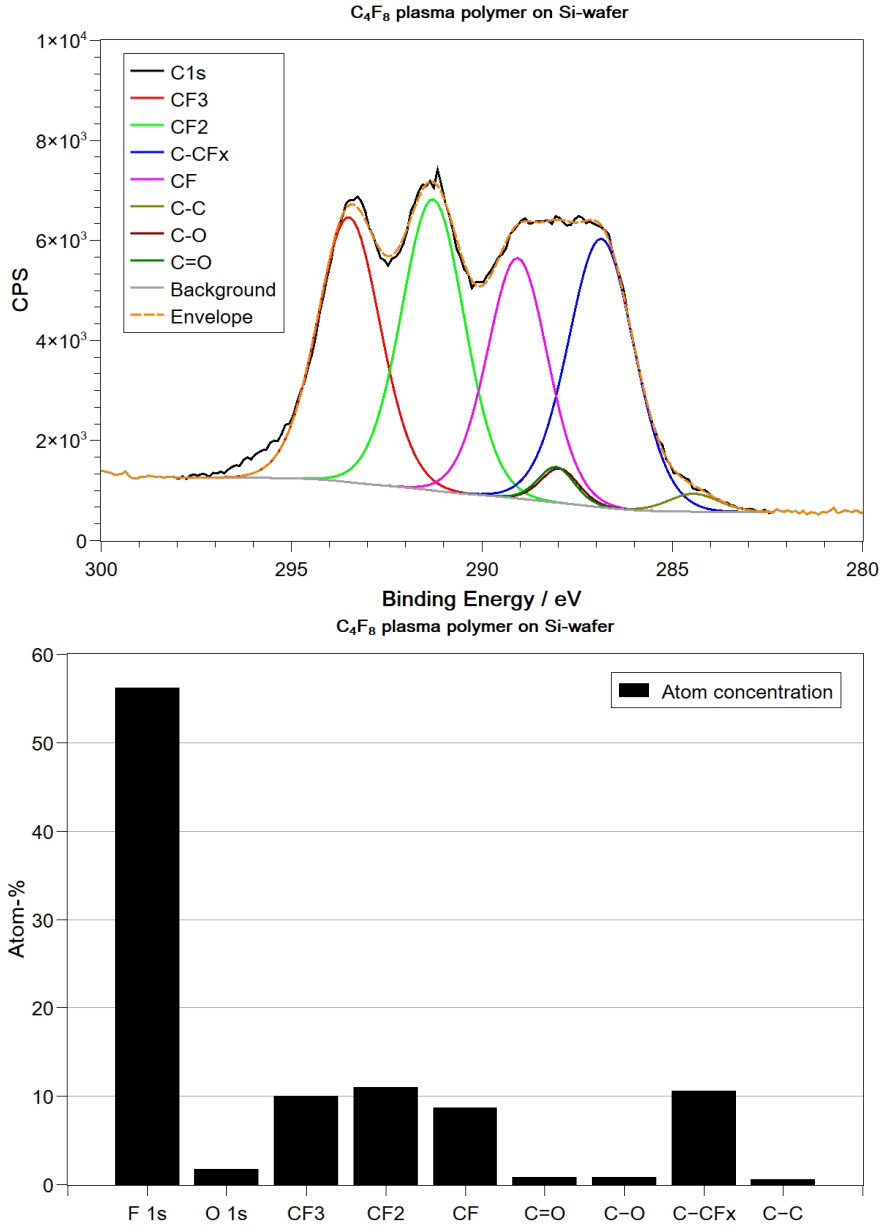


Figure A.23.: ESCA C 1s spectrum and atomic concentrations of the $C_4F_8$-plasma coating on a Si-wafer (samples of stamp 1).

## $CHF_3$ plasma coatings on a Si-wafer (samples of stamp 1)

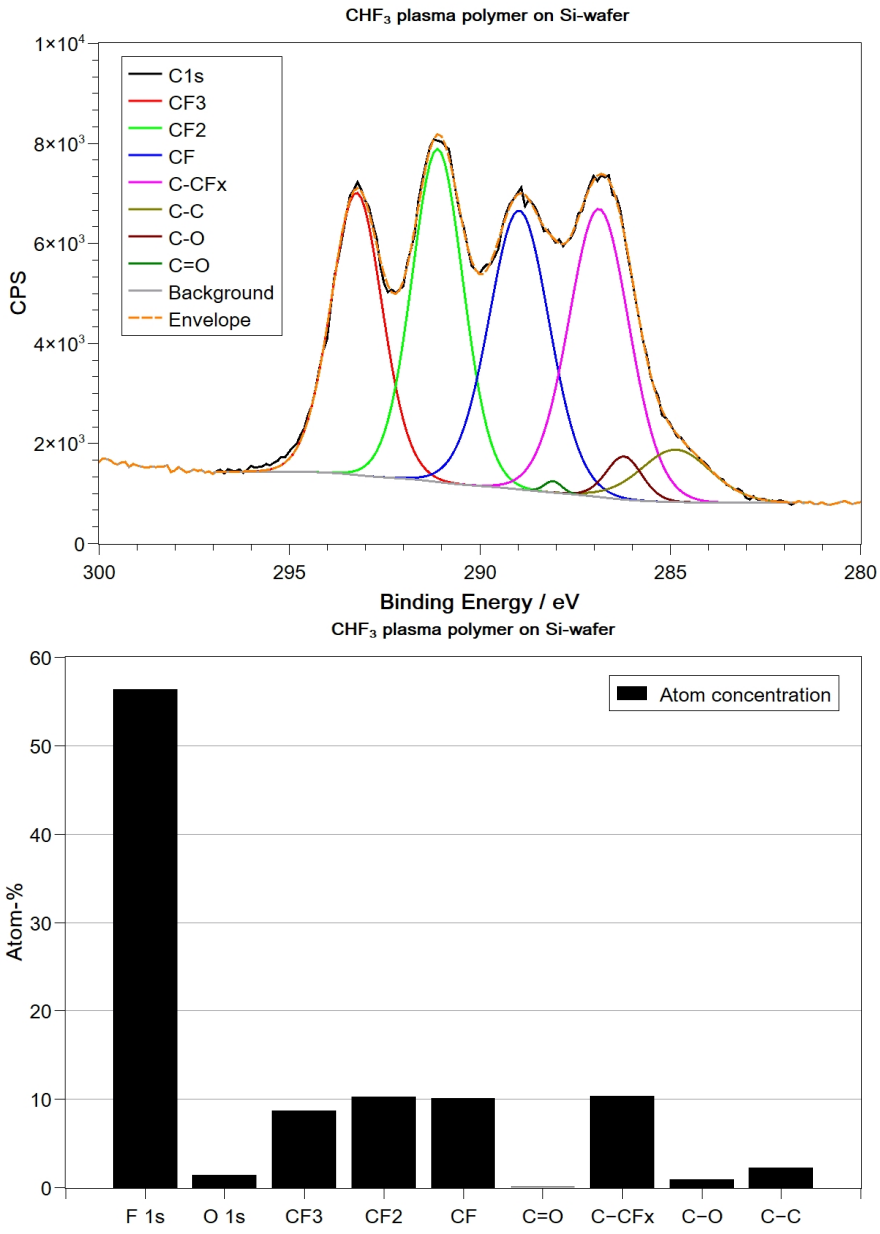


Figure A.24.: ESCA C 1s spectrum and atomic concentrations of the $CHF_3$-plasma coating on a Si-wafer (samples of stamp 1).

## $C_4F_8$ plasma coating on a Si-wafer (samples of stamp 2)

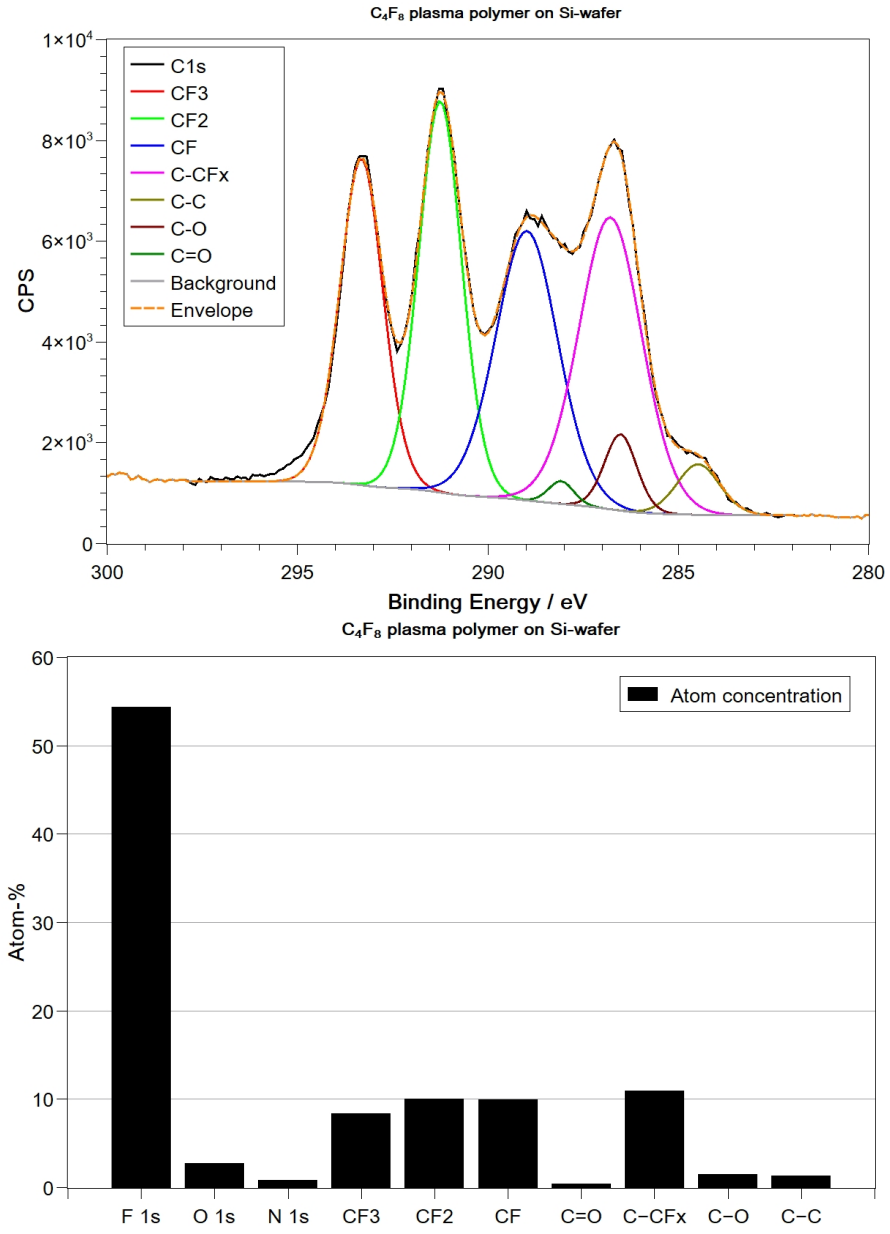


Figure A.25.: ESCA C 1s spectra of the $C_4F_8$-plasma coating on a Si-wafer (samples of stamp 2).

## $CHF_3$ plasma coating on a Si-wafer (samples of stamp 2)

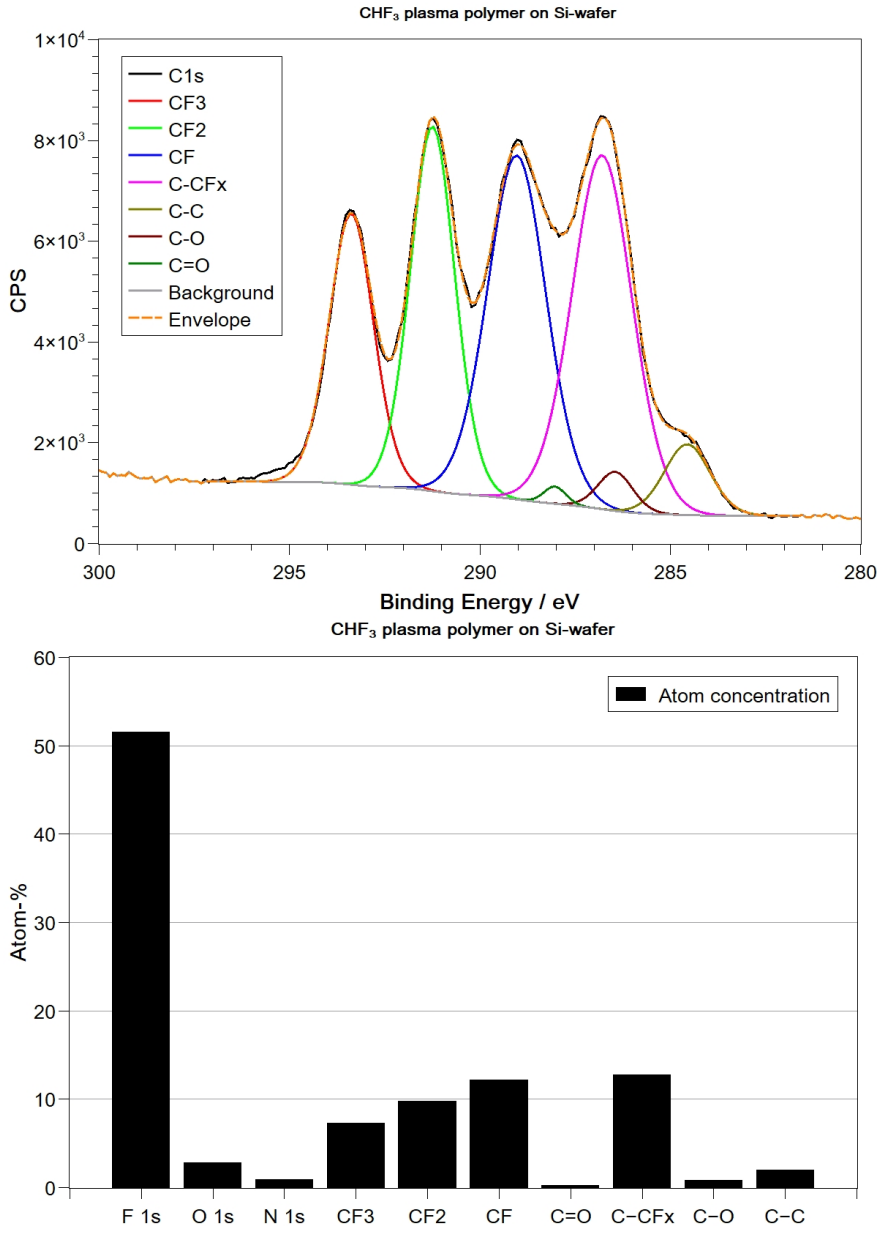


Figure A.26.: ESCA C 1s spectra of the $CHF_3$-plasma coating on a Si-wafer (samples of stamp 2).

## $C_4F_8$ plasma coating on a PU film (CMC 63630, samples of stamp 3)

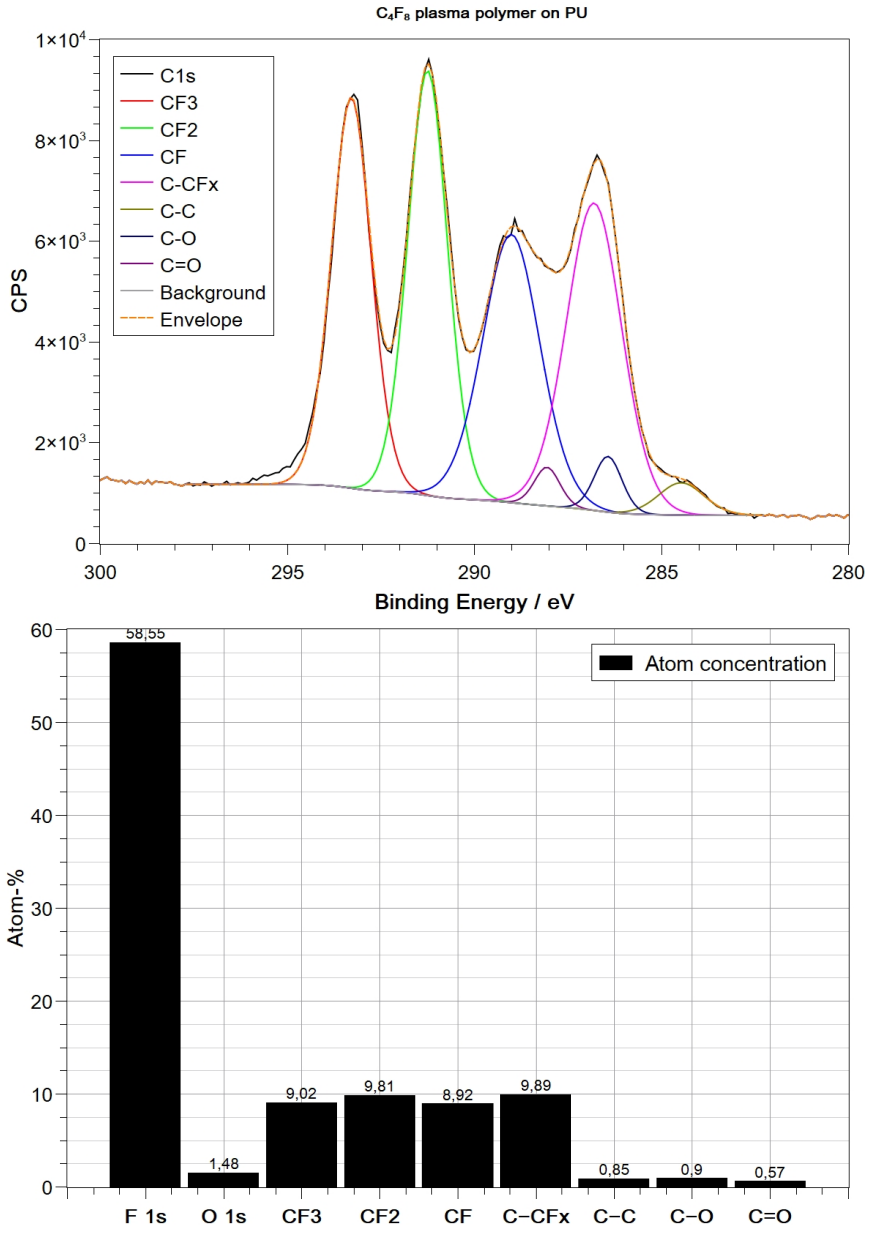


Figure A.27.: ESCA C 1s spectrum and atomic concentrations of the $C_4F_8$-plasma coating on a PU film (samples of stamp 3).

## Silicone-like plasma coating on a Si-wafer (samples of stamp 1)

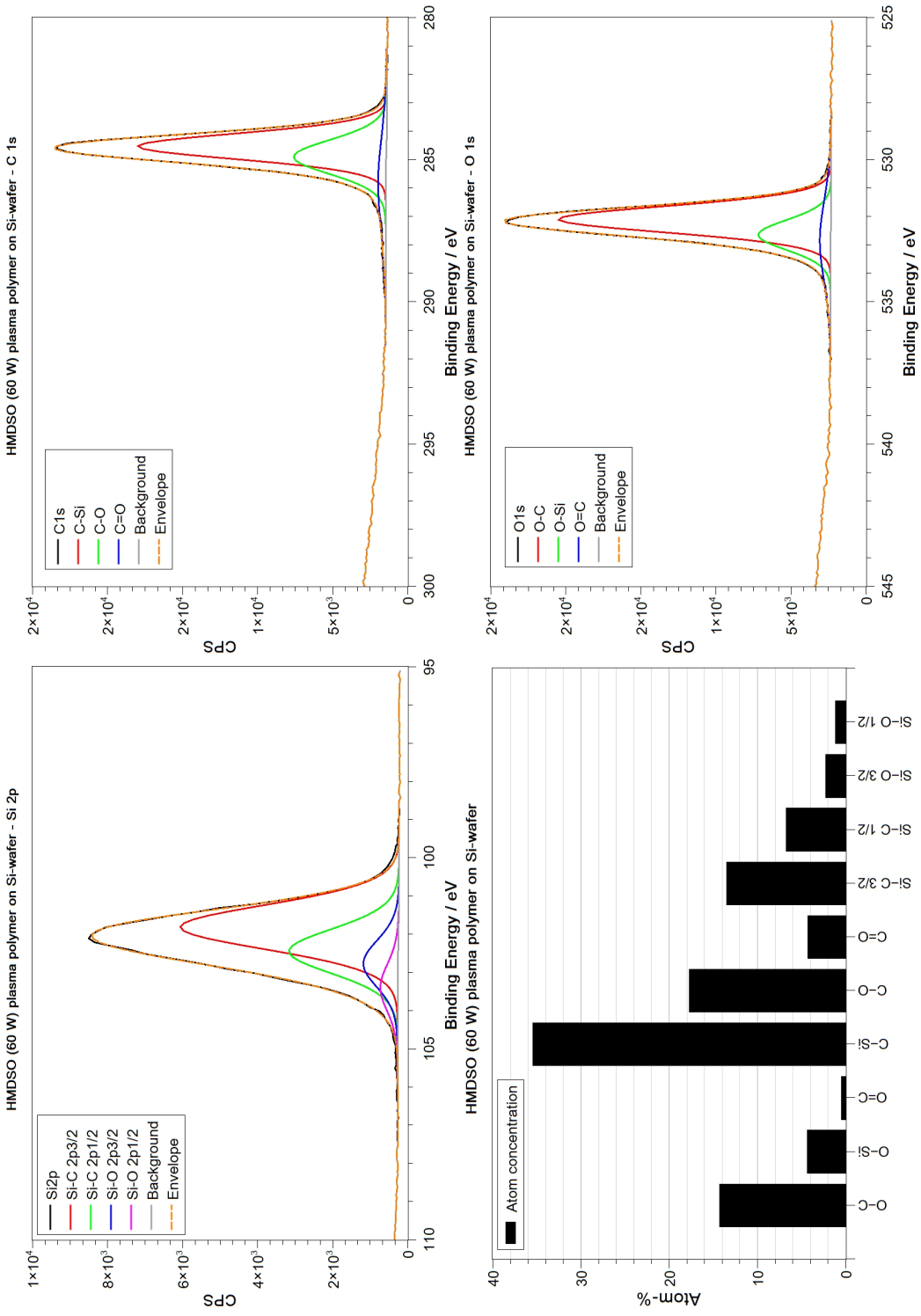


Figure A.28.: ESCA spectra and atomic concentrations of the HMDSO (60 W) plasma coating on a Si-wafer (samples of stamp 1).

**Silicone-like plasma coating on a PU film (CMC 63630, samples of stamp 3)**

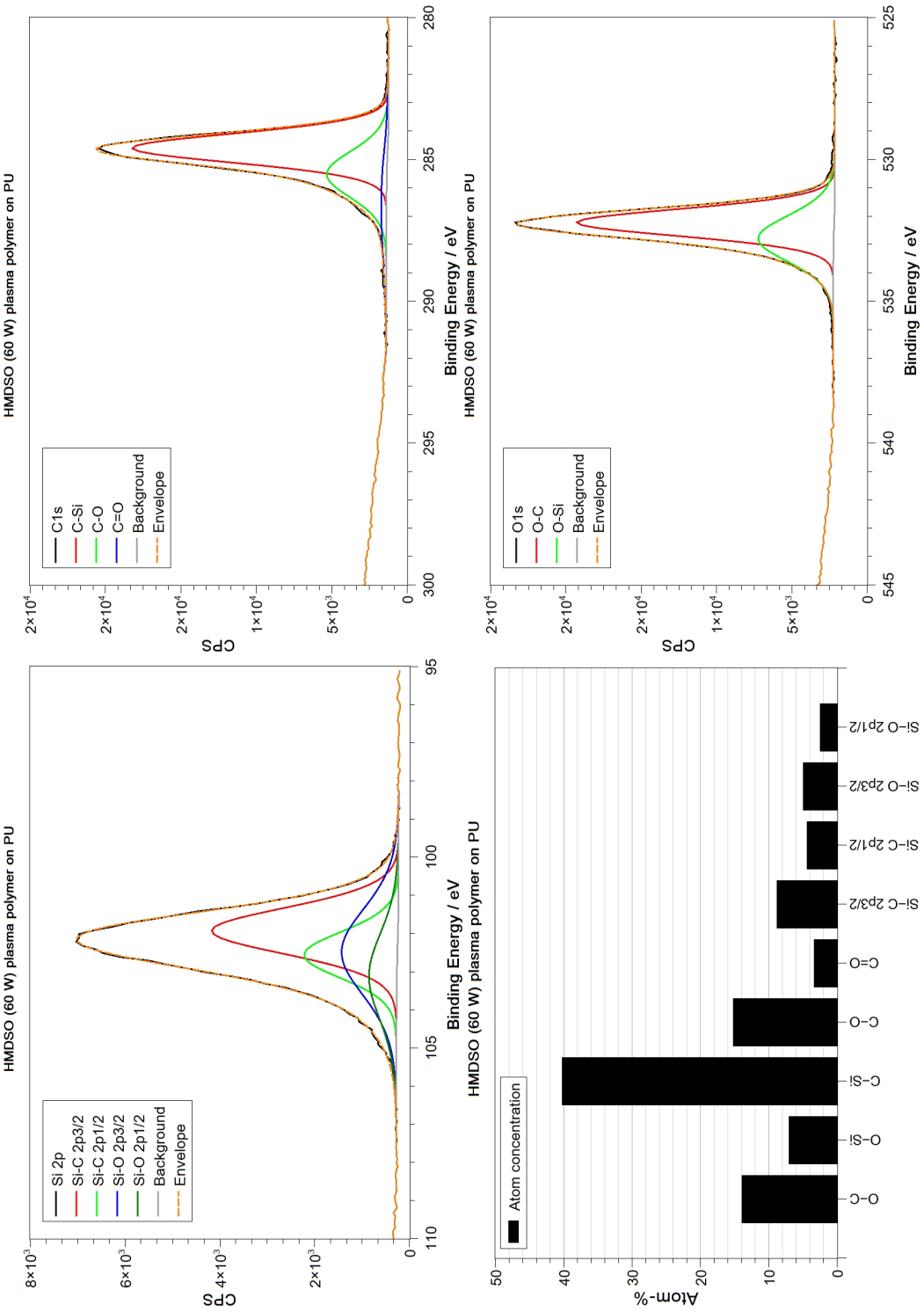


Figure A.29.: ESCA spectra and atomic concentrations of the HMDSO (60 W) plasma coating on a PU film (samples of stamp 3).

# A.4. Wetting behavior

## A.4.1. Water contact angle values

Table A.6.: Dynamic contact angles (CA) of $H_2O$ on functionalized PU surfaces and competing material surfaces.

| Stamp | Sample | Static CA | | Advancing CA | | Receding CA | |
|---|---|---|---|---|---|---|---|
| | | Mean (°) | SD (°) | Mean (°) | SD (°) | Mean (°) | SD (°) |
| | PU 3M 8674 | 81 | 1 | - | - | - | - |
| | PU LPT 4802T | 87 | - | - | - | - | - |
| | PU CMC 63630 | 75 | 4 | 83 | 5 | 44 | 2 |
| | PU CMC + C3F6 (50 W) | 101 | 4 | 117 | 1 | 84 | 0 |
| | PU CMC + O2 (200 W), C3F6 (50 W) | 102 | 3 | 111 | 2 | 57 | 1 |
| | PU CMC + HMDSO (60 W) | 95 | 2 | 117 | 3 | 81 | 6 |
| | PU CMC + HMDSO (200 W) | 96 | 1 | 102 | 3 | 56 | - |
| 5 | Aetztec DIN A4 | 88 | 1 | 105 | 1 | 48 | 1 |
| 5 | Aetztec DIN A4 + C3F6 | 120 | 1 | 126 | 1 | 60 | 1 |
| 4 | PU CMC 63615 150 µm C16 | 102 | 2 | - | - | - | - |
| 4 | PU CMC 63615 150 µm C16 + C3F6 | 114 | 1 | - | - | - | - |
| - | PU CMC 63630 300 µm sandpaper P80 + C3F6 | 108 | 1 | 93 | 1 | 65 | 1 |
| - | PU CMC 63630 300 µm sandpaper P400 + C3F6 | 109 | 1 | 107 | 1 | 80 | 1 |
| 4 | C16 | 115 | - | 124 | 2 | 63 | - |
| 4 | C16 + O2 (200 W), C3F6 (50 W) | 131 | - | 132 | 2 | 74 | - |
| 4 | C16 + HMDSO (60 W) | 130 | - | 135 | 2 | 92 | - |
| 4 | C16 + HMDSO (200 W) | 113 | 1 | 122 | 2 | 50 | 6 |
| 4 | C17 | 123 | 1 | - | - | - | - |
| 4 | C17 + O2 (200 W), C3F6 (50 W) | 120 | 1 | - | - | - | - |
| 4 | C17 + HMDSO (60 W) | 146 | 1 | - | - | - | - |
| 4 | C17 + HMDSO (200 W) | 98 | 1 | - | - | - | - |

Table A.6.: Dynamic contact angles (CA) of $H_2O$ on functionalized PU surfaces and competing material surfaces.

| Stamp | Sample | Static CA | | Advancing CA | | Receding CA | |
|---|---|---|---|---|---|---|---|
| | | Mean (°) | SD (°) | Mean (°) | SD (°) | Mean (°) | SD (°) |
| 2 | C1 | 110 | 3 | 144 | 1 | 135 | 5 |
| 2 | C1 + C4F8 (50 W) | 135 | 7 | 155 | 1 | 154 | 1 |
| 2 | E1 | 85 | 7 | 125 | 2 | 118 | 1 |
| 2 | E1 + C4F8 (50 W) | 118 | 7 | 153 | 1 | 151 | 2 |
| 3 | C6 | 124 | 1 | 122 | 5 | 86 | 6 |
| 3 | C6 + O2 (200 W), C3F6 (50 W) | 145 | - | 157 | - | 149 | 4 |
| 3 | C6 + HMDSO (60 W) | 136 | 1 | 150 | 4 | 146 | 4 |
| 3 | C6 + HMDSO (200 W) | 138 | 1 | 133 | 1 | 62 | - |
| 3 | C9 | 87 | 10 | 96 | 9 | 50 | 12 |
| 3 | C9 + O2 (200 W), C3F6 (50 W) | 144 | | 135 | 1 | 69 | - |
| 3 | C9 + HMDSO (60 W) | 125 | 1 | 151 | 4 | 147 | 1 |
| 3 | C9 + HMDSO (200 W) | 127 | 7 | 120 | 5 | 57 | - |
| | Al | 106 | - | 109 | 1 | 53 | 3 |
| | Ti | 98 | 3 | 102 | 5 | 44 | 10 |
| | Cu | 86 | - | 100 | - | 87 | 10 |
| | Glass | 34 | - | 40 | - | 33 | - |
| | Epoxy (CFRP) | 77 | - | 82 | - | 32 | - |
| | FEP | 101 | - | 108 | - | 92 | - |
| | PFA | 102 | - | 108 | - | 93 | - |
| | GH60-5 Nano (EADS) | 99 | - | 101 | - | 84 | - |
| | NuSil R2180 (EADS) | 115 | - | 108 | 2 | 80 | 5 |
| | PUR Topcoat (EADS) | 93 | 5 | 96 | - | 70 | - |
| | CFRP (EADS) | 95 | - | 94 | - | 74 | 2 |
| | Sicon DLC (EADS) | 93 | - | 95 | 2 | 60 | 5 |
| | Icephob ESL (EADS) | 91 | 1 | 80 | 7 | 51 | 6 |
| | Steel MTechF (EADS) | 93 | 1 | - | - | - | - |

## Comparison of measured ACA with theoretical limits for samples of stamp 1

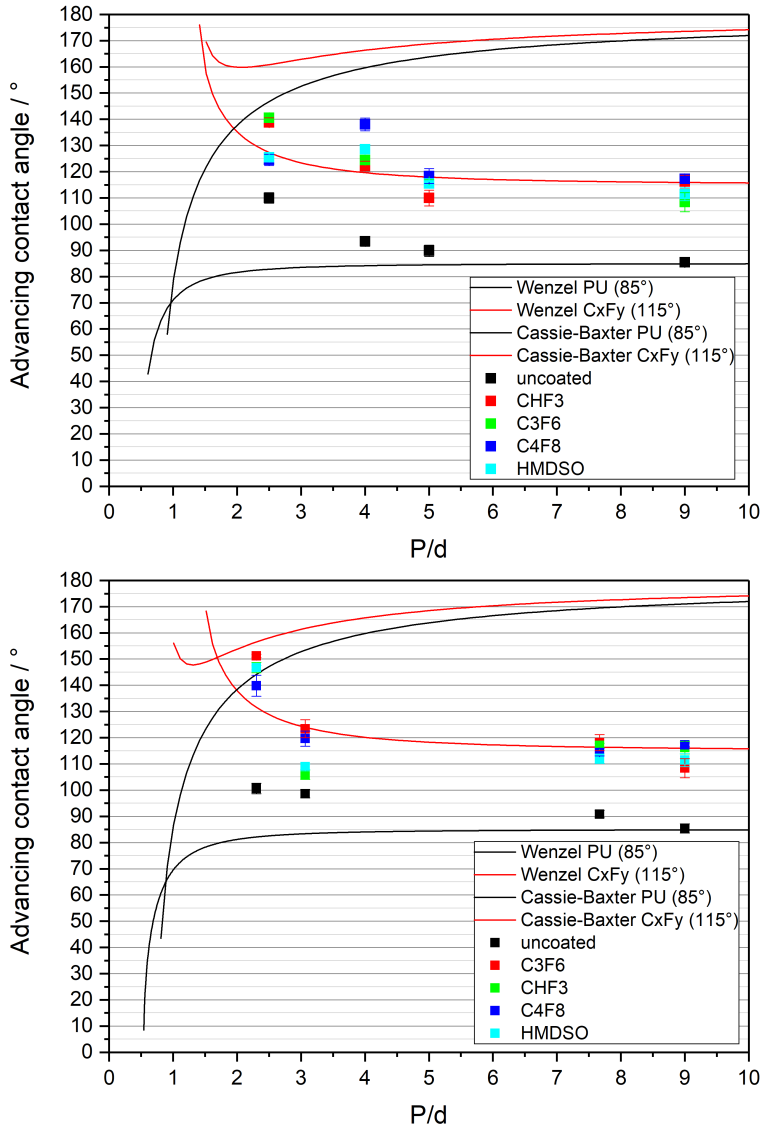


Figure A.30.: Comparison of measured advancing contact angles of water with theoretical limits, calculated with the Wenzel and the Cassie-Baxter theories, for samples of stamp 1 (top: cylinders, bottom: ellipses). Values for flat PU shown at $P/d = 9$ for comparison.

**Comparison of measured ACA with theoretical limits for samples of stamp 2**

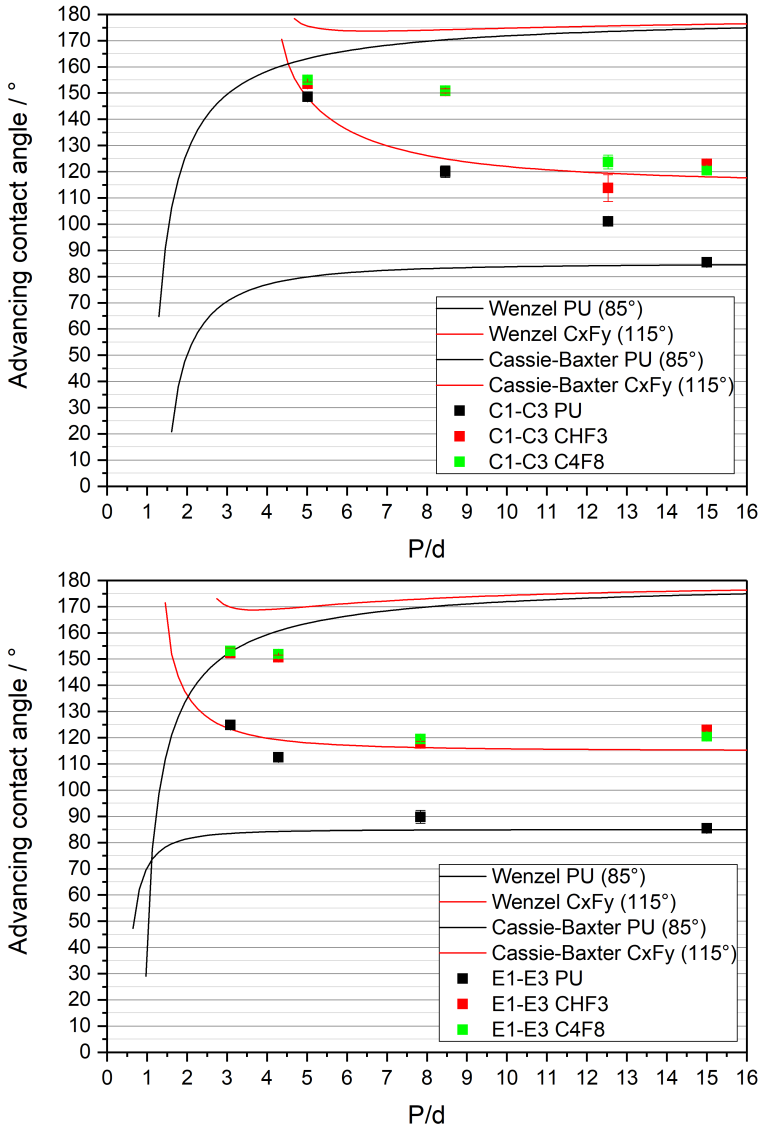


Figure A.31.: Comparison of measured advancing contact angles of water with theoretical limits, calculated with the Wenzel and the Cassie-Baxter theories, for samples of stamp 2 (top: cylinders, bottom: ellipses). Values for flat PU shown at $P/d = 15$ for comparison.

## A.4.2. Di-iodo-methane contact angle values

Table A.7.: Static contact angles measured with di-iodo-methane (DIM).

| Stamp | Sample | Static contact angle | |
|---|---|---|---|
| - | - | Mean (°) | StdDev (°) |
| | PU 3M 8674 | 42 | 1 |
| | PU LPT4802T | 64 | 1 |
| | PU CMC | 41 | 3 |
| | PU CMC + C3F6 (50 W) | - | - |
| | PU CMC + O2 (200 W), C3F6 (50 W) | 68 | 10 |
| | PU CMC + HMDSO (60 W) | 69 | 2 |
| | PU CMC + HMDSO (200 W) | 56 | 2 |
| 4 | C16 | 72 | 8 |
| 4 | C16 + O2 (200 W), C3F6 (50 W) | 89 | 11 |
| 4 | C16 + HMDSO (60 W) | 66 | 1 |
| 4 | C16 + HMDSO (200 W) | 69 | 3 |
| 3 | C6 | 89 | 2 |
| 3 | C6 + O2 (200 W), C3F6 (50 W) | 126 | 7 |
| 3 | C6 + HMDSO (60 W) | 82 | 1 |
| 3 | C6 + HMDSO (200 W) | 76 | 4 |
| 3 | C9 | 68 | 8 |
| 3 | C9 + O2 (200 W), C3F6 (50 W) | 88 | 1 |
| 3 | C9 + HMDSO (60 W) | 80 | 1 |
| 3 | C9 + HMDSO (200 W) | 61 | 2 |
| | Al | 63 | 4 |
| | Ti | 52 | 1 |
| | Cu | 49 | 1 |
| | Glass | 56 | 1 |
| | Epoxy (CFRP) | 39 | 4 |
| | FEP | 83 | 1 |
| | PFA | 83 | 3 |

### A.4.3. Surface free energy

Table A.8.: Surface free energies (SE) determined by water and DIM static contact angle measurements.

| Stamp<br>- | Samples<br>- | SE<br>(mN/m) | SE disperse<br>(mN/m) | SE polar<br>(mN/m) |
|---|---|---|---|---|
| | 3M 8674 | 41.69 | 38.53 | 3.16 |
| | LPT 4802 T | 30.17 | 26.20 | 3.97 |
| | PU CMC | 44.89 | 39.09 | 5.80 |
| | PU CMC + C3F6 (50 W) | - | - | - |
| | PU CMC + O2 (200 W), C3F6 (50 W) | 24.78 | 24.23 | 0.55 |
| | PU CMC + HMDSO (60 W) | 25.77 | 23.60 | 2.17 |
| | PU CMC + HMDSO (200 W) | 31.97 | 30.99 | 0.97 |
| 4 | C16 | 18.74 | 18.73 | 0.01 |
| 4 | C16 + O2 (200 W), C3F6 (50 W) | 18.97 | 18.23 | 0.74 |
| 4 | C16 + HMDSO (60 W) | 27.57 | 25.42 | 2.15 |
| 4 | C16 + HMDSO (200 W) | 23.43 | 23.43 | 0 |
| 3 | C6 | 12.99 | 12.98 | 0.01 |
| 3 | C6 + O2 (200 W), C3F6 (50 W) | 2.52 | 2.51 | 0.01 |
| 3 | C6 + HMDSO (60 W) | 18.00 | 16.47 | 1.53 |
| 3 | C6 + HMDSO (200 W) | 22.44 | 19.96 | 2.48 |
| 3 | C9 | 24.18 | 23.82 | 0.35 |
| 3 | C9 + O2 (200 W), C3F6 (50 W) | 15.54 | 13.44 | 2.10 |
| 3 | C9 + HMDSO (60 W) | 17.96 | 17.63 | 0.32 |
| 3 | C9 + HMDSO (200 W) | 30.14 | 28.06 | 2.08 |
| | Al | 27.02 | 26.95 | 0.07 |
| | Ti | 33.66 | 33.34 | 0.32 |
| | Cu | 37.65 | 35.16 | 2.49 |
| | Glass | 63.61 | 31.15 | 32.46 |
| | Epoxy (CFRP) | 45.40 | 40.51 | 4.90 |
| | FEP | 18.32 | 16.07 | 2.25 |
| | PFA | 18.12 | 15.88 | 2.24 |

## A.5. Development of the new icing test chamber

Images of the new icing test chamber and the ice test setup are shown in Figure A.32.

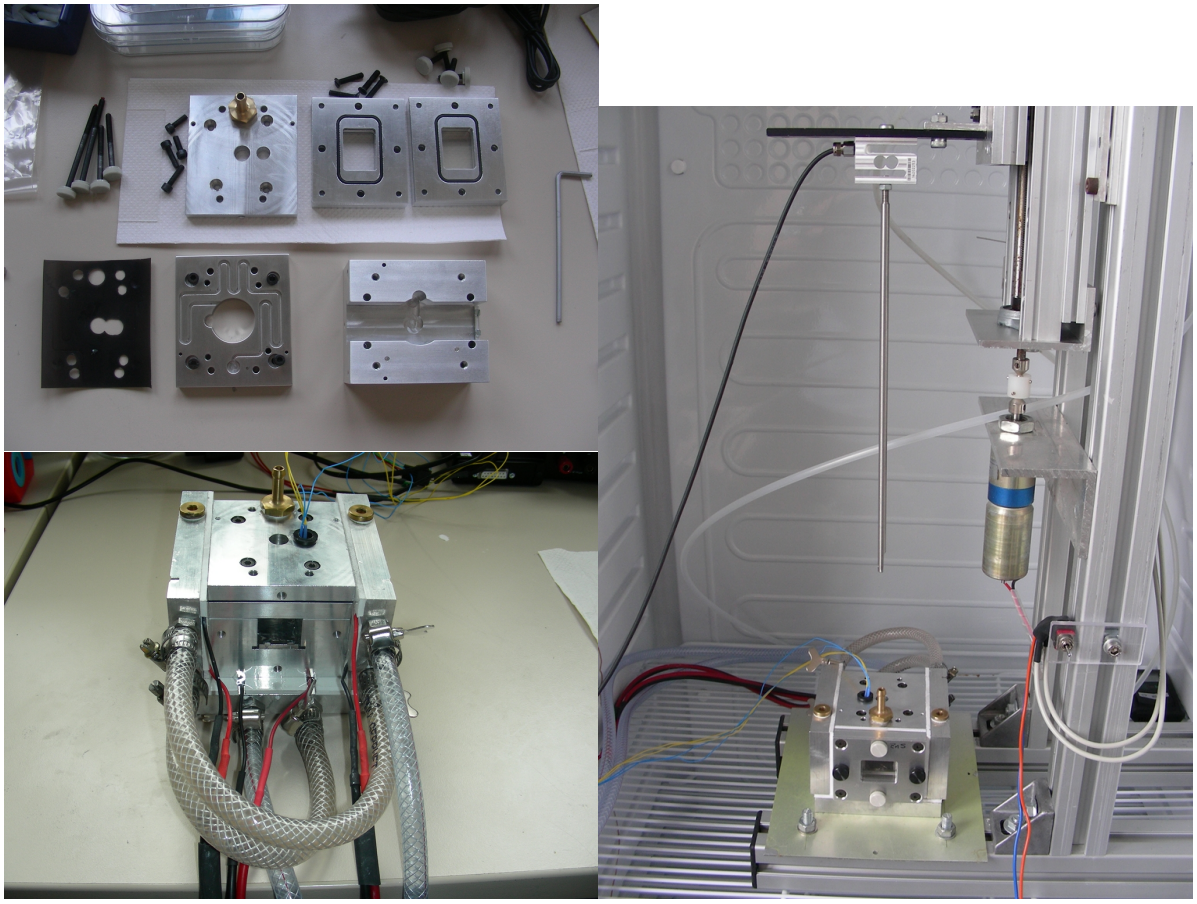

Figure A.32.: Images of the final concept of the newly developed icing test chamber (left) and of the ice test set-up (right).

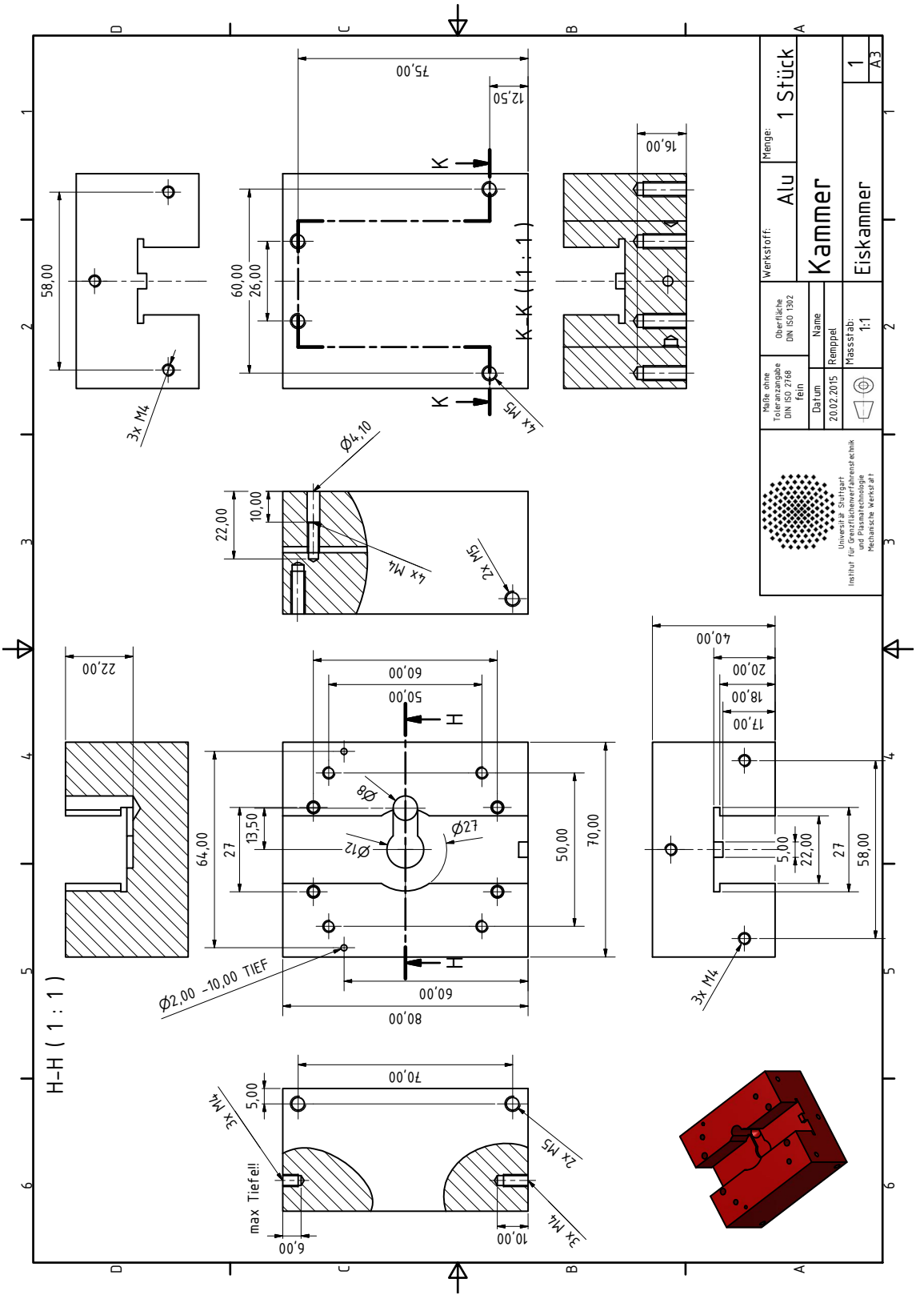


Figure A.33.: Final concept of the new icing test chamber: central aluminum block.

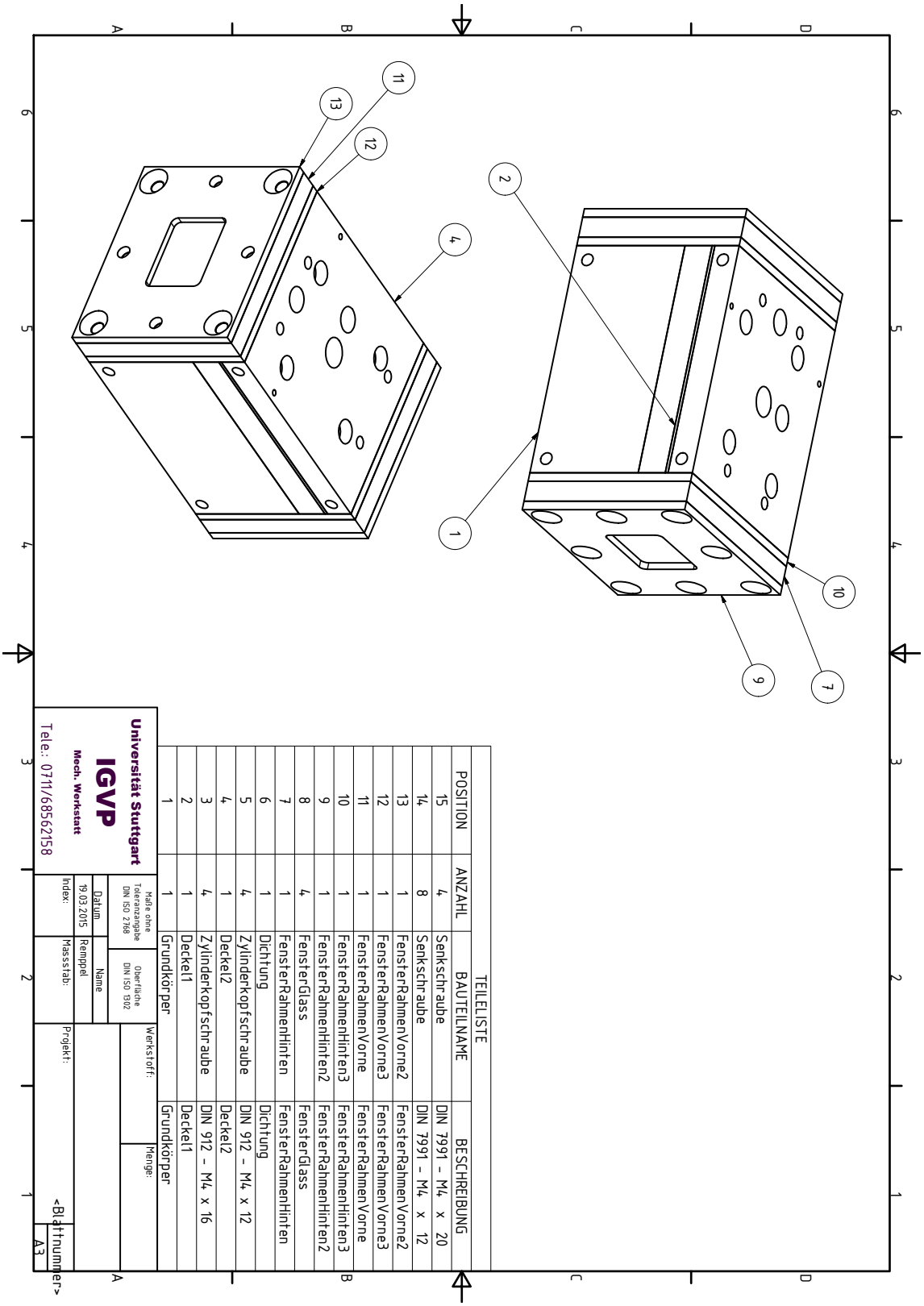


Figure A.34.: Final concept of the new icing test chamber: assembly.

# A.6. Ice adhesion

## A.6.1. Ice adhesion measurement values

Table A.9.: Ice adhesion values on the technical material surfaces and commercial anti-ice coatings.

| Sample<br>- | Ice adhesion, mean $\sigma_{ice}$<br>(kPa) | Ice adhesion, StdDev $\Delta\sigma_{ice}$<br>(kPa) | Type of fracture<br>- |
|---|---|---|---|
| Al | 140.34 | 58.21 | mixed |
| Ti | 62.11 | 8.62 | mixed |
| Cu | 394.23 | 234.39 | mixed |
| Glass | 160.08 | 28.87 | cohesive |
| Epoxy (CFRP) | 297.61 | 71.89 | cohesive |
| FEP | 500.74 | 122.05 | adhesive |
| PFA | 614.91 | 97.12 | adhesive |
| Steel MTechF (EADS) | - | - | - |
| GH60-5 Nano (EADS) | 230.62 | 38.79 | adhesive |
| Icephob ESL (EADS) | - | - | - |
| NuSil R2180 (EADS) | 760.45 | 65.54 | adhesive |
| PUR Topcoat (EADS) | 599.13 | 35.09 | mixed |

Table A.10.: Ice adhesion values on the functionalized PU surfaces.

| Stamp | Sample | Ice adhesion, mean $\sigma_{ice}$ | Ice adhesion, StdDev $\Delta\sigma_{ice}$ | Type of fracture |
|---|---|---|---|---|
| - | - | (kPa) | (kPa) | - |
| | PU 3M 8674 | - | - | - |
| | PU LPT 4802 T | - | - | - |
| | PU CMC | 447.10 | 77.10 | adhesive |
| | PU CMC + C3F6 (50 W) | 286.52 | 8.03 | adhesive |
| | PU CMC + O2 (200 W), C3F6 (50 W) | 370.78 | 65.91 | adhesive |
| | PU CMC + HMDSO (60 W) | 413.11 | 207.67 | adhesive |
| | PU CMC + HMDSO (200 W) | 365.07 | 45.70 | adhesive |
| 4 | C16 | 568.81 | 188.14 | mixed |
| 4 | C16 + O2 (200 W), C3F6 (50 W) | - | - | - |
| 4 | C16 + HMDSO (60 W) | 930.95 | 43.27 | mixed |
| 4 | C16 + HMDSO (200 W) | - | - | - |
| 4 | C17 + O2 (200 W), C3F6 (50 W) | - | - | - |
| 4 | C17 + HMDSO (200 W) | - | - | - |
| 2 | C1 | 572.75 | 29.18 | mixed |
| 2 | C1 + C4F8 (50 W) | 1387.94 | 156.57 | cohesive |
| 2 | E1 | - | - | - |
| 2 | E1 + C4F8 (50 W) | - | - | - |
| 3 | C6 | 1125.02 | 364.38 | mixed |
| 3 | C6 + O2 (200 W), C3F6 (50 W) | 2779.91 | 270.15 | mixed |
| 3 | C6 + HMDSO (60 W) | 2591.05 | 136.31 | mixed |
| 3 | C6 + HMDSO (200 W) | 930.00 | 134.97 | mixed |
| 3 | C6 + O2 (200 W), C3F6 (50 W) 0 %RH | 2449.88 | 480.71 | cohesive |
| 3 | C9 | 866.25 | 15.17 | mixed |
| 3 | C9 + O2 (200 W), C3F6 (50 W) | 1186.15 | 258.62 | mixed |
| 3 | C9 + HMDSO (60 W) | 1279.01 | 116.97 | mixed |
| 3 | C9 + HMDSO (200 W) | 839.01 | 88.00 | mixed |
| 3 | C9 + O2 (200 W), C3F6 (50 W) 0 %RH | 770.73 | - | mixed |

### A.6.2. Images of ice fractures on hexagonally arranged, cylindrical microstructure C1

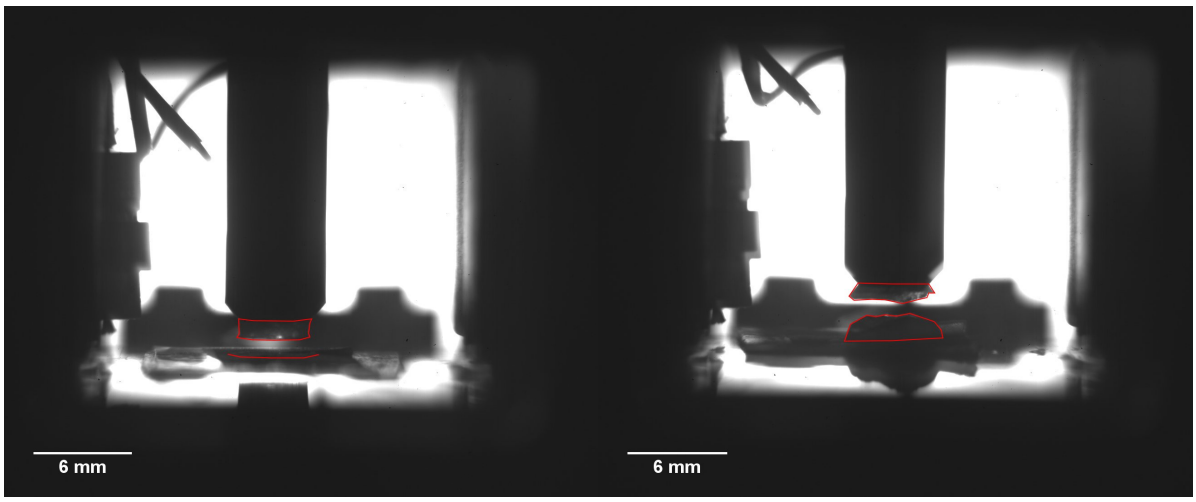


Figure A.35.: Images of ice adhesion measurement fractures on samples of stamp 2, C1 uncoated (left) and C1 + $C_4F_8$ (right).

### A.6.3. Images of ice fractures on hexagonally arranged, cylindrical microstructure C6 and C9

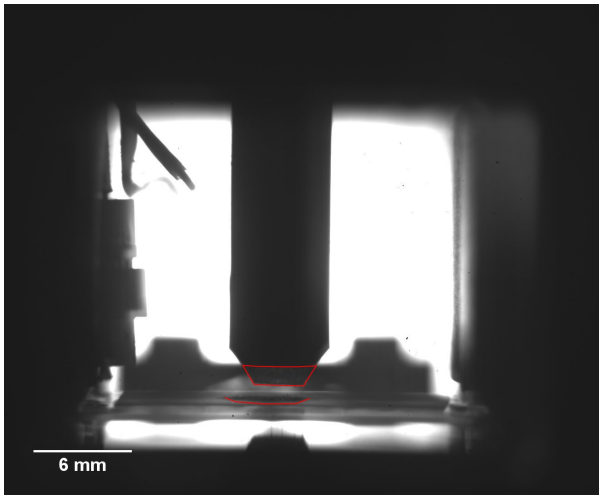


Figure A.36.: Image of ice adhesion measurement fractures on samples of stamp 3, C6 + $O_2$+$C_3F_6$.

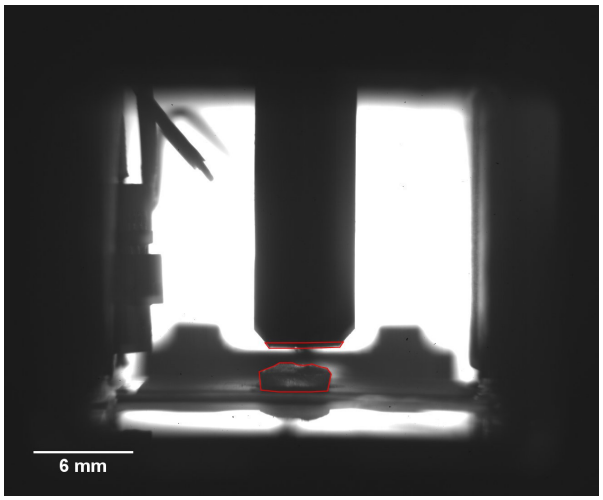


Figure A.37.: Image of ice adhesion measurement fracture on sample of stamp 3, C6 + HMDSO 60 W.

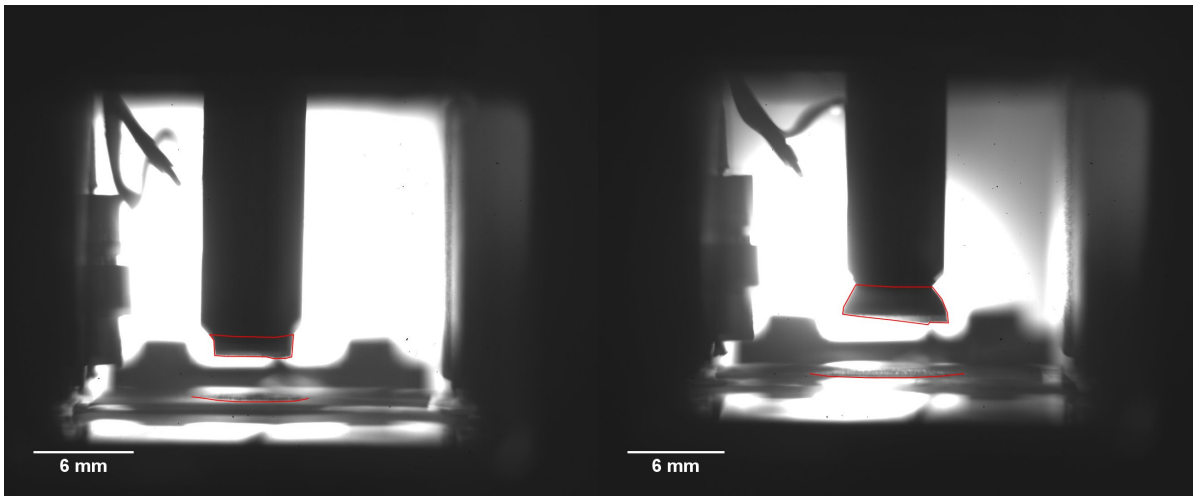


Figure A.38.: Images of ice adhesion measurement fractures on samples of stamp 3, C6 + HMDSO 200 W and C9 + HMDSO 200 W.

### A.6.4. Images of ice fractures on technical material surfaces

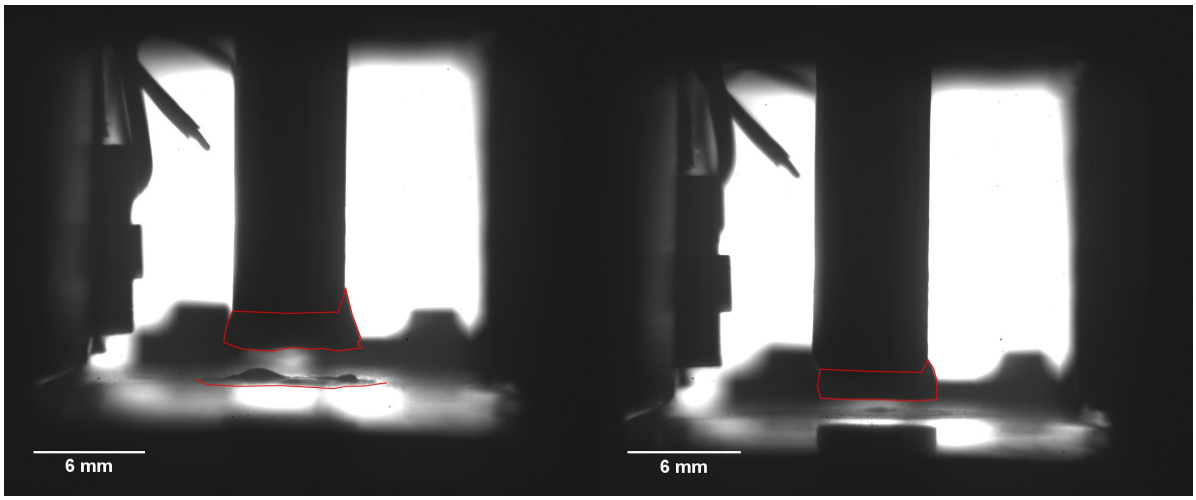


Figure A.39.: Images of ice adhesion measurement fractures on aluminum.

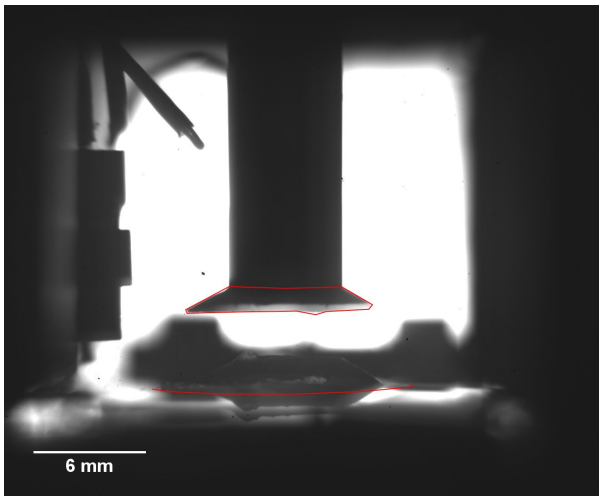


Figure A.40.: Image of ice adhesion measurement fractures on glass.

## A.6.5. Correlations of ice adhesion with surface wetting behavior

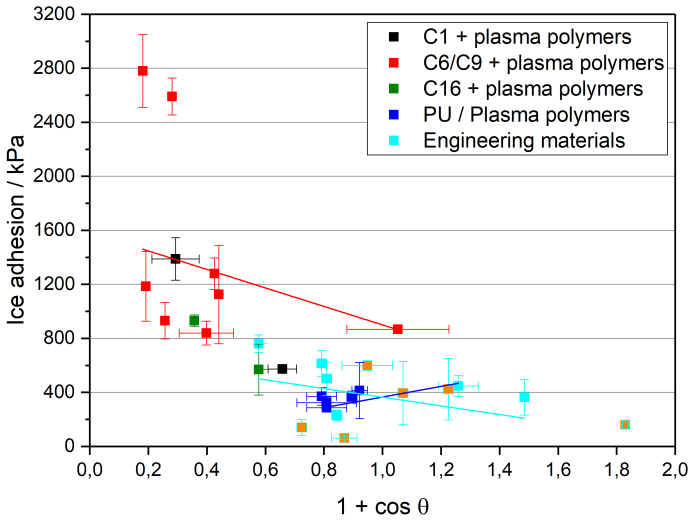


Figure A.41.: Ice adhesion values of all surfaces correlated with the equilibrium work of adhesion term.

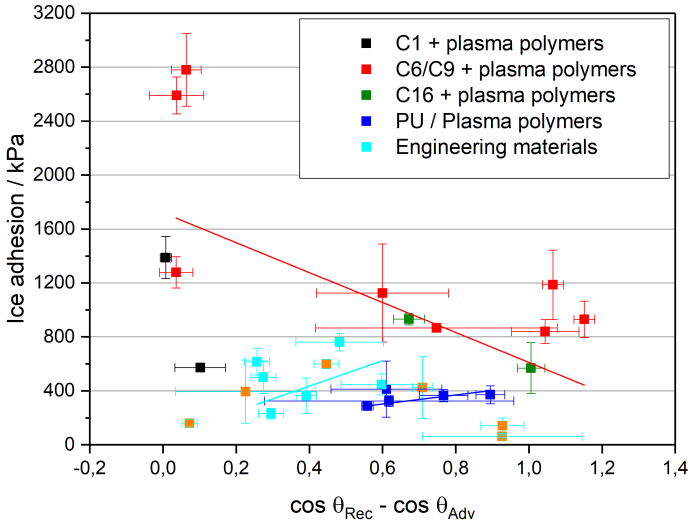


Figure A.42.: Ice adhesion values of all surfaces correlated with a term from the Furmidge equation for drop roll-off.

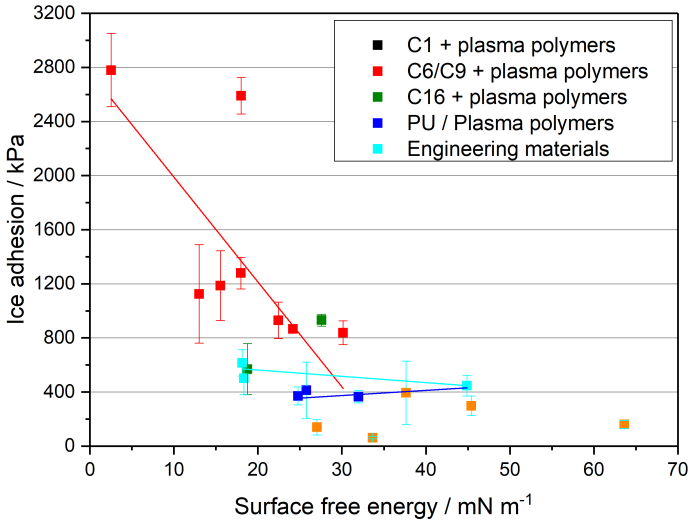


Figure A.43.: Ice adhesion values of all surfaces correlated with the surface free energy.

### A.6.6. Corrected ice adhesion in dependence of micrometer surface roughness

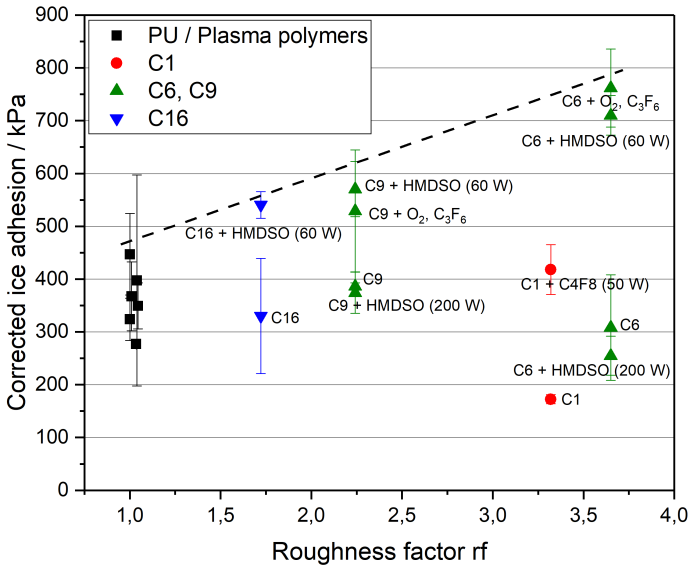


Figure A.44.: Corrected ice adhesion in dependence of the surface roughness factor $rf = A_{sl}/A_f$. The dashed line represents an upper limit.

## A.6.7. Ice adhesion in dependence of nanometer surface roughness

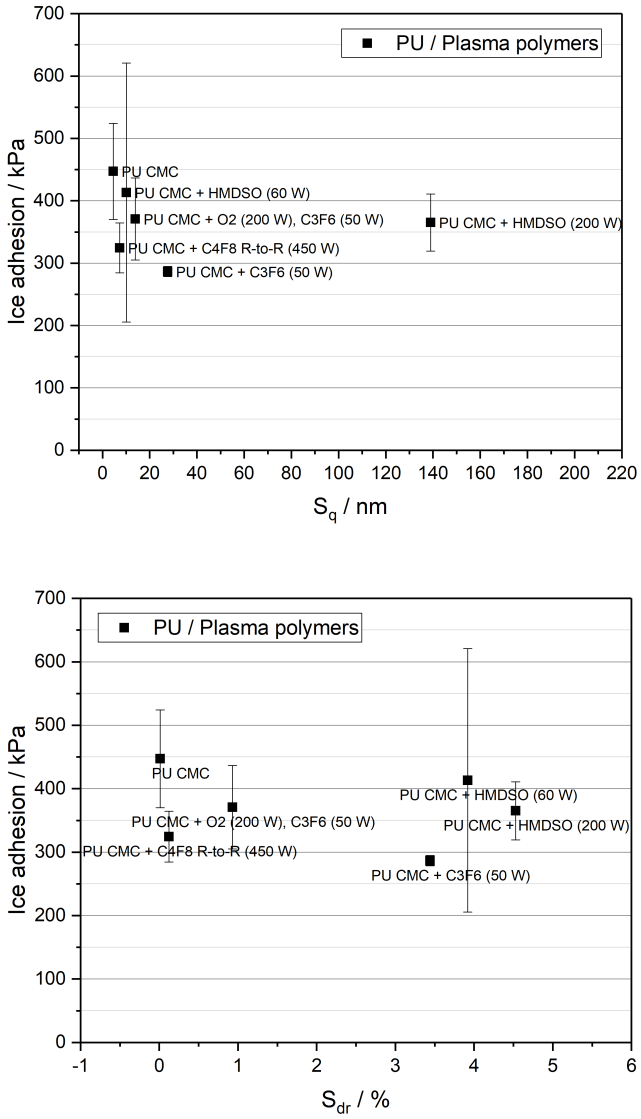


Figure A.45.: Ice adhesion in dependence of nanoscale RMS roughness $S_q$ and surface area ratio $S_{dr}$ determined by AFM measurements.

# A.7. Icing

## A.7.1. Heat transfer during the dynamic freezing experiment

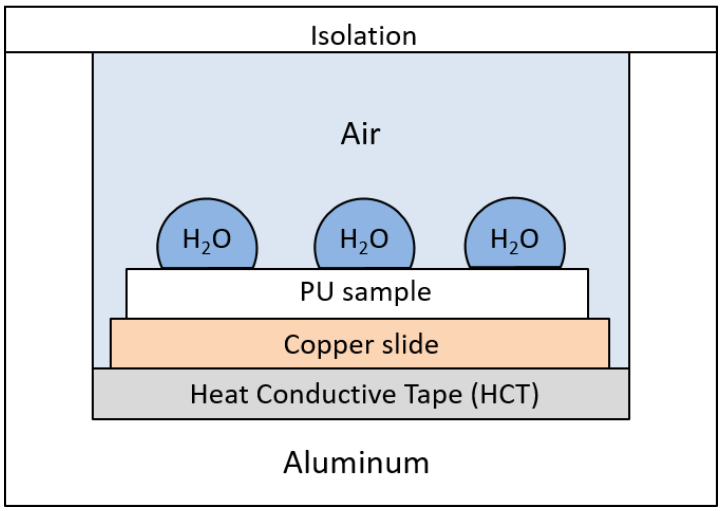


Figure A.46.: Schematic drawing of the experimental setup for dynamic water drop freezing experiments.

It is important to know the heat transfer rate of the water drops, the sample and the surroundings in order to be sure that the cooling rate of 1 K/min enables a thermodynamic equilibrium. The parameters in Table A.11 were used for the calculation of the heat conduction.

The density and specific heat capacity of the heat conduction tape (values marked by *) were estimated according to similar polymers, as no values are given in the corresponding datasheet.

At first, the total heat needed to be transported out of the chamber per minute is calculated. Then, the possible heat flux of each component is compared to the heat needed to be transported away. Finally, the maximum possible heat transfer through the chamber walls is calculated and compared to the minimum needed heat transfer in order to verify that quasi-steady state cooling is possible.

The aluminum chamber is cooled down by the three Peltier elements and assumed to have an even temperature distribution. As the PU sample is glued to the copper slide which is pressed down onto the heat conduction tape (ceramic material), heat transfer resistances at the layer interfaces are neglected. The following calculations were made with the values from Table A.11.

Table A.11.: Parameters for calculation of heat conduction out of the chamber.

| Material | Layer thickness $d_i$ | Heat conduction coefficient $\lambda_i$ | Dimensions L x W x H | Volume $V_i$ | Density $\rho_{Al}$ | Mass $m_i$ | Specific heat capacity $c_{p,i}$ |
|---|---|---|---|---|---|---|---|
| - | (mm) | (W/mK) | (mm) | ($m^3$) | ($kg/m^3$) | (g) | (J/gK) |
| Al | 20 | 230 | - | - | 2710 | - | 0.896 |
| HCT | 0.3 | 1.4 | 76 x 26 x 0.3 | 593e-9 | 1000* | 0.593 | 1* |
| Cu | 0.5 | 330 | 76 x 26 x 0.5 | 988e-9 | 8940 | 8.833 | 0.382 |
| PU | 0.35 | 0.245 | 3 x 3 x 0.35 | 3.15e-9 | 1140 | 3.591e-3 | 1.8 |
| Water | - | 0.556 | - | 25e-9 | 1000 | 0.025 | 4.19 |
| Air | - | 0.0262 | 80 x 22 x 20 | 35.2e-6 | 1.2 | 42.24e-3 | 1.005 |
| Ice | - | 2.33 | - | - | 917 | 0.025 | 2.11 |

The total heat needed to be transported out of the icing chamber (IC) inside for a reduction of $\Delta T = 1\,\mathrm{K}$ consists of the three water drops ($3 \cdot \Delta Q_{\mathrm{H_2O}}$), the chamber air ($\Delta Q_{\mathrm{air}}$) and the layers of the PU sample ($\Delta Q_{\mathrm{PU}}$), the copper sheet ($\Delta Q_{\mathrm{Cu}}$) and the heat conduction tape ($\Delta Q_{\mathrm{HCT}}$):

$$\begin{aligned}
\Delta Q &= \sum_i (m_i \cdot c_{p,i}) \cdot \Delta T, \\
\Delta Q &= 3 \cdot \Delta Q_{\mathrm{H_2O}} + \Delta Q_{\mathrm{air}} + \Delta Q_{\mathrm{PU}} + \Delta Q_{\mathrm{Cu}} + \Delta Q_{\mathrm{HCT}}, \\
\Delta Q &= (3 \cdot 0.105 + 0.04245 + 6.4638 \times 10^{-3} + 3.3742 + 0.593)\ \mathrm{J} = 4.3311\ \mathrm{J}. \qquad \text{(A.7)}
\end{aligned}$$

The total heat to be transported away per minute is

$$\dot{Q}_{\mathrm{IC,inside}} = 4.3311\ \mathrm{J/min} = 0.072185\ \mathrm{W}. \qquad \text{(A.8)}$$

The aluminum of the icing chamber also has to be cooled down and added to the heat

from the icing chamber inside:

$$\begin{aligned} \Delta Q_{\mathrm{Al}} &= (V_{\mathrm{chamber}} - V_{\mathrm{channel}}) \cdot \rho_{\mathrm{Al}} \cdot c_{p,\mathrm{Al}} \cdot \Delta T = 730.39\ \mathrm{J}, \\ \dot{Q}_{\mathrm{IC,Al}} &= 730.39\ \mathrm{J/min} = 12.17\ \mathrm{W}. \end{aligned} \tag{A.9}$$

If the aluminum chamber is included, the total heat to be transported away per minute is

$$\dot{Q}_{\mathrm{IC}} = \dot{Q}_{\mathrm{IC,inside}} + \dot{Q}_{\mathrm{IC,Al}} = (4.3311 + 730.39)\ \mathrm{J/min} = 734.72\ \mathrm{J/min} = 12.245\ \mathrm{W}. \tag{A.10}$$

The heat flux out of the air consists of conduction through the air and convection at the chamber walls:

$$\begin{aligned} \dot{Q}_{\mathrm{cond,air}} &= \frac{\lambda_{\mathrm{air}}}{d_{\mathrm{air}}} \cdot A_{\mathrm{Al,air}} \cdot \Delta T\ , \\ &= \frac{0.0262\ \mathrm{W/(mK)}}{0.01\ \mathrm{m}} \cdot 1.6 \times 10^{-3}\ \mathrm{m}^2 \cdot 1\ \mathrm{K}\ , \\ &= 4.192 \times 10^{-3}\ \mathrm{W}. \end{aligned} \tag{A.11}$$

$$\begin{aligned} \dot{Q}_{\mathrm{conv,air}} &= \alpha_{\mathrm{Al,air}} \cdot A_{\mathrm{Al,air}} \cdot \Delta T\ , \\ &= 5\ \mathrm{W/(m^2K)} \cdot ((2 \times 80 \times 20 + 80 \times 22) \times 10^{-6}\ \mathrm{m}^2) \cdot 1\ \mathrm{K}\ , \\ &= 0.0248\ \mathrm{W}. \end{aligned} \tag{A.12}$$

$$\dot{Q}_{\mathrm{total,air}} = \dot{Q}_{\mathrm{cond,air}} + \dot{Q}_{\mathrm{conv,air}} = 0.028992\,\mathrm{W} > \frac{\Delta Q_{\mathrm{air}}}{t} = 0.04245\,\mathrm{J/min} = 7.075 \times 10^{-4}\,\mathrm{W}. \tag{A.13}$$

Since the total heat flux through the air is larger than the heat of the air needed to be transported away, the quasi-steady state cooling is possible for the air.

The heat flux out of one water drop consists of conduction through the water (the radius 2.285 mm of a 25 µl half-sphere was used for the thickness $d_{\mathrm{w}}$):

$$\begin{aligned} \dot{Q}_{\mathrm{cond,H_2O}} &= \frac{\lambda_{\mathrm{H_2O}}}{d_{\mathrm{H_2O}}} \cdot A_{\mathrm{H_2O}} \cdot \Delta T\ , \\ &= \frac{0.556\ W/(mK)}{2.285 \times 10^{-3}\ m} \cdot 16.409 \times 10^{-6}\ m^2 \cdot 1\ K\ , \\ &= 3.993 \times 10^{-3}\ \mathrm{W} > \frac{\Delta Q_{\mathrm{H_2O}}}{t} = 0.105\ \mathrm{J/min} = 1.75 \times 10^{-3}\ \mathrm{W}. \end{aligned} \tag{A.14}$$

Since the total heat flux through the water is larger than the heat of the water drop needed to be transported away, the quasi-steady state cooling is possible for a water

drop.

The heat conduction through the sample layer system is:

$$\dot{Q}_{\text{layer}} = \left( \frac{1}{\frac{d_{\text{PU}}}{\lambda_{\text{PU}}} + \frac{d_{\text{Cu}}}{\lambda_{\text{Cu}}} + \frac{d_{\text{HCT}}}{\lambda_{\text{HCT}}}} \right) \cdot A_{\text{ICG}} \cdot \Delta T,$$
$$\dot{Q}_{\text{layer}} = \left( \frac{1}{\frac{0.35\times10^{-3}\ \text{m}}{0.245\ \text{W/(mK)}} + \frac{0.5\times10^{-3}\ \text{m}}{330\ \text{W/(mK)}} + \frac{0.3\times10^{-3}\ \text{m}}{1.4\ \text{W/(mK)}}} \right) \cdot 2.16 \times 10^{-3}\ \text{m}^2 \cdot 1\ \text{K},$$
$$\dot{Q}_{\text{layer}} = 1.3136\ \text{W}. \tag{A.15}$$

The heat needed to be transported through the layer system consists of the heats of the PU, the copper, the heat conduction tape (HCT) and the three water drops:

$$\frac{\Delta Q_{\text{layer}}}{t} = 3.9737\ \text{J/min} = 0.0662\ \text{W}\ ,$$
$$\frac{\Delta Q_{3\text{H}_2\text{O}}}{t} = 0.315\ \text{J/min} = 5.25 \times 10^{-3}\ \text{W}\ ,$$
$$\dot{Q}_{\text{cond,layer}} = 1.3136\ W > \frac{\Delta Q_{\text{layer}}}{t} + \frac{\Delta Q_{3\text{H}_2\text{O}}}{t} = 0.07145\ \text{W}. \tag{A.16}$$

Since the possible heat flux through the layer system is larger than the heat of the water drops and the layer system needed to be transported away, the quasi-steady state cooling is possible for the layer system.

For a temperature difference of 1 K, the heat conduction through the icing chamber ground (ICG) with area $A_{ICG}$, equal to one aluminum layer, can be modeled as:

$$\dot{Q}_{\text{ICG}} = \frac{\lambda_{\text{Al}}}{d_{\text{Al}}} \cdot A_{\text{ICG}} \cdot \Delta T,$$
$$\dot{Q}_{\text{ICG}} = \frac{230\ \text{W/(mK)}}{20 \times 10^{-3}\ \text{m}} \cdot 2.16 \times 10^{-3}\ \text{m}^2 \cdot 1\ \text{K},$$
$$\dot{Q}_{\text{ICG}} = 24.84\ \text{W}. \tag{A.17}$$

The heat of the three water drops, the layer system and the icing chamber ground needs to be transported through the icing chamber ground:

$$\Delta Q_{\text{ICG}} = (V_{\text{ICG}}) \cdot \rho_{\text{Al}} \cdot c_{p,\text{Al}} \cdot \Delta T = 271.95\ \text{J},$$
$$\frac{\Delta Q_{\text{ICG}}}{t} = 271.95\ \text{J/min} = 4.5326\ \text{W}, \tag{A.18}$$
$$\dot{Q}_{\text{ICG}} = 24.84\ \text{W} > \frac{\Delta Q_{3\text{H}_2\text{O}}}{t} + \frac{\Delta Q_{\text{layer}}}{t} + \frac{\Delta Q_{\text{ICG}}}{t} = 4.6041\ \text{W}. \tag{A.19}$$

Since the possible heat flux through the icing chamber ground is larger than the heat of the water drops, the layer system and the icing chamber ground needed to be transported away, the quasi-steady state cooling is possible for the icing chamber ground.

For a temperature difference of 1 K, the heat conduction through one icing chamber wall (ICW) with area $A_{ICW}$, equal to another aluminum layer would be:

$$\begin{aligned}\dot{Q}_{\mathrm{ICW}} &= \frac{\lambda_{\mathrm{Al}}}{d_{\mathrm{Al}}} \cdot A_{\mathrm{ICW}} \cdot \Delta T, \\ \dot{Q}_{\mathrm{ICW}} &= \frac{230\ \mathrm{W/(mK)}}{20 \times 10^{-3}\ \mathrm{m}} \cdot 1.6 \times 10^{-3}\ \mathrm{m}^2 \cdot 1\ \mathrm{K}, \\ \dot{Q}_{\mathrm{ICW}} &= 18.4\ \mathrm{W}. \end{aligned} \tag{A.20}$$

Then, the total heat conduction through all sides of the chamber is:

$$\begin{aligned}\dot{Q}_{\mathrm{IC,flux}} &= \dot{Q}_{\mathrm{ICG}} + 2 \cdot \dot{Q}_{\mathrm{ICW}}, \\ \dot{Q}_{\mathrm{IC,flux}} &= 61.64\ \mathrm{W}. \end{aligned} \tag{A.21}$$

The possible heat flux through the aluminum chamber is compared to the heat needed to be transported away per minute:

$$\dot{Q}_{\mathrm{IC,flux}} = 61.64\ \mathrm{W} > \dot{Q}_{\mathrm{IC}} = 12.245\ \mathrm{W}. \tag{A.22}$$

Since the possible total heat flux through the aluminum is larger than the total heat needed to be transported away, the quasi-steady state cooling is achieved for the aluminum chamber.

Each Peltier element has a power of about 200 W, the whole system therefore can deliver about 600 W. This high heat flux caused by a temperature difference of 1 K shows the low heat transfer resistance of the sample layer system and the aluminum layers. If only 1 K temperature difference is applied by the Peltier elements, the heat transfer rate through the aluminum layers is higher than the minimally needed one for taking away the heat from the water drops, air, sample layer system and aluminum of the chamber per minute. By this, it is shown that the whole system is cooled down in thermodynamic equilibrium at a rate of 1 K/min.

For maintaining a temperature of -20 °C inside of the chamber, in the lab room of 22 °C, the temperature difference of 42 K would equal an outward heat transfer of about 2589 W. Therefore, an effective cooling was only possible with the aid of an external water cooling cycle.

## A.7.2. Derivations for calculation of the nucleation temperature

Nucleation rate at $T_0 + \Delta T$:

$$J(T_0+\Delta T) = \frac{n\mathrm{k_B}(T_0+\Delta T)}{\mathrm{h}} \cdot A_{\mathrm{sl}} \cdot \exp\left(\frac{-\Delta F_{\mathrm{diff}}(T_0+\Delta T)}{\mathrm{k_B}(T_0+\Delta T)}\right) \cdot \exp\left(\frac{-\Delta G(T_0+\Delta T)}{\mathrm{k_B}(T_0+\Delta T)}\right) \tag{A.23}$$

Taylor approximation:

$$J(T_0+\Delta T) \approx \frac{n\mathrm{k_B}T_0}{\mathrm{h}} \cdot A_{\mathrm{sl}} \cdot \exp\left(-\frac{\Delta F_{\mathrm{diff}}(T_0)+\Delta G(T_0)}{\mathrm{k_B}T_0}\right) \cdot \tag{A.24}$$

$$\cdot \exp\left(-\frac{\partial}{\partial T}\left(\frac{\Delta F_{\mathrm{diff}}(T_0)}{\mathrm{k_B}T_0}\right)\cdot\Delta T - \frac{\partial}{\partial T}\left(\frac{\Delta G(T_0)}{\mathrm{k_B}T_0}\right)\cdot\Delta T\right) \tag{A.25}$$

Surface specific variables $a$ and $\lambda$:

$$a = \frac{n\mathrm{k_B}T_0}{\mathrm{h}} \cdot A_{\mathrm{sl}} \cdot \exp\left(-\frac{\Delta F_{\mathrm{diff}}(T_0)+\Delta G(T_0)}{\mathrm{k_B}T_0}\right) \tag{A.26}$$

$$\lambda = \frac{\partial}{\partial T}\left(\frac{\Delta F_{\mathrm{diff}}(T_0)}{\mathrm{k_B}T_0}\right) + \frac{\partial}{\partial T}\left(\frac{\Delta G(T_0)}{\mathrm{k_B}T_0}\right) \tag{A.27}$$

Helmholtz energy $\Delta F$ (free energy):

$$\Delta F_{\mathrm{diff}}(T) = \frac{\mathrm{k_B}ET^2}{(T-T_{\mathrm{R}})^2} \tag{A.28}$$

$$\frac{\partial}{\partial T}\left(\frac{\Delta F_{\mathrm{diff}}(T)}{\mathrm{k_B}T}\right) = \frac{E(-T-T_{\mathrm{R}})}{(T-T_{\mathrm{R}})^3} \tag{A.29}$$

Gibbs energy $\Delta G$ (free enthalpy):

$$\Delta G(T) = \frac{16\pi\gamma^3 f T_{\mathrm{m}}^2}{3(\Delta H_{\mathrm{f,v}}(T_{\mathrm{m}}-T))^2} \tag{A.30}$$

$$\frac{\partial}{\partial T}\left(\frac{\Delta G(T)}{\mathrm{k_B}T}\right) = \frac{-16\pi\gamma^3 f T_{\mathrm{m}}^2(T_{\mathrm{m}}^2-4T_{\mathrm{m}}T+3T^2)}{3\mathrm{k_B}\Delta H_{\mathrm{f,v}}^2(T_{\mathrm{m}}^2T-2T_{\mathrm{m}}T^2+T^3)^2} \tag{A.31}$$

## A.7.3. Ice nucleation and crystallization measurement values

Table A.12.: Values of icing behavior of the examined technical material surfaces, commercial anti-ice coatings and flat, uncoated or plasma-coated PU surfaces.

| Stamp<br>- | Sample<br>- | Roughness factor<br>$rf$ | Solid-liquid fraction<br>$f_{sl}$ | Nucleation temperature (calculated)<br>$T_N$ (°C) | Nucleation temperature (measured mean)<br>$T_N$ (°C) | Crystallization time (measured mean)<br>$\Delta t_C$ (s) |
|---|---|---|---|---|---|---|
| | Al | 1 | 1 | - | -16.05 | 9.83 |
| | Ti | 1 | 1 | - | -13.56 | 28.12 |
| | Cu | 1 | 1 | - | -12.02 | 9.53 |
| | Glass | 1 | 1 | - | -14.46 | 17.74 |
| | Epoxy (CFRP) | 1 | 1 | - | -15.01 | 36.62 |
| | FEP | 1 | 1 | - | -10.01 | 105.06 |
| | PFA | 1 | 1 | - | -19.41 | 17.84 |
| | Steel MTechF (EADS) | 1 | 1 | - | -17.02 | 17.54 |
| | GH60-5 Nano (EADS) | 1 | 1 | - | -16.10 | 13.04 |
| | Icephob ESL (EADS) | 1 | 1 | - | -14.17 | 35.59 |
| | NuSil R2180 (EADS) | 1 | 1 | - | - | - |
| | PUR Topcoat (EADS) | 1 | 1 | - | - | - |
| | PU 3M 8674 | - | - | - | -17.31 | 18.47 |
| | PU LPT4802T | - | - | - | -16.98 | 23.72 |
| | PU CMC | 1 | 1 | -17.106 | -17.02 | 21.23 |
| | PU CMC + C3F6 (50 W) | 1 | 1 | -17.103 | -17.76 | 29.30 |
| | PU CMC + O2 (200 W), C3F6 (50 W) | 1 | 1 | -17.107 | -15.17 | 40.33 |
| | PU CMC + HMDSO (60 W) | 1 | 1 | -17.102 | -20.04 | 24.25 |
| | PU CMC + HMDSO (200 W) | 1 | 1 | -17.111 | -15.91 | 34.25 |

Table A.13.: Values of icing behavior of the microstructured, uncoated or plasma-coated PU surfaces.

| Stamp<br>- | Sample<br>- | Roughness factor<br>$rf$ | solid-liquid fraction<br>$f_{sl}$ | Nucleation temperature (calculated)<br>$T_N$ / °C | Nucleation temperature (measured mean)<br>$T_N$ / °C | Crystallization time (measured mean)<br>$\Delta t_C$ / s |
|---|---|---|---|---|---|---|
| 4 | C16 | 1.72 | 1 | -17.032 | -18.46 | 31.97 |
| 4 | C16 + O2 (200 W), C3F6 (50 W) | 1.72 | 1 | -17.033 | -15.87 | 41.39 |
| 4 | C16 + HMDSO (60 W) | 1.72 | 1 | -17.028 | -13.63 | 59.95 |
| 4 | C16 + HMDSO (200 W) | 1.72 | 1 | -17.037 | -13.36 | 38.83 |
| 4 | C17 + O2 (200 W), C3F6 (50 W) | 1.65 | 1 | -17.039 | -16.71 | 39.18 |
| 4 | C17 + HMDSO (200 W) | 1.65 | 1 | -17.043 | -16.99 | 25.41 |
| 2 | C1 | 3.32 | 1 | -16.943 | -13.57 | 63.09 |
| 2 | C1 + C4F8 (50 W) | 3.32 | 0.4 | -17.064 | -12.51 | 45.72 |
| 2 | E1 | 2.19 | 1 | -16.999 | -6.24 | 95.64 |
| 2 | E1 + C4F8 (50 W) | 2.19 | 0.6 | -17.065 | -12.03 | 51.47 |
| 3 | C6 | 3.65 | 1 | -16.930 | -17.13 | 41.05 |
| 3 | C6 + O2 (200 W), C3F6 (50 W) | 3.65 | 0.2 | -17.149 | -17.46 | 53.47 |
| 3 | C6 + HMDSO (60 W) | 3.65 | 0.2 | -17.144 | -16.66 | 59.63 |
| 3 | C6 + HMDSO (200 W) | 3.65 | 0.6 | -17.005 | -15.45 | 43.01 |
| 3 | C9 | 2.24 | 1 | -16.996 | -17.11 | 35.23 |
| 3 | C9 + O2 (200 W), C3F6 (50 W) | 2.24 | 0.4 | -17.121 | -15.05 | 51.04 |
| 3 | C9 + HMDSO (60 W) | 2.24 | 0.4 | -17.116 | -16.00 | 49.39 |
| 3 | C9 + HMDSO (200 W) | 2.24 | 0.8 | -17.032 | -18.64 | 34.39 |
| 3 | C6 at 0 %RH | 3.65 | 1 | -16.930 | -16.26 | 19.09 |
| 3 | C6 + O2 (200 W), C3F6 (50 W) at 0 %RH | 3.65 | 0.1 | -17.243 | -18.65 | 38.43 |
| 3 | C6 + HMDSO (60 W) at 0 %RH | 3.65 | 0.1 | -17.238 | - | - |

### Overview of measured nucleation temperatures for all microstructures with fluorocarbon plasma coatings

Figure A.47 shows an overview of the measured nucleation temperatures of the uncoated or fluorocarbon plasma-coated microstructures and surfaces for comparison.

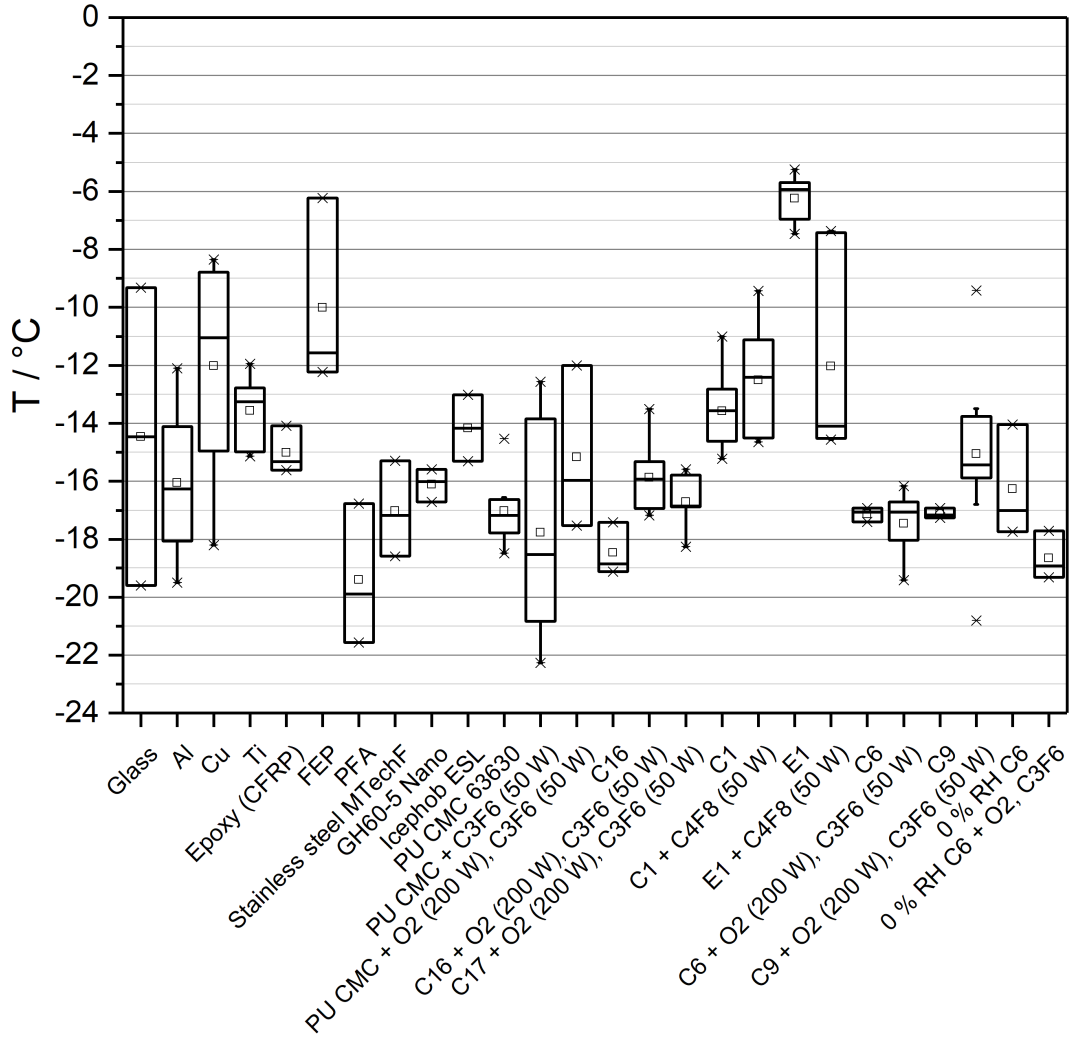


Figure A.47.: Overview of nucleation temperatures of the uncoated or fluorocarbon plasma-coated microstructures and surfaces for comparison.

## Overview of measured nucleation temperatures for all microstructures with silicone-like plasma coatings

Figure A.48 shows an overview of the measured nucleation temperatures of the uncoated or silicone-like plasma-coated microstructures and surfaces for comparison.

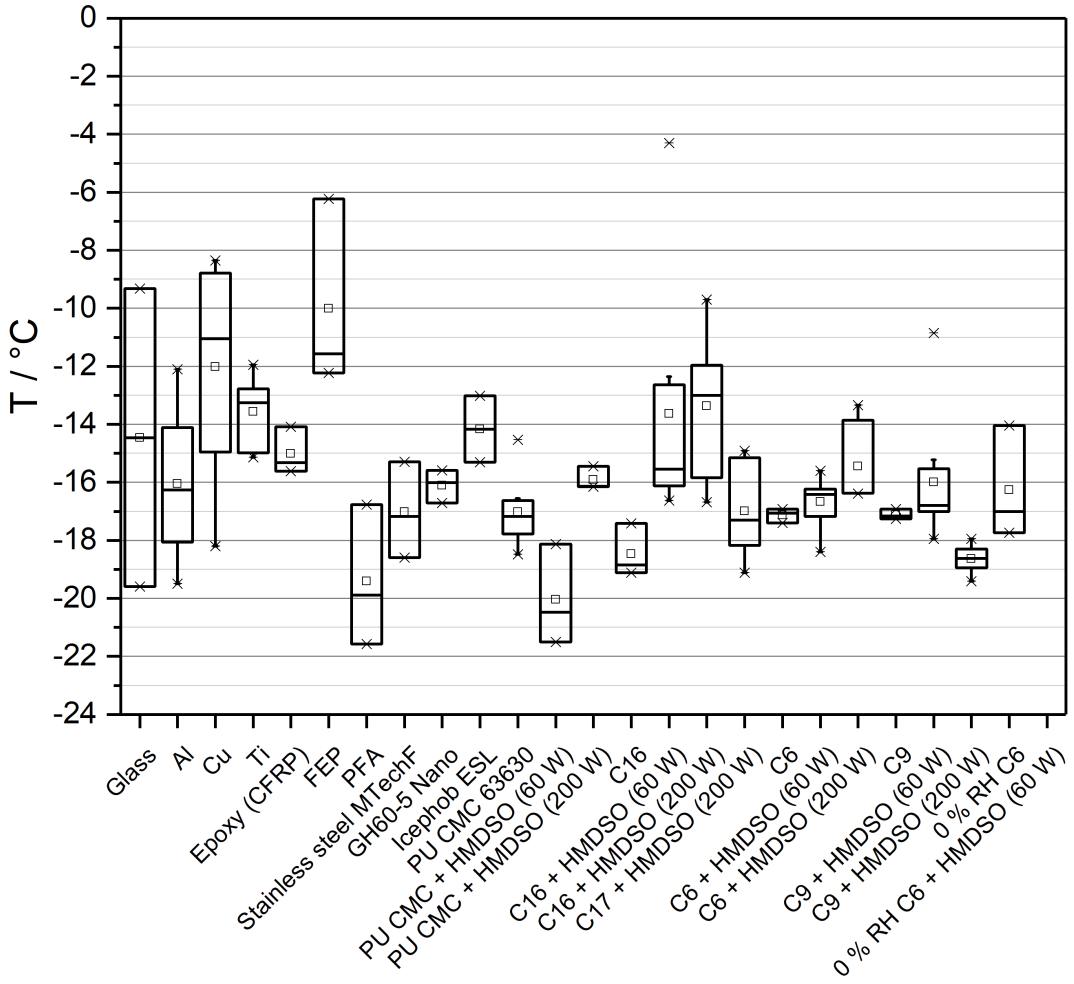


Figure A.48.: Overview of nucleation temperatures of the uncoated or silicone-like plasma-coated microstructures and surfaces for comparison.

## A.8. Temperature simulations of a freezing water drop

The simulation software COMSOL Multiphysics was used for several heat transfer simulations. A freezing water drop was modeled in two and in three dimensions on a flat and on a microstructured PU surface. The aim was to simulate the temperature of the freezing water drop and then to compare the freezing or crystallization times with the measured values of the static icing experiments. Therefor, the COMSOL Multiphysics "heat transfer with phase change" module was used. This module uses the same model properties as the normal "heat transfer" module, but it includes the material properties of two phases (e.g. ice as solid and water as liquid phase) and the linking factor alpha (between 0 and 1) in the corresponding model equations. The phase change is then modeled by a linear transition of alpha from 0 to 1 or the other way around the melting point (273.15 K for water) over a user-defined range (5 K for the models shown here). The water drop was modeled as the upper half of a sphere, where the upper half has a volume of 25 µl. Therefore, the water contact angle would be 90° on all the different surfaces, so no contact angle dependent wetting area is included in the models yet. The difference is in the water-surface contact area between the flat and the microstructured models, where the drop was placed on top of the microstructures resembling the Cassie-Baxter wetting state. The material properties of water were already present in the database, the data for ice and polyurethane were taken from [222]. The geometrical and material parameters were saved in a textfile and imported as a parameter list. No convective heat transfer was included in the models, since the air in the icing test chamber was at rest for the freezing experiments at 50 % rel. humidity. Only conductive heat transfer between the entities of the model and radiative heat transfer on the surface towards an ambient temperature of 295 K were simulated. Transient simulations were done with an initial temperature of the drop of 10 °C and a constant temperature of the surface of -10 °C (the surface temperature during the static icing experiment was -20 °C).

## A.8.1. 2D simulation models

### 2D flat surface model

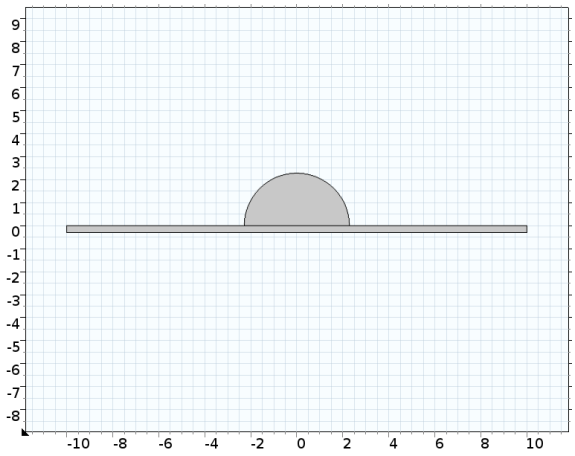


Figure A.49.: 2D model of a 25 µl water drop freezing on a flat PU surface.

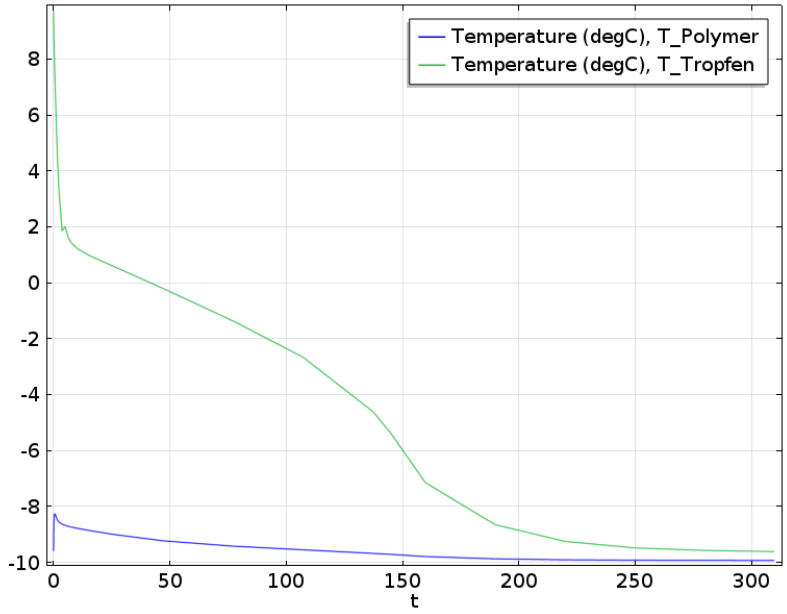


Figure A.50.: Simulated temperature curve of a 25 µl water drop freezing on a flat PU surface (2D model).

In the static icing experiment on uncoated or plasma-coated PU, the crystallization times were between about 40 s and 60 s as opposed to about 110 s to 140 s in the simulation.

### 2D microstructured surface model

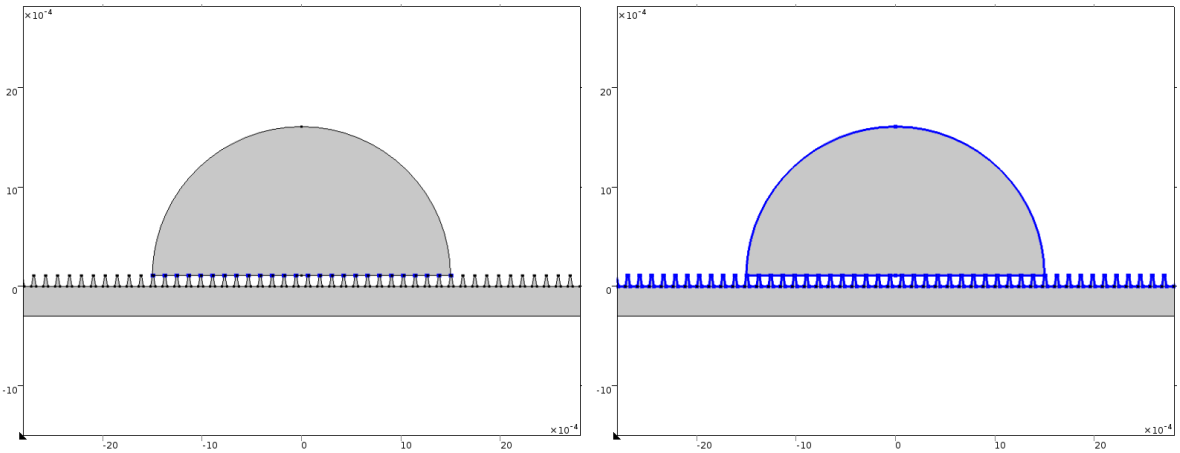

Figure A.51.: 2D model of the microstructured surface: conductive heat transfer interface (left) and radiative heat transfer interface (right).

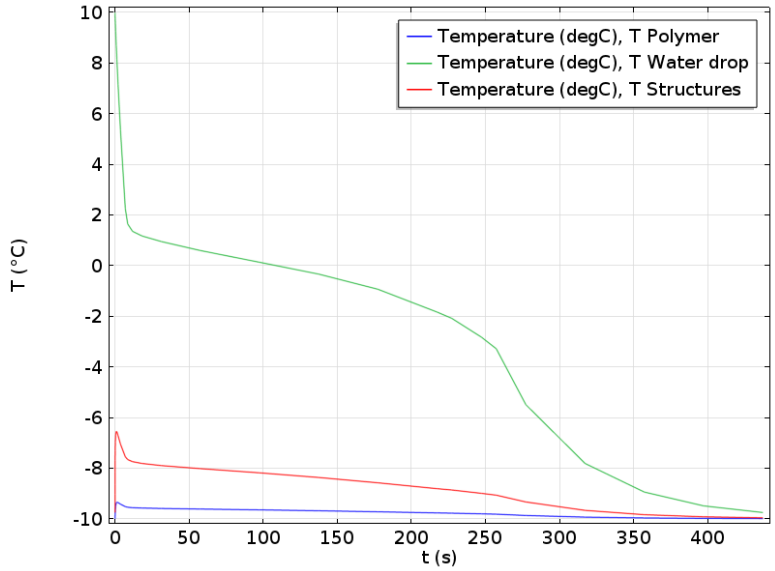


Figure A.52.: Simulated temperature curve of a 25 µl water drop freezing on a microstructured PU surface (2D model)

The longer crystallization time compared to the flat surface model because of the smaller heat flux and the reduced solid-liquid contact area can be seen clearly.

## A.8.2. 3D simulation models

### 3D flat surface model

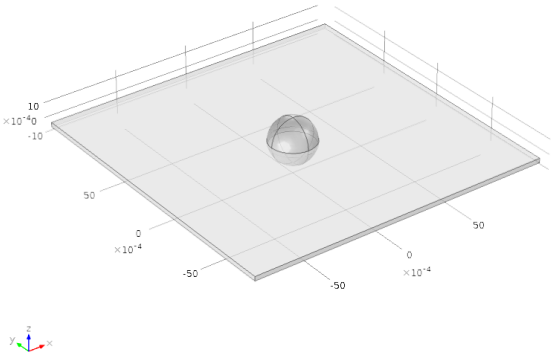

Figure A.53.: 3D model of a 25 µl water drop freezing on a flat PU surface.

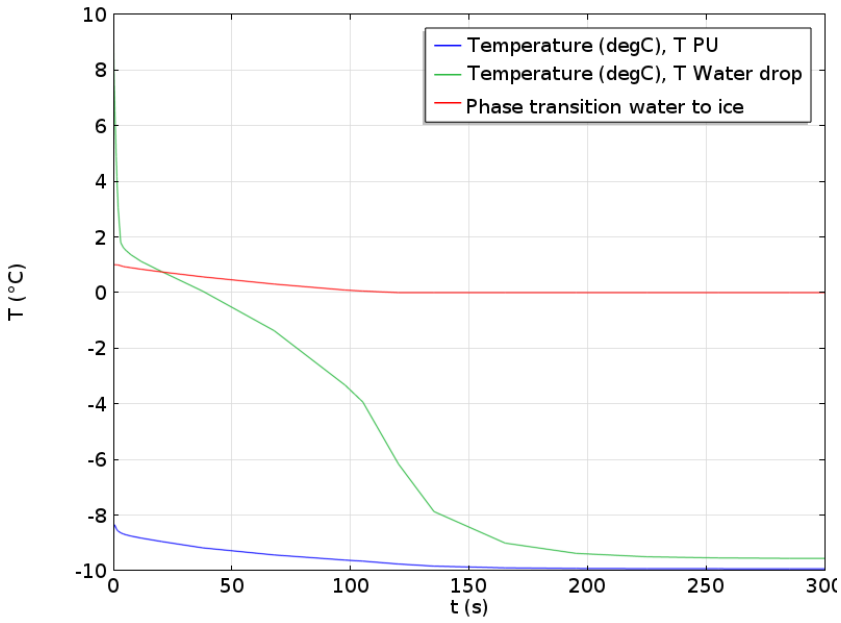


Figure A.54.: Simulated temperature curves from the 3D flat surface model.

This crystallization time value is similar to the one from the 2D flat surface model (about 110 s to 140 s).

### 3D microstructured surface model

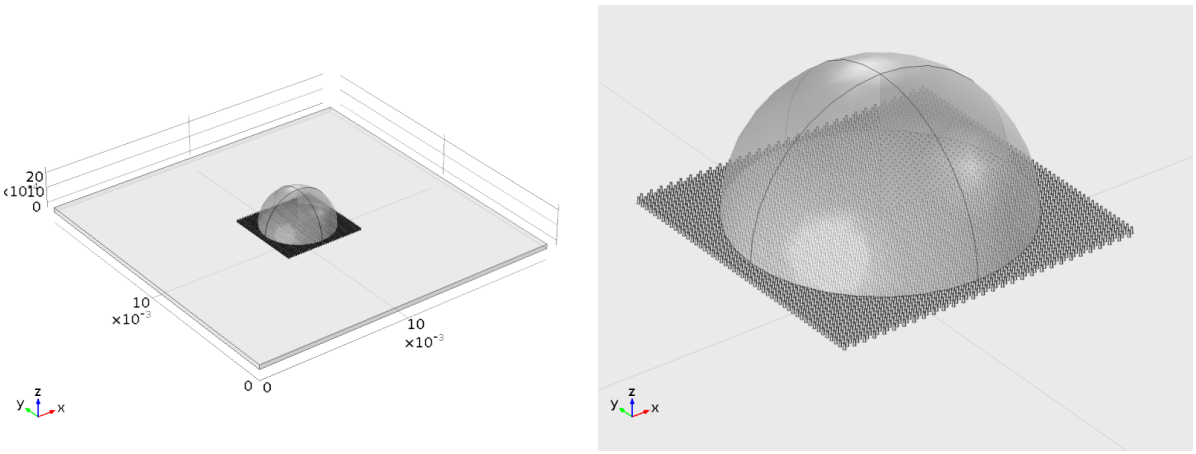


Figure A.55.: 3D model of a 25 µl water drop freezing on a microstructured PU surface.

The 3D microstructured surface model incorporated a few hundred microstructures beneath the drop and the model mesh node number was very large. The simulation was canceled after a few hours and therefore no data is available from this model.

Overall, the model simulations show longer crystallization times compared to the static icing experiment values in reality. The reasons are that no natural heat convection and heat conduction into the surrounding air was included in the models. Furthermore, the surface temperature was -20 °C in reality in contrast to -10 °C in the simulations. The drops wet the surface more than only in Cassie-Baxter state on the microstructured surfaces in reality increasing the solid-liquid contact area and therefore the heat transfer rate.

# A.9. Statistical basics and error estimation

## A.9.1. Statistical basics

### Definition of standard deviation

There are two different definitions of the (empirical) standard deviation of a variable. One is derived by inductive statistics and using the inductive variance:

$$s = \sqrt{\frac{\sum_i (x_i - \bar{x})^2}{(n-1)}} \tag{A.32}$$

The other one is derived by descriptive statistics and using the empirical variance:

$$\tilde{s} = \sqrt{\frac{\sum_i (x_i - \bar{x})^2}{n}} \tag{A.33}$$

### Correlation analysis

In order to check whether there is a linear correlation between the two variables x and y of a data set, the correlation coefficient or Pearson's $r$ is calculated. It standardizes the covariance $s_{xy}$ with the standard deviations $s_x$ amd $s_y$:

$$r = \frac{s_{xy}}{s_x \cdot s_y} \tag{A.34}$$

It can take on values between -1 and +1. The closer it is to -1 or +1, the better is the linear relation between the two variables. For r = 0, there is no linear relation.

### Regression analysis

Regression analysis is done for determination of the type of correlation of two variables, as there is not always a linear correlation. Therefore, often non-linear regression models are used. A curve, based on a non-linear equation of a mathematical approach useful for the type of data set, is compared and "fitted" to the data points by the method of "least squares". This method by Gaußminimizes the sum of the squared differences between the data points and the regression model values by adjusting the parameters of the non-linear equation. The coefficient of determination (COD) $R^2$ is a measure of quality of how much variation of the data can be explained by the used regression

model. It quantifies the relationship between the dependent (y) and independent (x) variables. $R^2$ can take on values between 0 and 1, where 0 means no linear relation and 1 means a perfect linear relation.

The variation of y is composed of the variation of residuals and the variation of regression values:

$$\sum_i (y_i - \bar{y})^2 = \sum_i (y_i - \hat{y}_i)^2 + \sum_i (\hat{y}_i - \bar{y})^2, \tag{A.35}$$

where $y_i$ are the measurement data points, $\bar{y}$ is the average value of the measurement data and $\hat{y}_i$ are the estimated regression values of the regression model.

For a simple linear regression, $R^2$ can be calculated from the squared Pearson's correlation coefficient $r_{xy}$, or the empirical covariance $s_{xy}$ and the empirical variances $s_x^2$ and $s_y^2$.

$$R^2 = r_{xy}^2 = \frac{s_{xy}^2}{s_x^2 \cdot s_y^2} \tag{A.36}$$

The definition of the coefficient of determination is

$$R^2 = 1 - \frac{\sum_i (y_i - \hat{y}_i)^2}{\sum_i (y_i - \bar{y})^2} = \frac{\sum_i (\hat{y}_i - \bar{y})^2}{\sum_i (y_i - \bar{y})^2}. \tag{A.37}$$

The coefficient of determination $R^2$ increases with an increasing number of independent variables, even if these independent variables do not improve the quality of the regression. Therefore, it is better to use the "corrected" or "adjusted" coefficient of determination $Adj.R^2$ for assessment of the quality of the regression model. It corrects the value of $R^2$ by the complexity of the model $p$, which is the number of the independent variables (not including constants). The definition of the adjusted coefficient of determination is

$$Adj.R^2 = R^2 - (1 - R^2) \cdot \frac{p}{n - p - 1}, \tag{A.38}$$

where $n$ is the number of data points and $p$ is the number of independent variables. The adjusted $R^2$ can also take on negative values and is smaller than the normal $R^2$.

## A.9.2. Error estimation

### Contact angle measurements

The measurement accuracy of the OCA 40 video system from dataphysics is $\pm 0.1°$ for contact angle measurements.

### Ice adhesion measurements

The measurement accuracy of the force sensor KD40s from ME Messysteme is 0.1 %, which equals 0.02 N for the 20 N type that was used.

### Icing behavior measurements

The measurement accuracy of the IR camera P620 from FLIR is ±2 °C or ±2 % of reading in the temperature range from -40 °C to +120 °C. The measured water drop temperatures were assumed to be equal to the sample surface temperature which was measured by a type K thermoelement connected to the Omega TC-08 measurement card with an accuracy of 0.2 % ± 0.5 °C. Therefore, the measured temperatures have a possible measurement error of only up to 0.5 °C. The dispensing accuracy of the LA-100 syringe pump from HHL Landgraf Laborsysteme for dispensing the 25 µl water drops is given with ±1 % which equals 0.25 µl. The accuracy of the Hamilton gas-tight syringes with 1 ml and 0.5 ml is ±1 % which equals 5 µl. The maximum dispensing error is therefore 5.25 µl.